Application of High Resolution Peripheral Quantitative Computed Tomography to the Study of Bone Microstructure and Matrix Mineral Density in Health and Disease

Ali Ghasem-Zadeh

ORCID ID (0000-0002-5284-9239)

June 2023

Faculty of Medicine, Dentistry and Health Sciences

Department of Medicine, Austin Health

The University of Melbourne

Victoria, Australia

Supervisors

Professor Ego Seeman

Dr. Sandra Iuliano

A thesis submitted in total fulfilment of the requirements

for the degree of Doctor of Philosophy

This page left blank intentionally.

ABSTRACT

Longevity increases the proportion of elderly persons in the community. Advancing age is accompanied by bone loss which compromises the volume, micro-architecture, and strength of both cortical and trabecular bone, particularly in women after menopause. Increasing fragility fracture risk is likely to be due to trabeculae thinning, perforation of trabeculae or reduction of trabecular numbers, thinning of the cortex and increased cortical porosity. Bone also becomes fragile due to changes in the material composition such as increased matrix mineral density, glycation of collagen and accumulation of unrepaired microdamage. These changes impact the mechanical properties of bone and make bones less able to resist loading, leading to an increased risk of fragility fractures.

The diagnosis of bone fragility is currently based on evaluation of clinical risk factor and with measurement of areal bone mineral density (aBMD) of the lumbar spine, and proximal hip using dual-energy X-ray absorptiometry (DXA). BMD is normally distributed. Over ~10% of people in the community have 'so-called' normal BMD (T-score >- 1.0 SD), ~60% of persons have osteopenia (T-score - 1.0 to -2.5 SD) and ~30% have a BMD T-score ≤ - 2.5 SD below the young normal mean, the diagnostic threshold for 'osteoporosis'. Because of the population distribution of BMD, most patients with fragility fractures in the community and most patients with diseases affecting the skeleton such as chronic kidney disease who suffer fragility fractures have osteopenia or normal BMD, not osteoporosis, so the use of aBMD threshold of ≤ – 2.5 SD has led to underestimation of the burden of bone fragility in the community.

High-Resolution peripheral Quantitative Computed Tomography (HR-pQCT) with 82 or 61-micron isotropic voxel size is an *in-vivo* imaging modality. HR-pQCT enables quantifying bone microarchitecture, distinguishing trabecular and cortical compartments, and measuring cortical and trabecular microarchitecture with minimal radiation exposure (5 µSv, equivalent to one day of background radiation) has made it an important modality to identify bone fragility in persons independent of their BMD level.

HR-pQCT is used in musculoskeletal research to quantify bone microstructure of appendicular regions of interest, both in normal and pathological conditions. However, there are limitations in the application of this imaging method and in the interpretation of findings, that need to be recognised such as accurate segmentation of cortical from trabecular bone using threshold or non-threshold-based image analysis algorithms and challenges in the correct choice of a region of interest (ROI) which is chosen as a fixed distance from the distal joint line. This region differs in persons differing in arm length; it is more distal in taller individuals, more proximal in shorter individuals. For this reason, sex differences, racial differences and growth related differences in microarchitecture may be the result of differences in the positioning of the region of interest.

The aim of this thesis was to address several of these technical limitations in methodology by using a non-threshold-based HR-pQCT image analysis and standardising the location of the ROI, so that sex- and race-specific differences in bone morphology could be correctly determined free of positioning errors. This method was applied in various disease states to establish the effects of disease on bone microarchitecture.

We investigated distal radius bone morphology of 158 healthy Asians and Caucasian women and men aged from 21 to 53 years using HR-pQCT. Errors in positioning the region of interest misrepresents accurate quantification of bone microarchitecture because it varies point by point (slice-by slice) along the length of a bone. For example, adjusting the scanned ROI resulted in a 0.51 SD higher cortical porosity in Asian women and 0.32 SD higher cortical porosity in Caucasian women. Failure to correct the ROI overestimated porosity by 0.21 SD in Asian men and by 0.39 SD in Caucasian men. Failure to correct the ROI comparing older Caucasian women, 33 postmenopausal women aged from 73 to 95 years, underestimate the age-related increase in porosity by 0.40 SD.

We investigated the effects of spinal paralysis on bone microstructure of distal radius and distal tibia and fibula of individuals with spinal cord injury. In this study, 32 men, 12 with tetraplegia and 20 with paraplegia, that were within 0.5 to 18.5 years of paralysis, were scanned by HR-pQCT. We report that following unloading caused by spinal cord injury, weight bearing regions

adapted to accommodate greater peak strains, and strain rates changes had more severe microarchitectural deterioration than non-weight bearing regions that are normally adapted to lower peak strains and strain rates prior injury. These observations highlight the site specificity of the strain thresholds regulating the cellular activity of mechano-transduction. The rapidity of the change and irreversible microarchitectural deterioration suggest prompt intervention with antiresorptive, anabolic therapy, or both, warrants consideration.

We also studied the effect of chronic kidney disease (CKD) on bone microstructure of 128 patients with CKD and compared them with 275 age- and sex-matched controls. We report that most patients with CKD stages 4-5D and kidney transplant recipients had osteopenia or normal femoral neck BMD, not osteoporosis. Despite these modest deficits in femoral neck BMD, distal tibial and distal radial microarchitecture and estimated failure load were compromised, even in patients with normal BMD. Cortical and trabecular distal tibia and distal radius microarchitecture, not femoral neck BMD, were independently associated with estimated failure load and accounted for over 85% of the variance in failure load estimated at these metaphyseal locations.

Resistance to fracture is achieved by modelling and remodelling adding bone to, or removing bone from, its periosteal (external) and endocortical, intracortical, and trabecular components of its endosteal (internal) surfaces. Quantification of macro/micro-structure of 18 radii and 5 femora human post-mortem specimens show that bone mass is constant along the radius, femur, and femoral neck. Along the metaphyseal regions, the constant mass was fashioned with a large void volume and high surface area/matrix volume forming mainly trabecular bone. At the mid-diaphyseal regions the same mass was fashioned with small intracortical and medullary void volumes and low surface area/matrix volume forming cortical bone. In addition, quantification of distal radius and tibia of 94 women, using HR-pQCT, showed that bigger bones are assemble with relatively less cortical mass of higher porosity and lower matrix mineral density.

In conclusion, the aging population is at higher risk of fragility fractures due to age-related bone loss and deteriorated bone microstructure. HR-pQCT provides three-dimensional bone microstructure analysis of human extremities as in-vivo, with minimal radiation exposure and high-resolution images. We offered a methodological solution for standardizing positioning and

scanning of ROI and accurately quantifying bone microarchitecture, and in pathological conditions. We investigated the impact of spinal cord injury on bone microstructure and the effects of chronic kidney disease on bone strength, highlighting the significance of cortical and trabecular microarchitecture in assessing bone health.

DECLARATION

This thesis consists solely of my original works towards the Doctor of Philosophy degree, except where explicitly stated in the preface. Proper acknowledgements have been included in the text for all materials cited from other researchers, as required. The thesis contains fewer than 100,000 words, not including tables, figures, the bibliography, and appendices.

Ali Ghasem-Zadeh

June 2023

PREFACE

This work presented was performed under the supervision of Professor Ego Seeman and Dr Sandra Iuliano in the Department of Endocrinology, Department of Medicine, Austin Health, The University of Melbourne. I was involved in the design and execution of the studies, including conducting scanning using High-Resolution Peripheral Quantitative Computed Tomography (HR-pQCT), performing quantitative image analysis, and drafting all manuscripts with guidance from Professor Ego Seeman. I performed statistical analyses with guidance from Dr Minh Bui. I presented all the findings as oral presentations at both national and international conferences.

No work used towards the thesis has been submitted for other qualifications or carried out prior to enrolment in the degree. No third-party editorial assistance was provided in preparation of this thesis. In summary, this thesis is my original work.

I coordinated with various departments including:

i) Department of Spinal Cord Injury, The Royal Talbot Rehabilitation Centre, Austin Health

ii) Department of Nephrology, Austin, and Royal Melbourne Hospitals

iii) Musculoskeletal Quantitative Imaging Research Group, Department of Radiology and Biomedical Imaging, University of California, San Francisco, CA, USA

iv) Department of Radiology, Stanford University, Stanford, CA, USA

v) McCaig Institute for Bone and Joint Health, University of Calgary, Calgary, AB, Canada

vi) School of Medical Science and Menzies Health Institute Queensland, Griffith University, Gold Coast, Australia

vii) Australian Synchrotron Radiation

viii) StrAx Corp, Melbourne, Australia

Contributions to published original papers.

Published papers as 1st author

Chapter 3: Quantifying sex, race, and age specific differences in bone microstructure requires measurement of anatomically equivalent regions

Primary author: **Ali Ghasem-Zadeh**

Co-authors: Andrew Burghardt, Xiao-Fang Wang, Sandra Iuliano, Serena Bonaretti, Minh Bui, Roger Zebaze, Ego Seeman

Published in journal **BONE**, 2017;101:206-13. DOI: 10.1016/j.bone.2017.05.010

I was involved in the conception, design, analysis, interpretation of data, and writing the manuscript. Minh Bui was involved in data analysis. Andrew Burghardt, Xiao-Fang Wang, Sandra Iuliano, Serena Bonaretti, and Ego Seeman were involved in revising the manuscript. Ego Seeman was involved in the conception, design, analysis, interpretation of data, funding acquisition, as well as revising the manuscript. Estimate of my proportion of the contribution: 75%

Chapter 4: Heterogeneity in microstructural deterioration following spinal cord injury

Primary author: **Ali Ghasem-Zadeh**

Co-authors: Mary P Galea, Andrew Nunn, Maya Panisset, Xiao-Fang Wang, Sandra Iuliano, Steven K Boyd, Mark R Forwood, Ego Seeman

Published in journal **BONE**, 2021 Vol. 142 Pages 115778, DOI: 0.1016/j.bone.2020.115778

I was involved in the conception, design, analysis, interpretation of data, and writing the

manuscript. Xiao-Fang Wang was involved in data analysis and revising the manuscript. Mary P Galea, Andrew Nunn, Maya Panisset, Xiao-Fang Wang, Sandra Iuliano, Steven K Boyd, Mark R Forwood and Ego Seeman were involved in revising the manuscript. ES was involved in the conception, design, analysis, interpretation of data, funding acquisition, as well as revising the manuscript. Estimate of my proportion of the contribution: 75%

Chapter 5: Bone Microarchitecture and Estimated Failure Load are Deteriorated Whether Patients with Chronic Kidney Disease have Normal Bone Mineral Density, Osteopenia or Osteoporosis

Primary author: **Ali Ghasem-Zadeh**

Co-authors: Minh Bui, Ego Seeman, Steven K Boyd, Sandra Iuliano, Rizwan Jaipurwala, Peter Mount, Nigel Toussaint, Cherie Chiang

Published in journal **BONE**, 2022, Vol. 154 Pages 116260, DOI: 10.1016/j.bone.2021.116260

I was involved in the conception, design, analysis, interpretation of data, and writing the manuscript. MB was involved in data analysis. Minh Bui, Ego Seeman, Steven K Boyd, Sandra Iuliano, Rizwan Jaipurwala, Peter Mount, Nigel Toussaint and Cherie Chiang were involved in revising the manuscript. ES, SI and CC were involved in the conception, design, analysis, interpretation of data, funding acquisition, as well as revising the manuscript. Estimate of my proportion of the contribution: 70%

PROJECT SET UP

Supervisors

- Prof Ego Seeman (Principal supervisor). Department of Endocrinology, Department of Medicine, Austin Health, The University of Melbourne

- Dr Sandra Iuliano (co-supervisor). Department of Endocrinology, Department of Medicine, Austin Health, The University of Melbourne

Advisory Committee

- Professor Elif Ekinci. Department of Medicine, Austin Health, The University of Melbourne

Sources of funding

None

PUBLICATIONS

Ali Ghasem-Zadeh, Andrew Burghardt, Xiao-Fang Wang, Sandra Iuliano, Serena Bonaretti, Minh Bui, Roger Zebaze, Ego Seeman **Quantifying sex, race, and age specific differences in bone microstructure requires measurement of anatomically equivalent regions** Published by journal of **BONE**, 2017;101:206-13. DOI: 10.1016/j.bone.2017.05.010

Ali Ghasem-Zadeh, Mary P Galea, Andrew Nunn, Maya Panisset, Xiao-Fang Wang, Sandra Iuliano, Steven K Boyd, Mark R Forwood, Ego Seeman **Heterogeneity in microstructural deterioration following spinal cord injury** Published by journal of **BONE**, 2021 Vol. 142 Pages 115778, DOI: 0.1016/j.bone.2020.115778

Ali Ghasem-Zadeh, Minh Bui, Ego Seeman, Steven K Boyd, Sandra Iuliano, Rizwan Jaipurwala, Peter Mount, Nigel Toussaint, Cherie Chiang **Bone Microarchitecture and Estimated Failure Load are Deteriorated Whether Patients with Chronic Kidney Disease have Normal Bone Mineral Density, Osteopenia or Osteoporosis** Published by journal of **BONE**, 2022, Vol. 154 Pages 116260, DOI: 10.1016/j.bone.2021.116260

Ali Ghasem-Zadeh, Ego Seeman. **Challenges in the Use of Cross-Sectional Data to Quantify Growth and Deterioration of Bone Structure During Advancing Age**. J Clin Densitom. 2017 Jan-Mar;20(1):5-7. doi: 10.1016/j.jocd.2016.08.006. PMID: 27618369

Ego Seeman E, **Ali Ghasem-Zadeh**. **Challenges in the Acquisition and Analysis of Bone Microstructure During Growth**. J Bone Miner Res. 2016 Dec;31(12):2239-2241. doi: 10.1002/jbmr.3015. PMID: 27736022

Additional Publications (21 papers)

- Russell N, **Ghasem-Zadeh A**, Hoermann R, Cheung A, Zajac J, Shore-Lorenti C, Ebeling P, Handelsman D, Grossmann M. Effects of transdermal estradiol on bone microarchitecture and density in men undergoing androgen deprivation therapy for prostate cancer: a randomized

placebo-controlled trial. European Journal of Endocrinology 2022 Aug 1. doi: 0.1530/EJE-22-0227. PMID: 35666800

- Bretherton I, **Ghasem-Zadeh A**, Leemaqz SY, Seeman E, Wang X, McFarlane T, Spanos C, Grossmann M, Zajac JD, Cheung AS.Bone Microarchitecture in Transgender Adults: a Cross Sectional Study. J Bone Miner Res. 2022 Jan 3. doi: 10.1002/jbmr.4497. PMID: 34981566

- Iuliano S, Poon S, Robbins J, Bui M, Wang X, De Groot L, Van Loan M, **Zadeh AG**, Nguyen T, Seeman E. Effect of dietary sources of calcium and protein on hip fractures and falls in older adults in residential care: cluster randomised controlled trial. BMJ. 2021 Oct 20;375: n2364. doi: 10.1136/bmj.n2364.PMID: 3467075

- Zendeli A, Bui M, Fischer L, **Ghasem-Zadeh A**, Schima W, Seeman E. High Cortico-Trabecular Transitional Zone Porosity and Reduced Trabecular Density in Men and Women with Stress Fractures. J Clin Med. 2021 Mar 8;10(5):1123. doi: 10.3390/jcm10051123.PMID: 33800284

- Ng Tang Fui M, Hoermann R, Bracken K, Handelsman DJ, Inder WJ, Stuckey BGA, Yeap BB, **Ghasem-Zadeh A**, Robledo KP, Jesudason D, Zajac JD, Wittert GA, Grossmann M. Effect of Testosterone Treatment on Bone Microarchitecture and Bone Mineral Density in Men: A 2-Year RCT. J Clin Endocrinol Metab. 2021 Jul 13;106(8): e3143-e3158. doi: 0.1210/clinem/dgab149. PMID: 33693907

- Cheung AS, Hoermann R, **Ghasem-Zadeh A**, Tinson AJ, Ly V, Milevski SV, Joon DL, Zajac JD, Seeman E, Grossmann M. Differing Effects of Zoledronic Acid on Bone Microarchitecture and Bone Mineral Density in Men Receiving Androgen Deprivation Therapy: A Randomized Controlled Trial. J Bone Miner Res. 2020 Oct;35(10):1871-1880. doi: 10.1002/jbmr.4106. PMID: 32542695

- Whittier DE, Boyd SK, Burghardt AJ, Paccou J, **Ghasem-Zadeh A**, Chapurlat R, Engelke K, Bouxsein ML. Guidelines for the assessment of bone density and microarchitecture in vivo using high-resolution peripheral quantitative computed tomography. Osteoporos Int. 2020 Sep;31(9):1607-1627. doi: 10.1007/s00198-020-05438-5. PMID: 32458029

- Wang XF, **Ghasem-Zadeh A**, Zhou B, Guo XE, Zhang Z, Seeman E. Dimorphism in axial and appendicular dimensions, cortical and trabecular microstructure and matrix mineral density in Chinese and Caucasian women. Bone. 2019 Nov; 128:115039. doi: 10.1016/j.bone.2019.115039.19.PMID: 31437567

- Zebaze R, Atkinson EJ, Peng Y, Bui M, **Ghasem-Zadeh A**, Khosla S, Seeman E. Increased Cortical Porosity and Reduced Trabecular Density Are Not Necessarily Synonymous With Bone Loss and Microstructural Deterioration. JBMR Plus. 2018 Oct 4;3(4): e10078. doi: 10.1002/jbm4.10078. eCollection 2019 PMID: 31044180

- Zebaze R, Osima M, Bui M, Lukic M, Wang X, **Ghasem-Zadeh A**, Eriksen EF, Vais A, Shore-Lorenti C, Ebeling PR, Seeman E, Bjørnerem Å. Adding Marrow Adiposity and Cortical Porosity to Femoral Neck Areal Bone Mineral Density Improves the Discrimination of Women With Nonvertebral Fractures From Controls. J Bone Miner Res. 2019 Aug;34(8):1451-1460. doi: 10.1002/jbmr.3721. 17.PMID: 30883870

- Cheuk KY, Wang XF, Wang J, Zhang Z, Yu FWP, Tam EMS, Hung VWY, Lee WYW, **Ghasem-Zadeh A**, Zebaze R, Zhu TY, Guo XE, Cheng JCY, Lam TP, Seeman E. Sexual Dimorphism in Cortical and Trabecular Bone Microstructure Appears During Puberty in Chinese Children. J Bone Miner Res. 2018 Nov;33(11):1948-1955. doi: 10.1002/jbmr.3551. PMID: 30001459

- Zhu JJ, Mahendran D, Lee MH, Seah J, Fourlanos S, Varadarajan S, **Ghasem-Zadeh A**, MacIsaac RJ, Seeman E. Systemic mastocytosis identified in two women developing fragility fractures during lactation. Osteoporos Int. 2018 Jul;29(7):1671-1674. doi: 10.1007/s00198-018-4498-5.4.PMID: 29619541

- Chiang CY, Zebaze R, Wang XF, **Ghasem-Zadeh A**, Zajac JD, Seeman E. Cortical Matrix Mineral Density Measured Noninvasively in Pre- and Postmenopausal Women and a Woman With Vitamin D-Dependent Rickets. J Bone Miner Res. 2018 Jul;33(7):1312-1317. doi: 10.1002/jbmr.3415.PMID: 29489033

- Borschmann K, Iuliano S, **Ghasem-Zadeh A**, Churilov L, Pang MYC, Bernhardt J.

Upright activity and higher motor function may preserve bone mineral density within 6 months of stroke: a longitudinal study. Arch Osteoporos. 2018 Jan 8;13(1):5. doi: 10.1007/s11657-017-0414-4.PMID: 29313169

- Bjørnerem Å, Wang X, Bui M, **Ghasem-Zadeh A**, Hopper JL, Zebaze R, Seeman E
Menopause-Related Appendicular Bone Loss is Mainly Cortical and Results in Increased Cortical Porosity. J Bone Miner Res. 2018 Apr;33(4):598-605. doi: 10.1002/jbmr.3333. Epub 2017 Dec 8. PMID: 29218771

- Ramchand SK, Seeman E, Wang XF, **Ghasem-Zadeh A**, Francis PA, Ponnusamy EJ, Bardin MS, Bui M, Zebaze R, Zajac JD, Grossmann M. Premenopausal women with early breast cancer treated with estradiol suppression have severely deteriorated bone microstructure. Bone. 2017 Oct; 103:131-135. doi: 10.1016/j.bone.2017.06.024. Epub 2017 Jul 1. PMID: 28673637

- Borschmann KN, Rewell SS, Iuliano S, **Ghasem-Zadeh A**, Davey RA, Ho H, Skeers PN, Bernhardt J, Howells DW. Reduced bone formation markers and altered trabecular and cortical bone mineral densities of non-paretic femurs observed in rats with ischemic stroke: A randomized controlled pilot study PLoS One. 2017 Mar 9;12(3): e0172889. doi: 10.1371/journal.pone.0172889.PMID: 28278253

- Zebaze R, Libanati C, McClung MR, Zanchetta JR, Kendler DL, Høiseth A, Wang A, **Ghasem-Zadeh A**, Seeman E. Denosumab Reduces Cortical Porosity of the Proximal Femoral Shaft in Postmenopausal Women with Osteoporosis. J Bone Miner Res. 2016 Oct;31(10):1827-1834. doi: 10.1002/jbmr.2855. PMID: 27082709

- Bjørnerem Å, **Ghasem-Zadeh A**, Wang X, Bui M, Walker SP, Zebaze R, Seeman E. Irreversible Deterioration of Cortical and Trabecular Microstructure Associated with Breastfeeding. J Bone Miner Res. 2017 Apr;32(4):681-687. doi: 10.1002/jbmr.3018.PMID: 27736021

- Bonaretti S, Vilayphiou N, Chan CM, Yu A, Nishiyama K, Liu D, Boutroy S, **Ghasem-Zadeh A**, Boyd SK, Chapurlat R, McKay H, Shane E, Bouxsein ML, Black DM, Majumdar S, Orwoll ES, Lang TF, Khosla S, Burghardt AJ. Operator variability in scan positioning is a major component of HR-pQCT precision error and is reduced by standardized training. Osteoporos Int. 2017 Jan;28(1):245-257. doi: 10.1007/s00198-016-3705-5. PMID: 27475931

- Cheuk KY, Tam EM, Yu FW, Yip BH, Hung VW, Wang X, **Ghasem-Zadeh A**, Zhu TY, Qin L, Cheng JC, Lam TP. A Critical Comparison Between Two Scanning Protocols of High-Resolution Peripheral Quantitative Computed Tomography at the Distal Radius in Adolescents. J Clin Densitom. 2016 Jul-Sep;19(3):305-15. doi: 10.1016/j.jocd.2016.04.002. PMID: 2713025

Conference Oral Presentations

2022, August, Gold Cost, Australia The 32nd Australian New Zealand Bone and Mineral Society. Variance in Bone Strength is conferred by Diversity of its Structure

2021, November, Virtual The 31st Australian New Zealand Bone and Mineral Society, virtual meeting. Bone Microarchitecture and Estimated Failure Load are Deteriorated Whether

Patients with Chronic Kidney Disease have Normal Bone Mineral Density, Osteopenia or Osteoporosis**. Finalist on Christopher and Margie Nordin Investigator Award**

2020, July, Virtual The 30th Australian New Zealand Bone and Mineral Society, virtual meeting, Heterogeneity in microstructural deterioration following spinal cord injury. **Finalist on Roger-Melick Investigator Award**

2019, October, Darwin The 29th Australian New Zealand Bone and Mineral Society, Darwin, Australia. Evaluation of bone microstructure of distal radius and distal tibia on human objects using phase-contrast synchrotron**. Finalist on Nordin Young Investigator Award**

2019, June, Melbourne Melbourne Bone Group Meeting, Australia. Application of Quantum Physics on Bone Imaging

2019, February, Calgary, Canada The 22nd International Workshop on Quantitative Musculoskeletal Imaging (QMSKI), Canada Increased Cortical Porosity and Reduced Trabecular Density Are Not Necessarily Synonymous with Bone Loss and Microstructural Deterioration.

2018, October, Tehran, Iran International Osteoporosis Foundation, Essentials of Densitometry, Diagnosis and Management Course and Osteoporosis Update conference, Tehran, Iran

2018, August, **Queenstown, New Zealand** The 28th Australian New Zealand Bone and Mineral Society Bone Microarchitecture in Patients with Chronic Kidney Disease.

2018, August Queenstown, New Zealand Musculoskeletal Research, Forum, Benefits and Limitations of Quantitative Imaging Techniques in the Assessment of Bone Fragility.

GRANTS or AWARDS

2023 Australian Synchrotron Radiation User Grant application- Micro-CT beam Line

2019 Australian Synchrotron Radiation User Grant application. IMBL

2019 Austin Medical Research Foundation (AMRF)-Research Higher Degree Award

2018 Australian Synchrotron Radiation User Grant application. IMBL

2018 ESCEO-Eli Lilly Scholarships, International Travel Grant

2017 Australia-Germany Joint Research Co-operation Scheme (DAAD-AU)

2016 Australian Spinal Network, international travel grant

2016 The European Calcified Tissue Society, St Catherine's College, Oxford, UK, PhD training course

ACKNOWLEDGMENTS

First and foremost, I would like to extend my gratitude to my principal supervisor and my mentor, Professor Ego Seeman, who has provided me with guidance, encouragement, and mentorship throughout this process. His determination to improve the global health by reducing the fragility fractures inspired me to complete my thesis and publish papers in top journals.

I would like to express my sincere gratitude to my co-supervisor, Dr. Sandra Iuliano, for her invaluable guidance throughout this project. Her expertise and support have been instrumental in shaping the outcome of my research.

I wish to acknowledge Prof Elif Ekinci for assisting in her advisory capacity. I thank Dr Xiao-Fang Wang, and A/Prof Cherie Chiang from the Department of Endocrinology, Austin Health and Royal Melbourne Hospital for being instrumental on recruiting participants with different ethnicity and gender and patients with chronic kidney disease. I am so grateful to research staff member of Department of Spinal Cord Injury of Austin Health for recruiting individuals with spinal cord injury. Dr Minh Bui has also been key, with his assistance in statistics, and I am grateful to him for his enthusiasm, and patience.

A major component of the studies was the Strax software analysis to measure bone microstructural parameters including the cortical porosity and matrix mineral density, I would like to extend my acknowledgment to all Strax Corp staff particularly Dr Yu Peng.

I would like to thank Prof Steven Boyd, from University of Calgary, Canada, for biomechanical testing using finite element analysis and Dr Andrew Burghardt from University of California, USA, for his inspired collaboration.

I would like to extend my sincere thanks to the University of Melbourne's Faculty of Medicine, Dentistry, and Health Sciences, specifically acknowledging Jo Mayal and the exceptional IT team at the University of Melbourne.

Lastly, I would like to express my heartfelt appreciation to my incredible family, especially my beloved wife, Shahla, who provided unwavering support, and endured more than her fair share of responsibilities throughout my studies. I am also grateful to my daughter, Anahita, and my son, Arian, for their understanding and encouragement during this journey. I want to dedicate this PhD to the entire members of my family, and above all, to the cherished memory of my admirable brother, Rashid.

ABBREVIATIONS

3D	Three Dimensional
25-OHD	25- hydroxycholecalciferol
aBMD	Areal Bone Mineral Density
BMD	Bone Mineral Density
BS	Bone Surface
BV/TV	Trabecular Bone Volume Fraction
CI	Confidence Interval
CKD-MBD	Chronic Kidney Disease Mineral and Bone Disorder
Conn D	Connectivity Density
CSA	Cross Sectional Area
CV	Coefficient Variation
DXA	Dual Energy X-ray Absorptiometry
eGFR	estimated Glomerular Filtration Rate
FEA	Finite Element Analysis
FES	Functional Electrical Stimulation
FN	Femoral Neck
HA	Hydroxyapatite
HR-pQCT	High Resolution Peripheral Quantitative Computed Tomography
MPa	Mega Pascal
N	Newton
OR	Odds Ratio
PTH	Parathyroid Hormone
SCI	Spinal Cord Injury
SMI	Structural Model Index

TABLE of CONTENTS

Abstract ..... **iii**

Declaration ..... **vi**

Preface ..... **vii**

Contribution to published papers……. ..... **viii**

Project set up ..... **x**

Publication, Grants and Awards ..... **xi**

Acknowledgements ..... **xvi**

Abbreviations ..... **xviii**

Table of contents ..... **xvii**

List of Figures ..... **xxiii**

List of Tables ..... **xxvii**

Literature Review

Chapter 1.1: Bone Fragility Fractures **1**

Fragility Fractures **2**

Epidemiology of Fragility Fractures **2**

Morbidity and mortality associated with fragility fractures **3**

Vertebral Fractures **3**

Hip Fractures **5**

Hip Fracture in Australia **8**

Non-vertebral, non-hip (NVNH) fractures **9**

Fragility fracture during COVID-19 pandemic **11**

Conclusions 12

Chapter 1.2: Pathogenesis of Bone Fragility 14

Introduction 15

Bone Modelling.....15

Bone remodelling.....16

Trabecular and cortical bone remodelling.....21

Bone remodelling during advancing age and menopause.....23

Conclusions 25

References.....26

Methodology

High Resolution–peripheral Quantitative Computed Tomography

Chapter 2.1: HR-pQCT 31

Introduction 32

Image Acquisition.....32

Position of the region of interest and its effect on bone microstructure.....33

Voxel size and its effect on bone structural analysis 37

Beam hardening.....39

Partial volume effects.....41

Motion (movement) artefact.....43

X-ray tube malfunctioning or failure.....45

Detectors malfunctioning and ring artefact.....46

Detectors and x-ray tube replacement.....47

Limitation of HR-pQCT on prediction of fragility fracture.....48

Future direction of HR-pQCT on prediction of fragility fracture.....48

Future direction of clinical CT on quantitative bone imaging.....49

Summary.....50

References.....50

2.2. Accuracy, reproducibility, least significant changes of bone microstructure parameters measured by HR-pQCT and compatibility of the 1st and 2nd generation of HR-pQCT.....53

Introduction 52

Precision.....54

Step-by-step evaluation of precision error.....55

Bone Density reproducibility.....55

Long term reproducibility.....58

Least CV (%) of microstructure parameters by HR-pQCT.....60

HR-pQCT; first-generation vs Second-generation 70

References 74

2.3. Finite Element Analysis.....76

Introduction 76

A Brief History and Explanation of Finite Element Analysis.....77

Estimation of failure load of distal radius and tibia using HR-pQCT images.....83

Validation 85

Our findings using FEA 87

Limitation of FEA 89

Summary and Conclusion.....90

References 92

Published Papers related to Chapter 2

a) Challenges in the Acquisition and Analysis of Bone Microstructure During Growth.....94

b) Challenges in the Use of Cross-Sectional Data to Quantify Growth and Deterioration of Bone Structure During Advancing Age..... **100**

Results

Chapter 3. Quantifying sex, race, and age specific differences in bone microstructure requires measurement of anatomically equivalent regions 106

Short summary.....**107**

Abstrcat.....**111**

Introduction.....**113**

Material and methods.....**115**

Results.....**116**

Discussion.....**127**

References.....**131**

Chapter 4. Heterogeneity in microstructural deterioration following spinal cord injury 134

Short summary.....**135**

Abstrcat.....**139**

Introduction.....**141**

Methods.....**144**

Results.....**144**

Discussion.....**152**

References.....**157**

Chapter 5. Bone microarchitecture and estimated failure load are deteriorated whether patients with chronic kidney disease have normal bone mineral density, osteopenia or osteoporosis.....163

Short summary.....**164**

Abstrcat.....**168**

Introduction.....**170**

Methods.....**171**

Results.....**174**

Discussion.....**181**

References.....**191**

Discission

Chapter 6.....196

Discission.....**196**

Conclusion.....**200**

Future directions.....**201**

References.....**203**

Bibliography.....204

Appendices related to Chapter 2.....226

Appendix related to Chapter 3.....267

Appendix related to Chapter 4.....276

Appendix related to Chapter 5.....285

Other related appendices.....293

List of Figures

Figure 1.1. Incidence of vertebra fractures in women and men from European Perspective Osteoporosis Study by age group**.....4**

Figure 1.2. Age specific incidence rates for hip, spine, and distal forearm facture in Caucasian women and men in Rochester, Minnesota, USA. **.....5**

Figure 1.3. Survival rates after the diagnosis of a vertebral, hip, or distal forearm fracture among residents of Rochester, Minnesota, USA. **.....6**

Figure 1.4. Comparison number of hospitalisations for fracture, myocardial infraction, stroke, and breast cancer within 2000-2011 in USA. **.....7**

Figure 1.5. Rate of hospitalisation for new hip fractures, by age and sex, 2015–16. **.....8**

Figure 1.6. Distribution of incident of hip, spine, major NHNV and minor NHNV fracture types. **.....10**

Figure 1.7. Structure of bone Cortical and trabecular bone, the periosteal surface, and the endocortical, trabecular, intracortical surface**.....17**

Figure 1.8. Comparison of structural aspect of bone remodelling between trabecular bone surface, Howship's Lacunae, with Haversian canals of cortical bone, Cutting Cone**……..19**

Figure 1.9. Bone remodelling activities in the surface of trabecular bone **.....21**

Figure 1.10 Cortical bone; Haversian canal surfaces and the endocortical surface and trabecular bone surface in the healthy bone **.....22**

Figure 1.11. Simplified mechanism of trabecular bone loss due to high turnover and negatively imbalanced bone remodelling**.....24**

Figure 2.1. Positioning and HR-pQCT scanning of the distal radius and tibia**……..... 33**

Figure 2.2. Location of scanning ROI of distal radius and the tibia**……..……. 34**

Figure 2.3. Comparison of reference line placement and distances between reference line and region of interest between fixed distance and relative offset **……..……...34**

Figure 2.4. Calculation of the number of slices and location of the corrected ROI**…...35**

Figure 2.5. The scout view of distal forearm and the reference line and identifying the scanning region of interest**…….....36**

Figure 2.6. Comparison the distal tibia of healthy person with person with spinal cord injury**……..….....37**

Figure 2.7. Trabecular bone packet with an average 50 µm thickness from the cement line to the border, facing the marrow cavity of a human lilac crest**..……..….....38**

Figure 2.8. Comparison of cadaveric femoral neck axial images scanned at different resolutions**..…….....39**

Figure 2.9. Changing energy spectrum of an x-ray beam as it passes through water. The mean energy of photons elevated with depth. The attenuated spectra have been rescaled to be equivalent in size to the unattenuated spectra **…….....40**

Figure 2.10. Density profile obtained across the centre of a uniform water phantom without beam hardening calibration correction and after calibration correction**…….....41**

Figure 2.11. Comparison of vertebral body scanned by clinical CT-Scanner with different resolution.**…….....42**

Figure 2.12. Image quality grading guideline suggested by the manufacturer. **…….....43**

Figure 2.13. Schematic drawing explaining the analysis process of mirrored parallelized projection. The 180° projection was mirrored and compared to the 0° projection to estimates of motion. For the ideal case where there is no motion, the difference image between the two parallelized projection images should be zero**……..44**

Figure 2.14. A big ring artefact in HR-pQCT density quality control phantom**……..47**

Figure 2.15. Axial image of bone density quality control phantom (QC) of HR-pQCT scanner**…….....54**

Figure 2.16. Right measured density vs actual density of rods of QC phantom**…..…....54**

Figure 2.17. The QC phantom scanned since early 2007 till March 2022. Figures A-E show the fluctuations on measurement of rods with density of 0 (equal to soft tissue),100, 200, 400 and 800 mgHA/cm3, respectively. Figure F shows the major drifts, and red boxes indicate the date of x-ray tube or detectors failure**…….....57**

Figure 2.18. A) Palmar and lateral view and positioning in the fibre cast view, C) Scout view, reference line and the location of scanned ROI, D) Coronal view and scanned ROI of the Distal Forearm Microstructure Phantom. **……..59**

Figure 2.19. XtremeCTI with nominal 82 micron voxels size (left panel) and XtremeCTII with 61 micron voxel size (right panel) . **…….....60**

Figure 2.20. Correlations and agreements of bone geometry, bone volumetric densities and bone microstructure indices between 1st and 2nd generation of HR-pQCT **…….……....71**

Figure 2.21. The process of conducting computed tomography-based finite element analysis for human bones……...**…….....75**

Figure 2.22. The process of conducting computed tomography-based finite element analysis for human bones……...**…….....75**

Figure 2.23. Comparison of bone stiffness between three family members. Both male members have larger and stronger bones, and that despite the "father" having the largest bone, it is not as strong as the "son". ……...**……..…....79**

Figure 2.24. Relationship between stress and strain. Left figure: The green area represents the Elastic zone, and after the yield point, increasing the strain the object under stress will be deformed irreversibly, the area between yield strain and ultimate strain Plastic zone (yellow area). Right figure: The area under curve of Stress- Strain represents the amount of absorbed energy by bone to reach the failure point, the area under curve is "Toughness". ……...**……..…….....80**

Figure 2.25 Comparison of 3 types of bone with different stiffness and toughness. Red colour represents the bone with high stiffness and low toughness (absorbing and damping energy) this type of bones are brittle like bone of patients with T2DM. The green line shows the moderate stiffness and toughness, like healthy bone. Low stiffness and higher toughness have been reported for patient with osteomalacia (blue lines). ……...**……..…….....81**

Figure 2.26 Details of the FE model generation: separation of cortical (A) and trabecular (B) compartments; geometrical meshing (C) mapping material properties based on the underlying HR-pQCT image (D) assignment of bone volume fraction (E) and anisotropy (the distribution of the maximal Young's modulus of the trabecular bone) (F) and applying boundary conditions (G). **…….....82**

Figure 2.27 Distal radii bone meshed using triangles (a) intact model, (b) longitudinal displacement under applied compressive load with von Mises stress distribution**…….....82**

Figure 2.28 Process of mechanical testing and finite element analysis. The minimum force is applied at a fixed vertical displacement (a), increased the force c) until the proximal femoral fracture occurs (e). The model of the proximal femur is made (b), a compressive load was applied (d)until predicted fracture (f)**.....85**

Figure 2.29 Compromised estimated failure load of distal tibia in individuals with tetraplegia or paraplegia, no differences found for distal radius for both groups in compression to sex- and age-matched controls, N=Newton.**.....86**

Figure 2.30 Comparison of estimated failure load in patients with CKD (yellow bars) versus controls (green bars) within a bone mineral (*p < 0.001). N=Newton.....**86**

Figure 3.1 a) The reference line corresponds to the mid-radiocarpal joint and calculation of the number of slices and location of the corrected ROI **117**

Figure 3.2 Axial and coronal sections of the distal radius radius.....**120**

Figure 3.3 Forearm length and total radial cross sectional area were higher in men than in women of each racial group (**p < 0.01). As shown by the double arrowheaded hatched lines, the differences by race in each sex were numerically smaller than sex differences in each race. **124**

Figure 3.4 Sexual dimorphism in (a) Asians (b) Caucasians, and racial dimorphisms in (c) women and (d) men, determined in the fixed (black bars) and in the corrected region of interest (grey bars).....**125**

Figure 3.5. Sexual and racial dimorphism in cortical porosity in the fixed region of interest, in the corrected region of interest, and in the fixed region of interest adjusted for total cross-sectional area (TCSA), forearm length and height.....**126**

Figure 4.1 Images of trabecular and cortical bone at the distal tibia.....**146**

Figure 4.2 Distal tibial total, cortical and trabecular volumetric bone mineral density (vBMD) and cortical porosity as a function of time since injury.....**147**

Figure 4.3 Comparison of deficits total, cortical and trabecular volumetric bone mineral density (vBMD) at the distal tibia (black bar), distal fibula (deep grey bars) and distal radius (light grey bars) in men with tetraplegia and paraplegia. Deficits are expressed as standard deviations from the mean in age-matched controls.....**151**

Figure 4.4 Differences in loading-induced microstrain within the range usually encountered by a bone do not modify modelling or remodelling.....**158**

Graphic Abstract.....**167**

Figure 5.1 Cortical and trabecular microarchitecture and femoral neck BMD are more deteriorated in patients with CKD (yellow dots) than in controls (green dots). The greater the cortical porosity, (a) the fewer the numbers of trabeculae, (b) the greater the trabecular separation but (c) no association with trabecular thickness. (d) Greater cortical porosity was associated with lower matrix mineral density and (e) greater inhomogeneity in trabecular spatial distribution. (f) Compared with a control, the patient with CKD had loss of homogeneity in distal tibial trabecular spatial distribution. Magnified section shows increased cortical porosity with trabecularized cortex producing fragments that may be mistaken as trabeculae and contribute to the inhomogeneity.....**176**

Figure 5.2. Comparison of bone microarchitecture and estimated failure load in patients with CKD (yellow bars) versus controls (green bars) within a bone mineral density (BMD) category (*p < 0.001). Comparison of matrix mineral density frequency distribution between patients with CKD and controls (right bottom panel), N=Newton. See text. (For interpretation of the references to colour in this figure legend, the reader is referred to the web version of this article)……..**178**

Figure 5.3. Univariate associations between estimated failure load at the distal tibia with tibial cortical and trabecular microarchitecture and femoral neck BMD in patients with CKD (yellow dots) and controls (green dots). N=Newton. See text. (For interpretation of the references to colour in this figure legend, the reader is referred to the web version of this article.)……..….**180**

List of Tables

Table 1.1. Annual incidence of NVNH fractures in Caucasian women and men**.....9**

Table 1.2. Remaining lifetime risk of fracture (%) of forearm and proximal humours in women and men at 50 and 80 years of age fix position of age groups. **.....10**

Table 2.1. Key parameters for HR-pQCT images acquisition men**.....32**
Table 2.2. Comparison of cortical thickness and cortical vBMD measurement of vertebrae body scanned by different resolution**……..…….....42**

Table 2.3. The mean, SD, and CV% of each rod of QC phantom scanned 10 times without repositioning**.....55**

Table 2.4. Mean, standard deviation and coefficient variation of bone microstructure parameters, without slice matching**.....60**

Table 2.5. Mean, standard deviation and coefficient variation of bone microstructure parameters, with slice matching**.....62**

Table 2.6. Mean, standard deviation, and CV (%) of trabecular apparent and material densities and non-parametric microstructure indices, without slice matching…..**.....61**

Table 2.7. Radius-slice matched CV (%) and least significant changes of 27 participants vBMDs and bone microstructure parameters of distal radius and tibia scanned twice with repositioning within same day**.....64**

Table 2.8. Tibia-slice matched, CV (%) and least significant changes of 27 participants vBMDs and bone microstructure parameters of distal radius and tibia scanned twice with repositioning within same day**.....65**

Table 2.9. Radius-slice unmatched, CV (%) and least significant changes of 27 participants vBMDs and bone microstructure parameters of distal radius and tibia scanned twice with repositioning within same day**.....66**

Table 2.10. Tibia-slice unmatched, CV (%) and least significant changes of 27 participants vBMDs and bone microstructure parameters of distal radius and tibia scanned twice with repositioning within same day..**.....67**

Table 3.1. Ex vivo distal radial morphology (n = 18 specimens) using the manufacturer's region of interest (ROI) positioned 1 or 2 mm distally or proximally**.....119**

Table 3.2. Characteristics of the participants**.....121**

Table 3.3. Distal radial microstructure in the fixed and corrected region of interest in Asian and Caucasian women and men. **..... 122**

Table 3.4. Sexual dimorphism in distal radial microstructure in the fixed ROI and in the corrected ROI in Asians and Caucasians**..... 122**

Table 3.5. Racial dimorphism in distal radial microstructure in women and men in the fixed and corrected region of interest**..... 122**

Table 4.1. Distal tibial microstructure in individuals with tetraplegia and paraplegia and controls**.....145**

Table 4.2. Distal fibula microstructure in individuals with quadriplegia and paraplegia and
ontrols**.....145**

Table 4.2. Distal fibula microstructure in individuals with quadriplegia and paraplegia and ontrols**.....146**

Table 4.3. Distal radial microstructure of individuals with tetraplegia and paraplegia and controls**.....148**

Table 4.4. Total, cortical and trabecular vBMD differences between tibia, fibula and radius in tetraplegic and paraplegic men. Difference expressed as age-adjusted standardized deviations (SD) with 95% confidence intervals (CIs). **.....149**

Table 5.1. Age, eGFR, serum PTH, vitamin D, total calcium and phosphate in patients with chronic kidney disease and kidney transplant recipients. Data expressed as Mean (SD**)……..……..174**

Table 5.2. Comparison of distal tibia microarchitecture, estimated failure load, lumbar spine, and femoral neck BMD in patients with CKD versus age- and sex-matched controls.**……..……...175**

Table 5.3. Comparison of distal tibia microarchitecture and estimated failure load in controls versus patients with CKD according to BMD category (normal, osteopenia and osteoporosis)..**…….....177**

Table 5.3. Univariate and multivariate analyses of associations between estimated failure load and tibial microarchitectural traits in patients with CKD (N = 103) **……..…179**

Table 5.S1. Univariate and multivariate analyses of associations between estimated failure load and tibial microarchitectural traits in patients with CKD (N = 103) **…...186**

Table 5.S2. Comparison of distal radius microarchitecture, estimated failure load in patients with CKD stage 4-5D versus kidney transplant recipients. **……...….187**

Table 5.S3. Comparison of distal radius microarchitecture, estimated failure load, lumbar spine, and femoral neck BMD in patients with CKD versus age- and sex-matched controls**……..……...188**

Table 5.S4. Comparison of distal radius microarchitecture, estimated failure load in controls versus patients with CKD according to BMD category (normal, osteopenia or osteoporosis)**…..……...189**

Table 5.S5. Univariate and multivariate analyses of association between estimated failure load and distal radius microarchitectural traits in patients with CKD (N =99)..**…..……...200**

CHAPTER 1

Bone Fragility Fractures

Chapter 1

1.1 Fragility Fractures

The term of ‘fragility fractures’ refers to fractures that occur in response to the minor trauma (1). Our bodies should be able to sustain a fall from its height without a fracture unless there is some underlying cause to suspect a bone disorder such as bone fragility. Fragility fractures differ in their incidence by age, sex, ethnic groups, geographic area and aetiology (2).

Epidemiology of Fragility Fractures

Fracture incidence in the general population is bimodal, with peaks occurring in the youth and in the elderly (3). The incidence of fragility fractures increases as age advances but differs by age, body weight, height, poor health, the propensity to fall, poor depth perception, history of bone related disease, previous fractures and environmental hazards (4).

Information released by *Osteoporosis Australia* indicates 4.74 million Australians over 50 years of age (66% of people over 50) have osteoporosis or osteopenia or poor bone health. In 2013 there was 1 fracture every 3.6 minutes in Australia. This equates to 395 fractures per day or 2,765 fractures per week. There will be 3,521 fractures per week by 2022 and it is expected there will be a 30% increase in the annual number of fractures resulting in 183,105 fractures per annum. The estimated total number of fractures over the next 10 years is over 1.6 million. This includes new fractures and re-fractures (5).

The similar trend reported for the US with more than 2 million incident fractures at a cost of $17 billion for 2005. By 2025, annual fractures and costs are projected to rise by almost 50% (6). Osteoporosis costs EU countries €37 billion every year base on International Osteoporosis Foundation report.

Chapter 1

Morbidity and mortality associated with fragility fractures

Bone fragility is a public health problem because it is associated with an increased risk of potentially serious fractures in a large proportion of the population. Fragility fractures generate a heavy burden of morbidity and financial cost (6). However, recent data indicate that some fractures are also associated with excess mortality (7). Hip fractures constitute the most severe complication of bone fragility because they can induce permanent physical disability, loss of self-sufficiency, institutionalisation and, above all, an increased risk of death (8).

Vertebral Fractures

Vertebral fragility fractures are recognised as a significant health problem facing the aged population and are considered the hallmark of osteoporosis. Vertebral and other fractures are independent risk factors for future fragility fractures (9).

Compared with hip fractures, the epidemiology of vertebral fracture is less well established due to the lack of a universally accepted definition, and a vast proportion of vertebral fractures escape clinical diagnosis. Only about a third of all vertebral deformities noted on radiographs come to medical attention, and less than 10% necessitate admission to hospital (10).

Due to issues mentioned above; the incidence of vertebral fractures could vary up to three-fold dependent on the criteria used to define vertebral fractures (11, 12). Many vertebral compression fractures follow minimal trauma, and controlled studies suggest that vertebral microarchitecture contributes to fracture risk independently of vertebral bone mass (2).

The rate of subsequent vertebral re-fracture is called ‘vertebral fracture cascade’. Lindsay et al. indicated the risk of sustaining a second vertebral fracture up to 20% in the first year of initial fractures (13), and other studies reported the risk of subsequent vertebral fracture to increase by 4–7-fold after an initial fracture, and then exponentially with greater numbers of prior vertebral fractures (14-16).

The European Perspective Osteoporosis Study (EPOS), by recruiting a total of 14,011 men and women aged 50 years and over from population-based registers in 29 European centres, has shown that the age-standardised incidence of morphometric fracture was 10.7/1000 and 5.7/1000 person-years in women and men, respectively. Repeat spinal radiographs were performed a mean of 3.8 years following the baseline film (**Fig. 1.1**) (17).

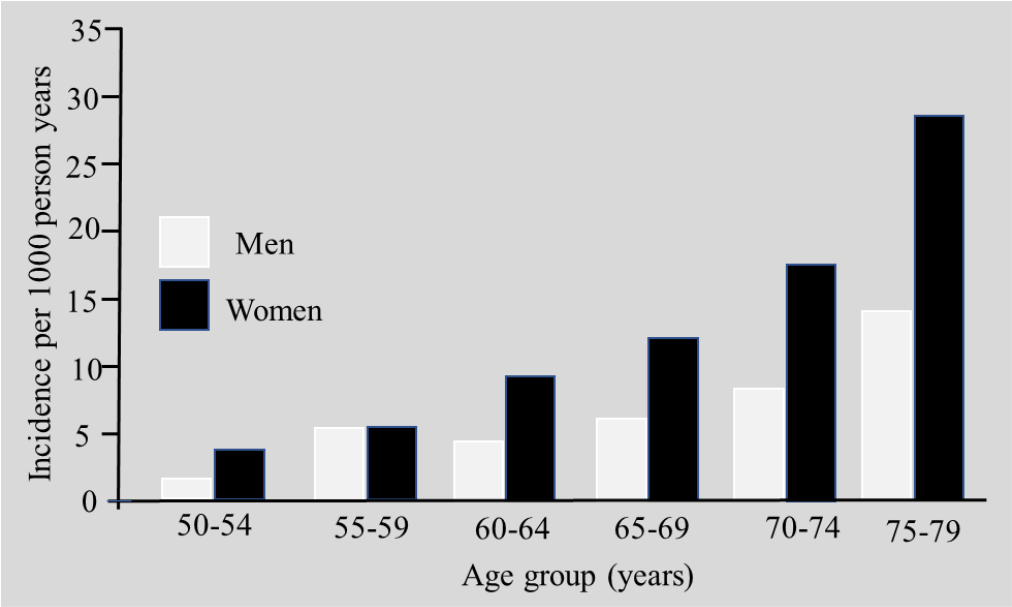

Figure 1.1. Incidence of vertebra fractures in women and men from European Perspective Osteoporosis Study by age group (17).

Osteoporosis Australia has reported 27,754 vertebral fractures or re-fractures for men and women 50 years and over (21,325 women vs 6,879 men) in 2014. By 2022 there are predicted to be 35,044 vertebral fractures, representing an average annual increase in vertebral fractures of 2.8% in

women and 3.1% in men over the same period. The total annual cost of vertebral fractures is predicted to increase by more than 30% by 2022, $226 million in 2013 to $226million in 2022 (5).

Hip Fractures

All fractures result in some degree of morbidity, but fractures at the hip are associated with the most devastating outcomes because of the higher morbidity and mortality in the patients with hip fracture. There are 3 types of proximal femur fragility fractures; femoral neck, pertrochantric and subtrochanteric fracture, with incidence rate ratio (Femoral Neck/ Trochanter) of 2.14 and 1.29 for women and men, respectively(18). It has been frequently reported that by ageing, the incidence of hip fracture increases (9, 19, 20). In this regard, Cooper and Sambrook et al., have shown an increase in hip fractures after 60 years old for both sexes **(Fig. 1.2**) (21, 22).

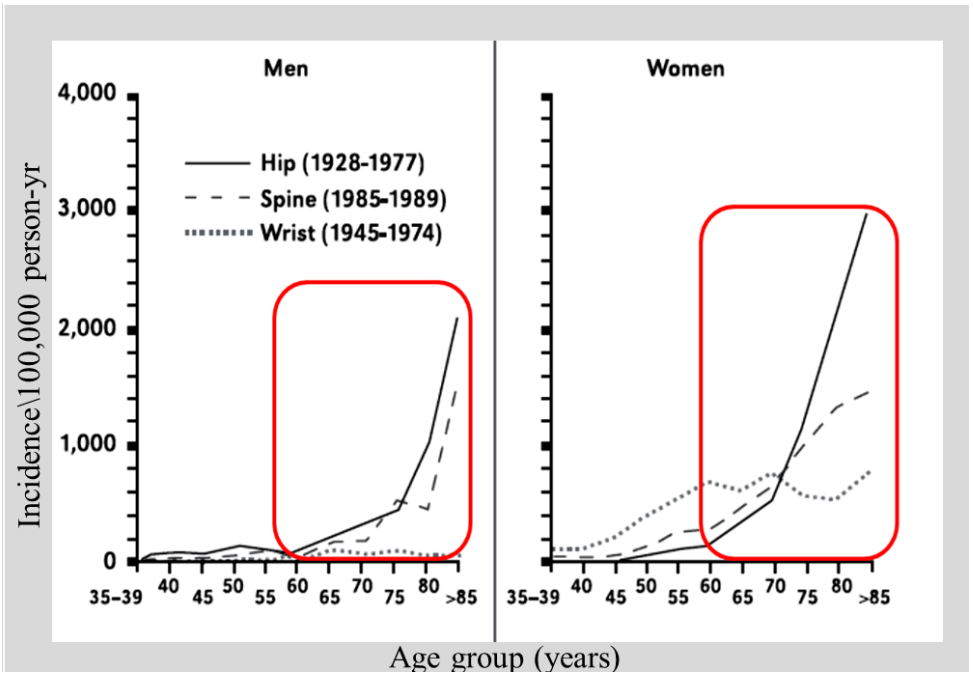

Figure 1.2. Age specific incidence rates for hip, spine, and distal forearm facture in Caucasian women and men in Rochester, Minnesota, USA (22).

It has been estimated 740,000 deaths per year associated with hip fracture (23), which account for 0.83% of the burden of non-communicable disease worldwide and 1.75% in Europe (24). The increment of incidence of proximal femur fragility fracture will be mainly due to an increase in the elderly population, especially in Asia, Latin America, the Middle East and Africa, which regions will account for over 70% of all fractures in the world by the year 2050 (18, 19).

Data from the Rochester Cohort showed that survival rates 5 years after hip and vertebral fractures were approximately 80% of those expected for men and women of similar age without fractures (**Fig. 1.3**) (21). Although hip fractures occur later, in comparison to the wrist and vertebral fractures, the impact of hip fractures are high and usually result in permanent disability (25).

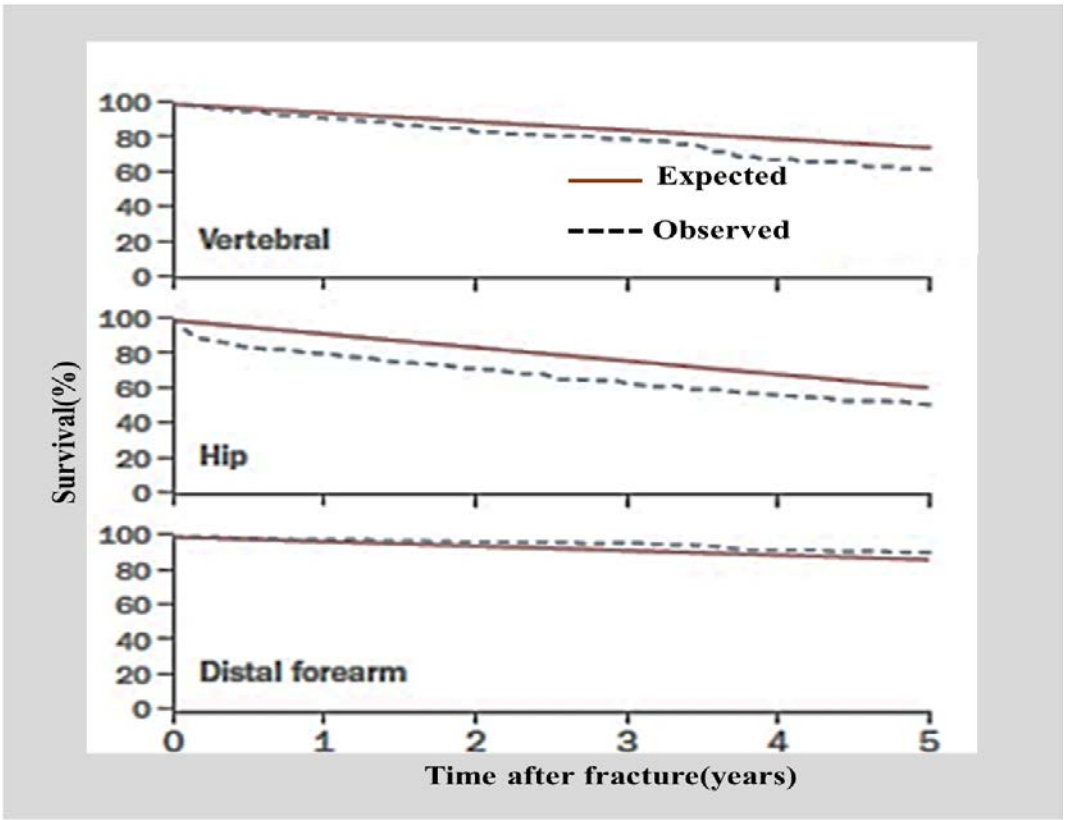

Figure 1.3. Survival rates after the diagnosis of a vertebral, hip, or distal forearm fracture among residents of Rochester, Minnesota, USA.

Based on National Osteoporosis Foundation (NOF) reports from 2000 to 2011, there were 4.9 million hospitalisations for osteoporotic fracture, 2.9 million for the myocardial infraction, 3.0 million for stroke, and 0.7 million for breast cancer in the USA. Fragility fractures accounted for more than 40% of the hospitalisations in these 4 outcomes, with an age-adjusted rate of 1124 admissions per 100,000 person-years. In comparison, myocardial infarction, stroke, and breast cancer had age-adjusted incidence rates of 668, 687, and 151 admissions per 100,000 person-years, respectively. The annual total population facility-related hospital cost was highest for hospitalisations due to fragility fractures ($5.1 billion), followed by a myocardial infraction ($4.3 billion), stroke ($3.0 billion), and breast cancer ($0.5 billion) (**Fig. 1.4**) (26).

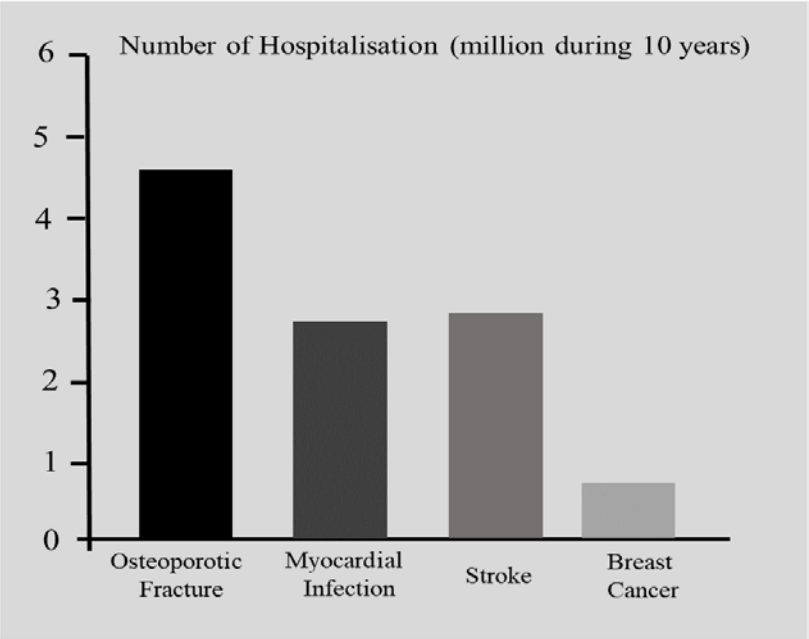

Figure 1.4. Comparison number of hospitalisations for fracture, myocardial infraction, stroke, and breast cancer within 2000-2011 in USA.

Hip fractures place considerable financial burden on the Australian health-care system. In 2013, it was estimated that about 26,000 hip fractures would occur in 2016, costing close to $1 billion dollars, with treatment of hip fractures accounting for about 44% of all fracture-related hospital expenditure (27).

Hip fracture in Australia

The age-adjusted incidence rate of hip fragility fracture has declined in Australia over the 10 years to 2007, by 20% and 14% among women and men, respectively. However, the absolute number of proximal femur fragility fracture continued to increase for both sexes due to population growth. There are more than 40 hip fractures per day in Australia, mostly on the people over 65 years, which half of them are aged over 85 years and almost 75% occurs in females (**Fig.1.5**)

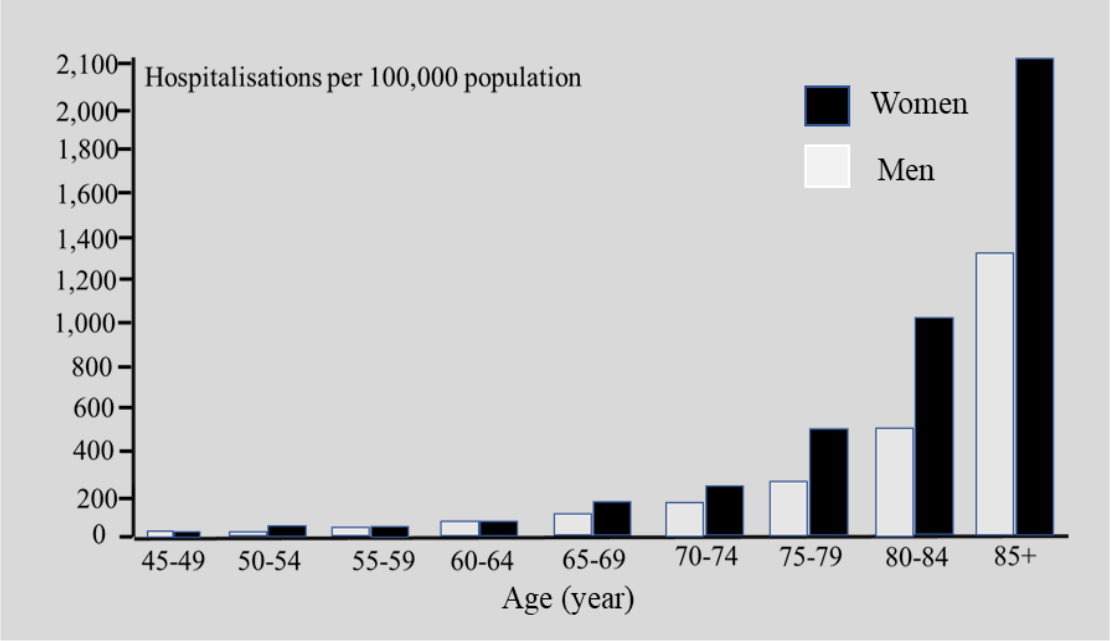

Figure 1.5. Rate of hospitalisation for new hip fractures, by age and sex, 2015–16.

The new data about incidence of hip fracture cross western areas of Victoria state of Australia, reported by Holloway at al., shows for men, the age-standardised rate of hospitalisations for hip fracture across the whole region was 19.2 per 10,000 population/year (95%CI 18.0–20.4) and for women, 40.0 (95%CI 38.3–41.7). The highest incidence rates for both sexes occurred in the less accessible Local Government Areas of Yarriambiack and Hindmarsh. In both sexes, approximately two thirds of individuals were discharged from acute hospital care within 14 days. Increasing age, higher remoteness and lower socioeconomic status were all associated with higher hip fracture rates.

Non-vertebral, non-hip (NVNH) fractures

Main attention in osteoporosis is focused on the spine and hip fragility fractures. However, there are insufficient data on the epidemiology and consequences of other fractures.

Non-vertebral non-hip (NVNH) fractures have a lower per-patient cost than either hip or vertebral fractures (6, 28), however NVNH fractures account for 90% of all fractures until 80 years of age and for 59% thereafter (29). The most common NVNH fractures in elderly individuals are distal radius, proximal humerus, and ribs. In women aged 80 years or over, forearm fractures have the highest incidence among NVNH fractures (29).

Table 1.1. Annual incidence of NVNH fractures in Caucasian women and men (29)

	Incidence per 10,000		
Fracture site	**Women**	**Men**	**Ratio**
Distal radius and ulna	243	182	1.33
Ankle	65	87	0.75
Humours	76	58	1.31
Clavicle	32	67	0.47
Metacarpal bones	19	117	0.16
Tarsal or metatarsal bones	52	73	0.71

For individuals aged 50, the lifetime risks for forearm and proximal humeral fractures are 22.9% and 12.9% in women and 10.7% and 4.1% in men, respectively (30).

Table 1.2. Remaining lifetime risk of fracture (%) of forearm and proximal humours in women and men at 50 and 80 years of age fix position of age groups.

	At 50 years			At 80 years		
	Women	**Men**	**Risk ratio**	**Women**	**Men**	**Risk ratio**
Forearm	22.9	10.7	2.14	19.3	9.1	2.12
Proximal humerus	12.9	4.1	3.14	7.7	2.5	3.08

Roux et al. reported the incidence of 57% minor NHNV, 26% major NHNV in 50,461 postmenopausal women over 1 year. Upper arm, lower leg, upper leg, and pelvis fractures accounted for 93% of major NHNV fractures; and wrist, ankle, and rib fractures made up 91% of minor NHNV fractures (Fig. 6) (31).

The incidence of Colle's fracture in Caucasian women increases between age 40 to 65 years then stabilises (32). However, in men, the incidence remained relatively stable from 20 to 80 years (33).

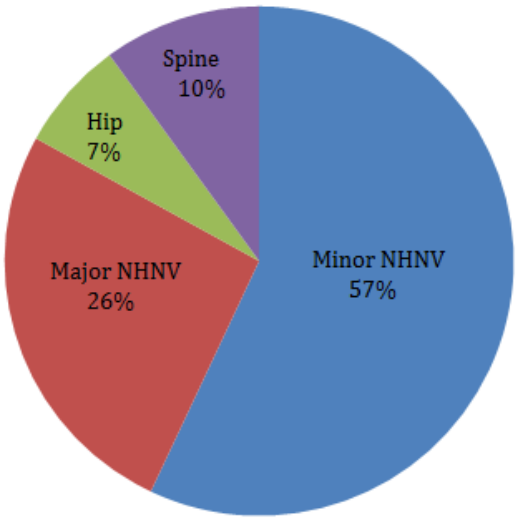

Figure 1.6. Distribution of incident of hip, spine, major NHNV and minor NHNV fracture types.

Chapter 1

Fragility fracture during COVID-19 pandemic

It is recognized that the COVID-19 pandemic has caused intense interruption to the delivery of healthcare services globally. This has affected the management of many long-term conditions including osteoporosis. Because of the prioritization of urgent services, the management of many chronic or long-term medical conditions such as osteoporosis has been challenging as resources are diverted from chronic disease care to combat the pandemic.

Measurement of BMD, or related laboratory exams, are largely provided by secondary-care facilities in Australia and these services have been disrupted, or even paused, during the pandemic due to rigorous infection control measures and social distancing or shortage of staff members in consequence of sever acute respiratory syndrome coronavirus 2 (SARS-CoV-2) infection. In addition, frail, and elderly patients who are particularly susceptible to fragility fracture associated with osteoporosis have been reluctant to attend hospitals for fear of contracting SARS-CoV-2. According to the report of the UK National Health Services, it has been estimated that there was 73% fewer DXA scan carried out in June 2020 compared to June 2019 (34).

Interestingly, it has been reported a declining rate of non-hip fracture during the pandemic. Ogliari and colleagues reported the declining number of non-hip fractures from a mean of 63.1 (12.6) per week to 26.0 (7.3) during the pandemic (35). The reason for the reduction in non-hip fracture has been speculated due to in part to fewer falls as a result of movement restrictions. However, there is no data about sarcopenia or osteo-sarcopenia, which is expected to be increased due to lack of sufficient physical activates during restrictions the pandemic.

Data on the rates of hip fracture during the pandemic have been conflicting, such as some studies have reported no changes compared with previous years (35), whereas others have described increases or decreases (36-38). Nevertheless, inadequate care the following discharge through

redeployment of key staff such as physiotherapists and occupational therapists to acute services may affect the duration of recovery of patients with hip fractures (34).

A large number of clinical risk factors have been associated with mortality in patients with COVID-19 disease, the most important of which are age, respiratory or cardiovascular disease, chronic kidney or liver diseases, neurological disorders, and immunosuppression (39). The QResearch data set from England shows that a history of hip, spine, humerus and wrist fractures was associated with an increased risk of death from SARS-Cov2 infection in women and men. In addition, individuals with previous fractures had an increased risk of hospital admission due to SRASS-Cov2 infections (40).

The data shows that vertebral fractures were common (about 36%) among those hospitalized with severe SARS Cov2 compared with the generalized population where the prevalence of VF ranged from 18-26% in women and 8-2% in men (41, 42). Patients with VFs were more likely to require non-invasive mechanical ventilation (48.8% vs. 27.4%, p=0.02) and mortality was higher in those with severe VFs (60%) compared with those with moderate or mild VFs (7% and 24%, respectively) (43). It seems the impaired respiratory function and kyphosis associated with VFs may decrease vital lung capacity and increase the risk of severe SRAS Cov2 infection.

Data from 21 studies, which reported mortality following hip fracture showed that COVID-19 positive have a seven-fold increased risk of death, compared to COVID-19 negative patients (43).

Conclusions

With the global shift towards an aging population, there will be a large increase in fracture burden worldwide over the next 50 years. Strategies are being developed to target more comprehensively those at high risk of fracture both for primary and secondary prevention, but much more needs to

be done at the policy level, bone quantitative imaging methods, artificial intelligent, including machine and deep learning, to identify people at the risk of fragility fracture at the early stages to reduce the burden of fragility fracture in future generations.

Pathogenesis of Bone Fragility

(A glance review)

1.2 Introduction

Fragility of bones is the result of genetics as well as environmental factors; seemingly, both factors play a part in development of macro- and microstructure of bones (44). Patients with fragility fractures may have abnormalities in bone microstructure and material properties such as larger or smaller bone size, fewer, separated, and thinner trabeculae, porous and thinned cortices, and too high or either too low matrix mineral density, which result in lower or impaired peak bone strength and predispose to fragility fracture (45).

The mineralized skeleton is defined by its periosteal (outer) surface and by the endocortical, trabecular, and intracortical components of its inner (endosteal) surface. Osteoblast and osteoclast activities produce net bone formation or resorption within bone surfaces, which modifies the size, shape, microarchitecture, and mass of the skeleton. Throughout life, bone modelling and remodelling work continuously on the skeleton to gain or maintain bone strength. While bone modelling dominates during growth, bone remodelling becomes more prominent after bone strength reaches its maximum.

Bone Modelling

Bone modelling involves independent process of bone formation and resorption that changes the shape of bone by forming and resorbing on different surfaces. There is no direct communication between osteoblasts and osteoclasts activities during bone modelling; however, these processes must be synchronized, perhaps by signals through the osteocyte network (46).

During growth, bone modelling is dominant to facilitate changes in bone length, size, and shape to accomplish peak bone strength, but continues to a lesser degree throughout adulthood

and old age in response to mechanical loading (47). Bone modelling continues after closure of the epiphyses, once skeletal maturity is attained, bone modelling is largely restricted to periosteal apposition, but it is insufficient to offset the loss of bone that occurs during advancing age.

Bone Remodelling

Bone remodelling is a lifelong process which continuously renews the material composition of bone by detecting and removing older or damaged bone and replacing it with new bone maintaining the mechanical integrity of the bone. Bone remodelling is bone surface dependent process which takes place asynchronously throughout the skeleton at anatomically distinct sites. Based on *Wolf's law* and the theory of *Mechanostat* bone remodelling direction (adding or removing the bone mass) would be mediated by magnitude and frequency of loading and has been adapted for each specific site(48, 49).

During bone remodelling cellular process occurring upon three components of bones inner (endosteal) surfaces and with lesser degree on the external (periosteal) surfaces (50, 51) (Fig. 1.7).

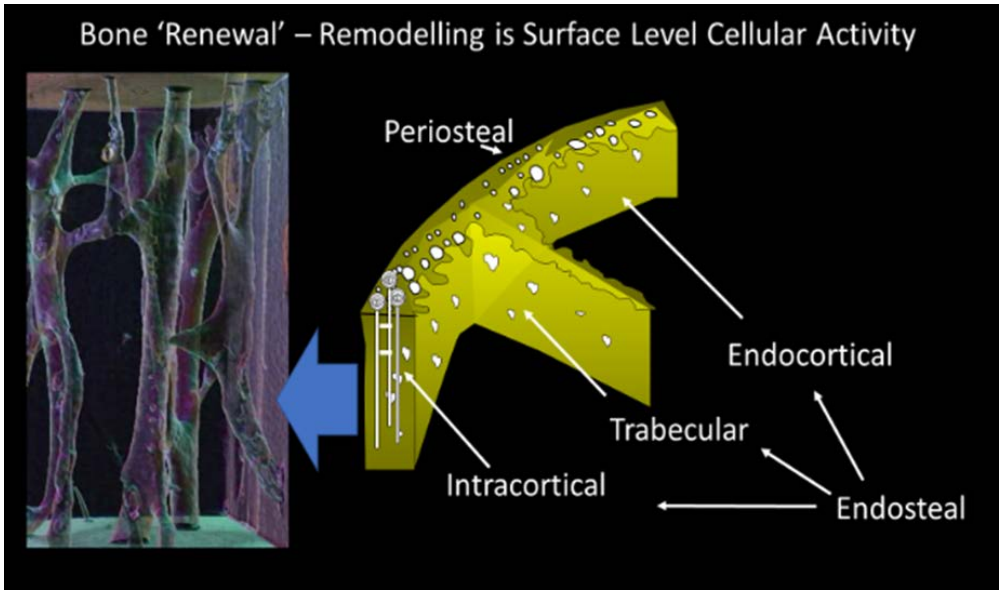

Figure 1.7. (Right panel) Structure of bone Cortical and trabecular bone, the periosteal surface, and the endocortical, trabecular, intracortical surface on which matrix remodelling is initiated. (Left panel) The intracortical surface formed by the lining of myriads of Haversian and Volkmann canals traversing the cortex. Adapted from reference 5.

During bone remodelling mineralised bone tissue is removed and replaced by new and less mineralised bone tissue. This cellular mechanism is carried out by basic multicellular units (BMUs) transient groups of cells. In each cycle of bone remodelling, quanta volume of bone is removed by osteoclasts and subsequently replaced by osteoblasts, at the same location. The resorption activity in a BMU in adult human bone takes approximately 3 weeks and formation response 3 to 4 months. The process of remodelling replaces about 5-10% of skeleton each year, with the entire adult human skeleton replaced in 10 years(51-53).

For many years, it was considered that bone remodelling is controlled primarily by actions upon bone of circulating hormones, such as PTH, 1,25(OH)2 vitamin D3 and sex hormones; however, discoveries of last three decades have revealed that locally generated cytokines are the key influences with influencing bone cells communications which are regulated by hormones withing complex ways. There are many hormonal and environmental triggers to

initiate the bone remodelling process; however, changes on magnitude and duration of mechanical loading initiates bone remodelling as external triggers. **Fig 1.8** explains the process of bone remodelling due to microcrack and osteocyte apoptosis (54).

The process of bone remodelling consists of 6 active sequential events: Activation, Resorption, Reversal, Formation, Mineralization, and Quiescence (55).

Activation

Bone remodelling can be initiated through different mechanisms. Once osteocytes have sensed a change in mechanical strain, death of osteocytes, or matrix changes in the form of microcracks the signals are conveyed to surface to initiate targeted bone remodelling. The signals activate bone remodelling process by recruiting mononuclear osteoclast precursors from hematopoietic. Fusion of the precursors cells forms multinucleated osteoclasts and functionally active osteoclasts stick to bone matrix. During this period the resting bone surface are converted into remodelling surface.

Resorption

Osteoclasts attach themselves to bone matrix and secret hydrochloric acid and other acids like Cathepsin K which degrade organic elements of the bone matrix. This process creates cersent-shapped resorption cavities called *Howship's Lacunae* on the cancellous bone surface and cutting cones of the evolving Haversian systems within cortical bone (**Fig.1.8**)

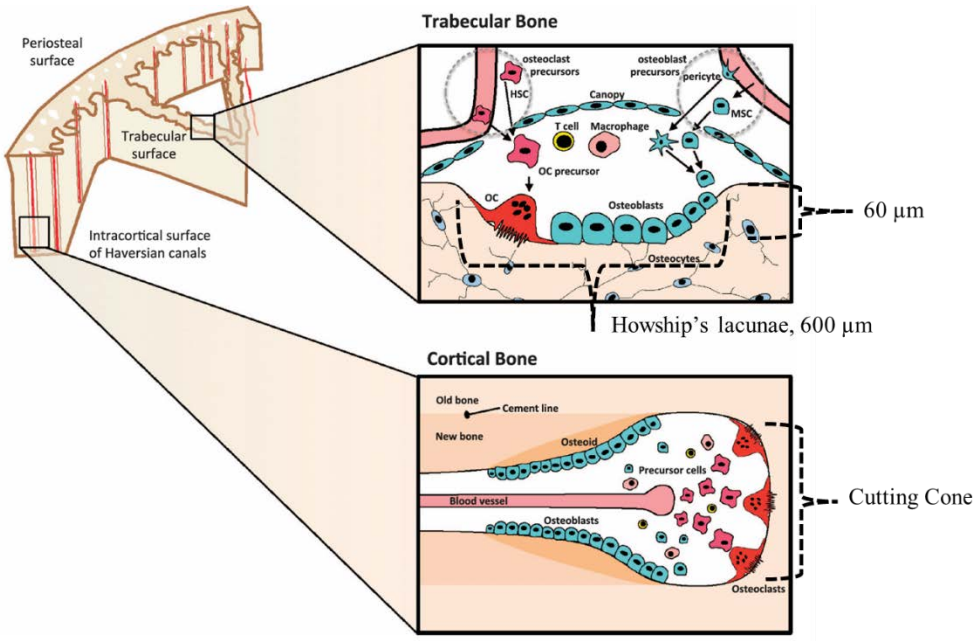

Figure 1.8. Comparison of structural aspect of bone remodelling between trabecular bone surface, Howship's Lacunae, with Haversian canals of cortical bone, Cutting Cone, adapted from reference 13.

Reversal

Reversal phase is coupling of bone resorption phase to bone formation phase by generating of osteogenic environment at the remodelling sits (56). During this phase, the resorption lacuna is occupied by mononuclear cells, including monocytes, osteocytes which were liberated from bone by osteoclasts and pre-osteoclasts and are being recruited to couple the resorption phase with formation phase.

Formation

In this phase, osteoblasts are recruited and differentiated from mesenchymal precursors. When they reach the bone surface, they become fully expressed osteoblast phenotype. Bone matrix

formation is a two-stages process in which osteoblasts initially synthesize the organic matrix, called *osteon*, and regulate its mineralisation (57).

Mineralisation

Once the collagenous organic matrix is synthesized osteoblasts trigger the mineralisation process, which occurs after a delay of about 20 days, called the mineralisation lag time. The mineral content of the matrix increases rapidly to 75% of the final mineralisation content over the first few days, called primary mineralisation which is initiated 5 to 10 days after bone matrix deposition (58). In contrast, secondary mineralization is a more gradual process that results in enlargement of crystals and lasts 24 to 30 months. This process consists of a slow and gradual maturation of the mineral component, including an increase in the number of crystals and/or an augmentation of crystal size toward their maximum dimensions and/or an increase of the perfection at crystal level (59).

Quiescence:

A period of inactivity which follows bone resorption and bone formation is finalized. In this period bone surface has turned to its original state of quiescence except that the bone is younger. Normally, 80% of trabecular bone surface and about 95% of the intracortical bone surface remain inactive with respect to bone remodelling(60).

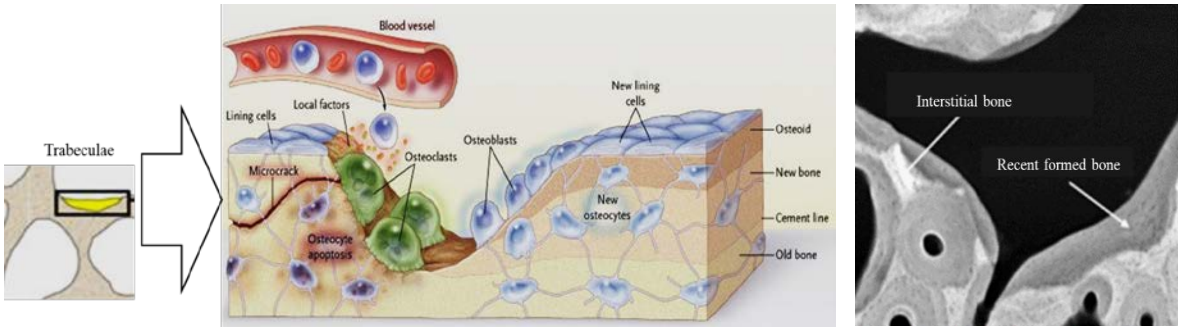

Figure 1.9.
Left panel) Bone remodelling activities in the surface of trabecular bone. A microcrack splits canaliculi, which causes osteocytic apoptosis, with the location and extent of the damage defined by signals to lining cells. Lining cells and osteocytes release local factors that attract cells from blood and marrow into the remodelling compartment in which osteoclastogenesis occurs. Osteoclasts resorb matrix and the microcrack, then successive teams of osteoblasts deposit new lamellar bone. Osteoblasts that are trapped in the matrix become osteocytes; others die or form new, flattened osteoblast lining cells. Adapted from reference 8.
Right panel) Human bone sample. A microradiograph of a 100 ± 1 μm-thick section illustrating the heterogeneity of the mineralization in the new formed and in the interstitial old bone tissue. The brighter interstitial lamellae had a mineral content of about 1.40 g/cm^3 while the least highly mineralised bone had a mineral content of about 1.00 g/cm^3. Adapted from reference 12.

Trabecular and cortical bone remodelling

The remodelling process occurs only on bone surfaces within trabecular or cortex. Contrary to remodelling sites in trabecular bone, which are close to red marrow (61), remodelling sites in cortical bone are distant from red marrow. Therefore, it is assumed that the mechanisms of bone remodelling are different in trabecular versus cortical bone, i.e. that the cells needed for bone remodelling in trabecular bone travelled directly from the red marrow to bone surfaces in trabecular bone, while cells reached cortical remodelling sites bone via the vasculature (62). Trabecular mineralised bone matrix are thin plates or rods with a relatively large surface area facilitating remodelling. The accessibility to being remodelled is an advantage for damage repair when remodelling is balanced, but a disadvantage when remodelling is unbalanced, and accelerated. Cortical bone has a large volume and is enveloped with a relatively smaller internal surface area (Haversian canal surfaces and the endocortical surface), so in comparison to

trabecular (63). Cortical bone has lower bone remodelling rate, when the microstructure of trabecular or cortical bone has not been deteriorated. **Fig 1.10** illustrates the comparison of trabecular and cortical bone surface available for bone remodelling.

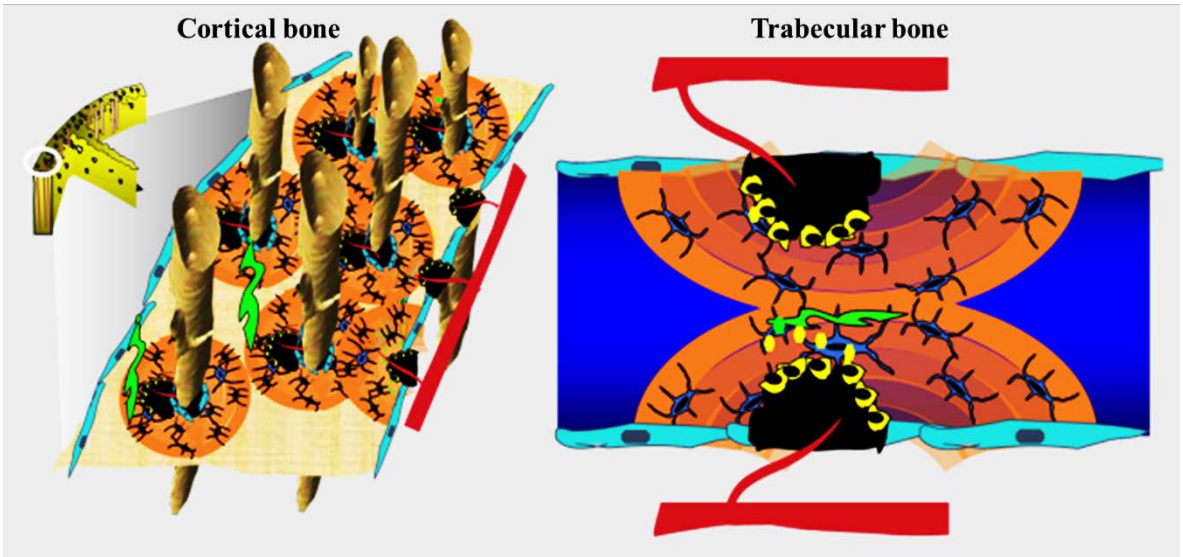

Figure 1.10 A) Cortical bone; Haversian canal surfaces (blue) and the endocortical surface (yellow). **B**) Trabecular bone surface (yellow). In the healthy bone, the surface to volume ratio in cortical bone is much lower than in trabecular bone, adapted form reference 20.

The intensity of remodelling is expressed by activation frequency, which is reciprocal of the average time interval between the initiation of remodelling at the same surface location, referred as the regeneration period.

Turnover refers to volume replacement, which depends not only the surface-defined activation frequency but on the surface -to-volume ratio. This geometrical property is about four to five times higher in typical cancellous bone than in typical cortical bone(64). Activation frequency is similar on the cancellous, endocortical and intracortical(65), so difference in turnover between cortical and trabecular entirely on the differences in surface-to-volume ratio. Turnover depends

also on distance from the surface; iliac interstitial bone has much lower turnover than inner cortical bone close to marrow(66).

Bone remodelling during advancing age and menopause

During young and healthy adulthood bone remodelling is balanced, the volume of bone resorbed is replaced by an identical volume of new bone so no net bone mass reduction or structural deterioration occurs (67). Advancing age is accompanied by bone loss in women and men, and there is evidence of remodelling imbalance in both sexes before 50 years. The rate of imbalanced bone remodelling increases during menopause in women and later in men. The remodelling imbalance is the necessary and sufficient morphological basis of bone loss in women and in men (68).

Abnormal bone remodelling involves some combination of **i**) loss of directional control of osteoclast or osteoblast differentiation, **ii**) increase in number of remodelling cycles or **iii**) incomplete new bone replacement.

All of bone related disease occurs as a consequence of the effects of cellular events in the bone remodelling cycle, during aging or sex hormones reduction, or other bone related abnormalities, bone remodelling balance becomes negative, and the volume of bone formed in the BMU is reduced.

The negative bone balance in each BMU means that each time a remodelling event occurs there is slightly less bone left over. This negative imbalance causes a decrease in bone mass and deterioration of bone microstructure and increase the risk of fragility fracture (69, 70). In addition to imbalanced bone remodelling, increased BMU activation frequency at the cellular level, which

leads to higher bone turnover, causes a greater number of bone remodelling units on the bone surface will be leading to microstructure deterioration (**Fig. 1.11**)(71, 72).

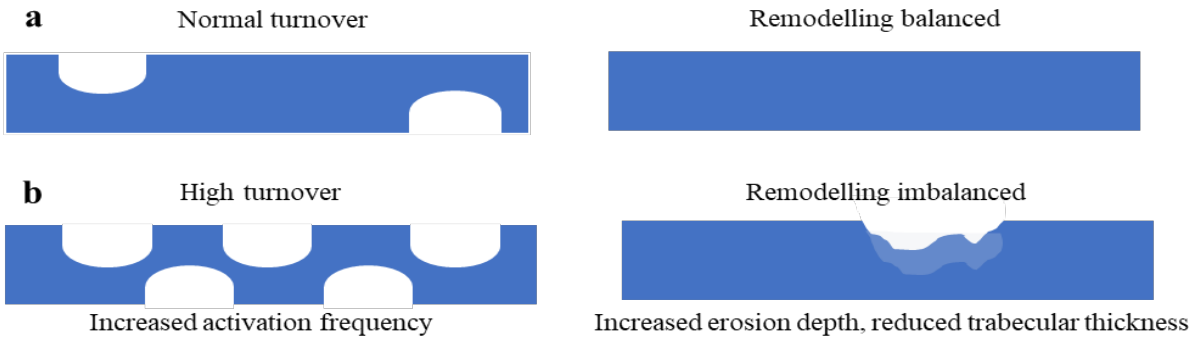

Figure 1.11. Simplified mechanism of trabecular bone loss due to **a**) high turnover **b**) negatively imbalanced bone remodelling.

Gonadal-derived sex steroid hormones are associated in the maintenance of bone integrity during adulthood in the women and men skeleton; testosterone and estrogen are crucial determinants for maintaining bone homeostasis, so the absence or decrease of either estrogen or testosterone levels, with age or gonadal dysfunction, leads to imbalance and negative bone remodelling rates causing reduction in the volume of bone formed in the BMU.

Fuller Albright demonstrated almost 80 years ago that osteoporosis in women was related to estrogen deficiency (73), now this is well-known that estrogen deficiency is major pathogenetic factor in the bone loss associated with the menopause and development of bone loss in postmenopausal women. Estrogens affect the generation, lifespan, and functional activity of both osteoclasts and osteoblasts. They decrease osteoclast formation and activity, while increase osteoclast apoptosis(74). In women around the time of menopause or shortly before, remodelling becomes unbalanced and rapid (75). After menopause, bone resorption increases by 90% while bone formation also increases but only 45% (76). This difference between bone resorption and

formation rate causes negative and imbalance bone remodelling, which leads to an accelerated bone loss during the first years after menopause.

In men, it has been well reported that hypogonadism and decrease in serum testosterone are important pathogenetic factors of bone loss. At the cellular level, testosterone increases lifespan of osteoblasts by decreasing apoptosis. Furthermore, androgens stimulate the proliferation of osteoblasts and differentiation of mature osteoblasts. Androgen has formidable effects on osteoblast formation, which maintain trabecular bone mass and microstructure, and favour periosteal formation in men (77).

Conclusion

Bone remodelling is a dynamic process, with different rates throughout the life, so a deep and comprehensive investigations of bone remodelling is required to develop more effective preventive and anabolic treatments in near future.

References

1. Heaney RP. Is there a role for bone quality in fragility fractures? Calcified tissue international. 1993;53 Suppl 1:S3-5; discussion S-6.
2. Cooper C. The epidemiology of fragility fractures: is there a role for bone quality? Calcified tissue international. 1993;53 Suppl 1:S23-6.
3. Walker-Bone K, Walter G, Cooper C. Recent developments in the epidemiology of osteoporosis. Curr Opin Rheumatol. 2002;14(4):411-5.
4. Friedman SM, Mendelson DA. Epidemiology of fragility fractures. Clinics in geriatric medicine. 2014;30(2):175-81.
5. Sanders JJWJA-OKM. Osteoporosis costing all Australians A new burden of disease analysis

2012 to 2022. 2018.
6. Burge R, Dawson-Hughes B, Solomon DH, Wong JB, King A, Tosteson A. Incidence and economic burden of osteoporosis-related fractures in the United States, 2005-2025. J Bone Miner Res. 2007;22(3):465-75.
7. Leboime A, Confavreux CB, Mehsen N, Paccou J, David C, Roux C. Osteoporosis and mortality. Joint Bone Spine. 2010;77 Suppl 2:S107-12.
8. Ip TP, Leung J, Kung AW. Management of osteoporosis in patients hospitalized for hip fractures. Osteoporos Int. 2010;21(Suppl 4):S605-14.
9. Cummings SR, Melton LJ. Epidemiology and outcomes of osteoporotic fractures. Lancet. 2002;359(9319):1761-7.
10. Cooper C, Atkinson EJ, O'Fallon WM, Melton LJ, 3rd. Incidence of clinically diagnosed vertebral fractures: a population-based study in Rochester, Minnesota, 1985-1989. J Bone Miner Res. 1992;7(2):221-7.
11. Black DM, Palermo L, Nevitt MC, Genant HK, Epstein R, San Valentin R, et al. Comparison of methods for defining prevalent vertebral deformities: the Study of Osteoporotic Fractures. J Bone Miner Res. 1995;10(6):890-902.
12. Eastell R, Cedel SL, Wahner HW, Riggs BL, Melton LJ, 3rd. Classification of vertebral fractures. J Bone Miner Res. 1991;6(3):207-15.
13. Lindsay R, Silverman SL, Cooper C, Hanley DA, Barton I, Broy SB, et al. Risk of new vertebral fracture in the year following a fracture. Jama. 2001;285(3):320-3.
14. Lunt M, O'Neill TW, Felsenberg D, Reeve J, Kanis JA, Cooper C, et al. Characteristics of a prevalent vertebral deformity predict subsequent vertebral fracture: results from the European Prospective Osteoporosis Study (EPOS). Bone. 2003;33(4):505-13.
15. Ross PD, Davis JW, Epstein RS, Wasnich RD. Pre-existing fractures and bone mass predict vertebral fracture incidence in women. Annals of internal medicine. 1991;114(11):919-23.
16. Ross PD, Genant HK, Davis JW, Miller PD, Wasnich RD. Predicting vertebral fracture incidence from prevalent fractures and bone density among non-black, osteoporotic women. Osteoporos Int. 1993;3(3):120-6.
17. European Prospective Osteoporosis Study G, Felsenberg D, Silman AJ, Lunt M, Armbrecht G, Ismail AA, et al. Incidence of vertebral fracture in europe: results from the European Prospective Osteoporosis Study (EPOS). J Bone Miner Res. 2002;17(4):716-24.
18. Lofman O, Berglund K, Larsson L, Toss G. Changes in hip fracture epidemiology: redistribution between ages, genders and fracture types. Osteoporos Int. 2002;13(1):18-25.
19. Gullberg B, Johnell O, Kanis JA. World-wide projections for hip fracture. Osteoporos Int. 1997;7(5):407-13.

20. Kanis JA, Oden A, McCloskey EV, Johansson H, Wahl DA, Cooper C, et al. A systematic review of hip fracture incidence and probability of fracture worldwide. Osteoporos Int. 2012;23(9):2239-56.
21. Cooper C, Melton LJ, 3rd. Epidemiology of osteoporosis. Trends Endocrinol Metab. 1992;3(6):224-9.
22. Sambrook P, Cooper C. Osteoporosis. Lancet. 2006;367(9527):2010-8.
23. Johnell O, Kanis JA. An estimate of the worldwide prevalence, mortality and disability associated with hip fracture. Osteoporos Int. 2004;15(11):897-902.
24. Johnell O, Kanis JA. An estimate of the worldwide prevalence and disability associated with osteoporotic fractures. Osteoporos Int. 2006;17(12):1726-33.
25. Kanis JA, Johnell O. The burden of osteoporosis. Journal of endocrinological investigation. 1999;22(8):583-8.
26. Singer A, Exuzides A, Spangler L, O'Malley C, Colby C, Johnston K, et al. Burden of illness for osteoporotic fractures compared with other serious diseases among postmenopausal women in the United States. Mayo Clinic proceedings. 2015;90(1):53-62.
27. Loefler A, Close J. Rising costs of hip fractures. Med J Aust. 2016;205(2):64-5.
28. Pike C, Birnbaum HG, Schiller M, Swallow E, Burge RT, Edgell ET. Economic burden of privately insured non-vertebral fracture patients with osteoporosis over a 2-year period in the US. Osteoporos Int. 2011;22(1):47-56.
29. van Staa TP, Dennison EM, Leufkens HG, Cooper C. Epidemiology of fractures in England and Wales. Bone. 2001;29(6):517-22.
30. Kanis JA, Johnell O, Oden A, Sembo I, Redlund-Johnell I, Dawson A, et al. Long-term risk of osteoporotic fracture in Malmo. Osteoporos Int. 2000;11(8):669-74.
31. Roux C, Wyman A, Hooven FH, Gehlbach SH, Adachi JD, Chapurlat RD, et al. Burden of non-hip, non-vertebral fractures on quality of life in postmenopausal women: the Global Longitudinal study of Osteoporosis in Women (GLOW). Osteoporos Int. 2012;23(12):2863-71.
32. Owen RA, Melton LJ, 3rd, Johnson KA, Ilstrup DM, Riggs BL. Incidence of Colles' fracture in a North American community. American journal of public health. 1982;72(6):605-7.
33. Nevitt MC, Cummings SR. Type of fall and risk of hip and wrist fractures: the study of osteoporotic fractures. Journal of the American Geriatrics Society. 1994;42(8):909.
34. Hampson G, Stone M, Lindsay JR, Crowley RK, Ralston SH. Diagnosis and Management of Osteoporosis During COVID-19: Systematic Review and Practical Guidance. Calcified tissue international. 2021;109(4):351-62.
35. Ogliari G, Lunt E, Ong T, Marshall L, Sahota O. The impact of lockdown during the COVID-19 pandemic on osteoporotic fragility fractures: an observational study. Arch Osteoporos. 2020;15(1):156.
36. Maniscalco P, Poggiali E, Quattrini F, Ciatti C, Magnacavallo A, Vercelli A, et al. Proximal femur fractures in COVID-19 emergency: the experience of two Orthopedics and Traumatology Departments in the first eight weeks of the Italian epidemic. Acta Biomed. 2020;91(2):89-96.
37. Malik-Tabassum K, Crooks M, Robertson A, To C, Maling L, Selmon G. Management of hip fractures during the COVID-19 pandemic at a high-volume hip fracture unit in the United Kingdom. J Orthop. 2020;20:332-7.
38. Arafa M, Nesar S, Abu-Jabeh H, Jayme MOR, Kalairajah Y. COVID-19 pandemic and hip fractures: impact and lessons learned. Bone Jt Open. 2020;1(9):530-40.
39. Williamson EJ, Walker AJ, Bhaskaran K, Bacon S, Bates C, Morton CE, et al. Factors associated with COVID-19-related death using OpenSAFELY. Nature. 2020;584(7821):430-6.
40. Clift AK, Coupland CAC, Keogh RH, Diaz-Ordaz K, Williamson E, Harrison EM, et al. Living risk prediction algorithm (QCOVID) for risk of hospital admission and mortality from coronavirus 19 in adults: national derivation and validation cohort study. Bmj. 2020;371:m3731.

41. di Filippo L, Formenti AM, Doga M, Pedone E, Rovere-Querini P, Giustina A. Radiological Thoracic Vertebral Fractures are Highly Prevalent in COVID-19 and Predict Disease Outcomes. J Clin Endocrinol Metab. 2021;106(2):e602-e14.
42. Genant HK, Jergas M, Palermo L, Nevitt M, Valentin RS, Black D, et al. Comparison of semiquantitative visual and quantitative morphometric assessment of prevalent and incident vertebral fractures in osteoporosis The Study of Osteoporotic Fractures Research Group. J Bone Miner Res. 1996;11(7):984-96.
43. Clement ND, Ng N, Simpson CJ, Patton RFL, Hall AJ, Simpson A, et al. The prevalence, mortality, and associated risk factors for developing COVID-19 in hip fracture patients: a systematic review and meta-analysis. Bone Joint Res. 2020;9(12):873-83.
44. Seeman E. Pathogenesis of bone fragility in women and men. Lancet. 2002;359(9320):1841-50.
45. Seeman E. Invited Review: Pathogenesis of osteoporosis. J Appl Physiol (1985). 2003;95(5):2142-51.
46. Johnson RW, McGregor NE, Brennan HJ, Crimeen-Irwin B, Poulton IJ, Martin TJ, et al. Glycoprotein130 (Gp130)/interleukin-6 (IL-6) signalling in osteoclasts promotes bone formation in periosteal and trabecular bone. Bone. 2015;81:343-51.
47. Robling AG, Turner CH. Mechanical signaling for bone modeling and remodeling. Crit Rev Eukaryot Gene Expr. 2009;19(4):319-38.
48. Wolff J. Das gesetz der transformation der knochen. A Hirshwald. 1892;1:1-152.
49. Frost HM. Bone “mass” and the “mechanostat”: a proposal. The anatomical record. 1987;219(1):1-9.
50. Zebaze RM, Ghasem-Zadeh A, Bohte A, Iuliano-Burns S, Mirams M, Price RI, et al. Intracortical remodelling and porosity in the distal radius and post-mortem femurs of women: a cross-sectional study. Lancet. 2010;375(9727):1729-36.
51. Eriksen EF. Normal and pathological remodeling of human trabecular bone: three dimensional reconstruction of the remodeling sequence in normals and in metabolic bone disease. Endocr Rev. 1986;7(4):379-408.
52. Courpron P, Meunier P, Vignon G. [Dynamics of bone remodeling explained by Harold Frost. Theory of the B. M.U. (basic multicellular unit)]. La Nouvelle presse medicale. 1975;4(6):421-4.
53. Parfitt AM. The coupling of bone formation to bone resorption: a critical analysis of the concept and of its relevance to the pathogenesis of osteoporosis. Metabolic bone disease & related research. 1982;4(1):1-6.
54. Seeman E, Delmas PD. Bone quality--the material and structural basis of bone strength and fragility. The New England journal of medicine. 2006;354(21):2250-61.
55. In: Orwoll ES, Bilezikian JP, Vanderschueren D, editors. Osteoporosis in Men (Second Edition). San Diego: Academic Press; 2010. p. 733-41.
56. Delaisse JM. The reversal phase of the bone-remodeling cycle: cellular prerequisites for coupling resorption and formation. BoneKEy reports. 2014;3:561.
57. Ramchand SK, Seeman E. Reduced Bone Modeling and Unbalanced Bone Remodeling: Targets for Antiresorptive and Anabolic Therapy. In: Stern PH, editor. Bone Regulators and Osteoporosis Therapy. Cham: Springer International Publishing; 2020. p. 423-50.
58. Boivin G, Meunier PJ. Methodological considerations in measurement of bone mineral content. Osteoporos Int. 2003;14 Suppl 5:S22-7; discussion S7-8.
59. Boivin G, Farlay D, Bala Y, Doublier A, Meunier PJ, Delmas PD. Influence of remodeling on the mineralization of bone tissue. Osteoporos Int. 2009;20(6):1023-6.
60. Parfitt AM. The cellular basis of bone remodeling: the quantum concept reexamined in light of recent advances in the cell biology of bone. Calcif Tissue Int. 1984;36 Suppl 1:S37-45.
61. Parfitt AM. The mechanism of coupling: a role for the vasculature. Bone. 2000;26(4):319-23.

62. Eriksen EF. Cellular mechanisms of bone remodeling. Rev Endocr Metab Disord. 2010;11(4):219-27.
63. Seeman E. Age- and menopause-related bone loss compromise cortical and trabecular microstructure. J Gerontol A Biol Sci Med Sci. 2013;68(10):1218-25.
64. Foldes J, Parfitt AM, Shih MS, Rao DS, Kleerekoper M. Structural and geometric changes in iliac bone: relationship to normal aging and osteoporosis. Journal of bone and mineral research : the official journal of the American Society for Bone and Mineral Research. 1991;6(7):759-66.
65. Han ZH, Palnitkar S, Rao DS, Nelson D, Parfitt AM. Effects of ethnicity and age or menopause on the remodeling and turnover of iliac bone: implications for mechanisms of bone loss. Journal of bone and mineral research : the official journal of the American Society for Bone and Mineral Research. 1997;12(4):498-508.
66. Parfitt AM. Misconceptions (2): turnover is always higher in cancellous than in cortical bone. Bone. 2002;30(6):807-9.
67. Parfitt AM. Targeted and nontargeted bone remodeling: relationship to basic multicellular unit origination and progression. Bone. 2002;30(1):5-7.
68. Gallagher JC, Riggs BL, DeLuca HF. Effect of estrogen on calcium absorption and serum vitamin D metabolites in postmenopausal osteoporosis. J Clin Endocrinol Metab. 1980;51(6):1359-64.
69. Ramchand SK, Seeman E, Wang XF, Ghasem-Zadeh A, Francis PA, Ponnusamy EJ, et al. Premenopausal women with early breast cancer treated with estradiol suppression have severely deteriorated bone microstructure. Bone. 2017;103:131-5.
70. Ng Tang Fui M, Hoermann R, Bracken K, Handelsman DJ, Inder WJ, Stuckey BGA, et al. Effect of Testosterone Treatment on Bone Microarchitecture and Bone Mineral Density in Men: A 2-Year RCT. J Clin Endocrinol Metab. 2021;106(8):e3143-e58.
71. Peel N. Disorders of bone metabolism. Surgery (Oxford). 2015;33(1):15-20.
72. Compston JE, Vedi S, Kaptoge S, Seeman E. Bone remodeling rate and remodeling balance are not co-regulated in adulthood: implications for the use of activation frequency as an index of remodeling rate. Journal of bone and mineral research : the official journal of the American Society for Bone and Mineral Research. 2007;22(7):1031-6.
73. Albright F, Smith PH, Richardson AMJJotAMA. Postmenopausal osteoporosis: its clinical features. 1941;116(22):2465-74.
74. Hughes DE, Dai A, Tiffee JC, Li HH, Mundy GR, Boyce BF. Estrogen promotes apoptosis of murine osteoclasts mediated by TGF-beta. Nature medicine. 1996;2(10):1132-6.
75. Bjørnerem Å, Ghasem-Zadeh A, Bui M, Wang X, Rantzau C, Nguyen TV, et al. Remodeling markers are associated with larger intracortical surface area but smaller trabecular surface area: a twin study. Bone. 2011;49(6):1125-30.
76. Clarke BL, Khosla S. Physiology of bone loss. Radiologic Clinics. 2010;48(3):483-95.
77. Vanderschueren D, Vandenput L, Boonen S, Lindberg MK, Bouillon R, Ohlsson C. Androgens and bone. Endocr Rev. 2004;25(3):389-425.

CHAPTER 2

High Resolution–peripheral Quantitative Computed Tomography

High Resolution–peripheral Quantitative Computed Tomography (HR-pQCT)

Introduction

Improving prediction of fragility fracture and obtaining insights into the pathophysiology of bone fragility requires quantification of the three-dimensional macro and microstructure of bone. X-ray computed tomography (CT) is an established method that achieves this goal. The first commercial x-ray CT scanner for medical diagnosis was made available by Hounsfield in 1971 (1). Improved efficiency of x-ray tubes and x-ray photon detectors have enhanced the quality and resolution of acquired images and created opportunities for the development of peripheral quantitative computed tomography (pQCT) scanners with 300 micrometres resolution and more recently for the development of high-resolution pQCT, (HR-pQCT) in 2005. HR-pQCT, with 82 micrometres (µm) isotropic voxel size, equal on x, y and z directions, and 2nd generation of HR-pQCT with 61 µm voxel size have a resolution permitting the quantification of bone microarchitecture of the distal radius and distal tibia. These improvements have made HR-pQCT the only *in- vivo* computed tomography scanner able to quantify trabeculae and cortical morphology in humans. Trabeculae thickness varies between 100-150 micrometre (µm) (2) and images with 82 or 61 µm voxel size are able to illustrate the dimension of trabeculae of human bones.

HR-pQCT acquires images based on the same principles as clinical CT scanners but does so at a higher resolution (due to smaller voxel size) with a trade-off of a smaller scanning field of view (a smaller scanning region of interest) but a reduction in radiation exposure of 5 micro Sievert (µSv) (3, 4). Limitations in the size of the region of interest permits scanning of peripheral sites only, such as the distal radius and distal tibia. The terminologies used for HR-pQCT image acquisition are shown in **Table 2.1**.

Table 2.1. Key parameters for HR-pQCT images acquisition.

Variable	Description	Unit
Voxel size	Three-dimensional discrete unit of a tomographic image	μm^3
X-ray energy (kVp)	Applied peak electric potential of X-ray tube that accelerates electrons generating X-ray photons	keV
Integration time	Duration of each tomographic projection	ms
Frame averaging	Number of repeated measurements at each tomography projection	n
Projections	Number of tomographic viewpoints used for reconstruction	n

μm^3: micrometer cube; ms: millisecond

During the last 18 years, HR-pQCT has been implemented as *in-vivo* method to quantify volumetric bone mineral density (vBMD), bone microstructure of cortical and trabecular compartments, of the distal radius and distal tibia. Applications of HR-pQCT include the assessment of growth and age-related changes in trabecular and cortical morphology (5-7) in males and females of different racial/ethnic origins, identification of risk factors associated with fragility fractures (8, 9) , bone mineral density and microstructure associated with pregnancy, lactation and diseases influencing bone metabolism (10-14), the effects of pharmaceutical interventions on bone microstructure (15), and the role of physical activity on bone (16).

Image Acquisition

Appropriate positioning of the patient's forearm and lower leg into the scanner gantry and correctly identifying the region of interest are essential to producing reliable imaging. As cortical and trabecular microarchitecture varies from millimetre to millimetre along the length

a bone, an error in position of even a few millimetres produces large errors in microstructure, errors that may be greater than age- or disease related changes (17).

The carbon fibre casts, designed and provided by the manufacturer (Scanco) should be used to immobilise the limbs to minimise movement during scanning that produces motion artefacts (3). The non-dominant limb is scanned provided there is no history of fracture or surgery, and no metal or fistula, otherwise the contralateral limb is scanned.

Once the limb is positioned in the gantry a plain x-ray or 'scout view' is obtained. This 2D image is used to define the region of interest to be scanned. The reference line is manually placed at the endplate of the distal radius and tibial plateau. As a default, the first axial slice is started at 9.5 mm at the distal radius, and 22.5 mm at the distal tibia, respectively (**Fig 2.1, 2.2**).

Figure 2.1. Positioning and HR-pQCT scanning of the distal radius (left panel) and the distal tibia (right panel).

Position of the region of interest and its effect on bone microstructure

There are two approaches used to define the scanning region of interest:

i) fixed offset distance

ii) relative offset distance, also known as the %-of-length offset

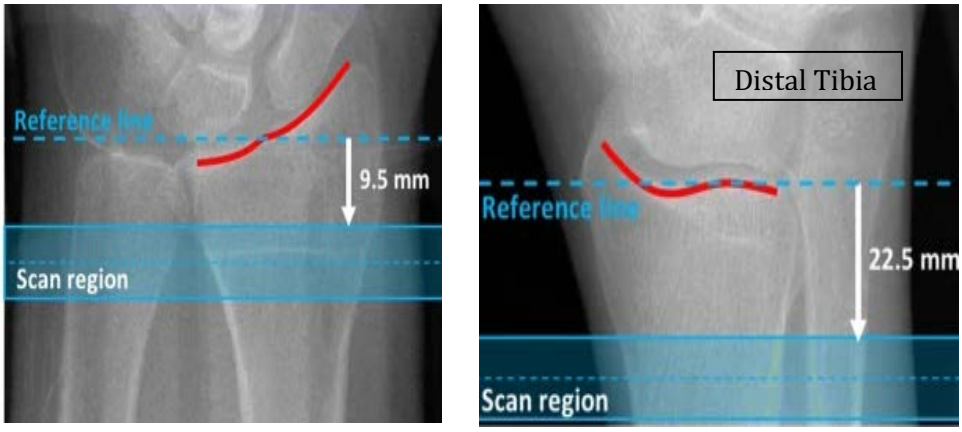

Figure 2.2. Location of scanning ROI of distal radius (left panel) and the distal tibia (right panel).

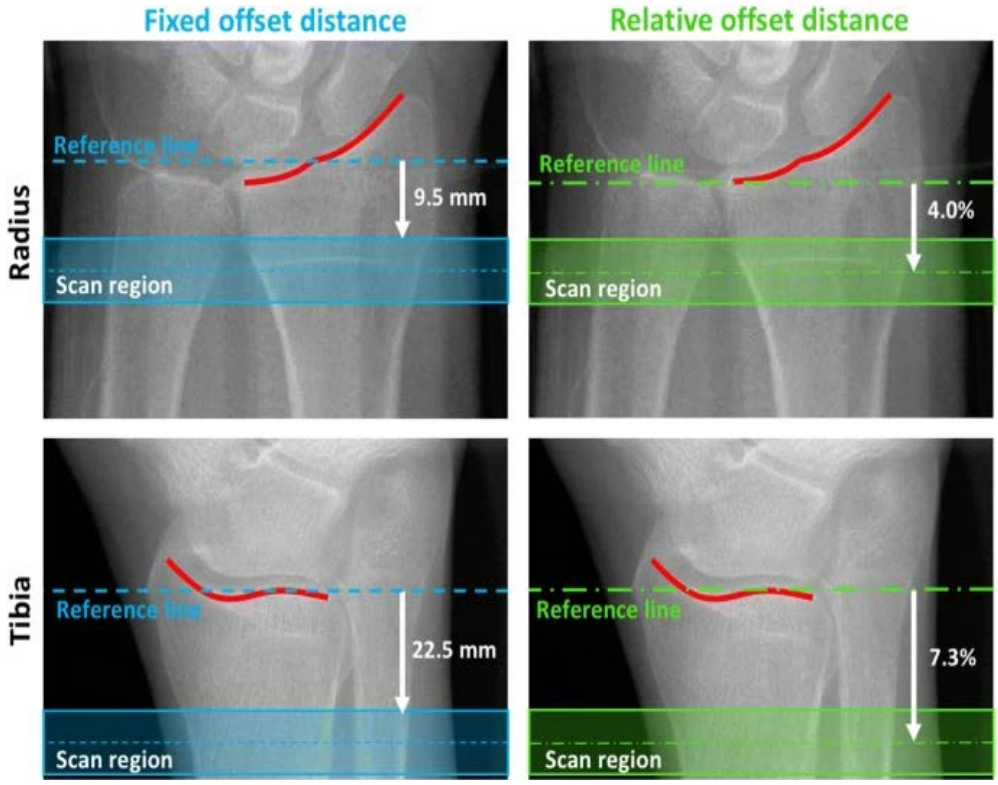

Figure 2.3. Comparison of reference line placement and distances between reference line and region of interest between fixed distance and relative offset distance. The place of reference line and distance between reference line and scanned ROI is based on forearm or tibia length.

Due to regional heterogeneity in bone microstructure point by point along the length of the distal radius or tibia, when the effects of growth, advancing age, sex, race, or drug therapy are quantified using HR-pQCT, the region of interest chosen must be anatomically comparable otherwise differences or absence of differences in microstructure may be the result of positioning errors, not bone biology. Using the fixed distance introduces significant errors as the region of interest in a taller person with longer limbs is more distal than in a shorter person with shorter limbs so comparison between males and females, and different racial groups that differ in size can result in measurements that are attributable to positioning not biology. On average, men and Caucasians have longer and wider bones than women and Asians, respectively (17). The influence of positioning the region of interest is discussed in the published papers in BONE (please see chapter 3), an invited manuscript published in the Journal of Clinical Densitometry (18) and a letter to the editor published in JBMR (19).

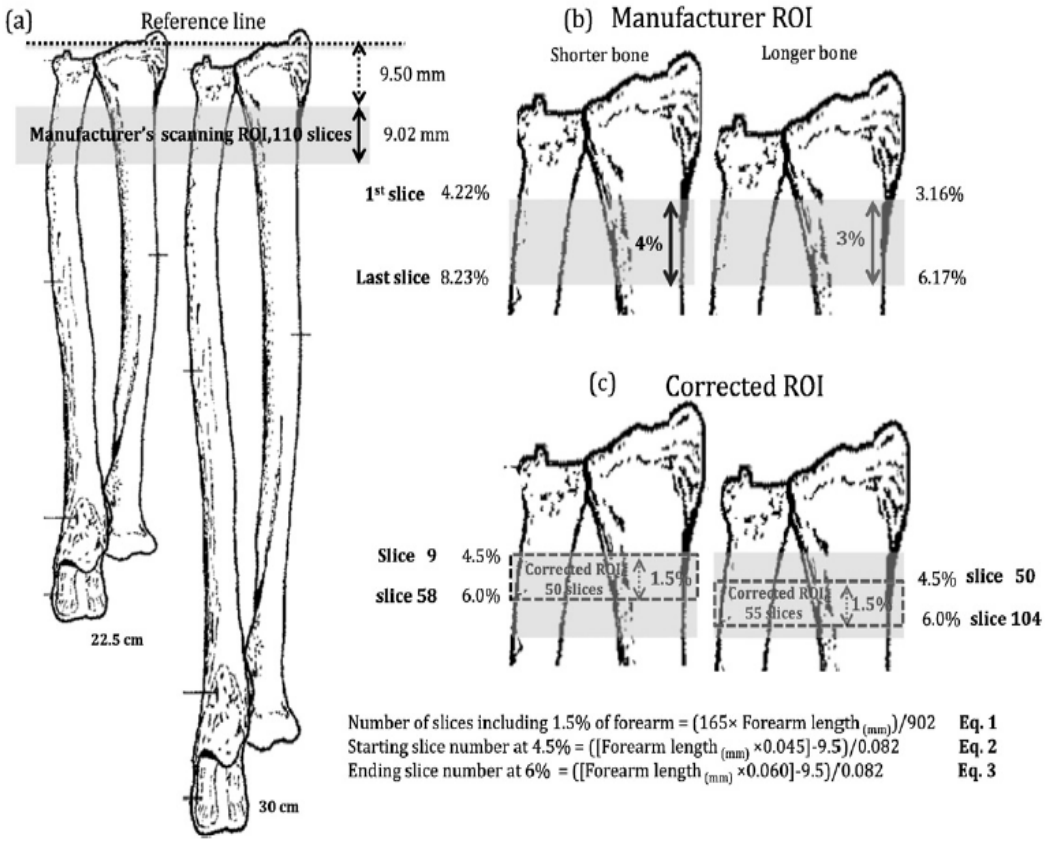

Figure 2.4. (a) The reference line corresponds to the mid-radiocarpal joint. The manufacturer's fixed ROI (grey rectangle) consists of 110 slices on the shorter (22.5 cm) and longer (30 cm) forearms. (b) The fixed ROI is 4% of the shorter bone and 3% of the longer bone. Positioning is more proximal for the shorter forearm (4.22–8.23% vs 3.16–6.17%). (c) Calculation of the number of slices and location of the corrected ROI is obtained using Eqs. (1)– (3) to identify 1st and last slices of the 110 slice ROI.

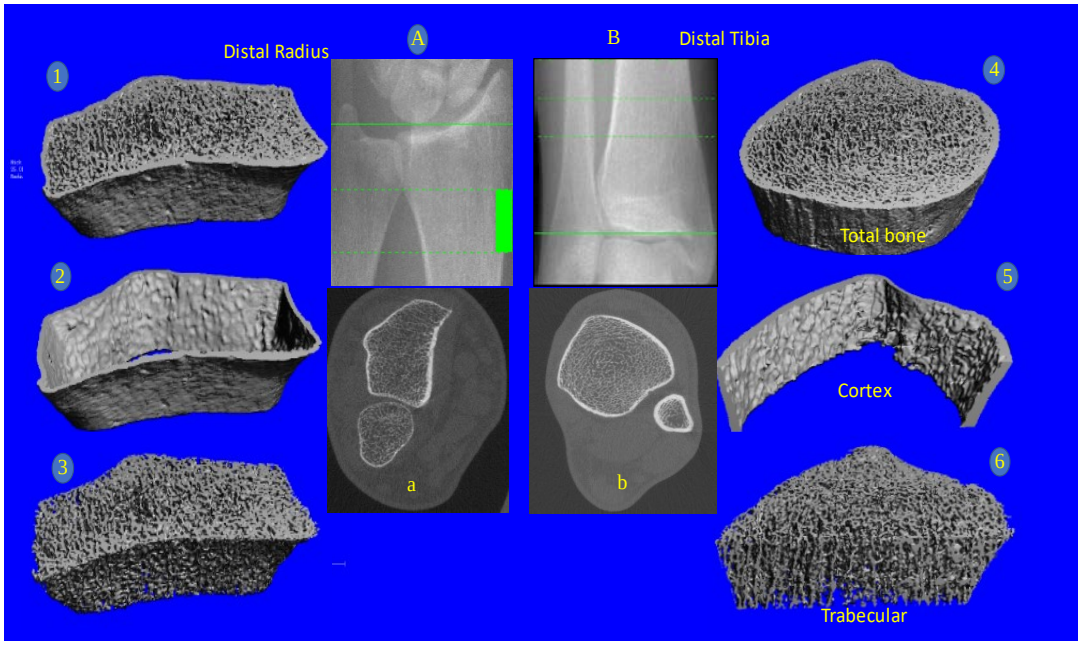

Figure 2.5. (A) The scout view of distal forearm and the reference line and identifying the scanning region of interest (doted lines). (B) The scout view of distal leg and the reference line and identifying the scanning region of interest (doted lines). (a) axial image of distal radius and ulna, (b) axial image of distal tibia and fibula. (1-3) total bone, cortical, and cortical compartment of distal radius, (4-6) total bone, cortical, and cortical compartment of distal tibia, respectively.

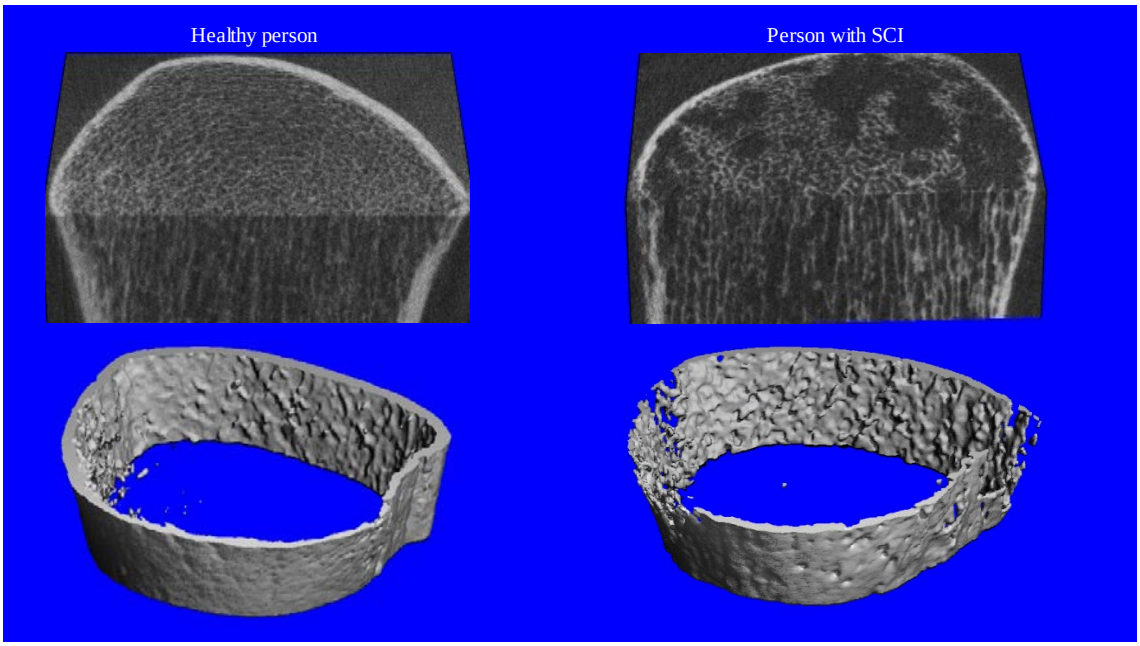

Figure 2.6. Comparison the distal tibia of healthy person with person with spinal cord injury. Thinner and porose cortex and deteriorated trabecular compartment with relatively thinner, fewer, and higher inhomogeneity of trabecular compartment are manifestation of deteriorated distal tibia in person with spinal cord injury.

Voxel size and its effect on bone structural analysis

Several parameters associated with reconstructing high-resolution images affect the quality of the images. The voxel size of images plays an important role on determining image quality and accuracy of measures of microstructure.

A 'voxel' describes the smallest distinguishable box-shaped part of a three-dimensional image. Larger voxel size reduces the resolution and quality of images, leading to increased noise, artefacts and loss of sharpness, each of which compromise the image quantification.

Trabecular bone loss, reduction in the number of trabeculae, thinning, and disconnection of trabeculae are hallmarks of bone loss. High resolution-CT images are able to capture these changes in response to aging or disease. Furthermore, monitoring these changes during treatment can offer valuable insights into the effectiveness of interventions aimed at reversing bone loss., Trabeculae thickness varies between 50-150 µm with an average 50 µm of

trabeculae packets (20), so any CT images with resolutions more than 100 µm will not be able to measure trabecular morphology directly. **Fig 2.8**. shows the femoral neck of human cadaveric bone scanned using a clinical CT scanner, with different voxel sizes and reconstructed with different image reconstruction algorithm. The same region of the femoral neck is scanned by HR-pQCT with 82 and 41 isotropic voxel sizes. As shown in the images, improving the resolution, individual trabeculae and larger cortical pores become visible. Blurred clinical CT images make cortical and trabecular segmentation challenging and limit the accuracy of the vBMD measurement of cortical and trabecular compartments.

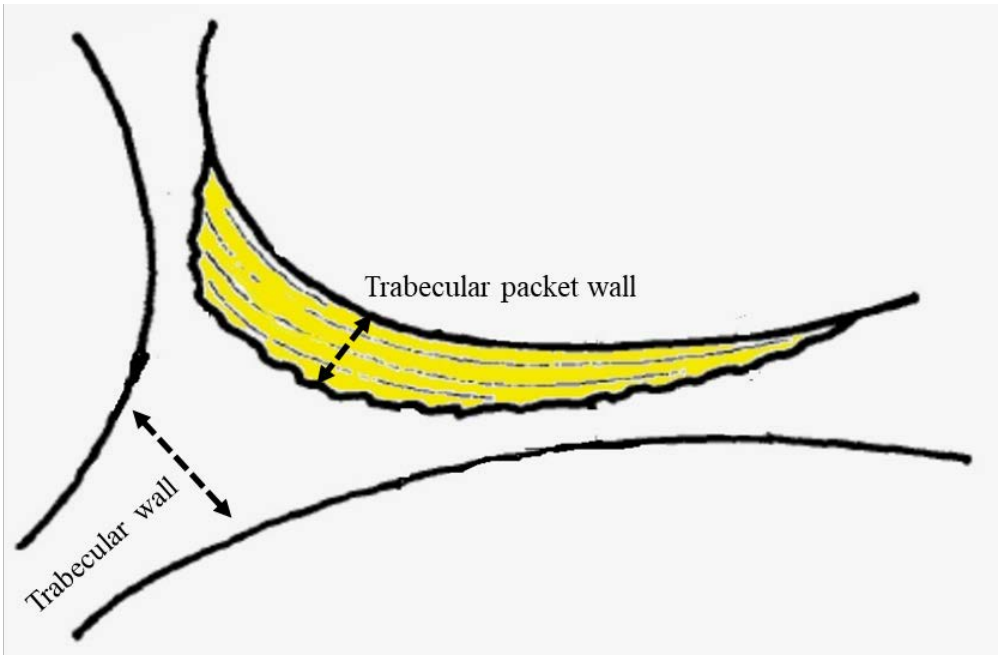

Figure 2.7. Trabecular bone packet with an average 50 µm thickness from the cement line to the border, facing the marrow cavity of a human lilac crest. Modified from reference 19.

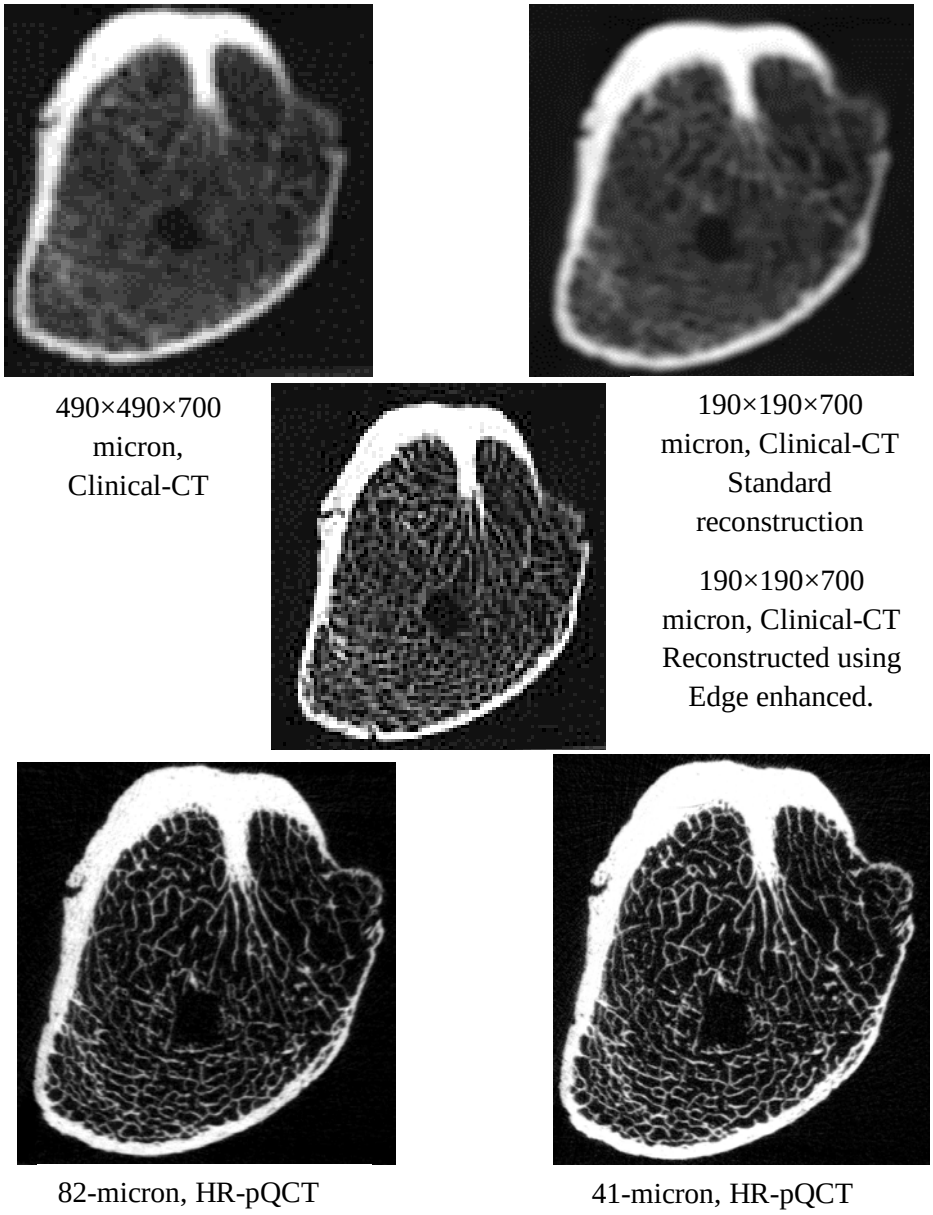

Figuer 2.8. Comparison of cadaveric femoral neck axial images scanned at different resolutions.

Beam hardening

X-ray beams are composed of photons with different energies. As the x-ray beam is transmitted through an object, it becomes 'harder'. The mean energy of residual photons increases because the lower energy photons are attenuated more than high-energy photons

(21). During interaction of x-ray photons with heterogeneous material composition like bone (which comprises a low density trabecular compartment with marrow surrounded by the high-density cortex, lower energy photons are attenuated by higher density material in the path of the x-ray beam, generating a higher energy transmitted x-rays beam. Tissues like fat or water in the trabecular compartment can no longer attenuate higher energy beam resulting in an underestimated linear attenuation profile or apparent density of the trabecular compartment.

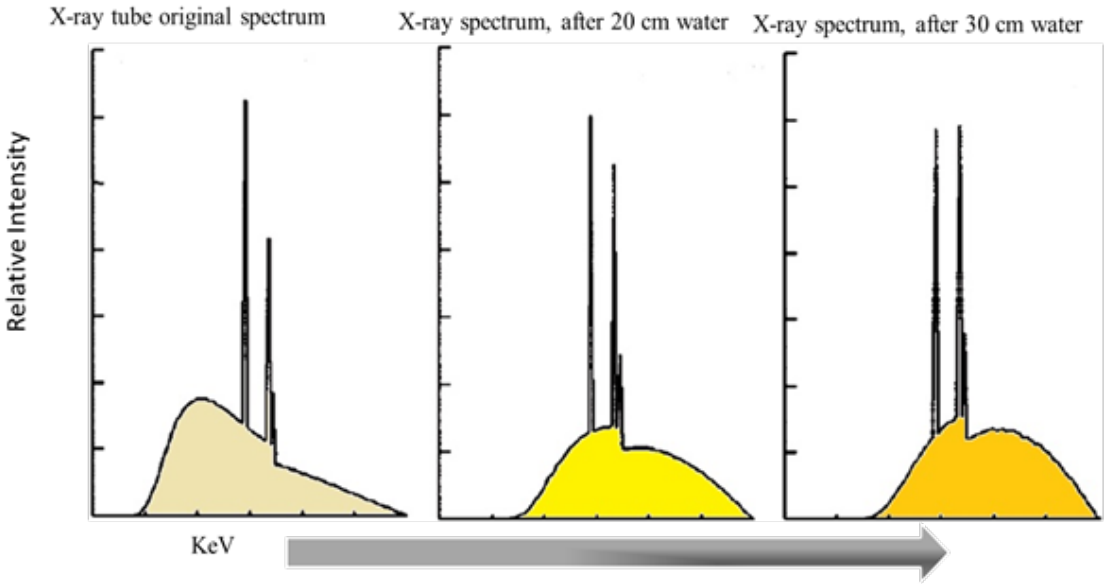

Figuer 2.9. Changing energy spectrum of an x-ray beam as it passes through water. The mean energy of photons elevated with depth. The attenuated spectra have been rescaled to be equivalent in size to the unattenuated spectra.

Aluminium and copper filters on pQCT and HR-pQCT x-ray tube scanners partly compensate for beam hardening by first attenuating the lower energy photons. In addition, the image reconstruction algorithm of a HR-pQCT scanner is able to reduce the beam hardening by applying a beam hardening image reconstruction filter **(Fig.2. 9,10**)

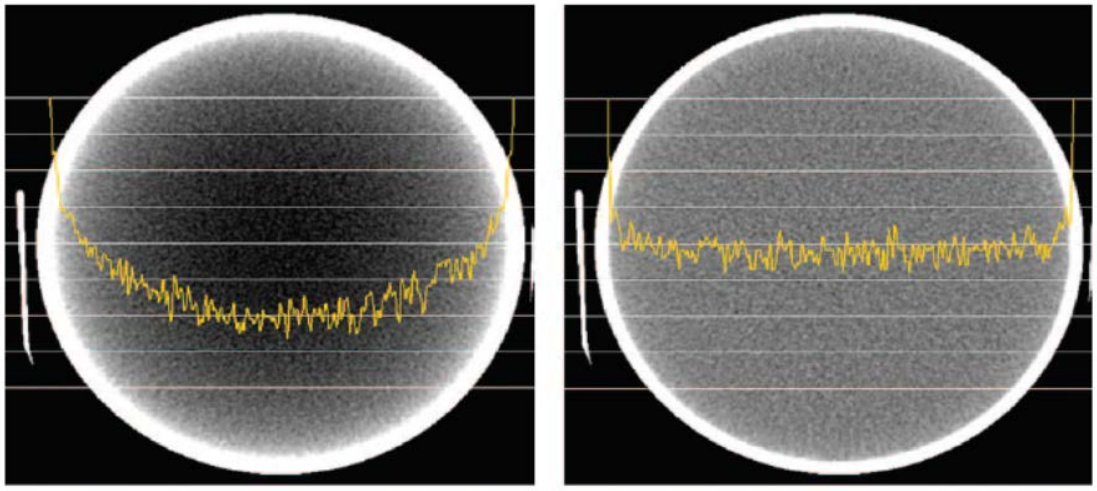

Figure 2.10. Density profile obtained across the centre of a uniform water phantom without beam hardening calibration correction (left panel) and after calibration correction (right panel).

Partial volume effects

Each voxel in a CT image represents the attenuation properties of the volume of the material within the voxel. If that volume is comprised of a number of different substances, then the resulting CT value represents the average of their x-ray photon attenuation values. This is the 'partial-volume effect'. Within CT images with larger voxel size boundaries may be blurred because the materials in any voxel can affect CT values of surrounding voxels. This artefact reduces the sharpness of the CT images and compromises accurate quantification of the structure. For example, in HR-pQCT this artefact affects the direct measurement of trabeculae, or small pores in cortical bone. Improvement in image resolution reduces the effect of this artefact. Non-threshold-based image analysis also addresses this problem in segmenting cortical from trabecular bone. In addition to figure 6, figure 9 shows the effect of images resolution and partial volume effect on cortical and trabecular measurements. By using larger voxel size some parts of trabecular area is included as part of the cortex which then reduces the vBMD of cortex. Table 2 shows the comparison of cortical thickness and vBMD of two images.

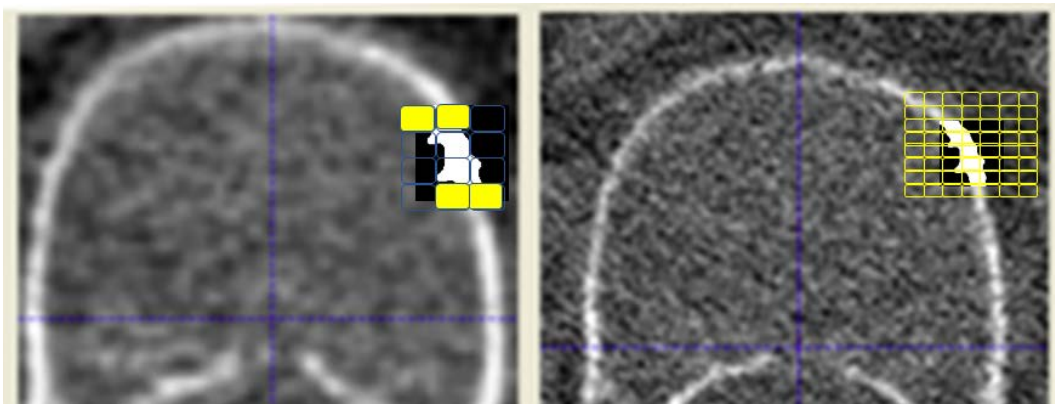

Figure 2.11. Comparison of vertebral body scanned by clinical CT-Scanner with different resolution.

Table 2.2. Comparison of cortical thickness and cortical vBMD measurement of vertebrae body scanned by different resolution.

	Voxel size	**Voxel size**
	0.72× 0.72 × 3 mm	0.16 × 0.16 × 0.33 mm
Cortical Thickness	3.3	1.9
Cortical vBMD (mg/ccm)	133	255

μm^3: micrometer cube; ms: millisecond. Relatively lower cortical thickness and higher cortical vBMD in the images with better resolution indicates the important influence of partial volume effects when analysing bone structure. These effects need to be carefully considered and accounted for to ensure accurate interpretation of cortical parameters and their implications for bone microstructure assessment.

Motion (movement) artefact

The image acquisition for the distal radius or tibia using HR-pQCT is around 3 minutes. Although the carbon fibre holder reduces motion artifact, this remains a problem for people, who are unable to remain still for the duration of image acquisition in particular teenagers and very old adults. Motion artefact occurs in 30% of people and most often at the distal radius. This artefact degrades the quality of images and resulting errors in the quantification of bone microstructure. In longitudinal studies, motion artefact may introduce an error in slice matching used to find the same region of interest between baseline and followed up images. Axial images with motion artefact influence the estimated total, cortical and trabecular cross-sectional areas, so finding the common number of slices (matched slices) is challenging in prospective studies. The HR-pQCT manufacturer (Scanco) suggested to record the type of motion artefact and grade them based on severity (**Fig. 2.12**).

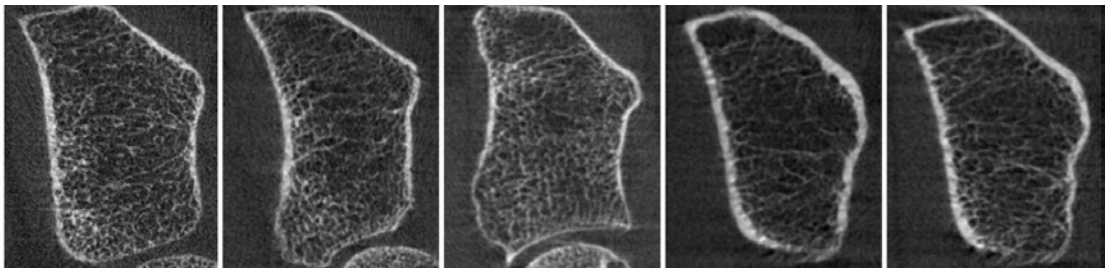

Figure 2.12. Image quality grading guideline suggested by the manufacturer. **a**) no visible motion artefact-acceptable for analysis, **b**) very slight artefacts- acceptable for analysis **c**) horizontal streaks visible-acceptable only for cortical and trabecular densities **d**) large horizontal streaks visible- not acceptable for analysis **e**) major horizontal streaks visible- not acceptable for analysis.

The detection of participants with motion artefacts is not confined to HR-pQCT imaging (22). The detection and correction of motion artefact is part of the three-dimensional computed tomography image reconstruction process. However, due to higher resolution, cone beam-based x-ray flux, and relatively longer scanning time, the frequency of motion artefact is higher in HR-pQCT imaging. Sode et al and others considered the effect of motion artefacts

on quality of images and suggested a quantitative technique for measuring motion in HR-pQCT images (23, 24). They developed a method of 'mirrored parallel projection' based on the assumption that if there was no motion, parallel projection images at 0° and 180° would be mirror images. Any differences between these two parallel projections are assumed to be due to motion during the image acquisition. Therefore, by comparing the differences between parallel projection images at 0° and mirrored parallel projection images at 180° using a similarity measure, the participant with motion artefact will be identified.

These investigators developed an equation (quantitative motion estimates, QMEs) to classify the magnitude of motion artefacts. They reported that coefficients of variation for the trabecular structure indices were larger than for the densitometric and cortical geometry indices due to motion artefact (23). This is attributed to motion artifacts, which can introduce additional variability in the assessment of trabecular structure.

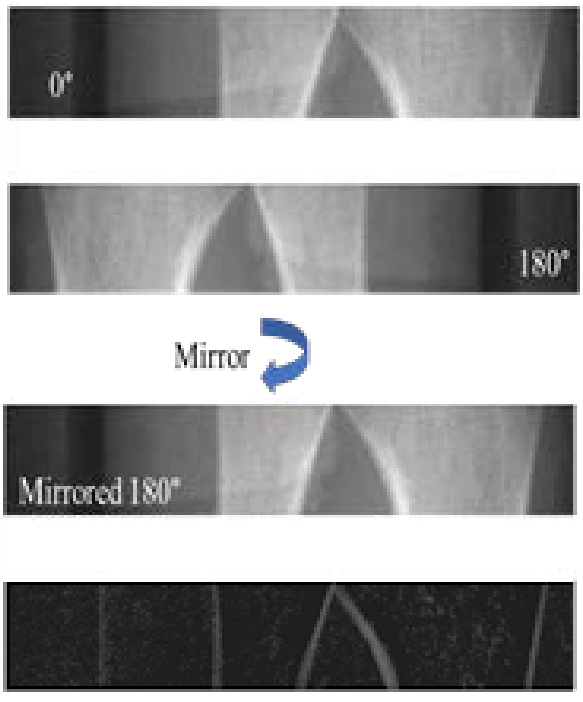

Figure 2.13. Schematic drawing explaining the analysis process of mirrored parallelized projection. The 180° projection was mirrored and compared to the 0° projection to estimates of motion. For the ideal case where there is no motion, the difference image between the two parallelized projection images should be zero.

Despite the development of algorithms aimed at mitigating the impact of motion artifacts on image quality, it is crucial to prioritize careful scanning techniques to minimise the occurrence of such artifacts. In addition to considering the age and sex of participant, it is important to acknowledge that the presence of motion artifacts during scanning is influenced by the conditions of the scanning environment. Factors such as

additional noise, a busy office, or the presence of friends or relatives can increase the likelihood of patient interruptions and involuntary movements, particularly in the upper extremities.

X-ray tube malfunctioning or failure

Consistency in generating x-ray beam with a sufficient photon flux is very important during HR-pQCT scanning. This is because the acquired images are used to quantify bone mineral density and bone microstructure parameters. Maintaining a consistent x-ray tube output ensures that the acquired images have consistent quality and provide reliable information about bone density and microstructure. It helps in reducing variability and ensures that measurements can be compared accurately over time and across different participants. To ensure the accuracy and reliability of HR-pQCT scans, it is recommended to perform pre-calibration procedures at regular intervals, specifically every 15 minutes and before each scanning session. Pre-calibration involves verifying and adjusting the scanner's settings and parameters to ensure proper functionality and consistent output.

In addition to ensuring the consistency of x-ray flux over short-term intervals, it is crucial to address the long-term consistency of the x-ray tube in HR-pQCT imaging. To address this, regular monitoring and maintenance of the x-ray tube should be implemented. This includes periodic inspections to assess the tube's performance and detect any signs of degradation or wear. Additionally, scheduled replacements or refurbishments of the x-ray tube may be necessary to ensure optimal imaging quality. However, the specific timing of these replacements will depend on the frequency of x-ray tube usage and may vary accordingly. In the production of x-rays less than 1% of the energy produces useful x-rays while the remaining 99% is transformed into heat. X-ray tubes have a limited lifespan because the characteristics and materials used begin a gradually degrade so performance gradually decreases until they

compromise photon flux. X-ray tube ageing, filament burn out, slow leaks, long term inactivity, glass crazing and target micro-cracking are the causes of x-ray tube failure; however, the arcing (connecting anode and cathode) is the most common cause of x-ray tube failure. Aging and losing the vacuum level are common reasons of x-ray tube arcing. In HR-pQCT systems, the average lifespan of the x-ray tube is approximately four years.

Detectors malfunctioning and ring artefact

Detectors play a critical role in HR-pQCT imaging by capturing the x-ray signals that pass through the scanned object. However, like any electronic component, detectors can experience malfunctions that can impact the quality and reliability of the imaging process. It can manifest in various ways including a complete failure, where the detector does not capture any signal, resulting in missing data for that specific region of interest. Partial malfunctioning may occur, leading to reduced sensitivity or inconsistent signal detection. This can result in inaccurate measurements, artifacts, or variations in image quality across different regions. To address this issue, regular quality control procedures are essential. These procedures involve periodic performance testing, calibration, and maintenance of the detectors. Quality control tests assess the detector response, linearity, uniformity, and stability. If any malfunctions or deviations from the expected performance are detected, appropriate actions can be taken, such as recalibration, repair, or replacement of the malfunctioning detector.

Ring artifacts are a common image artifact that can occur in any x-ray based computed tomography imaging. These artifacts appear as circular or semi-circular patterns in the reconstructed images and can impact the accurate assessment of bone microstructure.

Ring artifacts in HR-pQCT typically result from variations in detector sensitivity or inconsistencies in x-ray attenuation across the field of view. These variations can arise due to factors such as variations in the detector response, inhomogeneities in the x-ray beam intensity, or imperfections in the imaging system.

The presence of ring artifacts can introduce distortions and inaccuracies in the image data, potentially affecting the quantification and analysis of bone microstructure parameters. They can obscure fine details and structures of interest, making it challenging to extract accurate measurements.

To address ring artifacts in HR-pQCT or micro-CT, various techniques and algorithms have been developed (25). These methods aim to correct or minimise the impact of the artifacts on the image quality and data analysis. Common approaches include advanced image processing techniques such as filtering, interpolation, and Fourier-based methods. These methods aim to remove or reduce the ring artifacts while preserving the integrity and accuracy of the underlying image information.

Regular quality control procedures, including calibration and system maintenance, are crucial in managing and minimizing ring artifacts. By ensuring proper system calibration, optimising imaging parameters, and utilising appropriate image reconstruction algorithms, the occurrence and impact of ring artifacts can be moderated.

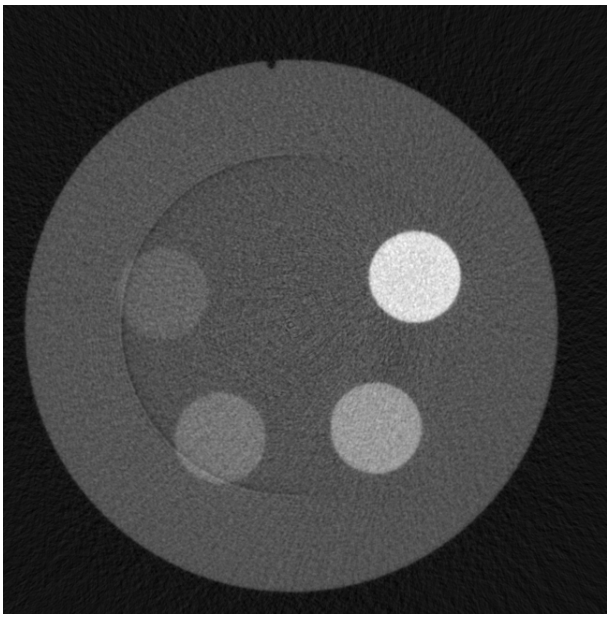

Figure 2.14. A big ring artefact in HR-pQCT density quality control phantom

Detectors and x-ray tube replacement

The detectors and x-ray tube replacement in HR-pQCT systems are essential for ensuring the optimal performance and accuracy of the imaging process. Over time, the detectors and x-ray tube in HR-pQCT scanners may experience functional deficiency. The fine calibration of x-ray tube and controlling the function of detectors is important for HR-pQCT scanning because as it is used to quantify structure, so any drift in mean energy x-ray beam or detector functions,

after replacement, will be leading to over/underestimation of bone mineral density and consequently bone microstructure. The HR-pQCT manufacture calibrates the function of scanner using density and geometry phantoms by scanning them several time after x-ray tube or detectors replacement.

Limitation of HR-pQCT on prediction of fragility fracture

A large number of microstructural parameters are available from HR-pQCT. There is currently no global agreement regarding which combination of measurements best predict the risk of fracture with high sensitivity and specificity (26-28). Bone is hierarchical structure with varying macro-, micro-, and nano-structural components (29) and collagen matrix, the water content (30). Measurement of porosity alone or trabecular density alone are not predictive of prevalent or incident fractures (31). Bone loss affects both cortical and trabecular compartments. We therefore developed the 'Structural Fragility Score' (31) which captures the deterioration in both cortical and trabecular compartments expressed as the increase in cortical porosity and decrease in trabecular density relative to the mean of each trait in premenopausal healthy women. We have now shown that this surrogate of bone fragility identifies women with prevalent fractures and women having incident fractures with 70% sensitivity and specificity (32). Further work is underway to improve the predictive strength of measurements of bone microstructure.

Future direction of HR-pQCT on prediction of fragility fracture

The future of use of HR-pQCT in identifying women and men at high risk of fragility fractures holds promising opportunities. Improving imaging quality and resolution will permit more accurate quantification of the microstructure of bone responsible for its strength. Advances have occurred in the use of artificial intelligence and deep learning for image analysis of large data sets. For example, we have shown that using only the three-dimensional image of the bone acquired using HR-pQCT (no other characteristics of the patient or the illness), it is possible to

identify and distinguish women having incident fractures from those women remaining fracture-free. the simplicity of this approach opens doors to wide-spread rapid screening of individuals (33).

A clinical aspect I am interested in assessing is the frequency distribution of microstructural parameters within young adult, pre-peri-, and postmenopausal women, and in men. Determining whether or not bone microstructural traits such as trabecular number, thickness, or cortical porosity are normally distributed or have a skewed distribution is unknown and has important implications. If the microstructural components become skewed as age advances, it implies that some individuals lose bone faster than others, and this skewing may help identify a threshold for detecting those at a high risk of fracture. Future studies are needed to determine material properties and other traits contributing to bone strength, for example, bone's external dimensions, its size bares a power relationship with its compressive and bending strength. Changes in the mineral content or matrix mineral density have an important effect on the stiffness of the matrix of bone. In addition, bone's water content also determines its strength. HR-pQCT is able to quantify external bone dimensions and matrix mineral density in vivo while newer methods of MRI can be applied to measure bone hydration, its water content. These advances make it possible to begin to explore the hierarchical basis of bone strength and the structural basis of the age-related loss of bone strength predisposing to fragility fractures.

Future direction of clinical CT on quantitative bone imaging

Photon Counting Detector - CT is a novel technology employing small detector elements to record individual photon interactions with scanned materials. PCD-CT offers several advantages, including enhanced spatial resolution, reduced electronic noise, improved contrast, and superior image quality. One of the key benefits of PCD-CT is its ability to differentiate between various material densities in scanned objects. However, this technique has a limitation

on bone microstructure assessment due to relatively larger pixel size (250 microns) at the moment (34).

Summary

HR-pQCT, as an in-vivo imaging technique in human, is an advanced imaging technique that offers high-resolution, and three-dimensional images of bone microstructure, enabling the evaluation of bone density and analysis of bone microarchitecture at peripheral skeletal sites. However, to fully harness the potential of HR-pQCT as a valuable tool in bone research, clinical diagnosis, and bone health monitoring, it is essential to overcome the associated technical challenges. Continuous advancements in image acquisition techniques, data processing algorithms, and standardisation efforts contribute to improving the accuracy, reproducibility, and clinical utility of HR-pQCT. By addressing these technical challenges, HR-pQCT can further establish itself as a valuable tool for advancing bone research, facilitating accurate clinical diagnoses, and monitoring bone health.

References

1. Hounsfield GN. Computerized transverse axial scanning (tomography). 1. Description of system. The British journal of radiology. 1973;46(552):1016-22.
2. Wehrli FW. Structural and functional assessment of trabecular and cortical bone by micro magnetic resonance imaging. Journal of magnetic resonance imaging : JMRI. 2007;25(2):390-409.
3. Whittier DE, Boyd SK, Burghardt AJ, Paccou J, Ghasem-Zadeh A, Chapurlat R, et al. Guidelines for the assessment of bone density and microarchitecture in vivo using high-resolution peripheral quantitative computed tomography. Osteoporos Int. 2020;31(9):1607-27.
4. Geusens P, Chapurlat R, Schett G, Ghasem-Zadeh A, Seeman E, de Jong J, et al. High-resolution in vivo imaging of bone and joints: a window to microarchitecture. Nature reviews Rheumatology. 2014;10(5):304-13.
5. Macdonald HM, Nishiyama KK, Kang J, Hanley DA, Boyd SK. Age-related patterns of trabecular and cortical bone loss differ between sexes and skeletal sites: a population-based HR-pQCT study. Journal of bone and mineral research : the official journal of the American Society for Bone and Mineral Research. 2011;26(1):50-62.
6. Burt LA, Liang Z, Sajobi TT, Hanley DA, Boyd SK. Sex- and Site-Specific Normative Data Curves for HR-pQCT. Journal of bone and mineral research : the official journal of the American Society for Bone and Mineral Research. 2016;31(11):2041-7.
7. Dalzell N, Kaptoge S, Morris N, Berthier A, Koller B, Braak L, et al. Bone micro-architecture and determinants of strength in the radius and tibia: age-related changes in a

population-based study of normal adults measured with high-resolution pQCT. Osteoporos Int. 2009;20(10):1683-94.
8. Samelson EJ, Broe KE, Xu H, Yang L, Boyd S, Biver E, et al. Cortical and trabecular bone microarchitecture as an independent predictor of incident fracture risk in older women and men in the Bone Microarchitecture International Consortium (BoMIC): a prospective study. The lancet Diabetes & endocrinology. 2019;7(1):34-43.
9. Sornay-Rendu E, Boutroy S, Duboeuf F, Chapurlat RD. Bone Microarchitecture Assessed by HR-pQCT as Predictor of Fracture Risk in Postmenopausal Women: The OFELY Study. Journal of bone and mineral research : the official journal of the American Society for Bone and Mineral Research. 2017;32(6):1243-51.
10. Sampaio-Barros MM, Alvarenga JC, Takayama L, Assad APL, Sampaio-Barros PD, Pereira RMR. Distal radius and tibia bone microarchitecture impairment in female patients with diffuse systemic sclerosis. Osteoporos Int. 2019;30(8):1679-91.
11. Ghasem-Zadeh A, Galea MP, Nunn A, Panisset M, Wang XF, Iuliano S, et al. Heterogeneity in microstructural deterioration following spinal cord injury. Bone. 2021;142:115778.
12. Ramchand SK, Seeman E, Wang XF, Ghasem-Zadeh A, Francis PA, Ponnusamy EJ, et al. Premenopausal women with early breast cancer treated with estradiol suppression have severely deteriorated bone microstructure. Bone. 2017;103:131-5.
13. Bjørnerem Å, Ghasem-Zadeh A, Wang X, Bui M, Walker SP, Zebaze R, et al. Irreversible Deterioration of Cortical and Trabecular Microstructure Associated With Breastfeeding. Journal of bone and mineral research : the official journal of the American Society for Bone and Mineral Research. 2017;32(4):681-7.
14. Borschmann K, Iuliano S, Ghasem-Zadeh A, Churilov L, Pang MYC, Bernhardt J. Upright activity and higher motor function may preserve bone mineral density within 6 months of stroke: a longitudinal study. Archives of osteoporosis. 2018;13(1):5.
15. Tsai JN, Nishiyama KK, Lin D, Yuan A, Lee H, Bouxsein ML, et al. Effects of Denosumab and Teriparatide Transitions on Bone Microarchitecture and Estimated Strength: the DATA-Switch HR-pQCT study. Journal of bone and mineral research : the official journal of the American Society for Bone and Mineral Research. 2017;32(10):2001-9.
16. Gabel L, Macdonald HM, Nettlefold L, McKay HA. Physical Activity, Sedentary Time, and Bone Strength From Childhood to Early Adulthood: A Mixed Longitudinal HR-pQCT study. Journal of bone and mineral research : the official journal of the American Society for Bone and Mineral Research. 2017;32(7):1525-36.
17. Ghasem-Zadeh A, Burghardt A, Wang XF, Iuliano S, Bonaretti S, Bui M, et al. Quantifying sex, race, and age specific differences in bone microstructure requires measurement of anatomically equivalent regions. Bone. 2017;101:206-13.
18. Ghasem-Zadeh A, Seeman E. Challenges in the Use of Cross-Sectional Data to Quantify Growth and Deterioration of Bone Structure During Advancing Age. Journal of clinical densitometry : the official journal of the International Society for Clinical Densitometry. 2017;20(1):5-7.
19. Seeman E, Ghasem-Zadeh A. Challenges in the Acquisition and Analysis of Bone Microstructure During Growth. Journal of bone and mineral research : the official journal of the American Society for Bone and Mineral Research. 2016;31(12):2239-41.
20. Lips P, Courpron P, Meunier PJ. Mean wall thickness of trabecular bone packets in the human iliac crest: changes with age. Calcified tissue research. 1978;26(1):13-7.
21. Barrett JF, Keat N. Artifacts in CT: recognition and avoidance. Radiographics : a review publication of the Radiological Society of North America, Inc. 2004;24(6):1679-91.
22. Yu H, Wang G. Data Consistency Based Rigid Motion Artifact Reduction in Fan-Beam CT. IEEE Transactions on Medical Imaging. 2007;26(2):249-60.
23. Sode M, Burghardt AJ, Pialat JB, Link TM, Majumdar S. Quantitative characterization of subject motion in HR-pQCT images of the distal radius and tibia. Bone. 2011;48(6):1291-7.

24. Pauchard Y, Ayres FJ, Boyd SK, editors. Measuring patient motion in HR-pQCT. 2009 IEEE International Symposium on Biomedical Imaging: From Nano to Macro; 2009 28 June-1 July 2009.
25. Kyriakou Y, Prell D, Kalender WA. Ring artifact correction for high-resolution micro CT. Physics in Medicine & Biology. 2009;54(17):N385.

26. Mikolajewicz N, Bishop N, Burghardt AJ, Folkestad L, Hall A, Kozloff KM, et al. HR-pQCT Measures of Bone Microarchitecture Predict Fracture: Systematic Review and Meta-Analysis. J Bone Miner Res. 2020;35(3):446-59.
27. Cheung WH, Hung VW, Cheuk KY, Chau WW, Tsoi KK, Wong RM, et al. Best Performance Parameters of HR-pQCT to Predict Fragility Fracture: Systematic Review and Meta-Analysis. J Bone Miner Res. 2021;36(12):2381-98.
28. Samelson EJ, Broe KE, Xu H, Yang L, Boyd S, Biver E, et al. Cortical and trabecular bone microarchitecture as an independent predictor of incident fracture risk in older women and men in the Bone Microarchitecture International Consortium (BoMIC): a prospective study. Lancet Diabetes Endocrinol. 2019;7(1):34-43.
29. Seeman E, Delmas PD. Bone quality--the material and structural basis of bone strength and fragility. N Engl J Med. 2006;354(21):2250-61.
30. Nyman JS, Ketsiri T, Louie EA, Harkins KD, Manhard MK, Gochberg DF, et al. Toward the use of MRI measurements of bound and pore water in fracture risk assessment. Bone. 2023;176:116863.
31. Zebaze R, Atkinson EJ, Peng Y, Bui M, Ghasem-Zadeh A, Khosla S, et al. Increased Cortical Porosity and Reduced Trabecular Density Are Not Necessarily Synonymous With Bone Loss and Microstructural Deterioration. JBMR Plus. 2019;3(4):e10078.
32. Chapurlat R, Bui M, Sornay-Rendu E, Zebaze R, Delmas PD, Liew D, et al. Deterioration of Cortical and Trabecular Microstructure Identifies Women With Osteopenia or Normal Bone Mineral Density at Imminent and Long-Term Risk for Fragility Fracture: A Prospective Study. J Bone Miner Res. 2020;35(5):833-44.
33. Chapurlat R, Ferrari S, Li X, Peng Y, Xu M, Bui M, et al. Deep Learning Using High-Resolution Images of Forearm Predicts Fracture. eLife Sciences Publications, Ltd; 2023.
34. Klintström B, Henriksson L, Moreno R, Malusek A, Smedby Ö, Woisetschläger M, et al. Photon-counting detector CT and energy-integrating detector CT for trabecular bone microstructure analysis of cubic specimens from human radius. Eur Radiol Exp. 2022;6(1):31.

Accuracy, reproducibility, least significant changes of bone microstructure parameters measured using HR-pQCT and compatibility of the 1st and 2nd generation of HR-pQCT

Introduction

High Resolution-peripheral Quantitative Computed Tomography (HR-pQCT), as high-resolution imaging and quantitative modality, is an important tool that has advanced our understanding of bone morphology and microstructure deterioration, and so providing new targets for investigations and identifying persons at risk of fragility fracture. This imaging technique enables a more precise prediction of fragility fracture than conventionally used methods and enables the efficacy of anti-resorptive and anabolic agents to be evaluated within a relatively short period. Measurements and monitoring minute skeletal changes over time using any imaging modality require a high level of accuracy and precision. A lower precision error (i.e., better reproducibility) ensures the sensitivity of measurements in capturing changes or treatments effects.

Accuracy

The accuracy of HR-pQCT for measuring bone microstructure has been evaluated using *ex vivo* imaging of bone using Micro-CT as the gold standard. By assessing cadaveric bone morphology, some studies have shown moderate to good agreement for bone mineral density and bone microstructure have been observed between HR-pQCT and Micro-CT ($r^2 = 0.59–0.98$) (1-3).

High correlations between HR-pQCT and Micro-CT have been reported for other bone parameters such as trabecular connectivity density ($r^2 = 0.90$) (2), mechanical stiffness ($r^2 = 0.73$) (2) and

cortical porosity (based on manufacture's method) ($r^2 = 0.80$) (4). Liu et al. investigated the correlation between *Individual Trabecular* assessed using HR-pQCT compared to Micro-CT images of a equal voxel size (80 μm) and reported good correlation ($r = 0.71 - 0.94$), that were also observed for plate-like trabecular and rod-like trabecular (5).

Precision

While accuracy is important, the precision or reproducibility is even more important for prospective studies that rely on repeated measurements of *in-vivo* participants to assess the consistency and reliability of outcomes. Precision errors can arise from various factors, including the specifications of the scanner's image acquisition hardware, the process of image reconstruction, the algorithms used for analysis, the expertise of the operator (s), and the design of the study design considerations, including the age range and sex of the population under study.

Beside the hardware related errors, precision errors in HR-pQCT images are influenced by several important factors. These include motion artifacts (6, 7), the positioning of the participant, the placement of reference lines to define the scanning region of interest, manual adjustments of periosteal and endocortical contours (8-10), as well as the utilisation of registration techniques to align the common region of interest (11).

Volumetric bone mineral densitometry (vBMD) measured using HR-pQCT is highly reproducible. Many studies have reported below 1% precision errors for vBMDs. However, bone microstructural parameters such as trabecular number and inhomogeneity, have greater precision errors ranging from 2.5% to 6.3% (6, 12-14) .Finite Element Analysis, which incorporates a combination of vBMD and microstructural parameters, has precision errors falling between of vBMD and microstructural parameters (<3.5 %) (12).

Step-by-step evaluation of precision error of HR-pQCT

Measuring precision error for each imaging modality is crucial due to variations in scanner models, scanner manufactures, image reconstruction methods, and image processing software. These differences can significantly influence the precision of measurements obtained from different scanners, highlighting the need to assess precision error specific to each imaging modality.

Some sources of error in precision, such as those originating from the x-ray tube and detectors, are not under the control of the operator. These errors, often referred to as "inherent errors," originate from components of the imaging system itself and can contribute to the overall precision error. It is important to consider and account for these inherent errors when evaluating the precision of imaging measurements.

To investigate the overall level and sources of precision errors such as errors on image acquisition of scanner, images reconstruction process, software of analysis and errors related to operator (s), we have conducted a step-by-step assessment of the precision error of HR-pQCT.

Bone Density reproducibility

To assess the HR-pQCT scanner image acquisition and its software's precision error, the density quality control phantom, which contains 4 rods with density of 100, 200,400 and 800 mgHA/cm^3, all embedded in the epoxy resin with density equivalent to soft tissue (0 mgHA/cm^3) (**Fig 1**) is scanned 15 times consecutively without repositioning during single day and within three hours.

The coefficient of variation (CV) for each density rod was calculated using the mean and standard deviation (SD) based on Equation **1**.

$$\mathbf{CV}\% = \frac{\text{Standard Deviation}}{\text{Mean}} \times 100 \quad \textbf{Equation 1}.$$

Figure 1. Axial image of bone density quality control phantom (QC) of HR-pQCT scanner.

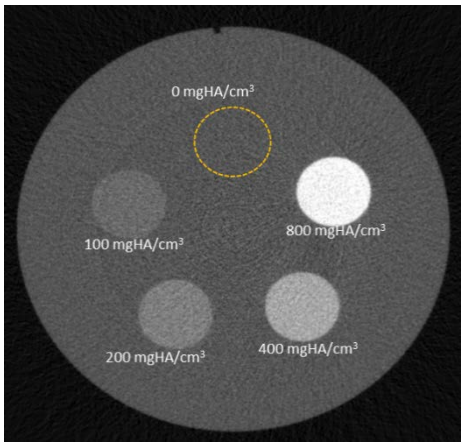

Figure 2.15 Axial image of bone density quality control phantom (QC)

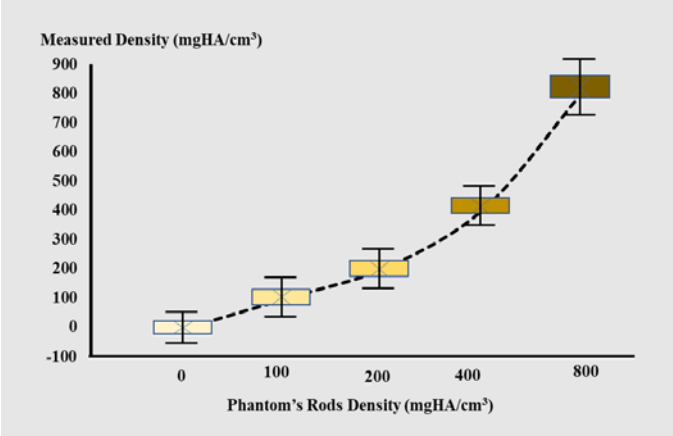

Figure 2.16 Right measured density *vs* actual density of rods of QC phantom.

Table 1 presents the mean, standard deviation (SD), and coefficient of variation (CV%) for each rod. Ideally, the density values of the rods would remain consistent when scanned at different times. However, the data in **Table 1** indicates slight errors for each rod. These variations can be attributed to two main factors:

i) Image acquisition process: The process of capturing tomographic images using the scanner can introduce variability, leading to differences in the density measurements of the rods.

ii) Image reconstruction and analysis algorithm: The algorithms used for reconstructing and analysing the acquired images may contribute to the observed variations in the density values of the rods.

It is important to consider these factors when interpreting the data and understanding the potential sources of error in density measurements.

Table 2.3. The mean, SD, and CV% of each rod of QC phantom scanned 10 times without repositioning

	Density of rod (mgHA/cm^3)				
	0	100	200	400	800
Mean(vBMD)	-1.33	101.17	203.41	407.98	803.88
SD	0.63	0.83	0.90	1.67	3.01
CV (%)	-*	0.82	0.44	0.41	0.37

HA=Hydroxyapatite, vBMD=Volumetric Bone Mineral Density, SD=Standard Deviation, CV= Coefficient Variation. * No CV% calculated for rod with 0 mgHA/cm^3.

Based on the principal of the interaction of photons with materials, and algorithm of the image reconstruction process on producing computed tomographic images, the CT images comprises different types of noises such as:

i) Gaussian noise: This type of noise follows a Gaussian distribution and is characterised by random variations in pixel values throughout the image. It can arise from various sources, such as *electronic noise* in the imaging system or statistical fluctuations, or *Quantum noise,* in the detected photons which is a fluctuation in the number of photons reaching the detector from point to point.

ii) Poisson noise: Poisson noise is inherent in imaging systems that rely on the detection of low-intensity photon counts. It is caused by the statistical nature of photon detection, resulting in fluctuations in the number of detected photons at each pixel. Poisson noise is more pronounced in regions with lower photon counts.

iii) Beam hardening artifacts: Beam hardening occurs when the poly chromatic x-ray beam passes through a material, causing preferential absorption of low-energy photons. This can result in streak or region(s) with low density artifacts in the reconstructed image, affecting the accuracy of density measurements.

iv) Ring artifacts: Ring artifacts manifest as concentric rings or arcs in the image and can occur due to irregularities or malfunctions in the CT detector array or errors in the calibration of the system. These artifacts can affect image quality and potentially impact quantitative analysis.

v) Motion artifacts: Motion during image acquisition, either from patient movement or involuntary physiological motion, can introduce blurring or streaking in the reconstructed image, leading to reduced image sharpness and potential misalignment of anatomical structures (15).

These type of noises or artefacts, which introduces precision errors, cannot be controlled by the operator(s), and are referred to as scanner's inherent errors.

In investigations using HR-pQCT, the relatively better CV% for high-density compartments (i.e., cortical vBMD) should be considered carefully due to the higher mean value density of cortex as a denominator. Because the density of cortical bone is higher than trabecular bone, resulting in a larger denominator when calculating the CV%. As a result, the CV% for cortical vBMD may appear lower compared to trabecular bone, which has a lower mean density. Therefore, while the relatively better CV% of the high-density compartment, such as cortical vBMD, can provide some reassurance, it is essential to carefully consider the underlying factors and interpret the results cautiously, taking into account the complexities of HR-pQCT measurements and the specific goals of the investigation.

Long term reproducibility

The long-term consistency and reproducibility of quantitative modalities is crucial for monitoring biological changes. As part of the quality assurance process, it is necessary to scan the quality control (QC) phantom daily before conducting HR-pQCT scans on participants.

In our department, the QC phantom has been scanned more than 24,000 times over the past 15 years. The following figures represent the long-term stability of the HR-pQCT scanner, with a few drifts that represent periods of detectors or x-ray tube failure or replacements (**Fig 3**).

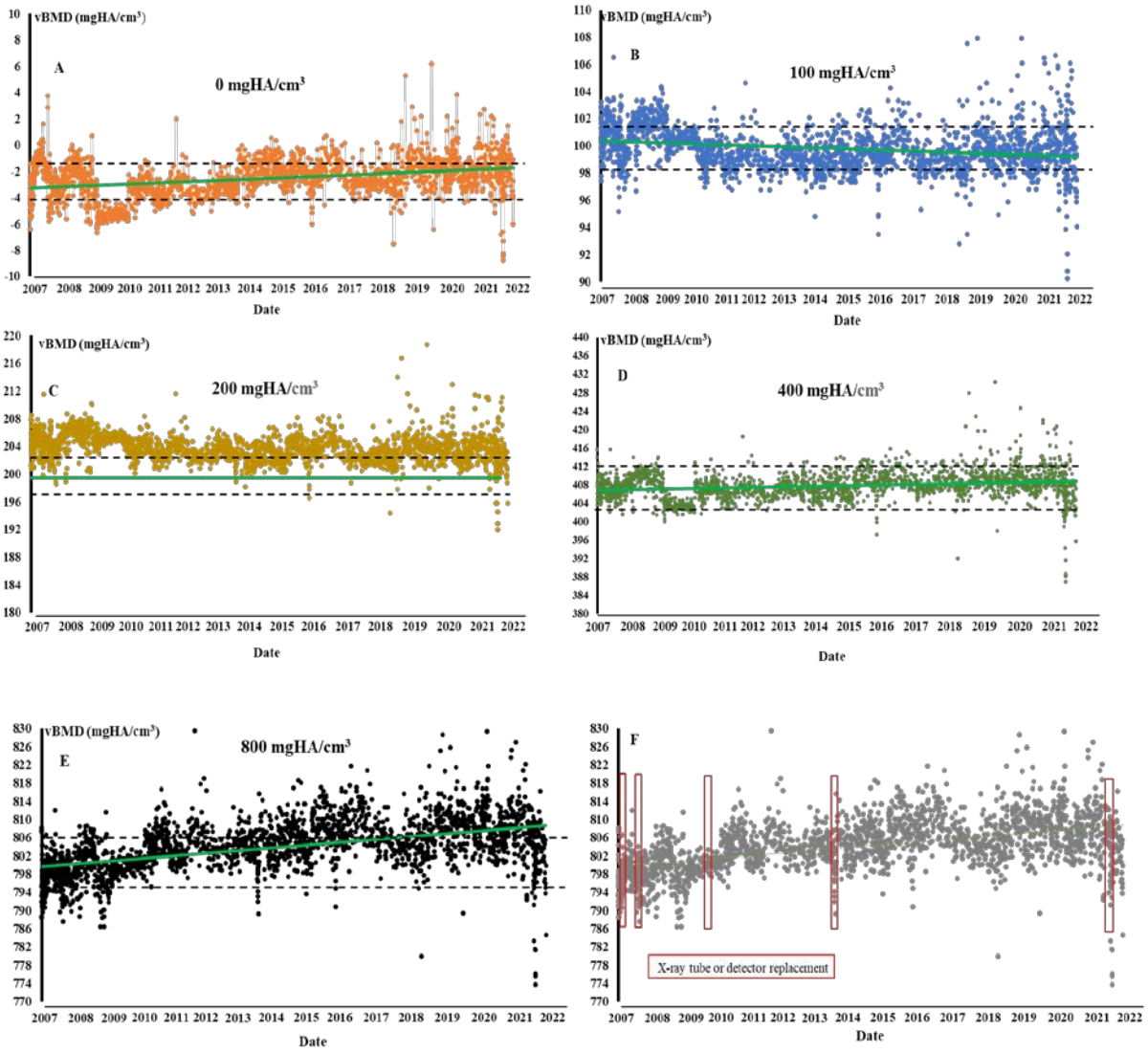

Figure 2.17. The QC phantom scanned since early 2007 to March 2022. Figures **A**-**E** show the fluctuations on measurement of rods with density of 0 (equal to soft tissue),100, 200, 400 and 800 mgHA/cm^3, respectively. Figure **F** shows the major drifts, and red boxes indicate the date of x-ray tube or detectors failure.

The long-term reproducibility of HR-pQCT is important. It ensures that measurements and assessments performed using HR-pQCT remain consistent and reliable over an extended period of

time. It enables accurate monitoring of changes in bone density, microstructure, and other parameters over time, facilitating the evaluation of disease progression, treatment efficacy, and overall bone health. Furthermore, reliable long-term reproducibility is essential for clinical trials and longitudinal studies, and the effective management of bone-related disorders.

Least CV (%) of microstructure parameters by HR-pQCT

The *Distal Forearm Microstructure Phantom* has been made of human cadaveric distal radius, distal ulna, carpal, and metacarpal bones (**Fig 2.18.A, B**). All bones are embedded in epoxy resin, imitating soft tissue, within anatomical and natural positioning.

To measure the least CV% of bone microstructure parameters, the Distal Forearm Microstructure Phantom was immobilised in the standard carbon fiber cast prior to scanning, as per the manufacturer's standard *in vivo* protocol- to simulate scanning the human distal forearm. A scout view scan was used to set the reference line and define the region of interest for each scan (**Fig 2.18.C**). The phantom has been scanned 10 times without repositioning within the same day and consecutively. A region of interest (110 parallel CT slices, 9.02 mm length) located 9.5 mm proximal to the reference line has been scanned at each time. The same image acquisition, image reconstruction, and analysis were used to collect the data following manufacturer protocols.

Each stack of images, comprising 110 slices, was analysed using the manufacturer's standard evaluation protocol without matching the slices (region of interest), as detailed in accordance with established guidelines (16).

In brief, the periosteal surface of the bone was outlined to separate the bone from the surrounding soft tissue. A semi-automatic edge-finding algorithm was used to detect the periosteal bone surface and facilitated the contour iteration process from the first slice through the subsequent 109 slices in a slice-by-slice manner. For every slice the contour line was observed, to make sure the line did not stray from the periosteal surface of the bone. Bone geometry outcomes were: total, cortical and trabecular bone area and volumetric bone mineral density values of total, cortical, and trabecular bone, and meta and inner trabecular compartment densities. Bone micro-architecture outcomes were: cortical thickness (Ct.Th), bone volume fraction (BV/TV), trabecular number (Tb.N), trabecular thickness (Tb.Th), trabecular separation (Tb.Sp), and trabecular bone pattern inhomogeneity (Tb.SpSD). The methods to define these outcome variables are described elsewhere (17-20).

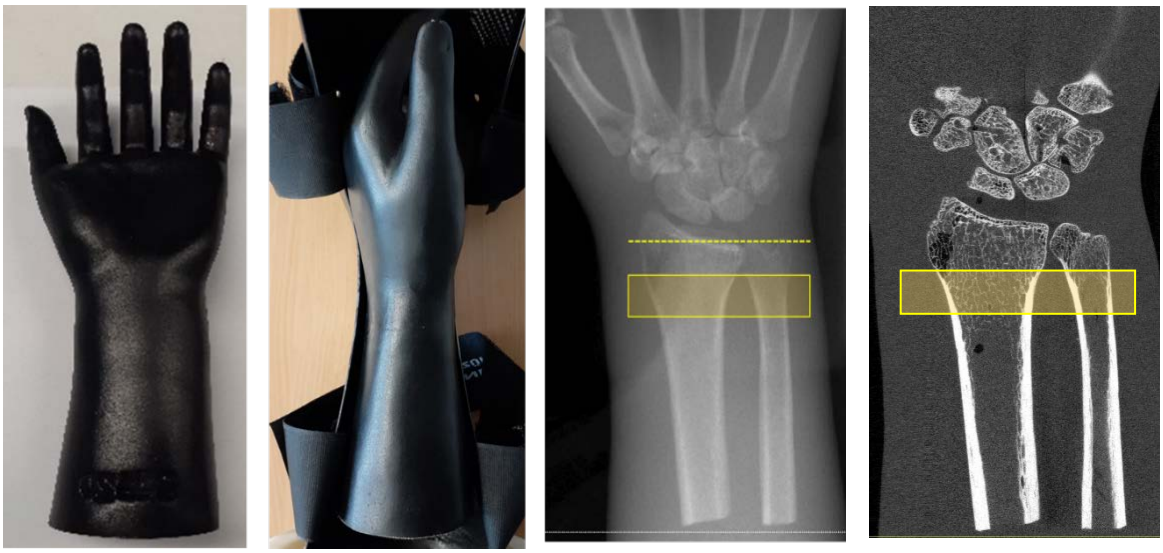

Figure 2.18. **A**) Palmar view, **B**) lateral view and positioning in the fibre cast view, **C**) Scout view, reference line and the location of scanned ROI, **D**) Coronal view and scanned ROI of the Distal Forearm Microstructure Phantom.

Table 2.3 shows the mean, standard deviation, and CV% for total, cortical and trabecular vBMD and cortical and trabecular compartments bone morphology parameters. Although the phantom was not repositioned between scans, differences were observed for all bone geometry and bone microstructure parameters. The CV of 0.60% for the total cross-sectional area is attributed to the comparison of data without slices matching. As the measurements of cross-sectional area were not conducted on the exact same slices for all samples this leads to minor variations in the measurements.

This lack of matching slices can contribute to the observed variability in results, as indicated by the coefficient of variation.

The CV% of vBMDs and bone microstructure parameters calculated following the **Equation 2**.

$$\mathbf{CV}\% = \frac{\text{Standard Deviation of 10 times repeated scans}}{\text{Mean of 10 times repeated scans}} \times 100 \qquad \textbf{Equation 2}.$$

Table 2.4 Mean, standard deviation and coefficient variation of bone microstructure parameters, without slice matching.

Parameters	**Mean**	**SD**	**CV (%)**
Cross Sectional Area of (mm^2)			
Total bone	273.4	1.60	0.60
Cortical bone	59.38	0.573	0.97
Medullary	208.20	2.040	0.98
Cortical Thickness (mm)	0.842	0.01	0.79
vBMD ($mgHA/cm^3$)			
Total bone	359.81	4.595	1.28
Cortical bone	918.33	6.772	0.74
Trabecular bone	185.15	1.753	0.95
Meta Trabecular	236.67	1.675	0.71
Inner Trabecular	149.45	1.828	1.22
Ratio of Meta/Inner*****	1.58	0.012	0.73
Trabecular bone volume fraction (%)	15.44	0.135	0.87
Number (1/mm)	1.32	0.006	0.48
Thickness (mm)	0.12	0.001	0.94
Separation (mm)	0.64	0.004	0.56
Inhomogeneity*****	0.29	0.003	1.06

No data for total cross-sectional area (TCSA) due to using TCSA to match the scanned region of interest between different scans, * No unit for ratio of Meta/Inner, Inhomogeneity is the SD of 1/Tb.N

The manufacturer's software has the capability to align the paired scans by identifying the common volume of interest. This process involves matching the slices of the baseline and follow-up scans to determine the optimal offset. A common 2D registration technique uses the total cross-sectional area of each slice to determine an optimal offset between paired (baseline and follow-up) scans resulting in a common volume of interest within a subset of the original slices acquired.

This 2D technique implemented by the Scanco software is primarily done to correct for discrepancies in the axial direction, ensuring alignment of the slices within the same plane. However, it does not account for variations in the tilt of the limb. As a result, if there are differences in the tilting or positioning of the limb between the baseline and follow-up scans, the software may not fully compensate for these variations during the registration process. It's important to be aware of this limitation and consider potential effects on the accuracy of the when analysing the data. Notably, the 2D registration technique precludes evaluation of periosteal bone apposition and thus limits the interpretation of studies where a change in bone size is anticipated, such as growth, exercise, or perhaps aging over an extended observation (21). Table 2.5 shows the CV% of parameters after slice-matching for followed up scans.

Table 2.5. Mean, standard deviation and coefficient variation of bone microstructure parameters, with slice matching.

Parameters	**Mean**	**SD**	**CV (%)**
Cross Sectional Area of (mm^2)			
Total bone*	272.0	-	-
Cortical bone	56.63	0.29	0.49
Medullary	207.33	0.23	0.11
Cortical Thickness (mm)	0.839	0.01	0.68
vBMD ($mgHA/cm^3$)			
Total bone	360.95	2.99	0.83
Cortical bone	919.16	4.61	0.50
Trabecular bone	185.54	1.76	0.95
Meta Trabecular	237.44	1.45	0.61
Inner Trabecular	149.63	1.92	1.28
Meta/Inner*	1.58	0.01	0.61
Trabecular bone volume fraction (%)	15.44	0.100	0.87
Number (1/mm)	1.318	0.004	0.32
Thickness (mm)	0.117	0.001	0.81
Separation (mm)	0.641	0.003	0.50
Inhomogeneity**	0.288	0.003	1.08

*All scans have the same total cross-sectional area due to slice matching. ** No data for total cross-sectional area (TCSA) due to using TCSA to match the scanned region of interest between different scans, * No unit for ratio of Meta/Inner, Inhomogeneity is the SD of 1/Tb.N.

In addition to standard parameters, the Scanco software provides non-parametric bone indices.

Table 2.6 shows the CV% of those parameters. These parameters are not matched.

Table 2.6 Mean, standard deviation, and CV (%) of trabecular apparent and material densities and non-parametric microstructure indices, without slice matching.

Parameters	Mean	SD	CV (%)
Apparent Density (mgHA/cm^3)	177.15	4.63	2.61
Material Density (mgHA/cm^3)	614.10	9.20	1.50
Tissue Volume (mm^3)	1700.90	26.10	1.53
Bone Volume (mm^3)	357.84	8.27	2.31
Trabecular Connectivity Density (1/mm^2)	2.69	0.06	2.23
Trabecular Bone Surface (mm^2)	3517.30	79.49	2.26
Structural Model Index (SMI)	1.77	0.04	2.41
Trabecular Degree of Anisotropy	1.49	0.02	1.50

In vivo reproducibility of HR-pQCT

To evaluate the *in-vivo* CV (%) of HR-pQCT, distal radius and distal tibia of 27 individuals (13 females and 14 males, age: 37.8 ± 16.5 years, range of 22.4 -75.3), were scanned twice, consecutively and with repositioning, with a 2 to 5-minute time interval. All images were analysed following the manufacture's guidelines. The vBMDs and bone microstructure parameters were determined with and without slice matching. The manufacturer software utilises the similar total cross-sectional areas of each slice to find a common volume of interest between different scans of the distal radius or tibia.

The Precision Error and Least Significant Changes calculated using the following equations:

$$\mathrm{CV\%}j = \left(\frac{SDj}{\bar{x}j}\right) \times 100\% \quad \text{Equation } \mathbf{1}$$

$$CV\%_{RMS} = \sqrt{\frac{\sum_{j=1}^{m} CV_j^2}{m}} \quad \text{Equation } \mathbf{2}$$

Where j refers to an individual participant, SDj is the standard deviation between the baseline and follow-up measurements (for that individual participant), *xj* is the mean of these two measurements, and *m* is the total number of participants in the analysis (22, 23).

$$\mathrm{LSC}_{(1\times1)} = \mathrm{Z} \times \mathrm{CV\%}\, RMS \sqrt{\frac{1}{n_1} + \frac{1}{n_1}} = 2.77 \times CV\%RMS \quad \text{Equation } \mathbf{3}$$

Tables **2.7** to **2.10** show the CV% and least significant changes for vBMDs and bone microstructural parameters of the distal radius and distal tibia. The unmatched results (i.e., slices are not matched to find common volume of interest) have relatively higher CV% and least significant changes in comparison to slice-matched results.

Table 2.7 Radius-slice matched CV (%) and least significant changes in vBMDs and bone microstructure parameters of distal radius and tibia of 27 participants scanned twice with repositioning within the same day.

Parameters, Radius	CV (Absolut value)	CV (%)	LSC (Absolut value)	LSC (%)
Bone Perimeter (mm)	0.368	0.38	1.020	1.05
Cross Sectional Area of (mm^2)				
Total bone	-	-	-	-
Cortical bone	0.687	0.97	1.904	2.69
Medullary	2.333	0.99	6.462	2.74
Cortical Thickness (mm)	0.014	1.24	0.038	3.43
vBMD ($mgHA/cm^3$)				
Total bone	4.232	0.96	11.722	2.66
Cortical bone	12.878	1.27	35.671	3.52
Trabecular bone	1.417	0.67	3.926	1.86
Meta Trabecular	2.261	0.74	6.262	2.05
Inner Trabecular	1.423	0.98	3.943	2.71
Ratio of Meta/Inner*	0.059	1.17	0.165	3.24
Trabecular BV/TV	0.001	0.70	0.003	1.94
Number(1/mm)	0.054	2.48	0.148	6.87
Thickness(mm)	0.003	2.32	0.008	6.43
Separation(mm)	0.016	2.55	0.043	7.06
Inhomogeneity of Trabecular*	0.009	3.16	0.025	8.75

No data for total cross-sectional area (TCSA) due to using TCSA to match the scanned region of interest between different scans, * No unit for ratio of Meta/Inner, Inhomogeneity is the SD of 1/Tb.N

Table 2.8 Tibia-slice matched, CV (%) and least significant changes of 27 participants vBMDs and bone microstructure parameters of distal radius and tibia scanned twice with repositioning within same day.

Parameters, Tibia	CV (Absolut value)	CV (%)	LSC (Absolut value)	LSC (%)
Bone Perimeter (mm)	0.287	0.22	0.796	0.61
Cross Sectional Area of (mm^2)				
Total bone	-	-	-	-
Cortical bone	0.861	0.60	2.384	1.66
Medullary	3.728	0.54	10.327	1.50
Cortical Thickness (mm)	0.010	0.74	0.028	2.05
vBMD ($mgHA/cm^3$)				
Total bone	2.166	0.61	5.999	1.69
Cortical bone	10.508	1.10	29.107	3.05
Trabecular bone	0.919	0.40	2.544	1.11
Meta Trabecular	1.315	0.40	3.642	1.11
Inner Trabecular	1.138	0.64	3.154	1.77
Ratio of Meta/Inner*	0.020	0.71	0.055	1.97
Trabecular BV/TV	0.001	0.33	0.002	0.91
Number (1/mm)	0.080	3.34	0.221	9.25
Thickness (mm)	0.004	3.19	0.012	8.84
Separation (mm)	0.022	3.35	0.061	9.28
Inhomogeneity of Trabecular*	0.011	3.22	0.031	8.92

No data for total cross-sectional area (TCSA) due to using TCSA to match the scanned region of interest between different scans, * No unit for ratio of Meta/Inner, Inhomogeneity is the SD of 1/Tb.N

Table 2.9 Radius-slice unmatched, CV (%) and least significant changes of 27 participants vBMDs and bone microstructure parameters of distal radius and tibia scanned twice with repositioning within same day.

Parameters, **Radius**	CV (Absolut value)	CV (%)	LSC (Absolut value)	LSC (%)
Bone Perimeter (mm)	1.049	1.21	2.90	3.35
Cross Sectional Area of (mm^2)				
Total bone	7.840	2.464	21.717	6.825
Cortical bone	1.69	2.51	4.70	6.95
Medullary	7.81	3.11	21.64	8.61
Cortical Thickness (mm)	0.03	3.62	0.09	10.03
vBMD ($mgHA/cm^3$)				
Total bone	9.31	2.31	25.80	6.40
Cortical bone	17.85	1.77	49.45	4.90
Trabecular bone	2.02	0.94	5.61	2.60
Meta Trabecular	2.66	0.87	7.37	2.41
Inner Trabecular	2.29	1.68	6.35	4.65
Ratio of Meta/Inner*	0.07	1.73	0.20	4.79
Trabecular BV/TV	0.002	0.96	0.005	2.66
Number (1/mm)	0.05	2.33	0.14	6.45
Thickness (mm)	0.003	2.58	0.008	7.15
Separation (mm)	0.015	2.41	0.041	6.68
Inhomogeneity of Trabecular	0.010	3.06	0.027	8.48

No data for total cross-sectional area (TCSA) due to using TCSA to match the scanned region of interest between different scans, * No unit for ratio of Meta/Inner, Inhomogeneity is the SD of 1/Tb.N

Table 2.10: Tibia-slice unmatched, CV (%) and least significant changes of 27 participants vBMDs and bone microstructure parameters of distal radius and tibia scanned twice with repositioning within same day.

Parameters, **Tibia**	CV (Absolut value)	CV (%)	LSC (Absolut value)	LSC (%)
Bone Perimeter(mm)	0.863	0.52	2.391	1.44
Cross Sectional Area of (mm^2)				
Total bone	24.121	1.424	66.816	3.945
Cortical bone	1.721	0.89	4.768	2.47
Medullary	10.600	1.35	29.363	3.74
Cortical Thickness (mm)	0.024	1.40	0.068	3.88
vBMD ($mgHA/cm^3$)				
Total bone	2.871	0.64	7.952	1.77
Cortical bone	13.055	1.25	36.163	3.46
Trabecular bone	1.555	0.60	4.307	1.66
Meta Trabecular	1.590	0.46	4.405	1.27
Inner Trabecular	2.021	1.10	5.597	3.05
Ratio of Meta/Inner*	0.028	1.07	0.078	2.96
Trabecular BV/TV	0.001	0.62	0.004	1.72
Number (1/mm)	0.080	3.25	0.221	9.00
Thickness (mm)	0.004	3.20	0.012	8.86
Separation (mm)	0.021	3.27	0.060	9.06
Inhomogeneity of Trabecular*	0.011	3.38	0.031	9.36

No data for total cross-sectional area (TCSA) due to using TCSA to match the scanned region of interest between different scans, * No unit for ratio of Meta/Inner, Inhomogeneity is the SD of 1/Tb.N

The CV% and power calculation are crucial components in study design of various research fields, including the assessment of bone microstructure using HR-pQCT. The CV% and power calculation are interconnected in study design. A lower CV% translates to lower variability, which can lead to more precise measurements and, consequently, a higher statistical power. With a higher statistical power, researchers have an increased likelihood of detecting significant differences or effects

between groups, if they exist. Power calculations inform the sample size determination, ensuring that the study is appropriately powered to detect the desired effect sizes and minimise the risk of Type II errors (false negatives) in hypothesis testing.

In conclusion, evaluating the CV% of HR-pQCT measurements before conducting a clinical trial is crucial for ensuring the reliability and precision of the study outcomes. It enables researchers to identify and address sources of measurement variability, optimise the study design, and determine an appropriate sample size, ultimately enhancing the quality and validity of the research findings.

HR-pQCT; first-generation *vs* Second-generation

In 2014, HR-pQCT underwent a significant upgrade, transitioning to a second generation of scanner and software, with notable improvements including a higher spatial resolution (voxel size:82 to 61 µm), faster scanning time (from 3 to 2 min), and a revised measurement algorithm for cortical and trabecular compartments.

The 2nd generation of HR-pQCT offers the capability to scan objects with both 82 and 61 µm voxel sizes. This flexibility allows for a range of applications and enables researchers to select the voxel size that best suits their specific imaging and analysis requirements It also facilitates data pooling with other centres that employ HR-pQCT scans using 82 µm voxel sizes. This data pooling facilitates larger sample sizes and strengthens the statistical power of studies, enhancing the overall validity and generalisability of the findings.

The main differences between the 1st and 2nd generation of HR-pQCT image analysis software lie in the algorithms are used for cortical thickness and trabecular thickness assessments. Cortical thickness (Ct.Th), as an average of the cortical compartment, is calculated as the volume of cortical compartment divided by the periosteal surface, using 1st generation algorithm; however, mean spacing of the periosteal and endocortical surfaces is used to calculated Ct.Th using the 2nd generation.

The ratio of segmented bone volume to total volume of the trabecular compartment, reported as a percentage, is called the 'Trabecular bone volume fraction -Trab. BV/TV (%)'. This ratio is derived using this equation (Tb.vBMD/1200 mg HA/cm^3) ×100 by the 1st generation, but the 2nd generation uses ratio of voxels in the mineralised bone phase to the total number of voxels in the trabecular compartment, therefore the measured BV/TV by the 2nd generation will be more accurate in cases with higher or lower mineralised trabecular compartment.

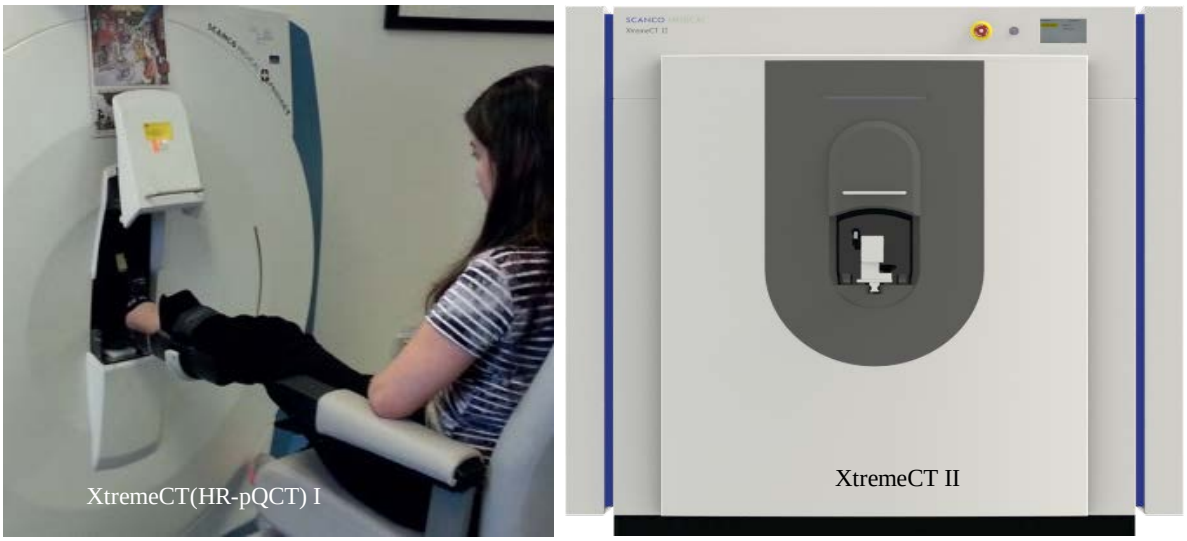

Fig 2.19 HR-pQCT1or XtremeCTI (left Panel), HR-pQCT2 or XtremeCTII (right Panel)

Based on 1st generation HR-pQCT software , the trabecular thickness (Tb.Th), average thickness of trabeculae, is calculated as the ratio of BV/TV to Trab.N; however, the 2nd generation Tb.Th is measured directly using 'mean spacing of the segmented trabecular structure using the distance transformation method'. In addition to the above-mentioned differences other are some differences between the two generations, are described in the position paper published in Osteoporosis International 2020 that I co-authored (21).

Most studies to date, including published vBMD and microstructure parameters population reference ranges, were performed using the 1st generation HR-pQCT scanners, therefore there a is need for collaboration across this field. It is not clear whether pooling bone microstructural indices produced by 1st and 2nd generations of the scanner is feasible in cross sectional or prospective studies.

In cross-sectional studies, additional considerations arise when pooling data from different scanner generations. Potential variations in measured values and differences in imaging protocols need to be appropriately addressed to ensure accurate and meaningful comparisons. To address this issue, we investigated the correlation between bone indices determined using 1st and 2nd generation HR-pQCT scanners by scanning the radii and tibiae of cadaveric samples.

Thirty-two human cadaveric radii and tibiae, we scanned using the manufacturer defined ROIs, on a 2nd generation HR-pQCT II (Monash University) with 61 and 82 µm voxel size without repositioning to avoid any potential repositioning errors. All images were reconstructed and evaluated following the manufacturer's protocols. Bone geometry, volumetric bone mineral density and trabecular bone microstructural indices were determined for comparison using both methods.

We found that total, cortical, and trabecular: (**i**) cross-sectional areas, and (**ii**) volumetric densities, were highly correlated (r^2>0.9, P<0.01). Trabecular indices (number, separation, and pattern inhomogeneity) were also well correlations (r^2>0.85, p <0.01), while trabecular bone volume fraction and thickness were not linearly correlated (**Fig 2.20**).

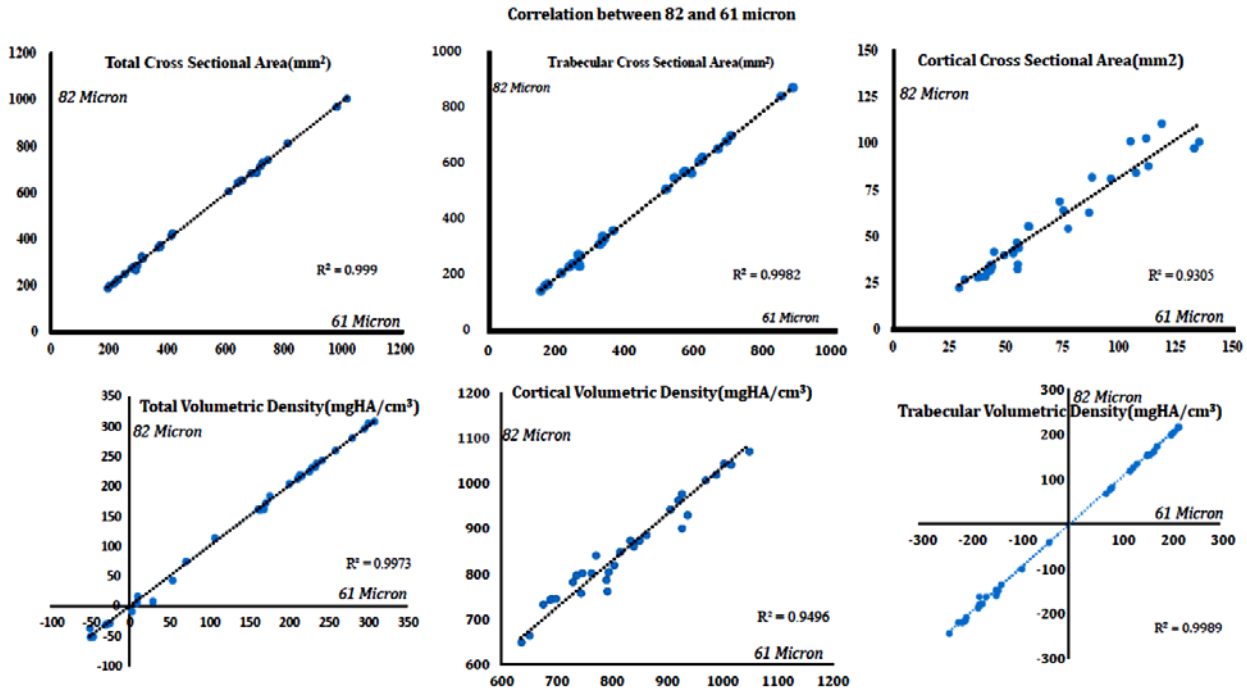

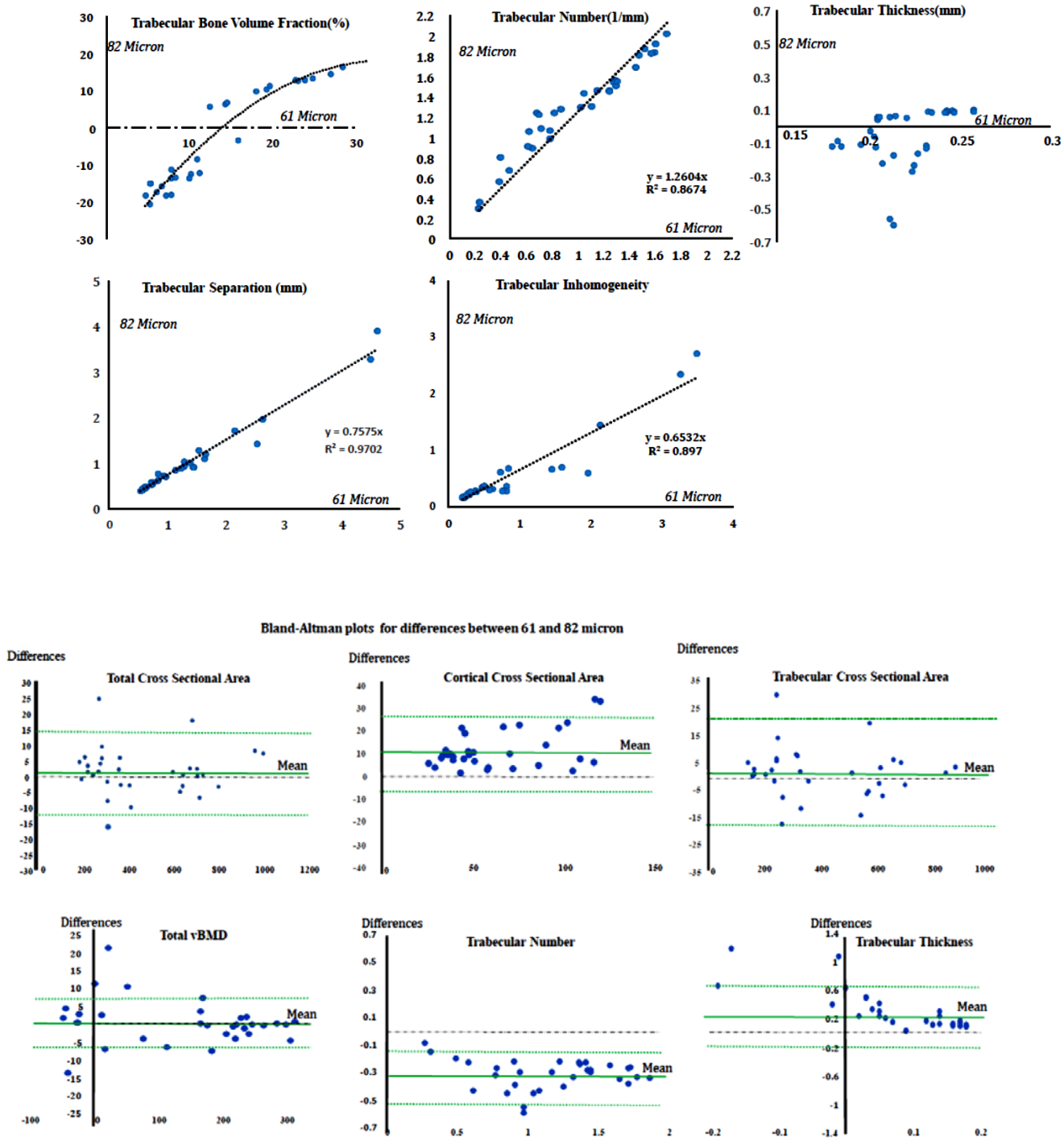

Fig 2.20 Correlations of bone geometry, volumetric densities and microstructure indices between 1st and 2nd generation HR-pQCT scanners.

Pooling bone geometric indices and volumetric densities from 1st and 2nd generation scanners is feasible; however, microstructural indices, particularly trabecular bone volume fraction and

trabecular thickness, caution should be exercised, and prior transformation may be necessary before pooling the data. By applying appropriate transformation methods, such as calibration equations or statistical adjustments, the microstructural indices can be aligned and harmonised across different scanner generations. This ensures that the pooled data accurately represents the underlying bone microstructure and enables valid comparisons and analyses.

References

1. Tjong W, Kazakia GJ, Burghardt AJ, Majumdar S. The effect of voxel size on high-resolution peripheral computed tomography measurements of trabecular and cortical bone microstructure. Med Phys. 2012;39(4):1893-903.

2. MacNeil JA, Boyd SK. Accuracy of high-resolution peripheral quantitative computed tomography for measurement of bone quality. Med Eng Phys. 2007;29(10):1096-105.

3. Liu XS, Zhang XH, Sekhon KK, Adams MF, McMahon DJ, Bilezikian JP, et al. High-resolution peripheral quantitative computed tomography can assess microstructural and mechanical properties of human distal tibial bone. J Bone Miner Res. 2010;25(4):746-56.

4. Nishiyama KK, Macdonald HM, Buie HR, Hanley DA, Boyd SK. Postmenopausal women with osteopenia have higher cortical porosity and thinner cortices at the distal radius and tibia than women with normal aBMD: an in vivo HR-pQCT study. J Bone Miner Res. 2010;25(4):882-90.

5. Liu XS, Shane E, McMahon DJ, Guo XE. Individual trabecula segmentation (ITS)-based morphological analysis of microscale images of human tibial trabecular bone at limited spatial resolution. J Bone Miner Res. 2011;26(9):2184-93.

6. Engelke K, Stampa B, Timm W, Dardzinski B, de Papp AE, Genant HK, et al. Short-term in vivo precision of BMD and parameters of trabecular architecture at the distal forearm and tibia. Osteoporos Int. 2012;23(8):2151-8.

7. Pialat JB, Burghardt AJ, Sode M, Link TM, Majumdar S. Visual grading of motion induced image degradation in high resolution peripheral computed tomography: impact of image quality on measures of bone density and micro-architecture. Bone. 2012;50(1):111-8.

8. Kawalilak CE, Johnston JD, Cooper DM, Olszynski WP, Kontulainen SA. Role of endocortical contouring methods on precision of HR-pQCT-derived cortical micro-architecture in postmenopausal women and young adults. Osteoporos Int. 2016;27(2):789-96.

9. de Waard EAC, Sarodnik C, Pennings A, de Jong JJA, Savelberg H, van Geel TA, et al. Reliability of HR-pQCT Derived Cortical Bone Structural Parameters When Using Uncorrected Instead of Corrected Automatically Generated Endocortical Contours in a Cross-Sectional Study: The Maastricht Study. Calcif Tissue Int. 2018;103(3):252-65.

10. Chiba K, Okazaki N, Kurogi A, Isobe Y, Yonekura A, Tomita M, et al. Precision of Second-Generation High-Resolution Peripheral Quantitative Computed Tomography: Intra- and Intertester Reproducibilities and Factors Involved in the Reproducibility of Cortical Porosity. J Clin Densitom. 2018;21(2):295-302.

11. Ellouz R, Chapurlat R, van Rietbergen B, Christen P, Pialat JB, Boutroy S. Challenges in longitudinal measurements with HR-pQCT: evaluation of a 3D registration method to improve bone microarchitecture and strength measurement reproducibility. Bone. 2014;63:147-57.

12. MacNeil JA, Boyd SK. Improved reproducibility of high-resolution peripheral quantitative computed tomography for measurement of bone quality. Med Eng Phys. 2008;30(6):792-9.

13. Boutroy S, Bouxsein ML, Munoz F, Delmas PD. In vivo assessment of trabecular bone microarchitecture by high-resolution peripheral quantitative computed tomography. J Clin Endocrinol Metab. 2005;90(12):6508-15.

14. Burghardt AJ, Buie HR, Laib A, Majumdar S, Boyd SK. Reproducibility of direct quantitative measures of cortical bone microarchitecture of the distal radius and tibia by HR-pQCT. Bone. 2010;47(3):519-28.

15. Duan X, Wang J, Leng S, Schmidt B, Allmendinger T, Grant K, et al. Electronic noise in CT detectors: Impact on image noise and artifacts. AJR Am J Roentgenol. 2013;201(4):W626-32.

16. Kawalilak CE, Johnston JD, Olszynski WP, Leswick DA, Kontulainen SA. Comparison of short-term in vivo precision of bone density and microarchitecture at the distal radius and tibia between postmenopausal women and young adults. J Clin Densitom. 2014;17(4):510-7.

17. Kazakia GJ, Burghardt AJ, Link TM, Majumdar S. Variations in morphological and biomechanical indices at the distal radius in subjects with identical BMD. J Biomech. 2011;44(2):257-66.

18. Laib A, Häuselmann HJ, Rüegsegger P. In vivo high resolution 3D-QCT of the human forearm. Technol Health Care. 1998;6(5-6):329-37.

19. Laib A, Hildebrand T, Häuselmann HJ, Rüegsegger P. Ridge number density: a new parameter for in vivo bone structure analysis. Bone. 1997;21(6):541-6.

20. Laib A, Rüegsegger P. Calibration of trabecular bone structure measurements of in vivo three-dimensional peripheral quantitative computed tomography with 28-microm-resolution microcomputed tomography. Bone. 1999;24(1):35-9.

21. Whittier DE, Boyd SK, Burghardt AJ, Paccou J, Ghasem-Zadeh A, Chapurlat R, et al. Guidelines for the assessment of bone density and microarchitecture in vivo using high-resolution peripheral quantitative computed tomography. Osteoporos Int. 2020;31(9):1607-27.

22. Kawalilak CE, Johnston JD, Olszynski WP, Kontulainen SA. Least significant changes and monitoring time intervals for high-resolution pQCT-derived bone outcomes in postmenopausal women. J Musculoskelet Neuronal Interact. 2015;15(2):190-6.

23. Glüer CC, Blake G, Lu Y, Blunt BA, Jergas M, Genant HK. Accurate assessment of precision errors: how to measure the reproducibility of bone densitometry techniques. Osteoporos Int. 1995;5(4):262-70.

Chapter 2

Finite Element Analysis

Introduction

Nature is an analogue realm in all aspects, and every image we perceive is composed of analogue data. The spectrum of colours or shades of grey used to depict an object is virtually infinite, and some of these nuances may not be discernible to the naked eye. However, when it comes to storing and analysing information in computers, we must convert the infinite analogue realm into discrete, sampled data. This process involves separating the continuous analogue information into discrete units, enabling efficient storage and analysis.

Bone strength plays a crucial role in determining the risk of fragility fractures; Measurement of bone strength provides valuable insight into predicting the risk of fragility facture. However, conducting direct and *in-vivo* measurement to estimate bone strength poses challenges due to the requirement for destructive testing and the associated potential for harm. Furthermore, considering the diverse array of influencing factors, including age, sex, weight, height, bone mass, and other conditions such as bone microstructure statues, is not feasible when relying solely on direct measurement of bone strength. Considering these challenges utilising virtual simulations, or computational modelling, within different conditions offers a viable alternative to calculate bone strength and predict the risk of fragility fractures precisely.

Finite element analysis (FEA) is a practical application of finite element for performing structural analysis. FEA is a powerful computational method employed to convert the vast and diverse range of material properties' information, including those of bone tissue, into discrete and analysable elements. FEA breaks down the structure into smaller, manageable elements, allowing for the approximation of its behaviour through numerical calculations. By utilising algebraic equations to analyse the behaviour of individual elements, FEA aids in comprehending and predicting the mechanical response of complicated structures under various conditions by dividing complex

structures into smaller, interconnected elements. These elements capture the essential characteristics of the material and enable the analysis of their responses to the applied forces, or other environmental factors. Through FEA, the seemingly infinite variations in material properties and behaviours can be effectively studied, providing valuable insights into the mechanical and structural aspects of diverse materials, including bone tissue (**Fig.2.21**) (1).

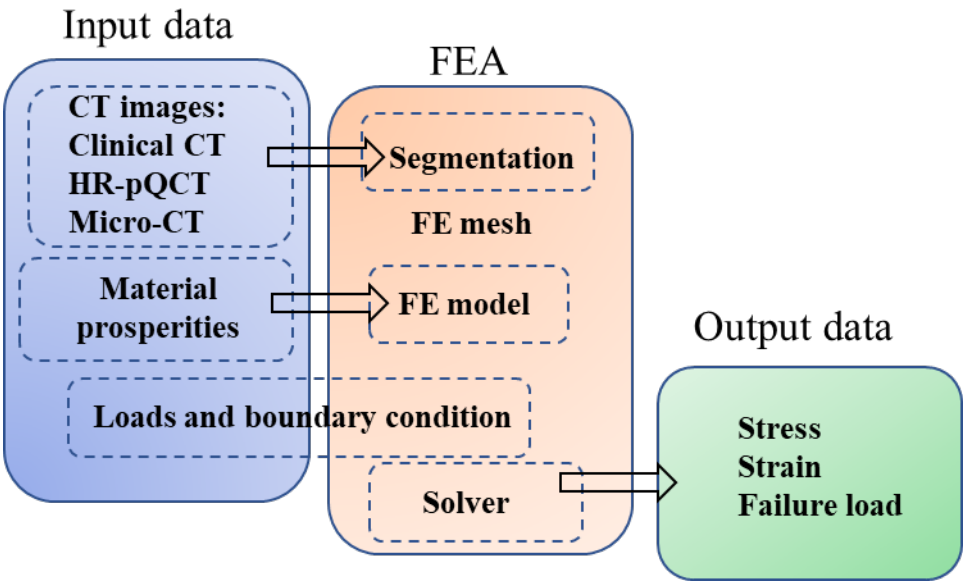

Figure 2.21. The process of conducting computed tomography-based finite element analysis for human bones. Adapted from Imai K. et al.

History of FE

In 1908, Walter Ritz made a significant breakthrough by developing a method to predict the stress and displacement behaviour of structures. However, it wasn't until the 1950s when Boeing, the renowned aerospace company, took a crucial step forward by utilising triangular stress elements to model the wings of airplanes which marked a pivotal advancement in the field. In 1960, Dr Ray Clough devised the term “finite element” (2). Nevertheless, the beginning of commercial FEA backs to time once digital computers replaced analogue ones with the ability of thousands of operations per second that truly revolutionised the field of FEA. This transition from analogue to digital computing opened new possibilities and allowed for the commercialisation of FEA. With the computational power provided by digital computers, engineers and scientists were able to efficiently analyse

complex structures and accurately predict their behaviour under various conditions. This breakthrough marked a significant milestone in the history of FEA, enabling its widespread adoption and application across various industries.

In the field of quantitative bone imaging, FEA estimate bone strength and predict the likely anatomical location(s) where failure is initiated, and fractures may progress. To apply FEA to living organisms, we require digital images that capture the internal structure of the object of interest. Computed tomography (CT) images consist of three-dimensionally distributed elements, voxel. Each voxel represents a specific location within the scanned object and contains a single value representing the x-ray coefficient attenuation as representative of bone mineral density or bone content. Improving the resolution of CT images involves reducing the size of each voxel, thereby allowing for more accurate and detailed information about the designated location **(Fig. 2.22)**. With advancements in imaging technology, it is now possible to acquire high-resolution CT images using HR-pQCT with voxel sizes as small as 82 or 61 microns. This level of resolution is particularly significant as it falls within the scale of trabecular thickness, making it the only *in-vivo* modality available for human studies that can capture such fine details (3).

Utilising these high-resolution CT images, FEA can estimate crucial biomechanical properties of bone, including strength, stiffness, and toughness, with acceptable accuracy (4). By simulating the mechanical behaviour of bone structures under various loading conditions, FEA provides valuable insights into bone biomechanics, helping in the assessment of fracture risk and the development of preventive measures. This non-invasive approach has proven particularly valuable in clinical research and has the potential to

enhance our understanding beyond bone mass. It enables the investigation of bone geometry and microstructure, and their effects on bone strength.

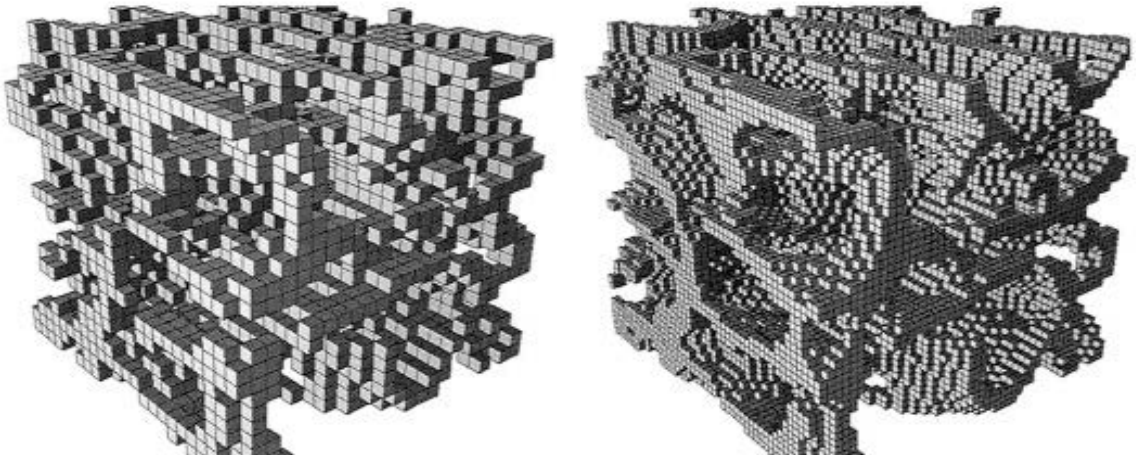

Figure 2.22. Finite element models of the femoral head trabecular specimen created at a voxel resolution of 168 μm (left) and 84 μm (right), smaller voxels provide more details. Adapted from Viguet-Carrin S et

The individual trabeculae and Haversian canals within bone are incredibly small, making direct mechanical testing to measure their properties nearly impossible at present. However, through the using of high-resolution imaging modalities such as High-Resolution peripheral Quantitative Computed Tomography (HR-pQCT) or Micro-CT and synchrotron radiation, it becomes feasible to estimate the mechanical properties of trabecular and cortical bone compartments. These imaging techniques enable for non-invasive assessment of various bone properties. However, it is important to note that certain aspects such as Haversian orientation and trabecular anisotropy are dependent on the resolution of the images obtained and cannot be easily assessed using current in-vivo imaging techniques (4, 5). Achieving a high enough resolution to capture such complicated details remains a challenge.

Nevertheless, ongoing advancements in imaging technologies hold promise for improving our ability to analyse and understand these finer structural characteristics of bone, particularly by using Nano-CT and Synchrotron Radiation.

The resistance of bone to fractures is influenced by several factors, including its mass, microstructure, bone turnover rate, and the intrinsic properties of the mineral and organic matrix. The hierarchical structure and geometric parameters of bone play a significant role in determining its stiffness, strength, toughness, energy absorption, and other mechanical properties (6). While FEA software provides valuable biomechanical data of bone, these estimates of bone strength do not encompass all the characteristics that contribute to bone strength, such as degree of bone mineralisation.

On the other hand, biomechanical properties of bone are partly influenced by bone geometry(7). Variations in cross-sectional area exist within and between sexes and races in the total, cortical, and trabecular compartments. Therefore, it is crucial to adjust FEA outputs for bone size when comparing between sexes or races (**Fig. 2.23**)(8). Normalising displacement by length, failure load by area, and energy by volume allows for the calculation of material properties such as strain, stress, and energy density (toughness). This approach replaces the load-displacement curve with a stress-strain curve, which is independent of sample shape and size (4).

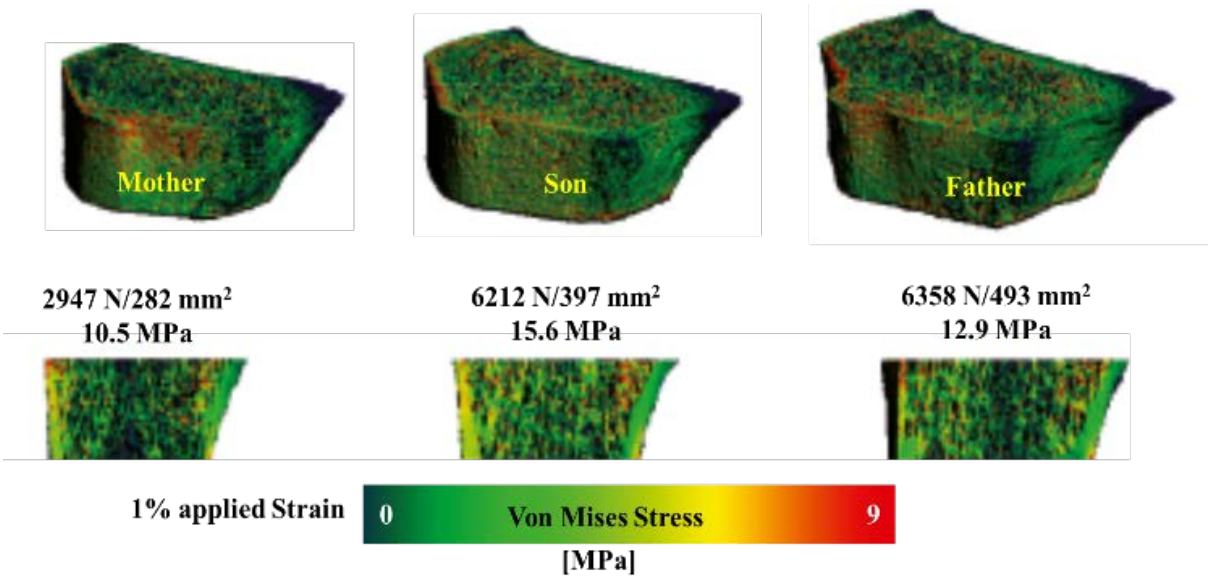

Figure 2.23. Comparison of bone stiffness between three family members. Both male members have larger and stronger bones, and that despite the "father" having the largest bone, it is not as strong as the "son". Adapted from Boyd SK.

In brief, any external load (*stress*) to bone causes a displacement (*strain*) at the location of applied force (*boundary condition*) and progression of loading induces more strain. There is a linear correlation between magnitude of stress and strain and the slop of this correlation, called stiffness (*Young's modulus*) and this part of the curve is the "*Elastic zone*". In this zone, the deformed material regains its original configuration upon removal of the load. However, the magnitude of strain after a certain level (*yield point* or *yield criterion*-) defining the limit of elasticity in a material and the onset of plastic deformation under stress- is not linear and exceeded applied stress initiates irreversible deformity on bone which leads to its *failure point*. This area of the curve (i.e., between *yield point* and *failure point*) is known as the "*Plastic zone*" (**Fig. 2.24**).

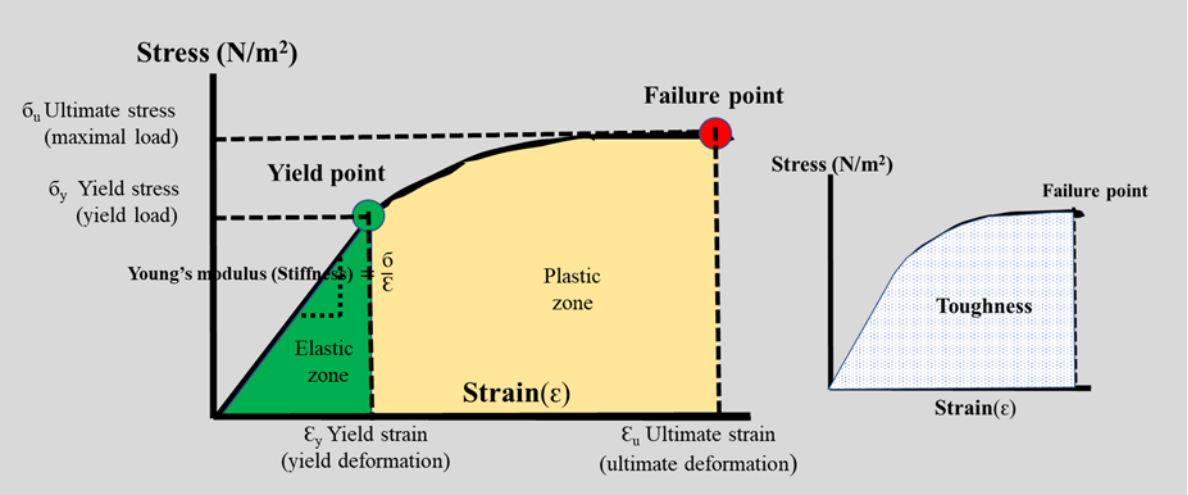

Figure 2.24. Relationship between stress and strain. Left figure: The green area represents the *Elastic zone*, and after the yield point, increasing the strain the object under stress will be deformed irreversibly, the area between yield strain and ultimate strain *Plastic zone* (yellow area). Right figure: The area under curve of Stress-Strain represents the amount of absorbed energy by bone to reach the failure point, the area under curve is "Toughness".

The bone matrix can be described as a two-phase system consisting of a mineral phase and collagen fibers. The mineral phase provides the bone with stiffness, while the collagen fibers contribute to its ability to absorb energy, also known as toughness (9). These two components work together to give bone its remarkable mechanical properties. Alterations of collagen properties as a consequence of disease or bone related treatments can therefore affect the mechanical properties of bone and increase fracture susceptibility (**Fig.2.25)**.

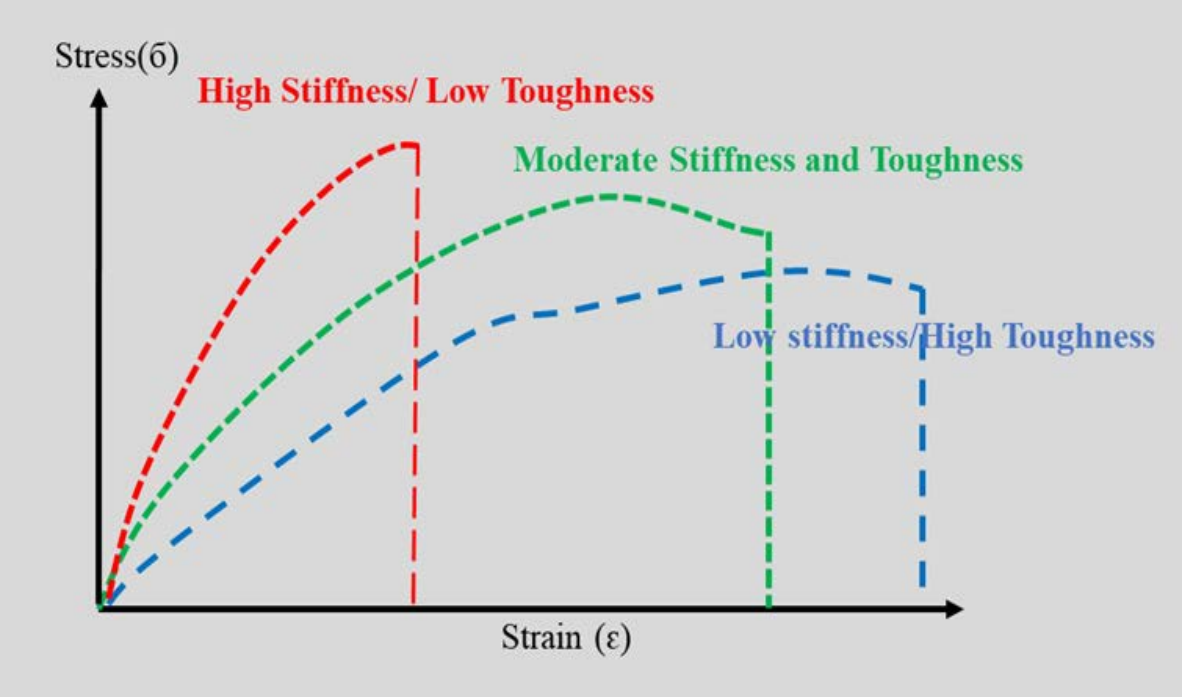

Figure 2.25. Comparison of 3 types of bone with different stiffness and toughness. Red colour represents the bone with high stiffness and low toughness (absorbing and damping energy) this type of bones are brittle like bone of patients with T2DM. The green line shows the moderate stiffness and toughness, like healthy bone. Low stiffness and higher toughness have been reported for patient with osteomalacia (blue lines). Adapted from basic concept of bone mechanics, David B. Burr

Estimation of failure load of distal radius and tibia using HR-pQCT images

Due to the relatively smaller voxel size of HR-pQCT images, the FE for HR-pQCT is called 'Micro Finite Element'. Micro Finite Element (μFE) models are generated using image processing language (IPL) software provided by the HR-pQCT manufacturer; however, there are other software to run μFEA, like FAIM (10).

The fundamental requirements for an FE model are selecting the bone geometry, assigning material properties, and defining boundary conditions to simulate loading conditions (11, 12).

Before conducting the analysis, an EF model is generated for bone structure, in which each voxel of images is converted to an equally sized brick-like element (**Fig. 6, 7**) (13, 14). During meshing stage, the bone compartments are differentiated. The cortical region which

is discretised with pentahedral, and trabecular region with tetrahedral elements based homogenised FE model (13). To delineate cortex from trabecular bone, a peeling algorithm is used by specifying a minimum cortical thickness of 6 voxels (~0.5 mm).

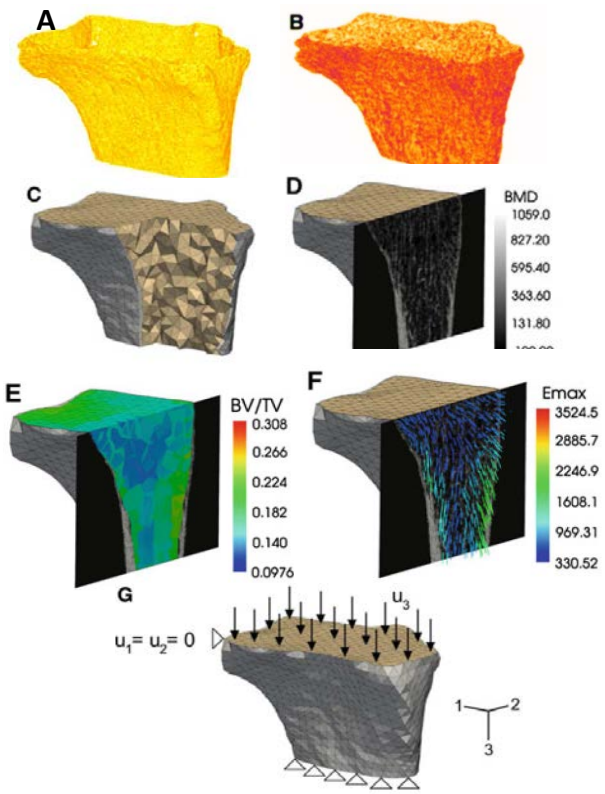

Figure 2.26. Details of the FE model generation: separation of cortical (**A**) and trabecular (**B**) compartments; geometrical meshing (**C**) mapping material properties based on the underlying HR-pQCT image (**D**) assignment of bone volume fraction (**E**) and anisotropy (the distribution of the maximal Young's modulus of the trabecular bone) (**F**) and applying boundary conditions (**G**). Adapted from Varga P et al.

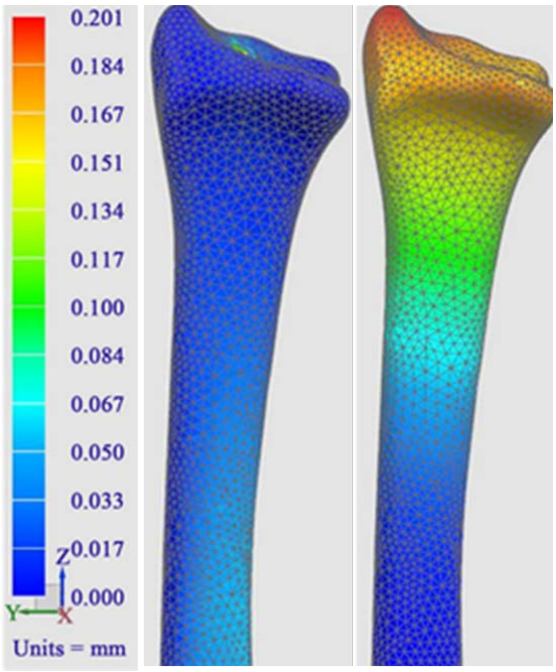

Figure2.27. Distal radii bone meshed using triangles (**a**) intact model, (**b**) longitudinal displacement under applied compressive load with von Mises stress distribution. Adapted from Zysk AM et al.

In the models, bone's elastic properties are specified for cortical and trabecular bone compartments. Elements representing cortical bone are assigned a Young's modulus of 20 GPa, and those representing trabecular bone tissue are assigned a Young's modulus of 17.5 GPa (15). The estimated failure load is computed based on a criterion developed by Pistoia

et al.(12), where the fracture is assumed to occur when 2% of the bone tissue is strained beyond a critical limit of 7000 microstrain.

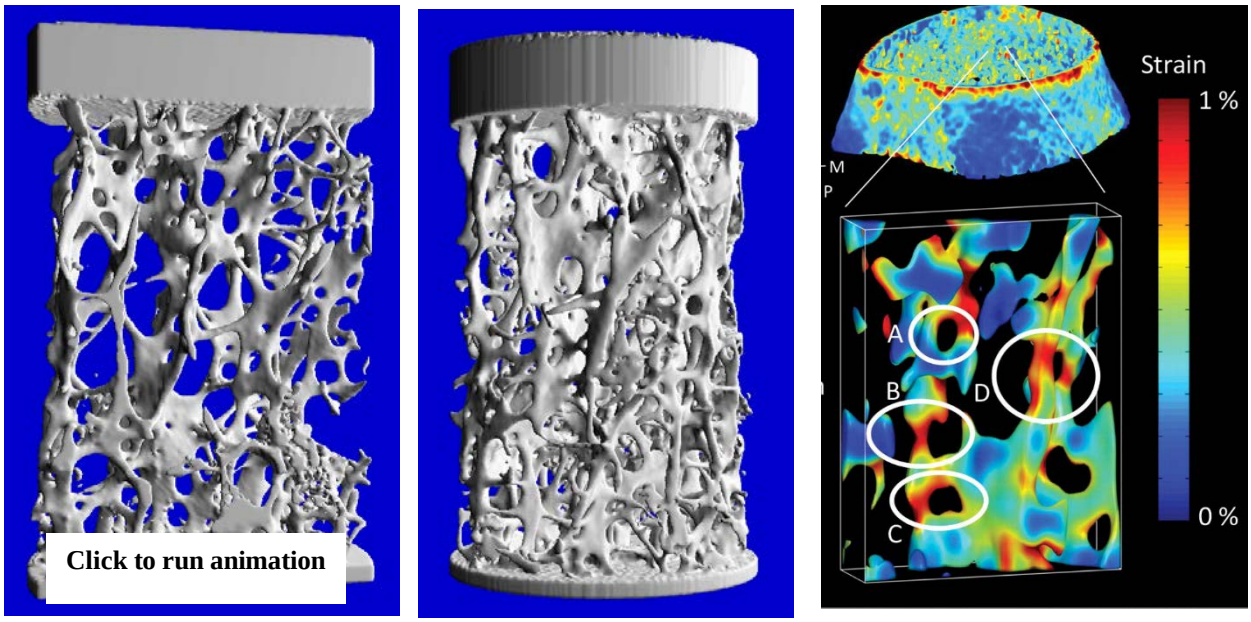

Figure 2.28. Animated the deteriorated (**left**) and healthy (**middle**) trabecular bone under compression load. Healthy trabecular bone relatively needs more force to reach the failure point in comparison to deteriorated trabecular. Illustration of cortical and trabeculae strain concentration(**right**). Courtesy from Prof Ralph Muller (ETH Zurich, Switzerland).

Validation

Validation of the Finite Element (FE) method is crucial for assessing the capabilities and limitations of FE modelling. Typically, validation involves comparing the results obtained from the FE model with experimental measurements (**Fig.2.28**) (16). However, when the FE model represents trabecular or cortical compartments separately, obtaining direct measurements can be challenging due to the lack of accurate delineation between these compartments (17). Nevertheless, incorporating Micro-CT images into the FE model can help mitigate this issue and improve accuracy.

Image-guided failure analysis (IGFA) is an alternative method which is used to validate finite element models by directly comparing 3D images of different bones at various stages of loading. This technique involves the use of a mechanical testing device that is compatible with Micro-CT imaging, enabling sequential 3D imaging of samples as they progress through different load levels until reaching failure point (18). IGFA provides a powerful means to validate finite element models by capturing the real-time changes in bone structure and behaviour during loading. By comparing the acquired 3D images with the corresponding FE model predictions, researchers can assess the accuracy and reliability of the model in simulating the mechanical response of the bone (19).

IGFA validates FE models by comparing real-time changes in bone structure and behaviour during loading. This involves comparing 3D images with FE model predictions to assess the accuracy and reliability of simulating bone's mechanical response.

The advantage of using IGFA lies in its ability to provide direct visual evidence of bone deformation, crack propagation, and ultimate failure, which may not be easily quantifiable through traditional experimental measurements alone. This method enhances the understanding of bone fracture mechanisms and enables the refinement and improvement of finite element models, resulting in more realistic simulations.

By combining the capabilities of Micro-CT imaging and mechanical testing, IGFA offers a comprehensive approach to validate and enhance the predictive capabilities of finite element models in analysing bone failure behaviour. This contributes to the advancement of fracture prediction and prevention strategies in the field of bone biomechanics.

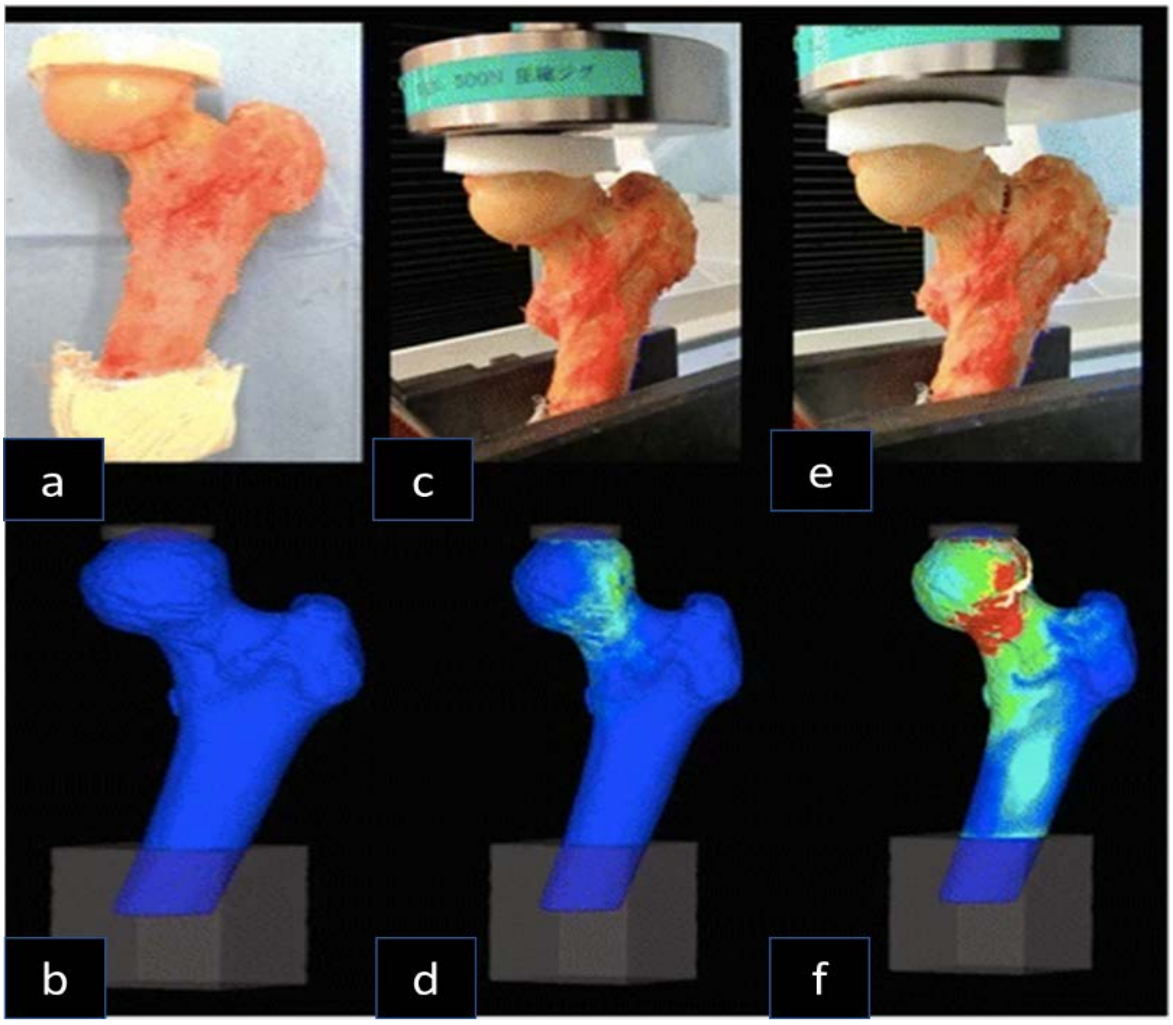

Figure 2.28. Process of mechanical testing and finite element analysis. The minimum force is applied at a fixed vertical displacement (**a)**, increased the force **c**) until the proximal femoral fracture occurs (**e**). The model of the proximal femur is made (**b**), a compressive load was applied (**d**)until predicted fracture (**f**). Adapted from Nazarian A. et al.

Our finding using FEA

We used μFEA (FAIM software, version 8.0) to estimate failure load of the distal tibia and radius of individuals with spinal cord injuries, resulting in tetraplegia or paraplegia, to sex- and age-matched controls. A uniaxial loading with a tissue elastic modulus of 6,829 MPa, a Poisson's ratio of 0.3, a critical strain of 7,000 micro-strain and a critical volume of 2%,

were defined. A 1% apparent strain was applied, and failure load is calculated as the load when 2% of elements exceeded the critical strain.

Men with tetraplegia and men with paraplegia had reduced estimated failure load of the distal tibia and distal fibula. Despite the presence of tetraplegia, we found no significant differences between cases and controls for the distal radius estimated failure load (**Fig. 2.29**) (20). Please refer to chapter 4 for more details.

Furthermore, our study explored the impact of chronic kidney disease (CKD) on bone strength using FEA and the same software as above mentioned Our finding shows significant reductions in the estimated failure load of the distal radius and tibia in patients with CKD who were classified as having BMD in the normal or osteopenia range compared to controls with same BMD classification. In CKD patients with osteoporosis, estimated distal tibial failure load was lower than in controls, but not significantly. Estimated distal radial failure load was significantly lower than controls for all three categories of BMD. (**Fig. 2.30**)(21). Please refer to chapter 5 for more details.

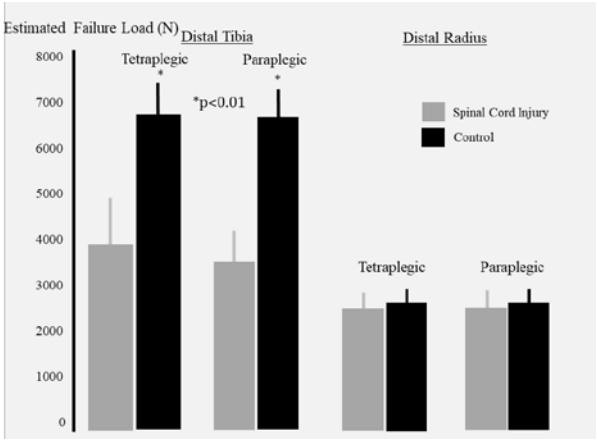

Figure 2.29. Compromised estimated failure load of distal tibia in individuals with tetraplegia or paraplegia, no differences found for distal radius for both groups in compression to sex- and age-matched controls, N=Newton.

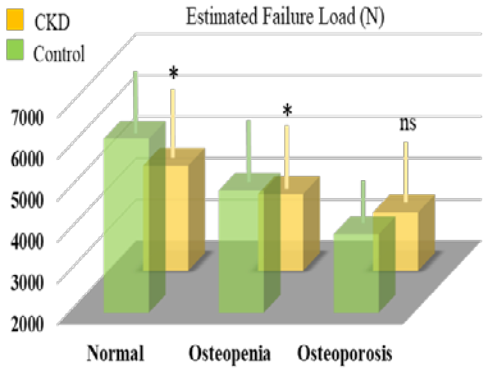

Figure 2.30. Comparison of estimated failure load in patients with CKD (yellow bars) versus controls (green bars) within a bone mineral (*p < 0.001). N=Newton.

These findings emphasise the potential influence of CKD on bone biomechanics and highlight the importance of considering factors beyond BMD alone when evaluating fracture risk in CKD patients. The utilisation of μFEA allows for a comprehensive assessment of bone strength and fracture risk, providing valuable insights for clinicians and researchers in developing appropriate preventive and treatment strategies for individuals with CKD.

Limitation of FEA

While Finite Element Analysis (FEA) is a powerful tool for predicting fragility fractures, it is important to acknowledge its limitations in this context.

One significant limitation of FEA is the accuracy of the input parameters used to model bone properties. Material properties such as bone density, elastic modulus, and yield strength vary among individuals and may not be accurately represented in FEA models. Additionally, the assumption of linear material behaviour may not fully capture the nonlinear response of bone under high-stress conditions, leading to potential inaccuracies in fracture predictions.

Bone remodelling rates have significant impact on the degree of mineralisation and bone's biomechanical properties. Cortical pores and medullary area contain different proportion of water and fat based on the age or condition of bone, which have different impact on damping the applied energy into bone. All above mentioned variables are not taking in account in each single voxel of CT-based images appropriately.

FEA models also rely on simplifications and assumptions to make the analysis computationally feasible. The complexity of bone structure, including trabecular and cortical regions, is often simplified in FEA models, potentially overlooking critical factors that contribute to fracture initiation and propagation.

Moreover, FEA predictions are highly sensitive to boundary conditions applied to the model. The selection of appropriate boundary conditions can be challenging, as the loading conditions experienced by bones in real-life scenarios are complex and difficult to accurately replicate in the analysis (22).

Another limitation is the computational cost and time required for FEA simulations. Generating a detailed and accurate model, meshing, and solving the equations can be time-consuming, particularly for large-scale models. This can limit the practicality of using FEA for real-time fracture risk assessment in certain clinical settings (23).

It is crucial to consider these limitations when interpreting FEA results and to complement them with other clinical assessments to effectively enhance fracture prediction to be used to develop prevention strategies.

Summary and Conclusion

Although bone looks composite of a mineral phase, calcium phosphate-based hydroxyapatite, embedded in an organic matrix of collagen protein, but its structure is highly complex and hierarchical which determines its strength. Despite the advancements in finite element analysis techniques, recent studies and reviews have indicated that the improvement in fracture prediction using strength-related variables, as opposed to bone mineral density, is generally modest. However, the greatest advantage in utilising strength-related variables has been demonstrated in the spine (24, 25) not proximal femur, this would be partly due to the complex shape of the proximal femur in comparison to the lumbar spine. In the near future, it is expected that the 3D images of the proximal femur using higher resolution will be achievable, and addition, using high performance computers may help to predict risk of

proximal femur fracture with higher precision. Still progress is needed to integrate FE outcomes into clinical workflow.

However, it is important to acknowledge the limitations of FEA. These include the accuracy of input parameters, simplifications in modelling bone structure, sensitivity to boundary conditions, and computational costs. Accurate representation of bone properties, such as density, elastic modulus, and yield strength, is crucial for reliable FEA predictions. Additionally, simplifications in bone structure modelling may overlook critical factors influencing fracture initiation and propagation. The selection of appropriate boundary conditions that replicate complex real-life loading conditions can be challenging. Furthermore, FEA simulations can be computationally expensive and time-consuming, particularly for large-scale models.

To overcome these limitations, advancements in modelling techniques and the incorporation of patient-specific data are crucial. Improving the accuracy of input parameters and incorporating more detailed representations of bone structure can enhance the reliability of FEA predictions. Furthermore, advancements in artificial intelligence and experimental validation can contribute to refining FEA models. Despite its limitations, FEA holds great promise for further advancements in the field of bone biomechanics and fracture prevention, particularly with ongoing research and technological advancements.

In conclusion, FEA has emerged as a valuable tool in the field of biomechanics, with extensive applications in predicting fragility fractures. By simulating and analysing the mechanical behaviour of bone structures, FEA provides valuable insights into fracture risk assessment and aids in understanding the underlying mechanisms of bone fractures, that may be used for treatment planning.

References

1. Imai K. Computed tomography-based finite element analysis to assess fracture risk and osteoporosis treatment. World J Exp Med. 2015;5(3):182-7.
2. Reddy JN. Introduction to the Finite Element Method. 2nd, editor: McGraw Hill; 1993.
3. Ulrich D, van Rietbergen B, Weinans H, Rüegsegger P. Finite element analysis of trabecular bone structure: a comparison of image-based meshing techniques. Journal of Biomechanics. 1998;31(12):1187-92.
4. Engelke K, van Rietbergen B, Zysset P. FEA to Measure Bone Strength: A Review. Clinical Reviews in Bone and Mineral Metabolism. 2016;14(1):26-37.
5. Martin RB, Ishida J. The relative effects of collagen fiber orientation, porosity, density, and mineralization on bone strength. J Biomech. 1989;22(5):419-26.
6. Fonseca H, Moreira-Gonçalves D, Coriolano HJ, Duarte JA. Bone quality: the determinants of bone strength and fragility. Sports Med. 2014;44(1):37-53.
7. Hart NH, Nimphius S, Rantalainen T, Ireland A, Siafarikas A, Newton RU. Mechanical basis of bone strength: influence of bone material, bone structure and muscle action. J Musculoskelet Neuronal Interact. 2017;17(3):114-39.
8. Boyd SK. Advanced Imaging in Biology and Medicine2009. 447 p.
9. Viguet-Carrin S, Garnero P, Delmas PD. The role of collagen in bone strength. Osteoporosis International. 2006;17(3):319-36.
10. Whittier DE, Manske SL, Kiel DP, Bouxsein M, Boyd SK. Harmonizing finite element modelling for non-invasive strength estimation by high-resolution peripheral quantitative computed tomography. J Biomech. 2018;80:63-71.
11. Macneil JA, Boyd SK. Bone strength at the distal radius can be estimated from high-resolution peripheral quantitative computed tomography and the finite element method. Bone. 2008;42(6):1203-13.
12. Pistoia W, van Rietbergen B, Lochmüller EM, Lill CA, Eckstein F, Rüegsegger P. Estimation of distal radius failure load with micro-finite element analysis models based on three-dimensional peripheral quantitative computed tomography images. Bone. 2002;30(6):842-8.
13. Varga P, Dall'Ara E, Pahr DH, Pretterklieber M, Zysset PK. Validation of an HR-pQCT-based homogenized finite element approach using mechanical testing of ultra-distal radius sections. Biomech Model Mechanobiol. 2011;10(4):431-44.
14. Zysk AM, Lewis G, Taxier D, Rose J. Biomechanical Comparison of Prototype of a Novel Intramedullary Injectable Bioresorbable Polymer-Bioresorbable Balloon Osteosynthesis and a Volar Locking Plate for Treatment of Distal Radius Fractures. World Journal of Engineering and Technology. 2017;05:309-23.
15. Boutroy S, Van Rietbergen B, Sornay-Rendu E, Munoz F, Bouxsein ML, Delmas PD. Finite element analysis based on in vivo HR-pQCT images of the distal radius is associated with wrist fracture in postmenopausal women. Journal of bone and mineral research : the official journal of the American Society for Bone and Mineral Research. 2008;23(3):392-9.
16. Miura M, Nakamura J, Matsuura Y, Wako Y, Suzuki T, Hagiwara S, et al. Prediction of fracture load and stiffness of the proximal femur by CT-based specimen specific finite element analysis: cadaveric validation study. BMC Musculoskelet Disord. 2017;18(1):536-.
17. Zebaze R, Ghasem-Zadeh A, Mbala A, Seeman E. A new method of segmentation of compact-appearing, transitional and trabecular compartments and quantification of cortical porosity from high resolution peripheral quantitative computed tomographic images. Bone. 2013;54(1):8-20.
18. Nazarian A, Müller R. Time-lapsed microstructural imaging of bone failure behavior. J Biomech. 2004;37(1):55-65.
19. Levchuk A, Schneider P, Meier M, Vogel P, Donaldson F, Müller R. An Automated Step-Wise Micro-Compression Device for 3D Dynamic Image-Guided Failure Assessment of Bone Tissue on a Microstructural Level Using Time-Lapsed Tomography. Frontiers in Materials. 2018;5.

20. Ghasem-Zadeh A, Galea MP, Nunn A, Panisset M, Wang XF, Iuliano S, et al. Heterogeneity in microstructural deterioration following spinal cord injury. Bone. 2021;142:115778.
21. Ghasem-Zadeh A, Bui M, Seeman E, Boyd SK, Iuliano S, Jaipurwala R, et al. Bone microarchitecture and estimated failure load are deteriorated whether patients with chronic kidney disease have normal bone mineral density, osteopenia or osteoporosis. Bone. 2022;154:116260.
22. Zysset PK, Dall'ara E, Varga P, Pahr DH. Finite element analysis for prediction of bone strength. Bonekey Rep. 2013;2:386.
23. Taylor WR, Roland E, Ploeg H, Hertig D, Klabunde R, Warner MD, et al. Determination of orthotropic bone elastic constants using FEA and modal analysis. J Biomech. 2002;35(6):767-73.
24. Zysset P, Qin L, Lang T, Khosla S, Leslie WD, Shepherd JA, et al. Clinical Use of Quantitative Computed Tomography-Based Finite Element Analysis of the Hip and Spine in the Management of Osteoporosis in Adults: the 2015 ISCD Official Positions-Part II. J Clin Densitom. 2015;18(3):359-92.
25. van Rietbergen B, Ito K. A survey of micro-finite element analysis for clinical assessment of bone strength: the first decade. J Biomech. 2015;48(5):832-41.

Challenges in the Acquisition and Analysis of Bone Microstructure During Growth

Ego Seeman [1,2,3]

Ali Ghasem-Zadeh[1]

[1]Department of Endocrinology, Austin Health, University of Melbourne, Melbourne, Australia

[2]Department of Medicine, Austin Health, University of Melbourne, Melbourne, Australia

[3]Institute of Health and Ageing, Australian Catholic University, Melbourne, Australia

J Bone Miner Res . 2016 Dec;31(12):2239-2241. doi: 10.1002/jbmr.3015. Epub 2016 Nov 1.

https://pubmed.ncbi.nlm.nih.gov/27736022/

Chapter 2

To The Editor

Gabel and colleagues (1) report sex and racial differences in distal tibial and distal radial microstructure. This was a mixed longitudinal study of white and Asian males and females aged from 9 to 20 years. The authors confirm that males grow larger bones than females. Cortical porosity was higher in males but there was no sex difference in cortical volumetric bone mineral density (vBMD), leading the authors to suggest, but not show, that cortical matrix mineral density may be higher in males. The findings are questionable given several methodological challenges we face studying growth.

First, assessment of bone microstructure is based on positioning a region of interest (ROI) of only 9.02 mm in length at the distal metaphysis of the radius and tibia (2, 3). In a longitudinal study, it is difficult to relocate the identical anatomical location in the same individual. In cross-sectional or longitudinal studies, it is difficult to know whether the same anatomical region has been chosen when individuals differ by sex or race and so differ in forearm and tibial lengths. In adults, a fixed distance from the joint line is chosen as beginning the 9.02 mm ROI (9.5 mm for radius and 22.5 mm for tibia). This approach positions the ROI more distally in taller persons. Because cortical porosity is higher more distally, finding a higher porosity in males than females may be the result of positioning, not biology. Hence, taking a percentage of the length of a long bone is recommended in adults (4).

Whether taking a percentage of the length of the radius and tibia is the correct approach when bone length is increasing rapidly during growth and at different rates at each growth plate is not known (5, 6). Growth of the radius occurs mainly at the distal growth plate so that the ROI first measured moves proximally. As the radius lengthens, using 7% of the lengthening bone moves that ROI proximally. However, if growth is nonlinear, it is unlikely that a fixed percentage of the lengthening bone will relocate the first ROI measured. The tibia initially grows equally at each growth plate so the first ROI at the distal metaphysis measured moves proximally. Later, most tibial growth occurs

at the proximal growth plate so the ROI measured earlier moves distally but the subsequent ROI chosen using 8% percent of the increasing length moves proximally.

Differences in positioning of the ROI by even 1 to 2 mm may exaggerate or obscure microstructural differences between sexes and races, particularly at the distal radial metaphysis, a heterogeneous irregular rhomboidal structure. Cortical porosity and trabecular density are high distally and decrease in nonlinear fashion, often by over 50% within a few millimeters (7). Positioning errors produce differences in microstructure that are the same order of magnitude as sex and racial differences reported when the positioning errors are corrected.

Second, males and whites enter puberty ~12 months later than their respective female and Asian counterparts so they have had more growth of the legs and trunk at the time of entering puberty. It is difficult to understand how an estimated measure of peak growth velocity of height controls for the longer prepubertal growth and so controls for "maturation" (8). Growth velocity of total height is highest at birth, it decreases precipitously then accelerates at 1 year of age because growth velocity of the legs, not trunk, increases and remains twice that of truncal growth until puberty when leg length decelerates and trunk length accelerates (**Fig. 1**, left panel). Peak height velocity is therefore driven by truncal growth, but measurements of the appendicular skeleton are being taken. A later age at puberty in males and whites produces longer legs than in their female and Asian counterparts, respectively (9, 10). A longer intrapubertal growth in males produces a longer trunk. Pooling whites and Asian (almost one-half the cohort) when comparing males and females adds to the difficulties. It remains plausible that sex and racial differences in height are the result of differences in the duration of prepubertal and intrapubertal growth in males and whites than females and Asians respectively, the rapidity of growth may not differ by sex or race (11-13).

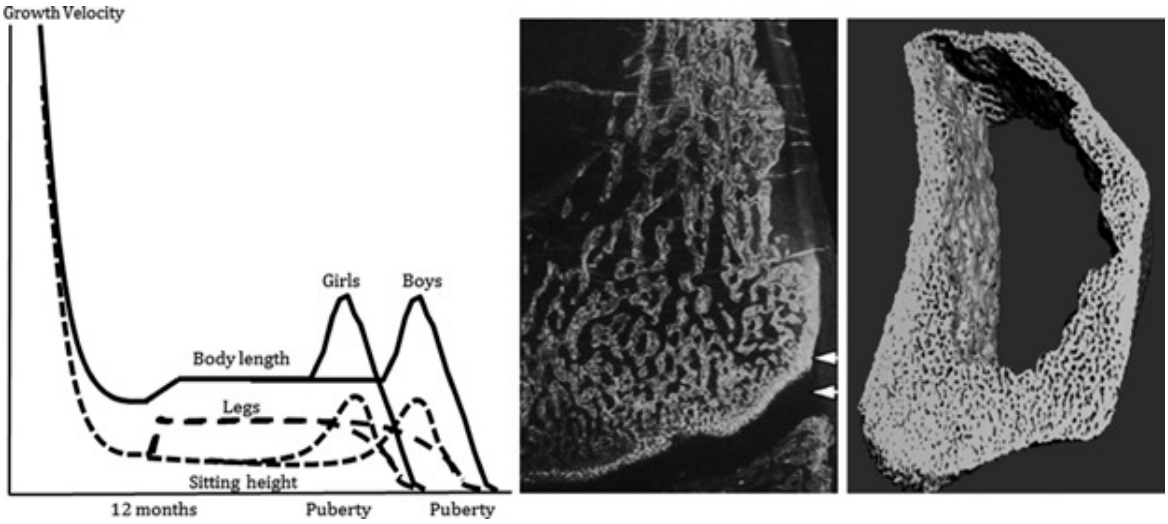

Figure 1. (Left panel) Growth velocity of the total body length decelerates after birth then accelerates at 1 year of age due to acceleration of the growth of the legs. Truncal growth accelerates at puberty. Males have a longer prepubertal and intrapubertal growth period than females. (Middle panel) Metaphyseal trabeculae coalesce to form the metaphyseal cortex (17). (Right panel) Incorrect segmentation of trabecular from cortical bone may result in this being "seen" as cortical bone.

Third, the authors report boys had higher porosity than girls but cortical vBMD was no different. They suggest, but do not show, that males may have higher matrix mineral density. Available evidence suggests the reverse is the case. The higher the porosity, the lower the matrix mineral density (14). This inverse association is likely to be the result of the rapidity of remodeling; excavation of cavities increases porosity, refilling with under mineralized matrix reduces matrix mineral density. This inconsistency signals the likelihood that there are errors in segmenting cortical and trabecular bone using thresholding and then calculating porosity in a cortex that is probably erroneously estimated (15, 16).

During growth of the distal radial metaphysis, trabeculae arising from the periphery of the growth plate coalesce ("corticalize"), forming the cortex by endochondral apposition (Fig. 1, middle panel).(17, 18) Longitudinal growth of the distal radius is rapid and transiently out paces osteoid apposition upon trabeculae so coalescence is delayed producing a transiently porous cortex. At a pixel size of 82 μm and a spatial resolution of about 100 μm, pixels containing incompletely coalesced trabeculae abutting against cortex may be registered as "cortical" bone and so

overestimate "cortical" thickness (**Fig. 1**, right panel). When porosity is calculated, the intertrabecular void may be erroneously included, leading to an overestimate of "cortical" porosity. Alternatively, porosity may be underestimated if mineralized matrix in a voxel containing part of a pore increases photon attenuation above the threshold designated to identify porosity.

Measurement of bone density using bone densitometry was a good beginning. Young investigators growing up under the shadow of the two-dimensional "areal" projection of a three-dimensional structure are unlikely to think about the morphological basis of bone fragility. Measurement of bone microstructure using high-resolution image analysis is changing the cerebral silence. However, this technology is not trouble-free press-button motoring. Understanding the microstructural changes that accompany growth, aging, and drug therapy requires attention to the challenges we face in image acquisition and analysis (19).

References

1. Gabel L, Macdonald HM, McKay HA. Sex differences and growth-related adaptations in bone microarchitecture, geometry, density and strength from childhood to early adulthood: a mixed longitudinal HR-pQCT Study. J Bone Miner Res. 20XX; XX(XX): XXXX–XXXX. DOI:10.1002/jbmr.2982.

2. Burrows M, Liu D, Perdios A, Moore S, Mulpuri K, McKay H. Assessing bone microstructure at the distal radius in children and adolescents using HR-pQCT: a methodological pilot study. J Clin Densitom.2010;13(4):451–5.

3. Cheuk KY, Tam EM, Yu FW, et al. A critical comparison between two scanning protocols of high-resolution peripheral quantitative computed tomography at the distal radius in adolescents. J Clin Densitom. 2016;19(3):305–15.

4.Ghasem-Zadeh A, Wang XF, Zebaze R, Seeman E. Sexual and racial dimorphism in bone microarchitecture requires adjustment of the region of interest for skeleton dimensions. J Bone Miner Res. 2016;31Suppl 1. [Poster session presented at: Annual Meeting American Society for Bone and Mineral Research (ASBMR); 2016 Sep 16–19; Atlanta, GA, USA; Presentation Number: SU0213]. Available from:http://www.asbmr.org/education/AbstractDetail?aid=86f1146f-e94e-47b9-9875-d52e78cb154e

5. Pritchett JW. Growth plate activity in the upper extremity. Clin Orthop Relat Res. 1991;268:235–42.

6.Pritchett JW. Longitudinal growth and growth-plate activity in the lower extremity. Clin Orthop Relat Res. 1992;275:274–9.

7. Ghasem-Zadeh A, Burghardt A, Zendeli A, et al. Assessing age, sex, and racial differences in cortical porosity requires adjustment for site-specific variation in the selected region of interest site

variation. J Bone Miner Res. 2014; 29 Suppl 1. [Poster session presented at: Annual Meeting American Society for Bone and Mineral Research (ASBMR); 2014 Se p 12–15; Houston, TX, USA; Presentation Number:SA0297]. Available from: http://www.asbmr.org/education/AbstractDetail?aid=974d22e0-fbac-4ebf-849c-353d6e60ab36

8. Bradney M, Karlsson MK, Duan Y, Stuckey S, Bass S, Seeman E. Heterogeneity in the growth of the axial and appendicular skeleton in boys: implications for the pathogenesis of bone fragility in men. J Bone Miner Res. 2000;15(10):1871–8.

9. Leung SS, Lau JT, Xu YY, et al. Secular changes in standing height, sitting height and sexual maturation of Chinese—the Hong Kong Growth Study, 1993. Ann Hum Biol. 1996; 23 (4): 297–306.10. Parfitt AM. The two faces of growth: benefits and risks to bone integrity. Osteoporos Int. 1994;4(6):382–98

10.Parfitt AM. The two faces of growth: benefits and risks to bone integrity. Osteoporos Int. 1994;4(6):382–98.

11.Wang XF, Duan Y, Seeman E. Similar trunk length but shorter leg length in Chinese than Caucasians: implications for racial differences in hip fracture rates. J Bone Miner Res. 2004;19 Suppl 1

12. Iuliano-Burns S, Hopper J, Seeman E. The age of puberty determines sexual dimorphism in bone structure: a male/female co-twin control study. J Clin Endocrinol Metab. 2009;94(5):1638–43.

13. Iuliano-Burns S, Mirwald RL, Bailey DA. Timing and magnitude of peak height velocity and peak tissue velocities for early, average, and late maturing boys and girls. Am J Hum Biol. 2001;13(1):1–8.

14. Boutroy S, Walker MD, Liu XS, et al. Lower cortical porosity and higher tissue mineral density in Chinese American versus white women. J Bone Miner Res. 2014;29(3):551–61.

15. Zebaze RM, Ghasem-Zadeh A, Bohte A, et al. Intracortical remodelling and porosity in the distal radius and post-mortem femurs of women: a cross-sectional study. Lancet. 2010 15;375(9727): 1729–36.

16. Zebaze R, Ghasem-Zadeh A, Mbala A, Seeman E. A new method of segmentation of compact-appearing, transitional and trabecular compartments and quantification of cortical porosity from high resolution peripheral quantitative computed tomographic images. Bone. 2013;54(1):8–20.

17. Cadet ER, Gafni RI, McCarthy EF, et al. Mechanisms responsible for longitudinal growth of the cortex: coalescence of trabecular bone into cortical bone. J Bone Joint Surg Am. 2003; 85-A (9):1739–48.

18. Bala Y, Bui QM, Wang XF, et al. Trabecular and cortical microstructure and fragility of the distal radius in women. J Bone Miner Res.2015;30(4):621–9.19. Seeman E, Martin TJ. Co-administration of antiresorptive and anabolic agents: a missed opportunity. J Bone Miner Res. 2015;30(5):753–64. Journal of Bone and Mineral Research2241

Challenges in the Use of Cross-Sectional Data to Quantify Growth and Deterioration of Bone Structure During Advancing Age

Ali Ghasem-Zadeh [*,1]

Ego Seeman [1,2]

[1]Departments of Endocrinology and Medicine, Austin Health, University of Melbourne, Melbourne, Australia

[2] Institute for Health and Aging, Australian Catholic University, Melbourne, Australia

J Clin Densitom. 2017 Jan-Mar;20(1):5-7. doi: 10.1016/j.jocd.2016.08.006. Epub 2016 Sep 8.

https://pubmed.ncbi.nlm.nih.gov/27618369/

Chapter 2

Editorial

In this issue of the Journal of Clinical Densitometry, Lindgren et al present data concerning peak bone mass of the extremities in young Swedish men. The work involved the use of peripheral quantitative computed tomography to assess peak radial and tibial metaphyseal and diaphyseal cortical and trabecular mass, volumetric bone mineral density (BMD), and other morphological features, rather than the use of areal BMD, a 2-dimensional areal projection of a 3-dimensional structure. The authors derived a reference range using a random sample of 1083 healthy Swedish men (1).

Contrary to what was proposed, the age at peak for bone traits was not discernible. There was also no detectable association between peak bone mass and strength, estimated by calculation of a cross-sectional polar moment of inertia. The authors also proposed that quantifying peak cortical and trabecular structures may identify persons at risk for fracture later in life and might do so better than areal BMD.

The work identifies several challenges we face using cross-sectional data to make inferences about longitudinal changes in bone morphology produced during growth and adulthood. These challenges include defining the age at which peak bone size, mass, and microstructure are achieved, and the changes in morphology during adulthood such as the age at which bone mass starts to decline and microstructure deteriorates, and whether bone size continues to increase due to slow periosteal apposition after epiphyseal closure (2,3,4).

The subjects of this study were males aged 18–28 yr. Puberty occurs at around 12–14 yr and is associated with a reduction in the rate of longitudinal appendicular growth but a concomitant acceleration in longitudinal truncal growth. The greater velocity of appendicular than axial longitudinal growth drives the increase in height between 1 yr of age and puberty. Longitudinal growth then slows, but mass continues to increase as cortical porosity decreases and matrix mineral

density increases (5-7). Most of these events are close to completion before 18 yr of age accounting for there being no identifiable age at peak for traits such as bone size and mass.

Another challenge using cross-sectional data is the effect of secular increases in stature. Trait differences between younger and older persons, or the lack of them, may be the result of secular changes in stature, which may either exaggerate or blunt the pattern of change across age depending on the phenotype studied. Indeed, secular changes are very heterogeneous; they are site, sex, race, and epoch specific. Even within the same community, the secular change may occur in 1 sex but not in the other; in the upper body, lower body, or both; or in 1 race but not in another (8-13).

The difficulties that arise may be relevant to this study even though there was only a decade between the youngest and oldest participants. For example, one explanation for the absence of a detectable peak in size and mass may be that persons forming the older cohort in a cross-sectional study had a smaller stature when they were young. The actual increase in height, bone width, and bone mass have been blunted because the persons forming the younger group are taller than those in the older group when the persons in the older group were young. This will underestimate the age-related increase in bone size produced by periosteal apposition during growth. In this cohort, it is plausible that there was a secular increase in height and this may partly explain the absence of a detectable peak in bone size or mass.

The authors wanted to determine whether peak bone mass predict bone strength. As the bending strength of bone is a fourth power function of the radial distance of a unit volume of bone (14), blunting of the increase in bone radius by secular changes may also underestimate the rise in bending strength that accompanies the rise in the radius of a cross section.

Another challenge is the use of a threshold-based segmentation (separation) of cortical from trabecular bone using peripheral quantitative computed tomography-derived images (15,16). This method may result in errors in metaphyseal regions but less so in diaphyseal regions. Metaphyseal cortical bone is formed, in part, by corticalization of trabeculae arising from the periphery of the growth plate (17,18). Trabecular are incorporated, adsorbed upon the endocortical surface, and

become the cortical bone of the metaphyseal region. More central trabeculae form the trabecular compartment (19).

If corticalization of trabeculae is delayed or incomplete, threshold-based segmentation erroneously leaves the trabeculae in the medullary canal, underestimating cortical thickness and area and overestimating trabecular density. Thus, in younger persons in a cross-sectional study, cortical thickness may be underestimated, even in 18 yr olds. This underestimation of cortical thickness in a young person will overestimate the increment in cortical thickness across age, whereas the increment in trabecular density will be underestimated (because younger people will seem to have higher "trabecular" density). The same issue does not occur in the diaphysis because cortical bone is formed by membranous bone formation.

The lack of association between mass and strength may be due to the constancy of mass along a bone (20). In a given individual, it is surprising and perhaps counterintuitive to find that the amount of material used to assemble a long bone is the same from cross section to cross section along the length of a long bone. What differs, and determines its strength, is the distribution of that same amount of material in space. For example, at the junction of the femoral shaft and femoral neck, the femoral neck is widest, and the cortices vary in thickness around a given cross section. The bending strength will vary depending on the radial distance of the amount of material at that point. Moving proximally, cortical thickness decreases while trabecular density increases. The varying configuration of the constant amount of material is achieved by varying the void volume (forming the medullary canal and the intracortical porosity). Larger bones are assembled with less matrix volume relative to their size; the medullary canal is wider, and the cortex is more porous and has a lower mineralization density (21,22).

In conclusion, skeletal growth is heterogeneous; final height is a function of the differing onset, tempo, and duration of growth of the trunk and appendicular skeleton. Long bones grow in length at their growth plates, but at some locations bones grow fast at their distal metaphyseal growth plate whereas others grow faster at the proximal metaphyseal (23). At each point around a perimeter of a

cross section, the rate of periosteal, endocortical, and intracortical modelling and remodelling varies, giving each cross section its unique size, shape, and microarchitecture. All of these phenomena vary by age, sex, and race. The study of growth is a fascinating journey for adults to think about and remember fondly.

References

1. Lindgren E., Karlsson M.K., Lorentzon M., Rosengren B.E.: Bone traits seem to develop also during the third decade in life-normative cross-sectional data on 1083 men aged 18–28 years. J Clin Densitom 2016; (in this issue)

2. Gilsanz V., Skaggs D.L., Kovanlikaya A., et. al.: Differential effect of race on the axial and appendicular skeletons of children. J Clin Endocrinol Metab 1998; 83: pp. 1420-1427.

3. Bonjour J.P., Theintz G., Law F., et. al.: Peak bone mass. Osteoporos Int 1994; 4: pp. 7-13.

4. Seeman E.: From density to structure: growing up and growing old on the surfaces of bone. J Bone Miner Res 1997; 12: pp. 509-521.

5. Bradney M., Karlsson M.K., Duan Y., et. al.: Heterogeneity in the growth of the axial and appendicular skeleton in boys: implications for the pathogenesis of bone fragility in men. J Bone Miner Res 2000; 15: pp. 1871-1878.

6. Karlberg J.: The infancy-childhood growth spurt. Acta Paediatr Scand Suppl 1990; 367: pp. 111-118.

7. Seeman E.: Growth in bone mass and size—are racial and gender differences in bone mineral density more apparent than real? J Clin Endocrinol Metab 1998; 83: pp. 1414-1419.

8. Bakwin H., McLaughlin S.M.: Secular increase in height is the end in sight? Lancet 1964; 2: pp. 1195-1196.

9. Meredith H.V.: Secular change in sitting height and lower limb height of children, youths, and young adults of Afro-black, European, and Japanese ancestry. Growth 1978; 42: pp. 37-41.

10. Hauspie R.C., Vercauteren M., Susanne C.: Secular changes in growth and maturation: an update. Acta Paediatr 1997; 423: pp. 20-27.

11. Danubio M.E., Sanna E.: Secular changes in human biological variables in Western countries: an updated review and synthesis. J Anthropol Sci 2008; 86: pp. 91-112.

12. Malina R.M., Brown K.H., Zavaleta A.N.: Relative lower extremity length in Mexican American and in American black and white youth. Am J Phys Anthropol 1987; 72: pp. 89-94.

13. Hamill P.V., Johnston F.E., Lemeshow S.: Height and weight of youths 12–17 years. United States. Vital Health Stat 11 1973; pp. 1-81.

14. Ruff C.B., Hayes W.C.: Sex differences in age-related remodeling of the femur and tibia. J Orthop Res 1988; 6: pp. 886-896.

15. Zebaze R.M., Ghasem-Zadeh A., Bohte A., et. al.: Intracortical remodelling and porosity in the distal radius and post-mortem femurs of women: a cross-sectional study. Lancet 2010; 375: pp. 1729-1736.

16. Zebaze R., Ghasem-Zadeh A., Mbala A., Seeman E.: A new method of segmentation of compact-appearing, transitional and trabecular compartments and quantification of cortical porosity from high resolution peripheral quantitative computed tomographic images. Bone 2013; 54: pp. 8-20.

17. Cadet E.R., Gafni R.I., McCarthy E.F., et. al.: Mechanisms responsible for longitudinal growth of the cortex: coalescence of trabecular bone into cortical bone. J Bone Joint Surg 2003; 85-A: pp. 1739-1748.

18. Bala Y., Bui Q.M., Wang X.F., et. al.: Trabecular and cortical microstructure and fragility of the distal radius in women. J Bone Miner Res 2015; 30: pp. 621-629.

19. Wang Q., Ghasem-Zadeh A., Wang X.F., et. al.: Trabecular bone of growth plate origin influences both trabecular and cortical morphology in adulthood. J Bone Miner Res 2011; 26: pp. 1577-1583.

20. Zebaze R.M., Jones A., Welsh F., et. al.: Femoral neck shape and the spatial distribution of its mineral mass varies with its size: clinical and biomechanical implications. Bone 2005; 37: pp. 243-252.

21. Bjornerem A., Bui Q.M., Ghasem-Zadeh A., et. al.: Fracture risk and height: an association partly accounted for by cortical porosity of relatively thinner cortices. J Bone Miner Res 2013; 28: pp. 2017-2026.

22. Boutroy S., Walker M.D., Liu X.S., et. al.: Lower cortical porosity and higher tissue mineral density in Chinese American versus white women. J Bone Miner Res 2014; 29: pp. 551-561.

23. Wang Q., Wang X.F., Iuliano-Burns S., et. al.: Rapid growth produces transient cortical weakness: a risk factor for metaphyseal fractures during puberty. J Bone Miner Res 2010; 25: pp. 1521-1526.

CHAPTER 3

Quantifying sex, race, and age specific differences in bone microstructure requires measurement of anatomically equivalent regions

Short summary

Quantifying sex, race, and age specific differences in bone microstructure requires measurement of anatomically equivalent regions

Bone microstructure, the spatial distribution of bone mass, plays an important role in determining bone strength. It is established that bone microstructure differs by age, sex, race, and the position along the length of a bone. For these reasons accurate measurement of bone microstructure is crucial for the management of bone disease as well as understanding the mechanisms responsible for the heterogeneity in bone microarchitecture.

High-resolution peripheral quantitative computed tomography (HR-pQCT) is a non-invasive in-vivo imaging technique that allows assessment of bone microstructure with high spatial resolution. However, in evaluating the effects of age, sex, disease and treatment on microarchitecture, it is important to measure in anatomically equivalent regions to avoid differences, or lack of differences, being due to positioning errors.

In this study, I aimed to quantify sex and race differences in bone microstructure to highlight the importance of measuring anatomically equivalent regions and how to ensure that errors in position can be identified and corrected.

Bone microstructure was quantified ex vivo in 18 cadaveric radii, scanning from the growth plate 4 cm onwards and in vivo in 158 Asian and Caucasian women and men at a fixed region of interest (ROI). To ensure accurate measurement, a corrected ROI was established at 4.5-6% of forearm length, and a fixed ROI was adjusted for cross-sectional

area (CSA), forearm length or height. The study also assessed the effects of aging by comparing 38 younger and 33 older women.

The findings indicated that adjacent cross-sections along the bone were assembled using comparable bone mass. However, larger distal cross-sections achieved their larger size by being assembled with more void volume (medullary cavity size) and higher intracortical porosity, not more mass. Cortices were thinner, more porous with a lower matrix mineral density (MMD), a larger medullary cross-sectional area (CSA), and a higher trabecular density. Conversely, smaller more proximal cross-sections had thicker, less porous cortices with higher MMD, a small medullary area, and minimal trabecular bone.

Taller persons had ROIs which moved proximally when corrected. Shorter persons had ROIs which moved distally when corrected, so sexual and racial dimorphisms lessened. In the corrected ROIs, in Caucasians, women had 0.6 SD higher porosity and 0.6 SD lower trabecular density than men. In Asians, women had 0.25 SD higher porosity and 0.5 SD lower trabecular density than men. In women, Asians had 0.8 SD lower porosity and 0.3 SD higher trabecular density than Caucasians. In men, Asians and Caucasians had similar porosity and trabecular density. Adjusting for age-related secular effects on forearm length resulted in an age-related increment in porosity from 2.08 SD to 2.48 SD.

In summary, because bone microstructure exhibits regional heterogeneity, it is crucial to select an anatomically comparable region of interest (ROI) when quantifying the effects of growth, aging, sex, race, or drug therapy using HR-pQCT. Failure to do so leads to observed differences, or lack of differences, being erroneously determined.

Chapter 3

Quantifying Sex, Race, and Age Specific Differences in Bone Microstructure Requires Measurement of Anatomically Equivalent Regions

Short title: Bone Microstructure is Region Specific

Ali Ghasem-Zadeh[1]

Andrew Burghardt[2]

Xiao-Fang Wang[1]

Sandra Iuliano[1]

Serena Bonaretti[2,3]

Minh Bui[4]

Roger Zebaze[1]

Ego Seeman[1, 5]

[1]Department of Medicine and Endocrinology, Austin Health, University of Melbourne, Melbourne, Australia
[2]Musculoskeletal Quantitative Imaging Research Group, Department of Radiology and Biomedical Imaging, University of California, San Francisco, CA, USA
[3]Department of Radiology, Stanford University, Stanford, CA, USA
[4] Centre for Epidemiology and Biostatistics, University of Melbourne, Melbourne, Australia
[5] Institute for Health and Aging, Australian Catholic University, Melbourne, Australia

Corresponding author: Ali Ghasem-Zadeh, Department of Endocrinology and Medicine, Repatriation Campus, Austin Health, Melbourne, Australia
Tel 6139496 2081, Fax 613 9496 3365, alig@unimelb.edu.au

Keywords**:** Age, Cortical porosity, HR-pQCT, Microstructure, Race, Site Variation, Sex

Word Count: Abstract: 312, Main text word count: 4,700, References: 1,074, Tables: 5, Figures: 5

Chapter 3

Highlights and graphical abstract

• Adjacent cross sections of metaphyses are assembled with similar amounts of bone.

• The similar mass is apportioned differently as cortical and trabecular bone and its mineralization from slice to slice.

• Differences in positioning of a region of interest (ROI) blunt or exaggerate sex or racial differences in morphology.

• Accurately quantifying sex, race and age-related differences in morphology requires assessment of anatomically equivalent ROIs.

Chapter 3

Abstract

Introduction: Individuals differ in forearm length. As microstructure differs along the radius, we hypothesized that errors may occur when sexual and racial dimorphisms are quantified at a fixed distance from the radio-carpal joint.

Methods: Microstructure was quantified ex vivo in 18 cadaveric radii using high resolution peripheral quantitative computed tomography and in vivo in 158 Asian and Caucasian women and men at a fixed region of interest (ROI), a corrected ROI positioned at 4.5–6% of forearm length and using the fixed ROI adjusted for cross sectional area (CSA), forearm length or height. Secular effects of age were assessed by comparing 38 younger and 33 older women.

Results: *Ex vivo*, similar amounts of bone mass fashioned adjacent cross sections. Larger distal cross sections had thinner, porous cortices of lower matrix mineral density (MMD), a larger medullary CSA and higher trabecular density. Smaller proximal cross-sections had thicker less porous cortices of higher MMD, a small medullary canal with little trabecular bone. Taller persons had more distally positioned fixed ROIs which moved proximally when corrected. Shorter persons had more proximally positioned fixed ROIs which moved distally when corrected, so dimorphisms lessened. In the corrected ROIs, in Caucasians, women had 0.6 SD higher porosity and 0.6 SD lower trabecular density than men ($p < 0.01$). In Asians, women had 0.25 SD higher porosity (NS) and 0.5 SD lower trabecular density than men ($p < 0.05$). In women, Asians had 0.8 SD lower porosity and 0.3 SD higher trabecular density than Caucasians ($p < 0.01$). In men, Asians and Caucasians had similar porosity and trabecular density. Results were similar using an adjusted fixed ROI. Adjusting for secular effects of age on forearm length resulted in the age-related increment in porosity increasing from 2.08 SD to 2.48 SD ($p < 0.05$).

Chapter 3

Conclusions: Assessment of sex, race and age-related differences in microstructure requires measurement of anatomically equivalent regions.

Chapter 3

1. Introduction

Long bones must be strong to tolerate loading, yet light to facilitate mobility. They must also be rigid to serve as levers, yet flexible to be able to deform elastically [1], [2]. These paradoxical properties are achieved by bone modelling and remodelling, cellular events that fashion and refashion bone's macro- and microstructure using void volume. Larger bones have a biomechanical advantage and so are assembled using less mass and more void relative to their size [3]. Smaller bones offset their biomechanical disadvantage by being assembled with more mass and less void relative to their size [4].

During growth, different amounts of periosteal apposition and endocortical resorption from point to point around a bone cross section, and from cross section to cross section along a bone, produce variation in external and medullary canal bone size and shape [5], [6], [7], [8]. Concurrent intracortical remodelling produces variation in osteonal and Haversian canal number and so porosity (canals seen in cross section).

Because of this regional heterogeneity, when the effects of growth, advancing age, sex, race, or drug therapy are quantified using high resolution peripheral quantitative computed tomography (HR-pQCT), the region of interest (ROI) chosen to measure this morphology must be anatomically comparable otherwise differences or absence of differences in microstructure between these groups may be the result of the positioning of the ROI, not bone biology.

Currently, a fixed ROI starting 9.5 mm proximal to mid radiocarpal joint of radius is used regardless of an individual's age, sex, race, height, or bone length, even though on average, men and Caucasians have longer and wider bones than women and Asians respectively [9]. As the fixed ROI is more distal in taller than shorter individuals [10], [11], [12], we hypothesized that sexual and racial dimorphisms may be partly due to differences in positioning of the ROI, not true sex and racial differences in morphology.

The same error is likely to arise comparing individuals of the same sex or same race but differing

in height. For example, the effect of advancing age on bone morphology is usually examined in cross sectional studies [13]. Earlier born persons, the older cohort in a cross-sectional sample, are likely to have been shorter when they were young than later born persons forming the younger cohort in the cross-sectional sample [14]. This secular difference in stature may blunt the estimated age-related increase in cortical porosity as later born taller persons are likely to have higher porosity because longer and wider long bones have more porous cortices [15].

Few, if any, studies have examined the biological relevance of errors in sex, race and age-specific differences in microstructure produced using the fixed ROI. Nor have there been attempts to correct any error produced so that a closer approximation of the true biological differences between sexes, races and age are quantified.

We assessed the heterogeneity in bone microstructure and matrix mineral density along the length of the distal radius using cadaveric specimens, and quantified sex, race and age-related differences in morphology using a fixed versus and corrected ROI. We report that trait differences were amenable to correction by positioning the ROI as a percentage of forearm length or by adjusting the fixed ROI by bone CSA, forearm length or height.

2. Material and methods

2.1.Ex vivo imaging

Radii were obtained at the National Disease Research Interchanges from 11 male cadavers aged 77–93 years and 7 female cadavers aged 56–88 years. Deaths were unrelated to bone disease. The specimens were scanned using HR-pQCT (XtremeCT; Scanco Medical, Brüttisellen, Switzerland) at the University of California, San Francisco (UCSF). The protocol applies 60 kVp, 900 μA, 100 ms integration time, and 82 μm isotropic voxel sizes was used to image the specimens.

Quality control was based on Shewart rules by daily scanning of a manufacturer's phantom containing rods of Hydroxyapatite (HA) (densities of 0, 100, 200, 400, and 800 mgHA/cm3)

embedded in a soft-tissue equivalent resin (QRM, Moehrendorf, Germany). The number of slices was extended to 9.02 mm distally and 18.04 mm proximally in the fixed ROI (9.5 mm from end plate) giving a total ROI of 36.08 mm containing 440 slices. All images were reconstructed automatically using the manufacturer's software. X-ray attenuation data were converted to equivalent hydroxyapatite (HA) densities. All procedures were approved by the UCSF ethics office.

2.2 In vivo imaging

We studied 158 healthy Asians of Chinese origin and Caucasian women and men aged from 21 to 53 years, and compared morphology in 38 Caucasian premenopausal women aged from 21.4 to 38 years and 33 postmenopausal Caucasian women aged from 73.1 to 95.3 years. Measurements were made at the Department of Endocrinology at Austin Health, Melbourne, Australia. The manufacturer's scanning protocol was used to scan the distal non-dominant forearm containing 110 slices, each 0.082 mm thick. The image acquisition, reconstruction and validation are reported [16]. Participants had no bone disease or drug treatment influencing bone morphology or history of fractures and all provided a written informed consent. Radiation exposure dose was ~ 5 μSv per measurement. The study was approved by the Austin Health Ethics Committee. The cortical porosity and other bone microstructural indices of the cadaveric radii and in vivo distal radius images were analysed using StrAx 1.0 Algorithm [17].

2.3. Adjusting the fixed ROI

Forearm length was measured as the distance between the ulnar styloid and olecranon processes by calliper (CV = 1%, equivalent to 2–3 mm based on measuring 30 individuals twice on separate occasions). To cover the same anatomical ROI and the equivalent number of slices in persons with a shorter or longer forearm, the corrected ROI started at 4.5% of forearm length calculated from the distal point (reference line) and extended 1.5% proximally (4.5–6%). The locations of the first and last slices and the number of slices were calculated based on forearm length using equations (Eqs. (1)–(3)) (Fig. 1).

2.4. Statistical analyses

Analyses were performed using SPSS (version 22.0). Paired t-tests were used to compare ROIs 1–2 mm proximal or distal to the manufacture's ROI in cadaveric radii ex vivo, and to compare fixed versus corrected ROIs in same individuals in vivo irrespective of sex or race. Two-sample t-tests were used to compare traits measured in the fixed and corrected ROIs between sexes, between races and between young and elderly women. Sex differences and racial differences

in morphology were expressed as standardized deviations (SDs) and these SDs were compared in the fixed and in the corrected ROIs. Trait differences between sexes, races and young and elderly Caucasian women were assessed using analysis of covariance (ANCOVA) adjusting for total CSA, forearm length or height differences. All results were expressed as mean ± SD, with significance set at 5% level (two-tailed).

3.Results

3.1. *Ex vivo – similar amounts of bone assemble of adjacent bone cross-sections*

The bone mass used to assemble each cross section was constant. Distally, the larger total CSA of the radial metaphysis was fashioned with a thin porous cortex of lower matrix mineral density and trabeculae within a larger medullary canal. More proximally, the constant bone mass fashioned the smaller total CSA with a thicker less porous cortex of higher matrix mineral density, a smaller medullary void volume containing progressively less trabecular bone (Table 1, Fig. 2).

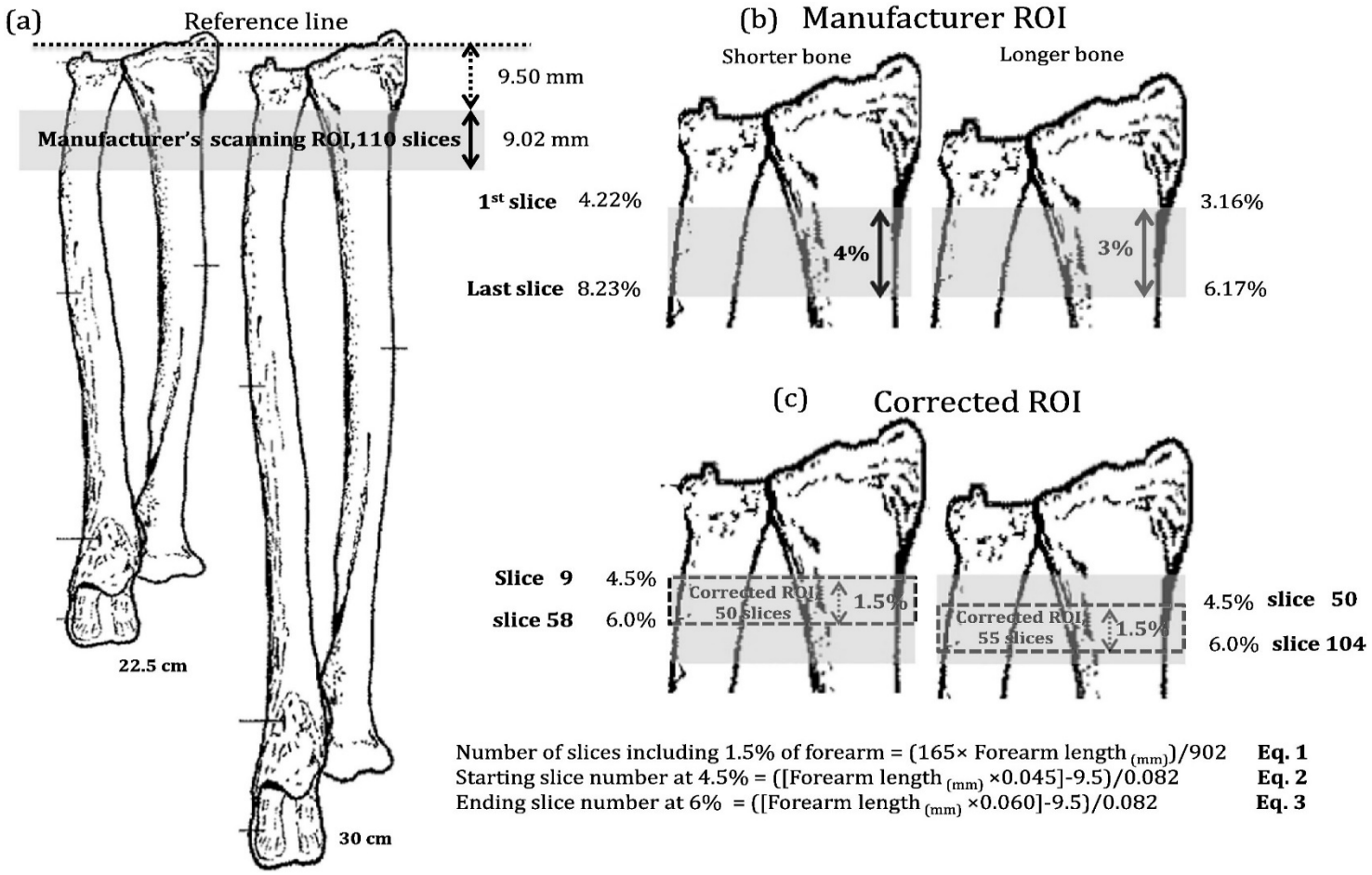

Figure 3.1

Fig. 1. (a) The reference line corresponds to the mid-radiocarpal joint. The manufacturer's fixed ROI (grey rectangle) consists of 110 slices on the shorter (22.5 cm) and longer (30 cm) forearm. (b) The fixed ROI is 4% of the shorter bone and 3% of the longer bone. Positioning is more proximal for the shorter forearm (4.22–8.23% vs 3.16–6.17%). (c) Calculation of the number of slices and location of the corrected ROI is obtained using Eqs. (1)– (3) to identify 1st and last slices of the 110 slice ROI.

3.2. In vivo – sexual and racial dimorphism

Men and Caucasians were taller and had longer forearms than women and Asians respectively (**Table 2, Fig. 3**). Sexual dimorphism in forearm length and total radial CSA was greater than racial dimorphism in these traits. For example, the mean sex difference in forearm length was 2.4 cm in each race, twice the racial differences of 1.1 cm in each sex. Details of traits measured in the fixed and corrected ROIs are shown in **Tables 3–5**, and **Fig. 4**. Dimorphisms measured in the fixed ROI lessened, were unaltered, and some reversed when measured in the corrected ROI. Comparing sexes, total and medullary CSAs were smaller in women than men of each race ($p < 0.01$). Caucasian women had 0.64 SD higher porosity and 0.63 SD lower trabecular density than Caucasian men ($p < 0.01$). Asian women had 0.25 SD higher porosity ($p = 0.72$) and 0.56 SD lower trabecular density than Asian men ($p < 0.05$).

Comparing races, total and medullary CSAs were smaller in Asians than Caucasians of each sex (all $p < 0.01$). Asian women had 0.83 SD lower porosity ($p < 0.01$) and 0.31 SD higher trabecular density than Caucasian women ($p = 0.19$). Asian and Caucasian men had similar porosity and trabecular density. MMD did not differ in Caucasian or Asian women and men. MMD was 0.86 SD higher in Asian women than Caucasian women (p b 0.05), not Asian and Caucasian men.

Table 3.1

Table1.
Ex vivo distal radial morphology (n = 18 specimens) using the manufacturer's region of interest (ROI) positioned 1 or 2 mm distally or proximally.

	2 mm distally	1 mm distally	Manufacturer's ROI	1 mm Proximally	2mm Proximally
Bone cross sectional areas (mm^2)					
Total	374.2 ± 96.0***	352.4 ± 90.0***	331.1 ± 84.4	312.0 ± 79.4***	296.3 ± 75.3***
Cortical	94.2 ± 23.0	94.0 ± 23.9	93.8 ± 24.1	94.0 ± 24.6	94.1 ± 24.9
Compact Cortex	32.3 ± 9.6**	32.9 ± 10.1**	33.6 ± 10.8	34.5 ± 11.6**	35.4 ± 12.3**
Transitional Zone	61.6 ± 15.1	60.7 ± 14.6 ns	60.2 ± 14.3	59.5 ± 14.1*	58.7 ± 13.8*
Medullary	148.0 ± 65.2	148.0 ± 66.2 ns	147.0 ± 66.9	145.3 ± 67.6*	142.9 ± 68.6*
Volumetric BMD ($mgHA/cm^3$)					
Total	257.9 ± 70.7***	258.9 ± 69.0***	290.1 ± 76.8	306.1 ± 79.5***	322.2 ± 82.2***
Cortical	257.9 ± 70.6**	258.9 ± 69.0**	290.1 ± 76.8	306.1 ± 79.5**	322.2 ± 82.2**
Trabecular	148.0 ± 65.2	148.0 ± 66.2	147.0 ± 67.0	145.3 ± 67.6*	142.9 ± 68.6*
Trabecular indices					
Number (1/mm)	2.17 ± 0.61	2.11 ± 0.67	2.06 ± 0.64	2.00 ± 0.64	2.00 ± 0.68
Separation (mm)	1.34 ± 0.41	1.35 ± 0.41	1.36 ± 0.41	1.38 ± 0.41*	1.40 ± 0.43**
Thickness (μm)	199 ± 11**	201 ± 12**	202 ± 12	203 ± 13**	204 ± 13**
Cortical indices					
Porosity (%)	68.8 ± 6.5***	66.3 ± 6.9***	63.7 ± 7.2	61.4 ± 7.4***	59.2 ± 7.6***
Thickness (mm)	1.46 ± 0.3**	1.50 ± 0.3**	1.55 ± 0.3	1.59 ± 0.3**	1.64 ± 0.3**
Matrix Mineral Density (%)	63.6 ± 1.2***	64.1 ± 1.3***	64.7 ± 1.3	65.1 ± 1.4***	65.6 ± 1.5***

Numbers are mean ± standard deviation.
P-value (p) for testing differences relative to manufacture's ROI: *P<0.05, **<0.01, ***<0.001

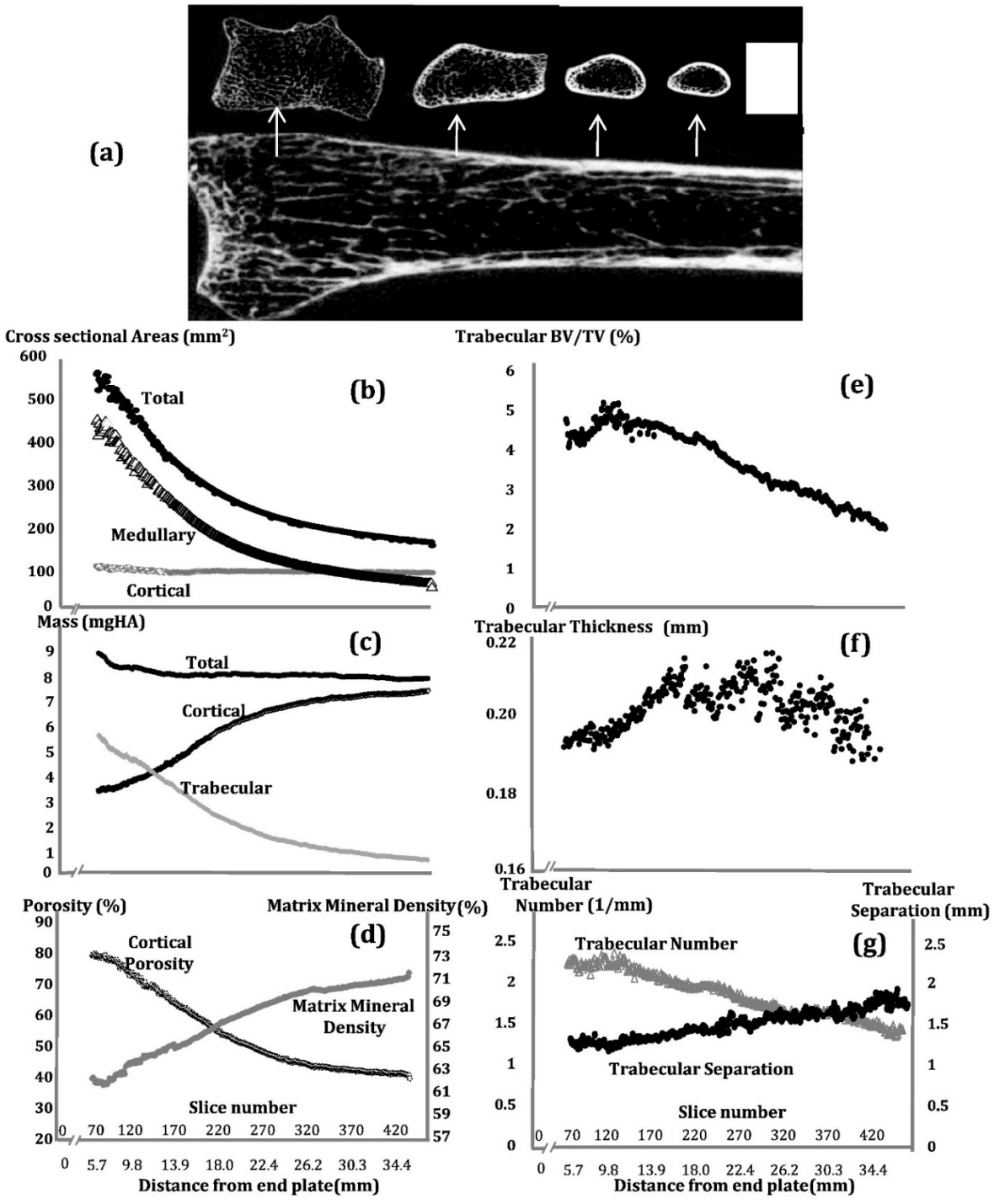

Figure 3.2

Fig. 2. (a) Axial and coronal sections of the distal radius. (b) Total and medullary cross-sectional areas decrease along the bone but cortical area is constant. (c) Total mass from cross section to cross section is constant but is assembled as varying proportions of cortical and trabecular bone depending on the position of the slice. (d) Cortical porosity and matrix mineral density vary from slice to slice along the bone and within a few millimetres. (e–g) Trabecular BV/TV, trabecular thickness, number and separation vary along the bone.

Table 3.2

Table 2.

Characteristics of the participants

	Asian women (N=40)	Asian men (N=37)	Caucasian women (N=33)	Caucasian men (N=48)
Age (yrs)	34.7 ± 9.0	36.6 ± 8.4	34.5 ± 10.0	34.2 ± 7.7
Forearm Length(cm)	24.6 ± 1.3	27.0 ± 1.4*	25.7 ± 1.5¥	28.1 ± 1.5* §
Height (cm)	160.9 ± 6.2	174.0 ± 7.1*	164.5 ± 8.1¥	177.1 ± 7.2* §
Weight (Kg)	58.1 ± 9.6	75.5 ± 12.9*	70.2 ± 15.0¥	81.0 ± 15.7*

Numbers are mean ± standard deviation.

* $P < 0.001$ comparing sexes of the same race.

¥ $P<0.05$ comparing races in women,

§ $P<0.05$ comparing races in men.

Table 3.3

Table3.

Distal radial microstructure in the fixed and corrected region of interest in Asian and Caucasian women and men.

	Asian women		Asian Men		Caucasian women		Caucasian Men	
	Fixed	Corrected	Fixed	Corrected	Fixed	Corrected	Fixed	Corrected
Total CSA(mm^2)	221.4 ± 40.3	234.1 ± 38.0**	304.9 ± 46.7	298.4 ± 44.3**	260.4 ± 60.9	267.5 ± 53.2*	354.6 ± 58.4	335.4 ± 50.0**
Cortical Area(mm^2)	87.6 ± 11.3	88.4 ± 11.0**	110.9 ± 13.7	109.9 ± 13.8**	91.9 ± 13.6	92.2 ± 13.3	120.5 ± 11.4	119.1 ± 11.6**
Medullary Area(mm^2)	133.8 ± 31.9	145.6 ± 29.9**	194.1 ± 36.7	188.6 ± 33.7*	168.4 ± 48.8	175.3 ± 41.7*	234.2 ± 51.9	216.2 ± 44.2**
Porosity of Total Cortex (%)	55.5 ± 5.2	58.0 ± 4.8**	57.7 ± 4.3	56.9 ± 3.8*	60.4 ± 5.8	61.9 ± 4.7**	60.8 ± 5.0	58.9 ± 4.8**
Total vBMD ($mgHA/cm^3$)	390.8 ± 65.8	361.1 ± 58.4**	374.9 ± 48.6	375.7 ± 43.7	335.9 ± 57.3	318.4 ± 46.8**	345.9 ± 58.3	356.4 ± 60.2**
Cortical vBMD ($mgHA/cm^3$)	725.5 ± 65.4	693.0 ± 59.1**	699.1 ± 54.6	709.1 ± 4.3*	664.7 ± 71.9	644.8 ± 58.9**	661.3 ± 63.2	684.5 ± 61.0**
Trabecular vBMD ($mgHA/cm^3$)	148.4 ± 46.1	150.6 ± 45.8**	168.9 ± 42.3	170.2 ± 40.9*	133.5 ± 41.4	137.6 ± 38.3**	171.4 ± 46.4	171.7 ± 47.6
Matrix Mineral Density (%)	64.9 ± 1.3	64.1 ± 1.1**	63.7 ± 1.1	63.7 ± 1.0	63.7 ± 1.2	63.1 ± 1.2**	63.1 ± 1.2	63.5 ± 1.3**

Mean ± standard deviation, * significant difference with $p<0.05$, ** significant difference with $p<0.01$.

Table 3.4

Table 4.

Sexual dimorphism in distal radial microstructure in the fixed ROI and in the corrected ROI in Asians and Caucasians.

	Fixed ROI(Asian)		Corrected ROI(Asian)		Fixed ROI(Caucasian)		Corrected ROI(Caucasian)	
	Women	Men	Women	Men	Women	Men	Women	Men
Total CSA(mm^2)	221.4 ± 40.3	304.9 ± 46.7**	234.1 ± 38.0	298.4 ± 44.3**	260.4 ± 60.9	354.6 ± 58.4**	267.5 ± 53.2	335.4 ± 50.0**
Cortical Area(mm^2)	87.6 ± 11.3	110.9 ± 13.7**	88.4 ± 11.0	109.9 ± 13.8**	91.9 ± 13.6	120.5 ± 11.4**	92.2 ±13.3	119.1 ± 11.6**
Medullary Area(mm^2)	133.8 ± 31.9	194.1 ± 36.7**	145.6 ± 29.9	188.6 ± 33.7**	168.4 ± 48.8	234.2 ± 51.9**	175.3 ± 41.7	216.2 ± 44.2**
Porosity of Total Cortex (%)	55.5 ± 5.2	57.7 ± 4.3*	58.0 ± 4.8	56.9 ± 3.8	60.4 ± 5.8	60.8 ± 5.0	61.9 ± 4.6	58.9 ± 4.8*
Total vBMD ($mgHA/cm^3$)	390.8 ± 65.8	374.9 ± 48.6	361.1 ± 58.4	375.7 ± 43.7	335.9 ± 57.3	345.9 ± 58.3	318.4 ± 46.8	356.4 ± 60.2**
Cortical vBMD ($mgHA/cm^3$)	725.5 ± 65.4	699.1 ± 54.6*	693.0 ± 59.1	709.1 ± 4.3	664.7 ± 71.9	661.3 ± 63.2	644.8 ± 58.9	684.5 ± 61.0**
Trabecular vBMD ($mgHA/cm^3$)	148.4 ± 46.1	168.9 ± 42.3*	150.6 ± 45.8	170.2 ± 40.9*	133.5 ± 41.4	171.4 ± 46.4**	137.6 ± 38.3	171.7 ± 47.6**
Matrix Mineral Density (%)	64.9 ± 1.3	63.75 ± 1.1**	64.1 ± 1.1	63.73 ± 1.0	63.71 ± 1.2	63.1 ± 1.2*	63.11 ± 1.2	63.5 ± 1.3

Mean ± standard deviation, * significant difference with $p<0.05$, ** significant difference with $p<0.01$.

Table 3.5

Table 5.

Racial dimorphism in distal radial microstructure in women and men in the fixed and corrected region of interest.

	Fixe ROI(Women)		Corrected ROI(Women)		Fixed ROI(Men)		Corrected ROI(Men)	
	Asian	Caucasian	Asian	Caucasian	Asian	Caucasian	Asian	Caucasian
Total CSA(mm^2)	221.4 ± 40.3	260.4 ± 60.9**	234.1 ± 38.0	267.5± 53.2**	304.9 ± 46.7	354.6 ± 58.4**	298.4 ± 44.3	335.4 ± 50.0**
Cortical Area(mm^2)	87.6 ± 11.3	91.9 ± 13.6	88.4 ± 11.0	92.2 ± 13.3	110.9 ± 13.7	120.5 ± 11.4**	109.9 ± 13.8	119.1 ± 11.6**
Medullary Area(mm^2)	133.8 ± 31.9	168.4 ± 48.8**	145.6 ± 29.9	175.3 ± 41.7**	194.1 ± 36.7	234.2 ± 51.9**	188.6 ± 33.7	216.2 ± 44.2**
Porosity of Total Cortex (%)	55.5 ± 5.2	60.45 ± 5.8**	58.0 ± 4.8	61.94 ± 4.7**	57.7 ± 4.3	60.8 ± 5.0 **	56.9 ± 3.8	58.9 ± 4.8
Total vBMD (mgHA/cm^3)	390.8 ± 65.8	335.9 ± 57.3**	361.1 ± 58.4	318.4 ± 46.8**	374.9 ± 48.6	345.9 ± 58.3	375.7 ± 43.7	356.4 ± 60.2
Cortical vBMD (mgHA/cm^3)	725.5 ± 65.4	664.7 ± 71.9**	693.0 ± 59.1	644.8 ± 58.9**	699.1 ± 54.6	661.3 ± 63.2	709.1 ± 4.3	684.5 ± 61.0
Trabecular vBMD (mgHA/cm^3)	148.4 ± 46.1	133.5 ± 41.4	150.6 ± 45.8	137.6 ± 38.3	168.9 ± 42.3	171.4 ± 46.4	170.2 ± 40.9	171.7 ± 47.6
Matrix Mineral Density (%)	64.9 ± 1.3	63.71 ± 1.2*	64.1 ± 1.1	63.1 ± 1.2*	63.75 ± 1.1	63.1 ± 1.2*	63.7 ± 1.0	63.5 ± 1.3

Mean ± standard deviation, * significant difference with $p<0.05$, ** significant difference with $p<0.01$.

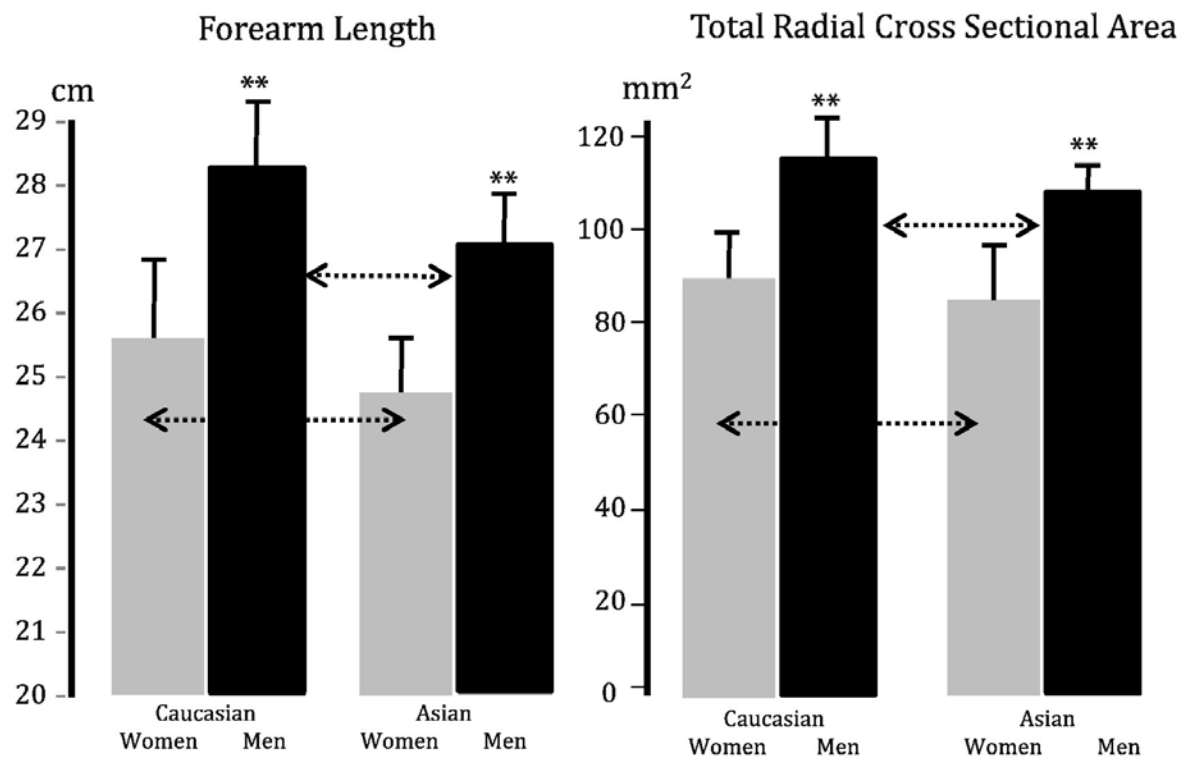

Figure 3.3

Fig. 3. Forearm length and total radial cross sectional area were higher in men than in women of each racial group (**p < 0.01). As shown by the double arrowheaded hatched lines, the differences by race in each sex were numerically smaller than sex differences in each race.

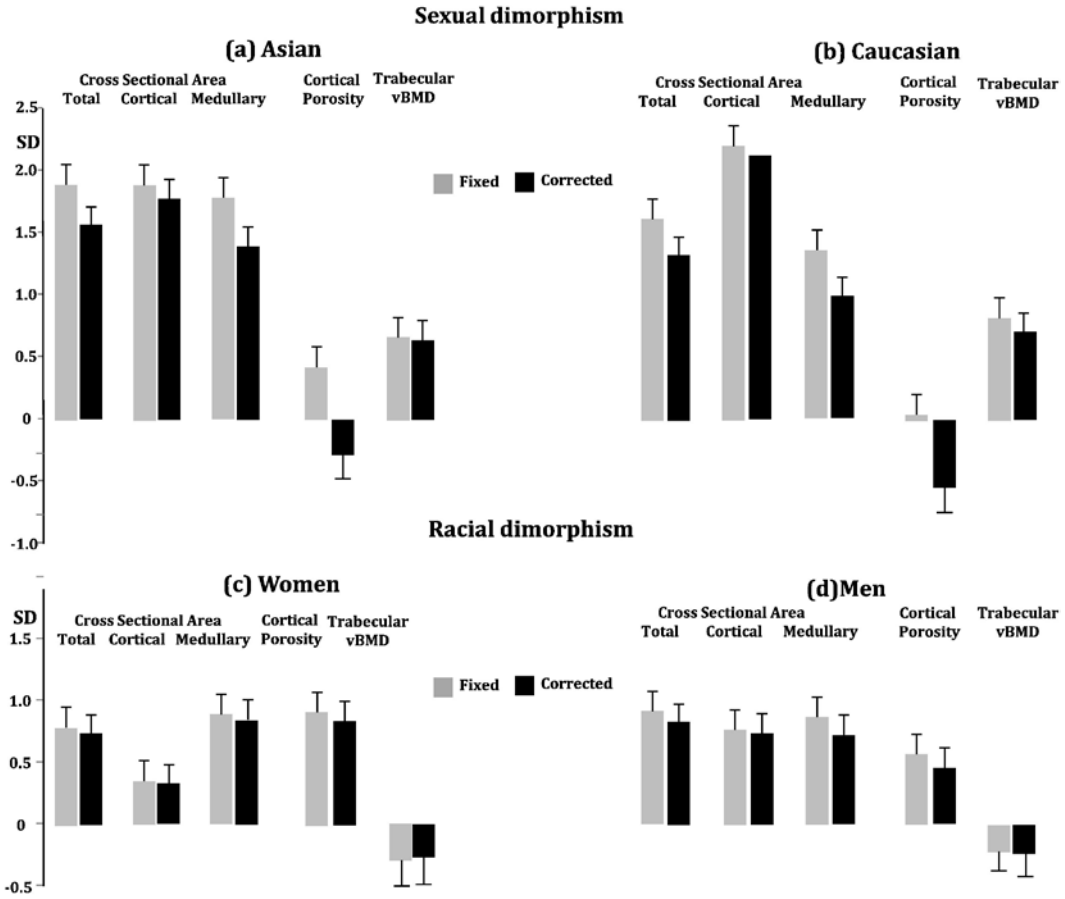

Figure 3.4

Fig. 4. Sexual dimorphism in (a) Asians (b) Caucasians, and racial dimorphisms in (c) women and (d) men, determined in the fixed (black bars) and in the corrected region of interest (grey bars). In general, trait differences (expressed as a standard deviations) lessened when measured in the corrected region of interest (see text and Tables 4 and 5).

Figure 3.5

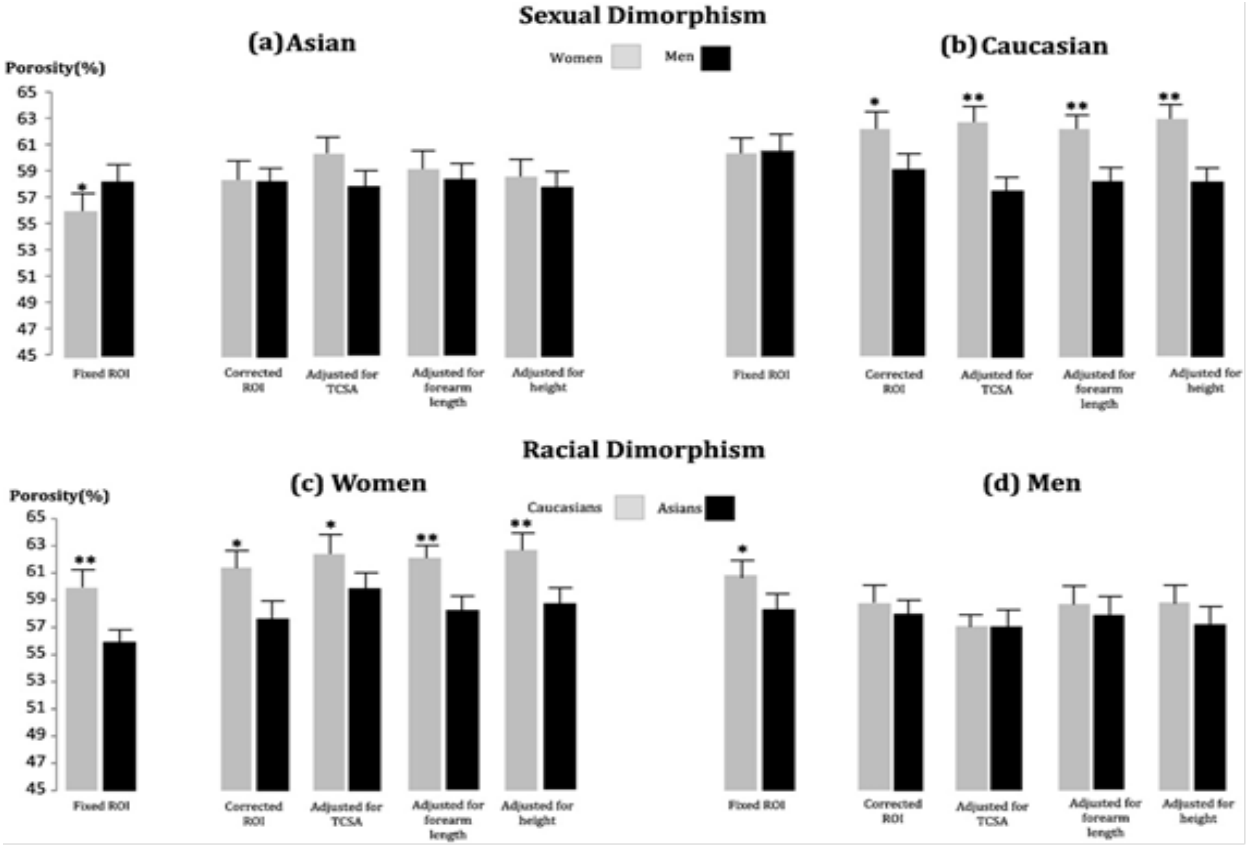

Fig. 5. Sexual and racial dimorphism in cortical porosity in the fixed region of interest, in the corrected region of interest, and in the fixed region of interest adjusted for total cross sectional area (TCSA), forearm length and height. (a) In Asians, the lower porosity in women than men was no longer seen after adjustment and porosity was higher after adjustment for total CSA. (b) In Caucasians, there was no sex difference using the fixed ROI but higher porosity in women than men becomes apparent using any one of the four approaches. (c) Higher porosity in Caucasian than Asian women was found with all approaches. (d) In Caucasian men, porosity was higher than in Asian men in the fixed ROI but not the corrected or any adjusted approaches. *$p < 0.05$, **$p < 0.01$.

3.3 .In vivo – adjusting the fixed ROI by CSA, forearm length or height

Instead of correcting the position of the ROI, when we adjusted the fixed ROI for CSA, forearm length or height, porosity was 1.07 SD higher in Caucasian women than Caucasian men (p b 0.01). Asian women had higher porosity than Asian men (p = NS). Asian women had 0.6 SD lower porosity than Caucasian women (p b 0.05). Cortical porosity did not differ in Asian and Caucasia men (Fig. 5). Dimorphisms in trabecular density did not differ before or after adjustment of the fixed ROI.

3.4. In vivo – secular effects of age on stature and microstructure

Caucasian elderly women were 1.6 SD shorter and had 0.97 SD shorter forearm length than young Caucasian women (p b 0.01). The fixed ROI was more proximal in elderly women resulting in a 2.08 SD higher cortical porosity than in younger women. After adjustment for forearm length, cortical porosity was 2.48 SD higher in older than younger women.

4. **Discussion**

In the study of cadaveric specimens of the distal radius, adjacent cross sections differed in size, shape, and microstructure but each cross section was assembled using virtually the same amount of bone matrix mass. The same is reported comparing cross sectional slices along the femoral neck [4]. Variation in size was achieved by varying intracortical and medullary void volumes, not bone matrix mass [18–21]. Distally, the bone was assembled with a thin porous cortex with a lower matrix mineral density and trabecular plates separated by ‘inter-trabecular’ void volume; features conferring lightness for mobility and dexterity. More proximally, the constant mass was fashioned as a thicker cortex with low porosity and higher matrix mineral density, a small medullary canal containing little or no trabecular bone.

Given the heterogeneity in bone size, microstructure and matrix mineral density from slice to slice

within a region of under 5 mm in length, positioning of a ROI in anatomically equivalent positions becomes important when comparing individuals differing in forearm length. This is a recognised requirement using pQCT scanning [22,23]. The need for cor- rect position of the ROI becomes particularly relevant using high resolution pQCT given this heterogeneity and the small ROI used.

The positioning of a ROI based on a percentage of forearm length instead of a fixed ROI was an attempt to measure anatomically equivalent regions in persons differing in forearm length. Men and Caucasians are taller and had longer forearms than women and Asians respectively. A fixed ROI was more distal in taller people and so overestimated po- rosity and trabecular density and under-estimated matrix mineral density. A fixed ROI was more proximal in a shorter person and so underestimated porosity and trabecular density and over-estimated matrix mineral density, the net effect being an exaggeration of sex and racial dimorphisms.

When corrected, the ROIs approximated; the more distal ROI in taller persons with longer forearms (Caucasians, males) moved proximally so that total and medullary areas decreased, porosity and trabecular density decreased and matrix mineral density increased, and the more proximal ROI in shorter persons with shorter forearms (Asians, women) moved distally so that the total and medullary areas increased, porosity and trabecular density increased, and matrix mineral density decreased. The net effect was a lessening or reversal of sex and racial dimorphisms.

The sexual and racial dimorphism may be, in part, the result of differences in remodelling rate. Women remodel their skeletons more rapidly than men after menopause [24], accounting for the higher porosity and lower trabecular density in Caucasian women than Caucasian men, and in Asian women than Asian men. We did not detect lower MMD in women than men in either race; perhaps due to younger age of the sample.

Asian women remodel their skeleton more slowly than Caucasian Women [25]. Accordingly, Asian women had lower porosity, higher trabecular density and higher MMD than Caucasian women. Men remodel their skeleton slowly. No differences were detected in porosity, trabecular density or MMD in

Sexual dimorphism was greater than racial dimorphism in this cohort because women and men of the same race differed in height and forearm length more than Asians and Caucasians of the same sex [26]. A reason for this may relate, in part, to the timing of puberty. Appendicular growth is rapid prior puberty. Males enter puberty about one year later than females and have a longer intra pubertal growth period. Chinese enter puberty only 6–9 months earlier than Caucasians so that the sex difference in the duration of pre-pubertal appendicular growth is greater than the racial difference, at least comparing Caucasians and Asians [27,28]. Whether this applies to other racial groups is not known [29].

Longer bones usually have a larger cross-sectional area, and wider long bones have higher porosity than narrower long bones [6]. Thus, in situations where forearm length is not available, we report that adjustment of the fixed ROI by CSA or height produced similar results for cortical porosity and trabecular density as found by correcting the position of the ROI.

Failure to correct the anatomical error may misrepresent fracture risk. For example, correcting the ROI resulted in a 0.51 SD higher porosity in Asian women and 0.32 SD higher porosity in Caucasian women. Failure to correct the ROI overestimated porosity by 0.21 SD in Asian men and by 0.39 SD in Caucasian men. Failure to correct the ROI comparing elderly Caucasian women underestimated the age-related increase in porosity by 0.40 SD. These discrepancies resemble the 0.40 SD higher cortical porosity in women with forearm fractures relative to controls [30].

This study has several limitations. Our purpose was to signal the need for caution in interpreting dimorphisms by sex, race and age given the small ROIs chosen in a heterogeneous structure like the distal radial metaphysis. However, we had no post-mortem samples from Asian sub- jects to establish the accuracy of each adjustment method. Sex, racial and age comparison were based on small sample sizes and we only measured Caucasian and Asians of Chinese origin, not other racial groups. Nor did we examine secular effects of age in men. We confined measurements to cortical porosity, trabecular morphology and matrix mineral density. We prefer to avoid making definitive statements concerning

the magnitude of sex, race and age related differences in macro- and microstructure because large cohorts are needed to provide robust data. We did not examine whether errors in repositioning in placebo controlled trials may obscure or exaggerate the effects of therapy on morphology. While differences in morphology were found in the fixed and corrected ROIs, evidence that these differences influence the sensitivity and specificity for fracture prediction is not available.

In conclusion, to the best of our knowledge this is the first study to provide a method that locates anatomically equivalent ROIs by repositioning the ROI according forearm length or adjusting the fixed ROI for cross sectional area, forearm length or height. Whatever the approach taken, the continued use of a fixed ROI without attention to differences in the dimensions of bone between individuals may result in misleading inferences concerning the pathogenesis of bone fragility, fracture risk, and effects of treatment.

Disclosures

A Ghasem-Zadeh is one of the inventors of the StrAx1.0 algorithm and serves as a reimbursed consultant for Straxcorp. R Zebaze has re-ceived grant and/or research support from Amgen, Merck Sharp & Dohme, Servier, Warner-Chilcott, AKP, Genzyme, Sonafi, GSK and Pfizer, and is one of the inventors of the StrAx1.0 algorithm. E Seeman has received research support and lectured at national and international meetings funded by from Allergan, Amgen, Asahi pharmaceuticals, Eli Lilly, and MSD. He is a director of the board, renumerated as Chief Medical Officer and is one of the inventors of the StrAx1.0 algorithm. AJ Burghardt has received research support from Ultragenyx Pharmaceutical. Other authors state they have no conflicts of interest.

Acknowledgements

This study was funded by Austin Medical Research Foundation Melbourne, Australia (2-1260) and NIH/NIMAS R01 AR 060700. Authors' roles: Study design and conduct: AGZ, XW, RZ, and ES. Data collection: AGZ, AB, SB, SI, XW. Responsibility for StrAx analysis: AGZ, RZ, Statistical

analyses: MB, XW, And AGZ. Drafting manuscript: AGZ, XW, SI and ES. Data interpretation and approving final version of manuscript: AGZ, XW, AB, SI, SB, MB, RZ, ES.

References

[1] J.D. Currey, Bones: Structure and Mechanics, Princeton University Press, Princeton, NJ, 2002 1–380.

[2] E. Seeman, Growth in bone mass and size—are racial and gender differences in bone mineral density more apparent than real? J. Clin. Endocrinol. Metab. 83 (5) (1998 May) 1414–1419.

[3] Q. Wang, S. Cheng, M. Alen, E. Seeman, Finnish Calex Study G, Bone's structural diver- sity in adult females is established before puberty, J. Clin. Endocrinol. Metab. 94 (5) (2009 May) 1555–1561.

[4] R.M. Zebaze, A. Jones, F. Welsh, M. Knackstedt, E. Seeman, Femoral neck shape and the spatial distribution of its mineral mass varies with its size: clinical and biomechanical implications, Bone 37 (2) (2005 Aug) 243–252.

[5] R.M. Zebaze, A. Jones, M. Knackstedt, G. Maalouf, E. Seeman, Construction of the fem- oral neck during growth determines its strength in old age, J. Bone Miner. Res. 22 (7) (2007 Jul) 1055–1061.

[6] Q. Wang, S. Cheng, M. Alen, E. Seeman, Finnish Calex Study G, Bone's structural diver- sity in adult females is established before puberty, J. Clin. Endocrinol. Metab. 94 (5) (2009 May) 1555–1561.

[7] G. Mall, M. Hubig, A. Buttner, J. Kuznik, R. Penning, M. Graw, Sex determination and estimation of stature from the long bones of the arm, Forensic Sci. Int. 117 (1–2) (2001 Mar 01) 23–30.

[8] X.F. Wang, Y. Duan, T.J. Beck, E. Seeman, Varying contributions of growth and ageing to racial and sex differences in femoral neck structure and strength in old age, Bone 36 (6) (2005 Jun) 978–986.

[9] S.K. Boyd, Site-specific variation of bone micro-architecture in the distal radius and tibia, J.

Clin. Densitom. 11 (3) (2008 Jul–Sep) 424–430.

[10] S. Bonaretti, N. Vilayphiou, C.M. Chan, A. Yu, K. Nishiyama, D. Liu, et al., Operator variability in scan positioning is a major component of HR-pQCT precision error and is reduced by standardized training, Osteoporos. Int. (2016 Jul 30).

[11] K.Y. Cheuk, E.M. Tam, F.W. Yu, B.H. Yip, V.W. Hung, X. Wang, et al., A critical comparison between two scanning protocols of high-resolution peripheral quantitative com- puted tomography at the distal radius in adolescents, J. Clin. Densitom. 19 (3) (2016 Jul–Sep) 305–315.

[12] V.V. Shanbhogue, S. Hansen, U. Halekoh, K. Brixen, Use of relative vs fixed offset distance to define region of interest at the distal radius and tibia in high-resolution peripheral quantitative computed tomography, J. Clin. Densitom. 18 (2) (2015 Apr–Jun) 217–225.

[13] B.L. Riggs, L.J. Melton, R.A. Robb, J.J. Camp, E.J. Atkinson, L. McDaniel, et al., A population-based assessment of rates of bone loss at multiple skeletal sites: evidence for substantial trabecular bone loss in young adult women and men, J. Bone Miner. Res. 23 (2) (2008 Feb) 205–214.

[14] R.C. Hauspie, M. Vercauteren, C. Susanne, Secular changes in growth and maturation: an update, Acta Paediatr. 423 (1997 Nov) 20–27.

[15] A. Bjornerem, Q.M. Bui, A. Ghasem-Zadeh, J.L. Hopper, R. Zebaze, E. Seeman, Fracture risk and height: an association partly accounted for by cortical porosity of relatively thinner cortices, J. Bone Miner. Res. 28 (9) (2013 Sep) 2017–2026.

[16] X.F. Wang, Q. Wang, A. Ghasem-Zadeh, A. Evans, C. McLeod, S. Iuliano-Burns, et al., Differences in macro- and microarchitecture of the appendicular skeleton in young Chinese and white women, J. Bone Miner. Res. 24 (12) (2009 Dec) 1946–1952.

[17] R. Zebaze, A. Ghasem-Zadeh, A. Mbala, E. Seeman, A new method of segmentation of compact-appearing, transitional and trabecular compartments and quantification of cortical porosity from high resolution peripheral quantitative computed tomographic images, Bone 54 (1) (2013 May) 8–20.

[18] L. Vico, M. Zouch, A. Amirouche, D. Frere, N. Laroche, B. Koller, et al., High-resolution pQCT analysis at the distal radius and tibia discriminates patients with recent wrist and femoral neck fractures, J. Bone Miner. Res. 23 (11) (2008 Nov) 1741–1750.

[19] E. Seeman, P.D. Delmas, Bone quality—the material and structural basis of bone strength and fragility, N. Engl. J. Med. 354 (21) (2006 May 25) 2250–2261.

[20] Y. Bala, Q.M. Bui, X.F. Wang, S. Iuliano, Q. Wang, A. Ghasem-Zadeh, et al., Trabecular and cortical microstructure and fragility of the distal radius in women, J. Bone Miner. Res. 30 (4) (2015

Apr) 621–629.

[21] R.M. Zebaze, A. Jones, M. Knackstedt, G. Maalouf, E. Seeman, Construction of the fem- oral neck during growth determines its strength in old age, J. Bone Miner. Res. 22 (7) (2007 Jul) 1055–1061.

[22] K. Engelke, J.E. Adams, G. Armbrecht, P. Augat, C.E. Bogado, M.L. Bouxsin, et al., Clinical use of quantitative computed tomography and peripheral quantitative computed to- mography in the management of osteoporosis in adults: the 2007 ISCD official positions, J. Clin. Densitometry 11 (1) (Jan–Mar 2008) 123–162.

[23] P. Augat, T. Fuerst, H.K. Genant, Quantitative bone mineral assessment at the forearm: a review, Osteoporos. Int. 8 (4) (1998) 299–310.

[24] S. Epstein, J. Poser, R. McClintock, C.C. Johnston Jr., G. Bryce, S. Hui, Differences in serum bone GLA protein with age and sex, Lancet 1 (8372) (Feb 11 1984) 307–310.

[25] J.S. Finkelstein, M. Sowers, G.A. Greendale, M.L. Lee, R.M. Neer, J.A. Cauley, et al., Ethnic variation in bone turnover in pre- and early perimenopausal women: effects of an- thropometric and lifestyle factors, J. Clin. Endocrinol. Metab. 87 (7) (Jul 2002) 3051–3056.

[26] X.F. Wang, Y. Duan, T.J. Beck, E. Seeman, Varying contributions of growth and ageing to racial and sex differences in femoral neck structure and strength in old age, Bone 36 (6) (2005) 978–986.

[27] A.S. Parent, G. Teilmann, A. Juul, N.E. Skakkebaek, J. Toppari, J.P. Bourguignon, The timing of normal puberty and the age limits of sexual precocity: variations around the world, secular trends, and changes after migration, Endocr. Rev. 24 (5) (Oct 2003) 668–693.

[28] K.F. Huen, S.S. Leung, J.T. Lau, A.Y. Cheung, N.K. Leung, M.C. Chiu, Secular trend in the sexual maturation of southern Chinese girls, Acta Paediatr. 86 (10) (Oct 1997) 1121–1124.

[29] D.S. Freedman, L.K. Khan, M.K. Serdula, W.H. Dietz, S.R. Srinivasan, G.S. Berenson, Relation of age at menarche to race, time period, and anthropometric dimensions: the Bogalusa Heart Study, Pediatrics 110 (4) (Oct 2002), e43.

[30] Y. Bala, R. Zebaze, A. Ghasem-Zadeh, E.J. Atkinson, S. Iuliano, J.M. Peterson, et al., Cor- tical porosity identifies women with osteopenia at increased risk for forearm fractures, J. Bone Miner. Res. 29 (6) (2014 Jun) 1356–1362.

CHAPTER 4

Heterogeneity in microstructural deterioration following spinal cord injury

Short summary

Heterogeneity in microstructural deterioration following spinal cord injury

After a spinal cord injury, bone loss occurs below the level of the injury; however, the severity of bone loss and the cellular activity involved in adapting bone to its loading are region specific. The tibia, being a weight-bearing region, undergoes higher loads and strain rates compared to less weight-bearing regions such as the fibula or non-weight-bearing regions such as the radius. Bone loss results in a reduction of bone volume and disruption of the microarchitecture of the remaining bone which compromises bone strength.

BMD measurements do not capture microstructural deterioration. Therefore, patients with spinal cord injury may exhibit bone fragility despite having osteopenia or so-called normal BMD. We therefore hypothesised that spinal cord injury will result in more bone loss and architectural disruption at weight bearing regions than less weight-bearing or non-weight bearing regions.

HR-pQCT was used to measure the volumetric bone mineral density (vBMD) of the distal tibia, distal fibula, and distal radius in 31 men with a mean age of 43.5 years, 12 with tetraplegia and 19 with paraplegia, with paralysis of 0.7 to 18.6 years. Controls included 102 healthy age- and sex-matched controls.

Compared to controls, men with paraplegia showed a decrease in total vBMD at the distal tibia and distal fibula, whereas no significant alteration was observed at the distal radius. Similarly, men with tetraplegia had lower total vBMD at the distal tibia and distal fibula, but interestingly, not at the distal radius despite having paralysis of all four limbs.

Both cortical and trabecular vBMD deficits were observed at the distal tibia. By contrast, vBMD deficits at the distal fibula were confided to trabecular bone and were less pronounced compared to the deficits seen at the distal tibia.

We concluded that following unloading caused by spinal cord injury, weight bearing regions, adapted to accommodate greater peak strains and strain rates, are at higher risk for bone loss and microarchitectural deterioration during unloading than non-weight bearing regions that are adapted to lower peak strains and strain rates. These observations highlight the site specificity of the strain thresholds regulating the cellular activity of mechano-transduction. The rapidity of the change and irreversible microarchitectural deterioration suggest prompt intervention with antiresorptive, anabolic therapy, or both, warrants consideration.

Chapter 4

Heterogeneity in microstructural deterioration following spinal cord injury

Short title: Bone Microstructure deterioration in spinal cord injury

Ali Ghasem-Zadeh*[1]

Mary P Galea [2]

Andrew Nunn [2]

Maya Panisset [2]

Xiao-Fang Wang [3]

Sandra Iuliano [3]

Steven K Boyd [4]

Mark R Forwood [1]

Ego Seeman [3]

[1] Depts of Medicine and Endocrinology, Austin Health, The University of Melbourne, Melbourne, Australia; Dept of Endocrinology, Austin Health, The University of Melbourne, Melbourne, Australia
[2] Depts of Medicine and Endocrinology, Austin Health, The University of Melbourne, Melbourne, Australia; Depts of Medicine and Victorian Spinal Cord Service, Austin Health, The University of Melbourne, Melbourne, Australia
[3] Depts of Medicine and Endocrinology, Austin Health, The University of Melbourne, Melbourne, Australia; Dept of Endocrinology, Austin Health, The University of Melbourne, Melbourne, Australia
[4] McCaig Institute for Bone and Joint Health, University of Calgary, Calgary, AB, Canada
[5] School of Medical Science and Menzies Health Institute Queensland, Griffith University, Gold Coast, Australia

Corresponding author: Ali Ghasem-Zadeh, Department of Endocrinology and Medicine, Repatriation Campus, Austin Health, Melbourne, Australia
Tel 6139496 2081, Fax 613 9496 3365, alig@unimelb.edu.au

Keywords**:** Cortical -bone, HR-pQCT, Microstructure, Paralysis, Spinal -cord -injury,

Trabecular bone, Unloading, Weight-bearing

Word Count: Abstract: 359, Main text word count: 4260, References: 1583, Tables: 4, Figures: 4

Highlights

• Weight-bearing regions have more compromised morphology than less weight-bearing regions after spinal cord injury.

• Higher cortical porosity, lower trabeculae density and lower matrix mineral density occur following spinal cord injury.

• Uncompromised distal radial microstructure following tetraplegia suggests this region is usually adapted to low strains.

Abstract

Background: Modelling and remodelling adapt bone morphology to accommodate strains commonly encountered during loading. If strains exceed a threshold threatening fracture, modelling-based bone formation increases bone volume reducing these strains. If unloading reduces strains below a threshold that inhibits resorption, increased remodelling-based bone resorption reduces bone volume restoring strains, but at the price of compromised bone volume and microstructure. As weight-bearing regions are adapted to greater strains, we hypothesized that microstructural deterioration will be more severe than at regions commonly adapted to low strains following spinal cord injury.

Methods: We quantified distal tibial, fibula and radius volumetric bone mineral density (vBMD) using high-resolution peripheral quantitative computed tomography in 31 men, mean age 43.5 years (range 23.5-75.0), 12 with tetraplegia and 19 with paraplegia of 0.7 to 18.6 years duration, and 102 healthy age- and sex-matched controls. Differences in morphology relative to controls were expressed as standardized deviation (SD) scores (mean ± SD). Standardized between-region differences in vBMD were expressed as SDs (95% confidence intervals, CI).

Results*:* Relative to controls, men with tetraplegia had deficits in total vBMD of −1.72 ± 1.38 SD at the distal tibia ($p < 0.001$) and − 0.68 ± 0.69 SD at distal fibula ($p = 0.041$), but not at the distal radius, despite paralysis. Deficits in men with paraplegia were −2.14 ± 1.50 SD ($p < 0.001$) at the distal tibia and −0.83 ± 0.98 SD ($p = 0.005$) at the distal fibula while distal radial total vBMD was 0.23 ± 1.02 ($p = 0.371$), not significantly increased, despite upper limb mobility. Comparing regions, in men with tetraplegia, distal tibial total vBMD was 1.04 SD (95%CI 0.07, 2.01) lower than at the distal fibula ($p = 0.037$) and 1.51 SD (95%CI 0.45, 2.57) lower than at the distal radius ($p = 0.007$); the latter two sites did not differ from each other. Results were similar in men with paraplegia, but total vBMD at the distal fibula was 1.06 SD (95%CI 0.35, 1.77) lower than at the distal radius (p =

0.004)

Conclusions: Microarchitectural deterioration following spinal cord injury is heterogeneous, perhaps partly because strain thresholds regulating the cellular activity of mechano-transduction are region specific.

Chapter 4

1. Introduction

Bone has paradoxical properties of strength for loading yet lightness for mobility, stiffness for leverage yet flexibility for energy absorption [1]. These properties are achieved by bone modelling and remodelling, a cellular machinery that adapts the spatial distribution of bone's mineralized matrix volume to its usual loading circumstances [2]. For example, in an individual, adjacent cross sections of a long bone are assembled using similar volumes of mineralized matrix [3]. Differences in the external size, shape and internal microarchitecture of each adjacent cross section along the bone are the result of differences in the volumes of the medullary and intracortical canals, not the volume of mineralized matrix [4].

Mass is minimized in larger cross sections by assembling them with relatively more void volume, not more matrix volume. The constant bone matrix volume is distributed radially by excavating a larger medullary canal producing a thinner cortex. The thinner cortex is distributed around a larger perimeter preserving cortical area and so compressive strength. The greater radial distribution of cortical mass increases bending and torsional strength disproportionately to the increase in matrix volume [5]. Smaller cross sections achieve robusticity by being assembled with a relatively thicker cortex and relatively less void volume, not less matrix volume [6].

The diversity in external bone size, shape, and architecture is largely the result of genetic variance [7]. However, focal differences in loading also contribute to this structural diversity because bone is mechanosensitive [2]. Bone adapts its structural design to accommodate a range of commonly encountered loading circumstances. These structural adaptations ensure that bone strains during loading remain within a range that does not threaten fracture during usual activities [2]. These strain ranges and the thresholds may also be region specific and selected for by genetic factors [8]. If strains exceed a threshold associated with a high risk of fracture, modelling and remodelling restore strains by increasing or redistributing total bone volume [2,9]. When unloading occurs, strains fall below a threshold inhibiting resorption, resorptive modelling or negatively balanced remodelling restore

strains by reducing bone volume and compromising bone microstructural strength [2,10].

Bone loss following spinal cord injury occurs below the level of the injury but the severity of bone loss and the cellular activity adapting bone to its loading are region specific [[11], [12], [13], [14], [15]]. Weight bearing regions like the tibia are subjected to higher loads and strain rates than less weight bearing regions, like the fibula [16], or non-weight bearing regions like the radius. Bone loss reduces bone volume and disrupts the microarchitecture of the remaining bone volume. The microarchitectural deterioration reduces bone strength as a power function of the bone loss causing it [[17], [18], [19]]. Bone mineral density (BMD) measurements do not capture microstructural deterioration and so, bone fragility may be present in patients with spinal cord injury with osteopenia or so-called normal BMD. We therefore hypothesized that weight bearing regions will have lost more bone and structural integrity than less weight-bearing or non-weight bearing bones after spinal cord injury.

2. Methods

2.1. Participants

We recruited 12 men with tetraplegia mean age 44.6 years (range 25.9–67.2) and 19 men with paraplegia, mean age 42.9 years (range 23.5–75.0) with injury of various grades [20]. Men with tetraplegia were studied 6.5 years, range 0.7–15.6, and men with paraplegia were studied 6.5 years (range 1.6–18.6) after the injury and compared with 102 age matched healthy male controls. Men aged under 18 years, with a history of distal tibia and radius fractures or treatment for osteoporosis were excluded. Participants provided informed consent prior to participation. The study was approved by the Austin Health Research Ethics Committee.

2.2. In vivo imaging

Image acquisition, reconstruction, analysis and validation have been reported [21,22]. Participants had distal radius, distal tibia and distal fibula microstructure quantified using HR-pQCT (Scanco Medical, Switzerland) at Austin Health. A region of interest of 9.02 mm was acquired starting 9.5

mm or 22.5 mm proximal to the joint line of the distal radius and tibia, respectively. The 49 most proximal slices of a region of interest were chosen for analysis. Images were reconstructed at a resolution of 82 μm. Total, cortical and medullary areas, and volumetric bone mineral density (vBMD) of total, trabecular and cortical compartments, trabecular number, thickness, separation, cortical porosity, and matrix mineral density were quantified using StrAx1.0 algorithm (Strax Corp, Melbourne, Australia).

A non-threshold based method selects attenuation profile curves and segments (separates) bone from background and cortical from trabecular bone [23]. Profile curves are produced as photons are attenuated by mineralized bone. Bone edges are identified as the beginning and end of the rise and fall of the attenuation profile. Analyzing ~3600 profiles around the perimeter of each cross-sectional slice segments the compartments. Porosity is quantified as the average void volume fraction of all voxels within each compartment.

Agreement between HR-pQCT and the gold standard (μCT of cadaveric specimens imaged at 19 μm voxel size) ranged from R2 = 0.87 to 0.99. Precision error in vivo was 0.54% for porosity. Quality control for the performance of HR-pQCT was based on daily scanning phantoms containing hydroxyapatite (densities 0, 100, 200, 400, and 800 mgHA/cm3) (QRM, Germany). Radiation exposure is 3–5 μSv per measurement [4,22]. The coefficients of variation (CV) of the measurements ranged from 0.54% to 3.98% [23]. Inhomogeneity of Trabecular Network is calculated based on the standard deviation of the spacing between mid-axis (ridges) of the trabeculae. Marching cubes and ruler intercept methods were applied to quantify trabecular Structural Model Index (SMI), Connectivity Density (ConnD), and Bone Surface (BS) using specified image analysis algorithm, developed by the manufacturer [24,25].

2.3. Bone strength

Micro finite element analysis (μFEA) was used to estimate Failure Load (FL) using the FAIM software (version 8.0). A uniaxial loading with a tissue elastic modulus of 6829 MPa, a Poisson's ratio of 0.3, a critical strain of 7000 micro-strain and a critical volume of 2%, were defined. A 1%

apparent strain was applied, and failure load is calculated as the load when 2% of elements exceeded the critical strain [25,26].

2.4 Statistical analysis

Statistical analyses were performed using STATA version 14.2 (StataCorp. 2018. Stata Statistical Software. College Station, TX: StataCorp LP). Normality was checked using the Shapiro-Wilk normality test. The Welch's t-test were used to compare traits between cases and controls. Two-tailed p-values <0.05 denoted statistical significance. Results were expressed as mean and standard deviation. Differences in standardized terms among sites were expressed as a SD adjusted for age based on simple linear regression.

3. Results

3.1. Weight bearing regions: distal tibia and distal fibula

Men with tetraplegia and men with paraplegia had reduced total, cortical and trabecular vBMD at the distal tibia relative to healthy controls (Table 1). Cortical porosity was higher, and cortical thickness and matrix mineral density were lower, relative to healthy controls. Trabecular vBMD was reduced due to fewer, thinner, more rod-like and more separated trabeculae, with loss of trabecular surface area and connectivity, and greater inhomogeneity of the trabecular network (Fig. 1). Failure load was reduced. Distal tibial vBMD was lower and cortical porosity was higher at later than earlier follow-up times (Fig. 2). At the distal fibula, total vBMD was lower in men with tetraplegia and men with paraplegia relative to controls, but with deficits confined to trabecular vBMD produced by fewer, more separated trabeculae, with loss of homogeneity in distribution (Table 2).

Table 4.1

Table1. Distal tibial microstructure in individuals with tetraplegia and paraplegia and controls.

	Tetraplegic			**Paraplegic**		
Parameters of distal tibia	Cases, n=12	Controls, n=79	P-value	Cases, n=17	Controls, n=81	P-value
Total vBMD (mgHA/cm^3)	236.7 (64.5)	334.1 (58.9)	**<0.001**	213.1 (75.2)	334.9 (58.9)	**<0.001**
Cortical vBMD (mgHA/cm^3)	572.9 (50.3)	677.5 (68.5)	**<0.001**	554.5 (86.4)	677.5 (65.7)	**<0.001**
Porosity (%)	67.2 (3.6)	59.1 (5.4)	**<0.001**	68.3 (6.3)	59.1 (5.1)	**<0.001**
Thickness(mm)	0.62 (0.14)	0.79(0.16)	**<0.001**	0.60 (0.18)	0.77 (0.16)	**<0.001**
Matrix Mineral Density (%)	64.7 (0.5)	65.4 (0.9)	**0.006**	64.2 (0.6)	65.4 (0.8)	**<0.001**
Trabecular vBMD (mgHA/cm^3)	98.3 (74.0)	169.2 (43.9)	**<0.001**	80.1 (63.8)	168.4 (45.7)	**<0.001**
Number (1/mm)	2.13 (1.09)	3.13(0.68)	**<0.001**	1.73 (0.86)	3.14 (0.69)	**<0.001**
Thickness(µm)	189 (15)	197(13)	0.076	190 (17)	197 (14)	0.074
SMI	2.28 (0.75)	1.52 (0.40)	**<0.001**	2.37 (0.53)	1.45 (0.46)	**<0.001**
Separation (mm)	1.94 (0.90)	1.13 (0.25)	**<0.001**	2.08 (0.77)	1.14 (0.25)	**<0.001**
Surface (mm^2)	12906 (8098)	16725 (5227)	**0.031**	10394 (4666)	16605 (4625)	**<0.001**
Connectivity Density (1/mm^3)	2.83 (2.11)	4.56 (1.54)	**<0.001**	2.14 (1.43)	4.38 (1.49)	**<0.001**
Inhomogeneity (mm)	0.51 (0.48)	0.21 (0.08)	**<0.001**	0.72 (0.61)	0.21 (0.08)	**<0.001**
Failure Load (N)	4074 (2521)	6909 (1407)	**<0.001**	3369 (1787)	6905 (1388)	**<0.001**

Table 4.2

Table 2. Distal fibula microstructure in individuals with quadriplegia and paraplegia and controls

	Tetraplegic			**Paraplegic**		
Parameters of distal fibula	Cases, n=11	Controls, n=60	P-value	Cases, n=15	Controls, n=63	P-value
Total vBMD (mgHA/cm^3)	571.1 (85.1)	637.6 (107.4)	**0.057**	555.1 (92.9)	643.2 (105.1)	**0.004**
Cortical vBMD (mgHA/cm^3)	912.0 (50.2)	932.5 (44.2)	0.171	915.6 (36.6)	929.7 (49.6)	0.304
Cortical Area(mm^2)	63.4 (17.8)	70.4 (13.9)	0.147	57.4 (10.9)	69.9 (13.24)	**0.002**
Cortical Thickness(mm)	1.34 (0.21)	1.52 (0.25)	**0.038**	1.29 (0.23)	1.52 (0.25)	**0.001**
Trabecular vBMD (mgHA/cm^3)	188.9 (78.2)	226.4 (50.7)	**0.043**	164.5 (46.4)	231.9 (50.5)	**<0.001**
Number (1/mm)	1.39 (0.47)	1.89 (0.39)	**<0.001**	1.24 (0.33)	1.90 (0.41)	**<0.001**
Separation (mm)	0.71 (0.38)	0.45 (0.11)	**<0.001**	0.74 (0.21)	0.46 (0.13)	**<0.001**
Thickness(µm)	111 (26)	101 (19)	0.134	111 (16)	104 (20)	0.170
Inhomogeneity (mm)	0.35 (0.17)	0.21 (0.07)	**<0.001**	0.40 (0.14)	0.21 (0.08)	**<0.001**

vBMD; Volumetric bone mineral density

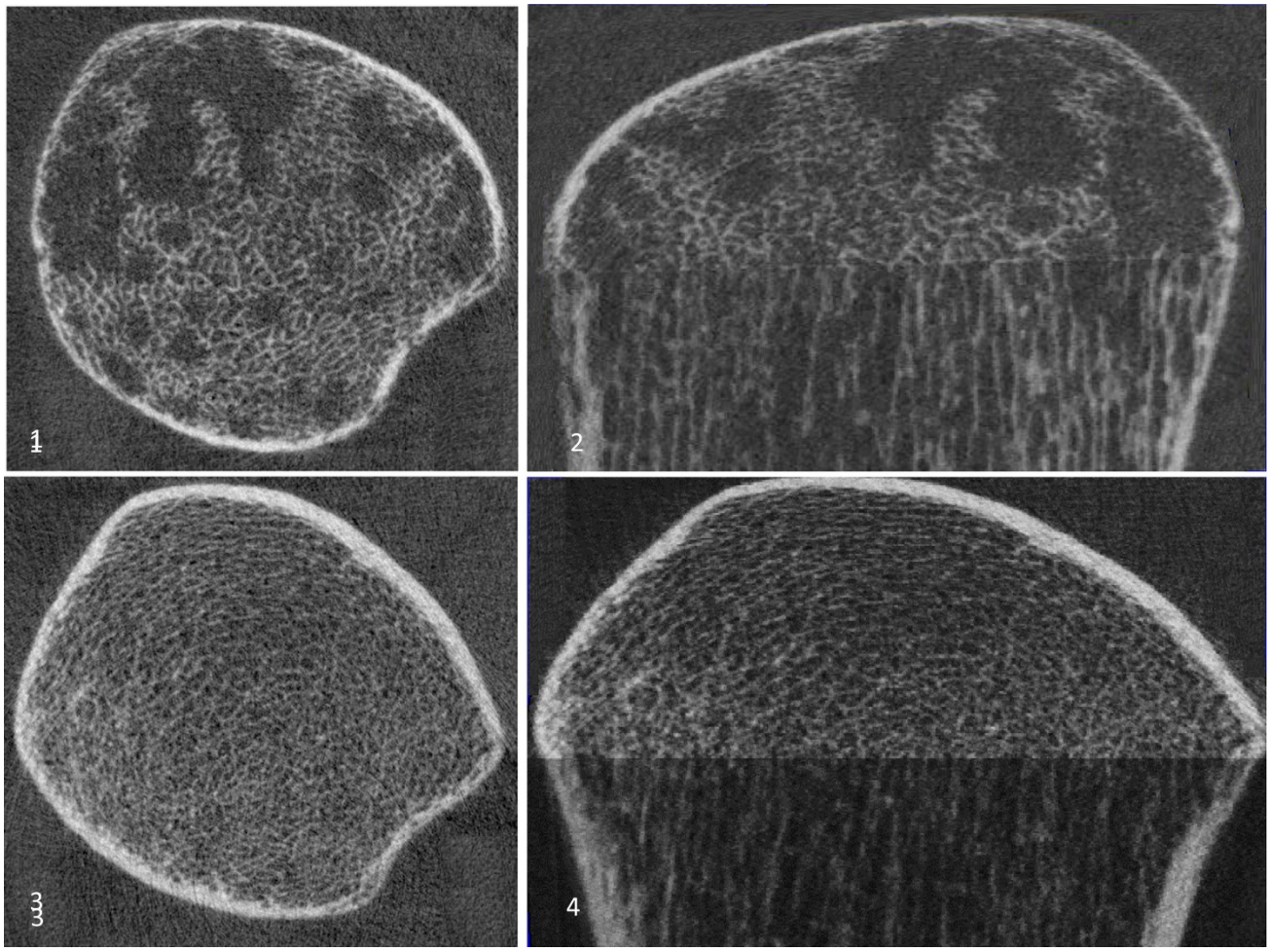

Figure 4.1

Fig. 1. Images of trabecular and cortical bone at the distal tibia.Axial and axial-coronal views of distal tibia of a 28 years male with spinal cord injury (panels 1, 2) and a healthy control (panels 3, 4). Cortices are thin and porous. Trabeculae are thinned, disconnected with loss of homogeneity in their distribution.

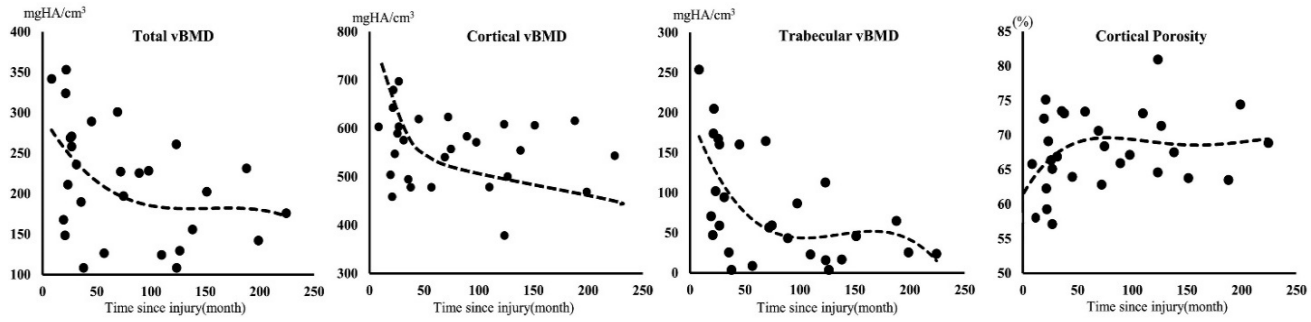

Figure 4.2

Fig. 2. Distal tibial total, cortical and trabecular volumetric bone mineral density (vBMD) and cortical porosity as a function of time since injury.

The regression lines were derived by plotting vBMD and cortical porosity from 0 to 50 months and then from 50 to 250 months. vBMD was lower and cortical porosity was higher at later than earlier follow up times.

3.2. Non-weight bearing region: distal radius

Despite the presence of tetraplegia, no deficits in distal radial total, cortical or trabecular vBMD were present. Trabecular thickness was increased in men with tetraplegia and men with paraplegia, and matrix mineral density was reduced, relative to healthy controls. Trabecular number and homogeneity were not deteriorated. Nor did failure load differ from controls **(Table 3**).

Chapter 4

Table 4.3

Table 3. Distal radial microstructure of individuals with tetraplegia and paraplegia and controls

	Tetraplegic			**Paraplegic**		
Parameters of distal radius	Cases, n=11	Controls, n=79	P-value	Cases, n=18	Controls, n=81	P-value
Total vBMD (mgHA/cm^3)	372.9 (72.5)	385.4 (68.6)	0.574	397.5 (73.0)	392.6 (67.8)	0.783
Cortical vBMD (mgHA/cm^3)	709.9 (63.3)	739.1 (68.5)	0.193	730.0 (66.2)	746.0 (72.8)	0.348
Porosity (%)	56.8 (4.9)	54.3 (5.6)	0.164	55.3 (5.4)	53.8 (5.2)	0.269
Thickness(mm)	0.74 (0.15)	0.79(0.17)	0.3373	0.86 (0.22)	0.78 (0.18)	0.0904
Matrix Mineral Density (%)	64.7 (0.7)	65.3 (0.9)	**0.037**	64.6 (0.7)	65.2 (0.8)	**0.004**
Trabecular vBMD (mgHA/cm^3)	152.7 (65.5)	160.2 (46.3)	0.635	173.5 (56.4)	164.0 (47.3)	0.457
Number (1/mm)	2.40 (0.70)	2.76 (0.58)	0.062	2.53 (0.52)	2.74 (0.54)	0.099
Thickness(µm)	205 (13)	197 (13)	0.063	212 (11)	198 (13)	**<0.001**
SMI	1.99 (0.62)	1.74 (0.41)	0.0695	1.79 (0.55)	1.70 (0.45)	0.4435
Separation (mm)	1.41 (0.55)	1.16 (0.25)	**0.013**	1.21 (0.28)	1.15 (0.25)	0.339
Surface (mm^2)	6408 (2489)	6818 (1786)	0.4831	6044 (1242)	6780 (1783)	0.0840
Connectivity Density (1/mm^3)	3.61 (1.37)	4.46 (1.21)	**0.0278**	4.01 (0.95)	4.35 (1.18)	0.2337
Inhomogeneity (mm)	0.25 (0.14)	0.19 (0.07)	**0.0194**	0.21 (0.07)	0.19 (0.06)	0.1976
Failure Load (N)	2499 (776)	2668 (652)	0.458	2600 (625)	2680 (662)	0.660

vBMD; Volumetric bone mineral density, SMI; Structure Model Index. SMI of 0 indicates plate-like structure, 3 indicates rod-like structure

Chapter 4

Table 4.4

Table 4. Total, cortical and trabecular vBMD differences between tibia, fibula and radius in tetraplegic and paraplegic men. Difference expressed as age-adjusted standardized deviations (SD) with 95% confidence intervals (CIs).

Deviation	**Tetraplegic**		**Paraplegic**	
Total vBMD	Mean difference, SD (CI)	p-value	Mean difference, SD (CI)	p-value
Tibia *vs.* Fibula	-1.04 (-2.01, -0.07)	**0.037**	-1.31 (-2.23, -0.39)	**0.007**
Tibia *vs.* Radius	-1.51 (-2.57 ,-0.45)	**0.007**	-2.37 (-3.22, 1.52)	**<0.001**
Fibula *vs.* Radius	-0.47 (-1.21, 0.27)	0.202	-1.06 (-1.77, -0.35)	**0.004**
Cortical vBMD				
Tibia *vs.* Fibula	-0.50 (-1.10, 0.10)	0.096	-1.05 (-1.69, -0.41)	**0.002**
Tibia *vs.* Radius	-0.54 (-1.13, 0.05)	0.070	-0.99(-1.65, -0.33)	**0.005**
Fibula *vs.* Radius	-0.04 (-0.65, 0.57)	0.893	0.06(-0.48, 0.60)	0.824
Trabecular vBMD				
Tibia *vs.* Fibula	-0.98 (-2.51, 0.55)	0.198	-1.03 (-2.07, 0.01)	0.051
Tibia *vs.* Radius	-1.73 (-3.25, -0.21)	**0.027**	-2.66 (-3.64, -1.68)	**<0.001**
Fibula *vs.* Radius	-0.75 (-1.98, 0.48)	0.219	-1.63 (-2.34, -0.92)	**<0.001**

Chapter 4

3.3. Comparisons of regions, cortical and trabecular bone

Table 4 shows the standardized mean difference between region with their 95% confidence intervals. Fig. 3 illustrates these differences with their p values. Deficits in total, cortical and trabecular vBMD were greater at the distal tibia than distal fibula or distal radius. Deficits were statistically significant in several, but not all, comparisons. Deficits were also significantly greater in some, but not all, comparisons of the distal fibula versus distal radius.

Chapter 4

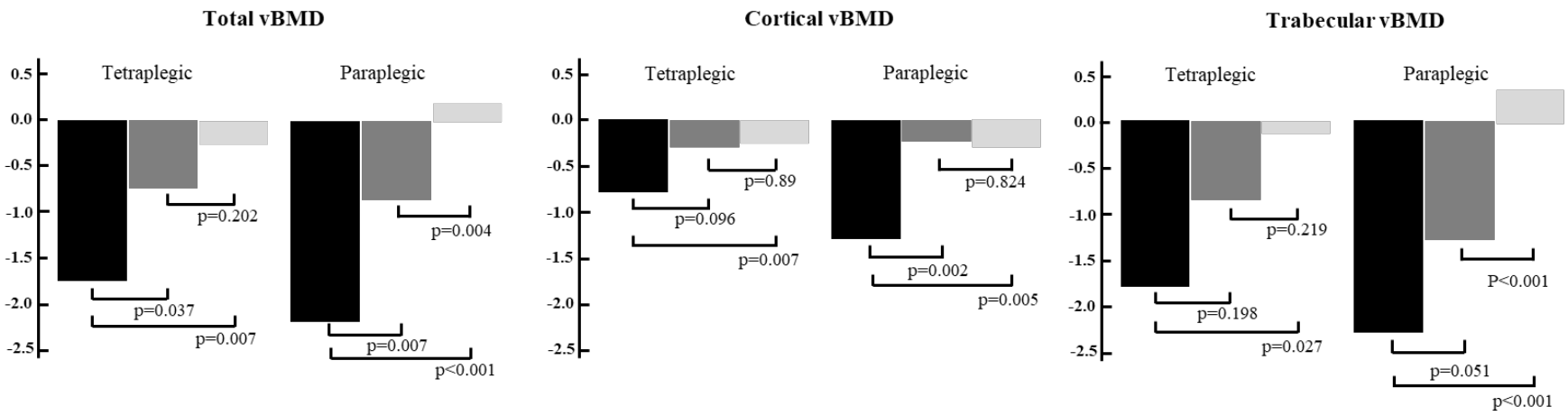

Figure 4.3

Figure 3. Comparison of deficits total, cortical and trabecular volumetric bone mineral density (vBMD) at the distal tibia (black bar), distal fibula (deep grey bars) and distal radius (light grey bars) in men with tetraplegia and paraplegia. Deficits are expressed as standard deviations from the mean in age-matched controls.

Chapter 4

4. Discussion

The purpose of this study was to quantify the microstructural deterioration of the distal metaphyseal regions of the appendicular skeleton in individuals with spinal cord injury. Relative to controls, men with tetraplegia or paraplegia had increased cortical porosity, reduced cortical thickness and matrix mineral density, complete loss of trabecular plates, reduced trabecular surface area, connectivity and loss of homogeneity of the interconnected plates seen as patching fallout of trabeculae. These changes resulted in loss of estimated strength at the distal tibia, a weight bearing site. More modest deficits were found at the distal fibula, a weight bearing site subjected to lower stresses during loading [27].

Most published studies, like those cited in a meta-analysis [12], focussed on the reduction in BMD, a measurement that does not capture the heterogeneity in cortical and trabecular morphology within and between regions of the skeleton. We report a hierarchy of deficits. The tibia experienced the greatest loss, followed by the fibula, with the least loss from the radius. These observations are consistent with the relative reduction in loading following spinal cord injury [12], with the tibia experiencing the greatest unloading, and the radius the least unloading relative to their customary loading.

We observed deficits in cortical and trabecular vBMD at the distal tibia, but deficits in vBMD at the distal fibula were confined to trabecular bone, and were less than the deficits at the distal tibia. The fibula is slender and largely cortical. Cortical bone has a lower surface area/matrix volume ratio than trabecular bone and so is less susceptible to being remodelled than trabecular bone following unloading [12]. As the fibula is subjected to lower strains than the tibia, we suggest that paralysis may have resulted in strains deviating less from their customary strain environment than the deviation of strains usually encountered at the tibia [16]. Consequently, loss of trabecular bone may have been sufficient to restore strains without the need to compromise cortical bone.

Eser et al. reported deficits in vBMD at the distal femur and proximal tibia were confined to trabecular bone despite these weight-bearing bones being subjected to higher strains than the radius [17]. The larger trabecular surface area/matrix volume ratio at these locations may also make these regions susceptible to more rapid trabecular than cortical bone loss.

Finding uncompromised distal radial microstructure in men with tetraplegia was unanticipated. However, scrutiny of the literature supports the likely validity of this observation. For example, in a meta-analysis [12], lower limb bones had greater deficits in bone mass than upper extremity bones. Eser et al. report rapid decreases in vBMD at the distal femur and tibia in patients with tetraplegia or paraplegia with little loss of bone at the distal radius in patients with paraplegia (as expected) and in the smaller number of patients with tetraplegia [28]. Studies of astronauts demonstrate preservation of radial bone, a structure commonly subjected to lower loads than weight bearing structures [29]. Modlesky et al. reported reduced distal femur and proximal tibia trabecular density using high-resolution magnetic resonance imaging in 10 men with long-term complete spinal cord injury compared to 8 controls. Despite complete SCI injury between C6-L1, radius BMD was not reduced relative to controls, as confirmed in this, and other studies [30].

No deficits at the distal radius of men with paraplegia were expected but evidence of higher vBMD in men with paraplegia than in healthy controls or men with tetraplegia might be expected due to mechanical usage for propulsion of a wheelchair. This was not observed. However, Goktepe et al. reported higher distal radial BMD in elite athletes with paraplegia, not sedentary subjects with paraplegia, an observation suggesting greater than usually encountered strains are needed to stimulate bone formation in this non-weight bearing bone [31]. The higher distal radial trabecular thickness in both tetraplegia and paraplegia than controls is likely to be due to preferential loss of thinner trabeculae as reported following rapid perimenopausal bone loss [32].

Likewise, in a study of dogs subjected to 40 weeks of immobilization, the greatest loss of bone occurred at the metacarpals (50%), compared to humeri which lost the least bone (28%) [10]. Although the forelimbs of quadrupeds are weight-bearing, the distal limb bones experience greater peak stresses during locomotion

than the proximal humerus [33]. Hsieh and colleagues reported using an in vivo loading of the ulna in rats that threshold strains are largest distally, where locomotor strains are typically higher than proximally. There was a correlation between greater peak strains and greater periosteal bone formation once a threshold was exceeded [34]. Schulte et al. also reported that bone formation in mice occurs at sites of high local mechanical strain while bone resorption occurred at sites of low local strain [35]. Christen et al. demonstrate a linear relationship between focal remodelling and local loading determined by micro finite element analysis in humans but non-mechanically determined component of this cellular activity fulfilling other demands for remodelling [36].

We propose that the heterogeneity of the morphological changes following spinal cord injury is likely to reflect the nature of bone as a mechanosensitive organ. Harold Frost, and many investigators since, suggested that bone modelling and remodelling adapt bone morphology to differences in microstrain imposed by unloading, physiological loading, overloading and pathological loading [2,5,8,9,15,37]. The mechanisms responsible for mechanotransduction are now better understood (Fig. 4). During loading, bone matrix deformation (strain) generates lacuna-canalicular fluid flow which induces shear stress on osteocytes, down regulating sclerostin, an inhibitor of bone formation and stimulator of bone resorption [38,39]. When sclerostin expression is suppressed, bone formation increases focally [39]. Concurrently, resorptive modelling, or negatively balanced remodelling, occur at other locations. This alters the spatial distribution of the mineralized matrix, adapting a region's microarchitecture to the new loading circumstances while avoiding an increase in total bone volume, which is energy requiring [1,2,40].

Reduced loading in individuals with spinal cord injury reduces canalicular fluid flow. Reduced strains upregulate sclerostin leading to reduced bone formation, increased bone resorption, bone loss and a reduction in bone volume which restores local strains at the price of compromised bone volume, microarchitecture and bone strength [41]. Sclerostin levels were not available in the present study. Published studies suggest that changes in sclerostin levels depend on the type and duration of SCI [42,43]. For example, Battaglino et al. reported that sclerostin levels were greatest in subjects with short-term SCI (≤5 years) and decreased during

the first 5 years post-injury [42]. By contrast, Maimoun et al. report lower concentration of sclerostin [43], a finding that should be associated with increased bone formation. Circulating concentrations may not be appropriate surrogates for the local action of this osteocyte product as reduced levels should be associated with increased bone formation.

In addition to changes in bone volume and microstructure, matrix mineral density was lower in men with tetraplegia and paraplegia, despite the absence of changes in morphology at the distal radius. This observation suggests that rapid remodelling has a systemic effect compromising bone properties above the level of the spinal cord injury. Shen et al. reported decreased mineral to collagen matrix ratio in the humeri of paraplegic mice [44]. This rapid remodelling may underly the so-called regional acceleratory phenomenon reported by Frost [45].

Stiffness, or resistance to bending, is a function of the degree of matrix mineralization and bone geometry, with the cross-sectional moment of inertia capturing the distribution of mass around the axis of loading [5]. As stiffness is determined by material and structural properties, both can vary independently, as matrix mineralization and microstructure did here. The change was greater at the distal tibia where both microstructure and matrix mineral density were compromised, contributing to the greater decline in estimated failure load.

Prevention of musculoskeletal deterioration following spinal cord injury remains challenging and has been attempted using functional electrical stimulation (FES)-rowing. Gibbons et al. report a case study of a patient with SCI in whom they suggest distal tibial bone loss measured using HR-pQCT was attenuated [46]. Draghici et al. measured distal tibia and distal radial microstructure also using HR-pQCT in an uncontrolled cross-sectional study of 13 men with SCI [47]. Time since injury, total distance rowed, and peak foot force together predicted trabecular, not cortical, morphology. These studies are difficult to interpret due to issues in design and execution. However, in a 6-month controlled prospective study of FES-cycling 30-min 3 times weekly initiated 4·5 weeks post SCI in 19 para- and tetraplegic patients compared with 19 patients with SCI left untreated, no evidence of attenuation of bone loss was observed [48]. By contrast, Fang et al. reported that 20

individuals with SCI treated for 12 months with FES–assisted rowing plus zoledronate improved distal femur stiffness by 4.6% estimated using finite element analysis, while stiffness decreased by 13.9% in those treated with rowing alone. No benefits were observed in either group at the proximal tibia. No group received drug therapy alone or no intervention [49]. In an uncontrolled study, Frotzler et al. reported improvement in thigh cross sectional area, distal femoral epiphysis trabecular and total BMD following 12 months of 3.7 hourly sessions per week FES-cycling in 11 subjects with complete SCI 11.0 years post injury [50]. Bone parameters in the femoral shaft decreased. Further studies are needed to address this therapeutic challenge.

This study has several limitations. This was a cross-sectional data with limited number of individuals with spinal cord injury and absence of data in the early months following spinal cord injury. For these reasons we could not document the precise temporal patterns of bone loss in each region. However, Edwards et al. reported early rapid bone loss of 3–5% per month [51]. Similarly, Eser et al. reported trabecular and cortical bone loss for the distal epiphyses and midshafts of the femur, tibia, and radius measured using peripheral quantitative computed tomography in 24 tetraplegic and 65 paraplegic men with SCI of 2 months and 50 years duration [17]. Bone mass and cortical area of the diaphyses, showed an exponential decrease with time since injury reaching a plateau after 3–8 years. While the upper limbs are not loaded by body weight, about 50% of this small group of subjects had level D grade ASIA impairment scale, in which most of the muscles are spared below the level of injury, an effect that may partly account for the preservation of bone structure. Analysis of cortical porosity of the fibula was not available. Height and weight measurements were not available so matching with controls was confined to age and sex. While unloading due to spinal cord injury plays a most important role in bone loss, bone loss is multifactorial [12,52]. Coexisting autonomic dysfunction was not quantified in this study and may contribute to bone loss, but few, if any, studies have quantified the contribution of the hemodynamic changes that may influence the skeleton [53,54].

In summary, fractures are common in patients with spinal cord injury and often occur at metaphyseal regions [55]. Bone fragility is the result of bone loss that is region specific and is, in part, a function of the change in mechanical load imposed on the region. Following unloading caused by spinal cord injury, weight bearing

regions, adapted to accommodate greater peak strains and strain rates, are at higher risk for bone loss and microarchitectural deterioration during unloading than non-weight bearing regions that are adapted to lower peak strains and strain rates. These observations highlight the site specificity of the strain thresholds regulating the cellular activity of mechano-transduction. The rapidity of the change and irreversible microarchitectural deterioration suggest prompt intervention with antiresorptive, anabolic therapy, or both, warrants consideration.

Chapter 4

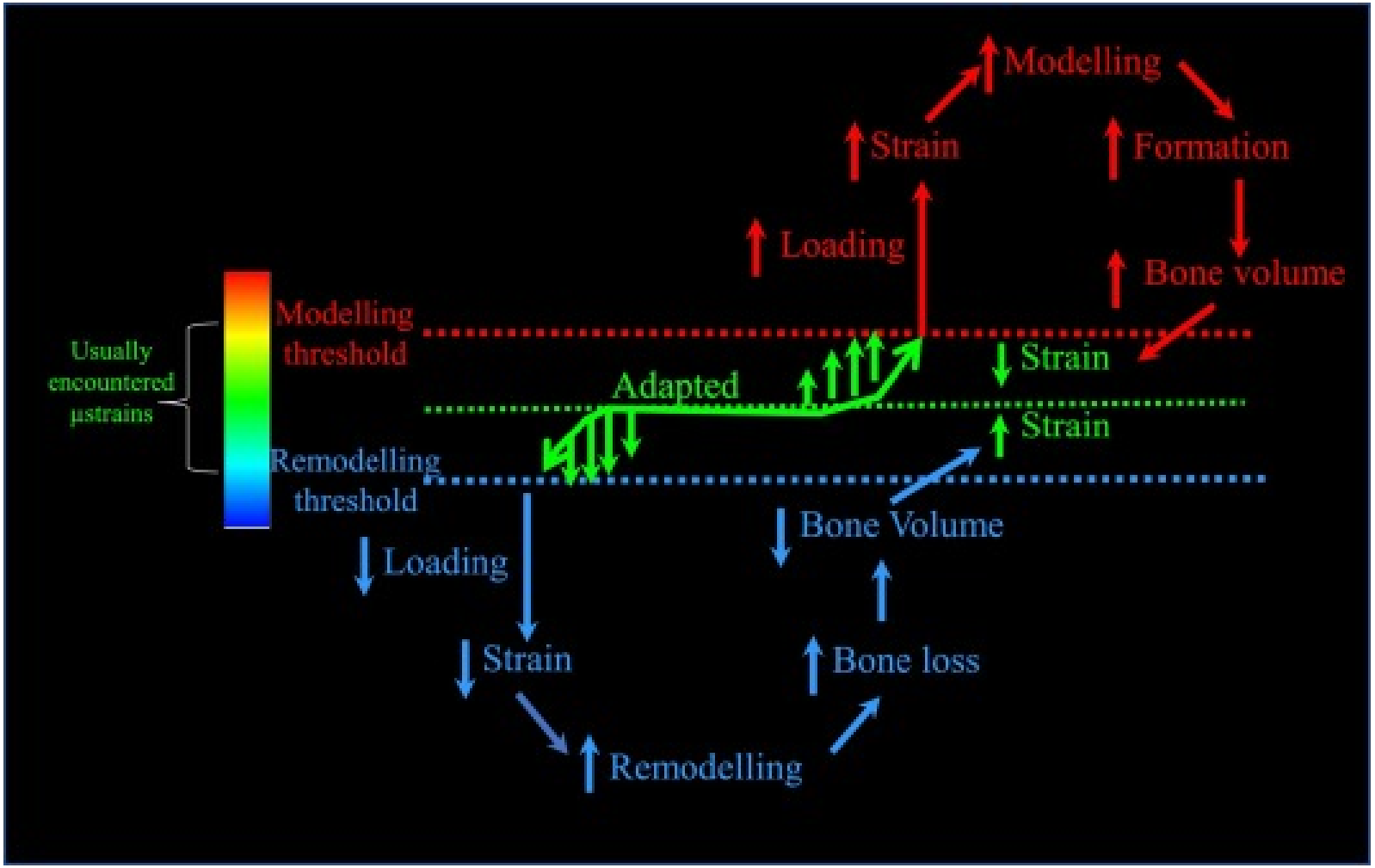

Figure 4.4

Fig. 4. Differences in loading-induced microstrain within the range usually encountered by a bone do not modify modelling or remodelling (green). When loading exceeds a strain threshold threatening fracture (red), modelling increases bone formation and bone volume restoring strains. When loading is reduced, as occurs in spinal cord injury, strains decrease below a threshold inhibiting remodelling (blue) result in initiation of unbalanced remodelling causing bone loss and a decrease in bone volume which restores strains. (For interpretation of the references to colour in this figure legend, the reader is referred to the web version of this article.)

Chapter 4

References

[1] J.D. Currey, The Mechanical Adaptations of Bones viii, Princeton University Press,Princeton, N.J, 1984 (294 pp.)

[2] H.M. Frost, Bone “mass” and the “mechanostat”: a proposal, Anat. Rec. 219 (1) (Sep 1987) 1–9 (Epub 1987/09/01).

[3] R.M. Zebaze, A. Jones, F. Welsh, M. Knackstedt, E. Seeman, Femoral neck shape and the spatial distribution of its mineral mass varies with its size: clinical and biomechanical implications, Bone. 37 (2) (Aug 2005) 243–252 (Epub 2005/06/09).

[4] A. Ghasem-Zadeh, A. Burghardt, X.F. Wang, S. Iuliano, S. Bonaretti, M. Bui, et al., Quantifying sex, race, and age specific differences in bone microstructure requires measurement of anatomically equivalent regions, Bone. 101 (Aug 2017) 206–213 (Epub 2017/05/16).

[5] M.R. Forwood, Mechanical effects on the skeleton: are there clinical implications? Osteoporos. Int. 12 (1) (2001) 77–83 (Epub 2001/04/18).

[6] C.B. Ruff, E. Trinkaus, A. Walker, C.S. Larsen, Postcranial robusticity in Homo. I: temporal trends and mechanical interpretation, Am. J. Phys. Anthropol. 91 (1) (May 1993) 21–53 (Epub 1993/05/01).

[7] A. Bjornerem, M. Bui, X. Wang, A. Ghasem-Zadeh, J.L. Hopper, R. Zebaze, et al., Genetic and environmental variances of bone microarchitecture and bone remodeling markers: a twin study, J. Bone Miner. Res. 30 (3) (Mar 2015) 519–527 (Epub 2014/11/20).

[8] A.G. Robling, C.H. Turner, Mechanotransduction in bone: genetic effects on mechanosensitivity in mice, Bone. 31 (5) (Nov 2002) 562–569 (Epub 2002/12/13).

[9] J.R. Mosley, B.M. March, J. Lynch, L.E. Lanyon, Strain magnitude related changes in whole bone architecture in growing rats, Bone. 20 (3) (Mar 1997) 191–198 (Epub 1997/03/01).

[10] H.K. Uhthoff, Z.F. Jaworski, Bone loss in response to long-term immobilisation, J. Bone Joint Surg. (Br.) 60-B (3) (Aug 1978) 420–429 (Epub 1978/08/01).

[11] D. Roberts, W. Lee, R.C. Cuneo, J. Wittmann, G. Ward, R. Flatman, et al., Longitudinal study of bone turnover after acute spinal cord injury, J. Clin. Endocrinol. Metab. 83 (2) (Feb 1998) 415–422 (Epub 1998/02/19).

[12] S.D. Jiang, L.S. Jiang, L.Y. Dai, Mechanisms of osteoporosis in spinal cord injury, Clin. Endocrinol. 65 (5) (Nov 2006) 555–565 (Epub 2006/10/24).

[13] L. Maimoun, C. Fattal, J.P. Micallef, E. Peruchon, P. Rabischong, Bone loss in spinal cord-injured patients: from physiopathology to therapy, Spinal Cord 44 (4) (Apr 2006) 203–210 (Epub 2005/09/15).

[14] F. Biering-Sorensen, H.H. Bohr, O.P. Schaadt, Longitudinal study of bone mineral content in the lumbar spine, the forearm and the lower extremities after spinal cord injury, Eur. J. Clin. Investig. 20 (3) (Jun 1990) 330–335 (Epub 1990/06/01).

[15] S.J. Kuruvilla, S.D. Fox, D.M. Cullen, M.P. Akhter, Site specific bone adaptation response to mechanical

loading, J. Musculoskelet. Neuronal Interact. 8 (1) (Jan-Mar 2008) 71–78 (Epub 2008/04/10).

[16] Q. Wang, M. Whittle, J. Cunningham, J. Kenwright, Fibula and its ligaments in load transmission and ankle joint stability, Clin. Orthop. Relat. Res. 330 (Sep 1996) 261–270 (Epub 1996/09/01).

[17] P. Eser, A. Frotzler, Y. Zehnder, L. Wick, H. Knecht, J. Denoth, et al., Relationship between the duration of paralysis and bone structure: a pQCT study of spinal cord injured individuals, Bone. 34 (5) (May 2004) 869–880 (Epub 2004/05/04).

[18] M.B. Schaffler, D.B. Burr, Stiffness of compact bone: effects of porosity and density, J. Biomech. 21 (1) (1988) 13–16 (Epub 1988/01/01).

[19] S. Coupaud, M.K. Gislason, M. Purcell, K. Sasagawa, K.E. Tanner, Patient-specific bone mineral density distribution in the tibia of individuals with chronic spinal cord injury, derived from multi-slice peripheral Quantitative Computed Tomography (pQCT) - a cross-sectional study, Bone. 97 (Apr 2017) 29–37 (Epub 2016/12/31).

[20] F.M. Maynard Jr., M.B. Bracken, G. Creasey, J.F. Ditunno Jr., W.H. Donovan, T. B. Ducker, et al., International standards for neurological and functional classification of spinal cord injury. American Spinal Injury Association, Spinal
Cord. 35 (5) (May 1997) 266–274 (Epub 1997/05/01).

[21] X.F. Wang, Q. Wang, A. Ghasem-Zadeh, A. Evans, C. McLeod, S. Iuliano-Burns, et al., Differences in macro- and microarchitecture of the appendicular skeleton in young Chinese and white women, J. Bone Miner. Res. 24 (12) (Dec 2009) 1946–1952 (Epub 2009/05/23).

22] P. Geusens, R. Chapurlat, G. Schett, A. Ghasem-Zadeh, E. Seeman, J. de Jong, et al., High-resolution in vivo imaging of bone and joints: a window to microarchitecture, Nat. Rev. Rheumatol. 10 (5) (May 2014) 304–313 (Epub 2014/03/07).

[23] R. Zebaze, A. Ghasem-Zadeh, A. Mbala, E. Seeman, A new method of segmentation of compact-appearing, transitional and trabecular compartments and quantification of cortical porosity from high resolution peripheral quantitative computed tomographic images, Bone. 54 (1) (May 2013) 8–20 (Epub 2013/01/22).

[24] T. Hildebrand, A. Laib, R. Muller, J. Dequeker, P. Ruegsegger, Direct three dimensional morphometric analysis of human cancellous bone: microstructural data from spine, femur, iliac crest, and calcaneus, J. Bone Miner. Res. 14 (7) (Jul 1999) 1167–1174 (Epub 1999/07/15).

[25] D.E. Whittier, S.K. Boyd, A.J. Burghardt, J. Paccou, A. Ghasem-Zadeh, R. Chapurlat, K. Engelke, ML. Bouxsein, Guidelines for the assessment of bone density and microarchitecture in vivo using high-resolution peripheral quantitative computed tomography, Osteoporos Int 31 (9) (2020) 1607–1627, https://doi.org/ 10.1007/s00198-020-05438-5 [Epub 2020 May 26].

[26] E.J. Samelson, K.E. Broe, H. Xu, L. Yang, S. Boyd, E. Biver, et al., Cortical and trabecular bone microarchitecture as an independent predictor of incident fracture risk in older women and men in the Bone Microarchitecture International
Consortium (BoMIC): a prospective a study, Lancet Diabetes Endocrinol. 7 (1) (Jan 2019) 34–43 (Epub 2018/12/07).

27] J.R. Funk, R.W. Rudd, J.R. Kerrigan, J.R. Crandall, The effect of tibial curvature and fibular loading on the

tibia index, Traffic Inj. Prev. 5 (2) (Jun 2004) 164–172 (Epub 2004/06/19).

[28] P. Eser, A. Frotzler, Y. Zehnder, H. Schiessl, J. Denoth, Assessment of anthropometric, systemic, and lifestyle factors influencing bone status in the legs of spinal cord injured individuals, Osteoporos. Int. 16 (1) (Jan 2005) 26–34 (Epub 2004/05/13).

[29] L. Vico, B. van Rietbergen, N. Vilayphiou, M.T. Linossier, H. Locrelle, M. Normand, et al., Cortical and trabecular bone microstructure did not recover at weightbearing skeletal sites and progressively deteriorated at non-weight-bearing sites during the year following international space station missions, J. Bone Miner. Res. 32 (10) (Oct 2017) 2010–2021 (Epub 2017/06/03).

[30] C.M. Modlesky, S. Majumdar, A. Narasimhan, G.A. Dudley, Trabecular bone microarchitecture is deteriorated in men with spinal cord injury, J. Bone Miner. Res. 19 (1) (Jan 2004) 48–55 (Epub 2004/02/03).

[31] A.S. Goktepe, B. Yilmaz, R. Alaca, K. Yazicioglu, H. Mohur, S. Gunduz, Bone density loss after spinal cord injury: elite paraplegic basketball players vs. paraplegic sedentary persons, Am. J. Phys. Med. Rehabil. 83 (4) (Apr 2004)
279–283 (Epub 2004/03/17).

[32] A. Bjornerem, X. Wang, M. Bui, A. Ghasem-Zadeh, J.L. Hopper, R. Zebaze, et al., Menopause-related appendicular bone loss is mainly cortical and results in increased cortical porosity, J. Bone Miner. Res. 33 (4) (Apr 2018) 598–605 (Epub 2017/12/09).

[33] A.A. Biewener, Bone strength in small mammals and bipedal birds: do safety factors change with body size? J. Exp. Biol. 98 (Jun 1982) 289–301 (Epub 1982/ 06/01).

[34] Y.F. Hsieh, A.G. Robling, W.T. Ambrosius, D.B. Burr, C.H. Turner, Mechanical loading of diaphyseal bone in vivo: the strain threshold for an osteogenic response varies with location, J. Bone Miner. Res. 16 (12) (Dec 2001) 2291–2297 (Epub 2002/01/05).

[35] F.A. Schulte, D. Ruffoni, F.M. Lambers, D. Christen, D.J. Webster, G. Kuhn, et al., Local mechanical stimuli regulate bone formation and resorption in mice at the tissue level, PLoS One 8 (4) (2013), e62172 (Epub 2013/05/03).

[36] P. Christen, K. Ito, R. Ellouz, S. Boutroy, E. Sornay-Rendu, R.D. Chapurlat, et al., Bone remodelling in humans is load-driven but not lazy, Nat. Commun. 5 (Sep 11 2014) 4855 (Epub 2014/09/12).

[37] L.M. McNamara, P.J. Prendergast, Bone remodelling algorithms incorporating both strain and microdamage stimuli, J. Biomech. 40 (6) (2007) 1381–1391 (Epub 2006/08/26).

[38] C.H. Turner, M.R. Forwood, M.W. Otter, Mechanotransduction in bone: do bone cells act as sensors of fluid flow? FASEB J. 8 (11) (Aug 1994) 875–878 (Epub 1994/08/01).

[39] A.G. Robling, P.J. Niziolek, L.A. Baldridge, K.W. Condon, M.R. Allen, I. Alam, et al., Mechanical stimulation of bone in vivo reduces osteocyte expression of Sost/sclerostin, J. Biol. Chem. 283 (9) (Feb 29, 2008) 5866–5875 (Epub 2007/12/20).

[40] S.L. Bass, L. Saxon, R.M. Daly, C.H. Turner, A.G. Robling, E. Seeman, et al., The effect of mechanical loading on the size and shape of bone in pre-, peri-, and postpubertal girls: a study in tennis players, J. Bone

Miner. Res. 17 (12) (Dec 2002) 2274–2280 (Epub 2002/12/10).

[41] X. Tian, W.S. Jee, X. Li, C. Paszty, H.Z. Ke, Sclerostin antibody increases bone mass by stimulating bone formation and inhibiting bone resorption in a hindlimb immobilization rat model, Bone 48 (2) (Feb 2011) 197–201 (Epub 2010/09/21).

[42] R.A. Battaglino, S. Sudhakar, A.A. Lazzari, E. Garshick, R. Zafonte, L.R. Morse, Circulating sclerostin is elevated in short-term and reduced in long-term SCI, Bone. 51 (3) (Sep 2012) 600–605 (Epub 2012/05/12).

[43] L. Maimoun, F. Ben Bouallegue, A. Gelis, S. Aouinti, T. Mura, P. Philibert, et al., Periostin and sclerostin levels in individuals with spinal cord injury and their relationship with bone mass, bone turnover, fracture and osteoporosis status, Bone. 127 (Oct 2019) 612–619 (Epub 2019/07/28).

[44] J. Shen, L. Fan, J. Yang, A.G. Shen, J.M. Hu, A longitudinal Raman microspectroscopic study of osteoporosis induced by spinal cord injury, Osteoporos. Int. 21 (1) (Jan 2010) 81–87 (Epub 2009/05/14).

[45] H.M. Frost, The regional acceleratory phenomenon: a review, Henry Ford Hosp. Med. J. 31 (1) (1983) 3–9 (Epub 1983/01/01).

CHAPTER 5

Bone microarchitecture and estimated failure load are deteriorated whether patients with chronic kidney disease have normal bone mineral density, osteopenia or osteoporosis

Short summary

Bone microarchitecture and estimated failure load are deteriorated whether patients with chronic kidney disease have normal bone mineral density, osteopenia or osteoporosis.

Age- and disease-related impairment of renal function have increased the numbers of persons requiring management of chronic kidney disease (CKD). Successful prolongation of life by drug therapy, dialysis, and kidney transplantation is accompanied by secondary hyperparathyroidism and unbalanced bone remodelling resulting on bone loss which compromises bone mass, microarchitecture, and strength predisposing to increased risk of fragility fracture. However, BMD measurements using DXA underestimate the bone fragility in patients with CKD because the BMD measurement does not capture the microarchitectural deterioration accompanying bone loss in patients with CKD.

In this cross-sectional study, I measured microarchitecture of the distal radius and distal tibia in 128 patients with CKD and 275 age- and sex-matched controls using HR-pQCT. Additionally, I measured failure load at the distal appendicular sites using finite element analysis, and femoral neck BMD using DXA.

The findings show that most patients with CKD stages 4-5D and kidney transplant recipients had osteopenia or normal femoral neck BMD, not osteoporosis. Despite these modest deficits in femoral neck BMD, distal radial and distal tibia microarchitecture and estimated failure load, were compromised. Within each BMD category – osteoporosis, osteopenia or normal BMD, relative to controls, microarchitecture was more compromised in patients than controls having the same BMD category: cortices were thinned, cortical vBMD was reduced due to increased porosity and decreased matrix mineral density. Trabecular vBMD was reduced due to fewer trabeculae that were disconnected and disrupted in their spatial distribution.

In univariate analyses, microarchitecture and FN-BMD were both associated with estimated failure load, however, in multivariable analyses, only microarchitecture was independently associated with estimated failure load and accounted for 87% of the variance in estimated strength.

I concluded that bone fragility is likely to be present in patients with CKD despite them having osteopenia or normal BMD. Therefore, assessing microarchitecture in these sites is likely to identify patients at the higher risk of fractures. These finding emphasise that bone fragility is likely to be present in patients with CKD despite them having osteopenia or normal BMD. Targeting and monitoring treatment based on the severity of microarchitectural deterioration is likely to be an effective means of reducing the fracture burden accompanying CKD.

Chapter 5

Bone microarchitecture and estimated failure load are deteriorated whether patients with chronic kidney disease have normal bone mineral density, osteopenia or osteoporosis

Short title: Bone Microstructure deterioration in patients with chronic kidney disease

Ali Ghasem-Zadeh*[1,6], Minh Bui [2], Ego Seeman[1,6], Steven K. Boyd [3], Sandra Iuliano [1,6], Rizwan Jaipurwala [1], Peter F. Mont [1,4], Nigel D Toussaint [5], Cherie Chiang [1,6]

[1] Dept of Medicine, Austin Health, The University of Melbourne, Melbourne, Australia
[2] Centre for Epidemiology and Biostatistics, Melbourne School of Population and Global Health, The University of Melbourne, Melbourne, Australia
[3] McCaig Institute for Bone and Joint Health, University of Calgary, Calgary, AB, Canada
[4] Dept of Nephrology, Austin Health, The University of Melbourne, Melbourne, Australia
[5] Dept of Nephrology, The Royal Melbourne Hospital, The University of Melbourne, Melbourne, Australia
[6] Depts of Medicine and Endocrinology, Austin Health, The University of Melbourne, Melbourne, Australia

Corresponding Author: Ali Ghasem-Zadeh
Department of Endocrinology, Austin Health, The University of Melbourne, Victoria, Australia.Tel +613 9496 2081, Email alig@unimelb.edu.au

Keywords: Bone microarchitecture, Chronic kidney disease, Cortical porosity, HR-pQCT, Osteopenia, Osteoporosis, Trabecular density

Word Count: Abstract: 311, Main text word count: 6149, References: 1146, Tables: 4, Figures: 4+ Graphic abstract, Supplementary Appendix SA1: 5

Chapter 5

Highlights and graphical abstract

•Microarchitecture is deteriorated in patients irrespective of their BMD category.

•Microarchitectural deterioration independently predicts bone failure load.

•BMD does not predict failure load independent of microarchitecture.

•Microarchitectural deterioration accounts for 87% of the variance in failure load.

•Targeting patients with microarchitectural deterioration may reduce fracture risk

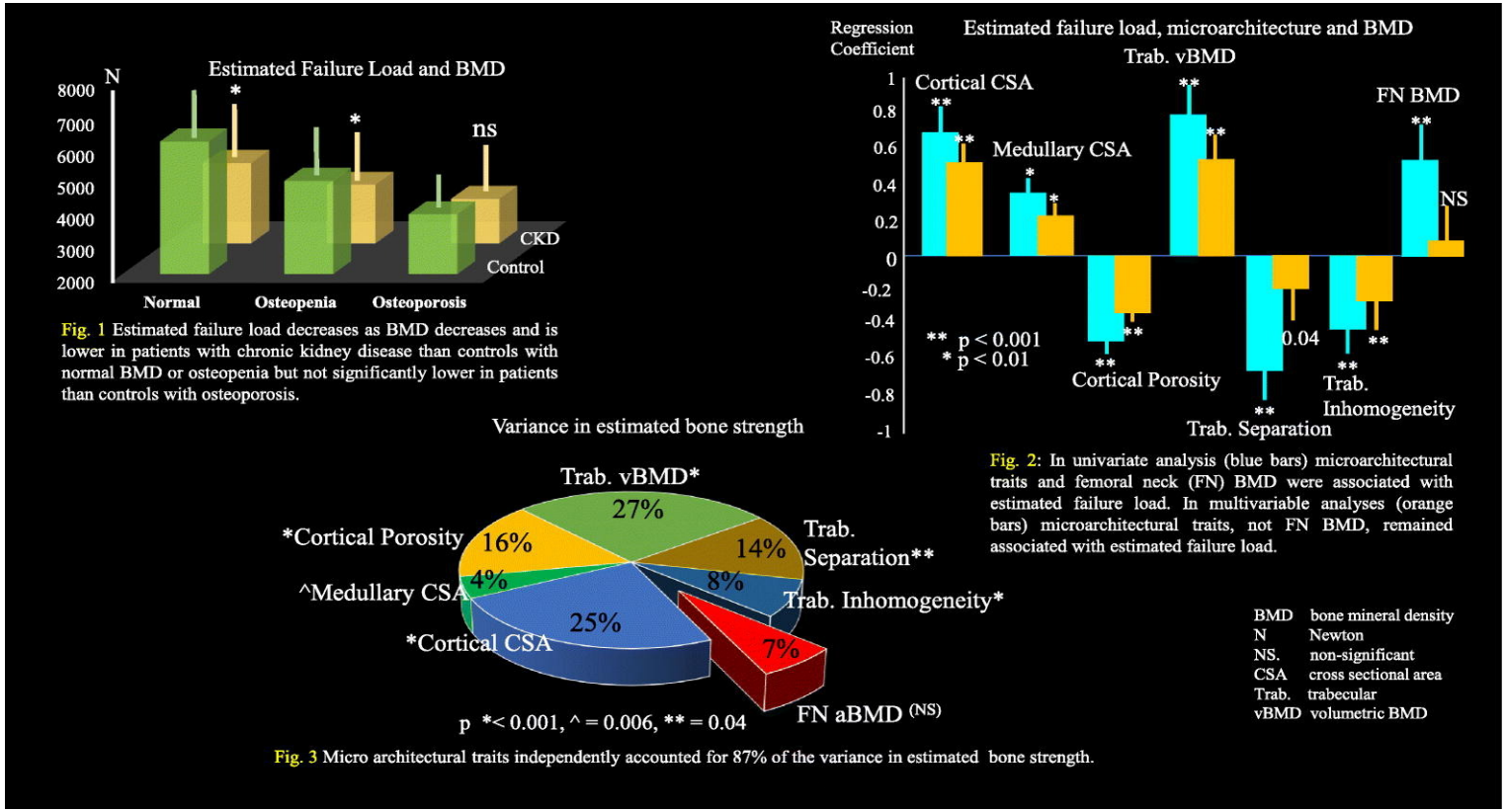

Fig. 1 Estimated failure load decreases as BMD decreases and is lower in patients with chronic kidney disease than controls with normal BMD or osteopenia but not significantly lower in patients than controls with osteoporosis.

Fig. 2: In univariate analysis (blue bars) microarchitectural traits and femoral neck (FN) BMD were associated with estimated failure load. In multivariable analyses (orange bars) microarchitectural traits, not FN BMD, remained associated with estimated failure load.

Fig. 3 Micro architectural traits independently accounted for 87% of the variance in estimated bone strength.

Abstract

Introduction: Measurement of bone mineral density (BMD) is recommended in patients with chronic kidney disease (CKD). However, most persons in the community and most patients with CKD have osteopenia, suggesting fracture risk is low. Bone loss compromises bone microarchitecture which increases fragility disproportionate to modest deficits in BMD. We therefore hypothesized that patients with CKD have reduced estimated failure load due to deterioration in microarchitecture irrespective of whether they have normal femoral neck (FN) BMD, osteopenia or osteoporosis.

Methods: We measured distal tibial and distal radial microarchitecture in 128 patients with CKD and 275 age- and sex-matched controls using high resolution peripheral quantitative computed tomography, FN-BMD using bone densitometry and estimated failure load at the distal appendicular sites using finite element analysis.

Results: Patients versus controls respectively had lower tibial cortical area 219 (40.7) vs. 237 (35.3) mm2, p0.002, lower cortical volumetric BMD 543 (80.7) vs. 642 (81.7) mgHA/cm3 due to higher porosity 69.6 (6.19) vs.61.9 (6.48)% and lower matrix mineral density 64.2 (0.62) vs. 65.1 (1.28)%, lower trabecular vBMD 92.2 (41.1) vs. 149 (43.0) mgHA/cm3 due to fewer and spatially disrupted trabeculae, lower FN-BMD 0.78 (0.12) vs. 0.94 (0.14) g/cm2 and reduced estimated failure load 3825 (1152) vs. 5778 (1467) N, all $p < 0.001$. Deterioration in microarchitecture and estimated failure load was most severe in patients and controls with osteoporosis. Patients with CKD with osteopenia and normal FN-BMD had more deteriorated tibial microarchitecture and estimated failure load than controls with BMD in the same category. In univariate analyses, microarchitecture and FN-BMD were both associated with estimated failure load. In multivariable analyses, only microarchitecture was independently associated with estimated failure load and accounted for 87% of the variance.

Conclusions: Bone fragility is likely to be present in patients with CKD despite them having osteopenia or normal BMD. Measuring microarchitecture may assist in targeting therapy to

those at risk of fracture.

Chapter 5

1. Introduction

Longevity increases the proportion of elderly persons in the community [1]. Age- and disease-related impairment of renal function increases the number of persons requiring management of chronic kidney disease (CKD) [2]. Prolongation of life by drug therapy, dialysis and kidney transplantation is accompanied by secondary hyperparathyroidism and unbalanced bone remodelling. The resulting bone loss compromises bone mass, microarchitecture and strength predisposing to increased morbidity, mortality and costs associated with fragility fracture [3]. To address this fracture burden, Kidney Disease Improving Global Outcomes guidelines recommend measurement of bone mineral density (BMD) [4]. However, BMD is normally distributed. Over ~60% of persons in the community have osteopenia (T-score - 2.5 to - 1.0 SD),~10% have so-called normal BMD (T-score > - 1 SD) and ~30% have a BMD T-score ≤ - 2.5 SD below the young normal mean, the diagnostic threshold for 'osteoporosis' [5]. Because of this population frequency distribution of BMD, most patients with fragility fractures in the community [5] and most patients with CKD who suffer fragility fractures have osteopenia or normal BMD, not osteoporosis [6]. Treatment is often withheld because fracture risk is mistakenly inferred to be low. Even in the presence of a fracture, treatment is withheld because the fracture is misinterpreted as being due to trauma not fragility given BMD is not in the 'osteoporosis' range [7].

Hence, targeting treatment exclusively to persons with 'osteoporosis' will fail to detect or treat over 70% of persons in the community at imminent risk of fracture [7] and will fail to detect or treat most persons with CKD at risk of fracture [6,8]. The absence of osteoporosis is not evidence of absence of bone fragility [9]. Persons with BMD in the osteopenic or normal range are at lower risk for fracture than those with osteoporosis, but they are not necessarily free of bone fragility [9].

Bone loss reduces bone mass and deteriorates the microarchitecture of the reduced bone mass. Measuring BMD captures the reduced bone mass, not the deterioration in microarchitecture. This is an important limitation because an increase in cortical porosity and decrease in trabecular density

reduce compression strength to the 7th and 3rd power respectively; disproportionate to the bone loss causing this microarchitectural deterioration and the modest BMD deficits of osteopenia or normal BMD [10].

Approaches are needed that identify persons at risk of fracture despite having modest deficits in BMD. Measurement of cortical and trabecular microarchitectural deterioration has been shown to identify postmenopausal women at imminent, intermediate and long-term risk for fragility fracture with greater sensitivity than BMD [9]. We therefore quantified bone microarchitecture and estimated failure load in women and men with CKD stages 4-5D, kidney transplant recipients and healthy age and sex matched controls to determine whether most patients with kidney disease, like most persons in the community, have osteopenia or normal BMD, not osteoporosis, but nevertheless differ from healthy persons by having compromised bone microarchitecture and reduced estimated failure load.

2. Methods

2.1. Participants

This study included 128 ambulant patients with CKD stages 4, 5 and 5D, and kidney transplantation attending the Renal and Endocrinology units of Austin Health and the Royal Melbourne Hospital, Melbourne, Australia. Inclusion criteria were age above 18 years old, estimated glomerular filtration rate (eGFR) < 30 (ml/min/1.73 m2), hemodialysis, or peritoneal dialysis and kidney transplantation for more than 3 months. Exclusion criteria were metabolic diseases affecting bone such as Paget disease and osteogenesis imperfecta. Secondary and tertiary hyperparathyroidism in CKD subjects were managed as per KDIGO 2017 Guidelines [11]. The dose of calcitriol was determined by the treating nephrologists. Immunosuppression protocols post renal transplantation was as per local institution guidelines. The patients with CKD were compared to 94 female (57.8 ± 6.3 years) and 181 male (56.3 ± 16.7 years) controls recruited from Bone Structure Study cohort. The Ethics Committee of Austin Health, The University of Melbourne, approved the study (H2006/02704) and all participants provided written informed consent.

2.2. Measurement of bone microarchitecture, BMD and biochemistry

All participants had microarchitecture quantified at the distal radius and distal tibia using high resolution peripheral quantitative computed tomography (HR-pQCT, XtremeCT; Scanco Medical, Brüttisellen, Switzerland) at Austin Health. The manufacturer's protocol applies 60 kVp, 900 μA, 100 ms integration time, 126 mm field of view used to image participants. Image acquisition, reconstruction, and validation are reported [12]. Quality control for the performance of HR-pQCT was based on daily scanning of a manufacturer's phantom containing rods of Hydroxyapatite (HA) embedded in a soft-tissue equivalent resin (QRM, Moehrendorf, Germany). Radiation exposure was 3–5 μSv per measurement. Subjects with motion artefact or degraded quality were excluded from analysis [13]. Bone microarchitecture was quantified using StrAx1.0 algorithm (Strax Corp, Melbourne, Australia) [14]. The 49 most proximal slices of a region of interest were chosen for analysis. Cortical and medullary areas, volumetric bone mineral density (vBMD) of cortical and trabecular compartments, cortical porosity, matrix mineral density, trabecular number, thickness, separation, and spatial inhomogeneity were quantified. The coefficients of variation (CV) of the measurements ranged from 0.54% to 3.98% [14]. BMD of lumbar spine and proximal femur was measured by the Lunar, Prodigy densitometer (GE Healthcare, Madison, WI). Serum was collected in all patients and female controls prior to bone densitometry or HR-pQCT scans. Samples were collected to measure serum parathyroid hormone (PTH), calcium, creatinine (Roche platform, coefficient of variation (CV) = 2.8%, 1.7%, 3.4% respectively), and circulating 25 hydroxyvitamin D (DiaSorin Liaison platform, CV =7.3%). eGFR was calculated using the CKD-EPI formula.

2.3. Estimation of failure load

Micro finite element analysis (μFEA) was used to calculate estimated failure load using the FAIM software (version 8.0). A uniaxial loading with a tissue elastic modulus of 6829 MPa, a Poisson's ratio of 0.3, a critical strain of 7000 microstrain and a critical volume of 2%, were defined. A 1% apparent strain was applied and estimated failure load was calculated as the load when 2% of

elements exceeded the critical strain [15]. The higher the failure load, the greater the strength of bone [16].

2.4 Statistical analysis

Summary statistics for characteristics of patients with CKD express the results in patients and controls as the mean and standard deviation (SD) separately for CKD stages 4-5D and kidney transplant recipients, males and females. Analyses were performed using bone microarchitectural parameters, estimated failure load, and femoral neck and lumbar spine BMD in patients with CKD and controls. Distribution of each microarchitectural and BMD variable was checked using Shapiro-Wilk normality test, and any non-normally distributed variable was transformed using square root, inverse and natural logarithm functions where appropriate. Comparison of the difference between controls and patients with CKD for microarchitectural variables, lumbar spine and femoral neck BMD and estimated failure load was conducted using robust regression, with controls as reference category adjusted for age and sex. The same procedure was applied when the data was stratified by BMD categories (normal BMD, osteopenia and osteoporosis). Relationships between estimated failure load and microarchitectural traits and femoral neck BMD in patients with CKD were assessed using linear regression. All variables were standardised to have mean 0 and standard deviation of 1 prior carried out analyses. Any predictor that had p-value <0.10 in the univariate analysis was considered for the multivariate analysis. As some microarchitectural variables were highly correlated, for example, between cortical vBMD and porosity (r = 0.99), and between trabecular vBMD and connectivity (r = 0.90), the presence of these variables together in the multivariate model caused collinearity. We therefore examined two multivariate models with cortical vBMD and trabecular connectivity in one model and cortical vBMD and trabecular connectivity in one model and cortical vBMD and trabecular vBMD in the other. The importance of each predictor in the multivariate model was assessed by its contribution to explained variance (R2) [17]. As we wanted to compare the performance of femoral neck BMD with microarchitectural traits, femoral neck BMD was kept in the multivariate model even if it was not significant. All analyses were performed using STATA, version 16.0

(http://www.stata.com), separately for distal tibia and distal radius.

3. Results

Demographic data of patients with CKD are shown in Table 1. The causes of end stage kidney disease included glomerulonephritis (55%), polycystic disease (18%), obstructive uropathy (13%), diabetes (2%) hypertension (1%) while 11% were unknown. All kidney transplant recipients had eGFR ≥30 ml/min/1.73 m2 (CKD stages 1T = 4.9%, 2T = 35.8%, 3aT = 30.9%, 3bT = 28.4%). For the remaining 47 patients who did not receive a kidney graft, 15 had CKD stage 4 and 32 had CKD 5D. Cortical and trabecular microarchitecture, estimated failure load, and BMD at the spine and hip did not differ in patients with CKD stages 4-5D and kidney transplant recipients relative to their respective controls so pooled results are shown below. Findings at the distal tibia and distal radius did not differ so the results for the distal tibia are shown below. Data in each patient group relative to their respective controls and data at the distal radius are presented in the supplementary section (Tables S1-S5).

Table 5.1

Table 1. Age, eGFR, serum PTH, vitamin D, total calcium and phosphate in patients with chronic kidney disease and kidney transplant recipients. Data expressed as Mean (SD).

	CKD stages 4-5D (*n* = 47)		**Kidney transplant (*n* = 81)**	
	Female (*n* = 23)	**Male (*n* = 24)**	**Female (*n* = 42)**	**Male (*n* = 39)**
Age (years)	61.4 (14.5)	59.0 (16.4)	58.1 (10.4)	58.6 (11.7)
eGFR (ml/min/1.73 m^2)	14.6 (8.5)	10.6 (7.0)	58.6 (19.4)	56.7 (16.9)
PTH (pmol/L)	21.8 (25.4)	23.8 (28.6)	10.3 (10.2)	8.6 (6.0)
Vitamin D (nmol/L)	69.2 (41.9)	80.0 (37.9)	84.0 (31.9)	88.1 (29.2)
Total calcium (mmol/L)	2.4 (0.1)	2.4 (0.2)	2.5 (0.2)	2.4 (0.1)
Phosphate (mmol/L)	1.3 (0.3)	1.8 (2.1)	1.1 (0.3)	1.0 (0.2)

eGFR = estimated glomerular filtration rate, PTH = parathyroid hormone.

Chapter 5

3.1. Distal tibia microarchitecture, failure load, lumbar spine BMD and

3.1 Distal tibia microarchitecture, failure load, lumbar spine BMD and femoral neck BMD

As shown in Table 2, patients had deficits relative to controls in the following traits - cortical area, cortical vBMD due to increased cortical porosity and decreased matrix mineral density, trabecular vBMD due to fewer, less connected, more widely separated and spatially disrupted trabeculae ('inhomogeneity'), estimated failure load, and BMD at the lumbar spine and femoral neck. Fig. 1 shows the higher the cortical porosity the (a) fewer, (b) the more separated the trabecular with (c) little association with trabecular thickness, but (d) an inverse association with matrix mineral density and (e) greater inhomogeneity in trabecular spatial distribution. Panel (f) shows tibial cortical porosity which trabecularized the cortex producing fragments that may be mistaken as trabeculae and contribute to the inhomogeneity. **Table 5.2**

Table 2. Comparison of distal tibia microarchitecture, estimated failure load, lumbar spine, and femoral neck BMD in patients with CKD versus age- and sex-matched controls.

	Control (*n* = 272)	**CKD (*n* = 126)**	**p**
	Mean (range)	**Mean (range)**	
Age	58.8 (62.3)	58.9 (62.3)	0.161
Bone microarchitecture	Mean (SD)	Mean (SD)	
Total bone CSA (mm^2)**	753 (153)	711 (146)	0.489
Cortical CSA (mm^2)	237 (35.3)	219 (40.7)	0.002
Medullary CSA (mm^2)**	517 (135)	492 (123)	0.920
Cortical vBMD ($mgHA/cm^3$)	642 (81.7)	543 (80.7)	<0.001
Porosity (%)**	61.9 (6.48)	69.6 (6.19)	<0.001
Matrix mineral density (%)	65.1 (1.28)	64.2 (0.62)	<0.001
Trabecular vBMD ($mgHA/cm^3$)	149 (43.0)	92.2 (41.1)	<0.001
Number (1/mm)	2.91 (0.68)	1.93 (0.59)	<0.001
Thickness (μm)*+	195 (143)	197 (146)	0.304
Connectivity ($1/mm^2$)	0.85 (0.17)	0.64 (0.20)	<0.001
Separation (mm)**	1.23 (0.28)	1.74 (0.36)	<0.001
Inhomogeneity*	0.23 (0.15)	0.46 (0.44)	<0.001
Estimated failure load (N)***	5778 (1467)	3825 (1152)	<0.001
Bone mineral density			
Lumbar spine BMD (g/cm^2)***	1.16 (0.18)	1.06 (0.17)	<0.001
T-Score	−0.35 (1.47)	−1.24 (1.31)	<0.001
Femoral neck BMD (g/cm^2)***	0.94 (0.14)	0.78 (0.12)	<0.001
T-Score	−0.89 (1.05)	−2.04 (0.87)	<0.001

Summary statistics presented by absolute mean, standard deviation (SD) where p-value was computed using transformed data if variable was not normally distributed using *inverse, **natural logarithm and ***square root functions; analyses were conducted using robust regression, adjusted for age and sex. Sample size for FEA analysis was 242 for controls and 119 for patients with CKD, and 218 to 225 for controls and 108 to 114 for patients with CKD for lumbar spine and femoral neck (bone mineral density BMD measurements). +The trabecular thickness' unit converted to micron to get more distinctive numbers. CSA = cross sectional area; HA = hydroxyapatite; vBMD = volumetric bone mineral density; N = Newton.

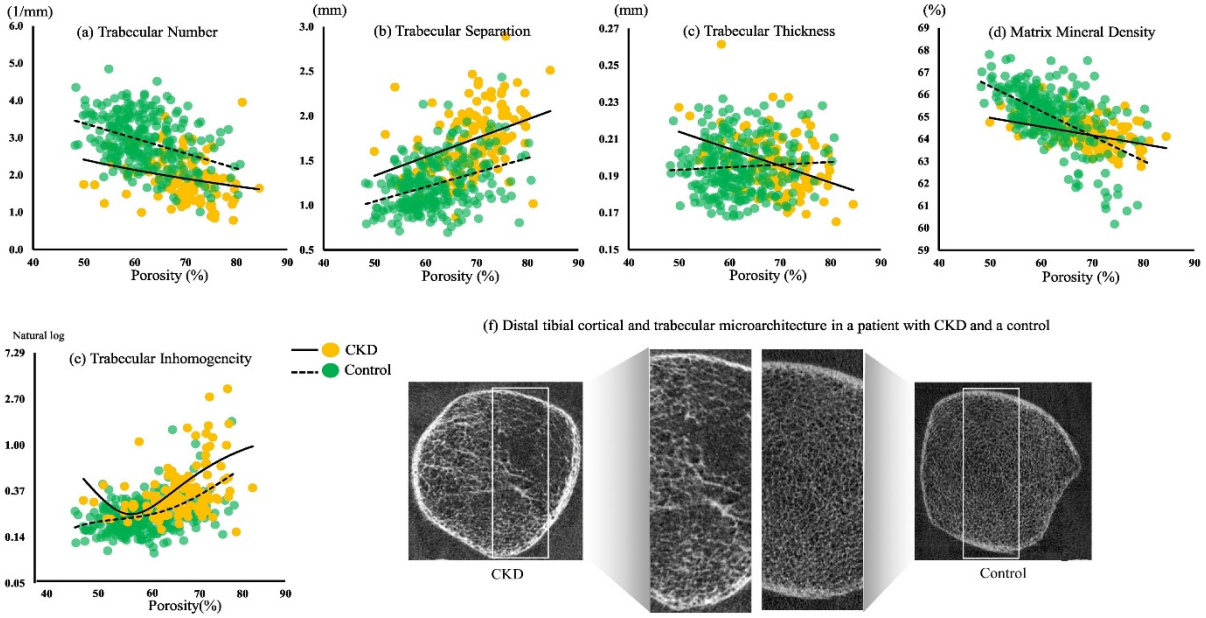

Fig. 1. Cortical and trabecular microarchitecture and femoral neck BMD are more deteriorated in patients with CKD (yellow dots) than in controls (green dots). The greater the cortical porosity, (a) the fewer the numbers of trabeculae, (b) the greater the trabecular separation but (c) no association with trabecular thickness. (d) Greater cortical porosity was associated with lower matrix mineral density and (e) greater inhomogeneity in trabecular spatial distribution. (f) Compared with a control, the patient with CKD had loss of homogeneity in distal tibial trabecular spatial distribution. Magnified section shows increased cortical porosity with trabecularized cortex producing fragments that may be mistaken as trabeculae and contribute to the inhomogeneity. (For interpretation of the references to colour in this figure legend, the reader is referred to the web version of this article).

Figure 5.1

3.2. Distal tibia microarchitecture and estimated failure load by femoral neck BMD categories

As shown in Table 3 and Fig. 2, across BMD categories, deterioration in microarchitectural traits and estimated failure load was most severe in patients and controls with osteoporosis, intermediate in patients and controls with osteopenia, and was least deteriorated in patients and controls with normal BMD. In patients with osteopenia and normal BMD, distal tibial microarchitecture and estimated failure load were more deteriorated relative to controls with the same BMD category. In patients with osteoporosis, estimated distal tibial failure load was lower than in controls, but not significantly. Estimated distal radial failure load was significantly lower than controls for all three categories of BMD (Table S4). The frequency distribution curve of cortical matrix mineral density was shifted left with a lower mean value in patients than in controls.

Table 5.3

Table 3. Comparison of distal tibia microarchitecture and estimated failure load in controls versus patients with CKD according to BMD category (normal, osteopenia and osteoporosis).

		Normal			Osteopenia			Osteoporosis		
		Control (*n* = 117)	CKD (*n* = 14)	p	Control (*n* = 96)	CKD (*n* = 67)	p	Control (n = 11)	CKD (*n* = 31)	p
Bone microarchitecture		Mean (SD)	Mean (SD)		Mean (SD)	Mean (SD)		Mean (SD)	Mean (SD)	
Total bone CSA (mm^2) **		753 (163)	751(117)	0.809	721 (138)	705(157)	0.673	723 (157)	704 (117)	0.344
Cortical CSA (mm^2)		241 (32.4)	228 (22.8)	0.008	225 (33.5)	215(40.7)	0.447	202 (35.0)	216 (41.4)	0.003
Medullary CSA (mm^2) **		512 (146)	524 (109)	0.551	496 (120)	490(135)	0.645	522 (137)	488 (92.3)	0.702
Cortical vBMD ($mgHA/cm^3$)		671 (64.4)	590 (64.5)	<0.001	608 (84.5)	548 80.9)	<0.001	528 (78.2)	512 (80.6)	0.024
Porosity (%) **		59.7 (5.11)	66.1 (4.95)	<0.001	64.5 (6.76)	69.1(6.28)	<0.001	70.7 (6.55)	71.9 (6.05)	0.018
Matrix mineral density (%)		65.2 (0.95)	64.4 (0.52)	<0.001	64.7 (1.69)	64.2 0.61)	0.006	64.5 (1.06)	64.2 (0.65)	0.454
Trabecular vBMD ($mgHA/cm^3$)		161(39.1)	118 (36.3)	<0.001	128 (37.6)	93.0 37.0)	<0.001	108 (54.7)	80.3 (47.9)	0.090
Number (1/mm)		3.02 (0.57)	2.32 (0.51)	<0.001	2.67 (0.71)	1.94 (0.59)	<0.001	2.27 (0.70)	1.81 (0.60)	0.004
Thickness (μm) *+		196 (135)	197 (127)	0.954	194 (160)	196 (141)	0.242	196 (135)	197 (127)	0.382
Connectivity ($1/mm^2$)		0.89(0.15)	0.74 (0.21)	0.012	0.78 (0.16)	0.64 (0.18)	<0.001	0.72 (0.21)	0.58 (0.22)	0.102
Separation (mm) **		1.17 (0.22)	1.53 (0.33)	<0.001	1.35 (0.30)	1.74 (0.34)	<0.001	1.52 (0.39)	1.83 (0.41)	0.012
Inhomogeneity *		0.21 (0.06)	0.28 (0.06)	<0.001	0.27 (0.21)	0.39 (0.23)	<0.001	0.34 (0.24)	0.62 (0.74)	0.014
Estimated failure load (N) ***		6199 (1177)	4541 (1190)	<0.001	4949 (1167)	3856 (1100)	<0.001	3893 (891)	3409 (1223)	0.107

Summary statistics were presented by mean and standard deviation (SD), where p-value was computed using transformed data if variable was not normally distributed using *inverse, **natural logarithm and ***square root functions; analyses were conducted using robust regression, adjusted for age and sex. +The trabecular thickness' unit converted to micron to get more distinctive numbers. CSA = cross sectional area; HA = hydroxyapatite; vBMD = volumetric bone mineral density; N = Newton.

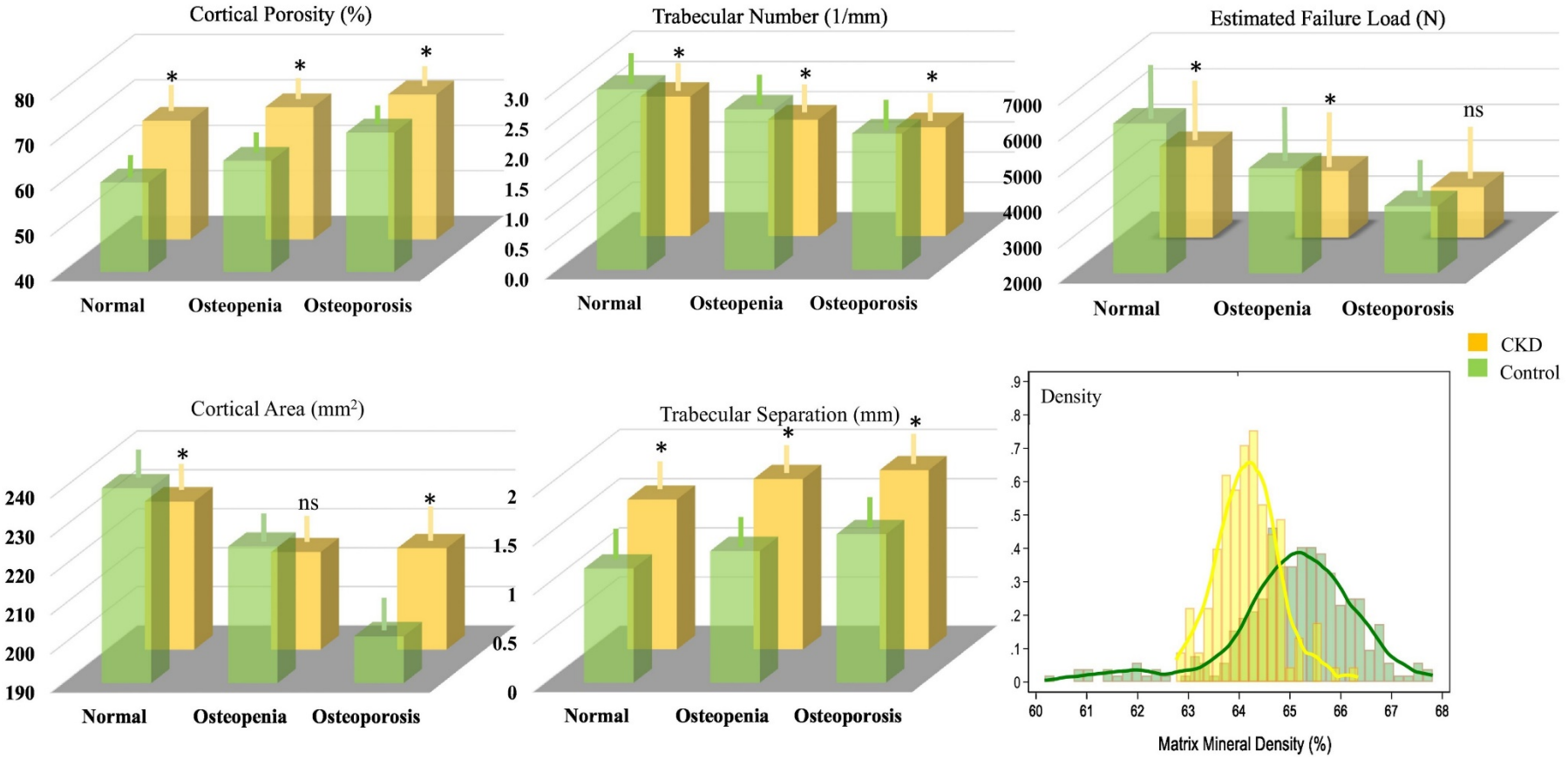

Fig. 2. Comparison of bone microarchitecture and estimated failure load in patients with CKD (yellow bars) versus controls (green bars) within a bone mineral density (BMD) category (*p < 0.001). Comparison of matrix mineral density frequency distribution between patients with CKD and controls (right bottom panel), N=Newton. See text. (For interpretation of the references to colour in this figure legend, the reader is referred to the web version of this article).

Figure 5.2

3.3. Predictors of estimated tibial bone failure load

As shown in **Table 4**, in univariate analyses, distal tibial cortical and trabecular microarchitecture and femoral neck BMD were each associated with estimated tibial failure load. In multivariable analyses, associations with estimated strength remained significant for microstructural traits but not for femoral neck BMD. Microarchitecture accounted for over 85% of the variance in estimated failure load (R^2 values were 0.879 and 0.868 for the multivariate model I and II respectively).

Table5.4

Table 4. Univariate and multivariate analyses of associations between estimated failure load and tibial microarchitectural traits in patients with CKD (*N* = 103).

	Univariate			**Multivariate Model I**				**Multivariate Model II**			
	Coef	**se**	**p**	**Coef**	**se**	**p**	**%R^2**	**Coef**	**se**	**p**	**%R^2**
Total bone CSA (mm^2)	0.450	0.100	<0.001								
Cortical CSA (mm^2)	0.640	0.083	<0.001	0.443	0.043	<0.001	25.4	0.413	0.048	<0.001	24.6
Medullary CSA (mm^2)	0.307	0.106	0.005	0.118	0.049	0.018	5.22	0.154	0.055	0.006	4.44
Cortical vBMD ($mgHA/cm^3$)	0.593	0.082	<0.001	0.341	0.048	<0.001	21.6				
Porosity (%)	-0.568	0.084	<0.001					−0.330	0.053	<0.001	15.9
Matrix mineral density (%)	0.236	0.102	0.023								
Trabecular vBMD ($mgHA/cm^3$)	0.773	0.067	<0.001					0.596	0.093	<0.001	26.7
Number (1/mm)	0.452	0.091	<0.001								
Thickness (μm)	0.477	0.097	<0.001								
Connectivity ($1/mm^2$)	0.796	0.064	<0.001	0.503	0.044	<0.001	38.8				
Separation (mm)	-0.632	0.078	<0.001					−0.169	0.082	0.041	13.8
Inhomogeneity*	0.459	0.094	<0.001					−0.355	0.073	<0.001	7.82
Femoral neck BMD	0.499	0.088	<0.001	0.033	0.042	0.431	9.02	0.024	0.045	0.603	6.77

All variables were standardised to have mean of 0 and standard deviation of 1; *data was transformed using inverse function; R-square (R^2) were 0.879 and 0.868 for the multivariate model I and II respectively; %R^2 = percentage of contribution to R-square by each bone trait. CSA = cross sectional area; HA = hydroxyapatite; vBMD = volumetric bone mineral density; N = Newton.

As shown **in Fig. 3**, there were significant associations between estimated failure load and several cortical and trabecular traits and between estimated failure load and femoral neck BMD in both patients and controls. At any given trait, estimated failure load was lower in the patients than controls.

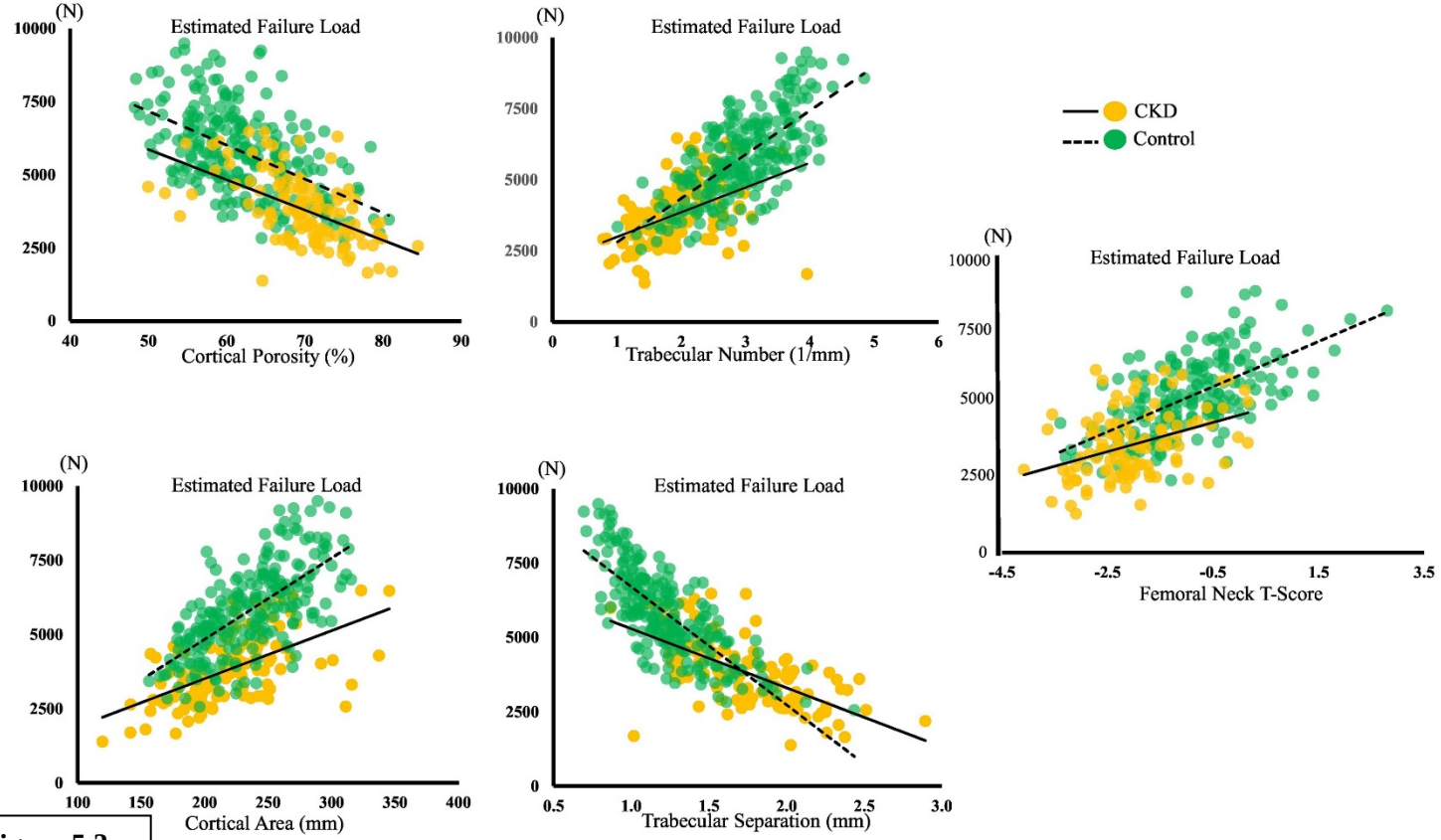

Figure 5.3

Fig. 3. Univariate associations between estimated failure load at the distal tibia with tibial cortical and trabecular microarchitecture and femoral neck BMD in patients with CKD (yellow dots) and controls (green dots). N=Newton. See text. (For interpretation of the references to colour in this figure legend, the reader is referred to the web version of this article.)

Chapter 5

4. Discussion

We report that most patients with CKD stages 4-5D and kidney transplant recipients had osteopenia or normal femoral neck BMD, not osteoporosis. Despite these modest deficits in femoral neck BMD, distal tibial and distal radial microarchitecture and estimated failure load were compromised. Cortical and trabecular distal tibia and distal radius microarchitecture, not femoral neck BMD, were independently associated with estimated failure load and accounted for over 85% of the variance in failure load estimated at these metaphyseal locations.

The findings were consistent within each BMD category – relative to controls, the cortices were reduced in area, cortical vBMD was reduced due to increased porosity and decreased matrix mineral density, trabecular vBMD was reduced due to fewer trabeculae that were disconnected and disrupted in their spatial distribution. Patients and controls with osteoporosis had more severe deterioration in microarchitecture and estimated failure load than patients and controls with osteopenia or normal BMD. In each of these three femoral neck BMD categories, patients had more deteriorated distal tibial and distal radial microarchitecture relative to controls with the same BMD category. Estimated failure load was also more severely deteriorated in patients than controls in all three BMD categories but the difference in patients with osteoporosis versus controls with osteoporosis achieved significance only at the distal radius, not distal tibia.

Persons with osteopenia and normal BMD are the source of most fragility fractures in the community because vastly greater numbers of persons in the community have these modest deficits in BMD [5]. It is likely that most patients with CKD in this study, and patients with CKD with fractures reported previously [6], [8], had osteopenia or normal BMD for the same reason. Thus, finding normal BMD or osteopenia in patients with CKD is no assurance of ‘normal’ bone strength and freedom from fracture risk.

BMD T-score > −1.0 SD is referred to as ‘normal’ but this terminology is misleading because bone loss

reduces bone mass but also deteriorates the microarchitecture of the reduced bone mass, irrespective of the assigned BMD category [18]. Compressive strength decreases as a 7th and 3rd power function of the increase in cortical porosity and decrease in trabecular density respectively, an increment in fragility disproportionate to the modest deficits in BMD produced by bone loss [10]. Indeed, we found that estimated failure load at the distal appendicular sites was independently associated with most microarchitectural traits at these locations, not femoral neck BMD.

Both distal tibial and distal radial cortical and trabecular microarchitecture were deteriorated in patients with CKD because widespread unbalanced bone remodelling occurs upon all three (intracortical, endocortical and trabecular) components of bone's inner (endosteal) envelope [19]. Finding correlations between cortical porosity and trabecular morphology in patients with CKD and in controls supports the notion that both bone compartments are compromised by bone loss produced by advancing age and by CKD.

Several investigators report deterioration in cortical bone but sparing of trabecular morphology or increased trabecular density in patients with primary [20], and secondary hyperparathyroidism of kidney disease [8]. This finding is likely to be due to an error in segmenting cortical from trabecular bone [14], [21]. Unbalanced intracortical remodelling upon the surface Haversian canals traversing the cortices fragment and trabecularizes the cortex adjacent to the medullary canal. The fragments are ‘seen’ as ‘trabecular’ bone by the threshold-based segmentation algorithm falsely elevating trabecular density, so it appears to be unaffected or increased in patients with CKD [8], [20], [22].

Finding normal or increased trabecular thickness is likely to be due to preferential loss of thin trabeculae, inclusion of thicker cortical fragments erroneously called ‘trabeculae’, or both. Thickening is unlikely to be due to increased trabecular bone formation as this requires intermittent not continuous PTH exposure as found in primary and secondary hyperparathyroidism [23]. We speculate that deterioration in trabecular

spatial distribution (‘inhomogeneity’) is likely to be due to more rapid bone loss of trabeculae positioned centrally in the medullary canal. These trabeculae may have a large surface area/bone volume configuration providing more surface for initiation of unbalanced remodelling than peripherally positioned trabeculae abutting the cortex [24]. Trabeculae populating the cortico-trabecular transitional zone may be fashioned with a lower surface area/bone volume configuration and so may be remodelled more slowly. Spatial inhomogeneity may also be due to inclusion of cortical fragments as ‘trabecular’ bone [12].

Rapid unbalanced remodelling compromises qualities of bone other than its cortical and trabecular microarchitecture [25]. For example, matrix mineralization density is reduced by replacing older, more mineralized bone, with young, less completely mineralized bone [26], [27]. As remodelling is unbalanced, the inverse association between porosity and matrix mineral density is due to replacement of older matrix with a smaller volume of new, less mineralized matrix. Kidney transplantation improves kidney function but hyperparathyroidism may persist resulting in continued rapid and unbalanced remodelling exacerbated by corticosteroid therapy which reduces bone formation by each remodelling event, worsening remodelling imbalance [28], [29]. This may account for the similar deficits in microarchitecture, BMD and estimated failure load in kidney transplant recipients and patients with CKD.

These results confirm previous work showing bone loss and deteriorated cortical and trabecular microarchitecture in patients with primary [30] and secondary hyperparathyroidism of CKD [8]. Cejka et al. reported lower cortical and trabecular vBMD and deteriorated trabecular microarchitecture of distal radius and distal tibia in patients undergoing hemodialysis [31]. Nishiyama et al., reported increased cortical porosity following kidney transplantation [32]. Trombetti et al. reported deteriorated cortical and trabecular microarchitecture and estimated failure load and stiffness [33]. This study advances previous work by demonstrating microarchitectural deterioration occurs irrespective of the BMD category, even so-called ‘normal’ BMD, and this deterioration compromises bone strength independent of BMD.

This study has several limitations. This was a cross-sectional with small numbers of patients with normal BMD and small numbers of controls with osteoporosis. For this reason, we may have been unable to detect some morphological differences, and some group differences failed to achieve statistical significance. We cannot distinguish whether lower peak, greater bone loss or both contributed to microstructural deterioration and deficits in BMD. In addition, only 24 subjects had had fractures so evaluation of bone morphology relative to patients without fractures and relative to controls was not possible. Attributing causation of bone disease is difficult because patients with CKD are heterogeneous in terms of the underlying cause and duration of kidney disease, duration of dialysis, exposure to glucocorticoids, kidney transplantation, gonadal status and other factors.

In summary, patients with CKD stages 4-5D and kidney transplant recipients are more likely to have osteopenia or normal BMD than osteoporosis. Despite the modest deficits in BMD, estimated breaking strength of bone is compromised, in part, due to microarchitectural deterioration of the reduced bone mass, a structural change which increases bone fragility disproportionate to the bone loss causing it. In conclusion, finding modest deficits in BMD does not exclude the presence of bone fragility. Assessment of bone microarchitecture might be helpful in identifying and targeting treatment to patients with CKD at risk of fracture.

CRediT authorship contribution statement

Study design and conduct: AGH, ES, CHCH. Data collection: AGZ, ES, SI, RJ, PM, NT, CHCH. Responsibility for StrAx analysis: AGZ, Responsibility for finite element analysis: SB. Statistical analyses: MB and AGH. Drafting manuscript: AGH, CHCH and ES. Data interpretation and approving final version of manuscript: AGH, MB, ES, SI, RJ, PM, NT, SB, and CHCH.

Chapter 5

Declaration of competing interest

A Ghasem-Zadeh is a shareholder in StraxCorp. E Seeman is shareholder in StraxCorp. S Boyd is a co-founder and co-owner of Numerics88 Solutions Inc.

Chapter 5

Appendix A. Supplementary data

SUPPLEMENTARY TABLES

Table 5.S1

Table S1: Comparison of distal tibia microarchitecture, estimated failure load, lumbar spine, and femoral neck BMD in patients with CKD stage 4-5D versus kidney transplant recipients.

	CKD stage 4-5D (n = 47)	**Kidney transplant recipients (n = 79)**	
Bone microarchitecture	Mean (SD)	Mean (SD)	p
Total Bone CSA (mm^2)**	703 (153)	715 (143)	0.708
Cortical CSA (mm^2)	218 (47.5)	219 (36.3)	0.486
Medullary CSA (mm^2)**	485 (124)	496 (123)	0.709
Cortical vBMD ($mgHA/cm^3$)	530 (91.6)	550 (73.1)	0.250
Porosity (%)**	70.6 (7.02)	69.0 (5.61)	0.284
Matrix Mineral Density (%)	64.1 (0.59)	64.2 (0.65)	0.983
Trabecular vBMD ($mgHA/cm^3$)	89.7 (42.8)	93.6 (40.3)	0.747
Number(1/mm)	1.91 (0.65)	1.95 (0.55)	0.622
Thickness(μm)*+	197 (173)	196 (128)	0.987
Connectivity($1/mm^2$)	0.64 (0.21)	0.64 (0.19)	0.987
Separation(mm)**	1.76 (0.37)	1.73 (0.36)	0.847
Inhomogeneity*	0.48 (0.46)	0.44 (0.42)	0.806
Estimated Failure Load (N)***	3731 (1195)	3880 (1130)	0.638
Bone mineral density	**n = 42**	**n = 70**	
Lumbar Spine BMD(g/cm^2) ***	1.09 (0.21)	1.04 (0.15)	0.343
T-Score	-1.08 (1.43)	-1.33 (1.24)	0.487
Femoral Neck BMD(g/cm^2) ***	0.76 (0.14)	0.78 (0.10)	0.446
T-Score	-2.18 (1.03)	-1.95 (0.76)	0.278

Chapter 5

Summary statistics presented by absolute mean and standard deviation (SD), where p-value (p) was computed using transformed data if variable was not normally distributed using *inverse,**natural logarithm and ***square root functions; analyses were conducted using robust regression, adjusted for age and sex; sample size for estimated failure load were 44 and 75 for CKD stage 4-5D and kidney transplant recipients respectively; +The trabecular thickness' unit converted to micron to get more distinctive numbers. CSA= Cross Sectional Area; HA= Hydroxyapatite; vBMD= volumetric Bone Mineral Density; N= Newton.

Table 5.S2

Table S2: Comparison of distal radius microarchitecture, estimated failure load in patients with CKD stage 4-5D versus kidney transplant recipients.

	CKD stage 4-5D (n=45)	**Kidney transplant recipients** (n=77)	
Bone microarchitecture	Mean (SD)	Mean (SD)	p
Total Bone CSA (mm^2)**	264 (64.1)	270 (66.3)	0.143
Cortical CSA (mm^2)	97.8 (21.5)	95.3 (20.8)	0.780
Medullary CSA (mm^2)**	166 (48.3)	175 (49.6)	0.062
Cortical vBMD ($mgHA/cm^3$)	592 (110)	610 (98.5)	0.570
Porosity (%)**	66.0 (8.68)	64.4 (7.62)	0.561
Matrix Mineral Density (%)	64.5 (0.85)	64.6 (0.79)	0.615
Trabecular vBMD ($mgHA/cm^3$)	87.8 (50.2)	83.2 (50.9)	0.491
Number(1/mm)	1.71 (0.64)	1.64 (0.61)	0.634
Thickness(µm)*+	202 (133)	198 (129)	0.184
Connectivity($1/mm^2$)	0.52 (0.25)	0.49 (0.26)	0.394
Separation(mm)**	1.79 (0.46)	1.83 (0.46)	0.554
Inhomogeneity*	0.44 (0.34)	0.44 (0.29)	0.547
Estimated Failure Load (N)***	1359 (552)	1377 (571)	0.859

Summary statistics were presented by absolute mean, standard deviation (SD) where p-value was computed using transformed data if variable was not normally distributed using *inverse, **natural logarithm and ***square root functions; sample size for estimated failure load were 43 and 74 for CKD stage 4-5D and post kidney transplant respectively; +The trabecular thickness' unit

converted to micron to get more distinctive numbers. CSA=Cross Sectional Area; HA= Hydroxyapatite; vBMD = volumetric Bone Mineral Density; N= Newton.

Table 5.S3

Table S3: Comparison of distal radius microarchitecture, estimated failure load, lumbar spine, and femoral neck BMD in patients with CKD versus age- and sex-matched controls.

	Control (n=266)	**CKD** (n=122)	
Bone microarchitecture	Mean (SD)	Mean (SD)	p
Total Bone CSA (mm^2)**	282 (65.9)	263 (65.3)	0.965
Cortical CSA (mm^2)	108 (20.7)	96.2 (21.0)	0.002
Medullary CSA (mm^2)**	175 (50.6)	172 (49.1)	0.135
Cortical vBMD ($mgHA/cm^3$)	720 (82.4)	603 (103)	<0.001
Porosity (%)**	55.8 (6.59)	65.0 (8.03)	<0.001
Matrix Mineral Density (%)	65.4 (0.85)	64.6 (0.81)	<0.001
Trabecular vBMD ($mgHA/cm^3$)	141 (49.3)	84.9 (50.5)	<0.001
Number(1/mm)	2.55 (0.56)	1.67 (0.62)	<0.001
Thickness(µm)*+	196 (150)	200 (131)	0.002
Connectivity($1/mm^2$)	0.77 (0.24)	0.50 (0.25)	<0.001
Separation(mm)**	1.27 (0.29)	1.81 (0.46)	<0.001
Inhomogeneity*	0.22 (0.13)	0.44 (0.31)	<0.001
Estimated Failure Load (N)***	2208 (678)	1370 (561)	<0.001

Summary statistics were presented by absolute mean, standard deviation (SD) where p-value was computed using transformed data if variable was not normally distributed using *inverse, **natural logarithm and ***square root functions; analyses were conducted using robust regression adjusted for age and sex; sample size for FEA was 238 for controls and 117 for CKD patients. +The trabecular thickness' unit converted to micron to get more distinctive numbers. CSA=Cross Sectional Area; HA= Hydroxyapatite; vBMD = volumetric Bone Mineral Density; N= Newton.

Chapter 5

Table 5.S4

Table S4: Comparison of distal radius microarchitecture, estimated failure load in controls versus patients with CKD according to BMD category (normal, osteopenia or osteoporosis).

	Normal			**Osteopenia**			**Osteoporosis**		
	Control (n=114)	**CKD (n=14)**		**Control (n=92)**	**CKD (n=65)**		**Control (n=11)**	**CKD (n=29)**	
Bone microarchitecture	Mean (SD)	Mean (SD)	p	Mean (SD)	Mean (SD)	p	Mean (SD)	Mean (SD)	p
Total Bone CSA (mm^2)**	282 (68.7)	273 (60.8)	0.539	268 (60.8)	262 (67.1)	0.472	271 (78.3)	276 (66.8)	0.011
Cortical CSA (mm^2)	109 (19.9)	103 (21.0)	0.058	102 (21.5)	92.0 (18.4)	0.003	95.1 (21.8)	99.0 (23.4)	0.003
Medullary CSA (mm^2)**	173 (54.4)	170 (45.0)	0.811	166 (44.2)	170 (52.4)	0.080	176 (58.6)	177 (48.2)	0.038
Cortical vBMD ($mgHA/cm^3$)	745 (67.0)	661 (83.6)	0.001	693 (90.3)	607 (105)	<0.001	635 (80.8)	570 (112)	<0.001
Porosity (%)**	53.9 (5.61)	60.5 (6.44)	<0.001	57.9 (7.28)	64.7 (8.20)	<0.001	62.5 (6.57)	67.6 (8.74)	<0.001
Matrix Mineral Density (%)	65.4 (0.82)	64.6 (0.90)	<0.001	65.3 (0.90)	64.6 (0.82)	<0.001	65.3 (1.11)	64.6 (0.79)	0.026
Trabecular vBMD ($mgHA/cm^3$)	151 (45.8)	111 (60.7)	0.002	120 (43.9)	82.6 (46.1)	<0.001	104 (52.4)	82.9 (47.4)	0.215
Number(1/mm)	2.62 (0.47)	1.92 (0.61)	<0.001	2.34 (0.55)	1.66 (0.60)	<0.001	2.02 (0.68)	1.69 (0.61)	0.011
Thickness(µm)*+	196 (136)	201 (159)	0.410	195 (160)	198 (114)	0.046	200 (195)	200 (118)	0.402
Connectivity($1/mm^2$)	0.83 (0.22)	0.61 (0.35)	0.003	0.67 (0.23)	0.48 (0.23)	<0.001	0.64 (0.25)	0.50 (0.23)	0.091
Separation(mm)**	1.21 (0.24)	1.64 (0.49)	<0.001	1.40 (0.30)	1.81 (0.44)	<0.001	1.53 (0.36)	1.83 (0.47)	0.008
Inhomogeneity*	0.20 (0.06)	0.31 (0.17)	<0.001	0.26 (0.14)	0.44 (0.30)	<0.001	0.42 (0.43)	0.41 (0.28)	0.067
Estimated Failure Load (N)***	2341 (616)	1718 (653)	<0.001	1873 (601)	1289 (438)	<0.001	1680 (421)	1297 (618)	0.003

Summary statistics were presented by mean and standard deviation (SD), where p-value was computed using transformed data if variable was not normally distributed using *inverse, **natural logarithm and ***square root functions; analyses were conducted using robust regression, adjusted for age and sex. Sample size for FEA was 100 for controls in normal group. +The trabecular thickness' unit converted to micron to get more distinctive numbers. CSA=Cross Sectional Area; HA= Hydroxyapatite; vBMD = volumetric Bone Mineral Density; N= Newton.

Chapter 5

Table 5.S5

Table S5: Univariate and multivariate analyses of association between estimated failure load and distal radius microarchitectural traits in patients with CKD (N =99).

	Univariate			Multivariate Model I				Multivariate Model II			
	Coef	se	p	Coef	se	p	%R^2	Coef	se	p	%R^2
Total Bone CSA (mm^2)	0.275	0.093	0.004								
Cortical CSA (mm^2)	0.614	0.078	<0.001	0.473	0.047	<0.001	33.9	0.504	0.050	<0.001	33.1
Medullary CSA (mm^2)	0.114	0.096	0.238								
Cortical vBMD ($mgHA/cm^3$)	0.552	0.077	<0.001	0.390	0.047	<0.001	26.6				
Porosity (%)	-0.537	0.078	<0.001					-0.345	0.053	<0.001	18.4
Matrix Mineral Density (%)	0.086	0.098	0.381								
Trabecular vBMD ($mgHA/cm^3$)	0.697	0.076	<0.001					0.333	0.147	0.026	17.9
Number(1/mm)	0.612	0.083	<0.001								
Thickness(µm)	0.344	0.099	0.001								
Connectivity($1/mm^2$)	0.699	0.074	<0.001	0.370	0.052	<0.001	32.1				
Separation(mm)	-0.664	0.078	<0.001					-0.254	0.123	0.042	15.9
Inhomogeneity*	0.527	0.086	<0.001					-0.240	0.100	0.019	9.20
Femoral Neck BMD	0.395	0.088	<0.001	0.038	0.047	0.423	7.43	0.025	0.051	0.621	5.55

All variables were standardised to have mean 0 and standard deviation of 1; *data was transformed using inverse function; R-square (R^2) were 0.816 and 0.800 for the multivariate model I and II respectively; %R^2 = percentage of contribution to R-square by each bone trait; CSA=Cross Sectional Area; HA= Hydroxyapatite; vBMD = volumetric Bone Mineral Density; N= Newton.

Chapter 5

References

[1] K. Christensen, G. Doblhammer, R. Rau, J.W. Vaupel, Ageing populations: the challenges ahead, Lancet 374 (9696) (2009) 1196–1208.

[2] P. Cockwell, L.A. Fisher, The global burden of chronic kidney disease, Lancet 395 (10225) (2020) 662–664. Epub 2020/02/18.

[3] L. Robertson, C. Black, N. Fluck, S. Gordon, R. Hollick, H. Nguyen, et al., Hip fracture incidence and mortality in chronic kidney disease: the GLOMMS-II record linkage cohort study, BMJ Open 8 (4) (Apr 12 2018), e020312. Epub 2018/04/15.

[4] M. Ketteler, G.A. Block, P. Evenepoel, M. Fukagawa, C.A. Herzog, L. McCann, et al., Executive summary of the 2017 KDIGO chronic kidney disease-mineral and bone disorder (CKD-MBD) guideline update: what's changed and why it matters, Kidney Int. 92 (1) (Jul 2017) 26–36. Epub 2017/06/26.

[5] E.S. Siris, Y.T. Chen, T.A. Abbott, E. Barrett-Connor, P.D. Miller, L.E. Wehren, et al., Bone mineral density thresholds for pharmacological intervention to prevent fractures, Arch. Intern. Med. 164 (10) (2004) 1108–1112. Epub 2004/05/26.

[6] M.H. Tariq, S.A.S. Sulaiman, Prevalence of osteopenia and osteoporosis among chronic kidney disease patients: a systematic review, Systematic Review, Open Urol. Nephrol. J. 13 (2020) 8. Epub 23/05/2020.

[7] W.D. Leslie, E. Seeman, S.N. Morin, L.M. Lix, S.R. Majumdar, The diagnostic threshold for osteoporosis impedes fracture prevention in women at high risk for fracture: a registry-based cohort study, Bone 114 (Sep 2018) 298–303. Epub 2018/07/17.

[8] T.L. Nickolas, E.M. Stein, E. Dworakowski, K.K. Nishiyama, M. Komandah-Kosseh, C.A. Zhang, et al., Rapid cortical bone loss in patients with chronic kidney disease, J. Bone Miner. Res. 28 (8) (2013) 1811–1820.

[9] R. Chapurlat, M. Bui, E. Sornay-Rendu, R. Zebaze, P.D. Delmas, D. Liew, et al., Deterioration of cortical and trabecular microstructure identifies women with osteopenia or normal bone mineral density at imminent and long-term risk for fragility fracture: a prospective study, J. Bone Miner. Res. 35 (5) (May 2020) 833–844. Epub

2019/12/11.

[10] M.B. Schaffler, D.B. Burr, Stiffness of compact bone: effects of porosity and density, J. Biomech. 21 (1) (1988) 13–16. Epub 1988/01/01.

[11] KDIGO 2017 clinical practice guideline update for the diagnosis, evaluation, prevention, and treatment of chronic kidney disease-mineral and bone disorder (CKD-MBD), Kidney international supplements. 7 (1) (Jul 2017) 1–59. Epub 2017/07/01.

[12] A. Laib, H.J. H¨auselmann, P. Rüegsegger, In vivo high resolution 3D-QCT of the human forearm, Technol. Health Care 6 (5–6) (Dec 1998) 329–337. Epub 1999/04/01.

[13] D.E. Whittier, S.K. Boyd, A.J. Burghardt, J. Paccou, A. Ghasem-Zadeh, R. Chapurlat, et al., Guidelines for the assessment of bone density and microarchitecture in vivo using high-resolution peripheral quantitative computed tomography, Osteoporos. Int. 31 (9) (Sep 2020) 1607–1627. Epub 2020/05/28.

[14] R. Zebaze, A. Ghasem-Zadeh, A. Mbala, E. Seeman, A new method of segmentation of compact-appearing, transitional and trabecular compartments and quantification of cortical porosity from high resolution peripheral quantitative computed tomographic images, Bone 54 (1) (May 2013) 8–20. Epub 2013/01/22.

[15] E.J. Samelson, K.E. Broe, H. Xu, L. Yang, S. Boyd, E. Biver, et al., Cortical and trabecular bone microarchitecture as an independent predictor of incident fracture risk in older women and men in the Bone Microarchitecture International Consortium (BoMIC): a prospective study, Lancet Diabetes Endocrinol. 7 (1) (Jan 2019) 34–43. Epub 2018/12/07.

[16] H.H. Malluche, D.S. Porter, D. Pienkowski, Evaluating bone quality in patients with chronic kidney disease, Nat. Rev. Nephrol. 9 (11) (2013) 671–680. Epub 2013/10/ 08.

[17] F. Huettner, M. Sunder, Axiomatic arguments for decomposing goodness of fit according to Shapley and Owen values, Electronic Journal of Statistics. 6 (none) (2012) 1239–1250, 12.

[18] J.A. Kanis, Assessment of fracture risk and its application to screening for postmenopausal osteoporosis: synopsis of a WHO report. WHO Study Group, Osteoporos Int. 4 (6) (Nov 1994) 368–381. Epub 1994/11/01.

Chapter 5

[19] K.J. Martin, E.A. Gonzalez, ´ Metabolic bone disease in chronic kidney disease, J. Am. Soc. Nephrol. 18 (3) (2007) 875–885.

[20] M. Parisien, F. Cosman, R.W. Mellish, M. Schnitzer, J. Nieves, S.J. Silverberg, et al., Bone structure in postmenopausal hyperparathyroid, osteoporotic, and normal women, J. Bone Miner. Res. 10 (9) (Sep 1995) 1393–1399. Epub 1995/09/01.

[21] R.M. Zebaze, A. Ghasem-Zadeh, A. Bohte, S. Iuliano-Burns, M. Mirams, R.I. Price, et al., Intracortical remodelling and porosity in the distal radius and post-mortem femurs of women: a cross-sectional study, Lancet 375 (9727) (2010) 1729–1736. Epub 2010/05/18.

[22] D.W. Dempster, M. Parisien, S.J. Silverberg, X.G. Liang, M. Schnitzer, V. Shen, et al., On the mechanism of cancellous bone preservation in postmenopausal women with mild primary hyperparathyroidism, J. Clin. Endocrinol. Metab. 84 (5) (May 1999) 1562–1566. Epub 1999/05/14.

[23] H. Dobnig, R.T. Turner, Evidence that intermittent treatment with parathyroid hormone increases bone formation in adult rats by activation of bone lining cells, Endocrinology 136 (8) (Aug 1995) 3632–3638. Epub 1995/08/01.

[24] M. Bui, A. Bjørnerem, A. Ghasem-Zadeh, G.S. Dite, J.L. Hopper, E. Seeman, Architecture of cortical bone determines in part its remodelling and structural decay, Bone 55 (2) (Aug 2013) 353–358. Epub 2013/05/07.

[25] E. Seeman, P.D. Delmas, Bone quality–the material and structural basis of bone strength and fragility, N. Engl. J. Med. 354 (21) (2006) 2250–2261. Epub 2006/ 05/26.

[26] B.M. Misof, S. Blouin, P. Roschger, J. Werzowa, K. Klaushofer, G. Lehmann, Bone matrix mineralization and osteocyte lacunae characteristics in patients with chronic kidney disease - mineral bone disorder (CKD-MBD), J. Musculoskelet. Neuronal Interact. 19 (2) (2019) 196–206.

[27] O. Akkus, A. Polyakova-Akkus, F. Adar, M.B. Schaffler, Aging of microstructural compartments in human compact bone, J. Bone Miner. Res. 18 (6) (Jun 2003) 1012–1019. Epub 2003/06/24.

[28] B.A. Julian, D.A. Laskow, J. Dubovsky, E.V. Dubovsky, J.J. Curtis, L.D. Quarles, Rapid loss of vertebral

mineral density after renal transplantation, N. Engl. J. Med. 325 (8) (1991) 544–550. Epub 1991/08/22.

[29] M.C. Monier-Faugere, H. Mawad, Q. Qi, R.M. Friedler, H.H. Malluche, High prevalence of low bone turnover and occurrence of osteomalacia after kidney

transplantation, J.Am.Soc.Nephrol. 11 (6) (Jun 2000) 1093–1099. Epub 2000/05/ 23.

[30] T.D. Vu, X.F. Wang, Q. Wang, N.E. Cusano, D. Irani, B.C. Silva, et al., New insights into the effects of primary hyperparathyroidism on the cortical and trabecular compartments of bone, Bone 55 (1) (Jul 2013) 57–63. Epub 2013/04/02.

[31] D. Cejka, J.M. Patsch, M. Weber, D. Diarra, M. Riegersperger, Z. Kikic, et al., Bone microarchitecture in hemodialysis patients assessed by HR-pQCT, Clin. J.Am.Soc. Nephrol. 6 (9) (Sep 2011) 2264–2271. Epub 2011/07/09.

[32] K.K. Nishiyama, Y. Pauchard, L.E. Nikkel, S. Iyer, C. Zhang, D.J. McMahon, et al., Longitudinal HR-pQCT and image registration detects endocortical bone loss in kidney transplantation patients, J. Bone Miner. Res. 30 (3) (Mar 2015) 554–561. Epub 2014/09/13.

[33] A. Trombetti, C. Stoermann, T. Chevalley, B. Van Rietbergen, F.R. Herrmann, P. Y. Martin, et al., Alterations of bone microstructure and strength in end-stage renal failure, Osteoporos. Int. 24 (5) (May 2013) 1721–1732. Epub 2012/10/27.

CHAPTER 6

Discussion and Conclusions

Chapter 6

Discussion

Longevity has led to an increase in the proportion of older adults in the community (1). Prolongation of life is accompanied by bone loss which compromises bone mass, bone microarchitecture and so, bone strength predisposing to fragility fractures and the accompanying increased morbidity, mortality, and costs to the community (2). Loss of bone mass compromises bone strength, but the deterioration of the microarchitecture has a profound independent effect on bone strength.

For example, compressive strength decreases as a 7^{th} and 3^{rd} power function of the increase in cortical porosity and decrease in trabecular density respectively. This power relationship increases bone fragility disproportionate to the deficits in bone mass produced by the bone loss (3). Bone loss in the cortical compartment increases cortical porosity, reduces cortical thickness, trabeculae thin, perforate, decrease in number and disconnect from each other and from the surrounding cortical shell.

During the last century, most methods used to capture the deterioration in bone mass and structure have focussed on the measurement of bone mass, not the architectural deterioration. Plain radiographs of the spine or hip were used to assess bone health (4). However, x-rays signal the presence of reduced bone mass only after 30% or more of the mass has been lost (5).

Several non-invasive imaging techniques have been developed including Radiographic Absorptiometry (RA) (6), Single Photon Absorptiometry (SPA) (7), Dual Photon Absorptiometry (DPA), Quantitative Computed Tomography (QCT), peripheral QCT (pQCT), Quantitative Ultrasound (QUS) and Quantitative Magnetic Resonance (QMR) (8). Dual-energy x-ray absorptiometry (DXA) is the most widely used technique. It provides a measure bone mineral density of the lumbar spine, proximal femur, and distal forearm. Since its introduction into clinical practice, the use of DXA, a non-invasive method, has accelerated the diagnosis and management of osteoporosis due to its ability to identify patients at

high risk of fracture and its ability to monitor changes in BMD in response to ageing, disease and drug therapy(5).

However, DXA has limitations as it measures bone mineral content not microarchitectural deterioration. DXA do not distinguish cortical and trabecular compartments because the technology acquired images are two dimensional 'areal' projections of a three-dimensional object. Additionally, BMD in the population is normally distributed and so over ~60% of persons in the community have osteopenia (T-score- 2.5 to -1.0 SD), ~10% have so-called 'normal' BMD (T-score > -1 SD) and ~30% have a BMD T-score ≤ - 2.5 SD below the young normal mean, the diagnostic threshold for 'osteoporosis' (9).

Due to this distribution, most patients who suffer fragility fractures have osteopenia or normal BMD, not osteoporosis defined as a BMD ≤ - 2.5 SD so that treatment is withheld because fracture risk is mistakenly perceived to be low given patients do not have osteoporosis. Even when a patient has a fracture, it is misinterpreted as being due to trauma rather than fragility, so treatment is still withheld because BMD is not in the 'osteoporosis' range (10).

The advent of High-Resolution peripheral Quantitative Computed Tomography (HR-pQCT) introduced a new approach to quantitative bone imaging. HR-pQCT provides *in-vivo* 3D images of cortical and trabecular bone of distal radius and tibia with high resolution (61-82 micrometre) combined with low radiation exposure and good precision (11-13). There are limitations using this technology (14). HR-pQCT imaging is confined to the distal radius and tibia. Consequently, this regional assessment of bone health may not reflect skeletal status of the spine or femoral neck, the site of fracture. However, these measurements do predict incident fractures with 70-80% sensitivity and specificity, superior to measurement of BMD or fracture risk assessment score (FRAX) (15)

I have conducted studies utilising HR-pQCT to investigate the effect of growth on the architecture of bone, spinal cord injury and chronic kidney disease.

Chapter 6

During studying cadaveric specimens of the distal radius, I found that adjacent cross sections varied in size, shape, and microstructure, yet each cross section was assembled using almost the same amount of bone matrix mass. Variation in size was achieved by varying intracortical and medullary void volumes, not bone matrix mass. Distally, the bone was assembled with a thin, porous cortex with a lower matrix mineral density and relatively more rod- or plate-like trabecular separated by 'inter-trabecular' void volume; features conferring lightness for mobility yet strength for load baring. More proximally, the constant mass was fashioned as a thicker cortex with low porosity and higher matrix mineral density, a small medullary canal containing little or no trabecular bone (14).

Because of abovementioned regional heterogeneity, when the effects of growth, advancing age, sex, race, or drug therapy are quantified using HR-pQCT, the region of interest (ROI) chosen to measure this morphology must be anatomically comparable, otherwise differences, or absence of differences in microstructure between these groups may be the result of positioning errors. Longer bones usually have a larger cross-sectional area, and wider long bones have higher porosity than more narrow long bones. Thus, in situations where forearm length is not available to accurately select the scanning ROI, I reported that adjustment of the fixed ROI by CSA or height corrects for positioning error and produces similar results for cortical porosity and trabecular density as found by correcting the position of the ROI. I found that failure to correct for positioning misrepresents fracture risk.

In the individuals with spinal cord injury, I found the greatest deficits in bone mass and abnormalities in microarchitecture of the cortical and trabecular vBMD were found at the distal tibia, a load baring bone while deficits in vBMD at the distal fibula were confined to trabecular bone and were less than the deficits at the distal tibia. The fibula is slender and largely cortical and is less loaded in comparison to tibia. Cortical bone has a lower surface area/matrix volume ratio than trabecular bone and so is less

susceptible to being remodelled than trabecular bone following unloading (16). Of particular importance, vBMD of the distal radius was not compromised despite them having tetraplegia (17).

These observations are consistent with the relative reduction in loading following spinal cord injury (18), with the tibia experiencing the greatest unloading, and the radius the least unloading. As the radius and fibula are subjected to lower strains than the tibia, paralysis may result in strains that deviate less from their customary strain environment than strains encountered at the tibia (16). Consequently, loss of trabecular bone at the fibula may have been sufficient to restore strains without the need to compromise cortical bone. At the radius, little or no bone loss occurs because this is a non-weight baring bone. The minimal effective strain in tetraplegia or weightlessness in space differs little from usual low strains imposed in daily life at these sites (17). I concluded that in the individuals with spinal cord injury, microarchitectural deterioration is heterogeneous because the strain thresholds regulating the cellular activity of mechano-transduction are region specific.

Increased fracture risk has been observed in patients with chronic kidney disease. Prolongation of life by drug therapy, dialysis and kidney transplantation is accompanied by secondary hyperparathyroidism and unbalanced bone remodelling (2). The unbalanced bone remodelling resulting bone loss compromises bone mass, microarchitecture and strength predisposing to increased risk of fragility fracture. However, BMD measurement using DXA method underestimate the bone fragility in patients with chronic kidney disease. Most of these patients do not have osteoporosis defined as a BMD $\leq$ - 2.5 SD (19). The BMD distribution is similar to the normal population and does not discriminate those at risk of fracture from those not at risk.

I hypothesised that patients with CKD at risk of fracture due to deterioration in microarchitecture irrespective of whether they have normal femoral neck (FN) BMD, osteopenia or osteoporosis. My findings show that deterioration in microarchitecture and estimated failure load was present in patients whether they had normal BMD, osteopenia or osteoporosis, and, whatever the BMD category, microarchitecture was more deteriorated than in controls.

In univariate analyses, microarchitecture and FN-BMD were both associated with estimated failure load. In multivariable analyses, microarchitecture was independently associated with estimated failure load and accounted for 87% of the variance. BMD was not independently associated with estimated failure load. These finding emphasis that bone fragility is likely to be present in patients with CKD despite them having osteopenia or normal BMD. Targeting and monitoring treatment based on the severity of microarchitectural deterioration may be an effective means of reducing fracture risk.

Conclusion

Bone regulates its spatial distribution making it strong for loading yet light for mobility, rigid for lever function yet flexible for energy absorption. These contradictory properties are achieved by bone modelling and remodelling. Bigger bones are assembled with relatively less mass and more void (higher porosity).

In individuals with spinal cord injury, microarchitectural deterioration is heterogeneous, partly because the strain thresholds regulating the cellular activity of mechano-transduction are region specific and its deterioration increases bone fragility as a power function, disproportionate to the bone loss causing it and often modest deficits in BMD.

In patients with chronic kidney disease microarchitectural deterioration accounts for >80% of the variance in bone strength, identifies persons needing prompt treatment and identifies treatment success or failure

Future directions

Bone exhibits a hierarchical structure that spans from the macrostructural level to the micro- nano- and pico-structural level. To understand the characteristics of bone at the different levels, the structure, organisation and mechanical properties of the underlying levels and their interactions need to be investigated. Achieving this requires the use of different imaging modalities.

Two major trends are appearing in the pursuit of defining the morphological basis of bone strength and the ability to identify persons at risk of fracture before the first fracture occurs. The first is the use of artificial intelligence to assess bone macro- and micro-structure and soft tissues such as muscle to predict risk of fragility fracture more precisely and more rapidly for clinical application. The second is the developing better methods to assess bone nano- and micro-structure within a relatively larger region of interest and with a reduced samples preparation process.

Artificial Intelligence

The rapidly evolving machine learning and deep learning technologies show promising results in automated bone macrostructure or bone mass assessment such as skeletal maturity on paediatric hand radiographs, determination of bone mineral density using chest computed tomography, and opportunistic osteoporosis screening. There is limited data to show the bone microstructure analysis using artificial intelligence (AI) predicts individuals at risk for a first incident fracture.

In the adult skeleton, osteocytes make up >90-95% of all bone cells, compared with 4-6% osteoblasts and 1-2% osteoclasts. Osteocytes are thought to function as a network of sensory cells mediating the effects of mechanical loading through an extensive lacuno-canalicular network and dendritic process that extends past to the bone surface and the bone marrow. In addition to responding to mechanical strain to send signals of bone resorption or formation, it has been shown that osteocytes regulate phosphate homoeostasis; therefore, the osteocyte network may also function as an endocrine gland.

There is evidence that osteocytes, as orchestrators of bone modelling and remodelling, have the ability to conduct and regulate both bone resorption and formation. Osteocytes (re)act exceptionally at the presence or lack of loading. They play major role in regulation of osteoclasts, by both inhibiting and activating of osteoclastic resorption. With loading, the osteocytes send signals inhibiting osteoclast activations. In contrast, deteriorated morphology, hypoxic, apoptotic or dying osteocytes, especially unloading, appear to send signals to osteoclast/preosteoclast on the bone surface to initiate resorption.

By advancing the three-dimensional and no-invasive imaging technologies, now the illustration and quantification of the osteocyte's morphology are feasible. Using synchrotron radiation with submicron resolution and phase-contrast imaging methods has brought the opportunity for quantification of osteocyte lacune morphology in animal and human subjects with minimal sample preparation. Our understanding of the pathophysiology of bone modelling and remodelling may be improved by studying and quantifying the osteocyte lacunes properties during ageing and other bone disorders. The data obtained through bone nano-structure quantification can be analysed using various computational methods to identify trends, patterns, and correlations in the structural properties of bone tissue. These analyses may include statistical analyses, machine learning, or modelling techniques, among others. Overall, quantification of bone micro- and nano-structure plays an important role in advancing our

understanding of bone strength achieved during growth and lost during advancing age and has implications for the development of new diagnostic and therapeutic approaches for prevention of bone loss or treatment osteoporosis.

References

1. Christensen K, Doblhammer G, Rau R, Vaupel JW. Ageing populations: the challenges ahead. Lancet. 2009;374(9696):1196-208.

2. Robertson L, Black C, Fluck N, Gordon S, Hollick R, Nguyen H, et al. Hip fracture incidence and mortality in chronic kidney disease: the GLOMMS-II record linkage cohort study. BMJ Open. 2018;8(4):e020312.

3. Schaffler MB, Burr DB. Stiffness of compact bone: effects of porosity and density. J Biomech. 1988;21(1):13-6.

4. Pocock NA. Quantitative diagnostic methods in osteoporosis: a review. Australas Radiol. 1998;42(4):327-34.

5. Genant HK, Engelke K, Fuerst T, Glüer CC, Grampp S, Harris ST, et al. Noninvasive assessment of bone mineral and structure: state of the art. J Bone Miner Res. 1996;11(6):707-30.

6. Morgan DB, Spiers FW, Pulvertaft CN, Fourman P. The amount of bone in the metacarpal and the phalanx according to age and sex. Clin Radiol. 1967;18(1):101-8.

7. Cameron JR, Sorenson J. MEASUREMENT OF BONE MINERAL IN VIVO: AN IMPROVED METHOD. Science. 1963;142(3589):230-2.

8. Davis CA, Genant HK, Dunham JS. The effects of bone on proton NMR relaxation times of surrounding liquids. Invest Radiol. 1986;21(6):472-7.

9. Siris ES, Chen YT, Abbott TA, Barrett-Connor E, Miller PD, Wehren LE, et al. Bone mineral density thresholds for pharmacological intervention to prevent fractures. Arch Intern Med. 2004;164(10):1108-12.

10. Leslie WD, Seeman E, Morin SN, Lix LM, Majumdar SR. The diagnostic threshold for osteoporosis impedes fracture prevention in women at high risk for fracture: A registry-based cohort study. Bone. 2018;114:298-303.

11. Boutroy S, Bouxsein ML, Munoz F, Delmas PD. In vivo assessment of trabecular bone microarchitecture by high-resolution peripheral quantitative computed tomography. J Clin Endocrinol Metab. 2005;90(12):6508-15.

12. Laib A, Häuselmann HJ, Rüegsegger P. In vivo high resolution 3D-QCT of the human forearm. Technology and Health Care. 1998;6:329-37.

13. Geusens P, Chapurlat R, Schett G, Ghasem-Zadeh A, Seeman E, de Jong J, et al. High-resolution in vivo imaging of bone and joints: a window to microarchitecture. Nat Rev Rheumatol. 2014;10(5):304-13.

14. Ghasem-Zadeh A, Burghardt A, Wang XF, Iuliano S, Bonaretti S, Bui M, et al. Quantifying sex, race, and age specific differences in bone microstructure requires measurement of anatomically equivalent regions. Bone. 2017;101:206-13.

15. Chapurlat R, Bui M, Sornay-Rendu E, Zebaze R, Delmas PD, Liew D, et al. Deterioration of Cortical and Trabecular Microstructure Identifies Women With Osteopenia or Normal Bone Mineral Density at Imminent and Long-Term Risk for Fragility Fracture: A Prospective Study. J Bone Miner Res. 2020;35(5):833-44.

16. Wang Q, Whittle M, Cunningham J, Kenwright J. Fibula and its ligaments in load transmission and ankle joint stability. Clin Orthop Relat Res. 1996(330):261-70.

17. Ghasem-Zadeh A, Galea MP, Nunn A, Panisset M, Wang XF, Iuliano S, et al. Heterogeneity in microstructural deterioration following spinal cord injury. Bone. 2021;142:115778.

18. Jiang SD, Jiang LS, Dai LY. Mechanisms of osteoporosis in spinal cord injury. Clin Endocrinol (Oxf). 2006;65(5):555-65.

19. Tariq MH, Sulaiman SA. Prevalence of osteopenia and osteoporosis among chronic kidney disease patients: a systematic review. The Open Urology & Nephrology Journal. 2020;13(1).

Bibliography

1. Heaney RP. Is there a role for bone quality in fragility fractures? Calcified tissue international. 1993;53 Suppl 1:S3-5; discussion S-6.

2. Cooper C. The epidemiology of fragility fractures: is there a role for bone quality? Calcified tissue international. 1993;53 Suppl 1:S23-6.

3. Walker-Bone K, Walter G, Cooper C. Recent developments in the epidemiology of osteoporosis. Curr Opin Rheumatol. 2002;14(4):411-5.

4. Friedman SM, Mendelson DA. Epidemiology of fragility fractures. Clinics in geriatric medicine. 2014;30(2):175-81.

5. Sanders JJWJA-OKM. Osteoporosis costing all Australians A new burden of disease analysis 2012 to 2022. 2018.

6. Burge R, Dawson-Hughes B, Solomon DH, Wong JB, King A, Tosteson A. Incidence and economic burden of osteoporosis-related fractures in the United States, 2005-2025. J Bone Miner Res. 2007;22(3):465-75.

7. Leboime A, Confavreux CB, Mehsen N, Paccou J, David C, Roux C. Osteoporosis and mortality. Joint Bone Spine. 2010;77 Suppl 2:S107-12.

8. Ip TP, Leung J, Kung AW. Management of osteoporosis in patients hospitalized for hip fractures. Osteoporos Int. 2010;21(Suppl 4):S605-14.

9. Cummings SR, Melton LJ. Epidemiology and outcomes of osteoporotic fractures. Lancet. 2002;359(9319):1761-7.

10. Cooper C, Atkinson EJ, O'Fallon WM, Melton LJ, 3rd. Incidence of clinically diagnosed vertebral fractures: a population-based study in Rochester, Minnesota, 1985-1989. J Bone Miner Res. 1992;7(2):221-7.

11. Black DM, Palermo L, Nevitt MC, Genant HK, Epstein R, San Valentin R, et al. Comparison of methods for defining prevalent vertebral deformities: the Study of Osteoporotic Fractures. J Bone Miner Res. 1995;10(6):890-902.

12. Eastell R, Cedel SL, Wahner HW, Riggs BL, Melton LJ, 3rd. Classification of vertebral fractures. J Bone Miner Res. 1991;6(3):207-15.

13. Lindsay R, Silverman SL, Cooper C, Hanley DA, Barton I, Broy SB, et al. Risk of new vertebral fracture in the year following a fracture. Jama. 2001;285(3):320-3.

14. Lunt M, O'Neill TW, Felsenberg D, Reeve J, Kanis JA, Cooper C, et al. Characteristics of a prevalent vertebral deformity predict subsequent vertebral fracture: results from the European Prospective Osteoporosis Study (EPOS). Bone. 2003;33(4):505-13.

15. Ross PD, Davis JW, Epstein RS, Wasnich RD. Pre-existing fractures and bone mass predict vertebral fracture incidence in women. Annals of internal medicine. 1991;114(11):919-23.

16. Ross PD, Genant HK, Davis JW, Miller PD, Wasnich RD. Predicting vertebral fracture incidence from prevalent fractures and bone density among non-black, osteoporotic women. Osteoporos Int. 1993;3(3):120-6.

17. European Prospective Osteoporosis Study G, Felsenberg D, Silman AJ, Lunt M, Armbrecht G, Ismail AA, et al. Incidence of vertebral fracture in europe: results from the European Prospective Osteoporosis Study (EPOS). J Bone Miner Res. 2002;17(4):716-24.

18. Lofman O, Berglund K, Larsson L, Toss G. Changes in hip fracture epidemiology: redistribution between ages, genders and fracture types. Osteoporos Int. 2002;13(1):18-25.

19. Gullberg B, Johnell O, Kanis JA. World-wide projections for hip fracture. Osteoporos Int. 1997;7(5):407-13.

20. Kanis JA, Oden A, McCloskey EV, Johansson H, Wahl DA, Cooper C, et al. A systematic review of hip fracture incidence and probability of fracture worldwide. Osteoporos Int. 2012;23(9):2239-56.

21. Cooper C, Melton LJ, 3rd. Epidemiology of osteoporosis. Trends Endocrinol Metab. 1992;3(6):224-9.

22. Sambrook P, Cooper C. Osteoporosis. Lancet. 2006;367(9527):2010-8.

23. Johnell O, Kanis JA. An estimate of the worldwide prevalence, mortality and disability associated with hip fracture. Osteoporos Int. 2004;15(11):897-902.

24. Johnell O, Kanis JA. An estimate of the worldwide prevalence and disability associated with osteoporotic fractures. Osteoporos Int. 2006;17(12):1726-33.

25. Kanis JA, Johnell O. The burden of osteoporosis. Journal of endocrinological investigation. 1999;22(8):583-8.

26. Singer A, Exuzides A, Spangler L, O'Malley C, Colby C, Johnston K, et al. Burden of illness for osteoporotic fractures compared with other serious diseases among postmenopausal women in the United States. Mayo Clinic proceedings. 2015;90(1):53-62.

27. Loefler A, Close J. Rising costs of hip fractures. Med J Aust. 2016;205(2):64-5.

28. Pike C, Birnbaum HG, Schiller M, Swallow E, Burge RT, Edgell ET. Economic burden of privately insured non-vertebral fracture patients with osteoporosis over a 2-year period in the US. Osteoporos Int. 2011;22(1):47-56.

29. van Staa TP, Dennison EM, Leufkens HG, Cooper C. Epidemiology of fractures in England and Wales. Bone. 2001;29(6):517-22.

30. Kanis JA, Johnell O, Oden A, Sembo I, Redlund-Johnell I, Dawson A, et al. Long-term risk of osteoporotic fracture in Malmo. Osteoporos Int. 2000;11(8):669-74.

31. Roux C, Wyman A, Hooven FH, Gehlbach SH, Adachi JD, Chapurlat RD, et al. Burden of non-hip, non-vertebral fractures on quality of life in postmenopausal women: the Global Longitudinal study of Osteoporosis in Women (GLOW). Osteoporos Int. 2012;23(12):2863-71.

32. Owen RA, Melton LJ, 3rd, Johnson KA, Ilstrup DM, Riggs BL. Incidence of Colles' fracture in a North American community. American journal of public health. 1982;72(6):605-7.

33. Nevitt MC, Cummings SR. Type of fall and risk of hip and wrist fractures: the study of osteoporotic fractures. Journal of the American Geriatrics Society. 1994;42(8):909.

34. Hampson G, Stone M, Lindsay JR, Crowley RK, Ralston SH. Diagnosis and Management of Osteoporosis During COVID-19: Systematic Review and Practical Guidance. Calcified tissue international. 2021;109(4):351-62.

35. Ogliari G, Lunt E, Ong T, Marshall L, Sahota O. The impact of lockdown during the COVID-19 pandemic on osteoporotic fragility fractures: an observational study. Arch Osteoporos. 2020;15(1):156.

36. Maniscalco P, Poggiali E, Quattrini F, Ciatti C, Magnacavallo A, Vercelli A, et al. Proximal femur fractures in COVID-19 emergency: the experience of two Orthopedics and Traumatology Departments in the first eight weeks of the Italian epidemic. Acta Biomed. 2020;91(2):89-96.

37. Malik-Tabassum K, Crooks M, Robertson A, To C, Maling L, Selmon G. Management of hip fractures during the COVID-19 pandemic at a high-volume hip fracture unit in the United Kingdom. J Orthop. 2020;20:332-7.

38. Arafa M, Nesar S, Abu-Jabeh H, Jayme MOR, Kalairajah Y. COVID-19 pandemic and hip fractures: impact and lessons learned. Bone Jt Open. 2020;1(9):530-40.

39. Williamson EJ, Walker AJ, Bhaskaran K, Bacon S, Bates C, Morton CE, et al. Factors associated with COVID-19-related death using OpenSAFELY. Nature. 2020;584(7821):430-6.

40. Clift AK, Coupland CAC, Keogh RH, Diaz-Ordaz K, Williamson E, Harrison EM, et al. Living risk prediction algorithm (QCOVID) for risk of hospital admission and mortality from coronavirus 19 in adults: national derivation and validation cohort study. Bmj. 2020;371:m3731.

41. di Filippo L, Formenti AM, Doga M, Pedone E, Rovere-Querini P, Giustina A. Radiological Thoracic Vertebral Fractures are Highly Prevalent in COVID-19 and Predict Disease Outcomes. J Clin Endocrinol Metab. 2021;106(2):e602-e14.

42. Genant HK, Jergas M, Palermo L, Nevitt M, Valentin RS, Black D, et al. Comparison of semiquantitative visual and quantitative morphometric assessment of prevalent and incident vertebral fractures in osteoporosis The Study of Osteoporotic Fractures Research Group. J Bone Miner Res. 1996;11(7):984-96.

43. Clement ND, Ng N, Simpson CJ, Patton RFL, Hall AJ, Simpson A, et al. The prevalence, mortality, and associated risk factors for developing COVID-19 in hip fracture patients: a systematic review and meta-analysis. Bone Joint Res. 2020;9(12):873-83.

44. Seeman E. Pathogenesis of bone fragility in women and men. Lancet. 2002;359(9320):1841-50.

45. Seeman E. Invited Review: Pathogenesis of osteoporosis. J Appl Physiol (1985). 2003;95(5):2142-51.

46. Johnson RW, McGregor NE, Brennan HJ, Crimeen-Irwin B, Poulton IJ, Martin TJ, et al. Glycoprotein130 (Gp130)/interleukin-6 (IL-6) signalling in osteoclasts promotes bone formation in periosteal and trabecular bone. Bone. 2015;81:343-51.

47. Robling AG, Turner CH. Mechanical signaling for bone modeling and remodeling. Crit Rev Eukaryot Gene Expr. 2009;19(4):319-38.

48. Wolff J. Das gesetz der transformation der knochen. A Hirshwald. 1892;1:1-152.
49. Frost HM. Bone "mass" and the "mechanostat": a proposal. The anatomical record. 1987;219(1):1-9.

50. Zebaze RM, Ghasem-Zadeh A, Bohte A, Iuliano-Burns S, Mirams M, Price RI, et al. Intracortical remodelling and porosity in the distal radius and post-mortem femurs of women: a cross-sectional study. Lancet. 2010;375(9727):1729-36.

51. Eriksen EF. Normal and pathological remodeling of human trabecular bone: three dimensional reconstruction of the remodeling sequence in normals and in metabolic bone disease. Endocr Rev. 1986;7(4):379-408.

52. Courpron P, Meunier P, Vignon G. [Dynamics of bone remodeling explained by Harold Frost. Theory of the B. M.U. (basic multicellular unit)]. La Nouvelle presse medicale. 1975;4(6):421-4.

53. Parfitt AM. The coupling of bone formation to bone resorption: a critical analysis of the concept and of its relevance to the pathogenesis of osteoporosis. Metabolic bone disease & related research. 1982;4(1):1-6.

54. Seeman E, Delmas PD. Bone quality--the material and structural basis of bone strength and fragility. The New England journal of medicine. 2006;354(21):2250-61.

55. In: Orwoll ES, Bilezikian JP, Vanderschueren D, editors. Osteoporosis in Men (Second Edition). San Diego: Academic Press; 2010. p. 733-41.

56. Delaisse JM. The reversal phase of the bone-remodeling cycle: cellular prerequisites for coupling resorption and formation. BoneKEy reports. 2014;3:561.

57. Ramchand SK, Seeman E. Reduced Bone Modeling and Unbalanced Bone Remodeling: Targets for Antiresorptive and Anabolic Therapy. In: Stern PH, editor. Bone Regulators and Osteoporosis Therapy. Cham: Springer International Publishing; 2020. p. 423-50.

58. Boivin G, Meunier PJ. Methodological considerations in measurement of bone mineral content. Osteoporos Int. 2003;14 Suppl 5:S22-7; discussion S7-8.

59. Boivin G, Farlay D, Bala Y, Doublier A, Meunier PJ, Delmas PD. Influence of remodeling on the mineralization of bone tissue. Osteoporos Int. 2009;20(6):1023-6.

60. Parfitt AM. The cellular basis of bone remodeling: the quantum concept reexamined in light of recent advances in the cell biology of bone. Calcif Tissue Int. 1984;36 Suppl 1:S37-45.

61. Parfitt AM. The mechanism of coupling: a role for the vasculature. Bone. 2000;26(4):319-23.
62. Eriksen EF. Cellular mechanisms of bone remodeling. Rev Endocr Metab Disord. 2010;11(4):219-27.

63. Seeman E. Age- and menopause-related bone loss compromise cortical and trabecular microstructure. J Gerontol A Biol Sci Med Sci. 2013;68(10):1218-25.

64. Foldes J, Parfitt AM, Shih MS, Rao DS, Kleerekoper M. Structural and geometric changes in iliac bone: relationship to normal aging and osteoporosis. Journal of bone and mineral research : the official journal of the American Society for Bone and Mineral Research. 1991;6(7):759-66.

65. Han ZH, Palnitkar S, Rao DS, Nelson D, Parfitt AM. Effects of ethnicity and age or menopause on the remodeling and turnover of iliac bone: implications for mechanisms of bone loss. Journal of bone

and mineral research : the official journal of the American Society for Bone and Mineral Research. 1997;12(4):498-508.

66. Parfitt AM. Misconceptions (2): turnover is always higher in cancellous than in cortical bone. Bone. 2002;30(6):807-9.

67. Parfitt AM. Targeted and nontargeted bone remodeling: relationship to basic multicellular unit origination and progression. Bone. 2002;30(1):5-7.

68. Gallagher JC, Riggs BL, DeLuca HF. Effect of estrogen on calcium absorption and serum vitamin D metabolites in postmenopausal osteoporosis. J Clin Endocrinol Metab. 1980;51(6):1359-64.

69. Ramchand SK, Seeman E, Wang XF, Ghasem-Zadeh A, Francis PA, Ponnusamy EJ, et al. Premenopausal women with early breast cancer treated with estradiol suppression have severely deteriorated bone microstructure. Bone. 2017;103:131-5.

70. Ng Tang Fui M, Hoermann R, Bracken K, Handelsman DJ, Inder WJ, Stuckey BGA, et al. Effect of Testosterone Treatment on Bone Microarchitecture and Bone Mineral Density in Men: A 2-Year RCT. J Clin Endocrinol Metab. 2021;106(8):e3143-e58.

71. Peel N. Disorders of bone metabolism. Surgery (Oxford). 2015;33(1):15-20.

72. Compston JE, Vedi S, Kaptoge S, Seeman E. Bone remodeling rate and remodeling balance are not co-regulated in adulthood: implications for the use of activation frequency as an index of remodeling rate. Journal of bone and mineral research : the official journal of the American Society for Bone and Mineral Research. 2007;22(7):1031-6.

73. Albright F, Smith PH, Richardson AMJJotAMA. Postmenopausal osteoporosis: its clinical features. 1941;116(22):2465-74.

74. Hughes DE, Dai A, Tiffee JC, Li HH, Mundy GR, Boyce BF. Estrogen promotes apoptosis of murine osteoclasts mediated by TGF-beta. Nature medicine. 1996;2(10):1132-6.

75. Bjørnerem Å, Ghasem-Zadeh A, Bui M, Wang X, Rantzau C, Nguyen TV, et al. Remodeling markers are associated with larger intracortical surface area but smaller trabecular surface area: a twin study. Bone. 2011;49(6):1125-30.

76. Clarke BL, Khosla S. Physiology of bone loss. Radiologic Clinics. 2010;48(3):483-95.

77. Vanderschueren D, Vandenput L, Boonen S, Lindberg MK, Bouillon R, Ohlsson C. Androgens and bone. Endocr Rev. 2004;25(3):389-425.

78. Hounsfield GN. Computerized transverse axial scanning (tomography). 1. Description of system. The British journal of radiology. 1973;46(552):1016-22.

79. Wehrli FW. Structural and functional assessment of trabecular and cortical bone by micro magnetic resonance imaging. Journal of magnetic resonance imaging : JMRI. 2007;25(2):390-409.

80. Whittier DE, Boyd SK, Burghardt AJ, Paccou J, Ghasem-Zadeh A, Chapurlat R, et al. Guidelines for the assessment of bone density and microarchitecture in vivo using high-resolution peripheral quantitative computed tomography. Osteoporos Int. 2020;31(9):1607-27.

81. Geusens P, Chapurlat R, Schett G, Ghasem-Zadeh A, Seeman E, de Jong J, et al. High-resolution in vivo imaging of bone and joints: a window to microarchitecture. Nature reviews Rheumatology. 2014;10(5):304-13.

82. Macdonald HM, Nishiyama KK, Kang J, Hanley DA, Boyd SK. Age-related patterns of trabecular and cortical bone loss differ between sexes and skeletal sites: a population-based HR-pQCT study. Journal of bone and mineral research : the official journal of the American Society for Bone and Mineral Research. 2011;26(1):50-62.

83. Burt LA, Liang Z, Sajobi TT, Hanley DA, Boyd SK. Sex- and Site-Specific Normative Data Curves for HR-pQCT. Journal of bone and mineral research : the official journal of the American Society for Bone and Mineral Research. 2016;31(11):2041-7.

84. Dalzell N, Kaptoge S, Morris N, Berthier A, Koller B, Braak L, et al. Bone micro-architecture and determinants of strength in the radius and tibia: age-related changes in a population-based study of normal adults measured with high-resolution pQCT. Osteoporos Int. 2009;20(10):1683-94.

85. Samelson EJ, Broe KE, Xu H, Yang L, Boyd S, Biver E, et al. Cortical and trabecular bone microarchitecture as an independent predictor of incident fracture risk in older women and men in the Bone Microarchitecture International Consortium (BoMIC): a prospective study. The lancet Diabetes & endocrinology. 2019;7(1):34-43.

86. Sornay-Rendu E, Boutroy S, Duboeuf F, Chapurlat RD. Bone Microarchitecture Assessed by HR-pQCT as Predictor of Fracture Risk in Postmenopausal Women: The OFELY Study. Journal of bone and mineral research : the official journal of the American Society for Bone and Mineral Research. 2017;32(6):1243-51.

87. Sampaio-Barros MM, Alvarenga JC, Takayama L, Assad APL, Sampaio-Barros PD, Pereira RMR. Distal radius and tibia bone microarchitecture impairment in female patients with diffuse systemic sclerosis. Osteoporos Int. 2019;30(8):1679-91.

88. Ghasem-Zadeh A, Galea MP, Nunn A, Panisset M, Wang XF, Iuliano S, et al. Heterogeneity in microstructural deterioration following spinal cord injury. Bone. 2021;142:115778.

89. Ramchand SK, Seeman E, Wang XF, Ghasem-Zadeh A, Francis PA, Ponnusamy EJ, et al. Premenopausal women with early breast cancer treated with estradiol suppression have severely deteriorated bone microstructure. Bone. 2017;103:131-5.

90. Bjørnerem Å, Ghasem-Zadeh A, Wang X, Bui M, Walker SP, Zebaze R, et al. Irreversible Deterioration of Cortical and Trabecular Microstructure Associated With Breastfeeding. Journal of bone and mineral research : the official journal of the American Society for Bone and Mineral Research. 2017;32(4):681-7.

91. Borschmann K, Iuliano S, Ghasem-Zadeh A, Churilov L, Pang MYC, Bernhardt J. Upright activity and higher motor function may preserve bone mineral density within 6 months of stroke: a longitudinal study. Archives of osteoporosis. 2018;13(1):5.

92. Tsai JN, Nishiyama KK, Lin D, Yuan A, Lee H, Bouxsein ML, et al. Effects of Denosumab and Teriparatide Transitions on Bone Microarchitecture and Estimated Strength: the DATA-Switch HR-pQCT study. Journal of bone and mineral research : the official journal of the American Society for Bone and Mineral Research. 2017;32(10):2001-9.

93. Gabel L, Macdonald HM, Nettlefold L, McKay HA. Physical Activity, Sedentary Time, and Bone Strength From Childhood to Early Adulthood: A Mixed Longitudinal HR-pQCT study. Journal of bone and mineral research : the official journal of the American Society for Bone and Mineral Research. 2017;32(7):1525-36.

94. Ghasem-Zadeh A, Burghardt A, Wang XF, Iuliano S, Bonaretti S, Bui M, et al. Quantifying sex, race, and age specific differences in bone microstructure requires measurement of anatomically equivalent regions. Bone. 2017;101:206-13.

95. Ghasem-Zadeh A, Seeman E. Challenges in the Use of Cross-Sectional Data to Quantify Growth and Deterioration of Bone Structure During Advancing Age. Journal of clinical densitometry : the official journal of the International Society for Clinical Densitometry. 2017;20(1):5-7.

96. Seeman E, Ghasem-Zadeh A. Challenges in the Acquisition and Analysis of Bone Microstructure During Growth. Journal of bone and mineral research : the official journal of the American Society for Bone and Mineral Research. 2016;31(12):2239-41.

97. Lips P, Courpron P, Meunier PJ. Mean wall thickness of trabecular bone packets in the human iliac crest: changes with age. Calcified tissue research. 1978;26(1):13-7.

98. Barrett JF, Keat N. Artifacts in CT: recognition and avoidance. Radiographics : a review publication of the Radiological Society of North America, Inc. 2004;24(6):1679-91.

99. Yu H, Wang G. Data Consistency Based Rigid Motion Artifact Reduction in Fan-Beam CT. IEEE Transactions on Medical Imaging. 2007;26(2):249-60.

100. Sode M, Burghardt AJ, Pialat JB, Link TM, Majumdar S. Quantitative characterization of subject motion in HR-pQCT images of the distal radius and tibia. Bone. 2011;48(6):1291-7.

101. Pauchard Y, Ayres FJ, Boyd SK, editors. Measuring patient motion in HR-pQCT. 2009 IEEE International Symposium on Biomedical Imaging: From Nano to Macro; 2009 28 June-1 July 2009.

102. Kyriakou Y, Prell D, Kalender WA. Ring artifact correction for high-resolution micro CT. Physics in Medicine & Biology. 2009;54(17):N385.

103. Tjong W, Kazakia GJ, Burghardt AJ, Majumdar S. The effect of voxel size on high-resolution peripheral computed tomography measurements of trabecular and cortical bone microstructure. Med Phys. 2012;39(4):1893-903.

104. MacNeil JA, Boyd SK. Accuracy of high-resolution peripheral quantitative computed tomography for measurement of bone quality. Med Eng Phys. 2007;29(10):1096-105.

105. Liu XS, Zhang XH, Sekhon KK, Adams MF, McMahon DJ, Bilezikian JP, et al. High-resolution peripheral quantitative computed tomography can assess microstructural and mechanical properties of human distal tibial bone. J Bone Miner Res. 2010;25(4):746-56.

106. Nishiyama KK, Macdonald HM, Buie HR, Hanley DA, Boyd SK. Postmenopausal women with osteopenia have higher cortical porosity and thinner cortices at the distal radius and tibia than women with normal aBMD: an in vivo HR-pQCT study. J Bone Miner Res. 2010;25(4):882-90.

107. Liu XS, Shane E, McMahon DJ, Guo XE. Individual trabecula segmentation (ITS)-based morphological analysis of microscale images of human tibial trabecular bone at limited spatial resolution. J Bone Miner Res. 2011;26(9):2184-93.

108. Engelke K, Stampa B, Timm W, Dardzinski B, de Papp AE, Genant HK, et al. Short-term in vivo precision of BMD and parameters of trabecular architecture at the distal forearm and tibia. Osteoporos Int. 2012;23(8):2151-8.

109. Pialat JB, Burghardt AJ, Sode M, Link TM, Majumdar S. Visual grading of motion induced image degradation in high resolution peripheral computed tomography: impact of image quality on measures of bone density and micro-architecture. Bone. 2012;50(1):111-8.

110. Kawalilak CE, Johnston JD, Cooper DM, Olszynski WP, Kontulainen SA. Role of endocortical contouring methods on precision of HR-pQCT-derived cortical micro-architecture in postmenopausal women and young adults. Osteoporos Int. 2016;27(2):789-96.

111. de Waard EAC, Sarodnik C, Pennings A, de Jong JJA, Savelberg H, van Geel TA, et al. Reliability of HR-pQCT Derived Cortical Bone Structural Parameters When Using Uncorrected Instead of Corrected Automatically Generated Endocortical Contours in a Cross-Sectional Study: The Maastricht Study. Calcif Tissue Int. 2018;103(3):252-65.

112. Chiba K, Okazaki N, Kurogi A, Isobe Y, Yonekura A, Tomita M, et al. Precision of Second-Generation High-Resolution Peripheral Quantitative Computed Tomography: Intra- and Intertester Reproducibilities and Factors Involved in the Reproducibility of Cortical Porosity. J Clin Densitom. 2018;21(2):295-302.

113. Ellouz R, Chapurlat R, van Rietbergen B, Christen P, Pialat JB, Boutroy S. Challenges in longitudinal measurements with HR-pQCT: evaluation of a 3D registration method to improve bone microarchitecture and strength measurement reproducibility. Bone. 2014;63:147-57.

114. MacNeil JA, Boyd SK. Improved reproducibility of high-resolution peripheral quantitative computed tomography for measurement of bone quality. Med Eng Phys. 2008;30(6):792-9.

115. Boutroy S, Bouxsein ML, Munoz F, Delmas PD. In vivo assessment of trabecular bone microarchitecture by high-resolution peripheral quantitative computed tomography. J Clin Endocrinol Metab. 2005;90(12):6508-15.

116. Burghardt AJ, Buie HR, Laib A, Majumdar S, Boyd SK. Reproducibility of direct quantitative measures of cortical bone microarchitecture of the distal radius and tibia by HR-pQCT. Bone. 2010;47(3):519-28.

117. Duan X, Wang J, Leng S, Schmidt B, Allmendinger T, Grant K, et al. Electronic noise in CT detectors: Impact on image noise and artifacts. AJR Am J Roentgenol. 2013;201(4):W626-32.

118. Kawalilak CE, Johnston JD, Olszynski WP, Leswick DA, Kontulainen SA. Comparison of short-term in vivo precision of bone density and microarchitecture at the distal radius and tibia between postmenopausal women and young adults. J Clin Densitom. 2014;17(4):510-7.

119. Kazakia GJ, Burghardt AJ, Link TM, Majumdar S. Variations in morphological and biomechanical indices at the distal radius in subjects with identical BMD. J Biomech. 2011;44(2):257-66.

120. Laib A, Häuselmann HJ, Rüegsegger P. In vivo high resolution 3D-QCT of the human forearm. Technol Health Care. 1998;6(5-6):329-37.

121. Laib A, Hildebrand T, Häuselmann HJ, Rüegsegger P. Ridge number density: a new parameter for in vivo bone structure analysis. Bone. 1997;21(6):541-6.

122. Laib A, Rüegsegger P. Calibration of trabecular bone structure measurements of in vivo three-dimensional peripheral quantitative computed tomography with 28-microm-resolution microcomputed tomography. Bone. 1999;24(1):35-9.

123. Whittier DE, Boyd SK, Burghardt AJ, Paccou J, Ghasem-Zadeh A, Chapurlat R, et al. Guidelines for the assessment of bone density and microarchitecture in vivo using high-resolution peripheral quantitative computed tomography. Osteoporos Int. 2020;31(9):1607-27.

124. Kawalilak CE, Johnston JD, Olszynski WP, Kontulainen SA. Least significant changes and monitoring time intervals for high-resolution pQCT-derived bone outcomes in postmenopausal women. J Musculoskelet Neuronal Interact. 2015;15(2):190-6.

125. Glüer CC, Blake G, Lu Y, Blunt BA, Jergas M, Genant HK. Accurate assessment of precision errors: how to measure the reproducibility of bone densitometry techniques. Osteoporos Int. 1995;5(4):262-70.

126. Imai K. Computed tomography-based finite element analysis to assess fracture risk and osteoporosis treatment. World J Exp Med. 2015;5(3):182-7.

127. Reddy JN. Introduction to the Finite Element Method. 2nd, editor: McGraw Hill; 1993.

128. Ulrich D, van Rietbergen B, Weinans H, Rüegsegger P. Finite element analysis of trabecular bone structure: a comparison of image-based meshing techniques. Journal of Biomechanics. 1998;31(12):1187-92.

129. Engelke K, van Rietbergen B, Zysset P. FEA to Measure Bone Strength: A Review. Clinical Reviews in Bone and Mineral Metabolism. 2016;14(1):26-37.

130. Martin RB, Ishida J. The relative effects of collagen fiber orientation, porosity, density, and mineralization on bone strength. J Biomech. 1989;22(5):419-26.

131. Fonseca H, Moreira-Gonçalves D, Coriolano HJ, Duarte JA. Bone quality: the determinants of bone strength and fragility. Sports Med. 2014;44(1):37-53.

132. Hart NH, Nimphius S, Rantalainen T, Ireland A, Siafarikas A, Newton RU. Mechanical basis of bone strength: influence of bone material, bone structure and muscle action. J Musculoskelet Neuronal Interact. 2017;17(3):114-39.

133. Boyd SK. Advanced Imaging in Biology and Medicine2009. 447 p.

134. Viguet-Carrin S, Garnero P, Delmas PD. The role of collagen in bone strength. Osteoporosis International. 2006;17(3):319-36.

135. Whittier DE, Manske SL, Kiel DP, Bouxsein M, Boyd SK. Harmonizing finite element modelling for non-invasive strength estimation by high-resolution peripheral quantitative computed tomography. J Biomech. 2018;80:63-71.

136. Macneil JA, Boyd SK. Bone strength at the distal radius can be estimated from high-resolution peripheral quantitative computed tomography and the finite element method. Bone. 2008;42(6):1203-13.

137. Pistoia W, van Rietbergen B, Lochmüller EM, Lill CA, Eckstein F, Rüegsegger P. Estimation of distal radius failure load with micro-finite element analysis models based on three-dimensional peripheral quantitative computed tomography images. Bone. 2002;30(6):842-8.

138. Varga P, Dall'Ara E, Pahr DH, Pretterklieber M, Zysset PK. Validation of an HR-pQCT-based homogenized finite element approach using mechanical testing of ultra-distal radius sections. Biomech Model Mechanobiol. 2011;10(4):431-44.

139. Zysk AM, Lewis G, Taxier D, Rose J. Biomechanical Comparison of Prototype of a Novel Intramedullary Injectable Bioresorbable Polymer-Bioresorbable Balloon Osteosynthesis and a Volar Locking Plate for Treatment of Distal Radius Fractures. World Journal of Engineering and Technology. 2017;05:309-23.

140. Boutroy S, Van Rietbergen B, Sornay-Rendu E, Munoz F, Bouxsein ML, Delmas PD. Finite element analysis based on in vivo HR-pQCT images of the distal radius is associated with wrist fracture

in postmenopausal women. Journal of bone and mineral research : the official journal of the American Society for Bone and Mineral Research. 2008;23(3):392-9.

141. Miura M, Nakamura J, Matsuura Y, Wako Y, Suzuki T, Hagiwara S, et al. Prediction of fracture load and stiffness of the proximal femur by CT-based specimen specific finite element analysis: cadaveric validation study. BMC Musculoskelet Disord. 2017;18(1):536-.

142. Zebaze R, Ghasem-Zadeh A, Mbala A, Seeman E. A new method of segmentation of compact-appearing, transitional and trabecular compartments and quantification of cortical porosity from high resolution peripheral quantitative computed tomographic images. Bone. 2013;54(1):8-20.

143. Nazarian A, Müller R. Time-lapsed microstructural imaging of bone failure behavior. J Biomech. 2004;37(1):55-65.

144. Levchuk A, Schneider P, Meier M, Vogel P, Donaldson F, Müller R. An Automated Step-Wise Micro-Compression Device for 3D Dynamic Image-Guided Failure Assessment of Bone Tissue on a Microstructural Level Using Time-Lapsed Tomography. Frontiers in Materials. 2018;5.

145. Ghasem-Zadeh A, Galea MP, Nunn A, Panisset M, Wang XF, Iuliano S, et al. Heterogeneity in microstructural deterioration following spinal cord injury. Bone. 2021;142:115778.

146. Ghasem-Zadeh A, Bui M, Seeman E, Boyd SK, Iuliano S, Jaipurwala R, et al. Bone microarchitecture and estimated failure load are deteriorated whether patients with chronic kidney disease have normal bone mineral density, osteopenia or osteoporosis. Bone. 2022;154:116260.

147. Zysset PK, Dall'ara E, Varga P, Pahr DH. Finite element analysis for prediction of bone strength. Bonekey Rep. 2013;2:386.

148. Taylor WR, Roland E, Ploeg H, Hertig D, Klabunde R, Warner MD, et al. Determination of orthotropic bone elastic constants using FEA and modal analysis. J Biomech. 2002;35(6):767-73.

149. Zysset P, Qin L, Lang T, Khosla S, Leslie WD, Shepherd JA, et al. Clinical Use of Quantitative Computed Tomography-Based Finite Element Analysis of the Hip and Spine in the Management of Osteoporosis in Adults: the 2015 ISCD Official Positions-Part II. J Clin Densitom. 2015;18(3):359-92.

150. van Rietbergen B, Ito K. A survey of micro-finite element analysis for clinical assessment of bone strength: the first decade. J Biomech. 2015;48(5):832-41.

151. Gabel L, Macdonald HM, McKay HA. Sex differences and growth-related adaptations in bone microarchitecture, geometry, density and strength from childhood to early adulthood: a mixed longitudinal HR-pQCT Study. J Bone Miner Res. 20XX; XX(XX): XXXX–XXXX. DOI:10.1002/jbmr.2982.

152. Burrows M, Liu D, Perdios A, Moore S, Mulpuri K, McKay H. Assessing bone microstructure at the distal radius in children and adolescents using HR-pQCT: a methodological pilot study. J Clin Densitom.2010;13(4):451–5.

153. Cheuk KY, Tam EM, Yu FW, et al. A critical comparison between two scanning protocols of high-resolution peripheral quantitative computed tomography at the distal radius in adolescents. J Clin Densitom. 2016;19(3):305–15.

154. Ghasem-Zadeh A, Wang XF, Zebaze R, Seeman E. Sexual and racial dimorphism in bone microarchitecture requires adjustment of the region of interest for skeleton dimensions. J Bone Miner Res. 2016;31Suppl 1. [Poster session presented at: Annual Meeting American Society for Bone and

Mineral Research (ASBMR); 2016 Sep 16–19; Atlanta, GA, USA; Presentation Number: SU0213]. Available from:http://www.asbmr.org/education/AbstractDetail?aid=86f1146f-e94e-47b9-9875-d52e78cb154e

155. Pritchett JW. Growth plate activity in the upper extremity. Clin Orthop Relat Res. 1991;268:235–42.

156. Pritchett JW. Longitudinal growth and growth-plate activity in the lower extremity. Clin Orthop Relat Res. 1992;275:274–9.

157. Ghasem-Zadeh A, Burghardt A, Zendeli A, et al. Assessing age, sex, and racial differences in cortical porosity requires adjustment for site-specific variation in the selected region of interest site variation. J Bone Miner Res. 2014; 29 Suppl 1. [Poster session presented at: Annual Meeting American Society for Bone and Mineral Research (ASBMR); 2014 Se p 12–15; Houston, TX, USA; Presentation Number:SA0297]. Available from: http://www.asbmr.org/education/AbstractDetail?aid=974d22e0-fbac-4ebf-849c-353d6e60ab36

158. Bradney M, Karlsson MK, Duan Y, Stuckey S, Bass S, Seeman E. Heterogeneity in the growth of the axial and appendicular skeleton in boys: implications for the pathogenesis of bone fragility in men. J Bone Miner Res. 2000;15(10):1871–8.

159. Leung SS, Lau JT, Xu YY, et al. Secular changes in standing height, sitting height and sexual maturation of Chinese—the Hong Kong Growth Study, 1993. Ann Hum Biol. 1996; 23 (4): 297–306.10. Parfitt AM. The two faces of growth: benefits and risks to bone integrity. Osteoporos Int. 1994;4(6):382–98

160. Parfitt AM. The two faces of growth: benefits and risks to bone integrity. Osteoporos Int. 1994;4(6):382–98.

161. Wang XF, Duan Y, Seeman E. Similar trunk length but shorter leg length in Chinese than Caucasians: implications for racial differences in hip fracture rates. J Bone Miner Res. 2004;19 Suppl 1

162. Iuliano-Burns S, Hopper J, Seeman E. The age of puberty determines sexual dimorphism in bone structure: a male/female co-twin control study. J Clin Endocrinol Metab. 2009;94(5):1638–43.

163. Iuliano-Burns S, Mirwald RL, Bailey DA. Timing and magnitude of peak height velocity and peak tissue velocities for early, average, and late maturing boys and girls. Am J Hum Biol. 2001;13(1):1–8.

164. Boutroy S, Walker MD, Liu XS, et al. Lower cortical porosity and higher tissue mineral density in Chinese American versus white women. J Bone Miner Res. 2014;29(3):551–61.

165. Zebaze RM, Ghasem-Zadeh A, Bohte A, et al. Intracortical remodelling and porosity in the distal radius and post-mortem femurs of women: a cross-sectional study. Lancet. 2010 15;375(9727): 1729–36.

166. Zebaze R, Ghasem-Zadeh A, Mbala A, Seeman E. A new method of segmentation of compact-appearing, transitional and trabecular compartments and quantification of cortical porosity from high resolution peripheral quantitative computed tomographic images. Bone. 2013;54(1):8–20.

167. Cadet ER, Gafni RI, McCarthy EF, et al. Mechanisms responsible for longitudinal growth of the cortex: coalescence of trabecular bone into cortical bone. J Bone Joint Surg Am. 2003; 85-A (9):1739–48.

168. Bala Y, Bui QM, Wang XF, et al. Trabecular and cortical microstructure and fragility of the distal radius in women. J Bone Miner Res.2015;30(4):621–9.19. Seeman E, Martin TJ. Co-administration of antiresorptive and anabolic agents: a missed opportunity. J Bone Miner Res. 2015;30(5):753–64. Journal of Bone and Mineral Research2241

169. Lindgren E., Karlsson M.K., Lorentzon M., Rosengren B.E.: Bone traits seem to develop also during the third decade in life-normative cross-sectional data on 1083 men aged 18–28 years. J Clin Densitom 2016; (in this issue)

170. Gilsanz V., Skaggs D.L., Kovanlikaya A., et. al.: Differential effect of race on the axial and appendicular skeletons of children. J Clin Endocrinol Metab 1998; 83: pp. 1420-1427.

171. Bonjour J.P., Theintz G., Law F., et. al.: Peak bone mass. Osteoporos Int 1994; 4: pp. 7-13.

172. Seeman E.: From density to structure: growing up and growing old on the surfaces of bone. J Bone Miner Res 1997; 12: pp. 509-521.

173. Bradney M., Karlsson M.K., Duan Y., et. al.: Heterogeneity in the growth of the axial and appendicular skeleton in boys: implications for the pathogenesis of bone fragility in men. J Bone Miner Res 2000; 15: pp. 1871-1878.

174. Karlberg J.: The infancy-childhood growth spurt. Acta Paediatr Scand Suppl 1990; 367: pp. 111-118.

175. Seeman E.: Growth in bone mass and size—are racial and gender differences in bone mineral density more apparent than real? J Clin Endocrinol Metab 1998; 83: pp. 1414-1419.

176. Bakwin H., McLaughlin S.M.: Secular increase in height is the end in sight? Lancet 1964; 2: pp. 1195-1196.

177. Meredith H.V.: Secular change in sitting height and lower limb height of children, youths, and young adults of Afro-black, European, and Japanese ancestry. Growth 1978; 42: pp. 37-41.

178. Hauspie R.C., Vercauteren M., Susanne C.: Secular changes in growth and maturation: an update. Acta Paediatr 1997; 423: pp. 20-27.

179. Danubio M.E., Sanna E.: Secular changes in human biological variables in Western countries: an updated review and synthesis. J Anthropol Sci 2008; 86: pp. 91-112.

180. Malina R.M., Brown K.H., Zavaleta A.N.: Relative lower extremity length in Mexican American and in American black and white youth. Am J Phys Anthropol 1987; 72: pp. 89-94.

181. Hamill P.V., Johnston F.E., Lemeshow S.: Height and weight of youths 12–17 years. United States. Vital Health Stat 11 1973; pp. 1-81.

182. Ruff C.B., Hayes W.C.: Sex differences in age-related remodeling of the femur and tibia. J Orthop Res 1988; 6: pp. 886-896.

183. Zebaze R.M., Ghasem-Zadeh A., Bohte A., et. al.: Intracortical remodelling and porosity in the distal radius and post-mortem femurs of women: a cross-sectional study. Lancet 2010; 375: pp. 1729-1736.

184. Zebaze R., Ghasem-Zadeh A., Mbala A., Seeman E.: A new method of segmentation of compact-appearing, transitional and trabecular compartments and quantification of cortical porosity from high resolution peripheral quantitative computed tomographic images. Bone 2013; 54: pp. 8-20.

185. Cadet E.R., Gafni R.I., McCarthy E.F., et. al.: Mechanisms responsible for longitudinal growth of the cortex: coalescence of trabecular bone into cortical bone. J Bone Joint Surg 2003; 85-A: pp. 1739-1748.

186. Bala Y., Bui Q.M., Wang X.F., et. al.: Trabecular and cortical microstructure and fragility of the distal radius in women. J Bone Miner Res 2015; 30: pp. 621-629.

187. Wang Q., Ghasem-Zadeh A., Wang X.F., et. al.: Trabecular bone of growth plate origin influences both trabecular and cortical morphology in adulthood. J Bone Miner Res 2011; 26: pp. 1577-1583.

188. Zebaze R.M., Jones A., Welsh F., et. al.: Femoral neck shape and the spatial distribution of its mineral mass varies with its size: clinical and biomechanical implications. Bone 2005; 37: pp. 243-252.

189. Bjornerem A., Bui Q.M., Ghasem-Zadeh A., et. al.: Fracture risk and height: an association partly accounted for by cortical porosity of relatively thinner cortices. J Bone Miner Res 2013; 28: pp. 2017-2026.

190. Boutroy S., Walker M.D., Liu X.S., et. al.: Lower cortical porosity and higher tissue mineral density in Chinese American versus white women. J Bone Miner Res 2014; 29: pp. 551-561.

191. Wang Q., Wang X.F., Iuliano-Burns S., et. al.: Rapid growth produces transient cortical weakness: a risk factor for metaphyseal fractures during puberty. J Bone Miner Res 2010; 25: pp. 1521-1526.

192. J.D. Currey, Bones: Structure and Mechanics, Princeton University Press, Princeton, NJ, 2002 1–380.

193. E. Seeman, Growth in bone mass and size—are racial and gender differences in bone mineral density more apparent than real? J. Clin. Endocrinol. Metab. 83 (5) (1998 May) 1414–1419.

194. Q. Wang, S. Cheng, M. Alen, E. Seeman, Finnish Calex Study G, Bone's structural diver- sity in adult females is established before puberty, J. Clin. Endocrinol. Metab. 94 (5) (2009 May) 1555–1561.

195. R.M. Zebaze, A. Jones, F. Welsh, M. Knackstedt, E. Seeman, Femoral neck shape and the spatial distribution of its mineral mass varies with its size: clinical and biomechanical implications, Bone 37 (2) (2005 Aug) 243–252.

196. R.M. Zebaze, A. Jones, M. Knackstedt, G. Maalouf, E. Seeman, Construction of the fem- oral neck during growth determines its strength in old age, J. Bone Miner. Res. 22 (7) (2007 Jul) 1055–1061.

197. Q. Wang, S. Cheng, M. Alen, E. Seeman, Finnish Calex Study G, Bone's structural diver- sity in adult females is established before puberty, J. Clin. Endocrinol. Metab. 94 (5) (2009 May) 1555–1561.

198. G. Mall, M. Hubig, A. Buttner, J. Kuznik, R. Penning, M. Graw, Sex determination and estimation of stature from the long bones of the arm, Forensic Sci. Int. 117 (1–2) (2001 Mar 01) 23–30.

199. X.F. Wang, Y. Duan, T.J. Beck, E. Seeman, Varying contributions of growth and ageing to racial and sex differences in femoral neck structure and strength in old age, Bone 36 (6) (2005 Jun) 978–986.

200. S.K. Boyd, Site-specific variation of bone micro-architecture in the distal radius and tibia, J. Clin. Densitom. 11 (3) (2008 Jul–Sep) 424–430.

201. S. Bonaretti, N. Vilayphiou, C.M. Chan, A. Yu, K. Nishiyama, D. Liu, et al., Operator variability in scan positioning is a major component of HR-pQCT precision error and is reduced by standardized training, Osteoporos. Int. (2016 Jul 30).

202. K.Y. Cheuk, E.M. Tam, F.W. Yu, B.H. Yip, V.W. Hung, X. Wang, et al., A critical comparison between two scanning protocols of high-resolution peripheral quantitative com- puted tomography at the distal radius in adolescents, J. Clin. Densitom. 19 (3) (2016 Jul–Sep) 305–315.

203. V.V. Shanbhogue, S. Hansen, U. Halekoh, K. Brixen, Use of relative vs fixed offset distance to define region of interest at the distal radius and tibia in high-resolution peripheral quantitative computed tomography, J. Clin. Densitom. 18 (2) (2015 Apr–Jun) 217–225.

204. B.L. Riggs, L.J. Melton, R.A. Robb, J.J. Camp, E.J. Atkinson, L. McDaniel, et al., A population-based assessment of rates of bone loss at multiple skeletal sites: evidence for substantial trabecular bone loss in young adult women and men, J. Bone Miner. Res. 23 (2) (2008 Feb) 205–214.

205. R.C. Hauspie, M. Vercauteren, C. Susanne, Secular changes in growth and maturation: an update, Acta Paediatr. 423 (1997 Nov) 20–27.

206. A. Bjornerem, Q.M. Bui, A. Ghasem-Zadeh, J.L. Hopper, R. Zebaze, E. Seeman, Fracture risk and height: an association partly accounted for by cortical porosity of relatively thinner cortices, J. Bone Miner. Res. 28 (9) (2013 Sep) 2017–2026.

207. X.F. Wang, Q. Wang, A. Ghasem-Zadeh, A. Evans, C. McLeod, S. Iuliano-Burns, et al., Differences in macro- and microarchitecture of the appendicular skeleton in young Chinese and white women, J. Bone Miner. Res. 24 (12) (2009 Dec) 1946–1952.

208. R. Zebaze, A. Ghasem-Zadeh, A. Mbala, E. Seeman, A new method of segmentation of compact-appearing, transitional and trabecular compartments and quantification of cortical porosity from high resolution peripheral quantitative computed tomographic images, Bone 54 (1) (2013 May) 8–20.

209. L. Vico, M. Zouch, A. Amirouche, D. Frere, N. Laroche, B. Koller, et al., High-resolution pQCT analysis at the distal radius and tibia discriminates patients with recent wrist and femoral neck fractures, J. Bone Miner. Res. 23 (11) (2008 Nov) 1741–1750.

210. E. Seeman, P.D. Delmas, Bone quality—the material and structural basis of bone strength and fragility, N. Engl. J. Med. 354 (21) (2006 May 25) 2250–2261.

211. Y. Bala, Q.M. Bui, X.F. Wang, S. Iuliano, Q. Wang, A. Ghasem-Zadeh, et al., Trabecular and cortical microstructure and fragility of the distal radius in women, J. Bone Miner. Res. 30 (4) (2015 Apr) 621–629.

212. R.M. Zebaze, A. Jones, M. Knackstedt, G. Maalouf, E. Seeman, Construction of the fem- oral neck during growth determines its strength in old age, J. Bone Miner. Res. 22 (7) (2007 Jul) 1055–1061.

222. K. Engelke, J.E. Adams, G. Armbrecht, P. Augat, C.E. Bogado, M.L. Bouxsin, et al., Clinical use of quantitative computed tomography and peripheral quantitative computed to- mography in the management of osteoporosis in adults: the 2007 ISCD official positions, J. Clin. Densitometry 11 (1) (Jan–Mar 2008) 123–162.

223. P. Augat, T. Fuerst, H.K. Genant, Quantitative bone mineral assessment at the forearm: a review, Osteoporos. Int. 8 (4) (1998) 299–310.

224. S. Epstein, J. Poser, R. McClintock, C.C. Johnston Jr., G. Bryce, S. Hui, Differences in serum bone GLA protein with age and sex, Lancet 1 (8372) (Feb 11 1984) 307–310.

225. J.S. Finkelstein, M. Sowers, G.A. Greendale, M.L. Lee, R.M. Neer, J.A. Cauley, et al., Ethnic variation in bone turnover in pre- and early perimenopausal women: effects of an- thropometric and lifestyle factors, J. Clin. Endocrinol. Metab. 87 (7) (Jul 2002) 3051–3056.

226. X.F. Wang, Y. Duan, T.J. Beck, E. Seeman, Varying contributions of growth and ageing to racial and sex differences in femoral neck structure and strength in old age, Bone 36 (6) (2005) 978–986.

227. A.S. Parent, G. Teilmann, A. Juul, N.E. Skakkebaek, J. Toppari, J.P. Bourguignon, The timing of normal puberty and the age limits of sexual precocity: variations around the world, secular trends, and changes after migration, Endocr. Rev. 24 (5) (Oct 2003) 668–693.

228. K.F. Huen, S.S. Leung, J.T. Lau, A.Y. Cheung, N.K. Leung, M.C. Chiu, Secular trend in the sexual maturation of southern Chinese girls, Acta Paediatr. 86 (10) (Oct 1997) 1121–1124.

229. D.S. Freedman, L.K. Khan, M.K. Serdula, W.H. Dietz, S.R. Srinivasan, G.S. Berenson, Relation of age at menarche to race, time period, and anthropometric dimensions: the Bogalusa Heart Study, Pediatrics 110 (4) (Oct 2002), e43.

230. Y. Bala, R. Zebaze, A. Ghasem-Zadeh, E.J. Atkinson, S. Iuliano, J.M. Peterson, et al., Cortical porosity identifies women with osteopenia at increased risk for forearm fractures, J. Bone Miner. Res. 29 (6) (2014 Jun) 1356–1362.

231. J.D. Currey, The Mechanical Adaptations of Bones viii, Princeton University Press,Princeton, N.J, 1984 (294 pp.)

232. H.M. Frost, Bone “mass” and the “mechanostat”: a proposal, Anat. Rec. 219 (1) (Sep 1987) 1–9 (Epub 1987/09/01).

233. R.M. Zebaze, A. Jones, F. Welsh, M. Knackstedt, E. Seeman, Femoral neck shape and the spatial distribution of its mineral mass varies with its size: clinical and biomechanical implications, Bone. 37 (2) (Aug 2005) 243–252 (Epub 2005/06/09).

234. A. Ghasem-Zadeh, A. Burghardt, X.F. Wang, S. Iuliano, S. Bonaretti, M. Bui, et al., Quantifying sex, race, and age specific differences in bone microstructure requires measurement of anatomically equivalent regions, Bone. 101 (Aug 2017) 206–213 (Epub 2017/05/16).

235. M.R. Forwood, Mechanical effects on the skeleton: are there clinical implications? Osteoporos. Int. 12 (1) (2001) 77–83 (Epub 2001/04/18).

236. C.B. Ruff, E. Trinkaus, A. Walker, C.S. Larsen, Postcranial robusticity in Homo. I: temporal trends and mechanical interpretation, Am. J. Phys. Anthropol. 91 (1) (May 1993) 21–53 (Epub 1993/05/01).

237. A. Bjornerem, M. Bui, X. Wang, A. Ghasem-Zadeh, J.L. Hopper, R. Zebaze, et al., Genetic and environmental variances of bone microarchitecture and bone remodeling markers: a twin study, J. Bone Miner. Res. 30 (3) (Mar 2015) 519–527 (Epub 2014/11/20).

238. A.G. Robling, C.H. Turner, Mechanotransduction in bone: genetic effects on mechanosensitivity in mice, Bone. 31 (5) (Nov 2002) 562–569 (Epub 2002/12/13).

239. J.R. Mosley, B.M. March, J. Lynch, L.E. Lanyon, Strain magnitude related changes in whole bone architecture in growing rats, Bone. 20 (3) (Mar 1997) 191–198 (Epub 1997/03/01).

240. H.K. Uhthoff, Z.F. Jaworski, Bone loss in response to long-term immobilisation, J. Bone Joint Surg. (Br.) 60-B (3) (Aug 1978) 420–429 (Epub 1978/08/01).

241. D. Roberts, W. Lee, R.C. Cuneo, J. Wittmann, G. Ward, R. Flatman, et al., Longitudinal study of bone turnover after acute spinal cord injury, J. Clin. Endocrinol. Metab. 83 (2) (Feb 1998) 415–422 (Epub 1998/02/19).

242. S.D. Jiang, L.S. Jiang, L.Y. Dai, Mechanisms of osteoporosis in spinal cord injury, Clin. Endocrinol. 65 (5) (Nov 2006) 555–565 (Epub 2006/10/24).

243. L. Maimoun, C. Fattal, J.P. Micallef, E. Peruchon, P. Rabischong, Bone loss in spinal cord-injured patients: from physiopathology to therapy, Spinal Cord 44 (4) (Apr 2006) 203–210 (Epub 2005/09/15).

244. F. Biering-Sorensen, H.H. Bohr, O.P. Schaadt, Longitudinal study of bone mineral content in the lumbar spine, the forearm and the lower extremities after spinal cord injury, Eur. J. Clin. Investig. 20 (3) (Jun 1990) 330–335 (Epub 1990/06/01).

245. S.J. Kuruvilla, S.D. Fox, D.M. Cullen, M.P. Akhter, Site specific bone adaptation response to mechanical loading, J. Musculoskelet. Neuronal Interact. 8 (1) (Jan-Mar 2008) 71–78 (Epub 2008/04/10).

246. Q. Wang, M. Whittle, J. Cunningham, J. Kenwright, Fibula and its ligaments in load transmission and ankle joint stability, Clin. Orthop. Relat. Res. 330 (Sep 1996) 261–270 (Epub 1996/09/01).

247. P. Eser, A. Frotzler, Y. Zehnder, L. Wick, H. Knecht, J. Denoth, et al., Relationship between the duration of paralysis and bone structure: a pQCT study of spinal cord injured individuals, Bone. 34 (5) (May 2004) 869–880 (Epub 2004/05/04).

248. M.B. Schaffler, D.B. Burr, Stiffness of compact bone: effects of porosity and density, J. Biomech. 21 (1) (1988) 13–16 (Epub 1988/01/01).

249. S. Coupaud, M.K. Gislason, M. Purcell, K. Sasagawa, K.E. Tanner, Patient-specific bone mineral density distribution in the tibia of individuals with chronic spinal cord injury, derived from multi-slice peripheral Quantitative Computed Tomography (pQCT) - a cross-sectional study, Bone. 97 (Apr 2017) 29–37 (Epub 2016/12/31).

250. F.M. Maynard Jr., M.B. Bracken, G. Creasey, J.F. Ditunno Jr., W.H. Donovan, T. B. Ducker, et al., International standards for neurological and functional classification of spinal cord injury. American Spinal Injury Association, Spinal
Cord. 35 (5) (May 1997) 266–274 (Epub 1997/05/01).

251. X.F. Wang, Q. Wang, A. Ghasem-Zadeh, A. Evans, C. McLeod, S. Iuliano-Burns, et al., Differences in macro- and microarchitecture of the appendicular skeleton in young Chinese and white women, J. Bone Miner. Res. 24 (12) (Dec 2009) 1946–1952 (Epub 2009/05/23).

252. P. Geusens, R. Chapurlat, G. Schett, A. Ghasem-Zadeh, E. Seeman, J. de Jong, et al., High-resolution in vivo imaging of bone and joints: a window to microarchitecture, Nat. Rev. Rheumatol. 10 (5) (May 2014) 304–313 (Epub 2014/03/07).

253. R. Zebaze, A. Ghasem-Zadeh, A. Mbala, E. Seeman, A new method of segmentation of compact-appearing, transitional and trabecular compartments and quantification of cortical porosity from high resolution peripheral quantitative computed tomographic images, Bone. 54 (1) (May 2013) 8–20 (Epub 2013/01/22).

254. T. Hildebrand, A. Laib, R. Muller, J. Dequeker, P. Ruegsegger, Direct three dimensional morphometric analysis of human cancellous bone: microstructural data from spine, femur, iliac crest, and calcaneus, J. Bone Miner. Res. 14 (7) (Jul 1999) 1167–1174 (Epub 1999/07/15).

252. D.E. Whittier, S.K. Boyd, A.J. Burghardt, J. Paccou, A. Ghasem-Zadeh, R. Chapurlat, K. Engelke, ML. Bouxsein, Guidelines for the assessment of bone density and microarchitecture in vivo using high-resolution peripheral quantitative computed tomography, Osteoporos Int 31 (9) (2020) 1607–1627, https://doi.org/ 10.1007/s00198-020-05438-5 [Epub 2020 May 26].

256. E.J. Samelson, K.E. Broe, H. Xu, L. Yang, S. Boyd, E. Biver, et al., Cortical and trabecular bone microarchitecture as an independent predictor of incident fracture risk in older women and men in the Bone Microarchitecture International
Consortium (BoMIC): a prospective a study, Lancet Diabetes Endocrinol. 7 (1) (Jan 2019) 34–43 (Epub 2018/12/07).

257. J.R. Funk, R.W. Rudd, J.R. Kerrigan, J.R. Crandall, The effect of tibial curvature and fibular loading on the tibia index, Traffic Inj. Prev. 5 (2) (Jun 2004) 164–172 (Epub 2004/06/19).

258. P. Eser, A. Frotzler, Y. Zehnder, H. Schiessl, J. Denoth, Assessment of anthropometric, systemic, and lifestyle factors influencing bone status in the legs of spinal cord injured individuals, Osteoporos. Int. 16 (1) (Jan 2005) 26–34 (Epub 2004/05/13).

259. L. Vico, B. van Rietbergen, N. Vilayphiou, M.T. Linossier, H. Locrelle, M. Normand, et al., Cortical and trabecular bone microstructure did not recover at weightbearing skeletal sites and progressively deteriorated at non-weight-bearing sites during the year following international space station missions, J. Bone Miner. Res. 32 (10) (Oct 2017) 2010–2021 (Epub 2017/06/03).

260. C.M. Modlesky, S. Majumdar, A. Narasimhan, G.A. Dudley, Trabecular bone microarchitecture is deteriorated in men with spinal cord injury, J. Bone Miner. Res. 19 (1) (Jan 2004) 48–55 (Epub 2004/02/03).

261. A.S. Goktepe, B. Yilmaz, R. Alaca, K. Yazicioglu, H. Mohur, S. Gunduz, Bone density loss after spinal cord injury: elite paraplegic basketball players vs. paraplegic sedentary persons, Am. J. Phys. Med. Rehabil. 83 (4) (Apr 2004)
279–283 (Epub 2004/03/17).

262. A. Bjornerem, X. Wang, M. Bui, A. Ghasem-Zadeh, J.L. Hopper, R. Zebaze, et al., Menopause-related appendicular bone loss is mainly cortical and results in increased cortical porosity, J. Bone Miner.

Res. 33 (4) (Apr 2018) 598–605 (Epub 2017/12/09).

263. A.A. Biewener, Bone strength in small mammals and bipedal birds: do safety factors change with body size? J. Exp. Biol. 98 (Jun 1982) 289–301 (Epub 1982/ 06/01).

264. Y.F. Hsieh, A.G. Robling, W.T. Ambrosius, D.B. Burr, C.H. Turner, Mechanical loading of diaphyseal bone in vivo: the strain threshold for an osteogenic response varies with location, J. Bone Miner. Res. 16 (12) (Dec 2001) 2291–2297 (Epub 2002/01/05).

265. F.A. Schulte, D. Ruffoni, F.M. Lambers, D. Christen, D.J. Webster, G. Kuhn, et al., Local mechanical stimuli regulate bone formation and resorption in mice at the tissue level, PLoS One 8 (4) (2013), e62172 (Epub 2013/05/03).

266. P. Christen, K. Ito, R. Ellouz, S. Boutroy, E. Sornay-Rendu, R.D. Chapurlat, et al., Bone remodelling in humans is load-driven but not lazy, Nat. Commun. 5 (Sep 11 2014) 4855 (Epub 2014/09/12).

267. L.M. McNamara, P.J. Prendergast, Bone remodelling algorithms incorporating both strain and microdamage stimuli, J. Biomech. 40 (6) (2007) 1381–1391 (Epub 2006/08/26).

268. C.H. Turner, M.R. Forwood, M.W. Otter, Mechanotransduction in bone: do bone cells act as sensors of fluid flow? FASEB J. 8 (11) (Aug 1994) 875–878 (Epub 1994/08/01).

269. A.G. Robling, P.J. Niziolek, L.A. Baldridge, K.W. Condon, M.R. Allen, I. Alam, et al., Mechanical stimulation of bone in vivo reduces osteocyte expression of Sost/sclerostin, J. Biol. Chem. 283 (9) (Feb 29, 2008) 5866–5875 (Epub 2007/12/20).

270. S.L. Bass, L. Saxon, R.M. Daly, C.H. Turner, A.G. Robling, E. Seeman, et al., The effect of mechanical loading on the size and shape of bone in pre-, peri-, and postpubertal girls: a study in tennis players, J. Bone Miner. Res. 17 (12) (Dec 2002) 2274–2280 (Epub 2002/12/10).

271. X. Tian, W.S. Jee, X. Li, C. Paszty, H.Z. Ke, Sclerostin antibody increases bone mass by stimulating bone formation and inhibiting bone resorption in a hindlimb immobilization rat model, Bone 48 (2) (Feb 2011) 197–201 (Epub 2010/09/21).

272. R.A. Battaglino, S. Sudhakar, A.A. Lazzari, E. Garshick, R. Zafonte, L.R. Morse, Circulating sclerostin is elevated in short-term and reduced in long-term SCI, Bone. 51 (3) (Sep 2012) 600–605 (Epub 2012/05/12).

273. L. Maimoun, F. Ben Bouallegue, A. Gelis, S. Aouinti, T. Mura, P. Philibert, et al., Periostin and sclerostin levels in individuals with spinal cord injury and their relationship with bone mass, bone turnover, fracture and osteoporosis status, Bone. 127 (Oct 2019) 612–619 (Epub 2019/07/28).

274. J. Shen, L. Fan, J. Yang, A.G. Shen, J.M. Hu, A longitudinal Raman microspectroscopic study of osteoporosis induced by spinal cord injury, Osteoporos. Int. 21 (1) (Jan 2010) 81–87 (Epub 2009/05/14).

275. H.M. Frost, The regional acceleratory phenomenon: a review, Henry Ford Hosp. Med. J. 31 (1) (1983) 3–9 (Epub 1983/01/01).

276. K. Christensen, G. Doblhammer, R. Rau, J.W. Vaupel, Ageing populations: the challenges ahead, Lancet 374 (9696) (2009) 1196–1208.

277. P. Cockwell, L.A. Fisher, The global burden of chronic kidney disease, Lancet 395

(10225) (2020) 662–664. Epub 2020/02/18.

278. L. Robertson, C. Black, N. Fluck, S. Gordon, R. Hollick, H. Nguyen, et al., Hip fracture incidence and mortality in chronic kidney disease: the GLOMMS-II record linkage cohort study, BMJ Open 8 (4) (Apr 12 2018), e020312. Epub 2018/04/15.

279. M. Ketteler, G.A. Block, P. Evenepoel, M. Fukagawa, C.A. Herzog, L. McCann, et al., Executive summary of the 2017 KDIGO chronic kidney disease-mineral and bone disorder (CKD-MBD) guideline update: what's changed and why it matters, Kidney Int. 92 (1) (Jul 2017) 26–36. Epub 2017/06/26.

280. E.S. Siris, Y.T. Chen, T.A. Abbott, E. Barrett-Connor, P.D. Miller, L.E. Wehren, et al., Bone mineral density thresholds for pharmacological intervention to prevent fractures, Arch. Intern. Med. 164 (10) (2004) 1108–1112. Epub 2004/05/26.

281. M.H. Tariq, S.A.S. Sulaiman, Prevalence of osteopenia and osteoporosis among chronic kidney disease patients: a systematic review, Systematic Review, Open Urol. Nephrol. J. 13 (2020) 8. Epub 23/05/2020.

282. W.D. Leslie, E. Seeman, S.N. Morin, L.M. Lix, S.R. Majumdar, The diagnostic threshold for osteoporosis impedes fracture prevention in women at high risk for fracture: a registry-based cohort study, Bone 114 (Sep 2018) 298–303. Epub 2018/07/17.

283. T.L. Nickolas, E.M. Stein, E. Dworakowski, K.K. Nishiyama, M. Komandah-Kosseh, C.A. Zhang, et al., Rapid cortical bone loss in patients with chronic kidney disease, J. Bone Miner. Res. 28 (8) (2013) 1811–1820.

284. R. Chapurlat, M. Bui, E. Sornay-Rendu, R. Zebaze, P.D. Delmas, D. Liew, et al., Deterioration of cortical and trabecular microstructure identifies women with osteopenia or normal bone mineral density at imminent and long-term risk for fragility fracture: a prospective study, J. Bone Miner. Res. 35 (5) (May 2020) 833–844. Epub 2019/12/11.

285. M.B. Schaffler, D.B. Burr, Stiffness of compact bone: effects of porosity and density, J. Biomech. 21 (1) (1988) 13–16. Epub 1988/01/01.

286. KDIGO 2017 clinical practice guideline update for the diagnosis, evaluation, prevention, and treatment of chronic kidney disease-mineral and bone disorder (CKD-MBD), Kidney international supplements. 7 (1) (Jul 2017) 1–59. Epub 2017/07/01.

287. A. Laib, H.J. H¨auselmann, P. Rüegsegger, In vivo high resolution 3D-QCT of the human forearm, Technol. Health Care 6 (5–6) (Dec 1998) 329–337. Epub 1999/04/01.

288. D.E. Whittier, S.K. Boyd, A.J. Burghardt, J. Paccou, A. Ghasem-Zadeh, R. Chapurlat, et al., Guidelines for the assessment of bone density and microarchitecture in vivo using high-resolution peripheral quantitative computed tomography, Osteoporos. Int. 31 (9) (Sep 2020) 1607–1627. Epub 2020/05/28.

289. R. Zebaze, A. Ghasem-Zadeh, A. Mbala, E. Seeman, A new method of segmentation of compact-appearing, transitional and trabecular compartments and quantification of cortical porosity from high resolution peripheral quantitative computed tomographic images, Bone 54 (1) (May 2013) 8–20. Epub 2013/01/22.

290. E.J. Samelson, K.E. Broe, H. Xu, L. Yang, S. Boyd, E. Biver, et al., Cortical and trabecular bone microarchitecture as an independent predictor of incident fracture risk in older women and men in the Bone Microarchitecture International Consortium (BoMIC): a prospective study, Lancet Diabetes Endocrinol. 7 (1) (Jan 2019) 34–43. Epub 2018/12/07.

291. H.H. Malluche, D.S. Porter, D. Pienkowski, Evaluating bone quality in patients with chronic kidney disease, Nat. Rev. Nephrol. 9 (11) (2013) 671–680. Epub 2013/10/ 08.

292. F. Huettner, M. Sunder, Axiomatic arguments for decomposing goodness of fit according to Shapley and Owen values, Electronic Journal of Statistics. 6 (none) (2012) 1239–1250, 12.

293. J.A. Kanis, Assessment of fracture risk and its application to screening for postmenopausal osteoporosis: synopsis of a WHO report. WHO Study Group, Osteoporos Int. 4 (6) (Nov 1994) 368–381. Epub 1994/11/01.

294. K.J. Martin, E.A. Gonzalez, ´ Metabolic bone disease in chronic kidney disease, J. Am. Soc. Nephrol. 18 (3) (2007) 875–885.

295. M. Parisien, F. Cosman, R.W. Mellish, M. Schnitzer, J. Nieves, S.J. Silverberg, et al., Bone structure in postmenopausal hyperparathyroid, osteoporotic, and normal women, J. Bone Miner. Res. 10 (9) (Sep 1995) 1393–1399. Epub 1995/09/01.

296. R.M. Zebaze, A. Ghasem-Zadeh, A. Bohte, S. Iuliano-Burns, M. Mirams, R.I. Price, et al., Intracortical remodelling and porosity in the distal radius and post-mortem femurs of women: a cross-sectional study, Lancet 375 (9727) (2010) 1729–1736. Epub 2010/05/18.

297. D.W. Dempster, M. Parisien, S.J. Silverberg, X.G. Liang, M. Schnitzer, V. Shen, et al., On the mechanism of cancellous bone preservation in postmenopausal women with mild primary hyperparathyroidism, J. Clin. Endocrinol. Metab. 84 (5) (May 1999) 1562–1566. Epub 1999/05/14.

298. H. Dobnig, R.T. Turner, Evidence that intermittent treatment with parathyroid hormone increases bone formation in adult rats by activation of bone lining cells, Endocrinology 136 (8) (Aug 1995) 3632–3638. Epub 1995/08/01.

299. M. Bui, A. Bjørnerem, A. Ghasem-Zadeh, G.S. Dite, J.L. Hopper, E. Seeman, Architecture of cortical bone determines in part its remodelling and structural decay, Bone 55 (2) (Aug 2013) 353–358. Epub 2013/05/07.

300. E. Seeman, P.D. Delmas, Bone quality–the material and structural basis of bone strength and fragility, N. Engl. J. Med. 354 (21) (2006) 2250–2261. Epub 2006/ 05/26.

301. B.M. Misof, S. Blouin, P. Roschger, J. Werzowa, K. Klaushofer, G. Lehmann, Bone matrix mineralization and osteocyte lacunae characteristics in patients with chronic kidney disease - mineral bone disorder (CKD-MBD), J. Musculoskelet. Neuronal Interact. 19 (2) (2019) 196–206.

302. O. Akkus, A. Polyakova-Akkus, F. Adar, M.B. Schaffler, Aging of microstructural compartments in human compact bone, J. Bone Miner. Res. 18 (6) (Jun 2003) 1012–1019. Epub 2003/06/24.

303. B.A. Julian, D.A. Laskow, J. Dubovsky, E.V. Dubovsky, J.J. Curtis, L.D. Quarles, Rapid loss of vertebral mineral density after renal transplantation, N. Engl. J. Med. 325 (8) (1991) 544–550. Epub 1991/08/22.

304. M.C. Monier-Faugere, H. Mawad, Q. Qi, R.M. Friedler, H.H. Malluche, High prevalence of low bone turnover and occurrence of osteomalacia after kidney transplantation, J.Am.Soc.Nephrol. 11 (6) (Jun 2000) 1093–1099. Epub 2000/05/ 23.

305. T.D. Vu, X.F. Wang, Q. Wang, N.E. Cusano, D. Irani, B.C. Silva, et al., New insights into the effects of primary hyperparathyroidism on the cortical and trabecular compartments of bone, Bone 55 (1) (Jul 2013) 57–63. Epub 2013/04/02.

306. D. Cejka, J.M. Patsch, M. Weber, D. Diarra, M. Riegersperger, Z. Kikic, et al., Bone microarchitecture in hemodialysis patients assessed by HR-pQCT, Clin. J.Am.Soc. Nephrol. 6 (9) (Sep 2011) 2264–2271. Epub 2011/07/09.

307. K.K. Nishiyama, Y. Pauchard, L.E. Nikkel, S. Iyer, C. Zhang, D.J. McMahon, et al., Longitudinal HR-pQCT and image registration detects endocortical bone loss in kidney transplantation patients, J. Bone Miner. Res. 30 (3) (Mar 2015) 554–561. Epub 2014/09/13.

308. A. Trombetti, C. Stoermann, T. Chevalley, B. Van Rietbergen, F.R. Herrmann, P. Y. Martin, et al., Alterations of bone microstructure and strength in end-stage renal failure, Osteoporos. Int. 24 (5) (May 2013) 1721–1732. Epub 2012/10/27.

309. Christensen K, Doblhammer G, Rau R, Vaupel JW. Ageing populations: the challenges ahead. Lancet. 2009;374(9696):1196-208.

310. Robertson L, Black C, Fluck N, Gordon S, Hollick R, Nguyen H, et al. Hip fracture incidence and mortality in chronic kidney disease: the GLOMMS-II record linkage cohort study. BMJ Open. 2018;8(4):e020312.

311. Schaffler MB, Burr DB. Stiffness of compact bone: effects of porosity and density. J Biomech. 1988;21(1):13-6.

312. Pocock NA. Quantitative diagnostic methods in osteoporosis: a review. Australas Radiol. 1998;42(4):327-34.

313. Genant HK, Engelke K, Fuerst T, Glüer CC, Grampp S, Harris ST, et al. Noninvasive assessment of bone mineral and structure: state of the art. J Bone Miner Res. 1996;11(6):707-30.

314. Morgan DB, Spiers FW, Pulvertaft CN, Fourman P. The amount of bone in the metacarpal and the phalanx according to age and sex. Clin Radiol. 1967;18(1):101-8.

315. Cameron JR, Sorenson J. MEASUREMENT OF BONE MINERAL IN VIVO: AN IMPROVED METHOD. Science. 1963;142(3589):230-2.

316. Davis CA, Genant HK, Dunham JS. The effects of bone on proton NMR relaxation times of surrounding liquids. Invest Radiol. 1986;21(6):472-7.

317. Siris ES, Chen YT, Abbott TA, Barrett-Connor E, Miller PD, Wehren LE, et al. Bone mineral density thresholds for pharmacological intervention to prevent fractures. Arch Intern Med. 2004;164(10):1108-12.

318. Leslie WD, Seeman E, Morin SN, Lix LM, Majumdar SR. The diagnostic threshold for osteoporosis impedes fracture prevention in women at high risk for fracture: A registry-based cohort study. Bone. 2018;114:298-303.

319. Boutroy S, Bouxsein ML, Munoz F, Delmas PD. In vivo assessment of trabecular bone microarchitecture by high-resolution peripheral quantitative computed tomography. J Clin Endocrinol Metab. 2005;90(12):6508-15.

320. Laib A, Häuselmann HJ, Rüegsegger P. In vivo high resolution 3D-QCT of the human forearm. Technology and Health Care. 1998;6:329-37.

321. Geusens P, Chapurlat R, Schett G, Ghasem-Zadeh A, Seeman E, de Jong J, et al. High-resolution in vivo imaging of bone and joints: a window to microarchitecture. Nat Rev Rheumatol. 2014;10(5):304-13.

322. Ghasem-Zadeh A, Burghardt A, Wang XF, Iuliano S, Bonaretti S, Bui M, et al. Quantifying sex, race, and age specific differences in bone microstructure requires measurement of anatomically equivalent regions. Bone. 2017;101:206-13.

323. Chapurlat R, Bui M, Sornay-Rendu E, Zebaze R, Delmas PD, Liew D, et al. Deterioration of Cortical and Trabecular Microstructure Identifies Women With Osteopenia or Normal Bone Mineral Density at Imminent and Long-Term Risk for Fragility Fracture: A Prospective Study. J Bone Miner Res. 2020;35(5):833-44.

324. Wang Q, Whittle M, Cunningham J, Kenwright J. Fibula and its ligaments in load transmission and ankle joint stability. Clin Orthop Relat Res. 1996(330):261-70.

325. Ghasem-Zadeh A, Galea MP, Nunn A, Panisset M, Wang XF, Iuliano S, et al. Heterogeneity in microstructural deterioration following spinal cord injury. Bone. 2021;142:115778.

326. Jiang SD, Jiang LS, Dai LY. Mechanisms of osteoporosis in spinal cord injury. Clin Endocrinol (Oxf). 2006;65(5):555-65.

327. Tariq MH, Sulaiman SA. Prevalence of osteopenia and osteoporosis among chronic kidney disease patients: a systematic review. The Open Urology & Nephrology Journal. 2020;13(1).

328. Mikolajewicz N, Bishop N, Burghardt AJ, Folkestad L, Hall A, Kozloff KM, et al. HR-pQCT Measures of Bone Microarchitecture Predict Fracture: Systematic Review and Meta-Analysis. J Bone Miner Res. 2020;35(3):446-59.

329. Cheung WH, Hung VW, Cheuk KY, Chau WW, Tsoi KK, Wong RM, et al. Best Performance Parameters of HR-pQCT to Predict Fragility Fracture: Systematic Review and Meta-Analysis. J Bone Miner Res. 2021;36(12):2381-98.

330. Samelson EJ, Broe KE, Xu H, Yang L, Boyd S, Biver E, et al. Cortical and trabecular bone microarchitecture as an independent predictor of incident fracture risk in older women and men in the Bone Microarchitecture International Consortium (BoMIC): a prospective study. Lancet Diabetes Endocrinol. 2019;7(1):34-43.

331. Seeman E, Delmas PD. Bone quality--the material and structural basis of bone strength and fragility. N Engl J Med. 2006;354(21):2250-61.

332. Nyman JS, Ketsiri T, Louie EA, Harkins KD, Manhard MK, Gochberg DF, et al. Toward the use of MRI measurements of bound and pore water in fracture risk assessment. Bone. 2023;176:116863.

333. Zebaze R, Atkinson EJ, Peng Y, Bui M, Ghasem-Zadeh A, Khosla S, et al. Increased Cortical Porosity and Reduced Trabecular Density Are Not Necessarily Synonymous With Bone Loss and Microstructural Deterioration. JBMR Plus. 2019;3(4):e10078.

334. Chapurlat R, Bui M, Sornay-Rendu E, Zebaze R, Delmas PD, Liew D, et al. Deterioration of Cortical and Trabecular Microstructure Identifies Women With Osteopenia or Normal Bone Mineral Density at Imminent and Long-Term Risk for Fragility Fracture: A Prospective Study. J Bone Miner Res. 2020;35(5):833-44.

335. Chapurlat R, Ferrari S, Li X, Peng Y, Xu M, Bui M, et al. Deep Learning Using High-Resolution Images of Forearm Predicts Fracture. eLife Sciences Publications, Ltd; 2023.

336. Klintström B, Henriksson L, Moreno R, Malusek A, Smedby Ö, Woisetschläger M, et al. Photon-counting detector CT and energy-integrating detector CT for trabecular bone microstructure analysis of cubic specimens from human radius. Eur Radiol Exp. 2022;6(1):31.

Appendix

Journal of Clinical Densitometry: Assessment & Management of Musculoskeletal Health, vol. 20, no. 1, 5–7, 2017
© 2016 The International Society for Clinical Densitometry.
1094-6950/20:5–7/$36.00
http://dx.doi.org/10.1016/j.jocd.2016.08.006

Editorial

Challenges in the Use of Cross-Sectional Data to Quantify Growth and Deterioration of Bone Structure During Advancing Age

Ali Ghasem-Zadeh,*[*,1] and Ego Seeman[1,2]

[1]*Departments of Endocrinology and Medicine, Austin Health, University of Melbourne, Melbourne, Australia; and*
[2]*Institute for Health and Aging, Australian Catholic University, Melbourne, Australia*

In this issue of the *Journal of Clinical Densitometry*, Lindgren et al present data concerning peak bone mass of the extremities in young Swedish men. The work involved the use of peripheral quantitative computed tomography to assess peak radial and tibial metaphyseal and diaphyseal cortical and trabecular mass, volumetric bone mineral density (BMD), and other morphological features, rather than the use of areal BMD, a 2-dimensional areal projection of a 3-dimensional structure. The authors derived a reference range using a random sample of 1083 healthy Swedish men *(1)*.

Contrary to what was proposed, the age at peak for bone traits was not discernible. There was also no detectable association between peak bone mass and strength, estimated by calculation of a cross-sectional polar moment of inertia. The authors also proposed that quantifying peak cortical and trabecular structures may identify persons at risk for fracture later in life, and might do so better than areal BMD.

The work identifies several challenges we face using cross-sectional data to make inferences about longitudinal changes in bone morphology produced during growth and adulthood. These challenges include defining the age at which peak bone size, mass, and microstructure are achieved, and the changes in morphology during adulthood such as the age at which bone mass starts to decline and microstructure deteriorates, and whether bone size continues to increase due to slow periosteal apposition after epiphyseal closure *(2–4)*.

The subjects of this study were males aged 18–28 yr. Puberty occurs at around 12–14 yr and is associated with a reduction in the rate of longitudinal appendicular growth but a concomitant acceleration in longitudinal truncal growth. The greater velocity of appendicular than axial longitudinal growth drives the increase in height between 1 yr of age and puberty. Longitudinal growth then slows, but mass continues to increase as cortical porosity decreases and matrix mineral density increases *(5–7)*. Most of these events are close to completion before 18 yr of age accounting for there being no identifiable age at peak for traits such as bone size and mass.

Another challenge using cross-sectional data is the effect of secular increases in stature. Trait differences between younger and older persons, or the lack of them, may be the result of secular changes in stature, which may either exaggerate or blunt the pattern of change across age depending on the phenotype studied. Indeed, secular changes are very heterogeneous; they are site, sex, race, and epoch specific. Even within the same community, the secular change may occur in 1 sex but not in the other; in the upper body, lower body, or both; or in 1 race but not in another *(8–13)*.

The difficulties that arise may be relevant to this study even though there was only a decade between the youngest and oldest participants. For example, one explanation for the absence of a detectable peak in size and mass may be that persons forming the older cohort in a cross-sectional study had a smaller stature when they were young. The actual increase in height, bone width, and bone mass have been blunted because the persons forming the younger group are taller than those in the older group when the persons in the older group were young. This will underestimate the age-related increase in bone size produced by periosteal apposition during growth. In this cohort, it is plausible that there was a secular increase in height and this may partly explain the absence of a detectable peak in bone size or mass.

The authors wanted to determine whether peak bone mass predict bone strength. As the bending strength of bone

Received 08/5/16; Accepted 08/13/16.
*Address correspondence to: Ali Ghasem-Zadeh, PhD, Departments of Endocrinology and Medicine, Austin Health, Repatriation Hospital, University of Melbourne, Level 2, Centaur Wing, Melbourne, VIC 3081, Australia. E-mail: alig@unimelb.edu.au

is a fourth power function of the radial distance of a unit volume of bone *(14)*, blunting of the increase in bone radius by secular changes may also underestimate the rise in bending strength that accompanies the rise in the radius of a cross section.

Another challenge is the use of a threshold-based segmentation (separation) of cortical from trabecular bone using peripheral quantitative computed tomography-derived images *(15,16)*. This method may result in errors in metaphyseal regions but less so in diaphyseal regions. Metaphyseal cortical bone is formed, in part, by corticalization of trabeculae arising from the periphery of the growth plate *(17,18)*. Trabecular are incorporated, adsorbed upon the endocortical surface, and become the cortical bone of the metaphyseal region. More central trabeculae form the trabecular compartment *(19)*.

If corticalization of trabeculae is delayed or incomplete, threshold-based segmentation erroneously leaves the trabeculae in the medullary canal, underestimating cortical thickness and area and overestimating trabecular density. Thus, in younger persons in a cross-sectional study, cortical thickness may be underestimated, even in 18 yr olds. This underestimation of cortical thickness in a young person will overestimate the increment in cortical thickness across age, whereas the increment in trabecular density will be underestimated (because younger people will seem to have higher "trabecular" density). The same issue does not occur in the diaphysis because cortical bone is formed by membranous bone formation.

The lack of association between mass and strength may be due to the constancy of mass along a bone *(20)*. In a given individual, it is surprising and perhaps counterintuitive to find that the amount of material used to assemble a long bone is the same from cross section to cross section along the length of a long bone. What differs, and determines its strength, is the distribution of that same amount of material in space. For example, at the junction of the femoral shaft and femoral neck, the femoral neck is widest and the cortices vary in thickness around a given cross section. The bending strength will vary depending on the radial distance of the amount of material at that point. Moving proximally, cortical thickness decreases while trabecular density increases. The varying configuration of the constant amount of material is achieved by varying the void volume (forming the medullary canal and the intracortical porosity). Larger bones are assembled with less matrix volume relative to their size; the medullary canal is wider and the cortex is more porous and has a lower mineralization density *(21,22)*.

In conclusion, skeletal growth is heterogeneous; final height is a function of the differing onset, tempo, and duration of growth of the trunk and appendicular skeleton. Long bones grow in length at their growth plates, but at some locations bones grow fast at their distal metaphyseal growth plate whereas others grow faster at the proximal metaphyseal *(23)*. At each point around a perimeter of a cross section, the rate of periosteal, endocortical, and intracortical modeling and remodeling varies, giving each cross section its unique size, shape, and microarchitecture. All of these phenomena vary by age, sex, and race. The study of growth is a fascinating journey for adults to think about and remember fondly.

References

1. Lindgren E, Karlsson MK, Lorentzon M, Rosengren BE. 2016 Bone traits seem to develop also during the third decade in life-normative cross-sectional data on 1083 men aged 18–28 years. J Clin Densitom (in this issue).
2. Gilsanz V, Skaggs DL, Kovanlikaya A, et al. 1998 Differential effect of race on the axial and appendicular skeletons of children. J Clin Endocrinol Metab 83(5):1420–1427.
3. Bonjour JP, Theintz G, Law F, et al. 1994 Peak bone mass. Osteoporos Int 4(Suppl 1):7–13.
4. Seeman E. 1997 From density to structure: growing up and growing old on the surfaces of bone. J Bone Miner Res 12(4):509–521.
5. Bradney M, Karlsson MK, Duan Y, et al. 2000 Heterogeneity in the growth of the axial and appendicular skeleton in boys: implications for the pathogenesis of bone fragility in men. J Bone Miner Res 15(10):1871–1878.
6. Karlberg J. 1990 The infancy-childhood growth spurt. Acta Paediatr Scand Suppl 367:111–118.
7. Seeman E. 1998 Growth in bone mass and size—are racial and gender differences in bone mineral density more apparent than real? J Clin Endocrinol Metab 83(5):1414–1419.
8. Bakwin H, McLaughlin SM. 1964 Secular increase in height is the end in sight? Lancet 2(7371):1195–1196.
9. Meredith HV. 1978 Secular change in sitting height and lower limb height of children, youths, and young adults of Afro-black, European, and Japanese ancestry. Growth 42(1):37–41.
10. Hauspie RC, Vercauteren M, Susanne C. 1997 Secular changes in growth and maturation: an update. Acta Paediatr 423:20–27.
11. Danubio ME, Sanna E. 2008 Secular changes in human biological variables in Western countries: an updated review and synthesis. J Anthropol Sci 86:91–112.
12. Malina RM, Brown KH, Zavaleta AN. 1987 Relative lower extremity length in Mexican American and in American black and white youth. Am J Phys Anthropol 72(1):89–94.
13. Hamill PV, Johnston FE, Lemeshow S. 1973 Height and weight of youths 12–17 years. United States. Vital Health Stat 11 (124):1–81.
14. Ruff CB, Hayes WC. 1988 Sex differences in age-related remodeling of the femur and tibia. J Orthop Res 6(6):886–896.
15. Zebaze RM, Ghasem-Zadeh A, Bohte A, et al. 2010 Intracortical remodelling and porosity in the distal radius and post-mortem femurs of women: a cross-sectional study. Lancet 375(9727):1729–1736.
16. Zebaze R, Ghasem-Zadeh A, Mbala A, Seeman E. 2013 A new method of segmentation of compact-appearing, transitional and trabecular compartments and quantification of cortical porosity from high resolution peripheral quantitative computed tomographic images. Bone 54(1):8–20.
17. Cadet ER, Gafni RI, McCarthy EF, et al. 2003 Mechanisms responsible for longitudinal growth of the cortex: coalescence of trabecular bone into cortical bone. J Bone Joint Surg 85-A(9):1739–1748.
18. Bala Y, Bui QM, Wang XF, et al. 2015 Trabecular and cortical microstructure and fragility of the distal radius in women. J Bone Miner Res 30(4):621–629.

Appendix

19. Wang Q, Ghasem-Zadeh A, Wang XF, et al. 2011 Trabecular bone of growth plate origin influences both trabecular and cortical morphology in adulthood. J Bone Miner Res 26(7):1577–1583.
20. Zebaze RM, Jones A, Welsh F, et al. 2005 Femoral neck shape and the spatial distribution of its mineral mass varies with its size: clinical and biomechanical implications. Bone 37(2):243–252.
21. Bjornerem A, Bui QM, Ghasem-Zadeh A, et al. 2013 Fracture risk and height: an association partly accounted for by cortical porosity of relatively thinner cortices. J Bone Miner Res 28(9):2017–2026.
22. Boutroy S, Walker MD, Liu XS, et al. 2014 Lower cortical porosity and higher tissue mineral density in Chinese American versus white women. J Bone Miner Res 29(3):551–561.
23. Wang Q, Wang XF, Iuliano-Burns S, et al. 2010 Rapid growth produces transient cortical weakness: a risk factor for metaphyseal fractures during puberty. J Bone Miner Res 25(7):1521–1526.

JBMR®

Challenges in the Acquisition and Analysis of Bone Microstructure During Growth

Ego Seeman[1,2,3] and Ali Ghasem-Zadeh[1]

[1]Department of Endocrinology, Austin Health, University of Melbourne, Melbourne, Australia
[2]Department of Medicine, Austin Health, University of Melbourne, Melbourne, Australia
[3]Institute of Health and Ageing, Australian Catholic University, Melbourne, Australia

To The Editor

Gabel and colleagues[1] report sex and racial differences in distal tibial and distal radial microstructure. This was a mixed longitudinal study of white and Asian males and females aged from 9 to 20 years. The authors confirm that males grow larger bones than females. Cortical porosity was higher in males but there was no sex difference in cortical volumetric bone mineral density (vBMD), leading the authors to suggest, but not show, that cortical matrix mineral density may be higher in males. The findings are questionable given several methodological challenges we face studying growth.

First, assessment of bone microstructure is based on positioning a region of interest (ROI) of only 9.02 mm in length at the distal metaphysis of the radius and tibia.[2,3] In a longitudinal study, it is difficult to relocate the identical anatomical location in the same individual. In cross-sectional or longitudinal studies, it is difficult to know whether the same anatomical region has been chosen when individuals differ by sex or race and so differ in forearm and tibial lengths. In adults, a fixed distance from the joint line is chosen as beginning the 9.02 mm ROI (9.5 mm for radius and 22.5 mm for tibia). This approach positions the ROI more distally in taller persons. Because cortical porosity is higher more distally, finding a higher porosity in males than females may be the result of positioning, not biology. Hence, taking a percentage of the length of a long bone is recommended in adults.[4]

Whether taking a percentage of the length of the radius and tibia is the correct approach when bone length is increasing rapidly during growth and at different rates at each growth plate is not known.[5,6] Growth of the radius occurs mainly at the distal growth plate so that the ROI first measured moves proximally. As the radius lengthens, using 7% of the lengthening bone moves that ROI proximally. However, if growth is nonlinear, it is unlikely that a fixed percentage of the lengthening bone will relocate the first ROI measured. The tibia initially grows equally at each growth plate so the first ROI at the distal metaphysis measured moves proximally. Later, most tibial growth occurs at the proximal growth plate so the ROI measured earlier moves distally but the subsequent ROI chosen using 8% percent of the increasing length moves proximally.

Differences in positioning of the ROI by even 1 to 2 mm may exaggerate or obscure microstructural differences between sexes and races, particularly at the distal radial metaphysis, a heterogeneous irregular rhomboidal structure. Cortical porosity and trabecular density are high distally and decrease in nonlinear fashion, often by over 50% within a few millimeters.[7] Positioning errors produce differences in microstructure that are the same order of magnitude as sex and racial differences reported when the positioning errors are corrected.

Second, males and whites enter puberty ~12 months later than their respective female and Asian counterparts so they have had more growth of the legs and trunk at the time of entering puberty. It is difficult to understand how an estimated measure of peak growth velocity of height controls for the longer prepubertal growth and so controls for "maturation."[8] Growth velocity of total height is highest at birth, it decreases precipitously then accelerates at 1 year of age because growth velocity of the legs, not trunk, increases and remains twice that of truncal growth until puberty when leg length decelerates and trunk length accelerates (Fig. 1, left panel). Peak height velocity is therefore driven by truncal growth but measurements of the appendicular skeleton are being taken. A later age at puberty in males and whites produces longer legs than in their female and Asian counterparts, respectively.[9,10] A longer intrapubertal growth in males produces a longer trunk. Pooling whites and Asian (almost one-half the cohort) when comparing males and females adds to the difficulties. It remains plausible that sex and racial differences in height are the result of differences in the *duration* of prepubertal and intrapubertal growth in males and whites than females and Asians respectively, the rapidity of growth may not differ by sex or race.[11–13]

Third, the authors report boys had higher porosity than girls but cortical vBMD was no different. They suggest, but do not show, that males may have higher matrix mineral density. Available evidence suggests the reverse is the case. The higher the porosity, the lower the matrix mineral density.[14] This inverse association is likely to be the result of the rapidity of remodeling; excavation of cavities increases porosity, refilling

Received in original form September 19, 2016; accepted October 4, 2016. Accepted manuscript online November 1, 2016.
Address correspondence to: Ego Seeman, MD, Department Endocrinology, Second Floor Centaur Wing, Austin Health, Waterdale Rd, Heidelberg 3081, Melbourne, Australia. E-mail: egos@unimelb.edu.au

Journal of Bone and Mineral Research, Vol. 31, No. 12, December 2016, pp 2239–2241
DOI: 10.1002/jbmr.3015
© 2016 American Society for Bone and Mineral Research

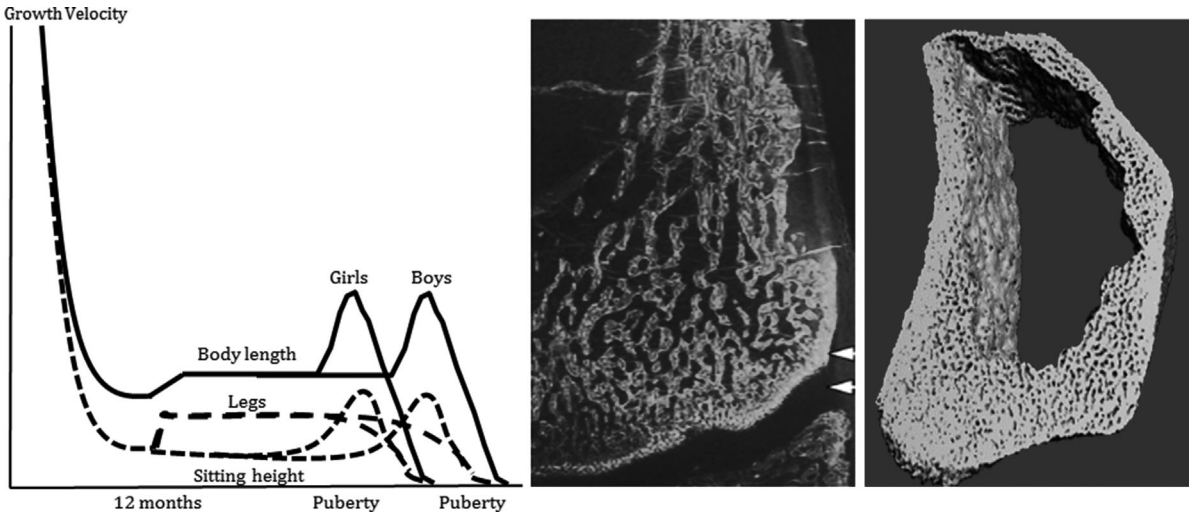

Fig. 1. (Left panel) Growth velocity of the total body length decelerates after birth then accelerates at 1 year of age due to acceleration of the growth of the legs. Truncal growth accelerates at puberty. Males have a longer prepubertal and intrapubertal growth period than females. (Middle panel) Metaphyseal trabeculae coalesce to form the metaphyseal cortex.[17] (Right panel) Incorrect segmentation of trabecular from cortical bone may result in this being "seen" as cortical bone.

with under mineralized matrix reduces matrix mineral density. This inconsistency signals the likelihood that there are errors in segmenting cortical and trabecular bone using thresholding and then calculating porosity in a cortex that is probably erroneously estimated.[15,16]

During growth of the distal radial metaphysis, trabeculae arising from the periphery of the growth plate coalesce ("corticalize"), forming the cortex by endochondral apposition (Fig. 1, middle panel).[17,18] Longitudinal growth of the distal radius is rapid and transiently out paces osteoid apposition upon trabeculae so coalescence is delayed producing a transiently porous cortex. At a pixel size of 82 μm and a spatial resolution of about 100 μm, pixels containing incompletely coalesced trabeculae abutting against cortex may be registered as "cortical" bone and so overestimate "cortical" thickness (Fig. 1, right panel). When porosity is calculated, the intertrabecular void may be erroneously included, leading to an overestimate of "cortical" porosity. Alternatively, porosity may be underestimated if mineralized matrix in a voxel containing part of a pore increases photon attenuation above the threshold designated to identify porosity.

Measurement of bone density using bone densitometry was a good beginning. Young investigators growing up under the shadow of the two-dimensional "areal" projection of a three-dimensional structure are unlikely to think about the morphological basis of bone fragility. Measurement of bone microstructure using high-resolution image analysis is changing the cerebral silence. However, this technology is not trouble-free press-button motoring. Understanding the microstructural changes that accompany growth, aging, and drug therapy requires attention to the challenges we face in image acquisition and analysis.[19]

References

1. Gabel L, Macdonald HM, McKay HA. Sex differences and growth-related adaptations in bone microarchitecture, geometry, density and strength from childhood to early adulthood: a mixed longitudinal HR-pQCT Study. J Bone Miner Res. 20XX; XX(XX): XXXX–XXXX. DOI:10.1002/jbmr.2982.
2. Burrows M, Liu D, Perdios A, Moore S, Mulpuri K, McKay H. Assessing bone microstructure at the distal radius in children and adolescents using HR-pQCT: a methodological pilot study. J Clin Densitom. 2010;13(4):451–5.
3. Cheuk KY, Tam EM, Yu FW, et al. A critical comparison between two scanning protocols of high-resolution peripheral quantitative computed tomography at the distal radius in adolescents. J Clin Densitom. 2016;19(3):305–15.
4. Ghasem-Zadeh A, Wang XF, Zebaze R, Seeman E. Sexual and racial dimorphism in bone microarchitecture requires adjustment of the region of interest for skeleton dimensions. J Bone Miner Res. 2016;31 Suppl 1. [Poster session presented at: Annual Meeting American Society for Bone and Mineral Research (ASBMR); 2016 Sep 16–19; Atlanta, GA, USA; Presentation Number: SU0213]. Available from: http://www.asbmr.org/education/AbstractDetail?aid=86f1146f-e94e-47b9-9875-d52e78cb154e
5. Pritchett JW. Growth plate activity in the upper extremity. Clin Orthop Relat Res. 1991;268:235–42.
6. Pritchett JW. Longitudinal growth and growth-plate activity in the lower extremity. Clin Orthop Relat Res. 1992;275:274–9.
7. Ghasem-Zadeh A, Burghardt A, Zendeli A, et al. Assessing age, sex, and racial differences in cortical porosity requires adjustment for site-specific variation in the selected region of interest site variation. J Bone Miner Res. 2014; 29 Suppl 1. [Poster session presented at: Annual Meeting American Society for Bone and Mineral Research (ASBMR); 2014 Se p 12–15; Houston, TX, USA; Presentation Number: SA0297]. Available from: http://www.asbmr.org/education/AbstractDetail?aid=974d22e0-fbac-4ebf-849c-353d6e60ab36
8. Bradney M, Karlsson MK, Duan Y, Stuckey S, Bass S, Seeman E. Heterogeneity in the growth of the axial and appendicular skeleton in boys: implications for the pathogenesis of bone fragility in men. J Bone Miner Res. 2000;15(10):1871–8.
9. Leung SS, Lau JT, Xu YY, et al. Secular changes in standing height, sitting height and sexual maturation of Chinese—the Hong Kong Growth Study, 1993. Ann Hum Biol. 1996; 23 (4): 297–306.
10. Parfitt AM. The two faces of growth: benefits and risks to bone integrity. Osteoporos Int. 1994;4(6):382–98.
11. Wang XF, Duan Y, Seeman E. Similar trunk length but shorter leg length in Chinese than Caucasians: implications for racial

15234681, 2016, 12, Downloaded from https://asbmr.onlinelibrary.wiley.com/doi/10.1002/jbmr.3015 by The University Of Melbourne, Wiley Online Library on [18/06/2023]. See the Terms and Conditions (https://onlinelibrary.wiley.com/terms-and-conditions) on Wiley Online Library for rules of use; OA articles are governed by the applicable Creative Commons License

differences in hip fracture rates. J Bone Miner Res. 2004;19 Suppl 1. [Poster session presented at: Annual Meeting American Society for Bone and Mineral Research (ASBMR); 2004 Oct 1–5; Seattle, WA, USA; Presentation Number: SA0382]. Available from: http://www.abstractsonline.com/viewer/viewAbstract.asp?CKey={0AA8B44D-7532-47A3-93E6-749B6DDACADB}&MKey={96915C07-D110-439D-BF0C-C23CD3392D2D}&AKey={D0C01D4F-E23B-45E2-ACD4-0AF8AC866B8B}&SKey={0E574113-B97E-4E07-A945-9B8D07087AD}

12. Iuliano-Burns S, Hopper J, Seeman E. The age of puberty determines sexual dimorphism in bone structure: a male/female co-twin control study. J Clin Endocrinol Metab. 2009;94(5):1638–43.
13. Iuliano-Burns S, Mirwald RL, Bailey DA. Timing and magnitude of peak height velocity and peak tissue velocities for early, average, and late maturing boys and girls. Am J Hum Biol. 2001;13(1):1–8.
14. Boutroy S, Walker MD, Liu XS, et al. Lower cortical porosity and higher tissue mineral density in Chinese American versus white women. J Bone Miner Res. 2014;29(3):551–61.
15. Zebaze RM, Ghasem-Zadeh A, Bohte A, et al. Intracortical remodelling and porosity in the distal radius and post-mortem femurs of women: a cross-sectional study. Lancet. 2010 15;375 (9727): 1729–36.
16. Zebaze R, Ghasem-Zadeh A, Mbala A, Seeman E. A new method of segmentation of compact-appearing, transitional and trabecular compartments and quantification of cortical porosity from high resolution peripheral quantitative computed tomographic images. Bone. 2013;54(1):8–20.
17. Cadet ER, Gafni RI, McCarthy EF, et al. Mechanisms responsible for longitudinal growth of the cortex: coalescence of trabecular bone into cortical bone. J Bone Joint Surg Am. 2003; 85-A(9):1739–48.
18. Bala Y, Bui QM, Wang XF, et al. Trabecular and cortical microstructure and fragility of the distal radius in women. J Bone Miner Res. 2015;30(4):621–9.
19. Seeman E, Martin TJ. Co-administration of antiresorptive and anabolic agents: a missed opportunity. J Bone Miner Res. 2015; 30(5):753–64.

15234681, 2016, 12, Downloaded from https://asbmr.onlinelibrary.wiley.com/doi/10.1002/jbmr.3015 by The University Of Melbourne, Wiley Online Library on [18/06/2023]. See the Terms and Conditions (https://onlinelibrary.wiley.com/terms-and-conditions) on Wiley Online Library for rules of use; OA articles are governed by the applicable Creative Commons License

Osteoporosis International (2020) 31:1607–1627
https://doi.org/10.1007/s00198-020-05438-5

POSITION PAPER

Guidelines for the assessment of bone density and microarchitecture in vivo using high-resolution peripheral quantitative computed tomography

D.E. Whittier[1,2] · S.K. Boyd[1,2] · A.J. Burghardt[3] · J. Paccou[4] · A. Ghasem-Zadeh[5] · R. Chapurlat[6,7] · K. Engelke[8,9] · M.L. Bouxsein[10,11]

Received: 12 March 2020 / Accepted: 23 April 2020 / Published online: 26 May 2020
© International Osteoporosis Foundation and National Osteoporosis Foundation 2020

Abstract

Introduction The application of high-resolution peripheral quantitative computed tomography (HR-pQCT) to assess bone microarchitecture has grown rapidly since its introduction in 2005. As the use of HR-pQCT for clinical research continues to grow, there is an urgent need to form a consensus on imaging and analysis methodologies so that studies can be appropriately compared. In addition, with the recent introduction of the second-generation HrpQCT, which differs from the first-generation HR-pQCT in scan region, resolution, and morphological measurement techniques, there is a need for guidelines on appropriate reporting of results and considerations as the field adopts newer systems.

Methods A joint working group between the International Osteoporosis Foundation, American Society of Bone and Mineral Research, and European Calcified Tissue Society convened in person and by teleconference over several years to produce the guidelines and recommendations presented in this document.

Results An overview and discussion is provided for (1) standardized protocol for imaging distal radius and tibia sites using HR-pQCT, with the importance of quality control and operator training discussed; (2) standardized terminology and recommendations on reporting results; (3) factors influencing accuracy and precision error, with considerations for longitudinal and multicenter study designs; and finally (4) comparison between scanner generations and other high-resolution CT systems.

Conclusion This article addresses the need for standardization of HR-pQCT imaging techniques and terminology, provides guidance on interpretation and reporting of results, and discusses unresolved issues in the field.

Keywords Bone microarchitecture · Guidelines · High-resolution peripheral quantitative computed tomography · Imaging protocol

Introduction

High-resolution peripheral quantitative computed tomography (HR-pQCT) is a non-invasive, low-radiation approach for assessing compartment-specific volumetric bone mineral density and bone microarchitecture in the peripheral skeleton, most commonly the distal radius and tibia. Until the introduction of the first HR-pQCT device in 2005 [1], assessment of human bone

✉ M.L. Bouxsein
mbouxsei@bidmc.harvard.edu

[1] McCaig Institute for Bone and Joint Health, Cumming School of Medicine, University of Calgary, Calgary, AB, Canada

[2] Department of Radiology, Cumming School of Medicine, University of Calgary, Calgary, AB, Canada

[3] Department of Radiology and Biomedical Imaging, University of California, San Francisco, CA, USA

[4] Department of Rheumatology, MABlab UR 4490, CHU Lille, Univ. Lille, 59000 Lille, France

[5] Departments of Endocrinology and Medicine, Austin Health, The University of Melbourne, Melbourne, Australia

[6] INSERM UMR 1033, Université de Lyon, Lyon, France

[7] Hôpital Edouard Herriot, Hospice Civils de Lyon, Lyon, France

[8] Department of Medicine 3, FAU University Erlangen-Nürnberg and Universitätsklinikum Erlangen, Erlangen, Germany

[9] Bioclinica, Inc., Hamburg, Germany

[10] Center for Advanced Orthopedic Studies, Beth Israel Deaconess Medical Center, Boston, MA, USA

[11] Harvard Medical School, Boston, MA, USA

microarchitecture was largely limited to histomorphometric or micro-CT analysis of iliac crest biopsies [2, 3] or technically challenging, limited resolution micro-magnetic resonance imaging. The ability to investigate bone microarchitecture in vivo has provided novel insights into differences due to age, sex, and ethnicity [4–13]; changes due to disease [14–17]; response to nutritional and pharmacologic treatments [18–22]; the impact of physical activity [23–26]; and deficits associated with increased fracture risk [27]. The use of HR-pQCT for clinical research studies has grown rapidly in the past decade, and as its application continues to expand, there is a need to establish recommendations for best practices and to discuss unresolved issues related to its use in clinical studies. Furthermore, with the recent introduction of a second-generation HR-pQCT device with improved resolution and longer scan region, it is important to highlight the differences and comparability between scanner generations, future HR-pQCT devices, and alternative systems, such as cone-beam CT.

Thus, the objective of this manuscript is to provide guidance on the technical aspects of HR-pQCT for use in the clinical setting, including best practices for acquisition and analysis of scans, as well as provide guidance on the presentation and interpretation of results. The work presented here is a product of a joint IOF-ASBMR-ECTS working group, which met in person and by teleconference over several years to produce this document. The final document was endorsed by the IOF, ASBMR, and ECTS.

Overview of HR-pQCT techniques

The following sections describe the steps involved in the conventional evaluation of bone mineral density and microarchitecture in vivo using HR-pQCT. Each section provides the best practices and considerations when conducting clinical studies. In most cases, the first-generation HR-pQCT (XtremeCT, Scanco Medical AG, Brütisellen, Switzerland) is used as a standard for outlining each step, as it is widely used today. However, these practices are intended to be applicable broadly to other HR-pQCT scanners, namely the second-generation HR-pQCT (XtremeCT II, Scanco Medical AG, Brütisellen, Switzerland), as well as future devices that may be developed by other manufacturers. The basic steps include image acquisition, image processing, image analysis, and reporting of results.

Imaging principles and radiation dose

HR-pQCT provides a method to non-invasively and three-dimensionally evaluate bone mineral density and microarchitecture at high resolutions. The benefit of HR-pQCT over comparable micro-CT systems is the ability to obtain images of human extremities in vivo due to the relatively larger gantry size, at the compromise of somewhat reduced resolution. The basic imaging principles are based on the interaction of ionizing radiation (i.e., X-rays) with matter. As an X-ray beam passes through matter, it is attenuated in relation to the density of the matter, with denser materials such as bone, resulting in greater attenuation than low-density materials, such as soft tissue. In computed tomography, X-ray attenuation data is acquired at multiple projections around the specimen, which allows for a 3D image to be reconstructed [28]. The effective radiation dose from a standard HR-pQCT scan at the distal radius or tibia is 3–5 μSv depending on the scanner generation [29]. In comparison with other common medical imaging techniques, this is considered a low radiation dose procedure. For example, a hip scan using dual-energy X-ray absorptiometry (DXA), commonly used for monitoring osteoporosis, has an effective dose of approximately 9 μSv, a standard chest X-ray has an effective dose of approximately 100 μSv, and a hip CT scan has an approximate effective dose of 286–506 μSv [30, 31].

Image acquisition

Positioning and selection of scan region

Properly positioning the patient's limb in the scanner and identifying the appropriate scan region are fundamental to all imaging protocols. The limb should be immobilized to minimize motion and properly positioned by using a padded, anatomically formed carbon fiber cast provided by the manufacturer. If not scanning bi-laterally, the technician should scan the non-dominant limb, unless prior fracture, surgery, or metal is present, in which case the contralateral side should be scanned.

Once the limb is placed into the gantry of the scanner, a 2D scout view is obtained to select the region of interest for the 3D measurement (this process takes approximately 2–4 min per limb). There are then two approaches used to define the region where the scan is acquired: (1) fixed offset distance and (2) relative offset distance, also called the %-of-length offset. For the fixed offset method, the operator places a reference line at the inflection point on the endplate of the distal radius or tibial plafond, and the scan region begins 9.5 mm and 22.5 mm proximal to the reference line for the radius and tibia, respectively (Fig. 1). The scan region then extends proximally from this point by 9.02 mm (110 slices) for first-generation scanners and 10.20 mm (168 slices) for second-generation scanners [1, 32]. This approach has been implemented in early studies using the second-generation HR-pQCT [32, 33]; however, due to the increased scan region, an additional 1.0 mm is acquired proximally, a predominantly cortical region. As a result, the manufacturer recommendation for the second-generation HR-pQCT is to use a fixed offset of 9.0 mm and 22.0 mm proximal to the reference line for the radius and tibia, respectively [29]. This difference positions the scan region so that it aligns with the center of the first-generation scan region, extending an additional 0.5 mm in both the proximal and distal region.

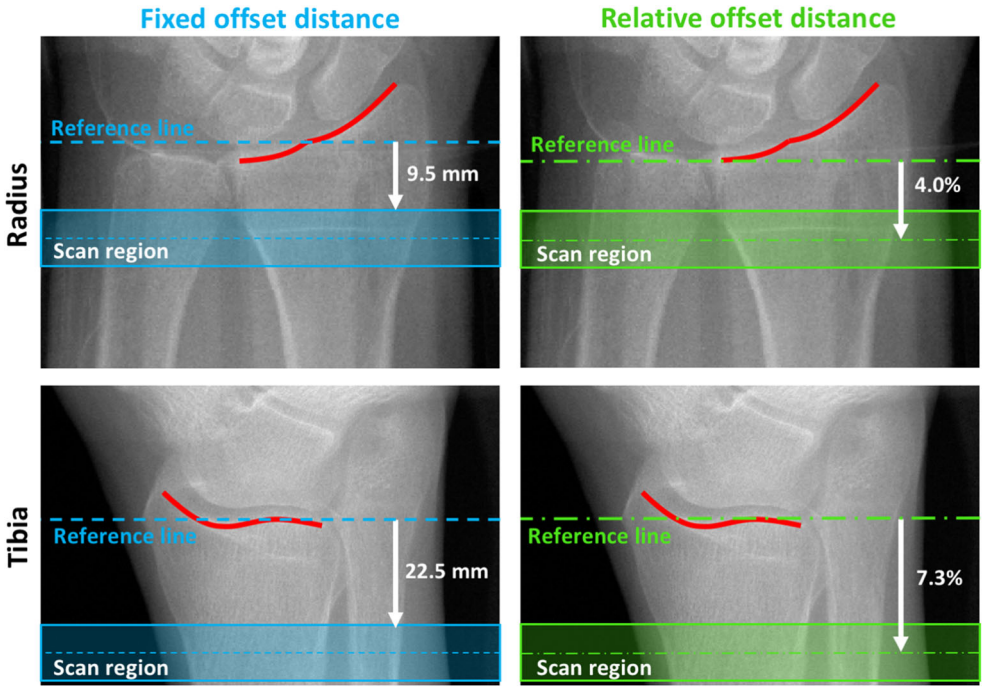

Fig. 1 Scout view from a first-generation HR-pQCT showing reference line placement for the fixed offset distance (left) and relative offset distance (right) methods for the radius and tibia [36]. The edge of the radiocarpal joint surface of the distal radius and tibial plafond are marked in red. Scan regions represented here are approximate and illustrate a scenario where the fixed and relative offsets are aligned

In the %-of-length approach, the operator measures the limb length and then selects a certain percent of the limb length, depending on the specific protocol, as the center point for the scan region. In this approach, the reference line placement is identical as above for the tibia, but for the radius, the reference line is placed at the proximal margin of the radial head (Fig. 1) [34, 35].

The limitation of a %-of-length measure is that it requires an accurate external physical limb length measurement prior to scanning, and it assumes that bone regions (epiphysis, metaphysis, and diaphysis) are proportional to limb length. The ulnar length is recommended as a surrogate for radial length because it is more reliable to identify the distal and proximal ends of the ulna. The ulnar length should be taken as the Euclidean distance between a horizontal surface on which the elbow is rested and the styloid process at the wrist. The tibial length should be taken as the Euclidean distance between the tibial plateau at the knee and the medial tibial malleolus at the ankle [36]. For a detailed description of measurement methods, we recommend the guidelines provided by Bonaretti and colleagues [36]. If using a %-of-length offset, for adults, we recommend the scan position be centered at 4.0% offset from the proximal margin of the radiocarpal joint surface of the distal radius, and 7.3% offset from the tibial plafond (Fig. 1). These relative offsets align, on average, with the standard fixed-length offset of the first-generation scanner. Centering the scan offset in this way yields equivalent variability in distal and proximal directions, minimizing bias introduced by differences in the relative length of the measured limb [37]. In longitudinal studies in adults, limb length should be measured at baseline, and the same length measurement used at follow-up visits in lieu of repeating the limb length measurement at each follow-up time point.

To date, most HR-pQCT studies in adults have employed the fixed offset distance approach, though this method is likely to confound the interpretation of results for studies that compare groups of differing heights (and therefore limb length), such as comparisons by sex and race/ethnicity, and even age, due to secular trends in limb length [37–40]. This is because a fixed distance offset from an anatomic reference results in measurements that are acquired at a relatively "too" distal location in individuals with long limbs and relatively "too" proximal position in individuals with short limbs. These differences cannot necessarily be made equivalent by statistical adjustment for height or limb length [37]. However, while the bone microarchitecture in the metaphyseal region is highly variable as a function of limb length [38], the difference in scan location between a relative (%-of-length) and a fixed offset approach is generally small. Nevertheless, an individual with a stature that is different from the population mean will have some measurement bias exceeding typical motion-induced errors due to positioning from a fixed offset [37, 41].

Another form of measurement error that arises from reference line placement is operator-driven variability. Bonaretti and colleagues reported that intra-operator variability in scan positioning corresponds to up to 4% of the total scan length, while inter-operator positioning variability is up to 7.5% of the total scan length [42]. This translates to significant measurement precision error, often exceeding the precision error attributable to subject motion. Standardized training for scan positioning, described by Bonaretti and colleagues, can reduce operator positioning error by approximately half [42].

In addition to the conventional scan region, it is possible to acquire scans more proximal to the standard position in order to investigate predominantly cortical bone, either as a proximal subset of slices extracted from a standard distal scan [43], an additional contiguous scan [44], or an independent scan proximal to the standard position [26, 45, 46]. Accordingly, there is some evidence that more proximal locations along the radius and tibia provide greater sensitivity to cortical bone changes. The second-generation HR-pQCT allows greater access to proximal scan positions at the forearm and tibia, and it is now possible to develop diaphyseal scan protocol centered at 30% of the ulnar/tibial length using the standard leg and forearm casts, and up to 66% of ulnar/tibial length using custom casts. Acquisition of scans at these regions allows for additional measurement of cortical bone, muscle, and fat, analogous to lower resolution pQCT [47, 48]; however, development of standardized scan acquisition and analysis protocols is ongoing.

In summary, it is recommended that research centers transition to a standardized protocol in future study designs, using the %-of-length offset scan region described above. However, given the historical use of a fixed offset scan region, there exist valuable cross-sectional and longitudinal datasets worldwide based upon this scan protocol. Consequently, the use of the fixed offset is an acceptable alternative, should studies need to compare results to historical databases. Due to differences across research centers, it is important to report in all publications how the scan region was selected, including choice of reference line placement, type of offset (fixed vs. relative), distance of offset, and total scan length.

Scan acquisition and motion artifacts

Scan acquisition varies depending on the in vivo measurement protocol, which is scanner and study specific. The standard protocol and scanner specifications for the commonly used HR-pQCT scanners, XtremeCT and XtremeCT II, are summarized in Table 1.

Scanned images should be inspected visually for motion artifacts, especially at the distal radius due to higher prevalence of motion at this location. Subject motion during image acquisition can lead to degraded image quality and introduce error, particularly for trabecular and cortical microarchitecture [41, 49, 50]. To determine what degree of motion is acceptable, several grading scales have been developed, where the most commonly used is a 5-level motion grading scale (best score is 1, worst score is 5) that aims to differentiate motion on the severity of artifacts, summarized in Fig. 2 [41]. However, even with a standardized scoring system, motion scoring remains subjective, and operator agreement has shown to remain only moderate, even with intensive training [49–51]. Automatic techniques analyzing CT projections have been suggested to provide a standardized approach [50]; however, these procedures have not yet been integrated into HR-pQCT protocols. Until automated techniques are integrated, the 5-level grading scale is recommended, with scoring done consistently by the same operator where possible. At the time of scanning, if motion artifacts with a score of three or more are observed, then it is recommended the scan be repeated.

In general, density-based measures are less sensitive to motion artifacts than structure-based measures. It is acceptable to include all outcome variables from scans with a motion score of three or less, as the precision error is not substantially compromised for density (< 1% error), microarchitecture (< 5% error), and biomechanical parameters, such as estimated failure load (< 4% error) [50]. Scans with a motion score of four may be acceptable for density-based measurements, but should not be used for

Table 1 Technical parameters of first-generation (XtremeCT) and second-generation (XtremeCT II) HR-pQCT standard in vivo scan protocol. Technical specifications adapted from Manske et al. [32]

	First-generation HR-pQCT (XtremeCT)	Second-generation HR-pQCT (XtremeCT II)
Technical specifications		
Energy (kVp)	59.4	68.0
Current (μA)	900	1470
Integration time (ms)	100	43
Field of view (cm)	12.6	14.0
Scan time (min)	2.8	2.0
Stack length (mm)	9.02	10.2
Isotropic voxel size (μm)	82.0	60.7
Spatial resolution (μm)	134.6–154.4	92.5–112.6
Effective patient dose (μSv)	3–5	5
Standard image processing specifications		
Image filtering	Laplace-Hamming filter: ε 0.5, cut-off 0.4	Gaussian filter: σ 0.8, support 1.0
Bone volume segmentation threshold	Global threshold: 400 permille (‰)	Trabecular: 320 mg HA/cm^3, Cortical: 450 mg HA/cm^3
Morphological analysis	Direct and derived measurements	Direct measurements

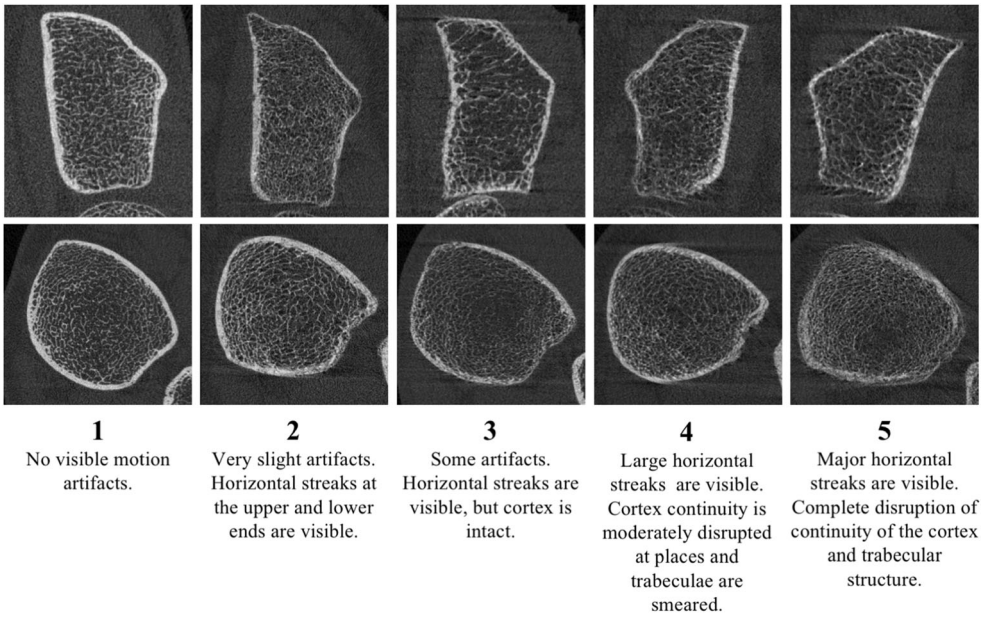

Fig. 2 Motion grading guideline as recommended by the manufacturer and presented by Sode et al. [41], with visual examples provided here for second-generation HR-pQCT radius (top row) and tibia (bottom row) scans

trabecular and cortical microarchitecture or biomechanical assessment. Scans with a motion artifact score of 5 should not be used.

Image processing

Segmentation of the cortical and trabecular bone compartments is necessary for density and structural analysis. Over the past decades, automated and semi-automated methods have been developed to improve accurate and repeatable extraction of the cortical and trabecular compartments.

Standard vs. extended cortical analysis

In the first-generation HR-pQCT standard analysis, the operator guides a semi-automated slice-by-slice contouring process to identify the periosteal boundary of the bone, thereby extracting the bone region from surrounding soft tissue (Fig. 3a). The bone region is extracted using a Laplace-Hamming filter and global threshold cut-off of 400 permille (‰) to generate the segmented bone volume be used for proceeding morphological analysis (Fig. 3b). Delineation of the cortical and trabecular compartments is done automatically using a filter and threshold-based algorithm, where the original greyscale bone region is smoothed using a high-Gaussian weighted filter, then a cut-off of 160 permille (‰) is used to identify voxels that belong to cortical bone [52]. However, this method is insufficient for extraction of the cortex when it is thin and/or highly porous (Fig. 3c) [53, 54] or when the trabecular structure is rich and well connected to the cortex. Thus, an alternate algorithm, the so-called "extended cortical analysis" which uses a dual-threshold segmentation technique, has been incorporated to provide a more robust extraction of the cortical and trabecular compartments [55, 56]. It involves a two-step algorithm to automatically identify the periosteal and then the endocortical surface. In the first step, a connectivity filter is applied to the previously generated segmented bone volume to create a mask of the whole bone region. In the second step, a dilation-erosion operation is applied to the background (i.e., marrow cavity) of the original segmented bone volume to remove trabeculae, thus leaving a mask of the cortical compartment (Fig. 3d) [55]. Once the compartments are defined, the

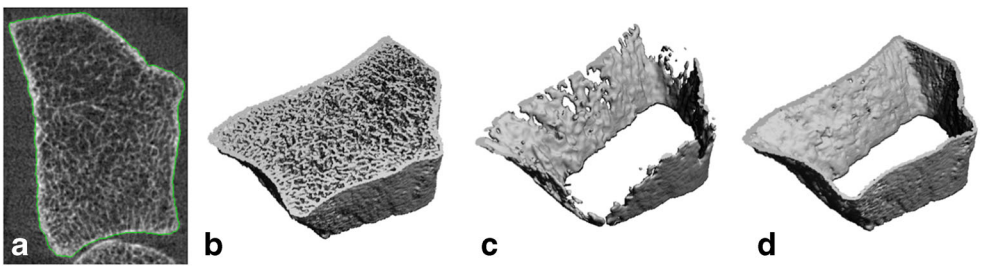

Fig. 3 Example of distal radius scan from a first-generation HR-pQCT and outputs from image processing protocol, where **a** is the greyscale slice-wise view with the periosteal contour (green) identified, **b** segmented whole bone volume, **c** cortical bone region extracted using the standard analysis protocol, and **d** cortical bone region extracted using the dual-threshold technique

extended cortical analysis allows for the assessment of cortical porosity and cortical tissue mineral density, as well as a direct measure of cortical thickness, described in detail in the later sections. With the deployment of the second-generation HR-pQCT scanner, the dual-threshold technique is the default segmentation method, and the image filtration and segmentation thresholds have been adjusted to account for the increased resolution, summarized in Table 1.

Manual correction

Although the dual-threshold technique improves the segmentation of the cortical and trabecular compartments, errors can persist. It is imperative that operators check the periosteal and endocortical contours visually for errors and apply manual corrections as necessary. Omitting corrections of the automatically generated contours leads to greater accuracy errors arising in very low- or high-density bone, resulting in a systematic bias with certain parameters, such as cortical density and thickness [57]. This has the potential to skew the results of studies that investigate osteoporotic or highly active populations; therefore, we advise that contours be checked and manually corrected [57].

Drawbacks to manual corrections include the increased time spent visually inspecting images and the potential for increased precision error that arises when manual corrections are applied [58, 59]. In particular, the endocortical contour can be highly subjective in low-density bone, and human interpretation by one or more operators introduces precision error. Nevertheless, inter-operator variability introduces less error than the accuracy error resulting from uncorrected contours [59], and short-term precision between using corrected versus uncorrected contours is comparable [58]. If manual corrections are applied, it is essential the operator has a suitable level of training to minimize precision error [57].

Image analysis

The defined cortical and trabecular compartments are the basis for measuring density and microarchitecture properties. Tables 2 and 3 provide a summary of common parameters, units, and methods of measurement from HR-pQCT modalities as have been previously described in the literature [1, 32].

Trabecular microarchitecture

Trabecular microarchitecture is assessed from the segmented image; however, the spatial resolution of the first-generation HR-pQCT limits the ability to measure trabecular thickness, and as a result, some of the trabecular morphology measures are derived using 2D stereologic methods rather than directly measured. Specifically, trabecular bone volume fraction (Tb.BV/TV) is computed as the ratio of the trabecular bone mineral density (Tb.BMD) and 1200 mg HA/cm^3, which is assumed to be the density of fully mineralized bone (Table 3). Alternatively, trabecular number (Tb.N) is directly measured using a ridge extraction technique [52]. Trabecular separation (Tb.Sp) and trabecular thickness (Tb.Th) are then derived from these two parameters assuming a plate-like morphology, as described in Table 3 [60].

In contrast, the second-generation HR-pQCT has sufficient spatial resolution to "directly" measure Tb.BV/TV, Tb.Th, and Tb.Sp. Accordingly, Tb.BV/TV is defined as the ratio of voxels in the mineralized bone phase to the total number of voxels in the trabecular compartment. Tb.Sp and Tb.Th are measured using the distance transformation method, where 3D distances are estimated by fitting maximal spheres inside the structure (or void space in the case of Tb.Sp) and taking the average sphere diameter as the mean thickness [61].

In addition to common morphometric indices, additional parameters have been developed to estimate the level of anisotropy in trabecular microarchitecture from HR-pQCT images. These non-metric indices include the structure model index (SMI) [60], connectivity density (Conn.D) [62], and mean intercept length (MIL) [63], outlined in Table 3. Another non-standard analysis includes individual trabecular bone segmentation (ITS)–based morphological analysis [64]. This approach performs a complete volumetric decomposition of individual trabecular plates and rods to characterize bone morphology and orientation of trabecular bone. These non-standard analyses are susceptible to resolution effects and demand cautious interpretation.

Cortical microarchitecture

Primary cortical microarchitecture parameters include the cortical thickness (Ct.Th) and cortical porosity (Ct.Po). The standard analysis for first-generation HR-pQCT derives Ct.Th from the mean cortical volume divided by the periosteal surface area. However, in the extended cortical analysis, the cortical thickness is directly measured using distance transformation methods once the cortical compartment has been extracted using the dual-threshold segmentation technique. Measurement of Ct.Po is limited by the spatial resolution of the HR-pQCT images, as Haversian canals can range in size from 30 to 350 μm. However, it is estimated that pores smaller than 90 μm contribute to only 5–8% of the total pore volume [65]. Measurement of Ct.Po is improved with the second-generation of HR-pQCT due to increased resolution [33].

Two methods currently exist to assess Ct.Po: (1) the threshold-based approach [55, 56] implemented in the XtremeCT analysis software provided by Scanco and (2) the density-based approach implemented in the StrAx1.0 software [43]. The threshold-based approach is a fully automated segmentation contouring approach integrated with extended

Table 2 Definition, units, and measurement of methods of common whole bone and cortical microarchitecture parameters obtained from available HR-pQCT systems. Italicized parameters are the minimum set to be reported when describing cortical bone morphology

Parameter	Abbreviation and standard units	Description	Measurement method	
			XtremeCT	XtremeCT II
Densities and areas				
Total bone mineral density	**Tt.BMD (mg HA/cm^3)**	Average mineral density within the periosteal surface	Calculated directly from the greyscale image data	
Cortical bone mineral density	**Ct.BMD (mg HA/cm^3)**	Average mineral density within the cortical compartment	Calculated directly from the greyscale image data	
Cortical tissue mineral density	Ct.TMD (mg HA/cm^3)	Average mineral density of the segmented cortical bone	Calculated directly from the greyscale image data, after pores have been masked from the region of interest.	
Total area	Tt.Ar (mm^2)	Measure of total cross-sectional area within the periosteal surface	Mean cross-sectional area of cortical compartment in all image slices	
Cortical area	Ct.Ar (mm^2)	Measure of the total cross-sectional area within the cortical bone compartment	Mean cross-sectional area of region within periosteal surface in all image slices	
Cortical bone microarchitecture				
Cortical thickness	**Ct.Th[d]| Ct.Th (mm)**	Average thickness of the cortical compartment	Volume of the cortical compartment divided by the periosteal surface[†]	Mean spacing of the periosteal and endocortical surfaces, measured using the distance transformation method[*]
Cortical perimeter	Ct.Pm (mm)	Length of periosteal perimeter	Mean of periosteal perimeter in all image slices	
Cortical porosity	**Ct.Po[d]| Ct.Po (%)**	Ratio of pore volume relative to the total volume of the cortical compartment, reported in percentage	Threshold-based approach: Ratio of volume of pores relative to the total volume in the cortical compartment[*] Density-based approach: The ratio of voxel-by-voxel void space to fully mineralized bone (1200 mg HA/cm^3) in compact cortical compartment[‡]	
Cortical pore volume	Ct.Po.V (mm^3)	Total volume of cortical pores	Summation of pore voxels in the intra-cortical region[*]	
Cortical pore diameter	Ct.Po.Dm (mm)	Average 3D diameter of the pore volumes	Mean spacing of the segmented cortical pores using the distance transform method[*]	

[d] Superscript should be used if reporting results using the derived measurement method

[*] Description of direct 3D morphological method of measurement

[†] Description of derived (indirect) morphological method of measurement

[‡] StrAx is a derived method with analysis bone compartments defined differently than the extended cortical analysis [55, 56] and is not integrated into the Scanco workflow

Ideally the minimum set of parameters reported are bolded

cortical analysis method. Briefly, intra-cortical porosity (Ct.Po) is calculated as the ratio of the total pore volume within the cortical compartment to the sum of the cortical volume [56]. This method has the advantage of segmenting the individual pores from the scan, which allows for structural information to be measured, including mean cortical pore diameter (Ct.Po.Dm); however, it is limited to capturing only pores within the limits of resolution and pores that do not intersect the periosteal or endocortical surfaces.

Alternatively, the density-based approach segments bone into a compact-appearing cortex, transitional zone, and trabecular compartment, described in detail elsewhere by Zebaze and colleagues [43]. In brief, Ct.Po is quantified in each of these regions by assuming that fully mineralized bone has a density between 1000 and 1200 mg HA/cm^3. Voxels with a density lower than 1000 mg HA/cm^3 indicate that some ratio of the voxel, proportional to its density, is composed of void space (i.e., pores). Porosity is quantified by estimating the ratio of void space present in each voxel and taking the mean across all voxels in the compartment of interest [43]. The density-based method of assessing Ct.Po aims to capture pores with diameters below the spatial resolution of the scanner; however, it relies on the assumption of a fixed bone tissue mineral density and is susceptible to image noise and beam hardening.

Table 3 Definition, units, and measurement of methods of common trabecular microarchitecture parameters obtained from available HR-pQCT systems. Italicized parameters are the minimum set to be reported when describing trabecular bone morphology

Parameter	Abbreviation and standard units	Description	Measurement method	
			XtremeCT	XtremeCT II
Density and area				
Trabecular bone mineral density	**Tb.BMD (mg HA/cm^3)**	Average mineral density within the trabecular compartment	Calculated directly from the greyscale image data	
Trabecular area	Tb.Ar (mm^2)	Cross-sectional area of the trabecular compartment	Mean cross-sectional area of trabecular compartment in all image slices	
Trabecular bone microarchitecture				
Trabecular bone volume fraction	Tb.BV/TV[d] | **Tb.BV/TV (%)**	Ratio of segmented bone volume to total volume of the trabecular compartment, reported as a percentage.	(Tb.BMD/1200 mg HA/cm^3) × 100[†]	Ratio of voxels in the mineralized bone phase to the total number of voxels in the trabecular compartment [*]
Trabecular number	**Tb.N (1/mm)**	Average number of trabeculae per unit length	Mean inverse of the spacing between mid-axis (ridges) of the trabeculae. Ridges are identified using ridge extraction technique[*]	
Trabecular separation	**Tb.Sp[d] | Tb.Sp (mm)**	Average distance between trabeculae	(1 – BV/TV)/Tb.N[†]	Mean separation between trabeculae measured using the distance transformation method applied to the background (void space) of the structure[*]
Trabecular thickness	**Tb.Th[d] | Tb.Th (mm)**	Average thickness of trabeculae	Ratio of BV/TV to Tb.N[†]	Mean spacing of the segmented trabecular structure, measured using the distance transformation method[*]
Inhomogeneity of trabecular network	Tb.1/N.SD (mm)	Measure of inhomogeneity of trabecular separation	The standard deviation of the spacing between mid-axis (ridges) of the trabeculae[*]	
Structural model index	SMI (unitless)	Quantification of structural appearance of trabeculae	Calculated from the derivative of the trabecular bone surface area. SMI of 0 indicates plate-like structure, 3 indicates rod-like structure, and 4 indicates sphere-like structure [60].	
Connectivity density	Conn.D (1/mm^3)	Measure of the connectivity of the trabeculae	Calculated using the Conn-Euler method [62]	
Degree of anisotropy	DA (unitless)	Measure of the anisotropy of the trabecular structure.	Estimated as the longest divided by the shortest principal directions of the mean intercept length ellipsoid. A DA of 1 is isotropic.	

[d] Superscript should be used if reporting results using the derived measurement method

[*] Description of direct 3D morphological method of measurement

[†] Description of derived (indirect) morphological method of measurement

Ideally the minimum set of parameters reported are bolded

A comparison of methods for in vivo assessment of Ct.Po revealed that both approaches are well correlated with gold standard porosity measurements from synchrotron radiation micro-computed tomography (SRμCT); however, each method has inherent systematic errors. In compact-appearing cortical bone specimens, the threshold-based approach underestimates Ct.Po by 3 to 11% as it does not capture smaller pores, whereas the density-based approach overestimates Ct.Po by 6 to 21% due to misclassifying image noise and artifacts as void space [65]. The threshold-based approach has improved accuracy in Ct.Po measurements with the second-generation HR-pQCT as this approach is resolution-dependent, whereas the density-based approach would not be impacted as it is not resolution-dependent. Both methods are widely adopted measures of Ct.Po, but due to methodologic differences, they cannot be directly compared and study methodologies should clearly state which method is used.

Finite element analysis

Morphometric parameters are numerous and provide valuable insight describing the structure of a bone, but the interpretation of these data can be complex. Finite element (FE) analysis is a computer modeling technique that, when coupled with HR-pQCT, provides a non-invasive approach to intrinsically account for the complex bone structure and estimate bone strength [66]. The fundamental requirements for an FE model are selecting the bone geometry, assigning material properties, and defining boundary conditions to simulate loading

conditions, typically determined through validation studies using experimental loading tests of cadaveric bones [67–69]. The application of FE procedures to HR-pQCT images has been explored in depth and is often referred to as micro-FE (μFE). Most HR-pQCT-based μFE models to date have defined constitutive properties that are linear, with uniform elastic material properties. However, non-linear models and density-based elastic material properties have also been implemented [67, 70–72]. Here, we outline key considerations and recommendations when choosing a μFE procedure, with a specific focus on linear, homogeneous models for standard HR-pQCT scan regions.

Model generation and boundary conditions

Geometry is determined from the segmented HR-pQCT image by converting it into an FE mesh, most commonly using a voxel-by-voxel conversion where each voxel is converted into a cubic hexahedral finite element [73]. First-generation HR-pQCT images typically result in FE models with 1–9 million elements [66] and second-generation in the range of 2–24 million elements, depending on the scan site and bone volume, resulting in a direct representation of the bone microarchitecture (Fig. 4).

Boundary conditions are selected to simulate a loading condition. Standard HR-pQCT scans are best suited for simulating a compression test along the z-axis (longitudinal axis), defined perpendicular to scan cross-section. One end is assigned a fixed constraint in the z-direction and a fixed displacement is applied to the opposite end resulting in 1% apparent strain. If the fixed constraint surface includes conditions that prevent lateral expansion during compression, the test is referred to as axial compression; otherwise, it is termed a uniaxial compression. The results of a compression test will differ slightly depending on whether axial or uniaxial boundary conditions are applied, but they are strongly linearly associated ($r^2 > 0.99$), and methods have been developed to allow harmonization by applying a linear correction factor [74].

Material properties must also be defined for the model, including Poisson's ratio and the elastic modulus (also called the tissue modulus or Young's modulus). A Poisson's ratio of 0.3 is conventionally used for all μFE models. However, selection of the elastic modulus requires closer consideration as it ultimately defines the stiffness of the material under tension or compression. The most common approach is to assign a uniform elastic modulus, previously determined through direct comparison to experimental loading tests, to all bone tissue in the model. A summary of common elastic modulus values (and their respective boundary conditions) for first- and second-generation HR-pQCT scanners are summarized in Table 4. The modulus utilized for a given scanner generation will not yield the same results if applied to another generation, as the elastic modulus is dependent on both the mesh resolution and segmentation protocol, which impact the bone structure extracted from the image. Hence, for second-generation HR-pQCT, an elastic modulus of 8748 MPa has been back-calculated from the modulus validated for the first-generation HR-pQCT [74], and 10,000 MPa has been determined from direct comparison to experimental loading tests [68].

FE outcomes

Table 5 provides a summary of common outcomes from μFE models, with proposed nomenclature and units. The most relevant primary outcomes include stiffness [kN/mm] and yield load, commonly referred to as the estimated failure load [kN]. A linear, elastic FE model intrinsically cannot directly measure failure load; however, non-linear approaches that are more appropriate for strength measurement are computationally demanding and therefore not often employed in high-resolution models [67, 75]. Instead, a failure criterion often used with linear FE models assumes bone yields when a specified volume of bone tissue (critical volume) exceeds a specified critical strain. This is often referred to as the "Pistoia criterion", and a typical set of yield parameters used assumes failure load can be estimated when the critical strain of 0.7% is exceeded for 2% for the bone tissue [76]; however, a complete table of commonly used yield parameters are provided in Table 4. Use of the Pistoia criterion for HR-pQCT-derived μFE models has led to strong correlations (r^2 = 0.73–0.95) with experimentally measured whole bone strength for the first-generation HR-pQCT [67, 77, 78], although some have suggested a 7.5% critical volume and 0.7% critical strain are more appropriate [77]. For the second-generation HR-pQCT, where scan volume and resolution differ, appropriate criterion needs to be adjusted [74]. A recent study by Arias-Moreno and colleagues determined that the appropriate failure criterion for the second-generation HR-pQCT should be a critical strain of 1.0% and critical volume of 5% under axial loading conditions [68]. Regardless of the specific parameters chosen, these variations of criteria provide highly comparable correlations with experimental bone strength and have been shown to be suitable predictors for failure load, but absolute values obtained using different yield parameters should not be directly compared. μFE-estimated failure load at the distal tibia scan site has also been shown to be well correlated to bone strength at the femoral neck and vertebra [79].

A common misconception is that μFE models predict failure load in a fall condition; however, boundary conditions in that scenario are prohibitively difficult to estimate with an enormous range of loading possibilities. Instead, standardized axial or uniaxial μFE tests of bone strength provide a reproducible approach that gives insight into the effect of bone microarchitecture on estimated bone strength. In addition to the failure load, there are several other μFE model outputs that provide additional insight into the biomechanical properties of bone, details are provided in Table 5.

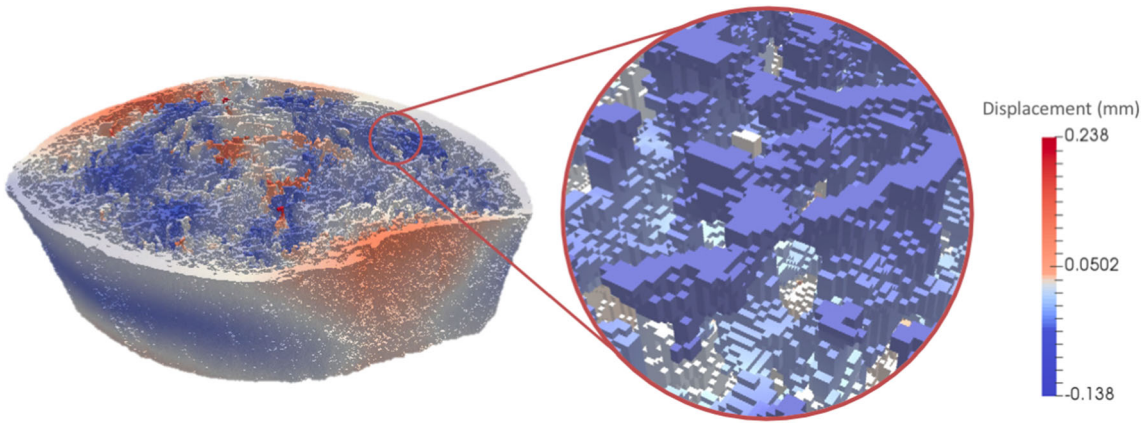

Fig. 4 Example of a segmented second-generation HR-pQCT tibia scan converted into an FE mesh using a voxel-by-voxel conversion approach. The model is composed of millions of hexahedral elements

In summary, for first-generation HR-pQCT, the choice of boundary conditions, elastic modulus, and yield criterion have varied among studies, but harmonization techniques are available to compare results using the different configurations summarized in Table 4 [74]. For the second-generation HR-pQCT, we recommend using an elastic modulus of 10,000 MPa with axial boundary conditions, and yield criterion of 1.0% critical strain and 5% critical volume. However, if this is not feasible, harmonization methods like those used for the first-generation HR-pQCT should be developed and used to compare results across studies [74]. As future systems become available, it will be necessary to determine the appropriate elastic modulus and yield criterion through back-calculation or direct validation for that particular system, ideally so that comparisons across HR-pQCT technologies are possible.

FE solvers

Due to the resolution of the images, μFE models tend to be very large, on the order of 10s of millions of degrees of freedom, and thus, the models pose a challenge for traditional commercial FE solvers. Fortunately, this problem has been overcome by the use of specialized solvers that are designed to leverage the fact that each element in the model (i.e., voxel) has the same hexahedral shape [80]. Scanco Medical provides built-in linear elastic FE software for the XtremeCT and XtremeCT II scanners, with libraries of pre-defined tests that may be applied. Specialized third-party FE solvers are also available that allow for faster computation time and flexibility, including commercial software (e.g., Numerics88 Solutions) as well as open-source versions (e.g., ParFE).

Table 4 Summary of elastic modulus, boundary conditions, and common yield criterion for first- and second-generation HR-pQCT. All models applied a 1% compressive strain in the axial direction and used a Poisson's ratio of 0.3. Unless specified, the proposed yield criterion and associated constitutive properties were compared with mechanical compressive loading tests; however, loading configurations relative to the scan region vary across studies [67–69, 74, 76, 77, 111]

Reference	Elastic modulus (MPa)	Boundary conditions	Yield criterion (critical strain, critical volume)
First-generation HR-pQCT			
Pistoia et al. Bone. 2002/Pistoia et al. J Clin. Dens. 2004*	10,000	Axial	0.7%, 2%
MacNeil et al. Bone 2008	6829	Uniaxial	0.7%, 2%
Mueller et al. Bone 2009	6829	Uniaxial	0.7%, 7.5%
Vilayphiou et al. Bone 2010†	Trabecular bone: 17,000 Cortical bone: 20,000	Axial	0.35%, 2%
Second-generation HR-pQCT			
Whittier et al. J Biomech 2018	8748	Uniaxial	0.7%, 2%
Arias-Moreno Osteoporosis Int 2019	10,000	Axial	1.0%, 5%

* Original validation studies were conducted using a 3D-pQCT scanner with 165 μm isotropic resolution; however, these parameter specifications have been frequently applied to first-generation HR-pQCT

† Yield criterion with associated tissue properties and boundary conditions were not explicitly validated in this study

Table 5 Definition, units, and measurement of methods of common micro-finite element analysis outcomes obtained from available HR-pQCT systems

Parameter	Abbreviation and standard units	Description
Primary model outputs		
Estimated failure load	FL (kN)	Estimate failure load is indirectly estimated from linear FE models using a yield criterion. When a specified volume of bone tissue (critical volume) exceeds a specified critical strain, the model is assumed to have yielded. This is often referred to as the Pistoia criterion.
Stiffness	Stiffness (kN/mm)	The total reaction force of the model divided by the applied displacement.
Additional model outputs		
Reaction force	RF (N)	The force required to induce the applied strain (typically 1%) in the model.
Compartment load distribution	$Load_{cort,dist}$ (%) $Load_{cort,prox}$ (%) $Load_{trab,dist}$ (%) $Load_{trab,prox}$ (%)	The ratio of the force carried by the trabecular and/or cortical compartments, at the distal and proximal ends of the model. It is sufficient to only report the load shared by one compartment, and the choice of reporting distal and/or proximal end is dependent on the research question.
Apparent modulus	E_a (kN/mm^2)	The average stress divided by the applied strain of the model. The average stress is the total reaction force divided by the average slice area. The applied strain is calculated as the applied displacement [mm] divided by the original height of the model (mm).
Tissue-level outputs*		
Average von Mises stress	$Stress_{VM}$ (MPa)	Scalar measure of the deviatoric stress accounting for the three principle axes. It can be used for yield criterion or as a heuristic measure of the magnitude of the stress at a given point.
Strain energy density	SED (J/mm^3)	The strain energy per unit volume of bone tissue. Strain energy is the increased energy associated with deformation in the FE model.

* These properties are scalar values defined for each element. Properties can be visualized on the model to inspect localized stress and strains, or expressed in terms of histograms. The average or median value across the model can be reported, and the histogram skewness or kurtosis can be used to provide insight into the strain distributions in the context of bone adaptation

Assumptions

It is important to be aware that μFE carries assumptions about tissue behavior. For instance, in μFE models, bone is assumed to be isotropic and behave purely linearly, both of which are only approximations of the true case. If applied to the atypical bone, this could possibly result in erroneous assumptions about bone strength in certain circumstances (e.g., osteogenesis imperfecta, fracture healing, or altered tissue-level properties) and care must be taken in designing studies and interpreting μFE results in these cases.

Image registration for longitudinal studies

A growing number of studies are producing longitudinal data to evaluate the effects of aging [10, 81] as well as pharmacologic [19, 82] or exercise interventions [25]. Small differences in participant positioning in follow-up scans can result in variations of axial position and in the degree of tilt, illustrated in Fig. 5, and this reduces the ability to detect longitudinal change, particularly for parameters that vary considerably along the length of the bone (e.g., cortical geometry). Despite procedures to ensure that positioning is standardized as much as possible during each image acquisition, small variations in the scan region are inevitable. Consequently, reproducibility has been shown to be suboptimal with precision errors for trabecular and cortical parameters of up to 7.0% and 20.3% RMS-CV% respectively in the radius [83]. Registration techniques reduce positioning errors and are necessary in longitudinal studies to ensure the same region of the image is analyzed at each time point.

2D registration

A common 2D registration technique uses the total cross-sectional area of each slice to determine an optimal offset

between paired (baseline and follow-up) scans resulting in a common volume of interest with a subset of the original slices acquired [56]. This 2D technique is implemented in the Scanco software. It is capable of correcting for discrepancies in an axial direction, but cannot take into consideration the variation in tilt of the limb (Fig. 5). Notably, the 2D registration technique precludes evaluation of periosteal bone apposition and thus limits the interpretation of studies where a change in bone size is anticipated, such as growth, exercise, or perhaps aging over an extended observation.

3D registration

Methods using 3D rigid registration account for both positional (axial) and angular differences in images by determining the necessary 3D transform (translational and rotational) between two images. The method is based on optimally overlapping all image data within a volume of interest (e.g., within the periosteal contours) and so noise or structures outside the bone of interest do not impact registration. It is somewhat more complex to implement because it requires an optimization process, typically including a pre-alignment (e.g., based on the center of masses of the two images) followed by an optimizer-guided alignment based on a metric of best overlap (e.g., mutual information), ultimately resulting in a 3D transform matrix [84]. Strategies to maximize efficiency and minimize risk of errors include using downscaled images for initial alignment, and then increasing to full resolution to refine the alignment. Nevertheless, as with any automated process, it can result in errors and therefore it is imperative to visually assess the degree of overlap to ensure a reasonable solution has been achieved. The resulting 3D transform is used to identify a common region between multiple scans in a series, and the masks for that region are transformed, rather than the images themselves, to prevent image degradation associated with interpolation [84]. Currently, the 3D registration procedures are not part of the standard Scanco software.

While 3D registration provides excellent reproducibility for morphological parameters, it is unfortunately not as effective for μFE analysis. The application of boundary conditions to non-parallel surfaces resulting from common regions of interest from 3D registration in μFE models is not trivial, and currently, there is ongoing research in this area. To date, reproducibility of μFE outputs has not been found to be greater with 3D than 2D registration; therefore, use of 3D registration is not yet recommended for μFE [84]. Instead, the recommended approach is to apply μFE to 2D registered data, but only relative changes should be compared in this context and not absolute outcomes, as a shorter segment of bone will yield different results from a full-height image. If absolute outcomes are to be compared, unregistered data should be used for μFE analyses and comparisons.

Additional considerations for image registration

Typically, in longitudinal studies, the periosteal and endocortical surfaces are defined independently between baseline and follow-up scans. However, in some cases, it may be preferable to compare changes in a fixed region over time, such as for detecting trabecularization of the cortical region. This can be accomplished by taking the defined cortical and trabecular regions at baseline and applying these to the follow-up scans (in lieu of re-defining the regions independently) [85]. This method ensures the exact same region of bone is compared between baseline and follow-up. Consequently, this approach precludes detecting changes in cortical thickness, perimeter, or changes in total, cortical, or trabecular areas. When conducting 3D registration, it is important to specify if trabecular and cortical compartments were defined independently or if regions were defined at baseline and applied during registration on follow-up scans.

There are circumstances where the value of registration may be diminished. In long-term treatment and aging studies, there can be significant changes in bone geometry and microstructure. This can lead to inaccuracies when using both 2D and 3D registration. Consequently, shorter intervals may be required to allow sequential transformations to take place, with smaller incremental changes, to allow a more optimal

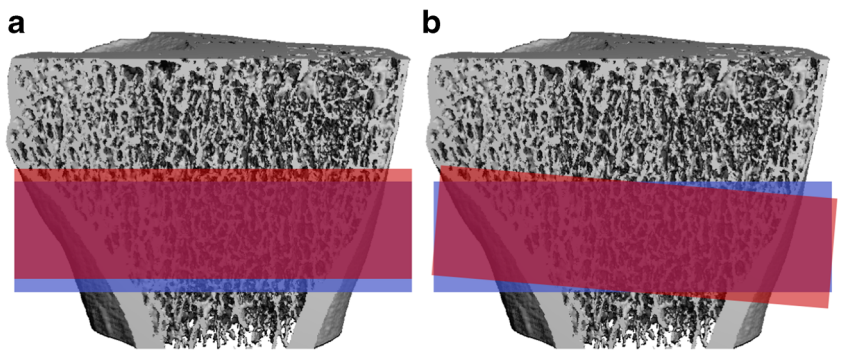

Fig. 5 Examples of axial (**a**) and angular (**b**) offsets in between scan regions captured at baseline (blue) and follow-up (red)

comparison of bone health between the start and end of the study. Furthermore, in children, bone growth leads to challenges because a fixed distance from the endplate will gradually become a more distal part of the bone and bone size is anticipated to change substantially [86]. Lastly, in the case of fracture healing, rapid remodeling occurs that changes overall bone geometry [71, 87] which poses challenges in terms of image registration and longitudinal comparison of bone morphology. It is imperative to visually inspect registered images to confirm that unexpected errors have not occurred during registration before the quantitative assessment is performed.

In general, follow-up scans should be registered to ensure the equivalent region is assessed, where 3D registration is the preferred method; however, if this approach is not feasible, 2D registration is an acceptable alternative. In both cases, a reasonable level of overlap must exist to include results from morphological or μFE analysis, so that the region is representative of the full scan length. An optimal minimum overlap between baseline and follow-up scans has not been validated, but we recommend a minimum volumetric overlap of 75%. There are circumstances where in a series of multiple follow-up scans there is one scan that is poorly positioned (i.e., less than 75% overlap). Rather than removing the entire series, that single scan can be removed so that the remainder of the subject's data can be used in the analysis. The choice of overlap cut-off should be specified in the study design and median or average overlap reported in the results.

Reporting results

Reporting density and morphometric data

The decision of which density and microarchitecture parameters to report depends on the research question. Nevertheless, with the goal of developing standardized procedures for using HR-pQCT in clinical studies, a minimum set of parameters should be reported to appropriately characterize the trabecular and cortical bone. As the research field shifts from the first-generation to the second-generation HR-pQCT, appropriate terminology is necessary, as certain morphological parameters, such as Tb.Th, have fundamentally different methods of measurement between scanner generations and thus cannot be directly compared.

Historically, with the introduction of direct 3D morphological measures, bone microarchitecture that was measured directly instead of derived was denoted with an asterisk (e.g., Tb.Sp*) [61]. However, this naming convention has not been used consistently in the literature. As direct measurement becomes more commonplace with regular use of the extended cortical analysis protocol and shift towards the second-generation HR-pQCT, we propose instead that direct measures be denoted without an asterisk (e.g., Tb.Sp), whereas derived measures be identified with the superscript "d" (e.g., $Tb.Sp^{d}$). Although the type of measurement method can often be inferred based on the scanner generation, it is more appropriate to use explicit nomenclature. Although inconsistencies exist in literature to date, this approach will help avoid confusion in future studies. For example, Ct.Th can be measured directly or derived using the first-generation HR-pQCT scanner, but if not explicitly stated it is not clear which approach was used. Tables 2 and 3 provide a summary of recommended terminology for common indices for future studies, and the minimum set of parameters to be reported are provided in bold.

Reporting μFE data

The choice of reported μFE outputs should be chosen with consideration of what biomechanical properties are most relevant to the research question. In many cases, μFE outputs are highly correlated, and it is not advised to report all available parameters without reasonable justification. Commonly reported parameters for standard HR-pQCT scans are summarized in Table 5. Primary outcomes are strength estimates (such as failure load) and stiffness; it is recommended at least one of these parameters is reported at a minimum; however, it is usually not necessary to report both due to high correlation (i.e., $r > 0.9$). Other insightful parameters include load distribution properties, specifically compartment load sharing at the distal and proximal ends of the scan region, or in certain cases stress/strain distributions within the model. As μFE outputs are highly dependent on model properties and loading conditions, it is important to provide sufficient details of the μFE analysis conducted (as summarized in Table 4) as well as the mesh generation method, and computational solver used. Additional information that is beneficial to report, especially for non-standard scan sites or techniques, is the model complexity (usually reported and the average number of elements in the models), the average computation time per model, and specifications of the computing system (i.e., hardware) used.

Precision error

An important factor in the clinical application of HR-pQCT is its ability to produce highly precise and accurate results. Precision error arises from a combination of technical and operational factors and is specific to the scanner, parameter, operator(s), and study design. As discussed throughout this article, important contributors to precision error are motion artifacts [49, 51], subject positioning and reference line placement [42], manual correction of periosteal and endocortical contours [58, 59, 88], and use of registration techniques [84]. Precision error is most often reported as the root-mean-squared coefficient of variance (RMS-CV%) of

repeated measurements in a group of individuals. Reported ranges of short-term precision for first- and second-generation HR-pQCT are summarized in Table 6 [27]. Although these ranges provide an idea of expected precision error, it is nevertheless dependent on the individual scanner and operators, and precision should be determined for each scanner and research center in a manner that reflects the study design. For cross-sectional study designs, precision should be measured without registration techniques applied. Longitudinal studies should report precision values with registration applied in a manner that reflects the technique that will be applied to the dataset. In addition, the precision measurements should be conducted on a cohort that reflects the demographics of the study (i.e., elderly versus younger subjects).

Reporting results from longitudinal studies

When reporting results for longitudinal studies, the method used for image registration should be reported, along with the average amount of overlap obtained between accepted baseline and follow-up scans, and the number of scans or subjects excluded from the analyses due to poor overlap. Depending on the study design, investigators may also consider reporting results in comparison with the least significant change (LSC), defined as the minimum change observed in an individual that can be considered statistically significant ($p < 0.05$), calculated by multiplying precision error by 2.77 [89]. A summary of ranges reported for LSC (primarily from the first-generation XtremeCT) is provided in Table 6; however, LSC should be estimated from the precision error of the specific scanner and registration methods used.

Considerations for multiple comparisons

Due to the large number of parameters that are produced using HR-pQCT and high correlation between some parameters, studies are susceptible to the issue of multiple comparisons and falsely positive statistical tests, or type I error. For example, there are often at least 11 parameters that are presented in HR-pQCT studies (see Tables 2 and 3) and this number is multiplied by two when examining both the radius and tibia. If a p value threshold of 0.05 is used to denote statistical significance between groups, then it is expected that by chance at least one comparison may be significant, when in reality it is not. When reporting results, investigators must interpret their results with this in mind.

Although there are no specific recommendations for how to address this issue, one approach could be to formally control for the potential of false-positive statistical tests, with the selection of statistical test dependent on the study design and power. The most conservative approach would be a Bonferroni correction, an alternate option is the Benjamini-Hochberg correction, which is advantageous as it accounts for the false discovery rate with a limited impact on power. It also favors large studies and it is easy to implement [90, 91]. Another way to preserve power in small studies could be to use a hierarchical method, adjusting for the false discovery rate [92]. Though not commonly employed for HR-pQCT studies, this method has the theoretical advantage of relying on a priori hypotheses in the analysis of HR-pQCT data. For instance, a first step could be to test for differences in total density, then in trabecular and cortical density if the comparison of total density is significant. Thereafter, the various parameters of each compartment can be tested if there is a significant difference for the compartment [93].

Quality control and training

Routine steps should be taken to ensure that the HR-pQCT system is working properly, and operators should be trained appropriately. The system should undergo routine service and maintenance check by the manufacturer annually.

Table 6 Precision error ranges, reported as the RMS-CV%, for first-generation (XtremeCT) and second-generation (XtremeCT II) scanners. First-generation ranges are from the meta-analysis conducted by Mikolajewicz and colleagues [27], and second-generation ranges were obtained from short-term reproducibility studies conducted to date [33, 88, 112]

Parameter	XtremeCT		XtremeCT II	
	Short-term precision (%)	LSC (%)	Short-term precision (%)	LSC (%)[†]
Density measurements	0.8–2.0	2.0–5.6	0.4–2.4	1.1–6.6
Area measurements	2.3–4.0	6.2–11.0	0.4–3.3	1.1–9.1
Trabecular microarchitecture	4.1–4.9	11.3–13.6	0.8–2.7	2.2–7.5
Cortical thickness	1.6–3.6	4.4–9.9	1.1–2.9	3.0–8.0
Cortical porosity	6.2–12.5	17.1–34.5	11.0–13.7	30.5–37. 9
μFE outputs	2.0–3.5	5.4–9.6	0.9–1.3	2.5–3.6

[†] LSC values were calculated by multiplying reported short-term precision error by 2.77

Daily and weekly quality control

The user should follow the manufacturer's protocol for quality control to ensure the system is functioning properly. This typically includes daily and weekly scans of a quality control phantom to check performance prior to in vivo scanning and to monitor the stability of density and microarchitecture parameters. A drift over time in the phantom measurements signals decay in the X-ray emission, which has the potential to confound longitudinal studies if not addressed. Use of Shewhart charts to track scanner stability is recommended, and although no specific guidelines for when a scanner should be recalibrated have been developed, typical changes on the order of 1.5% from the mean phantom density are considered a threshold for when an intervention should take place. Daily quality control scans should also be inspected visually to identify common artifacts, such as ring artifacts, or distortions that would affect measurement outcomes. These should only be corrected by the manufacturer during routine maintenance, but it is prudent for the user to carefully monitor image quality control.

Operator training

Operator training is an essential aspect of obtaining high-quality data. Although there is no formal training course or certification for operators of the HR-pQCT device, it is recommended that new operators undergo thorough training from experienced operators in patient management and positioning, location of the reference line, and manual correction of contours generated by the automated and semi-automated protocols. Unfortunately, limited formal training is available despite the knowledge that scan precision and inter-operator variability can be reduced using a standard training platform [42]. In terms of reference line placement, it is recommended that new operators complete the online training developed by UCSF (http://webapps.radiology.ucsf.edu/refline/) [42]. Comparable training for contouring has yet to be developed, and so it is recommended new operators receive training from an experienced operator, and guidelines previously reported be followed to minimize error bias [57]. In the future, standardized training courses should be offered.

Other considerations

Multi-center studies

Measurement of multi-center precision and cross-calibration is important when pooling data from multiple research groups and scan sites, as inter-scanner differences are a key source of error. When compared with single-center precision, HR-pQCT parameters are less precise across different scanners, which may be attributed to differences in quality control of scanners, calibration, and intrinsic manufacturer differences. Burghardt and colleagues reported LSC values for the first-generation HR-pQCT ranging from two to five times that of short-term single-center precision [94]. There is some evidence in that second-generation HR-pQCT scanners have notably improved inter-scanner precision, resulting in differences below LSC [95]. However, this may not apply broadly and cross-calibration procedures should still be employed for future studies using second-generation HR-pQCT. Although no standardized procedure exists for the estimation of multi-center precision, the use of a phantom that mimics geometry, microarchitecture, and composition of standard scan regions is recommended for cross-calibration [94]. This information collected can be employed to establish cross-calibration procedures to minimize inter-scanner errors; however, individual approaches vary and there is currently no standardized approach. Optimal methods for cross-calibration in multi-center studies have not yet been established and studies in this area are greatly needed. Of note, the issue of multi-center calibration is more important for cross-sectional studies; in longitudinal studies that have primary outcomes of individual change, the concern for inter-scanner variation is lessened.

Adjusting for different scanner generations

The introduction of the second-generation HR-pQCT poses a challenge of comparing research findings across different systems. Factors such as differences in resolution, scan region of interest, and measurement methods make it challenging to compare data from different generations, and this will be further confounded when future systems become available. Although it is possible for the second-generation HR-pQCT to be operated in a configuration mimicking the original system, this is not ideal because it defeats the purpose of having improved signal-to-noise and better quality images. Cross-calibration between scanner generations has demonstrated that some parameters from the first-generation can be converted to equivalent parameters for the second-generation; however, some parameters such as Tb.Th, which are highly dependent on resolution, should not be compared across systems [29, 33].

Beam hardening and scatter

Beam hardening and scatter effects that arise due to increased adipose (fat) tissue overlying the scan region, as might be expected in an obese population, can introduce measurable bias in HR-pQCT parameters [96]. Specifically, overlying adipose tissue can result in underestimation of density measurements and failure load, and altered trabecular microarchitecture, often leading to overestimation of bone microarchitecture impairment [96]. Similarly, high-density objects such as a clinical cast composed of plaster-of-Paris

or fiberglass can result in similar bias, due to beam hardening effects, and should be accounted for in a quantitative analysis if they are present in the scan [97, 98]. Future work is needed to determine the appropriate standardized procedures for overweight and obese individuals.

Bone tissue mineralization

Variations in bone tissue mineralization can influence morphological measurements obtained from HR-pQCT. Extraction of the bone structure uses a fixed threshold technique, and consequently, under-mineralized bone tissue that falls below the threshold may not be captured. In addition, μFE analysis usually assumes a uniform tissue modulus for all of the bone, and thus, variation in the degree of mineralization is not accounted for in bone strength estimates. Typical variability in tissue mineralization has little effect on morphological or μFE-derived outcomes [67, 99]. However, results must be interpreted carefully in situations that produce more extreme values of tissue mineralization, such as metabolic bone diseases (e.g., osteopetrosis) or pharmacologic treatments. In particular, induction of new bone formation by anabolic therapies may lead to a relatively undermineralized bone matrix, whereas potent anti-remodeling drugs lead to an increase in tissue mineralization.

Other high-resolution systems

The HR-pQCT systems discussed here focuses on available systems, manufactured by Scanco Medical AG. It is expected that HR-pQCT systems developed by other manufacturers will become available in the near future. In addition, existing imaging technologies are being adapted to study extremity bone microarchitecture as a substitute to HR-pQCT, namely cone-beam CT (CBCT) [100–103]. Current CBCT systems designed for extremity scanning offer larger scan lengths and shorter scanning times relative to HR-pQCT, with some systems allowing for scan acquisition in a weight-bearing configuration [103]. These benefits come with the trade-off of lower resolution, typically 127-μm nominal resolution reconstructed to a 75-μm voxel size [100]. Consequently, CBCT is susceptible to partial volume effects and can struggle to distinguish thinner trabecular structures that are visible with HR-pQCT [102]. As the application of CBCT for bone microarchitecture grows, and new HR-pQCT systems become available, the recommendations and guidelines outlined in this article should be considered.

Table 7 Summary of recommendations

Scan acquisition and analysis

- *The method of selecting scan site should be clearly indicated.* The relative offset outlined in this article and described in detail elsewhere [36] is recommended; however, a fixed offset may be used when comparing to historical datasets.
- *Image processing should use direct measurement methods following the extended cortical analysis.* Automatically generated contours should be checked and manually corrected for errors following guidelines outlines in detail elsewhere [57].
- *μFE analysis should use standardized constitutive properties and boundary conditions.* μFE specifications outlined in Table 4 are recommended for first-generation HR-pQCT and can be compared using harmonizing techniques. For second-generation HR-pQCT analysis, an elastic modulus of 10,000 MPa with axial boundary conditions and a yield criterion of 1.0% critical strain and 5% critical volume is recommended.
- *Longitudinal studies should employ 3D or 2D registration and exclude scans with less than 75% overlap.* μFE should not be applied to 3D-registered scans and instead 2D-registered or unregistered scans should be used.

Reporting results

- *Standardized nomenclature proposed here should be used for reporting results.* Nomenclature proposed in Tables 2, 3, and 5 should be used, and use of direct or indirect measurement techniques should be clearly indicated. The minimum parameters to describe trabecular bone morphology should include trabecular bone volume fraction, and trabecular number, thickness, and separation; for cortical bone morphology, cortical thickness, and cortical porosity should be reported.
- *Precision error should be measured and reported for each research center, specific to study protocol.* Cross-sectional studies should report precision with unregistered scans, and longitudinal studies should report precision with the registration technique used in the study design.

Quality control and training

- *Quality control should follow manufacturer maintenance protocol, including daily and weekly scanning of QC phantoms.* Scanner drift should be actively monitored, and the use of Shewhart charts to track scanner stability is recommended.
- *New operators should be trained by an experienced operator and available training tools used.* New operators should be trained in patient management and positioning, anatomical measurements, location of the reference line, and manual correction of contours generated by the automated and semi-automated protocols. Training should be supplemented with online reference line training developed by UCSF [42], and other online resources, as they become available.
- *Continuity across scanner generations (makes, models) should be assessed through cross-calibration.* It is important to understand relationships between parameters measured on different scanner generations [29, 33]. Typically, density-based parameters can be converted between scanner generations, but resolution-dependent parameters (e.g., Tb.Th) are problematic and should not be compared between generations.
- *Multi-center studies should report inter-scanner precision error*, and it is recommended that these are estimated using a calibration phantom that replicates geometry, densities, and microarchitecture of standard scan sites.

Pediatric studies

There is growing interest in the application of HR-pQCT in pediatrics for the study of normal skeletal acquisition [8], as well as the impact of disease [15] and physical activity [24] on skeletal acquisition. However, measurement of bone density and microarchitecture in children and adolescents poses unique challenges due to the complexities of long bone growth and presence of the growth plate near the scan region [86]. Non-linear bone growth and differences in maturation between sexes and ethnicities pose challenges in the appropriate selection of a standardized scan region. Several protocols have been proposed for the selection of the scan region to account for long bone growth [104], and although there is no consensus regarding the most appropriate scan site, there is an agreement that a relative offset should be used in children and adolescents. Further work is required to form a consensus on a standardized protocol for pediatric studies, including how to handle the transition from a pediatric to adult scanning protocol in longitudinal studies where participants are followed from childhood into adulthood.

Non-standard applications

HR-pQCT is specifically designed to measure the distal radius and distal tibia in adults, but its application to study bone microarchitecture at other sites has expanded in recent years. The introduction of XtremeCT II, which has a larger gantry and redesigned staging mechanism, permits knee and elbow joints to be imaged [105]. Furthermore, applications beyond the standard protocol have included the study of fracture healing at the distal radius [71], quantification of muscle morphometry [47], progression of inflammatory arthritis through quantification of joint space narrowing and development of erosions in finger and wrist joints [106, 107], and investigation of changes in bone microarchitecture at the knee due to injury or osteoarthritis [108]. These emerging applications are likely to become more prominent in HR-pQCT research and will require careful development of standardized protocols. A prominent example of this is the development of research focused on inflammatory arthritis, with as many as 20 research centers actively publishing in this area. Ongoing standardization of this novel application is overseen by the international consortium, SPECTRA (Study grouP for xtrEme-Computed Tomography in Rheumatoid Arthritis) [109, 110].

Summary of recommendations

Recommendations for best practices for the acquisition and analysis of HR-pQCT imaging techniques have been presented here, with nomenclature and recommendations on presenting and interpreting results. Many decisions on appropriate techniques and study design remain dependent on the research question. However, with the uptake in the clinical application of HR-pQCT, a certain degree of standardization is necessary to support the further advancement of the clinical application of HR-pQCT. The key recommendations for standard analysis of the distal radius and tibia HR-pQCT scans are summarized in Table 7. Implementation of these recommendations as "best practices" should facilitate the comparison of results across studies by minimizing technical variation in scan acquisition and analysis.

Acknowledgments These guidelines have been reviewed and endorsed by the Committee of Scientific Advisors of the International Osteoporosis Foundation, the European Calcified Tissue Society, and the American Society for Bone and Mineral Research.

Compliance with ethical standards

Conflicts of interest Dr. Boyd is a co-founder and co-owner of Numerics88 Solutions Inc., creator of finite element package FAIM. Dr. Ghasem-Zadeh is one of the inventors of the StrAx algorithm and consults for Strax Corp. Dr. Burghardt is a consultant and served on an Advisory Board to Mereo BioPharma.

References

1. Boutroy S, Bouxsein ML, Munoz F, Delmas PD (2005) In vivo assessment of trabecular bone microarchitecture by high-resolution peripheral quantitative computed tomography. J Clin Endocrinol Metab 90:6508–6515
2. Jobke B, Burghardt AJ, Muche B, Hahn M, Semler J, Amling M, Majumdar S, Busse B (2011) Trabecular reorganization in consecutive iliac crest biopsies when switching from bisphosphonate to strontium ranelate treatment. PLoS One 6:e23638
3. Jobke B, Muche B, Burghardt AJ, Semler J, Link TM, Majumdar S (2011) Teriparatide in bisphosphonate-resistant osteoporosis: microarchitectural changes and clinical results after 6 and 18 months. Calcif Tissue Int 89:130–139
4. Burt LA, Bhatla JL, Hanley DA, Boyd SK (2017) Cortical porosity exhibits accelerated rate of change in peri- compared with post-menopausal women. Osteoporos Int 28:1423–1431
5. Burt LA, Liang Z, Sajobi TT, Hanley DA, Boyd SK (2016) Sex- and site-specific normative data curves for HR-pQCT. J Bone Miner Res 31:2041–2047
6. Burt LA, Macdonald HM, Hanley DA, Boyd SK (2014) Bone microarchitecture and strength of the radius and tibia in a reference population of young adults: an HR-pQCT study. Arch Osteoporos 9:183
7. Gabel L, Macdonald HM, McKay HA (2017) Sex differences and growth-related adaptations in bone microarchitecture, geometry, density, and strength from childhood to early adulthood: a mixed longitudinal HR-pQCT study. J Bone Miner Res 32:250–263
8. Gabel L, Macdonald HM, Nettlefold LA, McKay HA (2018) Sex-, ethnic-, and age-specific centile curves for pQCT- and HR-pQCT-derived measures of bone structure and strength in adolescents and young adults. J Bone Miner Res 33:987–1000
9. Hansen S, Shanbhogue V, Folkestad L, Nielsen MM, Brixen K (2014) Bone microarchitecture and estimated strength in 499 adult

Danish women and men: a cross-sectional, population-based high-resolution peripheral quantitative computed tomographic study on peak bone structure. Calcif Tissue Int 94:269–281
10. Macdonald HM, Nishiyama KK, Kang J, Hanley DA, Boyd SK (2011) Age-related patterns of trabecular and cortical bone loss differ between sexes and skeletal sites: a population-based HR-pQCT study. J Bone Miner Res 26:50–62
11. Popp KL, Hughes JM, Martinez-Betancourt A, Scott M, Turkington V, Caksa S, Guerriere KI, Ackerman KE, Xu C, Unnikrishnan G, Reifman J, Bouxsein ML (2017) Bone mass, microarchitecture and strength are influenced by race/ethnicity in young adult men and women. Bone 103:200–208
12. Vilayphiou N, Boutroy S, Sornay-Rendu E, Van Rietbergen B, Chapurlat R (2016) Age-related changes in bone strength from HR-pQCT derived microarchitectural parameters with an emphasis on the role of cortical porosity. Bone 83:233–240
13. Milovanovic P, Adamu U, Simon MJ, Rolvien T, Djuric M, Amling M, Busse B (2015) Age- and sex-specific bone structure patterns portend bone fragility in radii and tibiae in relation to osteodensitometry: a high-resolution peripheral quantitative computed tomography study in 385 individuals. J Gerontol A Biol Sci Med Sci 70:1269–1275
14. Bacchetta J, Boutroy S, Vilayphiou N, Juillard L, Guebre-Egziabher F, Rognant N, Sornay-Rendu E, Szulc P, Laville M, Delmas PD, Fouque D, Chapurlat R (2010) Early impairment of trabecular microarchitecture assessed with HR-pQCT in patients with stage II-IV chronic kidney disease. J Bone Miner Res 25: 849–857
15. Braun C, Bacchetta J, Braillon P, Chapurlat R, Drai J, Reix P (2017) Children and adolescents with cystic fibrosis display moderate bone microarchitecture abnormalities: data from high-resolution peripheral quantitative computed tomography. Osteoporos Int 28:3179–3188
16. Nour MA, Burt LA, Perry RJ, Stephure DK, Hanley DA, Boyd SK (2016) Impact of growth hormone on adult bone quality in turner syndrome: a HR-pQCT study. Calcif Tissue Int 98:49–59
17. Samelson EJ, Demissie S, Cupples LA, Zhang X, Xu H, Liu CT, Boyd SK, McLean RR, Broe KE, Kiel DP, Bouxsein ML (2018) Diabetes and deficits in cortical bone density, microarchitecture, and bone size: Framingham HR-pQCT Study. J Bone Miner Res 33:54–62
18. Boyd SK, Burt LA, Sevick LK, Hanley DA (2015) The relationship between serum 25(OH)D and bone density and microarchitecture as measured by HR-pQCT. Osteoporos Int 26: 2375–2380
19. Burghardt AJ, Kazakia GJ, Sode M, de Papp AE, Link TM, Majumdar S (2010) A longitudinal HR-pQCT study of alendronate treatment in postmenopausal women with low bone density: relations among density, cortical and trabecular microarchitecture, biomechanics, and bone turnover. J Bone Miner Res 25:2558–2571
20. Tsai JN, Nishiyama KK, Lin D, Yuan A, Lee H, Bouxsein ML, Leder BZ (2017) Effects of denosumab and teriparatide transitions on bone microarchitecture and estimated strength: the DATA-Switch HR-pQCT study. J Bone Miner Res 32:2001–2009
21. Langsetmo L, Shikany JM, Burghardt AJ et al (2018) High dairy protein intake is associated with greater bone strength parameters at the distal radius and tibia in older men: a cross-sectional study. Osteoporos Int 29:69–77
22. Burt LA, Billington EO, Rose MS, Raymond DA, Hanley DA, Boyd SK (2019) Effect of high-dose vitamin D supplementation on volumetric bone density and bone strength: a randomized clinical trial. JAMA 322:736–745
23. Burt LA, Schipilow JD, Boyd SK (2016) Competitive trampolining influences trabecular bone structure, bone size, and bone strength. J Sport Health Sci 5:469–475
24. Gabel L, Macdonald HM, Nettlefold L, McKay HA (2017) Physical activity, sedentary time, and bone strength from childhood to early adulthood: a mixed longitudinal HR-pQCT study. J Bone Miner Res 32:1525–1536
25. Hughes JM, Gaffney-Stomberg E, Guerriere KI, Taylor KM, Popp KL, Xu C, Unnikrishnan G, Staab JS, Matheny RW Jr, McClung JP, Reifman J, Bouxsein ML (2018) Changes in tibial bone microarchitecture in female recruits in response to 8weeks of U.S. Army Basic Combat Training. Bone 113:9–16
26. Kazakia GJ, Tjong W, Nirody JA, Burghardt AJ, Carballido-Gamio J, Patsch JM, Link T, Feeley BT, Ma CB (2014) The influence of disuse on bone microstructure and mechanics assessed by HR-pQCT. Bone 63:132–140
27. Mikolajewicz N, Bishop N, Burghardt AJ et al (2019) HR-pQCT measures of bone microarchitecture predict fracture: systematic review and meta-analysis. J Bone Miner Res
28. Stauber M, Müller R (2008) Micro-computed tomography: a method for the non-destructive evaluation of the three-dimensional structure of biological specimens. Methods Mol Biol 455:273–292
29. Agarwal S, Rosete F, Zhang C, McMahon DJ, Guo XE, Shane E, Nishiyama KK (2016) In vivo assessment of bone structure and estimated bone strength by first- and second-generation HR-pQCT. Osteoporos Int 27:2955–2966
30. Bandirali M, Lanza E, Messina C, Sconfienza LM, Brambilla R, Maurizio R, Marchelli D, Piodi LP, di Leo G, Ulivieri FM, Sardanelli F (2013) Dose absorption in lumbar and femoral dual energy X-ray absorptiometry examinations using three different scan modalities: an anthropomorphic phantom study. J Clin Densitom 16:279–282
31. Wylie JD, Jenkins PA, Beckmann JT, Peters CL, Aoki SK, Maak TG (2018) Computed tomography scans in patients with young adult hip pain carry a lifetime risk of malignancy. Arthroscopy 34(155–163):e153
32. Manske SL, Zhu Y, Sandino C, Boyd SK (2015) Human trabecular bone microarchitecture can be assessed independently of density with second generation HR-pQCT. Bone 79:213–221
33. Manske SL, Davison EM, Burt LA, Raymond DA, Boyd SK (2017) The estimation of second-generation HR-pQCT from first-generation HR-pQCT using in vivo cross-calibration. J Bone Miner Res 32:1514–1524
34. Wang Q, Wang XF, Iuliano-Burns S, Ghasem-Zadeh A, Zebaze R, Seeman E (2010) Rapid growth produces transient cortical weakness: a risk factor for metaphyseal fractures during puberty. J Bone Miner Res 25:1521–1526
35. Burrows M, Liu D, Moore S, McKay H (2010) Bone microstructure at the distal tibia provides a strength advantage to males in late puberty: an HR-pQCT study. J Bone Miner Res 25:1423–1432
36. Bonaretti S, Majumdar S, Lang TF, Khosla S, Burghardt AJ (2017) The comparability of HR-pQCT bone measurements is improved by scanning anatomically standardized regions. Osteoporos Int 28:2115–2128
37. Shanbhogue VV, Hansen S, Halekoh U, Brixen K (2015) Use of relative vs fixed offset distance to define region of interest at the distal radius and tibia in high-resolution peripheral quantitative computed tomography. J Clin Densitom 18:217–225
38. Boyd SK (2008) Site-specific variation of bone micro-architecture in the distal radius and tibia. J Clin Densitom 11:424–430
39. Hauspie RC, Vercauteren M, Susanne C (1997) Secular changes in growth and maturation: an update. Acta Paediatr Suppl 423:20–27
40. Ghasem-Zadeh A, Burghardt A, Wang XF, Iuliano S, Bonaretti S, Bui M, Zebaze R, Seeman E (2017) Quantifying sex, race, and age specific differences in bone microstructure requires measurement of anatomically equivalent regions. Bone 101:206–213

41. Sode M, Burghardt AJ, Pialat JB, Link TM, Majumdar S (2011) Quantitative characterization of subject motion in HR-pQCT images of the distal radius and tibia. Bone 48:1291–1297
42. Bonaretti S, Vilayphiou N, Chan CM, Yu A, Nishiyama K, Liu D, Boutroy S, Ghasem-Zadeh A, Boyd SK, Chapurlat R, McKay H, Shane E, Bouxsein ML, Black DM, Majumdar S, Orwoll ES, Lang TF, Khosla S, Burghardt AJ (2017) Operator variability in scan positioning is a major component of HR-pQCT precision error and is reduced by standardized training. Osteoporos Int 28: 245–257
43. Zebaze R, Ghasem-Zadeh A, Mbala A, Seeman E (2013) A new method of segmentation of compact-appearing, transitional and trabecular compartments and quantification of cortical porosity from high resolution peripheral quantitative computed tomographic images. Bone 54:8–20
44. Schafer AL, Burghardt AJ, Sellmeyer DE, Palermo L, Shoback DM, Majumdar S, Black DM (2013) Postmenopausal women treated with combination parathyroid hormone (1-84) and ibandronate demonstrate different microstructural changes at the radius vs. tibia: the PTH and Ibandronate Combination Study (PICS). Osteoporos Int 24:2591–2601
45. Cheung AM, Majumdar S, Brixen K, Chapurlat R, Fuerst T, Engelke K, Dardzinski B, Cabal A, Verbruggen N, Ather S, Rosenberg E, de Papp AE (2014) Effects of odanacatib on the radius and tibia of postmenopausal women: improvements in bone geometry, microarchitecture, and estimated bone strength. Journal of bone and mineral research : the official journal of the American Society for Bone and Mineral Research 29:1786–1794
46. Patsch JM, Burghardt AJ, Yap SP, Baum T, Schwartz AV, Joseph GB, Link TM (2013) Increased cortical porosity in type 2 diabetic postmenopausal women with fragility fractures. Journal of bone and mineral research : the official journal of the American Society for Bone and Mineral Research 28:313–324
47. Wong AK (2016) A comparison of peripheral imaging technologies for bone and muscle quantification: a technical review of image acquisition. J Musculoskelet Neuronal Interact 16:265–282
48. Stagi S, Cavalli L, Cavalli T, de Martino M, Brandi ML (2016) Peripheral quantitative computed tomography (pQCT) for the assessment of bone strength in most of bone affecting conditions in developmental age: a review. Ital J Pediatr 42:88
49. Engelke K, Stampa B, Timm W, Dardzinski B, de Papp AE, Genant HK, Fuerst T (2012) Short-term in vivo precision of BMD and parameters of trabecular architecture at the distal forearm and tibia. Osteoporos Int 23:2151–2158
50. Pauchard Y, Liphardt AM, Macdonald HM, Hanley DA, Boyd SK (2012) Quality control for bone quality parameters affected by subject motion in high-resolution peripheral quantitative computed tomography. Bone 50:1304–1310
51. Pialat JB, Burghardt AJ, Sode M, Link TM, Majumdar S (2012) Visual grading of motion induced image degradation in high resolution peripheral computed tomography: impact of image quality on measures of bone density and micro-architecture. Bone 50: 111–118
52. Laib A, Hauselmann HJ, Ruegsegger P (1998) In vivo high resolution 3D-QCT of the human forearm. Technol Health Care 6: 329–337
53. Davis KA, Burghardt AJ, Link TM, Majumdar S (2007) The effects of geometric and threshold definitions on cortical bone metrics assessed by in vivo high-resolution peripheral quantitative computed tomography. Calcif Tissue Int 81:364–371
54. Nishiyama KK, Macdonald HM, Buie HR, Hanley DA, Boyd SK (2010) Postmenopausal women with osteopenia have higher cortical porosity and thinner cortices at the distal radius and tibia than women with normal aBMD: an in vivo HR-pQCT study. Journal of bone and mineral research : the official journal of the American Society for Bone and Mineral Research 25:882–890
55. Buie HR, Campbell GM, Klinck RJ, MacNeil JA, Boyd SK (2007) Automatic segmentation of cortical and trabecular compartments based on a dual threshold technique for in vivo micro-CT bone analysis. Bone 41:505–515
56. Burghardt AJ, Buie HR, Laib A, Majumdar S, Boyd SK (2010) Reproducibility of direct quantitative measures of cortical bone microarchitecture of the distal radius and tibia by HR-pQCT. Bone 47:519–528
57. Whittier DE, Mudryk AN, Vandergaag ID, Burt LA, Boyd SK (2019) Optimizing HR-pQCT workflow: a comparison of bias and precision error for quantitative bone analysis. Osteoporos Int
58. Kawalilak CE, Johnston JD, Cooper DM, Olszynski WP, Kontulainen SA (2016) Role of endocortical contouring methods on precision of HR-pQCT-derived cortical micro-architecture in postmenopausal women and young adults. Osteoporos Int 27: 789–796
59. de Waard EAC, Sarodnik C, Pennings A, de Jong JJA, Savelberg HHCM, van Geel TA, van der Kallen CJ, Stehouwer CDA, Schram MT, Schaper N, Dagnelie PC, Geusens PPMM, Koster A, van Rietbergen B, van den Bergh JPW (2018) Reliability of HR-pQCT derived cortical bone structural parameters when using uncorrected instead of corrected automatically generated endocortical contours in a cross-sectional study: the Maastricht Study. Calcif Tissue Int 103:252–265
60. Hildebrand T, Rüegsegger P (1997) Quantification of bone microarchitecture with the structure model index. Comput Methods Biomech Biomed Engin 1:15–23
61. Hildebrand T, Laib A, Müller R, Dequeker J, Rüegsegger P (1999) Direct three-dimensional morphometric analysis of human cancellous bone: microstructural data from spine, femur, iliac crest, and calcaneus. J Bone Miner Res 14:1167–1174
62. Odgaard A, Gundersen HJ (1993) Quantification of connectivity in cancellous bone, with special emphasis on 3-D reconstructions. Bone 14:173–182
63. Whitehouse WJ (1974) The quantitative morphology of anisotropic trabecular bone. J Microsc 101:153–168
64. Liu XS, Sajda P, Saha PK, Wehrli FW, Bevill G, Keaveny TM, Guo XE (2008) Complete volumetric decomposition of individual trabecular plates and rods and its morphological correlations with anisotropic elastic moduli in human trabecular bone. J Bone Miner Res 23:223–235
65. Jorgenson BL, Buie HR, McErlain DD, Sandino C, Boyd SK (2015) A comparison of methods for in vivo assessment of cortical porosity in the human appendicular skeleton. Bone 73:167–175
66. van Rietbergen B, Ito K (2015) A survey of micro-finite element analysis for clinical assessment of bone strength: the first decade. J Biomech 48:832–841
67. MacNeil JA, Boyd SK (2008) Bone strength at the distal radius can be estimated from high-resolution peripheral quantitative computed tomography and the finite element method. Bone 42: 1203–1213
68. Arias-Moreno AJ, Hosseini HS, Bevers M, Ito K, Zysset P, van Rietbergen B (2019) Validation of distal radius failure load predictions by homogenized- and micro-finite element analyses based on second-generation high-resolution peripheral quantitative CT images. Osteoporos Int 30:1433–1443
69. Pistoia W, van Rietbergen B, Lochmuller EM, Lill CA, Eckstein F, Rüegsegger P (2002) Estimation of distal radius failure load with micro-finite element analysis models based on three-dimensional peripheral quantitative computed tomography images. Bone 30:842–848
70. Christen D, Zwahlen A, Müller R (2014) Reproducibility for linear and nonlinear micro-finite element simulations with density derived material properties of the human radius. J Mech Behav Biomed Mater 29:500–507

71. de Jong JJ, Willems PC, Arts JJ, Bours SG, Brink PR, van Geel TA, Poeze M, Geusens PP, van Rietbergen B, van den Bergh JP (2014) Assessment of the healing process in distal radius fractures by high resolution peripheral quantitative computed tomography. Bone 64:65–74
72. Engelke K, van Rietbergen B, Zysset P (2016) FEA to measure bone strength: a review. Clinic Rev Bone Miner Metab 14:26–37
73. Müller R, Rüegsegger P (1995) Three-dimensional finite element modelling of non-invasively assessed trabecular bone structures. Med Eng Phys 17:126–133
74. Whittier DE, Manske SL, Kiel DP, Bouxsein M, Boyd SK (2018) Harmonizing finite element modelling for non-invasive strength estimation by high-resolution peripheral quantitative computed tomography. J Biomech 80:63–71
75. Christen D, Melton LJ 3rd, Zwahlen A, Amin S, Khosla S, Muller R (2013) Improved fracture risk assessment based on nonlinear micro-finite element simulations from HRpQCT images at the distal radius. Journal of bone and mineral research : the official journal of the American Society for Bone and Mineral Research 28:2601–2608
76. Pistoia W, van Rietbergen B, Lochmuller EM, Lill CA, Eckstein F, Rüegsegger P (2004) Image-based micro-finite-element modeling for improved distal radius strength diagnosis: moving from bench to bedside. J Clin Densitom 7:153–160
77. Mueller TL, Christen D, Sandercott S, Boyd SK, van Rietbergen B, Eckstein F, Lochmuller EM, Muller R, van Lenthe GH (2011) Computational finite element bone mechanics accurately predicts mechanical competence in the human radius of an elderly population. Bone 48:1232–1238
78. Varga P, Pahr DH, Baumbach S, Zysset PK (2010) HR-pQCT based FE analysis of the most distal radius section provides an improved prediction of Colles' fracture load in vitro. Bone 47: 982–988
79. Kroker A, Plett R, Nishiyama KK, McErlain DD, Sandino C, Boyd SK (2017) Distal skeletal tibia assessed by HR-pQCT is highly correlated with femoral and lumbar vertebra failure loads. J Biomech 59:43–49
80. van Rietbergen B, Weinans H, Huiskes R, Odgaard A (1995) A new method to determine trabecular bone elastic properties and loading using micromechanical finite-element models. J Biomech 28:69–81
81. Chen H, Zhou X, Fujita H, Onozuka M, Kubo KY (2013) Age-related changes in trabecular and cortical bone microstructure. Int J Endocrinol 2013:213234
82. Seeman E, Delmas PD, Hanley DA, Sellmeyer D, Cheung AM, Shane E, Kearns A, Thomas T, Boyd SK, Boutroy S, Bogado C, Majumdar S, Fan M, Libanati C, Zanchetta J (2010) Microarchitectural deterioration of cortical and trabecular bone: differing effects of denosumab and alendronate. Journal of bone and mineral research : the official journal of the American Society for Bone and Mineral Research 25:1886–1894
83. Paggiosi MA, Eastell R, Walsh JS (2014) Precision of high-resolution peripheral quantitative computed tomography measurement variables: influence of gender, examination site, and age. Calcif Tissue Int 94:191–201
84. Ellouz R, Chapurlat R, van Rietbergen B, Christen P, Pialat JB, Boutroy S (2014) Challenges in longitudinal measurements with HR-pQCT: evaluation of a 3D registration method to improve bone microarchitecture and strength measurement reproducibility. Bone 63:147–157
85. Nishiyama KK, Pauchard Y, Nikkel LE, Iyer S, Zhang C, McMahon DJ, Cohen D, Boyd SK, Shane E, Nickolas TL (2015) Longitudinal HR-pQCT and image registration detects endocortical bone loss in kidney transplantation patients. J Bone Miner Res 30:554–561
86. Adams JE, Engelke K, Zemel BS, Ward KA, International Society of Clinical D (2014) Quantitative computer tomography in children and adolescents: the 2013 ISCD Pediatric Official Positions. J Clin Densitom 17:258–274
87. de Jong JJA, Christen P, Plett RM, Chapurlat R, Geusens PP, van den Bergh JPW, Müller R, van Rietbergen B (2017) Feasibility of rigid 3D image registration of high-resolution peripheral quantitative computed tomography images of healing distal radius fractures. PLoS One 12:e0179413
88. Chiba K, Okazaki N, Kurogi A, Isobe Y, Yonekura A, Tomita M, Osaki M (2018) Precision of second-generation high-resolution peripheral quantitative computed tomography: intra- and intertester reproducibilities and factors involved in the reproducibility of cortical porosity. J Clin Densitom 21:295–302
89. Shepherd JA, Lu Y (2007) A generalized least significant change for individuals measured on different DXA systems. J Clin Densitom 10:249–258
90. Benjamini Y, Hochberg Y (1995) Controlling the false discovery rate: a practical and powerful approach to multiple testing. J R Stat Soc Series B Stat Methodol 57:289–300
91. Boutroy S, Khosla S, Sornay-Rendu E, Zanchetta MB, McMahon DJ, Zhang CA, Chapurlat RD, Zanchetta J, Stein EM, Bogado C, Majumdar S, Burghardt AJ, Shane E (2016) Microarchitecture and peripheral BMD are impaired in postmenopausal white women with fracture independently of total hip T-score: an international multicenter study. J Bone Miner Res 31:1158–1166
92. Yekutieli D (2008) Hierarchical flse discovery rate-controlling methodology. J Am Stat Assoc 103:309–316
93. Gensburger D, Boutroy S, Chapurlat R, Nove-Josserand R, Roche S, Rabilloud M, Durieu I (2016) Reduced bone volumetric density and weak correlation between infection and bone markers in cystic fibrosis adult patients. Osteoporos Int 27:2803–2813
94. Burghardt AJ, Pialat JB, Kazakia GJ, Boutroy S, Engelke K, Patsch JM, Valentinitsch A, Liu D, Szabo E, Bogado CE, Zanchetta MB, McKay HA, Shane E, Boyd SK, Bouxsein ML, Chapurlat R, Khosla S, Majumdar S (2013) Multicenter precision of cortical and trabecular bone quality measures assessed by high-resolution peripheral quantitative computed tomography. J Bone Miner Res 28:524–536
95. Cauley JA, Burghardt AJ, Harrison SL, Cawthon PM, Schwartz AV, Connor EB, Ensrud KE, Langsetmo L, Majumdar S, Orwoll E, for the Osteoporotic Fractures in Men (MrOS) Research Group (2018) Accelerated bone loss in older men: effects on bone microarchitecture and strength. J Bone Miner Res 33:1859–1869
96. Caksa S, Yuan A, Rudolph SE, Yu EW, Popp KL, Bouxsein ML (2019) Influence of soft tissue on bone density and microarchitecture measurements by high-resolution peripheral quantitative computed tomography. Bone 124:47–52
97. de Jong JJ, Arts JJ, Meyer U, Willems PC, Geusens PP, van den Bergh JP, van Rietbergen B (2016) Effect of a cast on short-term reproducibility and bone parameters obtained from HR-pQCT measurements at the distal end of the radius. J Bone Joint Surg Am 98:356–362
98. Whittier DE, Manske SL, Boyd SK, Schneider PS (2018) The correction of systematic error due to plaster and fiberglass casts on HR-pQCT bone parameters measured in vivo at the distal radius. J Clin Densitom
99. MacNeil JA, Boyd SK (2007) Accuracy of high-resolution peripheral quantitative computed tomography for measurement of bone quality. Med Eng Phys 29:1096–1105
100. de Charry C, Boutroy S, Ellouz R, Duboeuf F, Chapurlat R, Follet H, Pialat JB (2016) Clinical cone beam computed tomography compared to high-resolution peripheral computed tomography in the assessment of distal radius bone. Osteoporos Int 27:3073–3082

101. Klintstrom E, Smedby O, Moreno R, Brismar TB (2014) Trabecular bone structure parameters from 3D image processing of clinical multi-slice and cone-beam computed tomography data. Skelet Radiol 43:197–204
102. Mys K, Varga P, Gueorguiev B, Hemmatian H, Stockmans F, van Lenthe GH (2019) Correlation between cone-beam computed tomography and high-resolution peripheral computed tomography for assessment of wrist bone microstructure. J Bone Miner Res 34: 867–874
103. Brehler M, Cao Q, Moseley KF, Osgood G, Morris C, Demehri S, Yorkston J, Siewerdsen JH, Zbijewski W (2018) Robust quantitative assessment of trabecular microarchitecture in extremity cone-beam CT using optimized segmentation algorithms. Proc SPIE Int Soc Opt Eng 10578:
104. Kawalilak CE, Bunyamin AT, Bjorkman KM, Johnston JD, Kontulainen SA (2017) Precision of bone density and micro-architectural properties at the distal radius and tibia in children: an HR-pQCT study. Osteoporos Int 28:3189–3197
105. Kroker A, Besler BA, Bhatla JL, Shtil M, Salat P, Mohtadi N, Walker RE, Manske SL, Boyd SK (2019) Longitudinal effects of acute anterior cruciate ligament tears on peri-articular bone in human knees within the first year of injury. J Orthop Res 37:2325–2336
106. Burghardt AJ, Lee CH, Kuo D, Majumdar S, Imboden JB, Link TM, Li X (2013) Quantitative in vivo HR-pQCT imaging of 3D wrist and metacarpophalangeal joint space width in rheumatoid arthritis. Ann Biomed Eng 41:2553–2564
107. Nagaraj S, Finzel S, Stok KS, Barnabe C, Collaboration S (2016) High-resolution peripheral quantitative computed tomography imaging in the assessment of periarticular bone of metacarpophalangeal and wrist joints. J Rheumatol 43:1921–1934
108. Kroker A, Zhu Y, Manske SL, Barber R, Mohtadi N, Boyd SK (2017) Quantitative in vivo assessment of bone microarchitecture in the human knee using HR-pQCT. Bone 97:43–48
109. Manske SL, Brunet SC, Finzel S, Stok KS, Conaghan PG, Boyd SK, Barnabe C (2019) The SPECTRA collaboration OMERACT working group: construct validity of joint space outcomes with high-resolution peripheral quantitative computed tomography. J Rheumatol 46:1369–1373
110. Stok KS, Finzel S, Burghardt AJ, Conaghan PG, Barnabe C, Collaboration S (2017) The SPECTRA collaboration OMERACT special interest group: current research and future directions. J Rheumatol 44:1911–1915
111. Vilayphiou N, Boutroy S, Sornay-Rendu E, Van Rietbergen B, Munoz F, Delmas PD, Chapurlat R (2010) Finite element analysis performed on radius and tibia HR-pQCT images and fragility fractures at all sites in postmenopausal women. Bone 46:1030–1037
112. Hosseini HS, Dunki A, Fabech J, Stauber M, Vilayphiou N, Pahr D, Pretterklieber M, Wandel J, Rietbergen BV, Zysset PK (2017) Fast estimation of Colles' fracture load of the distal section of the radius by homogenized finite element analysis based on HR-pQCT. Bone 97:65–75

Publisher's note Springer Nature remains neutral with regard to jurisdictional claims in published maps and institutional affiliations.

Bone 101 (2017) 206–213

Contents lists available at ScienceDirect

Bone

journal homepage: www.elsevier.com/locate/bone

Full Length Article

Quantifying sex, race, and age specific differences in bone microstructure requires measurement of anatomically equivalent regions

Ali Ghasem-Zadeh [a,*], Andrew Burghardt [b], Xiao-Fang Wang [a], Sandra Iuliano [a], Serena Bonaretti [b,c], Minh Bui [d], Roger Zebaze [a], Ego Seeman [a,e]

[a] Department of Endocrinology and Medicine, Austin Health, University of Melbourne, Melbourne, Australia
[b] Musculoskeletal Quantitative Imaging Research Group, Department of Radiology and Biomedical Imaging, University of California, San Francisco, CA, USA
[c] Department of Radiology, Stanford University, Stanford, CA, USA
[d] Centre for Epidemiology and Biostatistics, University of Melbourne, Melbourne, Australia
[e] Institute for Health and Aging, Australian Catholic University, Melbourne, Australia

ARTICLE INFO

Article history:
Received 23 November 2016
Revised 29 April 2017
Accepted 10 May 2017
Available online 11 May 2017

Keywords:
Age
Cortical porosity
HR-pQCT
Microstructure
Race
Site variation
Sex

ABSTRACT

Introduction: Individuals differ in forearm length. As microstructure differs along the radius, we hypothesized that errors may occur when sexual and racial dimorphisms are quantified at a fixed distance from the radio-carpal joint.
Methods: Microstructure was quantified *ex vivo* in 18 cadaveric radii using high resolution peripheral quantitative computed tomography and *in vivo* in 158 Asian and Caucasian women and men at a fixed region of interest (ROI), a corrected ROI positioned at 4.5–6% of forearm length and using the fixed ROI adjusted for cross sectional area (CSA), forearm length or height. Secular effects of age were assessed by comparing 38 younger and 33 older women.
Results: Ex vivo, similar amounts of bone mass fashioned adjacent cross sections. Larger distal cross sections had thinner porous cortices of lower matrix mineral density (MMD), a larger medullary CSA and higher trabecular density. Smaller proximal cross-sections had thicker less porous cortices of higher MMD, a small medullary canal with little trabecular bone. Taller persons had more distally positioned fixed ROIs which moved proximally when corrected. Shorter persons had more proximally positioned fixed ROIs which moved distally when corrected, so dimorphisms lessened. In the corrected ROIs, in Caucasians, women had 0.6 SD higher porosity and 0.6 SD lower trabecular density than men ($p < 0.01$). In Asians, women had 0.25 SD higher porosity (NS) and 0.5 SD lower trabecular density than men ($p < 0.05$). In women, Asians had 0.8 SD lower porosity and 0.3 SD higher trabecular density than Caucasians ($p < 0.01$). In men, Asians and Caucasians had similar porosity and trabecular density. Results were similar using an adjusted fixed ROI. Adjusting for secular effects of age on forearm length resulted in the age-related increment in porosity increasing from 2.08 SD to 2.48 SD ($p < 0.05$).
Conclusion: Assessment of sex, race and age related differences in microstructure requires measurement of anatomically equivalent regions.

© 2017 Elsevier Inc. All rights reserved.

1. Introduction

Long bones must be strong to tolerate loading, yet light to facilitate mobility. They must also be rigid to serve as levers, yet flexible to be able to deform elastically [1,2]. These paradoxical properties are achieved by bone modelling and remodelling, cellular events that fashion and refashion bone's macro- and microstructure using void volume. Larger bones have a biomechanical advantage and so are assembled using less mass and more void relative to their size [3]. Smaller bones offset their biomechanical disadvantage by being assembled with more mass and less void relative to their size [4].

During growth, different amounts of periosteal apposition and endocortical resorption from point to point around a bone cross section, and from cross section to cross section along a bone, produce variation in external and medullary canal bone size and shape [5–8]. Concurrent intracortical remodelling produces variation in osteonal and Haversian canal number and so porosity (canals seen in cross section).

Because of this regional heterogeneity, when the effects of growth, advancing age, sex, race, or drug therapy are quantified using high resolution peripheral quantitative computed tomography (HR-pQCT), the region of interest (ROI) chosen to measure this morphology must be anatomically comparable otherwise differences or absence of differences in microstructure between these groups may be the result of the positioning of the ROI, not bone biology.

Currently, a fixed ROI starting 9.5 mm proximal to mid radiocarpal joint of radius is used regardless of an individual's age, sex, race, height,

* Corresponding author.
E-mail address: alig@unimelb.edu.au (A. Ghasem-Zadeh).

http://dx.doi.org/10.1016/j.bone.2017.05.010
8756-3282/© 2017 Elsevier Inc. All rights reserved.

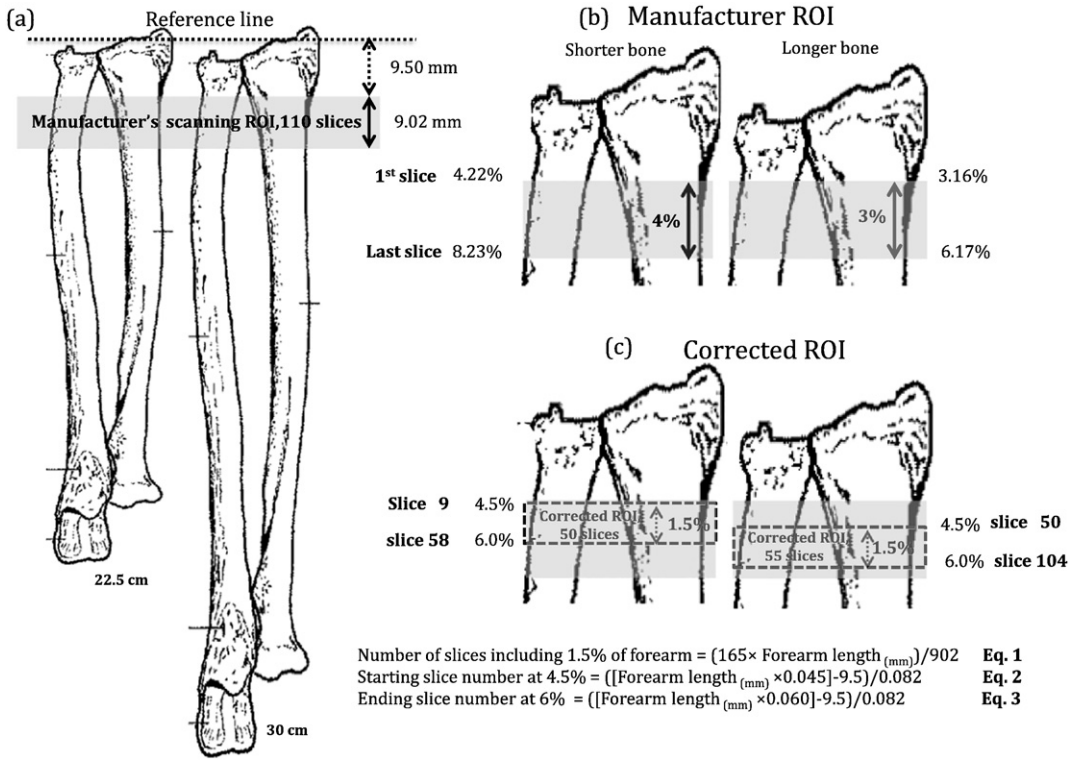

Fig. 1. (a) The reference line corresponds to the mid-radiocarpal joint. The manufacturer's fixed ROI (grey rectangle) consists of 110 slices on the shorter (22.5 cm) and longer (30 cm) forearm. (b) The fixed ROI is 4% of the shorter bone and 3% of the longer bone. Positioning is more proximal for the shorter forearm (4.22–8.23% *vs* 3.16–6.17%). (c) Calculation of the number of slices and location of the corrected ROI is obtained using Eqs. (1)–(3) to identify 1st and last slices of the 110 slice ROI.

or bone length, even though on average, men and Caucasians have longer and wider bones than women and Asians respectively [9]. As the fixed ROI is more distal in taller than shorter individuals [10–12], we hypothesized that sexual and racial dimorphisms may be partly due to differences in positioning of the ROI, not true sex and racial differences in morphology.

The same error is likely to arise comparing individuals of the same sex or same race but differing in height. For example, the effect of advancing age on bone morphology is usually examined in cross sectional studies [13]. Earlier born persons, the older cohort in a cross-sectional sample, are likely to have been shorter when they were young than later born persons forming the younger cohort in the cross-sectional sample [14]. This secular difference in stature may blunt the estimated age-related increase in cortical porosity as later born taller persons are likely to have higher porosity because longer and wider long bones have more porous cortices [15].

Table 1
Ex vivo distal radial morphology (n = 18 specimens) using the manufacturer's region of interest (ROI) positioned 1 or 2 mm distally or proximally.

	2 mm distally	1 mm distally	Manufacturer's ROI	1 mm proximally	2 mm proximally
Bone cross sectional areas (mm^2)					
Total	374.2 ± 96.0***	352.4 ± 90.0***	331.1 ± 84.4	312.0 ± 79.4***	296.3 ± 75.3***
Cortical	94.2 ± 23.0	94.0 ± 23.9	93.8 ± 24.1	94.0 ± 24.6	94.1 ± 24.9
Compact cortex	32.3 ± 9.6**	32.9 ± 10.1**	33.6 ± 10.8	34.5 ± 11.6**	35.4 ± 12.3**
Transitional zone	61.6 ± 15.1	60.7 ± 14.6 ns	60.2 ± 14.3	59.5 ± 14.1*	58.7 ± 13.8*
Medullary	148.0 ± 65.2	148.0 ± 66.2 ns	147.0 ± 66.9	145.3 ± 67.6*	142.9 ± 68.6*
Volumetric BMD ($mgHA/cm^3$)					
Total	257.9 ± 70.7***	258.9 ± 69.0***	290.1 ± 76.8	306.1 ± 79.5***	322.2 ± 82.2***
Cortical	257.9 ± 70.6**	258.9 ± 69.0**	290.1 ± 76.8	306.1 ± 79.5**	322.2 ± 82.2**
Trabecular	148.0 ± 65.2	148.0 ± 66.2	147.0 ± 67.0	145.3 ± 67.6*	142.9 ± 68.6*
Trabecular indices					
Number (1/mm)	2.17 ± 0.61	2.11 ± 0.67	2.06 ± 0.64	2.00 ± 0.64	2.00 ± 0.68
Separation (mm)	1.34 ± 0.41	1.35 ± 0.41	1.36 ± 0.41	1.38 ± 0.41*	1.40 ± 0.43**
Thickness (μm)	199 ± 11**	201 ± 12**	202 ± 12	203 ± 13**	204 ± 13**
Cortical indices					
Porosity (%)	68.8 ± 6.5***	66.3 ± 6.9***	63.7 ± 7.2	61.4 ± 7.4***	59.2 ± 7.6***
Thickness (mm)	1.46 ± 0.3**	1.50 ± 0.3**	1.55 ± 0.3	1.59 ± 0.3**	1.64 ± 0.3**
Matrix mineral density (%)	63.6 ± 1.2***	64.1 ± 1.3***	64.7 ± 1.3	65.1 ± 1.4***	65.6 ± 1.5***

Numbers are mean ± standard deviation.
p-Value (p) for testing differences relative to manufacture's ROI:
* $p < 0.05$.
** $p < 0.01$.
*** $p < 0.001$.

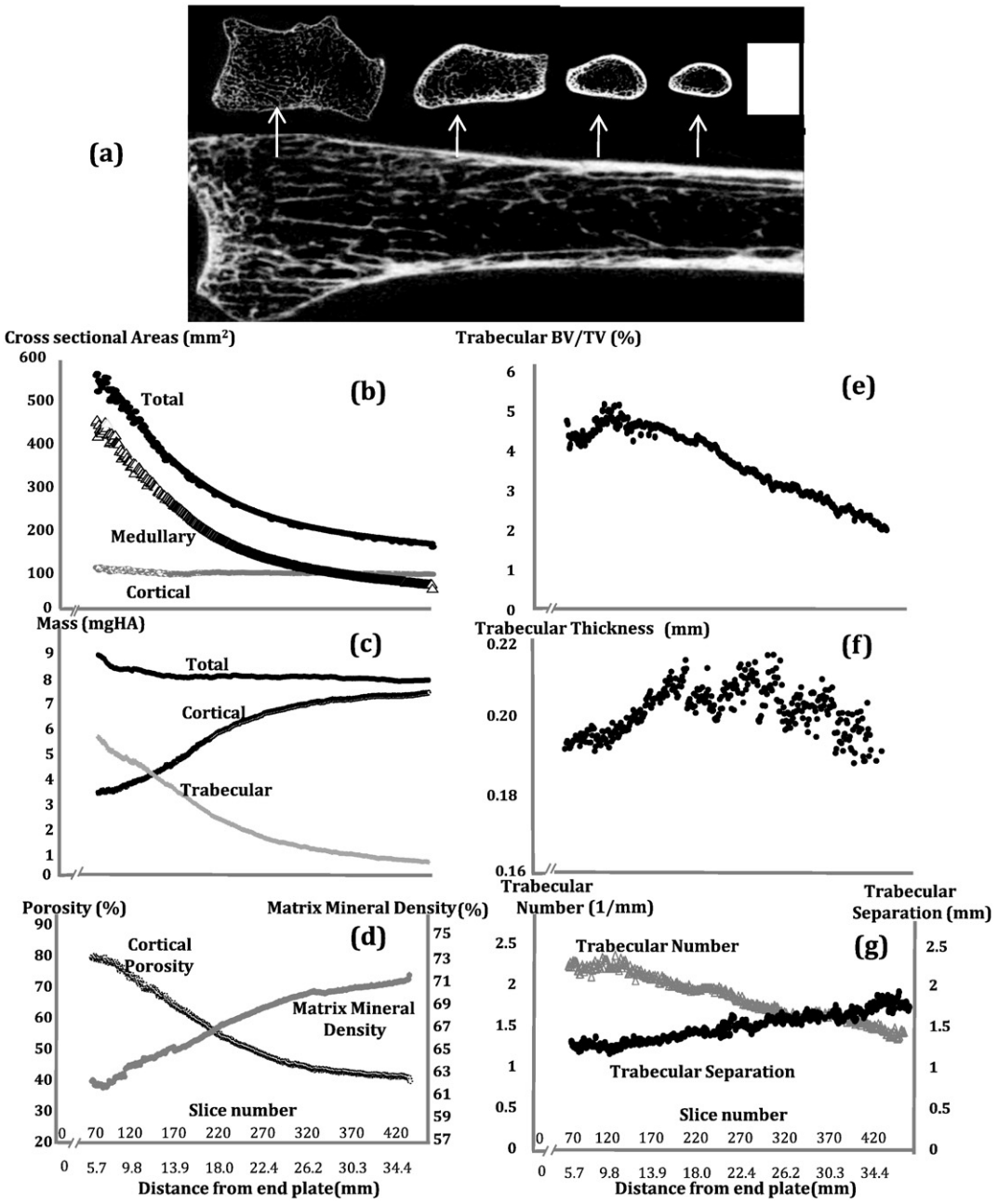

Fig. 2. (a) Axial and coronal sections of the distal radius. (b) Total and medullary cross sectional areas decrease along the bone but cortical area is constant. (c) Total mass from cross section to cross section is constant but is assembled as varying proportions of cortical and trabecular bone depending on the position of the slice. (d) Cortical porosity and matrix mineral density vary from slice to slice along the bone and within a few millimetres. (e–g) Trabecular BV/TV, trabecular thickness, number and separation vary along the bone.

Few, if any, studies have examined the biological relevance of errors in sex, race and age-specific differences in microstructure produced using the fixed ROI. Nor have there been attempts to correct any error produced so that a closer approximation of the true biological differences between sexes, races and age are quantified.

Table 2
Characteristics of the participants.

	Asian women (N = 40)	Asian men (N = 37)	Caucasian women (N = 33)	Caucasian men (N = 48)
Age (years)	34.7 ± 9.0	36.6 ± 8.4	34.5 ± 10.0	34.2 ± 7.7
Forearm length (cm)	24.6 ± 1.3	27.0 ± 1.4*	25.7 ± 1.5¥	28.1 ± 1.5*,§
Height (cm)	160.9 ± 6.2	174.0 ± 7.1*	164.5 ± 8.1¥	177.1 ± 7.2*,§
Weight (kg)	58.1 ± 9.6	75.5 ± 12.9*	70.2 ± 15.0¥	81.0 ± 15.7*

Numbers are mean ± standard deviation.
* $p < 0.001$ comparing sexes of the same race.
¥ $p < 0.05$ comparing races in women,
§ $p < 0.05$ comparing races in men.

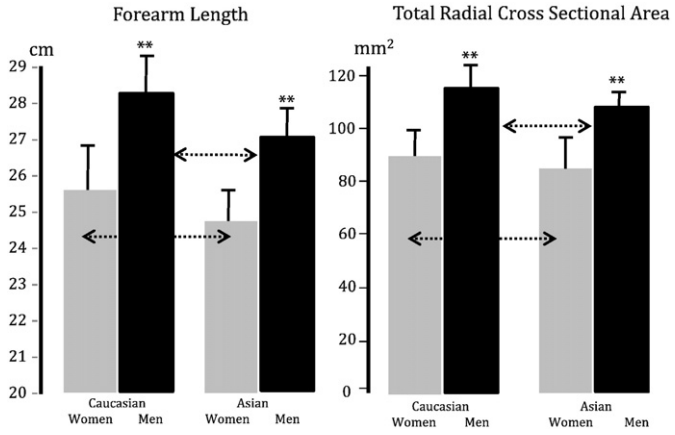

Fig. 3. Forearm length and total radial cross sectional area were higher in men than in women of each racial group (**$p < 0.01$). As shown by the double arrowheaded hatched lines, the differences by race in each sex were numerically smaller than sex differences in each race.

We assessed the heterogeneity in bone microstructure and matrix mineral density along the length of the distal radius using cadaveric specimens, and quantified sex, race and age-related differences in morphology using a fixed *versus* and corrected ROI. We report that trait differences were amenable to correction by positioning the ROI as a percentage of forearm length or by adjusting the fixed ROI by bone CSA, forearm length or height.

2. Material and methods

2.1. Ex vivo imaging

Radii were obtained at the National Disease Research Interchanges from 11 male cadavers aged 77–93 years and 7 female cadavers aged 56–88 years. Deaths were unrelated to bone disease. The specimens were scanned using HR-pQCT (XtremeCT; Scanco Medical, Brüttisellen, Switzerland) at the University of California, San Francisco (UCSF). The protocol applies 60 kVp, 900 μA, 100 ms integration time, and 82 μm isotropic voxel sizes was used to image the specimens.

Quality control was based on Shewart rules by daily scanning of a manufacturer's phantom containing rods of Hydroxyapatite (HA) (densities of 0, 100, 200, 400, and 800 mgHA/cm^3) embedded in a soft-tissue equivalent resin (QRM, Moehrendorf, Germany). The number of slices was extended to 9.02 mm distally and 18.04 mm proximally in the fixed ROI (9.5 mm from end plate) giving a total ROI of 36.08 mm containing 440 slices. All images were reconstructed automatically using the manufacturer's software. X-ray attenuation data were converted to equivalent hydroxyapatite (HA) densities. All procedures were approved by the UCSF ethics office.

2.2. In vivo imaging

We studied 158 healthy Asians of Chinese origin and Caucasian women and men aged from 21 to 53 years, and compared morphology in 38 Caucasian premenopausal women aged from 21.4 to 38 years and 33 postmenopausal Caucasian women aged from 73.1 to 95.3 years. Measurements were made at the Department of Endocrinology at Austin Health, Melbourne, Australia. The manufacturer's scanning protocol was used to scan the distal non-dominant forearm containing 110 slices, each 0.082 mm thick. The image acquisition, reconstruction and validation are reported [16]. Participants had no bone disease or drug treatment influencing bone morphology or history of fractures and all provided a written informed consent. Radiation exposure dose was ~5 μSv per measurement. The study was approved by the Austin Health Ethics Committee. The cortical porosity and other bone microstructural indices of the cadaveric radii and *in vivo* distal radius images were analysed using StrAx 1.0 Algorithm [17].

2.3. Adjusting the fixed ROI

Forearm length was measured as the distance between the ulnar styloid and olecranon processes by calliper (CV = 1%, equivalent to 2–3 mm based on measuring 30 individuals twice on separate occasions). To cover the same anatomical ROI and the equivalent number of slices in persons with a shorter or longer forearm, the corrected ROI started at 4.5% of forearm length calculated from the distal point (reference line) and extended 1.5% proximally (4.5–6%). The locations of the first and last slices and the number of slices were calculated based on forearm length using equations (Eqs. (1)–(3)) (Fig. 1).

2.4. Statistical analyses

Analyses were performed using SPSS (version 22.0). Paired *t*-tests were used to compare ROIs 1–2 mm proximal or distal to the manufacture's ROI in cadaveric radii *ex vivo*, and to compare fixed *versus* corrected ROIs in same individuals *in vivo* irrespective of sex or race. Two-sample *t*-tests were used to compare traits measured in the fixed and corrected ROIs between sexes, between races and between young and elderly women. Sex differences and racial differences in morphology were expressed as standardized deviations (SDs) and these SDs were compared in the fixed and in the corrected ROIs. Trait differences between sexes, races and young and elderly Caucasian women were assessed using analysis of covariance (ANCOVA) adjusting for total CSA, forearm length or height differences. All results were expressed as mean ± SD, with significance set at 5% level (two-tailed).

Table 3
Distal radial microstructure in the fixed and corrected region of interest in Asian and Caucasian women and men.

	Asian women		Asian men		Caucasian women		Caucasian men	
	Fixed	Corrected	Fixed	Corrected	Fixed	Corrected	Fixed	Corrected
Total CSA (mm^2)	221.4 ± 40.3	234.1 ± 38.0**	304.9 ± 46.7	298.4 ± 44.3**	260.4 ± 60.9	267.5 ± 53.2*	354.6 ± 58.4	335.4 ± 50.0**
Cortical area (mm^2)	87.6 ± 11.3	88.4 ± 11.0**	110.9 ± 13.7	109.9 ± 13.8**	91.9 ± 13.6	92.2 ± 13.3	120.5 ± 11.4	119.1 ± 11.6**
Medullary area (mm^2)	133.8 ± 31.9	145.6 ± 29.9**	194.1 ± 36.7	188.6 ± 33.7*	168.4 ± 48.8	175.3 ± 41.7*	234.2 ± 51.9	216.2 ± 44.2**
Porosity of total cortex (%)	55.5 ± 5.2	58.0 ± 4.8**	57.7 ± 4.3	56.9 ± 3.8*	60.4 ± 5.8	61.9 ± 4.7**	60.8 ± 5.0	58.9 ± 4.8**
Total vBMD (mgHA/cm^3)	390.8 ± 65.8	361.1 ± 58.4**	374.9 ± 48.6	375.7 ± 43.7	335.9 ± 57.3	318.4 ± 46.8**	345.9 ± 58.3	356.4 ± 60.2**
Cortical vBMD (mgHA/cm^3)	725.5 ± 65.4	693.0 ± 59.1**	699.1 ± 54.6	709.1 ± 4.3*	664.7 ± 71.9	644.8 ± 58.9**	661.3 ± 63.2	684.5 ± 61.0**
Trabecular vBMD (mgHA/cm^3)	148.4 ± 46.1	150.6 ± 45.8**	168.9 ± 42.3	170.2 ± 40.9*	133.5 ± 41.4	137.6 ± 38.3**	171.4 ± 46.4	171.7 ± 47.6
Matrix mineral density (%)	64.9 ± 1.3	64.1 ± 1.1**	63.7 ± 1.1	63.7 ± 1.0	63.7 ± 1.2	63.1 ± 1.2**	63.1 ± 1.2	63.5 ± 1.3**

Mean ± standard deviation.
* Significant difference with $p < 0.05$.
** Significant difference with $p < 0.01$.

Table 4
Sexual dimorphism in distal radial microstructure in the fixed ROI and in the corrected ROI in Asians and Caucasians.

	Fixed ROI (Asian)		Corrected ROI (Asian)		Fixed ROI (Caucasian)		Corrected ROI (Caucasian)	
	Women	Men	Women	Men	Women	Men	Women	Men
Total CSA (mm^2)	221.4 ± 40.3	304.9 ± 46.7**	234.1 ± 38.0	298.4 ± 44.3**	260.4 ± 60.9	354.6 ± 58.4**	267.5 ± 53.2	335.4 ± 50.0**
Cortical area (mm^2)	87.6 ± 11.3	110.9 ± 13.7**	88.4 ± 11.0	109.9 ± 13.8**	91.9 ± 13.6	120.5 ± 11.4**	92.2 ± 13.3	119.1 ± 11.6**
Medullary area (mm^2)	133.8 ± 31.9	194.1 ± 36.7**	145.6 ± 29.9	188.6 ± 33.7**	168.4 ± 48.8	234.2 ± 51.9**	175.3 ± 41.7	216.2 ± 44.2**
Porosity of total cortex (%)	55.5 ± 5.2	57.7 ± 4.3*	58.0 ± 4.8	56.9 ± 3.8	60.4 ± 5.8	60.8 ± 5.0	61.9 ± 4.6	58.9 ± 4.8*
Total vBMD ($mgHA/cm^3$)	390.8 ± 65.8	374.9 ± 48.6	361.1 ± 58.4	375.7 ± 43.7	335.9 ± 57.3	345.9 ± 58.3	318.4 ± 46.8	356.4 ± 60.2**
Cortical vBMD ($mgHA/cm^3$)	725.5 ± 65.4	699.1 ± 54.6*	693.0 ± 59.1	709.1 ± 4.3	664.7 ± 71.9	661.3 ± 63.2	644.8 ± 58.9	684.5 ± 61.0**
Trabecular vBMD ($mgHA/cm^3$)	148.4 ± 46.1	168.9 ± 42.3*	150.6 ± 45.8	170.2 ± 40.9*	133.5 ± 41.4	171.4 ± 46.4**	137.6 ± 38.3	171.7 ± 47.6**
Matrix mineral density (%)	64.9 ± 1.3	63.75 ± 1.1**	64.1 ± 1.1	63.73 ± 1.0	63.71 ± 1.2	63.1 ± 1.2*	63.11 ± 1.2	63.5 ± 1.3

Mean ± standard deviation,
* Significant difference with $p < 0.05$.
** Significant difference with $p < 0.01$.

3. Results

3.1. Ex vivo – similar amounts of bone assemble of adjacent bone cross-sections

The bone mass used to assemble each cross section was constant. Distally, the larger total CSA of the radial metaphysis was fashioned with a thin porous cortex of lower matrix mineral density and trabeculae within a larger medullary canal. More proximally, the constant bone mass fashioned the smaller total CSA with a thicker less porous cortex of higher matrix mineral density, a smaller medullary void volume containing progressively less trabecular bone (Table 1, Fig. 2).

3.2. In vivo – sexual and racial dimorphism

Men and Caucasians were taller and had longer forearms than women and Asians respectively (Table 2, Fig. 3). Sexual dimorphism in forearm length and total radial CSA was greater than racial dimorphism in these traits. For example, the mean sex difference in forearm length was 2.4 cm in each race, twice the racial differences of 1.1 cm in each sex.

Details of traits measured in the fixed and corrected ROIs are shown in Tables 3–5, and Fig. 4. Dimorphisms measured in the fixed ROI lessened, were unaltered, and some reversed when measured in the corrected ROI.

Comparing sexes, total and medullary CSAs were smaller in women than men of each race ($p < 0.01$). Caucasian women had 0.64 SD higher porosity and 0.63 SD lower trabecular density than Caucasian men ($p < 0.01$). Asian women had 0.25 SD higher porosity ($p = 0.72$) and 0.56 SD lower trabecular density than Asian men ($p < 0.05$).

Comparing races, total and medullary CSAs were smaller in Asians than Caucasians of each sex (all $p < 0.01$). Asian women had 0.83 SD lower porosity ($p < 0.01$) and 0.31 SD higher trabecular density than Caucasian women ($p = 0.19$). Asian and Caucasian men had similar porosity and trabecular density.

MMD did not differ in Caucasian or Asian women and men. MMD was 0.86 SD higher in Asian women than Caucasian women ($p < 0.05$), not Asian and Caucasian men.

3.3. In vivo – adjusting the fixed ROI by CSA, forearm length or height

Instead of correcting the position of the ROI, when we adjusted the fixed ROI for CSA, forearm length or height, porosity was 1.07 SD higher in Caucasian women than Caucasian men ($p < 0.01$). Asian women had higher porosity than Asian men ($p = NS$). Asian women had 0.6 SD lower porosity than Caucasian women ($p < 0.05$). Cortical porosity did not differ in Asian and Caucasia men (Fig. 5). Dimorphisms in trabecular density did not differ before or after adjustment of the fixed ROI.

3.4. In vivo – secular effects of age on stature and microstructure

Caucasian elderly women were 1.6 SD shorter and had 0.97 SD shorter forearm length than young Caucasian women ($p < 0.01$). The fixed ROI was more proximal in elderly women resulting in a 2.08 SD higher cortical porosity than in younger women. After adjustment for forearm length, cortical porosity was 2.48 SD higher in older than younger women.

4. Discussion

In the study of cadaveric specimens of the distal radius, adjacent cross sections differed in size, shape, and microstructure but each cross section was assembled using virtually the same amount of bone matrix mass. The same is reported comparing cross sectional slices along the femoral neck [4]. Variation in size was achieved by varying intracortical and medullary void volumes, not bone matrix mass [18–21]. Distally, the bone was assembled with a thin porous cortex with a lower matrix mineral density and trabecular plates separated by 'inter-trabecular'

Table 5
Racial dimorphism in distal radial microstructure in women and men in the fixed and corrected region of interest.

	Fixe ROI (women)		Corrected ROI (women)		Fixed ROI (men)		Corrected ROI (men)	
	Asian	Caucasian	Asian	Caucasian	Asian	Caucasian	Asian	Caucasian
Total CSA (mm^2)	221.4 ± 40.3	260.4 ± 60.9**	234.1 ± 38.0	267.5 ± 53.2**	304.9 ± 46.7	354.6 ± 58.4**	298.4 ± 44.3	335.4 ± 50.0**
Cortical area (mm^2)	87.6 ± 11.3	91.9 ± 13.6	88.4 ± 11.0	92.2 ± 13.3	110.9 ± 13.7	120.5 ± 11.4**	109.9 ± 13.8	119.1 ± 11.6**
Medullary area (mm^2)	133.8 ± 31.9	168.4 ± 48.8**	145.6 ± 29.9	175.3 ± 41.7**	194.1 ± 36.7	234.2 ± 51.9**	188.6 ± 33.7	216.2 ± 44.2**
Porosity of total cortex (%)	55.5 ± 5.2	60.45 ± 5.8**	58.0 ± 4.8	61.94 ± 4.7**	57.7 ± 4.3	60.8 ± 5.0 **	56.9 ± 3.8	58.9 ± 4.8
Total vBMD ($mgHA/cm^3$)	390.8 ± 65.8	335.9 ± 57.3**	361.1 ± 58.4	318.4 ± 46.8**	374.9 ± 48.6	345.9 ± 58.3	375.7 ± 43.7	356.4 ± 60.2
Cortical vBMD ($mgHA/cm^3$)	725.5 ± 65.4	664.7 ± 71.9**	693.0 ± 59.1	644.8 ± 58.9**	699.1 ± 54.6	661.3 ± 63.2	709.1 ± 4.3	684.5 ± 61.0
Trabecular vBMD ($mgHA/cm^3$)	148.4 ± 46.1	133.5 ± 41.4	150.6 ± 45.8	137.6 ± 38.3	168.9 ± 42.3	171.4 ± 46.4	170.2 ± 40.9	171.7 ± 47.6
Matrix mineral density (%)	64.9 ± 1.3	63.71 ± 1.2*	64.1 ± 1.1	63.1 ± 1.2*	63.75 ± 1.1	63.1 ± 1.2*	63.7 ± 1.0	63.5 ± 1.3

Mean ± standard deviation.
* Significant difference with $p < 0.05$.
** Significant difference with $p < 0.01$.

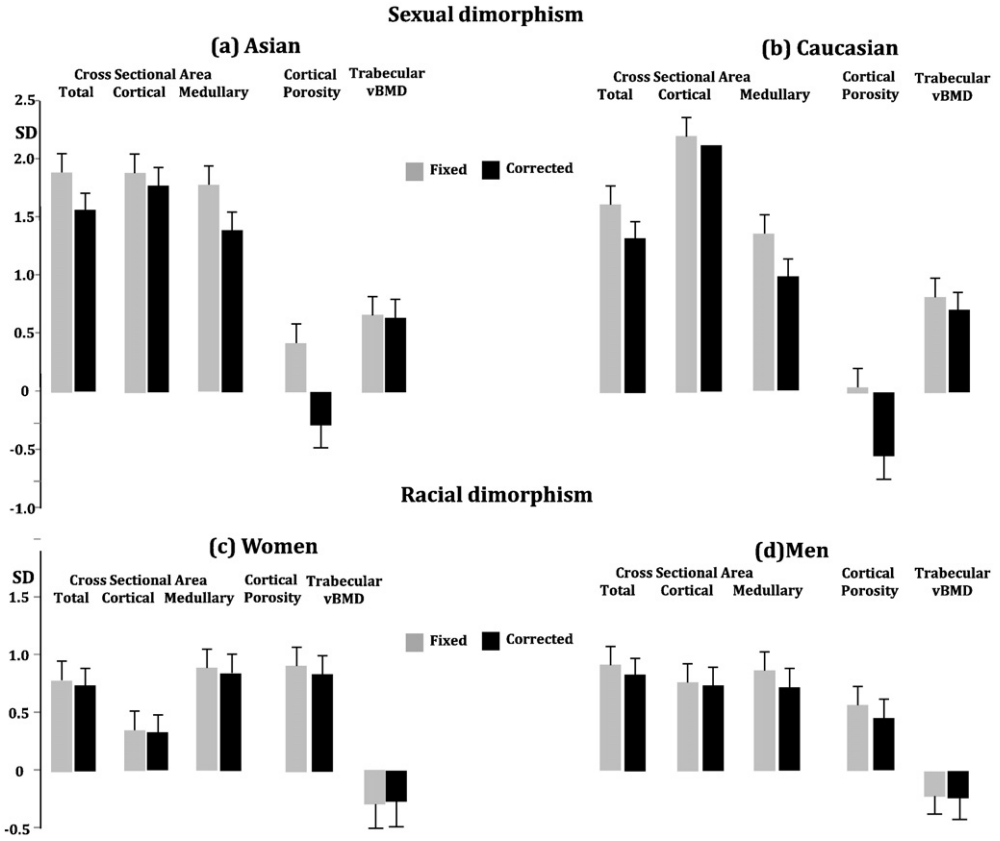

Fig. 4. Sexual dimorphism in (a) Asians (b) Caucasians, and racial dimorphisms in (c) women and (d) men, determined in the fixed (black bars) and in the corrected region of interest (grey bars). In general, trait differences (expressed as a standard deviations) lessened when measured in the corrected region of interest (see text and Tables 4 and 5).

void volume; features conferring lightness for mobility and dexterity. More proximally, the constant mass was fashioned as a thicker cortex with low porosity and higher matrix mineral density, a small medullary canal containing little or no trabecular bone.

Given the heterogeneity in bone size, microstructure and matrix mineral density from slice to slice within a region of under 5 mm in length, positioning of a ROI in anatomically equivalent positions becomes important when comparing individuals differing in forearm length. This is a recognised requirement using pQCT scanning [22,23]. The need for correct position of the ROI becomes particularly relevant using high resolution pQCT given this heterogeneity and the small ROI used.

The positioning of a ROI based on a percentage of forearm length instead of a fixed ROI was an attempt to measure anatomically equivalent regions in persons differing in forearm length. Men and Caucasians are taller and had longer forearms than women and Asians respectively. A fixed ROI was more distal in taller people and so overestimated porosity and trabecular density and under-estimated matrix mineral density. A fixed ROI was more proximal in a shorter person and so underestimated porosity and trabecular density and over-estimated matrix mineral density, the net effect being an exaggeration of sex and racial dimorphisms.

When corrected, the ROIs approximated; the more distal ROI in taller persons with longer forearms (Caucasians, males) moved proximally so that total and medullary areas decreased, porosity and trabecular density decreased and matrix mineral density increased, and the more proximal ROI in shorter persons with shorter forearms (Asians, women) moved distally so that the total and medullary areas increased, porosity and trabecular density increased and matrix mineral density decreased. The net effect was a lessening or reversal of sex and racial dimorphisms.

The sexual and racial dimorphism may be, in part, the result of differences in remodelling rate. Women remodel their skeletons more rapidly than men after menopause [24], accounting for the higher porosity and lower trabecular density in Caucasian women than Caucasian men, and in Asian women than Asian men. We did not detect lower MMD in women than men in either race; perhaps due to younger age of the sample.

Asian women remodel their skeleton more slowly than Caucasian Women [25]. Accordingly, Asian women had lower porosity, higher trabecular density and higher MMD than Caucasian women. Men remodel their skeleton slowly. No differences were detected in porosity, trabecular density or MMD in Asian and Caucasian men.

Sexual dimorphism was greater than racial dimorphism in this cohort because women and men of the same race differed in height and forearm length more than Asians and Caucasians of the same sex [26]. A reason for this may relate, in part, to the timing of puberty. Appendicular growth is rapid prior puberty. Males enter puberty about one year later than females and have a longer intrapubertal growth period. Chinese enter puberty only 6–9 months earlier than Caucasians so that the sex difference in the duration of pre-pubertal appendicular growth is greater than the racial difference, at least comparing Caucasians and Asians [27,28]. Whether this applies to other racial groups is not known [29].

Longer bones usually have a larger cross sectional area, and wider long bones have higher porosity than narrower long bones [6]. Thus, in situations where forearm length is not available, we report that adjustment of the fixed ROI by CSA or height produced similar results for cortical porosity and trabecular density as found by correcting the position of the ROI.

Failure to correct the anatomical error may misrepresent fracture risk. For example, correcting the ROI resulted in a 0.51 SD higher porosity in Asian women and 0.32 SD higher porosity in Caucasian women. Failure to correct the ROI overestimated porosity by 0.21 SD in Asian men and by 0.39 SD in Caucasian men. Failure to correct the ROI comparing elderly Caucasian women underestimated the age-related increase in

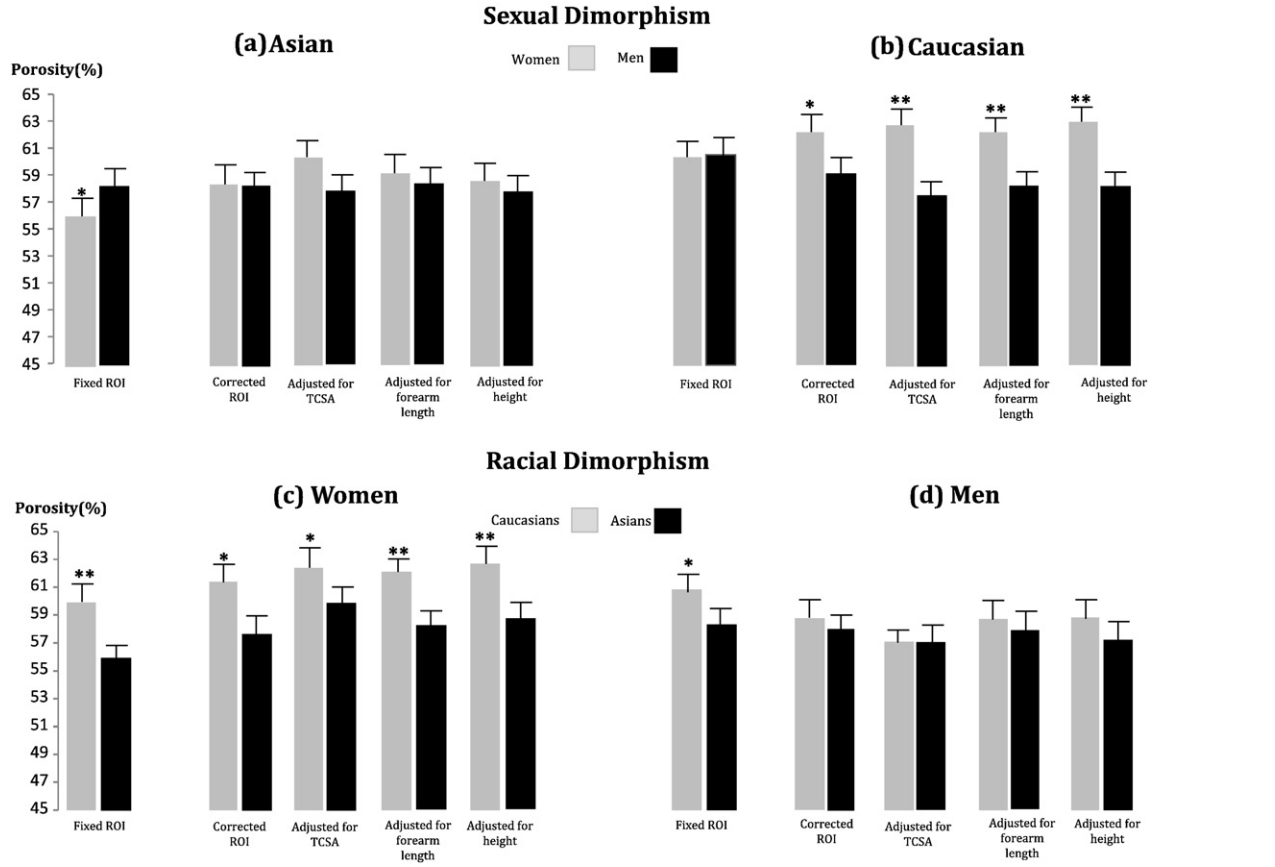

Fig. 5. Sexual and racial dimorphism in cortical porosity in the fixed region of interest, in the corrected region of interest, and in the fixed region of interest adjusted for total cross sectional area (TCSA), forearm length and height. (a) In Asians, the lower porosity in women than men was no longer seen after adjustment and porosity was higher after adjustment for total CSA. (b) In Caucasians, there was no sex difference using the fixed ROI but higher porosity in women than men becomes apparent using any one of the four approaches. (c) Higher porosity in Caucasian than Asian women was found with all approaches. (d) In Caucasian men, porosity was higher than in Asian men in the fixed ROI but not the corrected or any adjusted approaches. *$p < 0.05$, **$p < 0.01$.

porosity by 0.40 SD. These discrepancies resemble the 0.40 SD higher cortical porosity in women with forearm fractures relative to controls [30].

This study has several limitations. Our purpose was to signal the need for caution in interpreting dimorphisms by sex, race and age given the small ROIs chosen in a heterogeneous structure like the distal radial metaphysis. However, we had no post-mortem samples from Asian subjects to establish the accuracy of each adjustment method. Sex, racial and age comparison were based on small sample sizes and we only measured Caucasian and Asians of Chinese origin, not other racial groups. Nor did we examine secular effects of age in men. We confined measurements to cortical porosity, trabecular morphology and matrix mineral density. We prefer to avoid making definitive statements concerning the magnitude of sex, race and age related differences in macro- and microstructure because large cohorts are needed to provide robust data. We did not examine whether errors in repositioning in placebo controlled trials may obscure or exaggerate the effects of therapy on morphology. While differences in morphology were found in the fixed and corrected ROIs, evidence that these differences influence the sensitivity and specificity for fracture prediction is not available.

In conclusion, to the best of our knowledge this is the first study to provide a method that locates anatomically equivalent ROIs by repositioning the ROI according forearm length or adjusting the fixed ROI for cross sectional area, forearm length or height. Whatever the approach taken, the continued use of a fixed ROI without attention to differences in the dimensions of bone between individuals may result in misleading inferences concerning the pathogenesis of bone fragility, fracture risk, and effects of treatment.

Disclosures

A Ghasem-Zadeh is one of the inventors of the StrAx1.0 algorithm and serves as a reimbursed consultant for Straxcorp. R Zebaze has received grant and/or research support from Amgen, Merck Sharp & Dohme, Servier, Warner-Chilcott, AKP, Genzyme, Sonafi, GSK and Pfizer, and is one of the inventors of the StrAx1.0 algorithm. E Seeman has received research support and lectured at national and international meetings funded by from Allergan, Amgen, Asahi pharmaceuticals, Eli Lilly, and MSD. He is a director of the board, renumerated as Chief Medical Officer and is one of the inventors of the StrAx1.0 algorithm. AJ Burghardt has received research support from Ultragenyx Pharmaceutical. Other authors state they have no conflicts of interest.

Acknowledgements

This study was funded by Austin Medical Research Foundation Melbourne, Australia (2-1260) and NIH/NIMAS R01 AR 060700.

Authors' roles: Study design and conduct: AGZ, XW, RZ, and ES. Data collection: AGZ, AB, SB, SI, XW. Responsibility for StrAx analysis: AGZ, RZ, Statistical analyses: MB, XW, And AGZ. Drafting manuscript: AGZ, XW, SI and ES. Data interpretation and approving final version of manuscript: AGZ, XW, AB, SI, SB, MB, RZ, ES.

References

[1] J.D. Currey, Bones: Structure and Mechanics, Princeton University Press, Princeton, NJ, 2002 1–380.

[2] E. Seeman, Growth in bone mass and size—are racial and gender differences in bone mineral density more apparent than real? J. Clin. Endocrinol. Metab. 83 (5) (1998 May) 1414–1419.
[3] Q. Wang, S. Cheng, M. Alen, E. Seeman, Finnish Calex Study G, Bone's structural diversity in adult females is established before puberty, J. Clin. Endocrinol. Metab. 94 (5) (2009 May) 1555–1561.
[4] R.M. Zebaze, A. Jones, F. Welsh, M. Knackstedt, E. Seeman, Femoral neck shape and the spatial distribution of its mineral mass varies with its size: clinical and biomechanical implications, Bone 37 (2) (2005 Aug) 243–252.
[5] R.M. Zebaze, A. Jones, M. Knackstedt, G. Maalouf, E. Seeman, Construction of the femoral neck during growth determines its strength in old age, J. Bone Miner. Res. 22 (7) (2007 Jul) 1055–1061.
[6] Q. Wang, S. Cheng, M. Alen, E. Seeman, Finnish Calex Study G, Bone's structural diversity in adult females is established before puberty, J. Clin. Endocrinol. Metab. 94 (5) (2009 May) 1555–1561.
[7] G. Mall, M. Hubig, A. Buttner, J. Kuznik, R. Penning, M. Graw, Sex determination and estimation of stature from the long bones of the arm, Forensic Sci. Int. 117 (1–2) (2001 Mar 01) 23–30.
[8] X.F. Wang, Y. Duan, T.J. Beck, E. Seeman, Varying contributions of growth and ageing to racial and sex differences in femoral neck structure and strength in old age, Bone 36 (6) (2005 Jun) 978–986.
[9] S.K. Boyd, Site-specific variation of bone micro-architecture in the distal radius and tibia, J. Clin. Densitom. 11 (3) (2008 Jul–Sep) 424–430.
[10] S. Bonaretti, N. Vilayphiou, C.M. Chan, A. Yu, K. Nishiyama, D. Liu, et al., Operator variability in scan positioning is a major component of HR-pQCT precision error and is reduced by standardized training, Osteoporos. Int. (2016 Jul 30).
[11] K.Y. Cheuk, E.M. Tam, F.W. Yu, B.H. Yip, V.W. Hung, X. Wang, et al., A critical comparison between two scanning protocols of high-resolution peripheral quantitative computed tomography at the distal radius in adolescents, J. Clin. Densitom. 19 (3) (2016 Jul–Sep) 305–315.
[12] V.V. Shanbhogue, S. Hansen, U. Halekoh, K. Brixen, Use of relative vs fixed offset distance to define region of interest at the distal radius and tibia in high-resolution peripheral quantitative computed tomography, J. Clin. Densitom. 18 (2) (2015 Apr–Jun) 217–225.
[13] B.L. Riggs, L.J. Melton, R.A. Robb, J.J. Camp, E.J. Atkinson, L. McDaniel, et al., A population-based assessment of rates of bone loss at multiple skeletal sites: evidence for substantial trabecular bone loss in young adult women and men, J. Bone Miner. Res. 23 (2) (2008 Feb) 205–214.
[14] R.C. Hauspie, M. Vercauteren, C. Susanne, Secular changes in growth and maturation: an update, Acta Paediatr. 423 (1997 Nov) 20–27.
[15] A. Bjornerem, Q.M. Bui, A. Ghasem-Zadeh, J.L. Hopper, R. Zebaze, E. Seeman, Fracture risk and height: an association partly accounted for by cortical porosity of relatively thinner cortices, J. Bone Miner. Res. 28 (9) (2013 Sep) 2017–2026.
[16] X.F. Wang, Q. Wang, A. Ghasem-Zadeh, A. Evans, C. McLeod, S. Iuliano-Burns, et al., Differences in macro- and microarchitecture of the appendicular skeleton in young Chinese and white women, J. Bone Miner. Res. 24 (12) (2009 Dec) 1946–1952.
[17] R. Zebaze, A. Ghasem-Zadeh, A. Mbala, E. Seeman, A new method of segmentation of compact-appearing, transitional and trabecular compartments and quantification of cortical porosity from high resolution peripheral quantitative computed tomographic images, Bone 54 (1) (2013 May) 8–20.
[18] L. Vico, M. Zouch, A. Amirouche, D. Frere, N. Laroche, B. Koller, et al., High-resolution pQCT analysis at the distal radius and tibia discriminates patients with recent wrist and femoral neck fractures, J. Bone Miner. Res. 23 (11) (2008 Nov) 1741–1750.
[19] E. Seeman, P.D. Delmas, Bone quality—the material and structural basis of bone strength and fragility, N. Engl. J. Med. 354 (21) (2006 May 25) 2250–2261.
[20] Y. Bala, Q.M. Bui, X.F. Wang, S. Iuliano, Q. Wang, A. Ghasem-Zadeh, et al., Trabecular and cortical microstructure and fragility of the distal radius in women, J. Bone Miner. Res. 30 (4) (2015 Apr) 621–629.
[21] R.M. Zebaze, A. Jones, M. Knackstedt, G. Maalouf, E. Seeman, Construction of the femoral neck during growth determines its strength in old age, J. Bone Miner. Res. 22 (7) (2007 Jul) 1055–1061.
[22] K. Engelke, J.E. Adams, G. Armbrecht, P. Augat, C.E. Bogado, M.L. Bouxsin, et al., Clinical use of quantitative computed tomography and peripheral quantitative computed tomography in the management of osteoporosis in adults: the 2007 ISCD official positions, J. Clin. Densitometry 11 (1) (Jan–Mar 2008) 123–162.
[23] P. Augat, T. Fuerst, H.K. Genant, Quantitative bone mineral assessment at the forearm: a review, Osteoporos. Int. 8 (4) (1998) 299–310.
[24] S. Epstein, J. Poser, R. McClintock, C.C. Johnston Jr., G. Bryce, S. Hui, Differences in serum bone GLA protein with age and sex, Lancet 1 (8372) (Feb 11 1984) 307–310.
[25] J.S. Finkelstein, M. Sowers, G.A. Greendale, M.L. Lee, R.M. Neer, J.A. Cauley, et al., Ethnic variation in bone turnover in pre- and early perimenopausal women: effects of anthropometric and lifestyle factors, J. Clin. Endocrinol. Metab. 87 (7) (Jul 2002) 3051–3056.
[26] X.F. Wang, Y. Duan, T.J. Beck, E. Seeman, Varying contributions of growth and ageing to racial and sex differences in femoral neck structure and strength in old age, Bone 36 (6) (2005) 978–986.
[27] A.S. Parent, G. Teilmann, A. Juul, N.E. Skakkebaek, J. Toppari, J.P. Bourguignon, The timing of normal puberty and the age limits of sexual precocity: variations around the world, secular trends, and changes after migration, Endocr. Rev. 24 (5) (Oct 2003) 668–693.
[28] K.F. Huen, S.S. Leung, J.T. Lau, A.Y. Cheung, N.K. Leung, M.C. Chiu, Secular trend in the sexual maturation of southern Chinese girls, Acta Paediatr. 86 (10) (Oct 1997) 1121–1124.
[29] D.S. Freedman, L.K. Khan, M.K. Serdula, W.H. Dietz, S.R. Srinivasan, G.S. Berenson, Relation of age at menarche to race, time period, and anthropometric dimensions: the Bogalusa Heart Study, Pediatrics 110 (4) (Oct 2002), e43.
[30] Y. Bala, R. Zebaze, A. Ghasem-Zadeh, E.J. Atkinson, S. Iuliano, J.M. Peterson, et al., Cortical porosity identifies women with osteopenia at increased risk for forearm fractures, J. Bone Miner. Res. 29 (6) (2014 Jun) 1356–1362.

Osteoporos Int (2017) 28:245–257
DOI 10.1007/s00198-016-3705-5

ORIGINAL ARTICLE

Operator variability in scan positioning is a major component of HR-pQCT precision error and is reduced by standardized training

S. Bonaretti[1,2] · N. Vilayphiou[3] · C. M. Chan[4] · A. Yu[1] · K. Nishiyama[5] · D. Liu[6] · S. Boutroy[7] · A. Ghasem-Zadeh[8] · S. K. Boyd[9] · R. Chapurlat[7] · H. McKay[6] · E. Shane[5] · M. L. Bouxsein[10] · D. M. Black[11] · S. Majumdar[1] · E. S. Orwoll[12] · T. F. Lang[1] · S. Khosla[13] · A. J. Burghardt[1]

Received: 12 November 2015 / Accepted: 7 July 2016 / Published online: 30 July 2016
© International Osteoporosis Foundation and National Osteoporosis Foundation 2016

Abstract
Summary In this study, we determined that operator positioning precision contributes significant measurement error in high-resolution peripheral quantitative computed tomography (HR-pQCT). Moreover, we developed software to quantify intra- and inter-operator variability and demonstrated that standard positioning training (now available as a web-based application) can significantly reduce inter-operator variability.
Introduction HR-pQCT is increasingly used to assess bone quality, fracture risk, and anti-fracture interventions. The

✉ S. Bonaretti
serena.bonaretti@stanford.edu

N. Vilayphiou
nvilayphiou@scanco.ch

C. M. Chan
cchan14@berkeley.edu

A. Yu
Andrew.Yu@ucsf.edu

K. Nishiyama
kn2205@cumc.columbia.edu

D. Liu
danmei.liu@hiphealth.ca

S. Boutroy
stephanie.boutroy@inserm.fr

A. Ghasem-Zadeh
alig@unimelb.edu.au

S. K. Boyd
skboyd@ucalgary.ca

R. Chapurlat
roland.chapurlat@inserm.fr

H. McKay
heather.mckay@ubc.ca

E. Shane
es54@cumc.columbia.edu

M. L. Bouxsein
mbouxsei@bidmc.harvard.edu

D. M. Black
DennisB@psg.ucsf.edu

S. Majumdar
Sharmila.Majumdar@ucsf.edu

E. S. Orwoll
orwoll@ohsu.edu

T. F. Lang
thomas.lang@ucsf.edu

S. Khosla
khosla.sundeep@mayo.edu

A. J. Burghardt
andrew.burghardt@ucsf.edu

[1] Department of Radiology and Biomedical Imaging, University of California, San Francisco, CA, USA

[2] Present address: Department of Radiology, Stanford University, Stanford, CA, USA

[3] Scanco Medical AG, Brüttisellen, Switzerland

[4] University of California Berkeley, Berkeley, CA, USA

[5] Division of Endocrinology, Department of Medicine, Columbia University Medical Center, New York, NY, USA

[6] University of British Columbia, Vancouver, BC, Canada

contribution of the operator has not been adequately accounted in measurement precision. Operators acquire a 2D projection ("scout view image") and define the region to be scanned by positioning a "reference line" on a standard anatomical landmark. In this study, we (i) evaluated the contribution of positioning variability to in vivo measurement precision, (ii) measured intra- and inter-operator positioning variability, and (iii) tested if custom training software led to superior reproducibility in new operators compared to experienced operators.

Methods To evaluate the operator in vivo measurement precision, we compared precision errors calculated in 64 co-registered and non-co-registered scan-rescan images. To quantify operator variability, we developed software that simulates the positioning process of the scanner's software. Eight experienced operators positioned reference lines on scout view images designed to test intra- and inter-operator reproducibility. Finally, we developed modules for training and evaluation of reference line positioning. We enrolled six new operators to participate in a common training, followed by the same reproducibility experiments performed by the experienced group.

Results In vivo precision errors were up to threefold greater (Tt.BMD and Ct.Th) when variability in scan positioning was included. The inter-operator precision errors were significantly greater than the short-term intra-operator precision ($p < 0.001$). New trained operators achieved comparable intra-operator reproducibility to experienced operators and lower inter-operator reproducibility ($p < 0.001$). Precision errors were significantly greater for the radius than for the tibia.

Conclusion Operator reference line positioning contributes significantly to in vivo measurement precision and is significantly greater for multi-operator datasets. Inter-operator variability can be significantly reduced using a systematic training platform, now available online (http://webapps.radiology.ucsf.edu/refline/).

KEYWORDS HR-pQCT · Multicenter studies · Operator reproducibility · Precision · Standardization

Introduction

High-resolution peripheral quantitative computed tomography (HR-pQCT) is increasingly used [1] to assess bone quality [2, 3], to investigate age-, sex-, and race-related differences [4, 5], to evaluate bone diseases and monitor drug therapies [6–9], and to assess fracture risk [10, 11]. HR-pQCT allows the acquisition of in vivo high-resolution images (isotropic voxel size 82 μm, stack length = 9.02 mm) of the distal radius and distal tibia with low radiation dose (3 μSv). From the images, densitometric and structural parameters can be measured to characterize the bone as a whole and separately as cortical and trabecular compartments. In addition, the images can be used to perform finite element analysis to assess bone strength.

High measurement precision is fundamental to reliably calculate bone parameters [12]. In previous studies reported in the literature, precision errors for HR-pQCT were calculated from scan-rescan images with subject repositioning between the repetitions. Scan-rescan images are usually acquired longitudinally in short-, intermediate-, and long-term repetitions. HR-pQCT precision errors are smaller ex vivo (<1.5 %) than in vivo [13, 14], for the tibia (<5.2 %) than for the radius (<6.3 %) [3, 15], and for densitometric (<1.5 %) than for structural (<4.5 %) measurements [2, 4]. In general, precision errors are calculated as coefficient of variation of bone measurements extracted from co-registered scan-rescan images [16]. However, co-registration limits the measurement of bone parameters to a common volume between the scan-rescan images. Therefore, this calculation of measurement precision includes the effect of factors such as inherent scanner precision, limb positioning in the scanner, and image quality degradation due to motion artifacts, but notably excludes the variability introduced by the operator when defining the anatomic region to be scanned.

To define the anatomic region to be scanned, the operator acquires a 2D anterior-posterior projection of the proximal limb, commonly named "scout view image". On the scout view image, the operator visually identifies an anatomic landmark and manually intersects it with a horizontal reference line (Fig. 1). From the reference line, the anatomic volume to be scanned is offset by a standard distance. In the forearm, the anatomic landmark is traditionally an inflection in the curvature of the articular surface of the radius between the scaphoid and lunate fossae of the radiocarpal joint, whereas in the lower leg, the anatomic landmark is the apex of the distal articular plateau of the tibia at the tibiotalar joint. The anatomic landmark is often vague or absent in the forearm, whereas it is generally clearly visible in the lower leg.

[7] INSERM UMR 1033, Université de Lyon, Lyon, France

[8] Department of Medicine, Austin Health, University of Melbourne, Melbourne, Australia

[9] Department of Radiology, Cumming School of Medicine, University of Calgary, Calgary, Alberta, Canada

[10] Center for Advanced Orthopaedic Studies, Beth Israel Deaconess Medical Center, Boston, MA, USA

[11] Department of Epidemiology and Biostatistics, University of California, San Francisco, CA, USA

[12] Division of Endocrinology, Bone and Mineral Unit, Oregon Health & Science University, Portland, OR, USA

[13] Division of Endocrinology, Metabolism and Nutrition, Department of Internal Medicine, College of Medicine, Mayo Clinic, Rochester, MN, USA

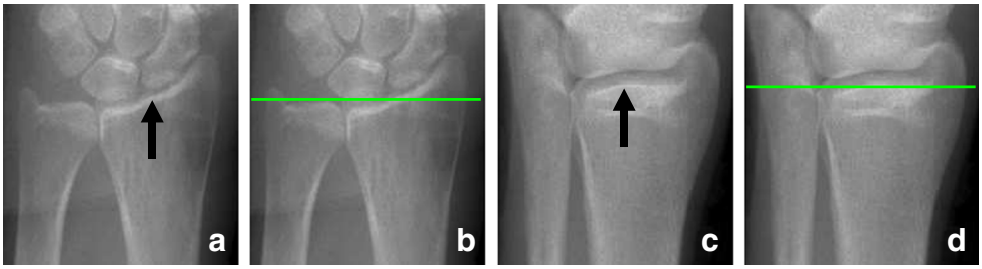

Fig. 1 Identification of the anatomic landmarks and positioning of the reference line in scout view images of the radius and tibia. The anatomic landmarks are (**a**) an inflection in the curvature of the articular surface of the radius between the scaphoid and lunate fossae of the radiocarpal joint for the forearm scan, and (**c**) the apex of the distal articular plateau of the tibia at the tibiotalar joint for the lower leg scan. To define the scan region, the operator manually positions a horizontal reference line (**b** and **d**) to intersect the landmark. The volume of interest is offset from this reference line by a fixed distance

Identification of the anatomic landmark and positioning of the reference line may vary within and between operators, affecting bone parameter measurements especially in the radius, where morphology changes remarkably along the bone axis [17, 18]. The variability in landmark identification is of paramount importance for cross-sectional or observational multicenter studies and when pooling cross-sectional datasets for retrospective analyses where multiple operators were involved in data collection. Furthermore, the reliability of using HR-pQCT to characterize an individual patient's skeletal status in a clinical context hinges on minimizing operator variability in the measurement procedure and high-quality reference data.

The goal of this study was to isolate and evaluate the contribution of operator reference line positioning to HR-pQCT measurement precision. Specifically, our first aim was to measure total precision error, including variability in scan positioning by the operator. We hypothesized that total precision error is significantly greater than what has been reported previously because the error due to positioning variability is removed by constraining the analysis to co-registered volumes of interest between repeat scans, which is the default behavior of the analysis output for follow-up measurements. The second aim was to explicitly quantify the contribution of scan positioning variability to the measurement precision error within and between operators. To this end, we developed software that simulates the acquisition interface of the HR-pQCT system and performed scan positioning reproducibility experiments. We hypothesized that operator variability in scan positioning is a major source of error for single and multicenter studies. Finally, the third aim was to evaluate the precision of new HR-pQCT operators who participated in a standard training curriculum. We developed training software for operators to perform scan positioning exercises on a collection of scout view images. We hypothesized that our training platform would lead to superior inter-operator precision errors.

Materials and methods

Study design

Our investigation of operator positioning variability and its contribution to measurement precision errors in HR-pQCT followed two complimentary study procedures (Fig. 2). First, we performed an in vivo scan-rescan reproducibility study to compare the *true* total precision error for HR-pQCT bone measurements (including scan positioning variability) to the precision error as it has previously been measured for HR-pQCT (excluding scan positioning variability). Specifically, we compared precision errors for bone parameters measured in the entire volumes acquired for each repeat scan, to those measured in volume of interest constrained to overlapping

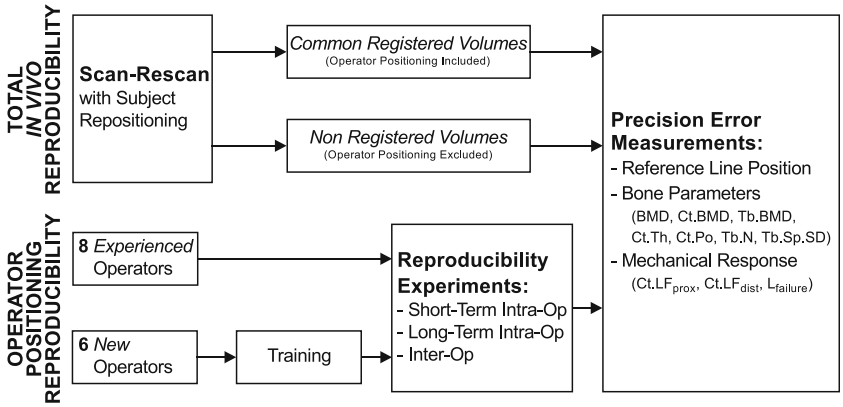

Fig. 2 Design of our study. First, we investigated the contribution of the HR-pQCT operators to total acquisition precision, and then we decomposed operator precision in intra- and inter-operator precision. In the last case, we also tested the efficacy of our training tool at reducing operator precision errors

slices between scan and rescan. Second, we isolated the error produced by operator positioning variability by calculating bone parameters in sub-volumes corresponding to variable operator-defined scan positions. We performed retrospective positioning experiments using custom scan simulation software and the scout view images collected for this second study in order to evaluate: (i) short-term intra-operator, (ii) long-term intra-operator, and (iii) inter-operator positioning precision. Based on the positioning experiments, we quantified the absolute reference line position precision and the corresponding precision errors for bone parameters. This second study was performed in (i) a group of experienced operators and (ii) a group of operators without previous HR-pQCT experience, who performed custom software training and evaluation exercises prior to their reproducibility experiments.

Operators

This study involved 14 HR-pQCT operators from different imaging centers situated in North America, Europe, and Australia. Of these, eight operators (S.B., S.B., N.P.D., A. G.-Z., M. H., D. L., K. N., and C. D.) had significant previous research experience with HR-pQCT at their respective institutions, but heterogeneous training histories. These operators participated only in the reproducibility experiments (Fig. 2). The remaining six operators (D.C., S.H., K.J., K.K., P.M., and N.W.) were clinical research technicians employed to perform HR-pQCT scans for the osteoporotic fractures in men (MrOS) study. These operators were licensed densitometry technicians without previous experience with HR-pQCT. Before participating in the reproducibility experiments, the operators were trained on reference line positioning to receive certification. Certification consisted of passing evaluation modules on reference line positioning and performing 10 acceptable imaging exams following the MrOS study protocol. Five of the MrOS operators participated in centralized training at a single MrOS clinical center, while one operator received identical on-site training by the same instructors (N.V. and A.J.B.) 4 weeks later.

Imaging

A total of 120 subjects were scanned at the University of California, San Francisco (UCSF) and at Mayo Clinic (60 at each center) using each center's first generation HR-pQCT system (XtremeCT, Scanco Medical AG, Brüttisellen, Switzerland). Subjects comprised 56 men and 64 women, with age range of 65–80 years (mean age = 71 ± 4 years). At each imaging center, a single operator scanned all subjects using an acquisition protocol provided by the organizing center (UCSF). After positioning the subject's non-dominant limb in a carbon fiber cast, the operator inserted the limb in the scanner and acquired standard dorsal-palmar (forearm) and oblique anterolateral-posteromedial (lower leg) scout view images. On this image, the operator identified the anatomic landmark and intersected the horizontal reference line with this position to define the tomographic scan region, according to the guidelines of the manufacturer. Volumetric images were acquired using standard in vivo settings (60 kVp, 900 μA, 100 ms integration time). For 34 subjects at UCSF and 30 subjects at Mayo Clinic, a single stack of slices was acquired (110 slices, 9.02 mm) at the standard fixed offset from the reference line (9.5 mm for the radius and 22.5 mm for the tibia) (Fig. 3a, b). All subjects were scanned twice at the same location with repositioning performed between acquisitions. These scan-rescan images were used to evaluate the contribution of operators in total acquisition reproducibility. For the remaining 26 subjects at UCSF and 30 subjects at Mayo Clinic, two sequential stacks (220 slices, 18.04 mm) were acquired. The double-stack volume was centered on the standard single-stack location. Therefore, the offset from the reference line to the distal-most slice of the scan was 4.99 mm for the radius and 17.99 mm for the tibia (Fig. 3c, d). For the double-stack protocol, all subjects were scanned once per anatomic site. These images were used to retrospectively investigate intra-operator and inter-operator positioning reproducibility and to compare operators with and without standardized training.

At scan time, the UCSF and Mayo Clinic operators assessed image quality by grading the central slice of a low-resolution reconstruction from 1 (no motion artifacts) to 5 (severe motion artifacts) [19]. The operator repeated an acquisition when the grade was equal to or greater than 3. If the best scan acquired was greater than grade 3, the image was excluded from the analysis. All subjects signed informed consent to participate in the study, and the Committees on Human Research at UCSF and Mayo Clinic approved study procedures.

Image analysis

The manufacturer's standard analysis protocol (IPL Version 5.08b, Scanco Medical) was used to semi-automatically segment all scans and calculate basic bone density and structure parameters. The software records mean values on a slice-by-slice basis, which is designed to facilitate future analysis of co-registered sub-volumes for longitudinal analyses. We utilized this feature to derive mean values for sub-volumes corresponding to positions defined by each operator in our reproducibility study. In particular, we calculated volumetric bone mineral densities of total (Tt.BMD), cortical (Ct.BMD), and trabecular (Tb.BMD) bone [20]. We computed cortical thickness (Ct.Th) using an annular approximation [20, 21], and cortical porosity (Ct.Po) using an extended cortical analysis [3, 22, 23]. Finally, we calculated trabecular number (Tb.N)

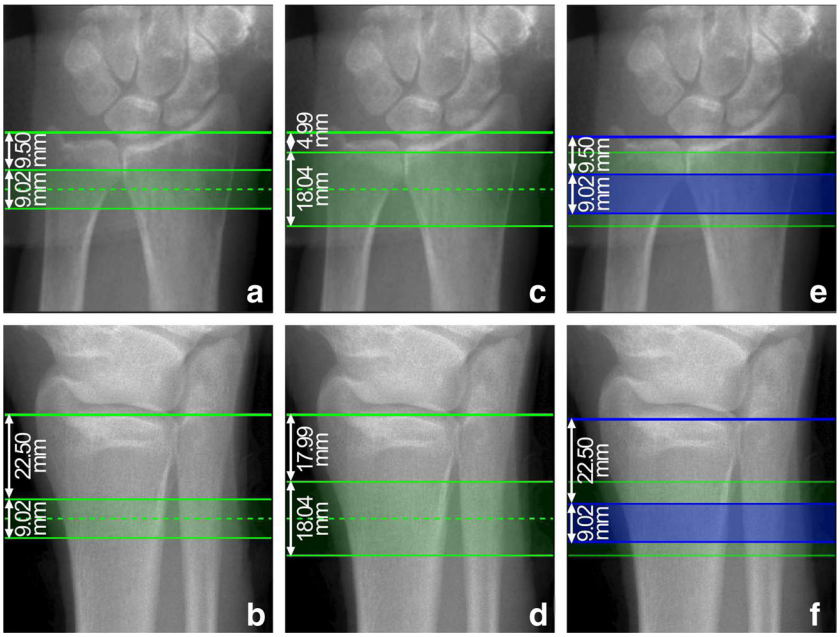

Fig. 3 Scout view images of the radius and tibia, illustrating the regions scanned in this study. (**a**, **b**) Standard-length, single stack volume: scan coverage starts at a fixed offset (9.50 mm for the radius and 22.50 mm for the tibia) from the reference line and extends 9.02 mm. (**c**, **d**) Double-length, two stack volume: scan coverage is centered on the standard stack position and extends 18.04 mm. (**e**, **f**) Standard-length sub-volume superimposed on the double-length volume, corresponding to retrospective operator reference line positioning: the standard stack (*blue*) starts at a fixed offset (9.50 mm for the radius and 22.50 mm for the tibia) from the reference line (*blue*) positioned by the operator in the scan simulation software, and extends for 9.02 mm within the double-length volume (*green*)

and heterogeneity (Tb.Sp.SD) directly using the distance transform method [24].

Mechanical response was estimated using micro-finite element (FE) analysis. From the segmented images, we automatically generated FE meshes converting image voxels to isotropic hexahedral elements [25]. We assigned Young's modulus of 6.829 GPa [26] and Poisson's ratio of 0.3 [27] to all elements, but we labeled cortical and trabecular bone differently to calculate compartmental load distributions at the distal and proximal boundaries of the model. We applied a 1 % uniaxial compressive strain to the nodes at the distal axial surface of the bone, and we constrained the nodes at the proximal axial surface. We solved the FE models using an iterative solver (Scanco FE Software v1.12; Scanco Medical AG). From the solutions, we extracted proximal cortical load fraction ($Ct.LF_{prox}$), distal cortical load fraction ($Ct.LF_{dist}$), and failure load ($L_{failure}$) [28].

Operator contribution to total acquisition reproducibility

We measured in vivo acquisition precision errors in standard-length stacks of scan-rescan images acquired with subject repositioning. From the 64 scan-rescan exams performed for the first part of our study, we analyzed 57 pairs of images of the radius and 63 pairs of images of the tibia. We excluded seven pairs of scan-rescan images of the radius and one pair of scan-rescan images of the tibia because of low image quality due to severe motion artifacts.

Scan and rescan images were co-registered by matching cross-sectional area of the bone, resulting in a slice-wise translation that provides an optimal overlap [29]. Positioning precision was calculated as root mean square of the slice shift (SD_{RMS}) between scan and rescan. The precision error for each bone parameter was calculated as root mean square of the coefficient of variation (CV_{RMS}, in %) for measurements computed from the entire 110-slice volumes for each paired scan (precision with operator positioning variability) and from sub-volumes constrained to overlapping slices between scan pairs (precision with operator positioning removed).

Operator positioning reproducibility

We directly measured precision errors contributed by operator variability in positioning the reference line by way of a retrospective reproducibility experiment. The 14 operators participating in this experiment performed reference line positioning on the set of scout view images that corresponded to our double-length acquisitions. The use of double-length stacks was critical to allow the analysis of 110-slice volumes that correspond to each operator's reference line positioning (Fig. 3e, f). From the 56 subjects enrolled for the second study, the image quality of 50 radius and 55 tibia scans was acceptable for analysis. To facilitate the reproducibility experiments, we developed software that simulates the graphical user interface of the HR-pQCT acquisition software (μCT Tomography v5.4C, Scanco Medical AG, Brüttisellen, Switzerland)

(Fig. 4b). The interface includes a pixel-to-pixel reproduction of the scout view image presentation, i.e., 1 pixel of the image corresponded to 1 pixel on the scanner's display. All text and graphical elements in the acquisition software were reproduced with the same values, colors, and layout. Graphical control elements were embedded on the left side of the simulation interface to enable control of the reproducibility experiments. The software was created using Matlab (Matlab 2012b, The MathWorks, Inc., Natick, MA, USA). Scout view images were loaded automatically and sequentially for reference line positioning. During the experiments, operators identified anatomical landmarks on each scout view image and positioned the reference line, following their usual acquisition protocol. To optimally recreate the acquisition environment, the operators performed the reproducibility experiments on the same video display used to perform HR-pQCT scans in their laboratory. The software was run from Apple MacBook or Windows PC laptops connected to the secondary video input of the scanner display. The three operator reproducibility experiments were performed in one single session that lasted approximately 1 h.

Three specific reproducibility experiments were performed to quantify:

- Short-term intra-operator precision: all 14 operators positioned reference lines on a subset of scout view images that were randomly repeated twice (a total of 45 scout view images of the radius and 48 scout view images of the tibia)
- Long-term intra-operator precision: the two operators that acquired the original images at UCSF and Mayo Clinic repositioned the reference lines on all the scout view images (50 for the radius and 55 for the tibia) 6–24 months after the original acquisition

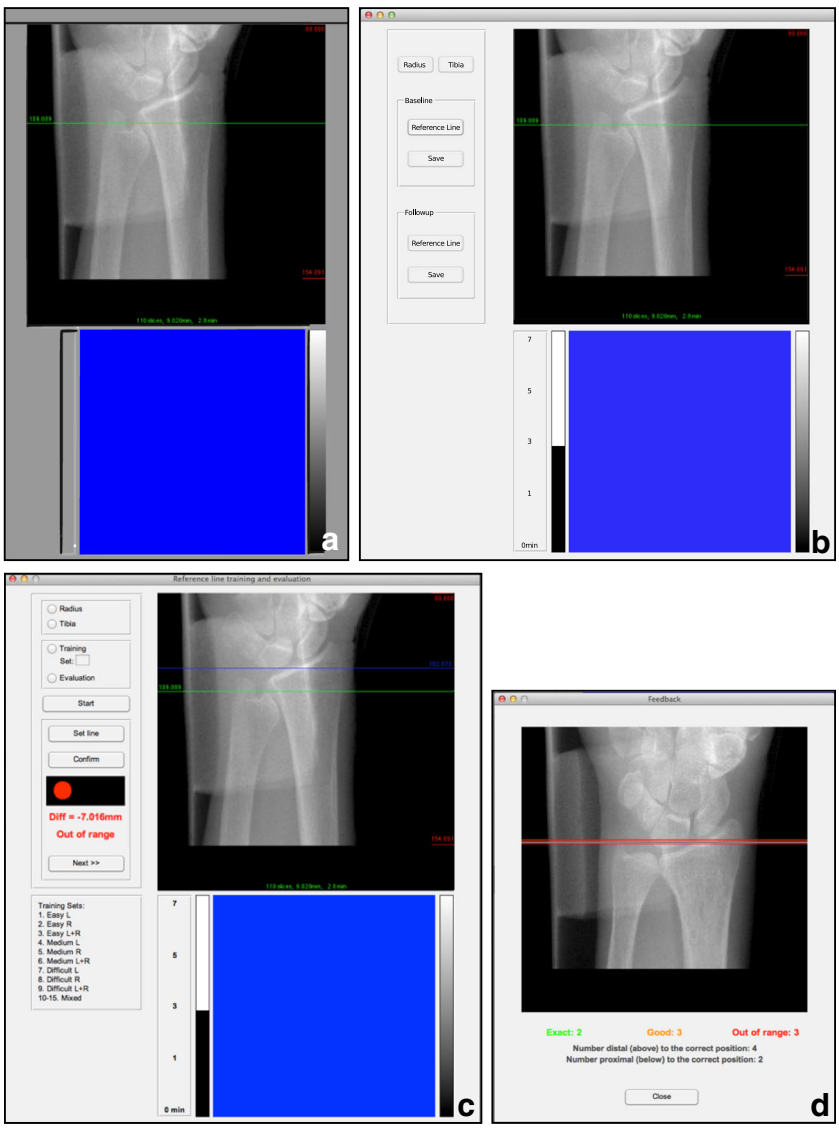

Fig. 4 The graphical user interface of the software used in this study. (**a**) Interface of the original acquisition software of the Scanco XtremeCT (μCT Tomography v5.4c). (**b**) Interface of the software created for the operator reproducibility study. The dimension of the top viewer was 512 × 512 pixels, and the dimension of the bottom viewer was 384 × 384 pixel. In the top viewer, the scout view is presented to the user as a pixel-level reproduction of the original acquisition software. (**c**) Interface of the training and evaluation software for reference line positioning. Operators could choose between training and evaluation modules, and limb and laterality on which to exercise and receive positioning feedback for each scout. (**d**) Summary feedback presented by the training software to the operator after completion of a scout view collection. The *green lines* ("exact" positioning) shows the ground truth position on a representative scout image, whereas *yellow lines* ("good" positioning) and *red lines* ("out of range" positioning) report distances from the ground truth for the preceding exercise

– Inter-operator precision: all 14 operators positioned reference lines on all scout view images (50 scout view images of the radius and 55 scout view images of the tibia)

Experienced operators were instructed to follow their local procedure for scan positioning, while the newly certified MrOS operators were instructed to follow a standard protocol provided to them as part of their training curriculum. Details of the positioning, training, and certification procedure are provided in detail in Appendix I. Short-term intra-operator and inter-operator precision errors were calculated for the experienced and new operators independently. The precision experiments for the MrOS operators were performed 8 ± 2 weeks after training and repeated to evaluate long-term precision at 17 months. For each reproducibility experiment, the positioning precision was calculated as the root mean square of the standard deviation of the absolute reference lines positions (SD_{RMS}). The corresponding bone parameter precision errors were calculated as root mean square of the coefficients of variation (CV_{RMS}) based on measurements performed in the 110-slice sub-volume corresponding to each reference line positioning. Statistical comparisons between short-term, long-term, and inter-operator precision errors, as well as between operator groups, were performed using Student's *t* test with Bonferroni corrections applied to account for multiple comparisons.

Results

Total in vivo precision errors

The variability in reference line positioning was 0.38 mm for the radius and 0.20 mm for the tibia ($p < 0.005$), corresponding to approximately 4.2 and 2.2 % of the total stack length, respectively. In vivo precision errors were greater for non-co-registered than co-registered images, both for the radius and tibia (Table 1). The differences were greater for densitometric and structural parameters than for mechanical parameters. In vivo precision errors were significantly higher for total, cortical, trabecular mineral density (Tt.BMD, Ct.BMD, and Tb.BMD), and geometric (Ct.Th) measurements when the variability in operator positioning was included in the measurement procedure (non-match). Significant differences in precision errors were not observed for the microstructural parameters (Ct.Po, Tb.N, and Tb.Sp.SD) or for FE-derived mechanical parameters. In general, precision errors were greater for the radius than for the tibia. Consequently, bone measurement errors were significantly greater for the radius than for the tibia ($p < 0.005$), except trabecular number, inter-trabecular heterogeneity, failure load, and proximal cortical load fraction.

Experienced operator reproducibility

Precision error measurements for operator variability in positioning are reported in Table 2. Short-term positioning precision was 0.3 mm. Short-term intra-operator positioning precision errors tended to be smaller than long-term intra-operator precision errors and significantly smaller than inter-operator precision errors ($p < 0.001$), both for the radius and tibia. Positioning precision errors were double for the radius than for the tibia. For both the radius and tibia, short-term intra-operator positioning errors were smaller than long-term intra-operator positioning errors and inter-operator positioning errors. The precision errors for bone parameter errors followed the trends of the positioning precision errors, with respect to short-term vs. long-term intra-operator and inter-operator precision, and radius vs. tibia. Among densitometric parameters, we observed the highest errors for Tt.BMD in the radius, where it reached 3.69 % for experienced operators in the inter-operator experiments, and for Tb.BMD for the tibia, where it reached 0.75 % for long-

Table 1 Precision of reference line positioning and corresponding in vivo precision errors for bone parameter measurements in the full 110-slice scans (non-match; includes operator positioning variability) and co-registered scan-rescan sub-volumes (match; excludes operator positioning variability)

Positioning precision (SD_{RMS} [mm])		Bone parameter precision (CV_{RMS} [%])							Biomechanics precision (CV_{RMS} [%])		
		Tt.BMD	Ct.BMD	Tb.BMD	Ct.Th	Ct.Po	Tb.N	Tb.Sp.SD	$L_{failure}$	$Ct.LF_{prox}$	$Ct.LF_{dist}$
Radius ($n = 57$; $o = 2$)											
Non-match	0.38[b]	3.33[a,b]	2.35[a,b]	1.63[a,b]	7.88[a,b]	12.02[b]	4.86	6.70	2.88	2.17	5.45[b]
Match	/	0.89[a,c]	0.77[a,c]	0.73[a]	2.12[a,c]	8.85[c]	4.27	5.72	2.69	1.88	4.34
Tibia ($n = 63$; $o = 2$)											
Non-match	0.20[b]	0.90[a,b]	1.54[a,b]	0.93[b]	2.52[a,b]	5.61[b]	5.71	5.61	2.76	1.96	3.95[b]
Match	/	0.43[a,c]	1.38[a,c]	0.76	1.30[a,c]	4.07[c]	5.82	6.33	2.73	1.87	3.73

n number of pairs of scan-rescan images, *o* number of operators

[a] Non-match vs. match comparison; $p < 0.001$

[b] Non-match radius vs. tibia comparison; $p < 0.005$

[c] Match radius vs. tibia comparison; $p < 0.005$

Table 2 Precision of reference line positioning and corresponding errors in bone parameter measurements due solely to operator positioning variability. Errors were calculated for short-term intra-operator, long-term intra-operator and inter-operator reproducibility. Operators were divided into groups: experienced operators without common training, and new operators with recent central training

	Positioning precision (SD_{RMS} [mm])	Bone parameter precision (CV_{RMS} [%])							Biomechanics precision (CV_{RMS} [%])		
		Tt.BMD	Ct.BMD	Tb.BMD	Ct.Th	Ct.Po	Tb.N	Tb.Sp.SD	$L_{failure}$	$Ct.LF_{prox}$	$Ct.LF_{dist}$
(a) Radius											
Short-term intra-op* ($n = 15$)											
Experienced ($o = 8$)	0.24 ± 0.05^{a}	$1.39 \pm 0.32^{a,c}$	$0.93 \pm 0.19^{a,c}$	0.40 ± 0.10^{a}	$3.17 \pm 0.65^{a,c}$	$2.78 \pm 0.81^{a,c}$	0.47 ± 0.14^{a}	0.83 ± 0.26^{a}	$0.42 \pm 0.12^{a,c}$	0.58 ± 0.12^{a}	$2.65 \pm 0.62^{a,c}$
New ($o = 6$)	0.28 ± 0.08^{c}	$1.50 \pm 0.25^{a,c}$	1.26 ± 0.40	0.72 ± 0.57	$3.46 \pm 1.24^{a,c}$	3.19 ± 0.96^{c}	0.69 ± 0.56	1.00 ± 0.44^{c}	0.41 ± 0.11^{c}	0.67 ± 0.25	3.03 ± 0.90^{c}
Long-term intra-op ($n = 50$; $o = 2$)	0.35	2.09^{c}	1.41^{c}	0.70	4.76	4.29^{c}	1.05	1.77	0.71^{c}	0.83	3.94
Inter-operator ($n = 50$)											
Experienced ($o = 8$)	$0.68^{a,b,c}$	$3.69^{a,b,c}$	$2.56^{a,b,c}$	$1.46^{a,b}$	$8.40^{a,b,c}$	$5.45^{a,b,c}$	$2.12^{a,b}$	$3.11^{a,b}$	$1.17^{a,b,c}$	$2.04^{a,b,c}$	$6.37^{a,b,c}$
New ($o = 6$)	$0.34^{b,c}$	$2.09^{a,b,c}$	$1.50^{b,c}$	0.87^{b}	$4.90^{a,b,c}$	$3.24^{b,c}$	1.32^{b}	$1.94^{a,b,c}$	$0.72^{a,b,c}$	$0.96^{b,c}$	$3.73^{a,b,c}$
(b) Tibia											
Short-term intra-op* ($n = 16$)											
Experienced ($o = 8$)	0.13 ± 0.07^{a}	$0.26 \pm 0.15^{a,c}$	$0.19 \pm 0.10^{a,c}$	0.26 ± 0.21^{a}	$0.94 \pm 0.50^{a,c}$	$0.69 \pm 0.33^{a,c}$	0.31 ± 0.18^{a}	0.48 ± 0.26^{a}	$0.07 \pm 0.03^{a,c}$	0.42 ± 0.16^{a}	$0.92 \pm 0.45^{a,c}$
New ($o = 6$)	$0.11 \pm 0.03^{a,c}$	0.31 ± 0.06^{c}	0.30 ± 0.07	0.28 ± 0.08	$0.52 \pm 0.29^{a,c}$	0.66 ± 0.22^{c}	0.31 ± 0.05	0.34 ± 0.02^{c}	$0.06 \pm 0.01^{a,c}$	0.39 ± 0.07	$0.75 \pm 0.24^{a,c}$
Long-term intra-op ($n = 55$; $o = 2$)	0.36	0.72^{c}	0.58^{c}	0.75	3.01	0.73^{c}	0.93	1.59	0.18^{c}	0.90	2.45
Inter-operator ($n = 55$)											
Experienced ($o = 8$)	$0.30^{a,b,c}$	$0.61^{a,b,c}$	$0.42^{a,b,c}$	$0.65^{a,b}$	$1.97^{a,b,c}$	$1.72^{a,b,c}$	$0.85^{a,b}$	$1.43^{a,b}$	$0.20^{a,b,c}$	$0.84^{a,b,c}$	$2.02^{a,b,c}$
New ($o = 6$)	$0.16^{a,b,c}$	$0.30^{b,c}$	$0.21^{b,c}$	0.32^{b}	$1.02^{a,b,c}$	$0.94^{b,c}$	0.41^{b}	$0.69^{a,b,c}$	$0.08^{a,b,c}$	$0.44^{b,c}$	$1.32^{a,b,c}$

n number of images, *o* number of operators

*For short-term intra-operator precision and corresponding bone parameters, values refer to mean ± standard deviation

[a] Short-term intra-operator vs. inter-operator comparison; $p < 0.001$

[b] Experienced vs. new operator comparison; $p < 0.001$

[c] Radius vs. tibia; $p < 0.001$

term intra-operator variability. Among geometrical and structural parameters, Ct.Th had the highest variations, especially in the radius where the inter-operator error reached 8.40 %. In terms of μFE parameters, precision errors were greatest for $Ct.LF_{dist}$, where it reached 6.37 % in the radius in the inter-operator reproducibility experiment. Inter-operator precision errors for $L_{failure}$ were modest (~1 %).

New operator reproducibility

Short-term positioning precision for the group of newly trained MrOS operators was not statistically different from the experienced operators at the radius or tibia. Accordingly, there were no significant differences in the short-term bone parameter precision errors between operator groups. In contrast, the inter-operator positioning precision at both the radius and tibia for the newly trained operators was significantly better than for the experienced operators with heterogeneous training histories (radius: 0.68 vs. 0.34 mm; tibia 0.30 vs. 0.16 mm; $p < 0.001$). Inter-operator positioning precision values for the newly trained operator group approached their respective short-term precision values (radius: 0.34 vs. 0.28 mm; tibia: 0.16 vs. 0.11 mm; $p < 0.001$), whereas the differentials between inter-operator and short-term positioning precision values were substantially greater for the experienced group (radius: 0.68 vs. 0.24 mm; tibia: 0.30 vs. 0.13 mm; $p < 0.001$). Long-term precision errors for the trainees were highly consistent with their initial performance. Intra-operator positioning SD_{RMS} was 0.25 mm for the radius (vs. 0.28 mm for the initial experiments) and 0.11 mm for the tibia (it was 0.11 mm initially). Similarly, inter-operator positioning SD_{RMS} was 0.36 mm (compared to 0.34 mm) and 0.14 mm (vs. 0.16 mm) for the radius and tibia, respectively. Bone parameter precision errors followed the trends of positioning precision errors.

Discussion

In this study, we analyzed the contribution of the operator to HR-pQCT acquisition precision. In particular, we investigated the scan localization process that requires an operator to position a horizontal reference line over a specific anatomic landmark on a scout view image. Our specific aims were to analyze operator reference line positioning in a set of scan-rescan images; to separately investigate short-term and long-term intra-operator precision and inter-operator precision; and to evaluate the efficacy of a training tool for reference line positioning. Operator reference line positioning contributed significantly to acquisition precision. Precision errors, and consequently bone parameter and mechanical measurements, were larger for the radius than for the tibia and for inter-operator than intra-operator cases. Short-term intra-operator errors were similar for experienced and trained operators, whereas inter-operator errors for trained operators were smaller than those for experienced operators and tended to be similar to short-term inter-operator errors.

Our first significant finding is that operatory variability in reference line positioning is a major component of in vivo precision error, for both the radius and tibia. Our scan-rescan precision errors measured in co-registered volumes (which inherently exclude positioning variability) were on the same order of magnitude as previously reported in other reproducibility studies ([2, 4, 13, 15, 16]). The error we measured in unregistered repeat scans was somewhat greater than what was reported by Ellouz et al. [16], though both studies observed significantly higher precision errors in unregistered vs. co-registered volumes. In the radius, precision errors for densitometric parameters were twofold greater, and Ct.Th threefold greater when operator positioning variability was included. In fact, the error due to positioning variability is greater for these parameters than the error due to severe motion artifacts [15, 19]. In general, precision errors for all bone parameters were significantly higher when variability in reference line positioning was included in the measurement, though the magnitude of the errors in trabecular structure and μFE parameters was less pronounced.

The precision errors measured by analyzing the full 110-slice volumes in our scan-rescan study are better estimates of true in vivo precision for cross-sectional studies [2–4, 13, 16]. On the other hand, positioning precision is less critical for longitudinal studies, where co-registration of baseline and follow-up acquisitions—necessary to measure changes in the same volume of interest—inherently removes variability in scan positioning. Therefore, the precision errors measured by analyzing co-registered volumes in our scan-rescan study (and most previous HR-pQCT reproducibility studies) are reasonable estimates of precision for longitudinal studies that employ image registration.

The second main outcome of our study is the direct quantification of precision errors due to operator positioning variability. The targeted investigation of operator positioning revealed that inter-operator variability is significantly greater than intra-operator variability, both for the radius and tibia. This underscores the critical need for standard training procedures for the operators charged with collecting valuable reference data and for multicenter studies. Long-term variability was greater than short-term intra-operator variability—suggesting operator drift is a possible scenario that could be addressed with regular training refreshers. The parameters most affected by positioning variability were cortical thickness and integral bone density. The sensitivity of these parameters to operator positioning precision is consistent with the significant variance in these properties along the distal-proximal axis [17, 18]. By the same token, trabecular microstructure and cortical porosity, which do not vary as dramatically across the scan volume, were less sensitive to positioning variability. The precision errors for apparent mechanical properties derived by μFE were modestly

sensitive to positioning variability (~1 % or less); however, load distributions between trabecular and cortical compartments were highly sensitive, especially in the radius. Finally, our operator reproducibility study demonstrated the relatively poorer reproducibility positioning the reference line in radius scout images, compared to tibia scout images, reflecting the challenge in landmark identification for the radius.

Our third principal finding is that inter-operator positioning precision errors were half for operators who used our training software to learn standard positioning procedures, compared to operators who had significant previous HR-pQCT experience, but heterogeneous individual training histories. In fact, the inter-operator precision values of our trainees approached their respective short-term intra-operator precision errors, whereas a significant discrepancy between intra- and inter-operator precision errors was found for the experienced group. In addition, we re-tested operator reproducibility of the MrOS trainees 17 months after certification. Encouragingly, the long-term performance indicated that the operators maintained or improved their personal precision performance, while comparability across the operators was maintained over approximately 1.5 years. This interval corresponds to three quarters of the data collection period for these MrOS visits. This suggests that our training platform could be a useful tool to homogenize operator positioning, especially for multicenter studies. These results also illustrate the importance of providing operators standardized positioning criteria and training. In this study, we gave operators precise guidelines (as detailed in Appendix 1) that provided a more detailed description of the procedure recommended by the manufacturer. In addition, while training, operators had immediate feedback on their positioning performance and had the opportunity to repeat training exercises until they achieved satisfactory scores. The current version of the software was specifically implemented for the MrOS study to certify the new operators. For general HR-pQCT operator training and certification, the software has subsequently been translated into a free web application (http://webapps.radiology.ucsf.edu/refline/). At the time of the paper publication, the webapp contains the same set of images used in this reproducibility study. In the future, we aim to develop modulus for other populations and anatomic sites, including protocols for pediatric and articular joint imaging [30–32].

The identification of the anatomical landmark was significantly more challenging for the radius compared to the tibia, with poorer positioning precision and larger resulting errors in bone parameter measurements. In fact, the anatomical landmark recommended by the manufacturer (a peak representing the confluence of the scaphoid and lunate fossae on the radial articular surface) is often not visible, and therefore requires a secondary process for localizing the reference line. Measurement precision errors at the radius are compounded by the substantial variability in geometry and density along the distal-proximal axis [17, 18]. In this study, positioning variability at the radius was significantly poorer than positioning variability for the tibia, demonstrating that the greater subjectivity involved in the landmark definition highly impacts positioning precision. Thus, improved landmark guidelines for the radius could significantly reduce measurement precision errors. The most straightforward solution would be to change the current anatomic landmark to a new anatomical landmark that is consistently visible in scout view images, less variable in its visual presentation, and features that are simple to precisely describe to operators. Possible new landmarks include the medial or the lateral margins of the radiocarpal articular surfaces of the radius (Fig. 5). The medial margin has the advantage that it would exclude variability due to the length of the joint surface (Fig. 5, length (d)), though it can be partially obscured by superposition of the ulna. On the other hand, the lateral margin is likely very precisely identifiable; however, it would include significant anatomic variability due to the length of the joint surface. One drawback of changing the landmark could be compromised comparability with existing data; however, adjusting the offset from the reference line to the scan region could be optimized to provide data comparability. An alternative would be software-based automatic positioning of the reference line at scan time [33]. Although we are actively working on this direction, automatic landmark detection involves significantly more hurdles to implement in a real-time product on the scanner. Furthermore, this represents a more significant methodological transition that will require agreement by the user community and the manufacturer. The third solution could be to train operators to recognize anatomic landmarks with

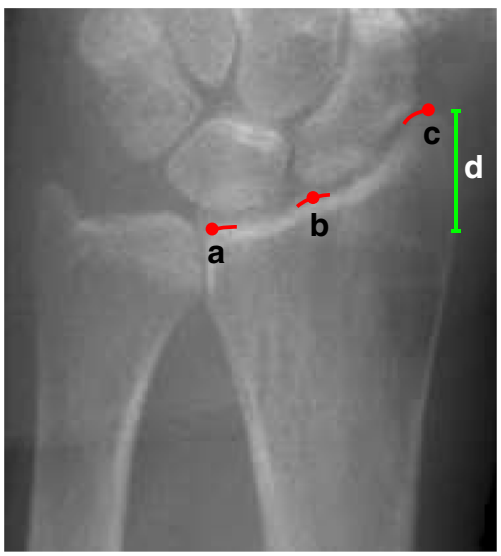

Fig. 5 Possible landmarks on the radius joint surface: **a** medial margin, **b** the notch defined by the scaphoid and lunate fossae and (**c**) lateral margin of the radiocarpal joint surface. Currently, HR-pQCT operators position the reference line that defines the region to be scanned at the notch between the scaphoid and lunate fossa of the radius (**b**). Medial (**a**) and lateral (**c**) margins represent the possible candidates for a more visible and easily identifiable anatomical landmark. The medial margin (**a**) might be preferable because it would exclude the subject-dependent joint height (**d**)

rigorously detailed and standardized protocols. In this study, we implemented this third solution and incorporated it into our training procedure and software. Operator training considerably decreased inter-operator positioning variability at the radius, which was half compared to the experienced operators, though still greater than variability observed at the tibia. Therefore, changing the anatomic landmark combined with standardized operator training is warranted to improve the precision errors for HR-pQCT of the radius.

Strengths and limitations must be acknowledged to this study. This was the first study that systematically isolated the contribution of the operators in HR-pQCT reproducibility. Measurements were performed on the same dataset for different operators, using double-length images from which we could extract pseudo-measurements based on reference line positions set by the different operators participating in our reproducibility studies. By evaluating sub-volumes within each dataset, we fixed all sources of acquisition variability except operator positioning. The experiments were performed under conditions closely approximating actual scanning, with software reproducing the XtremeCT interface and operators using their XtremeCT workstation's display to visualize the scout images. The dataset represents the main limitation of this study. For the new trained operators, images from the same dataset were used both for training and evaluation and for the precision study, albeit presented in different orders. Therefore, we did not test short- nor long-term precision in entirely independent datasets from the training data. However, the trained operators participated in the precision experiments 33–75 days after their software training and following the initiation of MrOS study data collection. The number of operators in a training group was small, though compared to the total number of operational HR-pQCT scanners, and this is not an insignificant number. It should also be noted that our tests did not account for small variations in the limb orientation that may impact the radiographic presentation of the scout image, and therefore contribute to reference line placement variability. Future experiments could systematically examine the degree to which realistic variability in the limb orientation impacts scan positioning precision. Finally, for practical considerations, we were only able to perform reproducibility experiments after the MrOS operators completed training. In the future, it would be worthwhile to test positioning precision in the same group of operators before and after completion of the training procedure. However, it is important for investigators to consider if "re-training" operators involved in ongoing data collection is advisable. It would be our recommendation that centers utilize the training platform for new technician hires or for experienced technicians transitioning to new studies.

In conclusion, we demonstrated that scan positioning precision has a large impact on HR-pQCT measurement errors. Scan positioning has not been recognized as source of measurement error in the previous reproducibility studies and not accounted for in published precision data to date. This finding has significant implications particularly for cross-sectional study design. We also demonstrated that inter-operator precision errors are significantly lower for the operators that participate in standardized training procedures compared to the experienced operators without a standard training history. Our data also suggest that the selection of a new landmark for positioning distal radius scans should be considered to reduce the error introduced by anatomical variability. We released our scan positioning training tool as a web-based application and plan to extend its functionality to include training modules for pediatric protocols and potential protocols for other anatomic sites such as the hand, foot, and knee.

Acknowledgments The authors thank Isra Saeed and Louise McCready for subject recruitment, Margaret Holets for data acquisition, James Peterson for data management, and Nicholas P. Derrico and the MrOS operators that took part in this study: Deborah Cusick, Shannon Hanson, Kristi Jacobson, Kyla Kent, Patricia Miller, and Nita Webb.

This study was funded by the NIH/NIAMS R01 AR060700 and by The Osteoporotic Fractures in Men (MrOS) study, which is supported by the National Institutes of Health funding. The following institutes provide support: the National Institute on Aging (NIA), the National Institute of Arthritis and Musculoskeletal and Skin Diseases (NIAMS), the National Center for Advancing Translational Sciences (NCATS), and NIH Roadmap for Medical Research under the following grant numbers: U01 AG027810, U01 AG042124, U01 AG042139, U01 AG042140, U01 AG042143, U01 AG042145, U01 AG042168, U01 AR066160, and UL1 TR000128.

Compliance with ethical standards All subjects signed informed consent to participate in the study, and the Committees on Human Research at UCSF and Mayo Clinic approved study procedures.

Conflict of interest Nicolas Vilayphiou is an employee of Scanco Medical AG. Serena Bonaretti, Caroline Mai Chan, Andrew Yu, Kyle Nishiyama, Danmei Liu, Stephanie Boutroy, Ali Ghasem-Zadeh, Steven K. Boyd, Roland Chapurlat, Heather McKay, Elizabeth Shane, Mary Bouxsein, Dennis M. Black, Sharmila Majumdar, Eric S. Orwoll, Thomas Lang, Sundeep Khosla, and Andrew J. Burghardt declare that they have no conflict of interest.

Appendix: HR-pQCT operator training

To train new operators, we developed custom software and a detailed scan positioning protocol. The software comprised two modules, one to train reference line positioning and one to evaluate positioning performance for the purposes of operator certification. The graphical user interface reproduces the original acquisition software (Fig. 6(c)). Graphical control elements on the left side of the interface allowed the user to select training or evaluation modules, and from a series of scout view collections (eight scout images each) according to anatomic site, laterality, and difficulty. In training mode, the software provides operators both immediate and summary feedback on their positioning accuracy. The immediate feedback consists of a traffic light that is illuminated after each reference line is positioned. A green, yellow, or red light is shown, corresponding to "exact", "good", or "out of range" positions, respectively. The final feedback consists of a separate window displaying a summary report of operator performance after completing the selected collection (Fig. 4d). Positioning feedback was determined by comparing the user's reference line position to a gold standard reference position. The gold standard positions were determined through independent consensus of three

experienced operators at UCSF. Exact indicates that the operator and reference positions coincided; good indicates that the operator position was within 2 pixels from the reference position; and out of range indicates that the operator position was greater than 2 pixels from the reference position. Two pixels corresponded to 0.34 mm, which was the short-term standard deviation among experienced operators.

We created training and evaluation collections for the radius and tibia from the double-length scans described in "Methods". A horizontal mirror image of each scout view image was created to have an equal number of "left" and "right" limb images, for a total of 112 scout view images per anatomic site. We divided the scout view images into two groups depending on the degree of difficulty in positioning the reference line. Difficulty was assigned based on the presence or absence of a clear anatomic landmark, as assessed by an experienced UCSF operator. From each of these two groups, 49 images were randomly selected to create the training collections, and we used the remaining seven images to create the evaluation datasets. Both for training and evaluation modules, we created 15 collections of eight images randomly selected within their visibility group. Before accessing the reproducibility experiments, the six new operators had to complete all the datasets of the training module at least once, and had to succeed on at least three sets for the radius and three sets for the tibia. A set was considered successful when the sum of exact and good positions was seven out of eight positions.

Together with the training and evaluation software, we provided specific guidelines to identify the anatomic landmark and to position the reference line, as follow (Fig. 6). For the radius, we defined the anatomic landmark as the peak of the radiocarpal articular surface of the radius, which separates the radiopaque subchondral bone (bright signal) from the radiolucent joint space (dark signal) (Fig. 6 (a, b)). When the peak is clearly visible, the reference line must intersect the peak (Fig. 6 (a)), whereas when the peak is not visible, the reference line must intersect the mid-point of the joint surface (Fig. 5b). The hiker analogy in Fig. 6 (e–h) illustrates the concept. Similarly, for the tibia, the anatomic landmark is the peak of the edge of the tibial plafond, which separates the radiopaque subchondral bone (bright signal) from the radiolucent joint space (dark signal) (Fig. 6 (c, d)). When the peak is clearly visible, the reference line must intersect the center of the peak (Fig. 6 (c)), whereas when the peak is not visible, the reference line must intersect the flat plafond (Fig. 6 (d)).

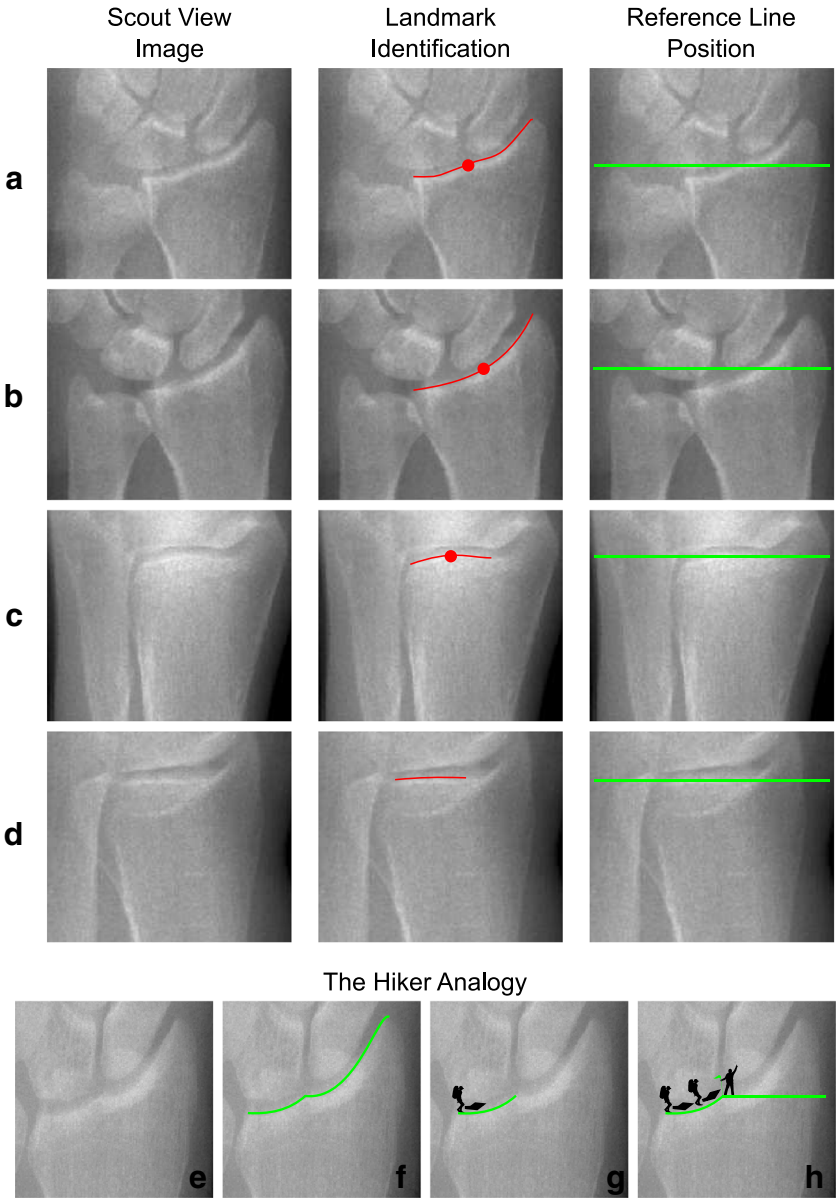

Fig. 6 Guidelines for reference line positioning recommended for the training and evaluation software. In the radius, the reference line intersects (**a**) the peak when visible or (**b**) the mid-articular surface when the peak is not visible. Similarly, in the tibia, the reference line intersects (**c**) the peak when visible or (**d**) the flat plafond when the peak is not visible. In the radius, the hiker analogy easily explains the positioning of the reference line. The articular surface of the radius (**e**) can be considered as a hiking path (**f**). The hiker walks along the path (**g**) until he reaches the peak where he plants his flag, which coincides with the location where the reference line intersects the edge that represents the articular surface of the radius (**h**)

References

1. Cheung AM, Adachi JD, Hanley DA, Kendler DL, Davison KS, Josse R et al (2013) High-resolution peripheral quantitative computed tomography for the assessment of bone strength and structure: a review by the Canadian Bone Strength Working Group. Curr Osteoporos Rep 11:136–146
2. Boutroy S, Bouxsein ML, Munoz F, Delmas PD (2005) In vivo assessment of trabecular bone microarchitecture by high-resolution peripheral quantitative computed tomography. J Clin Endocrinol Metab 90:6508–6515
3. Burghardt AJ, Buie HR, Laib A, Majumdar S, Boyd SK (2010) Reproducibility of direct quantitative measures of cortical bone microarchitecture of the distal radius and tibia by HR-pQCT. Bone 47:519–528
4. Khosla S, Riggs BL, Atkinson EJ, Oberg AL, McDaniel LJ, Holets M et al (2006) Effects of sex and age on bone microstructure at the ultradistal radius: a population-based noninvasive in vivo assessment. J Bone Miner Res 21:124–131
5. Macdonald HM, Nishiyama KK, Kang J, Hanley DA, Boyd SK (2011) Age-related patterns of trabecular and cortical bone loss differ between sexes and skeletal sites: a population-based HR-pQCT study. J Bone Miner Res 26:50–62
6. Kazakia GJ, Tjong W, Nirody JA, Burghardt AJ, Carballido-Gamio J, Patsch JM et al (2014) The influence of disuse on bone microstructure and mechanics assessed by HR-pQCT. Bone 63:132–140
7. Zhu TY, Griffith JF, Qin L, Hung VW, Fong T-N, Au S-K et al (2014) Alterations of bone density, microstructure and strength of the distal radius in male patients with rheumatoid arthritis: a case-control study with HR-pQCT. J Bone Miner Res:1–42
8. Rizzoli R, Laroche M, Krieg M-A, Frieling I, Thomas T, Delmas P et al (2010) Strontium ranelate and alendronate have differing effects on distal tibia bone microstructure in women with osteoporosis. Rheumatol Int 30:1341–1348
9. Seeman E, Delmas PD, Hanley DA, Sellmeyer D, Cheung AM, Shane E et al (2010) Microarchitectural deterioration of cortical and trabecular bone: differing effects of denosumab and alendronate. J Bone Miner Res 25:1886–1894
10. Melton LJ, Christen D, Riggs BL, Achenbach SJ, Müller R, van Lenthe GH et al (2010) Assessing forearm fracture risk in postmenopausal women. Osteoporos Int 21:1161–1169
11. Christen D, Melton LJ, Zwahlen A, Amin S, Khosla S, Müller R (2013) Improved fracture risk assessment based on nonlinear micro-finite element simulations from HRpQCT images at the distal radius. J Bone Miner Res 28:2601–2608
12. Glüer C, Blake G, Lu Y, Blunt B (1995) Accurate assessment of precision errors: how to measure the reproducibility of bone densitometry techniques. Osteoporos Int 5:262–270
13. MacNeil JA, Boyd SK (2008) Improved reproducibility of high-resolution peripheral quantitative computed tomography for measurement of bone quality. Med Eng Phys 30:792–799
14. Burghardt AJ, Pialat J-B, Kazakia GJ, Boutroy S, Engelke K, Patsch JM et al (2013) Multicenter precision of cortical and trabecular bone quality measures assessed by high-resolution peripheral quantitative computed tomography. J Bone Miner Res 28:524–536
15. Engelke K, Stampa B, Timm W, Dardzinski B, de Papp AE, Genant HK et al (2012) Short-term in vivo precision of BMD and parameters of trabecular architecture at the distal forearm and tibia. Osteoporos Int 23:2151–2158
16. Ellouz R, Chapurlat R, van Rietbergen B, Christen P, Pialat J-B, Boutroy S (2014) Challenges in longitudinal measurements with HR-pQCT: evaluation of a 3D registration method to improve bone microarchitecture and strength measurement reproducibility. Bone 63:147–157
17. Boyd SK (2008) Site-specific variation of bone micro-architecture in the distal radius and tibia. J Clin Densitom 11:424–430
18. Mueller TL, van Lenthe GH, Stauber M, Gratzke C, Eckstein F, Müller R (2009) Regional, age and gender differences in architectural measures of bone quality and their correlation to bone mechanical competence in the human radius of an elderly population. Bone 45:882–891
19. Pialat JB, Burghardt AJ, Sode M, Link TM, Majumdar S (2012) Visual grading of motion induced image degradation in high resolution peripheral computed tomography: impact of image quality on measures of bone density and micro-architecture. Bone 50:111–118
20. Laib A, Häuselmann HJ, Rüegsegger P (1998) In vivo high resolution 3D-QCT of the human forearm. Technol Health Care 6:329–337
21. Davis KA, Burghardt AJ, Link TM, Majumdar S (2007) The effects of geometric and threshold definitions on cortical bone metrics assessed by in vivo high-resolution peripheral quantitative computed tomography. Calcif Tissue Int 81:364–371
22. Burghardt AJ, Kazakia GJ, Ramachandran S, Link TM, Majumdar S (2010) Age- and gender-related differences in the geometric properties and biomechanical significance of intracortical porosity in the distal radius and tibia. J Bone Miner Res 25:983–993
23. Buie HR, Campbell GM, Klinck RJ, MacNeil JA, Boyd SK (2007) Automatic segmentation of cortical and trabecular compartments based on a dual threshold technique for in vivo micro-CT bone analysis. Bone 41:505–515
24. Hildebrand T, Ru P (1997) A new method for the model-independent assessment of thickness in three-dimensional images. J Microsc 185:67–75
25. Müller R, Rüegsegger P (1995) Three-dimensional finite element modelling of non-invasively assessed trabecular bone structures. Med Eng Phys 17:126–133
26. MacNeil J, Boyd SK (2008) Bone strength at the distal radius can be estimated from high-resolution peripheral quantitative computed tomography and the finite element method. Bone 42:1203–1213
27. Van Rietbergen B, Odgaard A, Kabel J, Huiskes R (1996) Direct mechanics assessment of elastic symmetries and properties of trabecular bone architecture. J Biomech 29:1653–1657
28. Mueller TL, Christen D, Sandercott S, Boyd SK, van Rietbergen B, Eckstein F et al (2011) Computational finite element bone mechanics accurately predicts mechanical competence in the human radius of an elderly population. Bone 48:1232–1238
29. Laib A, Hildebrand T, Häuselmann H, Rüegsegger P (1997) Ridge number density: a new parameter for in vivo bone structure analysis. Bone 21:541–546
30. Kirmani S, Christen D, van Lenthe GH, Fischer PR, Bouxsein ML, McCready LK et al (2009) Bone structure at the distal radius during adolescent growth. J Bone Miner Res 24:1033–1042
31. Burrows M, Liu D, McKay H (2010) High-resolution peripheral QCT imaging of bone micro-structure in adolescents. Osteoporos Int 21:515–20
32. Barnabe C, Feehan L (2012) High-resolution peripheral quantitative computed tomography imaging protocol for metacarpophalangeal joints in inflammatory arthritis: the SPECTRA collaboration. J Rheumatol 39:7–9
33. Carballido-Gamio J, Bonaretti S, Holets M, Saeed I, McCready L, Majumdar S et al (2013) Automated scan prescription for HR-pQCT: a multi-atlas prospective registration approach. ASBMR

Bone 142 (2021) 115778

Contents lists available at ScienceDirect

Bone

journal homepage: www.elsevier.com/locate/bone

Full Length Article

Heterogeneity in microstructural deterioration following spinal cord injury

Ali Ghasem-Zadeh [a,b,*], Mary P. Galea [a,c], Andrew Nunn [a,c], Maya Panisset [a,c], Xiao-Fang Wang [a,b], Sandra Iuliano [a,b], Steven K. Boyd [d], Mark R. Forwood [e], Ego Seeman [a,b]

[a] Depts of Medicine and Endocrinology, Austin Health, The University of Melbourne, Melbourne, Australia
[b] Dept of Endocrinology, Austin Health, The University of Melbourne, Melbourne, Australia
[c] Depts of Medicine and Victorian Spinal Cord Service, Austin Health, The University of Melbourne, Melbourne, Australia
[d] McCaig Institute for Bone and Joint Health, University of Calgary, Calgary, AB, Canada
[e] School of Medical Science and Menzies Health Institute Queensland, Griffith University, Gold Coast, Australia

ARTICLE INFO

Keywords:
Cortical -bone
HR-pQCT
Microstructure
Paralysis
Spinal -cord -injury
Trabecular bone
Unloading
Weight-bearing

ABSTRACT

Background: Modelling and remodelling adapt bone morphology to accommodate strains commonly encountered during loading. If strains exceed a threshold threatening fracture, modelling-based bone formation increases bone volume reducing these strains. If unloading reduces strains below a threshold that inhibits resorption, increased remodelling-based bone resorption reduces bone volume restoring strains, but at the price of compromised bone volume and microstructure. As weight-bearing regions are adapted to greater strains, we hypothesized that microstructural deterioration will be more severe than at regions commonly adapted to low strains following spinal cord injury.

Methods: We quantified distal tibial, fibula and radius volumetric bone mineral density (vBMD) using high-resolution peripheral quantitative computed tomography in 31 men, mean age 43.5 years (range 23.5-75.0), 12 with tetraplegia and 19 with paraplegia of 0.7 to 18.6 years duration, and 102 healthy age- and sex-matched controls. Differences in morphology relative to controls were expressed as standardized deviation (SD) scores (mean ± SD). Standardized between-region differences in vBMD were expressed as SDs (95% confidence intervals, CI).

Results: Relative to controls, men with tetraplegia had deficits in total vBMD of −1.72 ± 1.38 SD at the distal tibia ($p < 0.001$) and − 0.68 ± 0.69 SD at distal fibula ($p = 0.041$), but not at the distal radius, despite paralysis. Deficits in men with paraplegia were −2.14 ± 1.50 SD ($p < 0.001$) at the distal tibia and −0.83 ± 0.98 SD ($p = 0.005$) at the distal fibula while distal radial total vBMD was 0.23 ± 1.02 ($p = 0.371$), not significantly increased, despite upper limb mobility. Comparing regions, in men with tetraplegia, distal tibial total vBMD was 1.04 SD (95%CI 0.07, 2.01) lower than at the distal fibula ($p = 0.037$) and 1.51 SD (95%CI 0.45, 2.57) lower than at the distal radius ($p = 0.007$); the latter two sites did not differ from each other. Results were similar in men with paraplegia, but total vBMD at the distal fibula was 1.06 SD (95%CI 0.35, 1.77) lower than at the distal radius ($p = 0.004$).

Conclusion: Microarchitectural deterioration following spinal cord injury is heterogeneous, perhaps partly because strain thresholds regulating the cellular activity of mechano-transduction are region specific.

1. Introduction

Bone has paradoxical properties of strength for loading yet lightness for mobility, stiffness for leverage yet flexibility for energy absorption [1]. These properties are achieved by bone modelling and remodelling, a cellular machinery that adapts the spatial distribution of bone's mineralized matrix volume to its usual loading circumstances [2]. For example, in an individual, adjacent cross sections of a long bone are assembled using similar volumes of mineralized matrix [3]. Differences in the external size, shape and internal microarchitecture of each adjacent cross section along the bone are the result of differences in the volumes of the medullary and intracortical canals, not the volume of mineralized matrix [4].

Mass is minimized in larger cross sections by assembling them with

* Corresponding author at: Dept of Endocrinology, 2nd floor, Centaur Wing, Repatriation Campus, Austin Health, Waterdale Rd, West Heidelberg, 3081, Victoria, Australia.
E-mail address: alig@unimelb.edu.au (A. Ghasem-Zadeh).

https://doi.org/10.1016/j.bone.2020.115778
Received 19 August 2020; Received in revised form 23 November 2020; Accepted 25 November 2020
Available online 28 November 2020
8756-3282/© 2020 Elsevier Inc. All rights reserved.

relatively more void volume, not more matrix volume. The constant bone matrix volume is distributed radially by excavating a larger medullary canal producing a thinner cortex. The thinner cortex is distributed around a larger perimeter preserving cortical area and so compressive strength. The greater radial distribution of cortical mass increases bending and torsional strength disproportionately to the increase in matrix volume [5]. Smaller cross sections achieve robusticity by being assembled with a relatively thicker cortex and relatively less void volume, not less matrix volume [6].

The diversity in external bone size, shape, and architecture is largely the result of genetic variance [7]. However, focal differences in loading also contribute to this structural diversity because bone is mechanosensitive [2]. Bone adapts its structural design to accommodate a range of commonly encountered loading circumstances. These structural adaptations ensure that bone strains during loading remain within a range that does not threaten fracture during usual activities [2]. These strain ranges and the thresholds may also be region specific and selected for by genetic factors [8]. If strains exceed a threshold associated with a high risk of fracture, modelling and remodelling restore strains by increasing or redistributing total bone volume [2,9]. When unloading occurs, strains fall below a threshold inhibiting resorption, resorptive modelling or negatively balanced remodelling restore strains by reducing bone volume and compromising bone microstructural strength [2,10].

Bone loss following spinal cord injury occurs below the level of the injury but the severity of bone loss and the cellular activity adapting bone to its loading are region specific [11–15]. Weight bearing regions like the tibia are subjected to higher loads and strain rates than less weight bearing regions, like the fibula [16], or non-weight bearing regions like the radius. Bone loss reduces bone volume and disrupts the microarchitecture of the remaining bone volume. The microarchitectural deterioration reduces bone strength as a power function of the bone loss causing it [17–19]. Bone mineral density (BMD) measurements do not capture microstructural deterioration and so, bone fragility may be present in patients with spinal cord injury with osteopenia or so-called normal BMD. We therefore hypothesized that weight bearing regions will have lost more bone and structural integrity than less weight-bearing or non-weight bearing bones after spinal cord injury.

2. Methods

2.1. Participants

We recruited 12 men with tetraplegia mean age 44.6 years (range 25.9–67.2) and 19 men with paraplegia, mean age 42.9 years (range 23.5–75.0) with injury of various grades [20]. Men with tetraplegia were studied 6.5 years, range 0.7–15.6, and men with paraplegia were studied 6.5 years (range 1.6–18.6) after the injury and compared with 102 age matched healthy male controls. Men aged under 18 years, with a history of distal tibia and radius fractures or treatment for osteoporosis were excluded. Participants provided informed consent prior to participation. The study was approved by the Austin Health Research Ethics Committee.

2.2. Image acquisition and analysis

Image acquisition, reconstruction, analysis and validation have been reported [21,22]. Participants had distal radius, distal tibia and distal fibula microstructure quantified using HR-pQCT (Scanco Medical, Switzerland) at Austin Health. A region of interest of 9.02 mm was acquired starting 9.5 mm or 22.5 mm proximal to the joint line of the distal radius and tibia, respectively. The 49 most proximal slices of a region of interest were chosen for analysis. Images were reconstructed at a resolution of 82 μm. Total, cortical and medullary areas, and volumetric bone mineral density (vBMD) of total, trabecular and cortical compartments, trabecular number, thickness, separation, cortical porosity, and matrix mineral density were quantified using StrAx1.0 algorithm (Strax Corp, Melbourne, Australia).

A non-threshold based method selects attenuation profile curves and segments (separates) bone from background and cortical from trabecular bone [23]. Profile curves are produced as photons are attenuated by mineralized bone. Bone edges are identified as the beginning and end of the rise and fall of the attenuation profile. Analyzing ~3600 profiles around the perimeter of each cross-sectional slice segments the compartments. Porosity is quantified as the average void volume fraction of all voxels within each compartment.

Agreement between HR-pQCT and the gold standard (μCT of cadaveric specimens imaged at 19 μm voxel size) ranged from $R^2 = 0.87$ to 0.99. Precision error *in vivo* was 0.54% for porosity. Quality control for the performance of HR-pQCT was based on daily scanning phantoms containing hydroxyapatite (densities 0, 100, 200, 400, and 800 mgHA/cm^3) (QRM, Germany). Radiation exposure is 3–5 μSv per measurement [4,22]. The coefficients of variation (CV) of the measurements ranged from 0.54% to 3.98% [23]. Inhomogeneity of Trabecular Network is calculated based on the standard deviation of the spacing between mid-axis (ridges) of the trabeculae. Marching cubes and ruler intercept methods were applied to quantify trabecular Structural Model Index (SMI), Connectivity Density (ConnD), and Bone Surface (BS) using specified image analysis algorithm, developed by the manufacturer [24,25].

2.3. Bone strength

Micro finite element analysis (μFEA) was used to estimate Failure Load (FL) using the FAIM software (version 8.0). A uniaxial loading with a tissue elastic modulus of 6829 MPa, a Poisson's ratio of 0.3, a critical strain of 7000 micro-strain and a critical volume of 2%, were defined. A 1% apparent strain was applied, and failure load is calculated as the load when 2% of elements exceeded the critical strain [25,26].

2.4. Statistical analysis

Statistical analyses were performed using STATA version 14.2 (StataCorp. 2018. Stata Statistical Software. College Station, TX: StataCorp LP). Normality was checked using the Shapiro-Wilk normality test. The Welch's *t*-test were used to compare traits between cases and controls. Two-tailed *p*-values <0.05 denoted statistical significance. Results were expressed as mean and standard deviation. Differences in standardized terms among sites were expressed as a SD adjusted for age based on simple linear regression.

3. Results

3.1. Weight bearing regions: distal tibia and distal fibula

Men with tetraplegia and men with paraplegia had reduced total, cortical and trabecular vBMD at the distal tibia relative to healthy controls (Table 1). Cortical porosity was higher, and cortical thickness and matrix mineral density were lower, relative to healthy controls. Trabecular vBMD was reduced due to fewer, thinner, more rod-like and more separated trabeculae, with loss of trabecular surface area and connectivity, and greater inhomogeneity of the trabecular network (Fig. 1). Failure load was reduced. Distal tibial vBMD was lower and cortical porosity was higher at later than earlier follow-up times (Fig. 2). At the distal fibula, total vBMD was lower in men with tetraplegia and men with paraplegia relative to controls, but with deficits confined to trabecular vBMD produced by fewer, more separated trabeculae, with loss of homogeneity in distribution (Table 2).

3.2. Non-weight bearing region: distal radius

Despite the presence of tetraplegia, no deficits in distal radial total, cortical or trabecular vBMD were present. Trabecular thickness was

Table 1
Distal tibial microstructure in individuals with tetraplegia and paraplegia and controls.

Parameters of distal tibia	Tetraplegic			Paraplegic		
	Cases, $n = 12$	Controls, $n = 79$	p-Value	Cases, $n = 17$	Controls, $n = 81$	p-Value
Total vBMD (mgHA/cm^3)	236.7 (64.5)	334.1 (58.9)	<0.001	213.1 (75.2)	334.9 (58.9)	<0.001
Cortical vBMD (mgHA/cm^3)	572.9 (50.3)	677.5 (68.5)	<0.001	554.5 (86.4)	677.5 (65.7)	<0.001
Porosity (%)	67.2 (3.6)	59.1 (5.4)	<0.001	68.3 (6.3)	59.1 (5.1)	<0.001
Thickness (mm)	0.62 (0.14)	0.79(0.19)	0.002	0.60 (0.18)	0.77 (0.16)	0.002
Matrix mineral density (%)	64.7 (0.5)	65.4 (0.9)	<0.001	64.2 (0.6)	65.4 (0.8)	<0.001
Trabecular vBMD (mgHA/cm^3)	98.3 (74.0)	169.2 (43.9)	0.007	80.1 (63.8)	168.4 (45.7)	<0.001
Number (1/mm)	2.13 (1.09)	3.13(0.68)	0.009	1.73 (0.86)	3.14 (0.69)	<0.001
Thickness (μm)	189 (15)	197(13)	0.130	190 (17)	197 (14)	0.128
SMI	2.28 (0.75)	1.52 (0.40)	0.005	2.37 (0.53)	1.45 (0.46)	<0.001
Separation (mm)	1.94 (0.90)	1.13 (0.25)	0.010	2.08 (0.77)	1.14 (0.25)	<0.001
Surface (mm^2)	12,906 (8098)	16,725 (5227)	0.138	10,394 (4666)	16,605 (4625)	<0.001
Connectivity density (1/mm^3)	2.83 (2.11)	4.56 (1.54)	0.017	2.14 (1.43)	4.38 (1.49)	<0.001
Inhomogeneity (mm)	0.51 (0.48)	0.21 (0.08)	0.053	0.72 (0.61)	0.21 (0.08)	0.003
Failure load (N)	4074 (2521)	6909 (1407)	0.004	3369 (1807)	6905 (1388)	<0.001

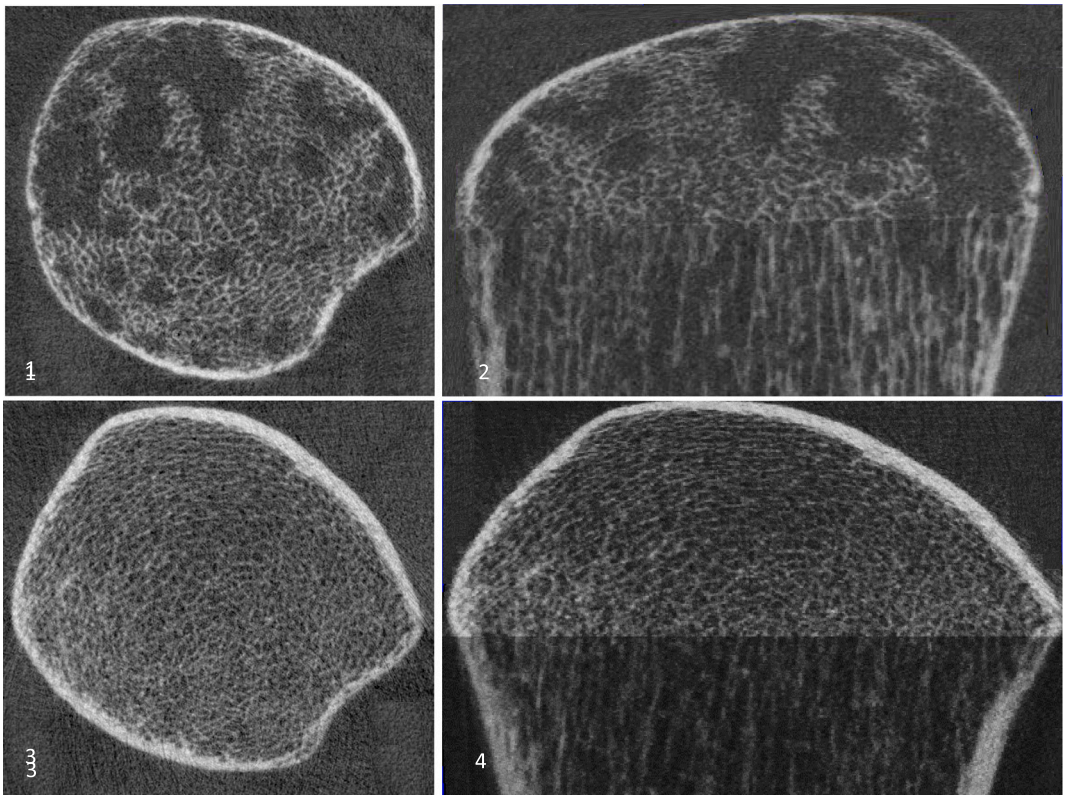

Fig. 1. Images of trabecular and cortical bone at the distal tibia.
Axial and axial-coronal views of distal tibia of a 28 years male with spinal cord injury (panels 1, 2) and a healthy control (panels 3, 4). Cortices are thin and porous. Trabeculae are thinned, disconnected with loss of homogeneity in their distribution.

increased in men with tetraplegia and men with paraplegia, and matrix mineral density was reduced, relative to healthy controls. Trabecular number and homogeneity were not deteriorated. Nor did failure load differ from controls (Table 3).

3.3. Comparisons of regions, cortical and trabecular bone

Table 4 shows the standardized mean difference between region with their 95% confidence intervals. Fig. 3 illustrates these differences with their *p* values. Deficits in total, cortical and trabecular vBMD were greater at the distal tibia than distal fibula or distal radius. Deficits were statistically significant in several, but not all, comparisons. Deficits were also significantly greater in some, but not all, comparisons of the distal fibula *versus* distal radius.

4. Discussion

The purpose of this study was to quantify the microstructural deterioration of the distal metaphyseal regions of the appendicular skeleton in individuals with spinal cord injury. Relative to controls, men with tetraplegia or paraplegia had increased cortical porosity, reduced cortical thickness and matrix mineral density, complete loss of trabecular plates, reduced trabecular surface area, connectivity and loss of homogeneity of the interconnected plates seen as patching fallout of trabeculae. These changes resulted in loss of estimated strength at the distal tibia, a weight bearing site. More modest deficits were found at the distal fibula, a weight bearing site subjected to lower stresses during loading [27].

Most published studies, like those cited in a meta-analysis [12],

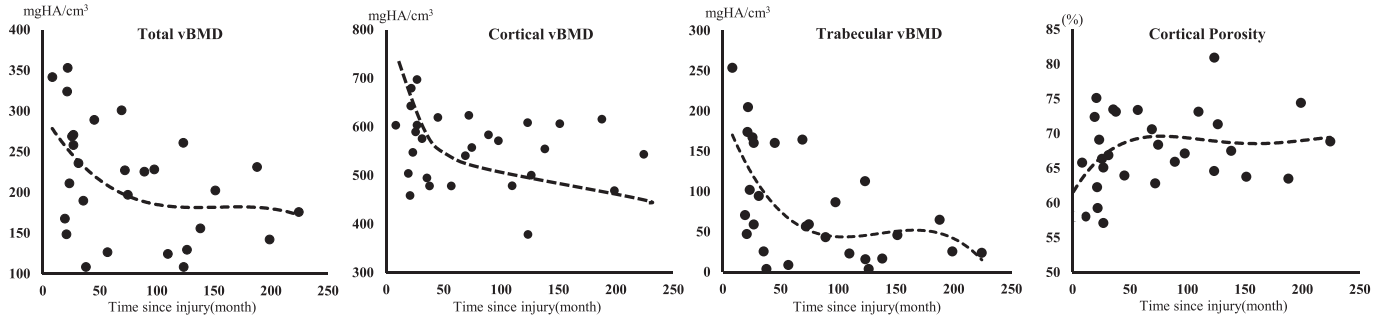

Fig. 2. Distal tibial total, cortical and trabecular volumetric bone mineral density (vBMD) and cortical porosity as a function of time since injury.
The regression lines were derived by plotting vBMD and cortical porosity from 0 to 50 months and then from 50 to 250 months. vBMD was lower and cortical porosity was higher at later than earlier follow up times.

Table 2
Distal fibula microstructure in individuals with quadriplegia and paraplegia and controls.

Parameters of distal fibula	Tetraplegic			Paraplegic		
	Cases, $n = 11$	Controls, $n = 60$	p-Value	Cases, $n = 15$	Controls, $n = 63$	p-Value
Total vBMD (mgHA/cm^3)	571.1 (85.1)	637.6 (107.4)	0.035	555.1 (92.9)	643.2 (105.1)	0.004
Cortical vBMD (mgHA/cm^3)	912.0 (50.2)	932.5 (44.2)	0.227	915.6 (36.6)	929.7 (49.6)	0.222
Cortical area (mm^2)	63.4 (17.8)	70.4 (13.9)	0.240	57.4 (10.9)	69.9 (14.0)	<0.001
Cortical thickness (mm)	1.34 (0.21)	1.52 (0.25)	0.027	1.29 (0.23)	1.52 (0.25)	0.002
Trabecular vBMD (mgHA/cm^3)	188.9 (78.1)	226.4 (50.7)	0.151	164.5 (46.4)	231.9 (50.5)	<0.001
Number (1/mm)	1.39 (0.47)	1.89 (0.39)	0.005	1.24 (0.33)	1.90 (0.41)	<0.001
Separation (mm)	0.71 (0.38)	0.45 (0.11)	0.043	0.75 (0.21)	0.45 (0.13)	<0.001
Thickness (μm)	111 (26)	101 (19)	0.248	111 (16)	104 (20)	0.128
Inhomogeneity (mm)	0.35 (0.17)	0.21 (0.07)	0.017	0.38 (0.12)	0.21 (0.08)	<0.001

vBMD; volumetric bone mineral density.

Table 3
Distal radial microstructure of individuals with tetraplegia and paraplegia and controls.

Parameters of distal radius	Tetraplegic			Paraplegic		
	Cases, n = 11	Controls, n = 79	p-Value	Cases, $n = 18$	Controls, n = 81	p-Value
Total vBMD (mgHA/cm^3)	372.9 (72.5)	385.4 (68.6)	0.598	397.5 (73.0)	392.6 (67.8)	0.794
Cortical vBMD (mgHA/cm^3)	709.9 (63.3)	739.1 (69.7)	0.180	730.0 (66.2)	746.0 (65.0)	0.360
Porosity (%)	56.8 (4.9)	54.3 (5.6)	0.145	55.3 (5.4)	53.8 (5.2)	0.285
Thickness (mm)	0.74 (0.15)	0.79(0.18)	0.325	0.86 (0.23)	0.78 (0.18)	0.0904
Matrix mineral density (%)	64.7 (0.7)	65.3 (0.9)	0.020	64.6 (0.7)	65.2 (0.8)	0.002
Trabecular vBMD (mgHA/cm^3)	152.7 (65.5)	160.2 (46.3)	0.720	173.5 (56.4)	164.0 (47.3)	0.511
Number (1/mm)	2.40 (0.70)	2.76 (0.58)	0.127	2.53 (0.52)	2.74 (0.54)	0.096
Thickness (μm)	205 (13)	197 (13)	0.085	212 (11)	198 (13)	<0.001
SMI	1.99 (0.62)	1.74 (0.41)	0.220	1.79 (0.55)	1.70 (0.45)	0.524
Separation (mm)	1.41 (0.55)	1.16 (0.25)	0.166	1.21 (0.28)	1.15 (0.25)	0.410
Surface (mm^2)	6408 (2489)	6818 (1786)	0.608	6044 (1242)	6780 (1783)	0.044
Connectivity density (1/mm^3)	3.61 (1.37)	4.46 (1.21)	0.073	4.01 (0.95)	4.35 (1.18)	0.200
Inhomogeneity (mm)	0.25 (0.14)	0.19 (0.07)	0.190	0.21 (0.07)	0.19 (0.06)	0.272
Failure load (N)	2499 (776)	2668 (652)	0.526	2600 (625)	2680 (662)	0.651

vBMD; volumetric bone mineral density, SMI; structure Model Index. SMI of 0 indicates plate-like structure, 3 indicates rod-like structure.

focussed on the reduction in BMD, a measurement that does not capture the heterogeneity in cortical and trabecular morphology within and between regions of the skeleton. We report a hierarchy of deficits. The tibia experienced the greatest loss, followed by the fibula, with the least loss from the radius. These observations are consistent with the relative reduction in loading following spinal cord injury [12], with the tibia experiencing the greatest unloading, and the radius the least unloading relative to their customary loading.

We observed deficits in cortical and trabecular vBMD at the distal tibia, but deficits in vBMD at the distal fibula were confined to trabecular bone, and were less than the deficits at the distal tibia. The fibula is slender and largely cortical. Cortical bone has a lower surface area/matrix volume ratio than trabecular bone and so is less susceptible to being remodelled than trabecular bone following unloading [12]. As the fibula is subjected to lower strains than the tibia, we suggest that paralysis may have resulted in strains deviating less from their customary strain environment than the deviation of strains usually encountered at the tibia [16]. Consequently, loss of trabecular bone may have been sufficient to restore strains without the need to compromise cortical bone.

Eser et al. reported deficits in vBMD at the distal femur and proximal tibia were confined to trabecular bone despite these weight-bearing bones being subjected to higher strains than the radius [17]. The larger trabecular surface area/matrix volume ratio at these locations may also make these regions susceptible to more rapid trabecular than cortical bone loss.

Finding uncompromised distal radial microstructure in men with tetraplegia was unanticipated. However, scrutiny of the literature supports the likely validity of this observation. For example, in a meta-analysis [12], lower limb bones had greater deficits in bone mass than

Table 4
Total, cortical and trabecular vBMD differences between tibia, fibula and radius in tetraplegic and paraplegic men.
Difference expressed as age-adjusted standardized deviations (SD) with 95% confidence intervals (CIs).

Deviation	Tetraplegic		Paraplegic	
	Mean difference, SD (CI)	p-Value	Mean difference, SD (CI)	p-Value
Total vBMD				
Tibia *vs.* fibula	−1.04 (−2.01, −0.07)	0.037	−1.31 (−2.23, −0.39)	0.007
Tibia *vs.* radius	−1.51 (−2.57, −0.45)	0.007	−2.37 (−3.22, 1.52)	<0.001
Fibula *vs.* radius	−0.47 (−1.21, 0.27)	0.202	−1.06 (−1.77, −0.35)	0.004
Cortical vBMD				
Tibia *vs.* fibula	−0.50 (−1.10, 0.10)	0.096	−1.05 (−1.69, −0.41)	0.002
Tibia *vs.* radius	−0.54 (−1.13, 0.05)	0.070	−0.99 (−1.65, −0.33)	0.005
Fibula *vs.* radius	−0.04 (−0.65, 0.57)	0.893	0.06 (−0.48, 0.60)	0.824
Trabecular vBMD				
Tibia *vs.* fibula	−0.98 (−2.51, 0.55)	0.198	−1.03 (−2.07, 0.01)	0.051
Tibia *vs.* radius	−1.73 (−3.25, −0.21)	0.027	−2.66 (−3.64, −1.68)	<0.001
Fibula *vs.* radius	−0.75 (−1.98, 0.48)	0.219	−1.63 (−2.34, −0.92)	<0.001

upper extremity bones. Eser et al. report rapid decreases in vBMD at the distal femur and tibia in patients with tetraplegia or paraplegia with little loss of bone at the distal radius in patients with paraplegia (as expected) and in the smaller number of patients with tetraplegia [28]. Studies of astronauts demonstrate preservation of radial bone, a structure commonly subjected to lower loads than weight bearing structures [29]. Modlesky et al. reported reduced distal femur and proximal tibia trabecular density using high-resolution magnetic resonance imaging in 10 men with long-term complete spinal cord injury compared to 8 controls. Despite complete SCI injury between C6-L1, radius BMD was not reduced relative to controls, as confirmed in this, and other studies [30].

No deficits at the distal radius of men with paraplegia were expected but evidence of higher vBMD in men with paraplegia than in healthy controls or men with tetraplegia might be expected due to mechanical usage for propulsion of a wheelchair. This was not observed. However, Goktepe et al. reported higher distal radial BMD in elite athletes with paraplegia, not sedentary subjects with paraplegia, an observation suggesting greater than usually encountered strains are needed to stimulate bone formation in this non-weight bearing bone [31]. The higher distal radial trabecular thickness in both tetraplegia and paraplegia than controls is likely to be due to preferential loss of thinner trabeculae as reported following rapid perimenopausal bone loss [32].

Likewise, in a study of dogs subjected to 40 weeks of immobilization, the greatest loss of bone occurred at the metacarpals (50%), compared to humeri which lost the least bone (28%) [10]. Although the forelimbs of quadrupeds are weight-bearing, the distal limb bones experience greater peak stresses during locomotion than the proximal humerus [33]. Hsieh and colleagues reported using an *in vivo* loading of the ulna in rats that threshold strains are largest distally, where locomotor strains are typically higher than proximally. There was a correlation between greater peak strains and greater periosteal bone formation once a threshold was exceeded [34]. Schulte et al. also reported that bone formation in mice occurs at sites of high local mechanical strain while bone resorption occurred at sites of low local strain [35]. Christen et al. demonstrate a linear relationship between focal remodelling and local loading determined by micro finite element analysis in humans but non-mechanically determined component of this cellular activity fulfilling other demands for remodelling [36].

We propose that the heterogeneity of the morphological changes following spinal cord injury is likely to reflect the nature of bone as a mechanosensitive organ. Harold Frost, and many investigators since, suggested that bone modelling and remodelling adapt bone morphology to differences in microstrain imposed by unloading, physiological loading, overloading and pathological loading [2,5,8,9,15,37]. The mechanisms responsible for mechanotransduction are now better understood (Fig. 4). During loading, bone matrix deformation (strain) generates lacuna-canalicular fluid flow which induces shear stress on osteocytes, down regulating sclerostin, an inhibitor of bone formation and stimulator of bone resorption [38,39]. When sclerostin expression is suppressed, bone formation increases focally [39]. Concurrently, resorptive modelling, or negatively balanced remodelling, occur at other locations. This alters the spatial distribution of the mineralized matrix, adapting a region's microarchitecture to the new loading circumstances while avoiding an increase in total bone volume, which is energy requiring [1,2,40].

Reduced loading in individuals with spinal cord injury reduces canalicular fluid flow. Reduced strains upregulate sclerostin leading to reduced bone formation, increased bone resorption, bone loss and a reduction in bone volume which restores local strains at the price of compromised bone volume, microarchitecture and bone strength [41]. Sclerostin levels were not available in the present study. Published studies suggest that changes in sclerostin levels depend on the type and duration of SCI [42,43]. For example, Battaglino et al. reported that sclerostin levels were greatest in subjects with short-term SCI (≤5 years) and decreased during the first 5 years post-injury [42]. By contrast, Maimoun et al. report lower concentration of sclerostin [43], a finding that should be associated with increased bone formation. Circulating concentrations may not be appropriate surrogates for the local action of this osteocyte product as reduced levels should be associated with

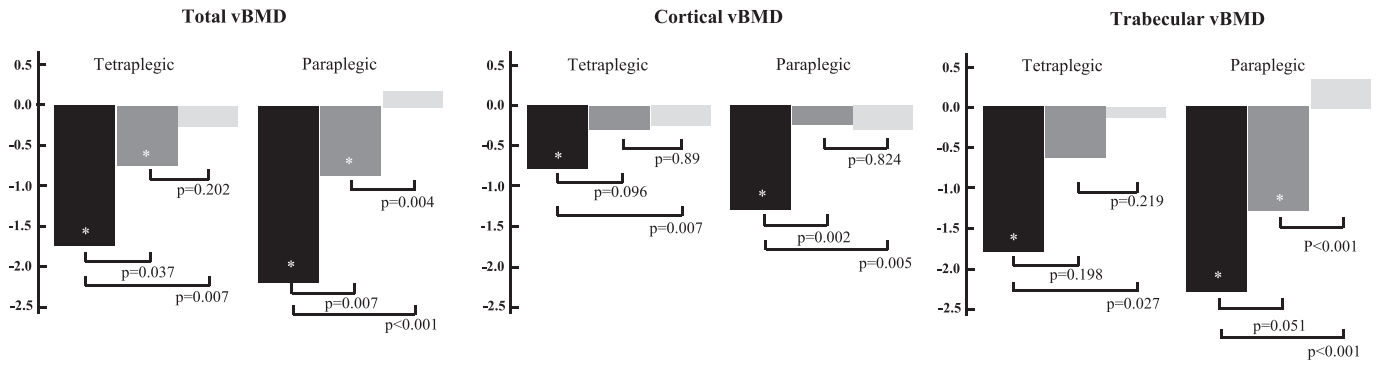

Fig. 3. Comparison of deficits total, cortical and trabecular volumetric bone mineral density (vBMD) at the distal tibia (black bar), distal fibula (deep grey bars) and distal radius (light grey bars) in men with tetraplegia and paraplegia. Deficits are expressed as standard deviations from the mean in age-matched controls.

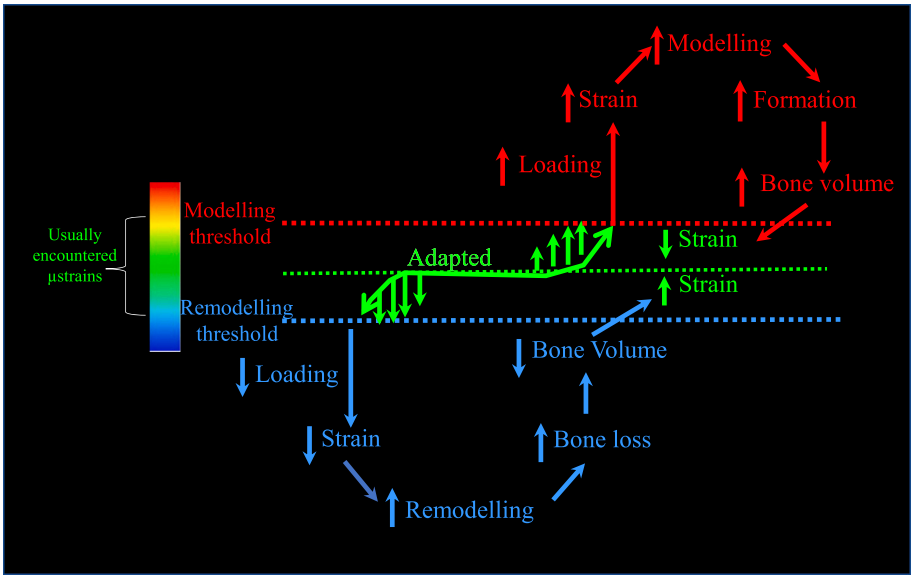

Fig. 4. Differences in loading-induced microstrain within the range usually encountered by a bone do not modify modelling or remodelling (green). When loading exceeds a strain threshold threatening fracture (red), modelling increases bone formation and bone volume restoring strains. When loading is reduced, as occurs in spinal cord injury, strains decrease below a threshold inhibiting remodelling (blue) result in initiation of unbalanced remodelling causing bone loss and a decrease in bone volume which restores strains. (For interpretation of the references to colour in this figure legend, the reader is referred to the web version of this article.)

increased bone formation.

In addition to changes in bone volume and microstructure, matrix mineral density was lower in men with tetraplegia and paraplegia, despite the absence of changes in morphology at the distal radius. This observation suggests that rapid remodelling has a systemic effect compromising bone properties above the level of the spinal cord injury. Shen et al. reported decreased mineral to collagen matrix ratio in the humeri of paraplegic mice [44]. This rapid remodelling may underly the so-called regional acceleratory phenomenon reported by Frost [45].

Stiffness, or resistance to bending, is a function of the degree of matrix mineralization and bone geometry, with the cross-sectional moment of inertia capturing the distribution of mass around the axis of loading [5]. As stiffness is determined by material and structural properties, both can vary independently, as matrix mineralization and microstructure did here. The change was greater at the distal tibia where both microstructure and matrix mineral density were compromised, contributing to the greater decline in estimated failure load.

Prevention of musculoskeletal deterioration following spinal cord injury remains challenging and has been attempted using functional electrical stimulation (FES)-rowing. Gibbons et al. report a case study of a patient with SCI in whom they suggest distal tibial bone loss measured using HR-pQCT was attenuated [46]. Draghici et al. measured distal tibia and distal radial microstructure also using HR-pQCT in an uncontrolled cross-sectional study of 13 men with SCI [47]. Time since injury, total distance rowed, and peak foot force together predicted trabecular, not cortical, morphology. These studies are difficult to interpret due to issues in design and execution. However, in a 6-month controlled prospective study of FES-cycling 30-min 3 times weekly initiated 4·5 weeks post SCI in 19 para- and tetraplegic patients compared with 19 patients with SCI left untreated, no evidence of attenuation of bone loss was observed [48]. By contrast, Fang et al. reported that 20 individuals with SCI treated for 12 months with FES–assisted rowing plus zoledronate improved distal femur stiffness by 4.6% estimated using finite element analysis, while stiffness decreased by 13.9% in those treated with rowing alone. No benefits were observed in either group at the proximal tibia. No group received drug therapy alone or no intervention [49]. In an uncontrolled study, Frotzler et al. reported improvement in thigh cross sectional area, distal femoral epiphysis trabecular and total BMD following 12 months of 3.7 hourly sessions per week FES-cycling in 11 subjects with complete SCI 11.0 years post injury [50]. Bone parameters in the femoral shaft decreased. Further studies are needed to address this therapeutic challenge.

This study has several limitations. This was a cross-sectional data with limited number of individuals with spinal cord injury and absence of data in the early months following spinal cord injury. For these reasons we could not document the precise temporal patterns of bone loss in each region. However, Edwards et al. reported early rapid bone loss of 3–5% per month [51]. Similarly, Eser et al. reported trabecular and cortical bone loss for the distal epiphyses and midshafts of the femur, tibia, and radius measured using peripheral quantitative computed tomography in 24 tetraplegic and 65 paraplegic men with SCI of 2 months and 50 years duration [17]. Bone mass and cortical area of the diaphyses, showed an exponential decrease with time since injury reaching a plateau after 3–8 years. While the upper limbs are not loaded by body weight, about 50% of this small group of subjects had level D grade ASIA impairment scale, in which most of the muscles are spared below the level of injury, an effect that may partly account for the preservation of bone structure. Analysis of cortical porosity of the fibula was not available. Height and weight measurements were not available so matching with controls was confined to age and sex. While unloading due to spinal cord injury plays a most important role in bone loss, bone loss is multifactorial [12,52]. Coexisting autonomic dysfunction was not quantified in this study and may contribute to bone loss, but few, if any, studies have quantified the contribution of the hemodynamic changes that may influence the skeleton [53,54].

In summary, fractures are common in patients with spinal cord injury and often occur at metaphyseal regions [55]. Bone fragility is the result of bone loss that is region specific and is, in part, a function of the change in mechanical load imposed on the region. Following unloading caused by spinal cord injury, weight bearing regions, adapted to accommodate greater peak strains and strain rates, are at higher risk for bone loss and microarchitectural deterioration during unloading than non-weight bearing regions that are adapted to lower peak strains and strain rates. These observations highlight the site specificity of the strain thresholds regulating the cellular activity of mechano-transduction. The rapidity of the change and irreversible microarchitectural deterioration suggest prompt intervention with antiresorptive, anabolic therapy, or both, warrants consideration.

Authors' roles

Study design and conduct: AGZ, ES, MPG and AN. Data collection: AGZ, XFW, SI, MP. Responsibility for StrAx analysis: AGZ, Responsibility for finite element analysis: SB. Statistical analyses: AGZ, and XFW.

Drafting manuscript: AGZ, MPG and ES. Data interpretation and approving final version of manuscript: AGZ, MPG, AN, MP, XFW, SI, SB, MRF and ES.

Declaration of competing interest

A Ghasem-Zadeh is renumerated as image analyst and shareholder in StraxCorp. E Seeman has received research support and lectured at national and international meetings funded by from Allergan, Amgen, Asahi pharmaceuticals, Eli Lilly, and MSD. He is a director of the board, renumerated as Chief Medical Officer, shareholder in StraxCorp, and is one of the inventors of the StrAx1.0 algorithm. S Boyd is a co-founder and co-owner of Numerics88 Solutions Inc., creator of finite element.

References

[1] J.D. Currey, The Mechanical Adaptations of Bones viii, Princeton University Press, Princeton, N.J, 1984 (294 pp.).
[2] H.M. Frost, Bone "mass" and the "mechanostat": a proposal, Anat. Rec. 219 (1) (Sep 1987) 1–9 (Epub 1987/09/01).
[3] R.M. Zebaze, A. Jones, F. Welsh, M. Knackstedt, E. Seeman, Femoral neck shape and the spatial distribution of its mineral mass varies with its size: clinical and biomechanical implications, Bone. 37 (2) (Aug 2005) 243–252 (Epub 2005/06/09).
[4] A. Ghasem-Zadeh, A. Burghardt, X.F. Wang, S. Iuliano, S. Bonaretti, M. Bui, et al., Quantifying sex, race, and age specific differences in bone microstructure requires measurement of anatomically equivalent regions, Bone. 101 (Aug 2017) 206–213 (Epub 2017/05/16).
[5] M.R. Forwood, Mechanical effects on the skeleton: are there clinical implications? Osteoporos. Int. 12 (1) (2001) 77–83 (Epub 2001/04/18).
[6] C.B. Ruff, E. Trinkaus, A. Walker, C.S. Larsen, Postcranial robusticity in Homo. I: temporal trends and mechanical interpretation, Am. J. Phys. Anthropol. 91 (1) (May 1993) 21–53 (Epub 1993/05/01).
[7] A. Bjornerem, M. Bui, X. Wang, A. Ghasem-Zadeh, J.L. Hopper, R. Zebaze, et al., Genetic and environmental variances of bone microarchitecture and bone remodeling markers: a twin study, J. Bone Miner. Res. 30 (3) (Mar 2015) 519–527 (Epub 2014/11/20).
[8] A.G. Robling, C.H. Turner, Mechanotransduction in bone: genetic effects on mechanosensitivity in mice, Bone. 31 (5) (Nov 2002) 562–569 (Epub 2002/12/13).
[9] J.R. Mosley, B.M. March, J. Lynch, L.E. Lanyon, Strain magnitude related changes in whole bone architecture in growing rats, Bone. 20 (3) (Mar 1997) 191–198 (Epub 1997/03/01).
[10] H.K. Uhthoff, Z.F. Jaworski, Bone loss in response to long-term immobilisation, J. Bone Joint Surg. (Br.) 60-B (3) (Aug 1978) 420–429 (Epub 1978/08/01).
[11] D. Roberts, W. Lee, R.C. Cuneo, J. Wittmann, G. Ward, R. Flatman, et al., Longitudinal study of bone turnover after acute spinal cord injury, J. Clin. Endocrinol. Metab. 83 (2) (Feb 1998) 415–422 (Epub 1998/02/19).
[12] S.D. Jiang, L.S. Jiang, L.Y. Dai, Mechanisms of osteoporosis in spinal cord injury, Clin. Endocrinol. 65 (5) (Nov 2006) 555–565 (Epub 2006/10/24).
[13] L. Maimoun, C. Fattal, J.P. Micallef, E. Peruchon, P. Rabischong, Bone loss in spinal cord-injured patients: from physiopathology to therapy, Spinal Cord 44 (4) (Apr 2006) 203–210 (Epub 2005/09/15).
[14] F. Biering-Sorensen, H.H. Bohr, O.P. Schaadt, Longitudinal study of bone mineral content in the lumbar spine, the forearm and the lower extremities after spinal cord injury, Eur. J. Clin. Investig. 20 (3) (Jun 1990) 330–335 (Epub 1990/06/01).
[15] S.J. Kuruvilla, S.D. Fox, D.M. Cullen, M.P. Akhter, Site specific bone adaptation response to mechanical loading, J. Musculoskelet. Neuronal Interact. 8 (1) (Jan-Mar 2008) 71–78 (Epub 2008/04/10).
[16] Q. Wang, M. Whittle, J. Cunningham, J. Kenwright, Fibula and its ligaments in load transmission and ankle joint stability, Clin. Orthop. Relat. Res. 330 (Sep 1996) 261–270 (Epub 1996/09/01).
[17] P. Eser, A. Frotzler, Y. Zehnder, L. Wick, H. Knecht, J. Denoth, et al., Relationship between the duration of paralysis and bone structure: a pQCT study of spinal cord injured individuals, Bone. 34 (5) (May 2004) 869–880 (Epub 2004/05/04).
[18] M.B. Schaffler, D.B. Burr, Stiffness of compact bone: effects of porosity and density, J. Biomech. 21 (1) (1988) 13–16 (Epub 1988/01/01).
[19] S. Coupaud, M.K. Gislason, M. Purcell, K. Sasagawa, K.E. Tanner, Patient-specific bone mineral density distribution in the tibia of individuals with chronic spinal cord injury, derived from multi-slice peripheral Quantitative Computed Tomography (pQCT) - a cross-sectional study, Bone. 97 (Apr 2017) 29–37 (Epub 2016/12/31).
[20] F.M. Maynard Jr., M.B. Bracken, G. Creasey, J.F. Ditunno Jr., W.H. Donovan, T. B. Ducker, et al., International standards for neurological and functional classification of spinal cord injury. American Spinal Injury Association, Spinal Cord. 35 (5) (May 1997) 266–274 (Epub 1997/05/01).
[21] X.F. Wang, Q. Wang, A. Ghasem-Zadeh, A. Evans, C. McLeod, S. Iuliano-Burns, et al., Differences in macro- and microarchitecture of the appendicular skeleton in young Chinese and white women, J. Bone Miner. Res. 24 (12) (Dec 2009) 1946–1952 (Epub 2009/05/23).
[22] P. Geusens, R. Chapurlat, G. Schett, A. Ghasem-Zadeh, E. Seeman, J. de Jong, et al., High-resolution in vivo imaging of bone and joints: a window to microarchitecture, Nat. Rev. Rheumatol. 10 (5) (May 2014) 304–313 (Epub 2014/03/07).
[23] R. Zebaze, A. Ghasem-Zadeh, A. Mbala, E. Seeman, A new method of segmentation of compact-appearing, transitional and trabecular compartments and quantification of cortical porosity from high resolution peripheral quantitative computed tomographic images, Bone. 54 (1) (May 2013) 8–20 (Epub 2013/01/22).
[24] T. Hildebrand, A. Laib, R. Muller, J. Dequeker, P. Ruegsegger, Direct three-dimensional morphometric analysis of human cancellous bone: microstructural data from spine, femur, iliac crest, and calcaneus, J. Bone Miner. Res. 14 (7) (Jul 1999) 1167–1174 (Epub 1999/07/15).
[25] D.E. Whittier, S.K. Boyd, A.J. Burghardt, J. Paccou, A. Ghasem-Zadeh, R. Chapurlat, K. Engelke, ML. Bouxsein, Guidelines for the assessment of bone density and microarchitecture in vivo using high-resolution peripheral quantitative computed tomography, Osteoporos Int 31 (9) (2020) 1607–1627, https://doi.org/10.1007/s00198-020-05438-5 [Epub 2020 May 26].
[26] E.J. Samelson, K.E. Broe, H. Xu, L. Yang, S. Boyd, E. Biver, et al., Cortical and trabecular bone microarchitecture as an independent predictor of incident fracture risk in older women and men in the Bone Microarchitecture International Consortium (BoMIC): a prospective study, Lancet Diabetes Endocrinol. 7 (1) (Jan 2019) 34–43 (Epub 2018/12/07).
[27] J.R. Funk, R.W. Rudd, J.R. Kerrigan, J.R. Crandall, The effect of tibial curvature and fibular loading on the tibia index, Traffic Inj. Prev. 5 (2) (Jun 2004) 164–172 (Epub 2004/06/19).
[28] P. Eser, A. Frotzler, Y. Zehnder, H. Schiessl, J. Denoth, Assessment of anthropometric, systemic, and lifestyle factors influencing bone status in the legs of spinal cord injured individuals, Osteoporos. Int. 16 (1) (Jan 2005) 26–34 (Epub 2004/05/13).
[29] L. Vico, B. van Rietbergen, N. Vilayphiou, M.T. Linossier, H. Locrelle, M. Normand, et al., Cortical and trabecular bone microstructure did not recover at weight-bearing skeletal sites and progressively deteriorated at non-weight-bearing sites during the year following international space station missions, J. Bone Miner. Res. 32 (10) (Oct 2017) 2010–2021 (Epub 2017/06/03).
[30] C.M. Modlesky, S. Majumdar, A. Narasimhan, G.A. Dudley, Trabecular bone microarchitecture is deteriorated in men with spinal cord injury, J. Bone Miner. Res. 19 (1) (Jan 2004) 48–55 (Epub 2004/02/03).
[31] A.S. Goktepe, B. Yilmaz, R. Alaca, K. Yazicioglu, H. Mohur, S. Gunduz, Bone density loss after spinal cord injury: elite paraplegic basketball players vs. paraplegic sedentary persons, Am. J. Phys. Med. Rehabil. 83 (4) (Apr 2004) 279–283 (Epub 2004/03/17).
[32] A. Bjornerem, X. Wang, M. Bui, A. Ghasem-Zadeh, J.L. Hopper, R. Zebaze, et al., Menopause-related appendicular bone loss is mainly cortical and results in increased cortical porosity, J. Bone Miner. Res. 33 (4) (Apr 2018) 598–605 (Epub 2017/12/09).
[33] A.A. Biewener, Bone strength in small mammals and bipedal birds: do safety factors change with body size? J. Exp. Biol. 98 (Jun 1982) 289–301 (Epub 1982/06/01).
[34] Y.F. Hsieh, A.G. Robling, W.T. Ambrosius, D.B. Burr, C.H. Turner, Mechanical loading of diaphyseal bone in vivo: the strain threshold for an osteogenic response varies with location, J. Bone Miner. Res. 16 (12) (Dec 2001) 2291–2297 (Epub 2002/01/05).
[35] F.A. Schulte, D. Ruffoni, F.M. Lambers, D. Christen, D.J. Webster, G. Kuhn, et al., Local mechanical stimuli regulate bone formation and resorption in mice at the tissue level, PLoS One 8 (4) (2013), e62172 (Epub 2013/05/03).
[36] P. Christen, K. Ito, R. Ellouz, S. Boutroy, E. Sornay-Rendu, R.D. Chapurlat, et al., Bone remodelling in humans is load-driven but not lazy, Nat. Commun. 5 (Sep 11 2014) 4855 (Epub 2014/09/12).
[37] L.M. McNamara, P.J. Prendergast, Bone remodelling algorithms incorporating both strain and microdamage stimuli, J. Biomech. 40 (6) (2007) 1381–1391 (Epub 2006/08/26).
[38] C.H. Turner, M.R. Forwood, M.W. Otter, Mechanotransduction in bone: do bone cells act as sensors of fluid flow? FASEB J. 8 (11) (Aug 1994) 875–878 (Epub 1994/08/01).
[39] A.G. Robling, P.J. Niziolek, L.A. Baldridge, K.W. Condon, M.R. Allen, I. Alam, et al., Mechanical stimulation of bone in vivo reduces osteocyte expression of Sost/sclerostin, J. Biol. Chem. 283 (9) (Feb 29, 2008) 5866–5875 (Epub 2007/12/20).
[40] S.L. Bass, L. Saxon, R.M. Daly, C.H. Turner, A.G. Robling, E. Seeman, et al., The effect of mechanical loading on the size and shape of bone in pre-, peri-, and postpubertal girls: a study in tennis players, J. Bone Miner. Res. 17 (12) (Dec 2002) 2274–2280 (Epub 2002/12/10).
[41] X. Tian, W.S. Jee, X. Li, C. Paszty, H.Z. Ke, Sclerostin antibody increases bone mass by stimulating bone formation and inhibiting bone resorption in a hindlimb-immobilization rat model, Bone 48 (2) (Feb 2011) 197–201 (Epub 2010/09/21).
[42] R.A. Battaglino, S. Sudhakar, A.A. Lazzari, E. Garshick, R. Zafonte, L.R. Morse, Circulating sclerostin is elevated in short-term and reduced in long-term SCI, Bone. 51 (3) (Sep 2012) 600–605 (Epub 2012/05/12).
[43] L. Maimoun, F. Ben Bouallegue, A. Gelis, S. Aouinti, T. Mura, P. Philibert, et al., Periostin and sclerostin levels in individuals with spinal cord injury and their relationship with bone mass, bone turnover, fracture and osteoporosis status, Bone. 127 (Oct 2019) 612–619 (Epub 2019/07/28).
[44] J. Shen, L. Fan, J. Yang, A.G. Shen, J.M. Hu, A longitudinal Raman microspectroscopic study of osteoporosis induced by spinal cord injury, Osteoporos. Int. 21 (1) (Jan 2010) 81–87 (Epub 2009/05/14).
[45] H.M. Frost, The regional acceleratory phenomenon: a review, Henry Ford Hosp. Med. J. 31 (1) (1983) 3–9 (Epub 1983/01/01).

[46] R.S. Gibbons, G.S. Beaupre, G.J. Kazakia, FES-rowing attenuates bone loss following spinal cord injury as assessed by HR-pQCT, Spinal Cord Ser. Cases 2 (2016) 15041 (Epub 2017/01/06).
[47] A.E. Draghici, J.A. Taylor, M.L. Bouxsein, S.J. Shefelbine, Effects of FES-rowing exercise on the time-dependent changes in bone microarchitecture after spinal cord injury: a cross-sectional investigation, JBMR Plus. 3 (9) (Sep 2019), e10200 (Epub 2019/11/02).
[48] P. Eser, E.D. de Bruin, I. Telley, H.E. Lechner, H. Knecht, E. Stüssi, Effect of electrical stimulation-induced cycling on bone mineral density in spinal cord-injured patients, Eur. J. Clin. Investig. 33 (5) (May 2003) 412–419 (Epub 2003/04/26).
[49] Y. Fang, L.R. Morse, N. Nguyen, R.A. Battaglino, R.F. Goldstein, K.L. Troy, Functional electrical stimulation (FES)-assisted rowing combined with zoledronic acid, but not alone, preserves distal femur strength and stiffness in people with chronic spinal cord injury, Osteoporos Int. (2020), https://doi.org/10.1007/s00198-020-05610-x [Epub ahead of print].
[50] A. Frotzler, S. Coupaud, C. Perret, T.H. Kakebeeke, K.J. Hunt, N.N. Donaldson, et al., High-volume FES-cycling partially reverses bone loss in people with chronic spinal cord injury, Bone. 43 (1) (Jul 2008) 169–176 (Epub 2008/04/29).
[51] W.B. Edwards, T.J. Schnitzer, K.L. Troy, Bone mineral and stiffness loss at the distal femur and proximal tibia in acute spinal cord injury, Osteoporos. Int. 25 (3) (Mar 2014) 1005–1015 (Epub 2013/11/06).
[52] S.D. Jiang, L.Y. Dai, L.S. Jiang, Osteoporosis after spinal cord injury, Osteoporos. Int. 17 (2) (Feb 2006) 180–192 (Epub 2005/10/12).
[53] A. Chantraine, C. van Ouwenaller, H.J. Hachen, P. Schinas, Intra-medullary pressure and intra-osseous phlebography in paraplegia, Paraplegia. 17 (4) (Nov 1979) 391–399 (Epub 1979/11/01).
[54] S.S. Shim, H.E. Hawk, W.Y. Yu, The relationship between blood flow and marrow cavity pressure of bone, Surg Gynecol Obstet 135 (3) (Sep 1972) 353–360 (Epub 1972/09/01).
[55] Y. Zehnder, M. Luthi, D. Michel, H. Knecht, R. Perrelet, I. Neto, et al., Long-term changes in bone metabolism, bone mineral density, quantitative ultrasound parameters, and fracture incidence after spinal cord injury: a cross-sectional observational study in 100 paraplegic men, Osteoporos. Int. 15 (3) (Mar 2004) 180–189 (Epub 2004/01/15).

Bone 154 (2022) 116260

Contents lists available at ScienceDirect

Bone

journal homepage: www.elsevier.com/locate/bone

Full Length Article

Bone microarchitecture and estimated failure load are deteriorated whether patients with chronic kidney disease have normal bone mineral density, osteopenia or osteoporosis

Ali Ghasem-Zadeh [a,f,*], Minh Bui [b], Ego Seeman [a,f], Steven K. Boyd [c], Sandra Iuliano [a,f], Rizwan Jaipurwala [a,f], Peter F. Mount [a,d], Nigel D. Toussaint [e], Cherie Chiang [a,f]

[a] Dept of Medicine, Austin Health, The University of Melbourne, Melbourne, Australia
[b] Centre for Epidemiology and Biostatistics, Melbourne School of Population and Global Health, The University of Melbourne, Melbourne, Australia
[c] McCaig Institute for Bone and Joint Health, University of Calgary, Calgary, AB, Canada
[d] Dept of Nephrology, Austin Health, The University of Melbourne, Melbourne, Australia
[e] Dept of Nephrology, The Royal Melbourne Hospital, The University of Melbourne, Melbourne, Australia
[f] Depts of Medicine and Endocrinology, Austin Health, The University of Melbourne, Melbourne, Australia

ARTICLE INFO

Keywords:
Bone microarchitecture
Chronic kidney disease
Cortical porosity
HR-pQCT
Osteopenia
Osteoporosis
Trabecular density

ABSTRACT

Introduction: Measurement of bone mineral density (BMD) is recommended in patients with chronic kidney disease (CKD). However, most persons in the community and most patients with CKD have osteopenia, suggesting fracture risk is low. Bone loss compromises bone microarchitecture which increases fragility disproportionate to modest deficits in BMD. We therefore hypothesized that patients with CKD have reduced estimated failure load due to deterioration in microarchitecture irrespective of whether they have normal femoral neck (FN) BMD, osteopenia or osteoporosis.

Methods: We measured distal tibial and distal radial microarchitecture in 128 patients with CKD and 275 age- and sex-matched controls using high resolution peripheral quantitative computed tomography, FN-BMD using bone densitometry and estimated failure load at the distal appendicular sites using finite element analysis.

Results: Patients versus controls respectively had: lower tibial cortical area 219 (40.7) vs. 237 (35.3) mm^2, $p = 0.002$, lower cortical volumetric BMD 543 (80.7) vs. 642 (81.7) $mgHA/cm^3$ due to higher porosity 69.6 (6.19) vs. 61.9 (6.48)% and lower matrix mineral density 64.2 (0.62) vs. 65.1 (1.28)%, lower trabecular vBMD 92.2 (41.1) vs. 149 (43.0) $mgHA/cm^3$ due to fewer and spatially disrupted trabeculae, lower FN-BMD 0.78 (0.12) vs. 0.94 (0.14) g/cm^2 and reduced estimated failure load 3825 (1152) vs. 5778 (1467) N, all $p < 0.001$. Deterioration in microarchitecture and estimated failure load was most severe in patients and controls with osteoporosis. Patients with CKD with osteopenia and normal FN-BMD had more deteriorated tibial microarchitecture and estimated failure load than controls with BMD in the same category. In univariate analyses, microarchitecture and FN-BMD were both associated with estimated failure load. In multivariable analyses, only microarchitecture was independently associated with estimated failure load and accounted for 87% of the variance.

Conclusions: Bone fragility is likely to be present in patients with CKD despite them having osteopenia or normal BMD. Measuring microarchitecture may assist in targeting therapy to those at risk of fracture.

1. Introduction

Longevity increases the proportion of elderly persons in the community [1]. Age- and disease-related impairment of renal function increases the number of persons requiring management of chronic kidney disease (CKD) [2]. Prolongation of life by drug therapy, dialysis and kidney transplantation is accompanied by secondary hyperparathyroidism and unbalanced bone remodelling. The resulting bone loss compromises bone mass, microarchitecture and strength predisposing to increased morbidity, mortality and costs associated with fragility fracture [3].

To address this fracture burden, Kidney Disease Improving Global

* Corresponding author at: Department of Endocrinology, Austin Health, The University of Melbourne, Victoria, Australia.
E-mail address: alig@unimelb.edu.au (A. Ghasem-Zadeh).

https://doi.org/10.1016/j.bone.2021.116260
Received 7 September 2021; Received in revised form 28 October 2021; Accepted 15 November 2021
Available online 18 November 2021
8756-3282/© 2021 Elsevier Inc. All rights reserved.

Outcomes guidelines recommend measurement of bone mineral density (BMD) [4]. However, BMD is normally distributed. Over ~60% of persons in the community have osteopenia (T-score −2.5 to −1.0 SD), ~10% have so-called normal BMD (T-score > −1 SD) and ~30% have a BMD T-score ≤ −2.5 SD below the young normal mean, the diagnostic threshold for 'osteoporosis' [5]. Because of this population frequency distribution of BMD, most patients with fragility fractures in the community [5] and most patients with CKD who suffer fragility fractures have osteopenia or normal BMD, not osteoporosis [6]. Treatment is often withheld because fracture risk is mistakenly inferred to be low. Even in the presence of a fracture, treatment is withheld because the fracture is misinterpreted as being due to trauma not fragility given BMD is not in the 'osteoporosis' range [7].

Hence, targeting treatment exclusively to persons with 'osteoporosis' will fail to detect or treat over 70% of persons in the community at imminent risk of fracture [7] and will fail to detect or treat most persons with CKD at risk of fracture [6,8]. The absence of osteoporosis is not evidence of absence of bone fragility [9]. Persons with BMD in the osteopenic or normal range are at lower risk for fracture than those with osteoporosis, but they are not necessarily free of bone fragility [9].

Bone loss reduces bone mass and deteriorates the microarchitecture of the reduced bone mass. Measuring BMD captures the reduced bone mass, not the deterioration in microarchitecture. This is an important limitation because an increase in cortical porosity and decrease in trabecular density reduce compression strength to the 7th and 3rd power respectively; disproportionate to the bone loss causing this microarchitectural deterioration and the modest BMD deficits of osteopenia or normal BMD [10].

Approaches are needed that identify persons at risk of fracture despite having modest deficits in BMD. Measurement of cortical and trabecular microarchitectural deterioration has been shown to identify postmenopausal women at imminent, intermediate and long-term risk for fragility fracture with greater sensitivity than BMD [9]. We therefore quantified bone microarchitecture and estimated failure load in women and men with CKD stages 4-5D, kidney transplant recipients and healthy age and sex matched controls to determine whether most patients with kidney disease, like most persons in the community, have osteopenia or normal BMD, not osteoporosis, but nevertheless differ from healthy persons by having compromised bone microarchitecture and reduced estimated failure load.

2. Methods

2.1. Participants

This study included 128 ambulant patients with CKD stages 4, 5 and 5D, and kidney transplantation attending the Renal and Endocrinology units of Austin Health and the Royal Melbourne Hospital, Melbourne, Australia. Inclusion criteria were age above 18 years old, estimated glomerular filtration rate (eGFR) < 30 (ml/min/1.73 m^2), hemodialysis, or peritoneal dialysis and kidney transplantation for more than 3 months. Exclusion criteria were metabolic diseases affecting bone such as Paget disease and osteogenesis imperfecta. Secondary and tertiary hyperparathyroidism in CKD subjects were managed as per KDIGO 2017 Guidelines [11]. The dose of calcitriol was determined by the treating nephrologists. Immunosuppression protocols post renal transplantation was as per local institution guidelines. The patients with CKD were compared to 94 female (57.8 ± 6.3 years) and 181 male (56.3 ± 16.7 years) controls recruited from Bone Structure Study cohort. The Ethics Committee of Austin Health, The University of Melbourne, approved the study (H2006/02704) and all participants provided written informed consent.

2.2. Measurement of bone microarchitecture, BMD and biochemistry

All participants had microarchitecture quantified at the distal radius and distal tibia using high resolution peripheral quantitative computed tomography (HR-pQCT, XtremeCT; Scanco Medical, Brüttisellen, Switzerland) at Austin Health. The manufacturer's protocol applies 60 kVp, 900 μA, 100 ms integration time, 126 mm field of view used to image participants. Image acquisition, reconstruction, and validation are reported [12]. Quality control for the performance of HR-pQCT was based on daily scanning of a manufacturer's phantom containing rods of Hydroxyapatite (HA) embedded in a soft-tissue equivalent resin (QRM, Moehrendorf, Germany). Radiation exposure was 3–5 μSv per measurement. Subjects with motion artefact or degraded quality were excluded from analysis [13].

Bone microarchitecture was quantified using StrAx1.0 algorithm (Strax Corp, Melbourne, Australia) [14]. The 49 most proximal slices of a region of interest were chosen for analysis. Cortical and medullary areas, volumetric bone mineral density (vBMD) of cortical and trabecular compartments, cortical porosity, matrix mineral density, trabecular number, thickness, separation, and spatial inhomogeneity were quantified. The coefficients of variation (CV) of the measurements ranged from 0.54% to 3.98% [14]. BMD of lumbar spine and proximal femur was measured by the Lunar, Prodigy densitometer (GE Healthcare, Madison, WI). Serum was collected in all patients and female controls prior to bone densitometry or HR-pQCT scans. Samples were collected to measure serum parathyroid hormone (PTH), calcium, creatinine (Roche platform, coefficient of variation (CV) = 2.8%, 1.7%, 3.4% respectively), and circulating 25 hydroxyvitamin D (DiaSorin Liaison platform, CV = 7.3%). eGFR was calculated using the CKD-EPI formula.

2.3. Estimation of failure load

Micro finite element analysis (μFEA) was used to calculate estimated failure load using the FAIM software (version 8.0). A uniaxial loading with a tissue elastic modulus of 6829 MPa, a Poisson's ratio of 0.3, a critical strain of 7000 microstrain and a critical volume of 2%, were defined. A 1% apparent strain was applied and estimated failure load was calculated as the load when 2% of elements exceeded the critical strain [15]. The higher the failure load, the greater the strength of bone [16].

2.4. Statistical analysis

Summary statistics for characteristics of patients with CKD express the results in patients and controls as the mean and standard deviation (SD) separately for CKD stages 4-5D and kidney transplant recipients, males and females. Analyses were performed using bone microarchitectural parameters, estimated failure load, and femoral neck and lumbar spine BMD in patients with CKD and controls. Distribution of each microarchitectural and BMD variable was checked using Shapiro-Wilk normality test, and any non-normally distributed variable was transformed using square root, inverse and natural logarithm functions where appropriate. Comparison of the difference between controls and patients with CKD for microarchitectural variables, lumbar spine and femoral neck BMD and estimated failure load was conducted using robust regression, with controls as reference category adjusted for age and sex. The same procedure was applied when the data was stratified by BMD categories (normal BMD, osteopenia and osteoporosis).

Relationships between estimated failure load and microarchitectural traits and femoral neck BMD in patients with CKD were assessed using linear regression. All variables were standardised to have mean 0 and standard deviation of 1 prior carried out analyses. Any predictor that had p-value <0.10 in the univariate analysis was considered for the multivariate analysis. As some microarchitectural variables were highly correlated, for example, between cortical vBMD and porosity ($r = 0.99$), and between trabecular vBMD and connectivity ($r = 0.90$), the presence of these variables together in the multivariate model caused collinearity. We therefore examined two multivariate models with cortical vBMD and trabecular connectivity in one model and cortical vBMD and trabecular

vBMD in the other. The importance of each predictor in the multivariate model was assessed by its contribution to explained variance (R^2) [17]. As we wanted to compare the performance of femoral neck BMD with microarchitectural traits, femoral neck BMD was kept in the multivariate model even if it was not significant. All analyses were performed using STATA, version 16.0 (http://www.stata.com), separately for distal tibia and distal radius.

3. Results

Demographic data of patients with CKD are shown in Table 1. The causes of end stage kidney disease included glomerulonephritis (55%), polycystic disease (18%), obstructive uropathy (13%), diabetes (2%) hypertension (1%) while 11% were unknown. All kidney transplant recipients had eGFR ≥30 ml/min/1.73 m^2 (CKD stages 1T = 4.9%, 2T = 35.8%, 3aT = 30.9%, 3bT = 28.4%). For the remaining 47 patients who did not receive a kidney graft, 15 had CKD stage 4 and 32 had CKD 5D. Cortical and trabecular microarchitecture, estimated failure load, and BMD at the spine and hip did not differ in patients with CKD stages 4-5D and kidney transplant recipients relative to their respective controls so pooled results are shown below. Findings at the distal tibia and distal radius did not differ so the results for the distal tibia are shown below. Data in each patient group relative to their respective controls and data at the distal radius are presented in the supplementary section (Tables S1-S5).

3.1. Distal tibia microarchitecture, failure load, lumbar spine BMD and femoral neck BMD

As shown in Table 2, patients had deficits relative to controls in the following traits - cortical area, cortical vBMD due to increased cortical porosity and decreased matrix mineral density, trabecular vBMD due to fewer, less connected, more widely separated and spatially disrupted trabeculae ('inhomogeneity'), estimated failure load, and BMD at the lumbar spine and femoral neck. Fig. 1 shows the higher the cortical porosity the (a) fewer, (b) the more separated the trabecular with (c) little association with trabecular thickness, but (d) an inverse association with matrix mineral density and (e) greater inhomogeneity in trabecular spatial distribution. Panel (f) shows tibial cortical porosity which trabecularized the cortex producing fragments that may be mistaken as trabeculae and contribute to the inhomogeneity.

3.2. Distal tibia microarchitecture and estimated failure load by femoral neck BMD categories

As shown in Table 3 and Fig. 2, across BMD categories, deterioration in microarchitectural traits and estimated failure load was most severe in patients and controls with osteoporosis, intermediate in patients and controls with osteopenia, and was least deteriorated in patients and controls with normal BMD. In patients with osteopenia and normal BMD, distal tibial microarchitecture and estimated failure load were more deteriorated relative to controls with the same BMD category. In patients with osteoporosis, estimated distal tibial failure load was lower than in controls, but not significantly. Estimated distal radial failure load was significantly lower than controls for all three categories of BMD (Table S4). The frequency distribution curve of cortical matrix mineral density was shifted left with a lower mean value in patients than in controls.

Table 1
Age, eGFR, serum PTH, vitamin D, total calcium and phosphate in patients with chronic kidney disease and kidney transplant recipients. Data expressed as Mean (SD).

	CKD stages 4-5D (n = 47)		Kidney transplant (n = 81)	
	Female (n = 23)	Male (n = 24)	Female (n = 42)	Male (n = 39)
Age (years)	61.4 (14.5)	59.0 (16.4)	58.1 (10.4)	58.6 (11.7)
eGFR (ml/min/1.73 m^2)	14.6 (8.5)	10.6 (7.0)	58.6 (19.4)	56.7 (16.9)
PTH (pmol/L)	21.8 (25.4)	23.8 (28.6)	10.3 (10.2)	8.6 (6.0)
Vitamin D (nmol/L)	69.2 (41.9)	80.0 (37.9)	84.0 (31.9)	88.1 (29.2)
Total calcium (mmol/L)	2.4 (0.1)	2.4 (0.2)	2.5 (0.2)	2.4 (0.1)
Phosphate (mmol/L)	1.3 (0.3)	1.8 (2.1)	1.1 (0.3)	1.0 (0.2)

eGFR = estimated glomerular filtration rate, PTH = parathyroid hormone.

Table 2
Comparison of distal tibia microarchitecture, estimated failure load, lumbar spine, and femoral neck BMD in patients with CKD versus age- and sex-matched controls.

	Control (n = 272)	CKD (n = 126)	p
	Mean (range)	Mean (range)	
Age	58.8 (62.3)	58.9 (62.3)	0.161
Bone microarchitecture	Mean (SD)	Mean (SD)	
Total bone CSA (mm^2)**	753 (153)	711 (146)	0.489
Cortical CSA (mm^2)	237 (35.3)	219 (40.7)	0.002
Medullary CSA (mm^2)**	517 (135)	492 (123)	0.920
Cortical vBMD (mgHA/cm^3)	642 (81.7)	543 (80.7)	<0.001
Porosity (%)**	61.9 (6.48)	69.6 (6.19)	<0.001
Matrix mineral density (%)	65.1 (1.28)	64.2 (0.62)	<0.001
Trabecular vBMD (mgHA/cm^3)	149 (43.0)	92.2 (41.1)	<0.001
Number (1/mm)	2.91 (0.68)	1.93 (0.59)	<0.001
Thickness (μm)*+	195 (143)	197 (146)	0.304
Connectivity (1/mm^2)	0.85 (0.17)	0.64 (0.20)	<0.001
Separation (mm)**	1.23 (0.28)	1.74 (0.36)	<0.001
Inhomogeneity*	0.23 (0.15)	0.46 (0.44)	<0.001
Estimated failure load (N)***	5778 (1467)	3825 (1152)	<0.001
Bone mineral density			
Lumbar spine BMD (g/cm^2)***	1.16 (0.18)	1.06 (0.17)	<0.001
T-Score	−0.35 (1.47)	−1.24 (1.31)	<0.001
Femoral neck BMD (g/cm^2)***	0.94 (0.14)	0.78 (0.12)	<0.001
T-Score	−0.89 (1.05)	−2.04 (0.87)	<0.001

Summary statistics presented by absolute mean, standard deviation (SD) where p-value was computed using transformed data if variable was not normally distributed using *inverse, **natural logarithm and ***square root functions; analyses were conducted using robust regression, adjusted for age and sex. Sample size for FEA analysis was 242 for controls and 119 for patients with CKD, and 218 to 225 for controls and 108 to 114 for patients with CKD for lumbar spine and femoral neck (bone mineral density BMD measurements). +The trabecular thickness' unit converted to micron to get more distinctive numbers. CSA = cross sectional area; HA = hydroxyapatite; vBMD = volumetric bone mineral density; N = Newton.

3.3. Predictors of estimated tibial bone failure load

As shown in Table 4, in univariate analyses, distal tibial cortical and trabecular microarchitecture and femoral neck BMD were each associated with estimated tibial failure load. In multivariable analyses, associations with estimated strength remained significant for microstructural traits but not for femoral neck BMD. Microarchitecture accounted for over 85% of the variance in estimated failure load (R^2 values were 0.879 and 0.868 for the multivariate model I and II respectively).

As shown in Fig. 3, there were significant associations between estimated failure load and several cortical and trabecular traits and between estimated failure load and femoral neck BMD in both patients and controls. At any given trait, estimated failure load was lower in the patients than controls.

4. Discussion

We report that most patients with CKD stages 4-5D and kidney

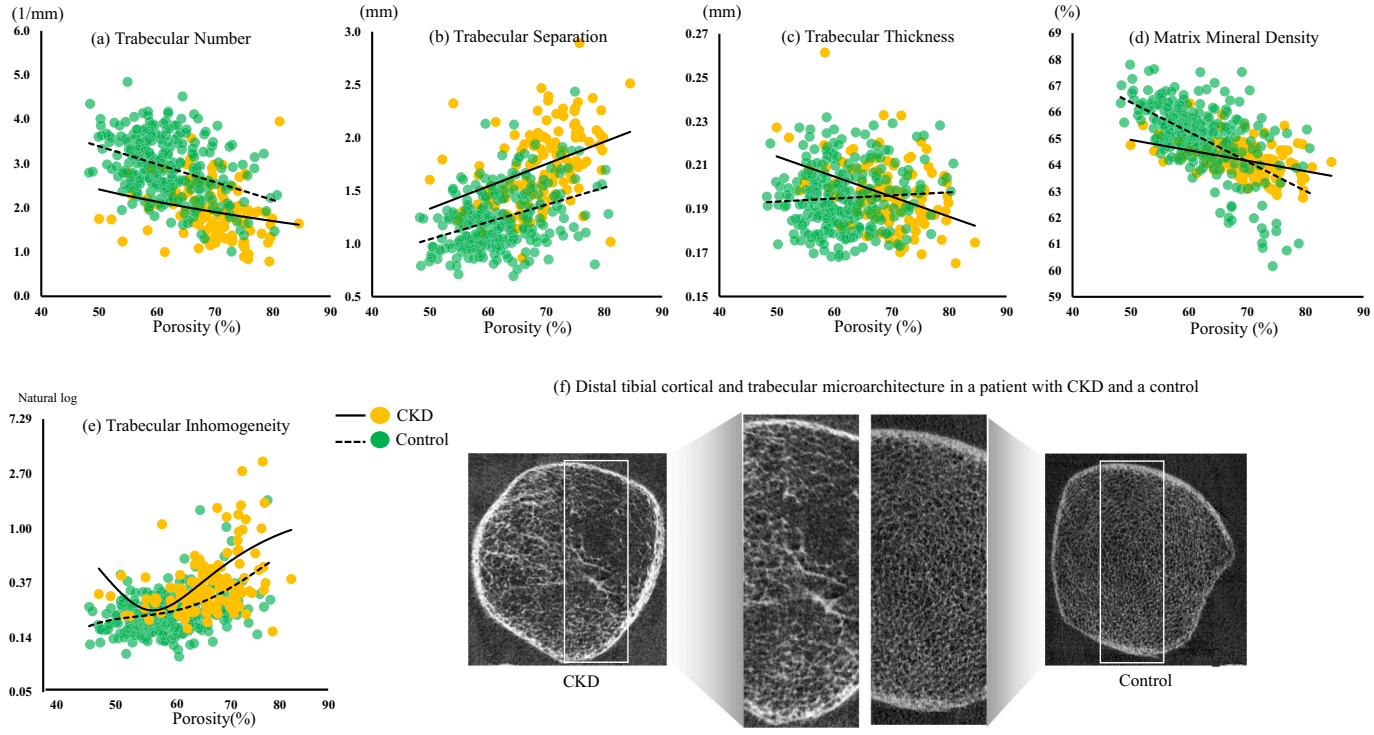

Fig. 1. Cortical and trabecular microarchitecture and femoral neck BMD are more deteriorated in patients with CKD (yellow dots) than in controls (green dots). The greater the cortical porosity, (a) the fewer the numbers of trabeculae, (b) the greater the trabecular separation but (c) no association with trabecular thickness. (d) Greater cortical porosity was associated with lower matrix mineral density and (e) greater inhomogeneity in trabecular spatial distribution. (f) Compared with a control, the patient with CKD had loss of homogeneity in distal tibial trabecular spatial distribution. Magnified section shows increased cortical porosity with trabecularized cortex producing fragments that may be mistaken as trabeculae and contribute to the inhomogeneity. (For interpretation of the references to colour in this figure legend, the reader is referred to the web version of this article.)

Table 3
Comparison of distal tibia microarchitecture, estimated failure load in controls versus patients with CKD according to BMD category (normal, osteopenia and osteoporosis).

Bone microarchitecture	Normal			Osteopenia			Osteoporosis		
	Control (n = 117)	CKD (n = 14)	p	Control (n = 96)	CKD (n = 67)	p	Control (n = 11)	CKD (n = 31)	p
	Mean (SD)	Mean (SD)		Mean (SD)	Mean (SD)		Mean (SD)	Mean (SD)	
Total bone CSA (mm^2)**	753 (163)	751 (117)	0.809	721 (138)	705 (157)	0.673	723 (157)	704 (117)	0.344
Cortical CSA (mm^2)	241 (32.4)	228 (22.8)	0.008	225 (33.5)	215 (40.7)	0.447	202 (35.0)	216 (41.4)	0.003
Medullary CSA (mm^2)**	512 (146)	524 (109)	0.551	496 (120)	490 (135)	0.645	522 (137)	488 (92.3)	0.702
Cortical vBMD ($mgHA/cm^3$)	671 (64.4)	590 (64.5)	<0.001	608 (84.5)	548 (80.9)	<0.001	528 (78.2)	512 (80.6)	0.024
Porosity (%)**	59.7 (5.11)	66.1 (4.95)	<0.001	64.5 (6.76)	69.1 (6.28)	<0.001	70.7 (6.55)	71.9 (6.05)	0.018
Matrix mineral density (%)	65.2 (0.95)	64.4 (0.52)	<0.001	64.7 (1.69)	64.2 (0.61)	0.006	64.5 (1.06)	64.2 (0.65)	0.454
Trabecular vBMD ($mgHA/cm^3$)	161 (39.1)	118 (36.3)	<0.001	128 (37.6)	93.0 (37.0)	<0.001	108 (54.7)	80.3 (47.9)	0.090
Number (1/mm)	3.02 (0.57)	2.32 (0.51)	<0.001	2.67 (0.71)	1.94 (0.59)	<0.001	2.27 (0.70)	1.81 (0.60)	0.004
Thickness (μm)*+	196 (135)	197 (127)	0.954	194 (160)	196 (141)	0.242	196 (135)	197 (127)	0.382
Connectivity ($1/mm^2$)	0.89 (0.15)	0.74 (0.21)	0.012	0.78 (0.16)	0.64 (0.18)	<0.001	0.72 (0.21)	0.58 (0.22)	0.102
Separation (mm)**	1.17 (0.22)	1.53 (0.33)	<0.001	1.35 (0.30)	1.74 (0.34)	<0.001	1.52 (0.39)	1.83 (0.41)	0.012
Inhomogeneity*	0.21 (0.06)	0.28 (0.06)	<0.001	0.27 (0.21)	0.39 (0.23)	<0.001	0.34 (0.24)	0.62 (0.74)	0.014
Estimated failure load (N)***	6199 (1177)	4541 (1190)	<0.001	4949 (1167)	3856 (1100)	<0.001	3893 (891)	3409 (1223)	0.107

Summary statistics were presented by mean and standard deviation (SD), where p-value was computed using transformed data if variable was not normally distributed using *inverse, **natural logarithm and ***square root functions; analyses were conducted using robust regression, adjusted for age and sex. +The trabecular thickness' unit converted to micron to get more distinctive numbers. CSA = cross sectional area; HA = hydroxyapatite; vBMD = volumetric bone mineral density; N = Newton.

transplant recipients had osteopenia or normal femoral neck BMD, not osteoporosis. Despite these modest deficits in femoral neck BMD, distal tibial and distal radial microarchitecture and estimated failure load were compromised. Cortical and trabecular distal tibia and distal radius microarchitecture, not femoral neck BMD, were independently associated with estimated failure load and accounted for over 85% of the variance in failure load estimated at these metaphyseal locations.

The findings were consistent within each BMD category – relative to controls, the cortices were reduced in area, cortical vBMD was reduced due to increased porosity and decreased matrix mineral density, trabecular vBMD was reduced due to fewer trabeculae that were disconnected and disrupted in their spatial distribution. Patients and controls with osteoporosis had more severe deterioration in microarchitecture and estimated failure load than patients and controls with

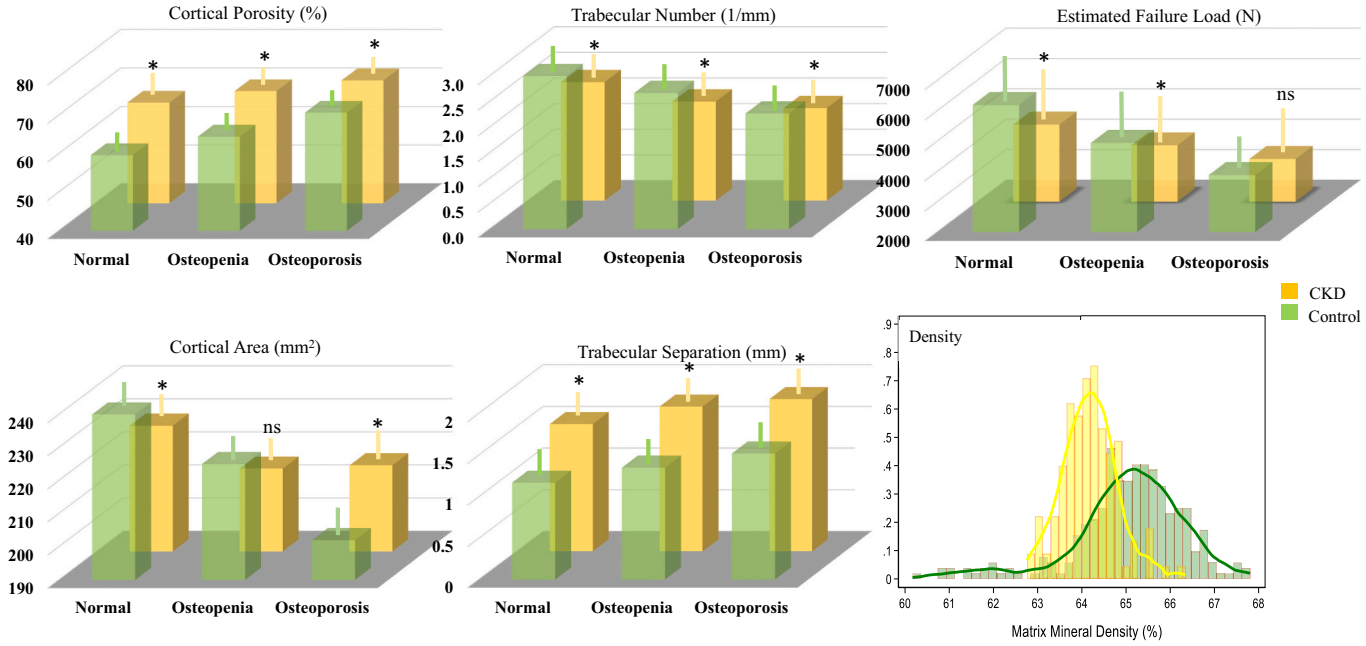

Fig. 2. Comparison of bone microarchitecture and estimated failure load in patients with CKD (yellow bars) versus controls (green bars) within a bone mineral density (BMD) category (*$p < 0.001$). Comparison of matrix mineral density frequency distribution between patients with CKD and controls (right bottom panel), N=Newton. See text. (For interpretation of the references to colour in this figure legend, the reader is referred to the web version of this article.)

Table 4
Univariate and multivariate analyses of associations between estimated failure load and tibial microarchitectural traits in patients with CKD ($N = 103$).

	Univariate			Multivariate Model I				Multivariate Model II			
	Coef	se	p	Coef	se	p	%R^2	Coef	se	p	%R^2
Total bone CSA (mm^2)	0.450	0.100	<0.001								
Cortical CSA (mm^2)	0.640	0.083	<0.001	0.443	0.043	<0.001	25.4	0.413	0.048	<0.001	24.6
Medullary CSA (mm^2)	0.307	0.106	0.005	0.118	0.049	0.018	5.22	0.154	0.055	0.006	4.44
Cortical vBMD ($mgHA/cm^3$)	0.593	0.082	<0.001	0.341	0.048	<0.001	21.6				
Porosity (%)	-0.568	0.084	<0.001					−0.330	0.053	<0.001	15.9
Matrix mineral density (%)	0.236	0.102	0.023								
Trabecular vBMD ($mgHA/cm^3$)	0.773	0.067	<0.001					0.596	0.093	<0.001	26.7
Number (1/mm)	0.452	0.091	<0.001								
Thickness (μm)	0.477	0.097	<0.001								
Connectivity ($1/mm^2$)	0.796	0.064	<0.001	0.503	0.044	<0.001	38.8				
Separation (mm)	-0.632	0.078	<0.001					−0.169	0.082	0.041	13.8
Inhomogeneity*	0.459	0.094	<0.001					−0.355	0.073	<0.001	7.82
Femoral neck BMD	0.499	0.088	<0.001	0.033	0.042	0.431	9.02	0.024	0.045	0.603	6.77

All variables were standardised to have mean of 0 and standard deviation of 1; *data was transformed using inverse function; R-square (R^2) were 0.879 and 0.868 for the multivariate model I and II respectively; %R^2 = percentage of contribution to R-square by each bone trait. CSA = cross sectional area; HA = hydroxyapatite; vBMD = volumetric bone mineral density; N = Newton.

osteopenia or normal BMD. In each of these three femoral neck BMD categories, patients had more deteriorated distal tibial and distal radial microarchitecture relative to controls with the same BMD category. Estimated failure load was also more severely deteriorated in patients than controls in all three BMD categories but the difference in patients with osteoporosis versus controls with osteoporosis achieved significance only at the distal radius, not distal tibia.

Persons with osteopenia and normal BMD are the source of most fragility fractures in the community because vastly greater numbers of persons in the community have these modest deficits in BMD [5]. It is likely that most patients with CKD in this study, and patients with CKD with fractures reported previously [6,8], had osteopenia or normal BMD for the same reason. Thus, finding normal BMD or osteopenia in patients with CKD is no assurance of 'normal' bone strength and freedom from fracture risk.

BMD T-score > −1.0 SD is referred to as 'normal' but this terminology is misleading because bone loss reduces bone mass but also deteriorates the microarchitecture of the reduced bone mass, irrespective of the assigned BMD category [18]. Compressive strength decreases as a 7th and 3rd power function of the increase in cortical porosity and decrease in trabecular density respectively, an increment in fragility disproportionate to the modest deficits in BMD produced by bone loss [10]. Indeed, we found that estimated failure load at the distal appendicular sites was independently associated with most microarchitectural traits at these locations, not femoral neck BMD.

Both distal tibial and distal radial cortical and trabecular microarchitecture were deteriorated in patients with CKD because widespread unbalanced bone remodelling occurs upon all three (intracortical, endocortical and trabecular) components of bone's inner (endosteal) envelope [19]. Finding correlations between cortical porosity and trabecular morphology in patients with CKD and in controls supports the notion that both bone compartments are compromised by bone loss produced by advancing age and by CKD.

Several investigators report deterioration in cortical bone but

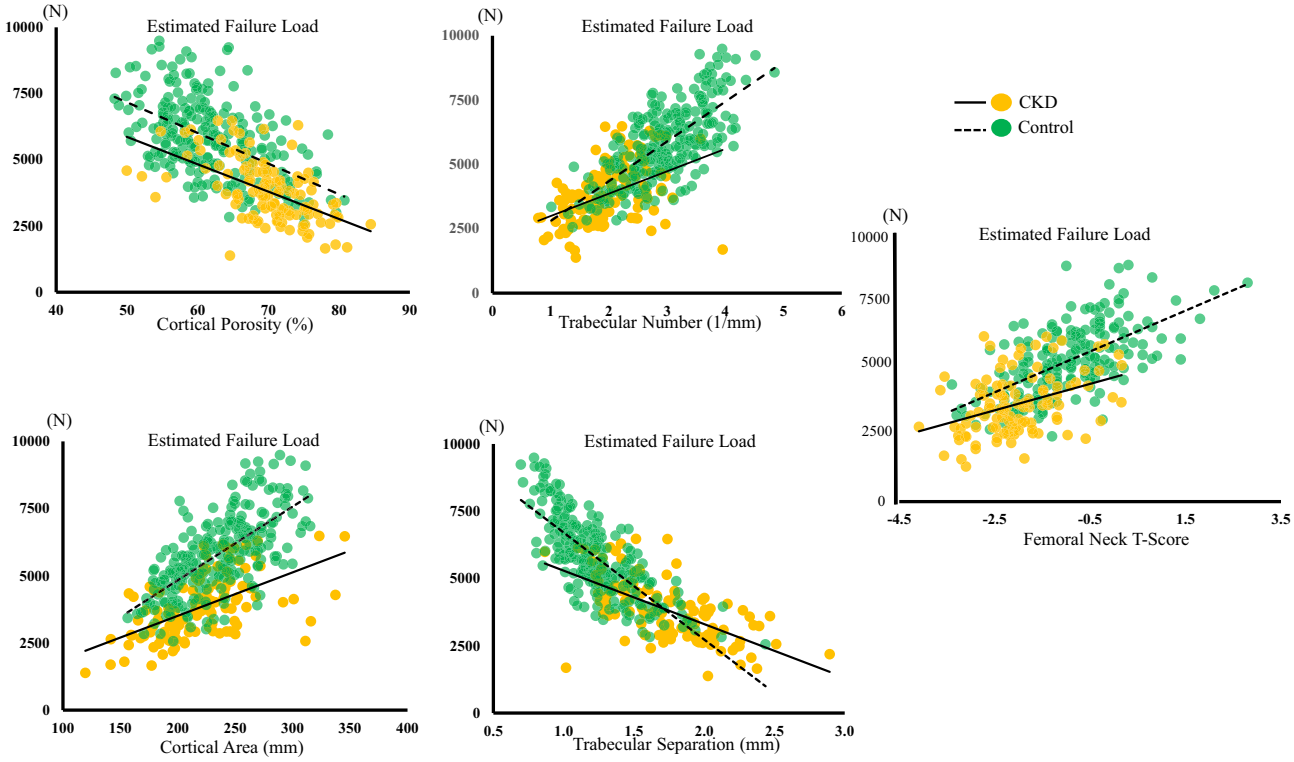

Fig. 3. Univariate associations between estimated failure load at the distal tibia with tibial cortical and trabecular microarchitecture and femoral neck BMD in patients with CKD (yellow dots) and controls (green dots). N=Newton. See text. (For interpretation of the references to colour in this figure legend, the reader is referred to the web version of this article.)

sparing of trabecular morphology or increased trabecular density in patients with primary [20], and secondary hyperparathyroidism of kidney disease [8]. This finding is likely to be due to an error in segmenting cortical from trabecular bone [14,21]. Unbalanced intracortical remodelling upon the surface Haversian canals traversing the cortices fragment and trabecularizes the cortex adjacent to the medullary canal. The fragments are 'seen' as 'trabecular' bone by the threshold-based segmentation algorithm falsely elevating trabecular density, so it appears to be unaffected or increased in patients with CKD [8,20,22].

Finding normal or increased trabecular thickness is likely to be due to preferential loss of thin trabeculae, inclusion of thicker cortical fragments erroneously called 'trabeculae', or both. Thickening is unlikely to be due to increased trabecular bone formation as this requires intermittent not continuous PTH exposure as found in primary and secondary hyperparathyroidism [23]. We speculate that deterioration in trabecular spatial distribution ('inhomogeneity') is likely to be due to more rapid bone loss of trabeculae positioned centrally in the medullary canal. These trabeculae may have a large surface area/bone volume configuration providing more surface for initiation of unbalanced remodelling than peripherally positioned trabeculae abutting the cortex [24]. Trabeculae populating the cortico-trabecular transitional zone may be fashioned with a lower surface area/bone volume configuration and so may be remodelled more slowly. Spatial inhomogeneity may also be due to inclusion of cortical fragments as 'trabecular' bone [12].

Rapid unbalanced remodelling compromises qualities of bone other than its cortical and trabecular microarchitecture [25]. For example, matrix mineralization density is reduced by replacing older, more mineralized bone, with young, less completely mineralized bone [26,27]. As remodelling is unbalanced, the inverse association between porosity and matrix mineral density is due to replacement of older matrix with a smaller volume of new, less mineralized matrix. Kidney transplantation improves kidney function but hyperparathyroidism may persist resulting in continued rapid and unbalanced remodelling exacerbated by corticosteroid therapy which reduces bone formation by each remodelling event, worsening remodelling imbalance [28,29]. This may account for the similar deficits in microarchitecture, BMD and estimated failure load in kidney transplant recipients and patients with CKD.

These results confirm previous work showing bone loss and deteriorated cortical and trabecular microarchitecture in patients with primary [30] and secondary hyperparathyroidism of CKD [8]. Cejka et al. reported lower cortical and trabecular vBMD and deteriorated trabecular microarchitecture of distal radius and distal tibia in patients undergoing hemodialysis [31]. Nishiyama et al., reported increased cortical porosity following kidney transplantation [32]. Trombetti et al. reported deteriorated cortical and trabecular microarchitecture and estimated failure load and stiffness [33]. This study advances previous work by demonstrating microarchitectural deterioration occurs irrespective of the BMD category, even so-called 'normal' BMD, and this deterioration compromises bone strength independent of BMD.

This study has several limitations. This was a cross-sectional with small numbers of patients with normal BMD and small numbers of controls with osteoporosis. For this reason, we may have been unable to detect some morphological differences, and some group differences failed to achieve statistical significance. We cannot distinguish whether lower peak, greater bone loss or both contributed to microstructural deterioration and deficits in BMD. In addition, only 24 subjects had had fractures so evaluation of bone morphology relative to patients without fractures and relative to controls was not possible. Attributing causation of bone disease is difficult because patients with CKD are heterogeneous in terms of the underlying cause and duration of kidney disease, duration of dialysis, exposure to glucocorticoids, kidney transplantation, gonadal status and other factors.

In summary, patients with CKD stages 4-5D and kidney transplant recipients are more likely to have osteopenia or normal BMD than osteoporosis. Despite the modest deficits in BMD, estimated breaking strength of bone is compromised, in part, due to microarchitectural deterioration of the reduced bone mass, a structural change which increases bone fragility disproportionate to the bone loss causing it. In

conclusion, finding modest deficits in BMD does not exclude the presence of bone fragility. Assessment of bone microarchitecture might be helpful in identifying and targeting treatment to patients with CKD at risk of fracture.

CRediT authorship contribution statement

Study design and conduct: AGH, ES, CHCH. Data collection: AGZ, ES, SI, RJ, PM, NT, CHCH. Responsibility for StrAx analysis: AGZ, Responsibility for finite element analysis: SB. Statistical analyses: MB and AGH. Drafting manuscript: AGH, CHCH and ES. Data interpretation and approving final version of manuscript: AGH, MB, ES, SI, RJ, PM, NT, SB, and CHCH.

Declaration of competing interest

A Ghasem-Zadeh is a shareholder in StraxCorp. E Seeman is shareholder in StraxCorp. S Boyd is a co-founder and co-owner of Numerics88 Solutions Inc.

Appendix A. Supplementary data

Supplementary data to this article can be found online at https://doi.org/10.1016/j.bone.2021.116260.

References

[1] K. Christensen, G. Doblhammer, R. Rau, J.W. Vaupel, Ageing populations: the challenges ahead, Lancet 374 (9696) (2009) 1196–1208.

[2] P. Cockwell, L.A. Fisher, The global burden of chronic kidney disease, Lancet 395 (10225) (2020) 662–664. Epub 2020/02/18.

[3] L. Robertson, C. Black, N. Fluck, S. Gordon, R. Hollick, H. Nguyen, et al., Hip fracture incidence and mortality in chronic kidney disease: the GLOMMS-II record linkage cohort study, BMJ Open 8 (4) (Apr 12 2018), e020312. Epub 2018/04/15.

[4] M. Ketteler, G.A. Block, P. Evenepoel, M. Fukagawa, C.A. Herzog, L. McCann, et al., Executive summary of the 2017 KDIGO chronic kidney disease-mineral and bone disorder (CKD-MBD) guideline update: what's changed and why it matters, Kidney Int. 92 (1) (Jul 2017) 26–36. Epub 2017/06/26.

[5] E.S. Siris, Y.T. Chen, T.A. Abbott, E. Barrett-Connor, P.D. Miller, L.E. Wehren, et al., Bone mineral density thresholds for pharmacological intervention to prevent fractures, Arch. Intern. Med. 164 (10) (2004) 1108–1112. Epub 2004/05/26.

[6] M.H. Tariq, S.A.S. Sulaiman, Prevalence of osteopenia and osteoporosis among chronic kidney disease patients: a systematic review, Systematic Review, Open Urol. Nephrol. J. 13 (2020) 8. Epub 23/05/2020.

[7] W.D. Leslie, E. Seeman, S.N. Morin, L.M. Lix, S.R. Majumdar, The diagnostic threshold for osteoporosis impedes fracture prevention in women at high risk for fracture: a registry-based cohort study, Bone 114 (Sep 2018) 298–303. Epub 2018/07/17.

[8] T.L. Nickolas, E.M. Stein, E. Dworakowski, K.K. Nishiyama, M. Komandah-Kosseh, C.A. Zhang, et al., Rapid cortical bone loss in patients with chronic kidney disease, J. Bone Miner. Res. 28 (8) (2013) 1811–1820.

[9] R. Chapurlat, M. Bui, E. Sornay-Rendu, R. Zebaze, P.D. Delmas, D. Liew, et al., Deterioration of cortical and trabecular microstructure identifies women with osteopenia or normal bone mineral density at imminent and long-term risk for fragility fracture: a prospective study, J. Bone Miner. Res. 35 (5) (May 2020) 833–844. Epub 2019/12/11.

[10] M.B. Schaffler, D.B. Burr, Stiffness of compact bone: effects of porosity and density, J. Biomech. 21 (1) (1988) 13–16. Epub 1988/01/01.

[11] KDIGO 2017 clinical practice guideline update for the diagnosis, evaluation, prevention, and treatment of chronic kidney disease-mineral and bone disorder (CKD-MBD), Kidney international supplements. 7 (1) (Jul 2017) 1–59. Epub 2017/07/01.

[12] A. Laib, H.J. Häuselmann, P. Rüegsegger, In vivo high resolution 3D-QCT of the human forearm, Technol. Health Care 6 (5–6) (Dec 1998) 329–337. Epub 1999/04/01.

[13] D.E. Whittier, S.K. Boyd, A.J. Burghardt, J. Paccou, A. Ghasem-Zadeh, R. Chapurlat, et al., Guidelines for the assessment of bone density and microarchitecture in vivo using high-resolution peripheral quantitative computed tomography, Osteoporos. Int. 31 (9) (Sep 2020) 1607–1627. Epub 2020/05/28.

[14] R. Zebaze, A. Ghasem-Zadeh, A. Mbala, E. Seeman, A new method of segmentation of compact-appearing, transitional and trabecular compartments and quantification of cortical porosity from high resolution peripheral quantitative computed tomographic images, Bone 54 (1) (May 2013) 8–20. Epub 2013/01/22.

[15] E.J. Samelson, K.E. Broe, H. Xu, L. Yang, S. Boyd, E. Biver, et al., Cortical and trabecular bone microarchitecture as an independent predictor of incident fracture risk in older women and men in the Bone Microarchitecture International Consortium (BoMIC): a prospective study, Lancet Diabetes Endocrinol. 7 (1) (Jan 2019) 34–43. Epub 2018/12/07.

[16] H.H. Malluche, D.S. Porter, D. Pienkowski, Evaluating bone quality in patients with chronic kidney disease, Nat. Rev. Nephrol. 9 (11) (2013) 671–680. Epub 2013/10/08.

[17] F. Huettner, M. Sunder, Axiomatic arguments for decomposing goodness of fit according to Shapley and Owen values, Electronic Journal of Statistics. 6 (none) (2012) 1239–1250, 12.

[18] J.A. Kanis, Assessment of fracture risk and its application to screening for postmenopausal osteoporosis: synopsis of a WHO report. WHO Study Group, Osteoporos Int. 4 (6) (Nov 1994) 368–381. Epub 1994/11/01.

[19] K.J. Martin, E.A. González, Metabolic bone disease in chronic kidney disease, J. Am. Soc. Nephrol. 18 (3) (2007) 875–885.

[20] M. Parisien, F. Cosman, R.W. Mellish, M. Schnitzer, J. Nieves, S.J. Silverberg, et al., Bone structure in postmenopausal hyperparathyroid, osteoporotic, and normal women, J. Bone Miner. Res. 10 (9) (Sep 1995) 1393–1399. Epub 1995/09/01.

[21] R.M. Zebaze, A. Ghasem-Zadeh, A. Bohte, S. Iuliano-Burns, M. Mirams, R.I. Price, et al., Intracortical remodelling and porosity in the distal radius and post-mortem femurs of women: a cross-sectional study, Lancet 375 (9727) (2010) 1729–1736. Epub 2010/05/18.

[22] D.W. Dempster, M. Parisien, S.J. Silverberg, X.G. Liang, M. Schnitzer, V. Shen, et al., On the mechanism of cancellous bone preservation in postmenopausal women with mild primary hyperparathyroidism, J. Clin. Endocrinol. Metab. 84 (5) (May 1999) 1562–1566. Epub 1999/05/14.

[23] H. Dobnig, R.T. Turner, Evidence that intermittent treatment with parathyroid hormone increases bone formation in adult rats by activation of bone lining cells, Endocrinology 136 (8) (Aug 1995) 3632–3638. Epub 1995/08/01.

[24] M. Bui, A. Bjørnerem, A. Ghasem-Zadeh, G.S. Dite, J.L. Hopper, E. Seeman, Architecture of cortical bone determines in part its remodelling and structural decay, Bone 55 (2) (Aug 2013) 353–358. Epub 2013/05/07.

[25] E. Seeman, P.D. Delmas, Bone quality–the material and structural basis of bone strength and fragility, N. Engl. J. Med. 354 (21) (2006) 2250–2261. Epub 2006/05/26.

[26] B.M. Misof, S. Blouin, P. Roschger, J. Werzowa, K. Klaushofer, G. Lehmann, Bone matrix mineralization and osteocyte lacunae characteristics in patients with chronic kidney disease - mineral bone disorder (CKD-MBD), J. Musculoskelet. Neuronal Interact. 19 (2) (2019) 196–206.

[27] O. Akkus, A. Polyakova-Akkus, F. Adar, M.B. Schaffler, Aging of microstructural compartments in human compact bone, J. Bone Miner. Res. 18 (6) (Jun 2003) 1012–1019. Epub 2003/06/24.

[28] B.A. Julian, D.A. Laskow, J. Dubovsky, E.V. Dubovsky, J.J. Curtis, L.D. Quarles, Rapid loss of vertebral mineral density after renal transplantation, N. Engl. J. Med. 325 (8) (1991) 544–550. Epub 1991/08/22.

[29] M.C. Monier-Faugere, H. Mawad, Q. Qi, R.M. Friedler, H.H. Malluche, High prevalence of low bone turnover and occurrence of osteomalacia after kidney transplantation, J.Am.Soc.Nephrol. 11 (6) (Jun 2000) 1093–1099. Epub 2000/05/23.

[30] T.D. Vu, X.F. Wang, Q. Wang, N.E. Cusano, D. Irani, B.C. Silva, et al., New insights into the effects of primary hyperparathyroidism on the cortical and trabecular compartments of bone, Bone 55 (1) (Jul 2013) 57–63. Epub 2013/04/02.

[31] D. Cejka, J.M. Patsch, M. Weber, D. Diarra, M. Riegersperger, Z. Kikic, et al., Bone microarchitecture in hemodialysis patients assessed by HR-pQCT, Clin. J.Am.Soc. Nephrol. 6 (9) (Sep 2011) 2264–2271. Epub 2011/07/09.

[32] K.K. Nishiyama, Y. Pauchard, L.E. Nikkel, S. Iyer, C. Zhang, D.J. McMahon, et al., Longitudinal HR-pQCT and image registration detects endocortical bone loss in kidney transplantation patients, J. Bone Miner. Res. 30 (3) (Mar 2015) 554–561. Epub 2014/09/13.

[33] A. Trombetti, C. Stoermann, T. Chevalley, B. Van Rietbergen, F.R. Herrmann, P. Y. Martin, et al., Alterations of bone microstructure and strength in end-stage renal failure, Osteoporos. Int. 24 (5) (May 2013) 1721–1732. Epub 2012/10/27.

ORIGINAL ARTICLE

JBMR®

Irreversible Deterioration of Cortical and Trabecular Microstructure Associated With Breastfeeding

Åshild Bjørnerem,[1,2] Ali Ghasem-Zadeh,[3] Xiaofang Wang,[3] Minh Bui,[4] Susan P Walker,[5] Roger Zebaze,[3] and Ego Seeman[3,6]

[1]Department of Clinical Medicine, UiT The Arctic University of Norway, Tromsø, Norway
[2]Department of Obstetrics and Gynecology, University Hospital of North Norway, Tromsø, Norway
[3]Endocrine Centre and Department of Medicine, Austin Health, University of Melbourne, Melbourne, Australia
[4]Centre for Epidemiology and Biostatistics, School of Population and Global Health, University of Melbourne, Melbourne, Australia
[5]Mercy Hospital for Women, Department of Obstetrics and Gynecology, University of Melbourne, Melbourne, Australia
[6]Institute of Health and Ageing, Australian Catholic University, Melbourne, Australia

ABSTRACT

Estrogen deficiency associated with menopause is accompanied by an increase in the rate of bone remodeling and the appearance of a remodeling imbalance; each of the greater number of remodeling transactions deposits less bone than was resorbed, resulting in microstructural deterioration. The newly deposited bone is also less completely mineralized than the older bone resorbed. We examined whether breastfeeding, an estrogen-deficient state, compromises bone microstructure and matrix mineral density. Distal tibial and distal radial microarchitecture were quantified using high-resolution peripheral quantitative computed tomography in 58 women before, during, and after breastfeeding and in 48 controls during follow-up of 1 to 5 years. Five months of exclusive breastfeeding increased cortical porosity by 0.6% (95% confidence interval [CI] 0.3–0.9), reduced matrix mineralization density by 0.26% (95% CI 0.12–0.41) (both $p < 0.01$), reduced trabecular number by 0.22 per mm (95% CI 0.15–0.28), and increased trabecular separation by 0.07 mm (95% CI 0.05–0.08) (all $p < 0.001$). Relative to prebreastfeeding, at a median of 2.6 years (range 1 to 4.8) after cessation of breastfeeding, cortical porosity remained 0.58 SD (95% CI 0.48–0.68) higher, matrix mineralization density remained 1.28 SD (95% CI 1.07–1.49) lower, and trabeculae were 1.33 SD (95% CI 1.15–1.50) fewer and 1.06 SD (95% CI 0.91–1.22) more greatly separated (all $p < 0.001$). All deficits were greater than in controls. The results were similar at distal radius. Bone microstructure may be irreversibly deteriorated after cessation of breastfeeding at appendicular sites. Studies are needed to establish whether this deterioration compromises bone strength and increases fracture risk later in life. © 2016 American Society for Bone and Mineral Research.

KEY WORDS: CORTICAL POROSITY; LACTATION; MATRIX MINERALIZATION; TRABECULAR BONE MICROARCHITECTURE

Introduction

All factors influencing bone's structural strength express their effects through a final common cellular machinery of bone remodeling.[1,2] Bone remodeling is balanced during young adulthood. Equal volumes of old or damaged bone are removed and replaced by new bone upon the endocortical surface of the cortex maintaining cortical thickness, upon the surfaces of the intracortical canals maintaining their diameters, and upon trabecular surfaces maintaining their thickness, number, and connectivity.[3,4]

With the appearance of estrogen deficiency at menopause, bone remodeling becomes unbalanced; each remodeling event resorbs more bone than it replaces, producing cortical thinning and porosity, perforation, and complete loss of trabeculae. Remodeling rate also accelerates; more remodeling sites appear upon the endocortical, intracortical, and trabecular surfaces, accelerating structural deterioration.[5] The rapid remodeling also reduces matrix mineralization density by replacing older, more mineralized bone with young, less completely mineralized bone.[4–6]

Breastfeeding is an estrogen-deficient state associated with bone loss.[6–9] Bone remodeling accelerates and may also become unbalanced. Studies in rodent and other animal models demonstrate that trabeculae perforate, their numbers decrease, and cortical porosity increases.[10–18] This structural deterioration has been reported to be reversible in some animal models.[7,17,18] Bone loss during breastfeeding in humans is reported, but whether the microstructural deterioration is reversible after cessation of breastfeeding in human subjects is uncertain.[19–29]

As trabecular bone loss, trabecular thinning, and perforation proceed rapidly after estrogen deficiency, the resulting bone fragility is attributed to deterioration in trabecular bone.

Received in original form July 25, 2016; revised form October 4, 2016; accepted October 11, 2016. Accepted manuscript online October 13, 2016.
Address correspondence to: Ashild Bjørnerem, MD, Department of Clinical Medicine, Faculty of Health Sciences, UiT The Arctic University of Norway, 9037 Tromsø, Norway. E-mail: ashild.bjornerem@uit.no
For a Commentary on this article, please see Kovacs (J Bone Miner Res. 2017;32:676–680. DOI: 10.1002/jbmr.3090).
Journal of Bone and Mineral Research, Vol. 32, No. 4, April 2017, pp 681–687
DOI: 10.1002/jbmr.3018
© 2016 American Society for Bone and Mineral Research

However, ~80% of the skeleton is cortical; trabecular bone comprises only ~20% of the skeleton. The slower remodeling and loss of the fourfold larger cortical bone volume contributes more to total bone loss in absolute terms than rapid trabecular bone loss during aging.[30,31] Moreover, unbalanced intracortical remodeling is the main source of cortical bone loss and produces cortical porosity.[30] Increasing porosity of a compact structure like cortical bone reduces strength more than increasing porosity of an already porous structure like trabecular bone.[32]

No study has been done examining the microstructural basis of bone loss or its reversibility during more than 1.5 years postpartum follow-up. We hypothesized that the rapid unbalanced remodeling associated with breastfeeding will produce bone loss, structural deterioration, and will reduce the completeness of matrix mineralization by replacing older bone with young bone. We also hypothesized that deficits in trabecular and cortical microstructure are likely partly irreversible because complete loss of trabeculae by perforation and formation of large pores may be incompletely restored after completion of breastfeeding and return of normal menstrual cyclicity.

Materials and Methods

We recruited 100 healthy pregnant women aged 20 to 42 years with a singleton pregnancy and term delivery at The Mercy Hospital for Women, Heidelberg, Melbourne, Australia, from 2008 to 2009. Initial assessment was at a mean of 14 days (range 3 to 25) post-delivery. The second assessment occurred after a median of 5 months (range 2 to 6) in women who breastfed 6 to 10 times per day exclusively without formula or bottle feeding (Table 1). To accurately capture changes during exclusive breastfeeding, each woman had the second assessment within 14 days of cessation of exclusive breastfeeding because the shift to intermittent breastfeeding is followed shortly by resumption of menses and possible slowing of remodeling as estrogen levels rise.[23] The third and final assessment occurred after a median total follow-up since delivery of 3.6 years (range 0.9 to 5.4). Total follow-up included a median of total breastfeeding for 13 months (range 3 to 31), exclusive breastfeeding for 5 months, intermittent breastfeeding (2 to 4 times daily combined with other nutrition for 7 months (range 0 to 25), and 2.6 years (range 1 to 4.8) follow-up after stopping breastfeeding. Resumption of menses occurred 7 months post-delivery (range 1 to 14) (which was shortly after cessation of exclusive breastfeeding), and follow-up after resumption of menses was 3 years (range 1.5 to 5.1).

We excluded 8 women who did not breastfeed, 6 who became pregnant, 10 who were lost to follow-up, as well as 18 women with movement artefacts during scanning of distal tibia and 24 women with movement artefact of distal radius. This left 58 breastfeeding women with three valid distal tibia scans and 52 women with three valid distal radial scans. We recruited a control group of 48 healthy non-pregnant non-lactating premenopausal women aged 18 to 44 years, followed for a median of 2.1 years (range 1.1 to 5.3) with two valid scans of distal tibia and 42 of them had two valid scans of distal radius. All participants gave written informed consent. The study was approved by the Austin and Mercy Human Research Ethics Committees.

High-resolution 3-dimensional peripheral quantitative computed tomography (HR-pQCT; XtremeCT, Scanco Medical AG, Brüttisellen, Switzerland) was used to obtain images at the non-dominant distal tibia and distal radius.[33] A total of 110 slices were obtained at 22.5 and 9.5 mm from a reference line at the endplate of the distal tibia and radius, respectively. The 49 most proximal slices were chosen because the thicker cortex allows accurate assessment of porosity. Porosity within the total cortex and its compartments (compact cortex, outer and inner transitional zones), matrix mineralization density, trabecular number, thickness, separation, and bone volume/tissue volume (BV/TV) were quantified using StrAx1.0, a non-threshold-based method for quantifying microarchitecture in vivo.[34] The method automatically segments bone into its compartments (Straxcorp, Melbourne, Australia). The in vivo precision was 0.5 to 3.0%.[34] Daily quality control was carried out by scanning a phantom containing rods of hydroxyapatite (QRM, Moehrendorf, Germany).

StrAx1.0 analysis uses an algorithm that separates bone from background (soft tissue) and bone into its compact-appearing cortex, the fragmented cortex forming an outer and inner transitional zone and the trabecular compartment. From the segmented image, porosity is quantified as the proportion of voxels within the cortical compartment that contain void. Once deposited, osteoid is mineralized reaching $\geq$80% of full mineralization (1200 mgHA/cc) within days. Matrix mineralization is quantified using StrAx1.0 by determining the mean density of voxels with attenuation between 80% and 100% of fully mineralized bone. These voxels are unlikely to contain a pore because a pore results in voxel attenuation $<$80% of the maximum. So, variation attenuation within 80% and 100% of full mineralization reflects heterogeneity in mineralization. Voxels attenuating photons $<$80% are used to calculate porosity.

Areal bone mineral density (aBMD) at the spine and total hip was assessed using dual-energy X-ray absorptiometry (DXA, Lunar GE Prodigy, Madison, WI, USA) at baseline and after end of lactation and end of follow-up (first and third visits but not at the second visit).

Analysis of variance (ANOVA) was used to compare baseline features in women who breastfed and controls. Then *t* tests were used to determine whether the within-group mean change in absolute terms differed from zero (i) during exclusive breastfeeding (second minus first measurement), (ii) after end of exclusive breastfeeding (third minus second measurement), and (iii) across the total follow-up in breastfeeding group (third minus first measurement), and in controls (second minus first measurement). In addition, change in standardized terms relative to prebreastfeeding was calculated by dividing total change by baseline standard deviation (SD) for each trait. Annual rates of change in absolute terms were calculated for each period by dividing each of the changes by its respective follow-up. ANOVA was used to test whether the change in each trait in absolute terms in women who breastfed differed from the change in controls after adjustment for baseline age, parity, height, and weight. Analyses were performed using SAS Software package, v9.3 (SAS Institute Inc., Cary, NC, USA). Two-sided $p < 0.05$ was the level of significance chosen. The results with mean $\pm$ standard deviation (SD) are shown in the tables, whereas the results below show the mean values only to facilitate comprehension. The 95% confidence intervals (CI) are presented short in parentheses.

Results

The total follow-up of women who breastfed was a median of 3.6 years (range 0.9 to 5.4), which included exclusive

15234681, 2017, 4, Downloaded from https://asbmr.onlinelibrary.wiley.com/doi/10.1002/jbmr.3018 by The University Of Melbourne, Wiley Online Library on [17/06/2023]. See the Terms and Conditions (https://onlinelibrary.wiley.com/terms-and-conditions) on Wiley Online Library for rules of use; OA articles are governed by the applicable Creative Commons License

Table 1. Baseline Features, Duration of Lactation, and Follow-up in 58 Women Who Breastfed and 48 Controls

	Breastfed	Controls
Age (years)	33.5 (24.8–42.8)	33.4 (18.1–44.6)
Height (cm)	163.7 (146–178)	164.0 (150–184)
Weight (kg)	72.7 (48–102)	67.6 (45–117)
Parity (range)	1.9 (1–4)	0.8 (0–3)[c]
White ethnicity, *n* (%)	50 (86.2)	39 (81.3)
Distal tibia	$n = 58$	$n = 48$
Total cortical porosity (%)	56.9 ± 4.0	57.8 ± 4.1
Compact cortex porosity (%)	38.4 ± 3.7	38.0 ± 3.7
Outer transitional zone porosity (%)	39.6 ± 2.7	39.4 ± 3.1
Inner transitional zone porosity (%)	83.5 ± 2.5	84.5 ± 2.7
Matrix mineralization density (%)	66.1 ± 1.0	65.5 ± 1.3[b]
Trabecular number (1/mm)	2.97 ± 0.49	2.63 ± 0.55[c]
Trabecular thickness (mm)	0.187 ± 0.011	0.196 ± 0.014[c]
Trabecular separation (mm)	1.24 ± 0.21	1.34 ± 0.27[a]
Trabecular bone volume/tissue volume (%)	4.67 ± 1.53	4.13 ± 1.53
Distal radius	$n = 52$	$n = 43$
Total cortical porosity (%)	51.8 ± 5.0	51.7 ± 6.4
Compact cortex porosity (%)	34.7 ± 3.5	35.1 ± 4.7
Outer transitional zone porosity (%)	38.2 ± 2.5	38.8 ± 3.8
Inner transitional zone porosity (%)	84.4 ± 3.0	84.9 ± 2.8
Matrix mineralization density (%)	66.3 ± 1.3	66.1 ± 1.7
Trabecular number (1/mm)	2.40 ± 0.46	2.25 ± 0.47
Trabecular thickness (mm)	0.187 ± 0.011	0.194 ± 0.013[b]
Trabecular separation (mm)	1.35 ± 0.33	1.39 ± 0.34
Trabecular bone volume/tissue volume (%)	3.29 ± 1.77	2.97 ± 1.58
Duration of exclusive lactation (months)*	5.0 (2–6)	
Duration of total (any) lactation (months)*	13.0 (3–31)	
Resumption of menses (months postpartum)*	7.1 (1–14)	
Follow-up after resumption of menses (years)*	3.0 (1.5–5.1)	
Follow-up after end of any lactation (years)*	2.6 (1–4.8)	
Total follow-up (years)*	3.6 (0.9–5.4)	2.1 (1.1–5.3)[c]

Mean (range), mean ± standard deviation, or *median (range).
[a]$p < 0.05$, [b]$p < 0.01$, [c]$p < 0.001$ differences between groups.

breastfeeding for a median of 5 months (range 2 to 6), intermittent breastfeeding for a median of 7 months (range 0 to 25), and no breastfeeding at all for a median of 2.6 years (range 1 to 4.8) (Table 1). Baseline age, height, weight, and tibial cortical porosity did not differ between women who breastfed and controls. However, trabecular number was higher (2.97 versus 2.63 per mm), trabeculae were thinner (0.187 versus 0.196) but less separated (1.24 versus 1.34 mm), and the degree of matrix mineralization was higher (66.1 versus 65.5%) compared with controls, respectively (all $p < 0.05$).

Exclusive breastfeeding

During a median of 5 months of exclusive breastfeeding, distal tibia cortical porosity increased by 0.6% (95% CI 0.3–0.9), whereas the degree of matrix mineralization decreased by 0.26% (0.12–0.41), trabecular number decreased by 0.22 per mm (0.15–0.28), thickness increased by 0.004 mm (0.003–0.005), separation increased by 0.07 mm (0.05–0.08), and BV/TV decreased by 0.29% (0.20–0.38) (all $p < 0.001$, Table 2).

Intermittent breastfeeding, with other nutrition and resumption of menses

Despite the cessation of breastfeeding for a median of 2.6 years and regular menses for 3.0 years, distal tibia cortical porosity continued to increase by a further 1.8% (95% CI 1.4–2.1), whereas matrix mineralization continued to decrease by 0.97% (0.79–1.14), trabecular number decreased by a further 0.43 per mm (0.36–0.51), thickness increased by 0.014 mm (0.011–0.016), separation increased by 0.16 mm (0.13–0.18), and BV/TV decreased by 0.78% (0.66–0.90) (all $p < 0.001$).

After stopping breastfeeding

Residual deficits in microarchitecture and material composition were observed at a median of 2.6 years after complete cessation of any breastfeeding. Relative to measurements done before breastfeeding, cortical porosity remained 2.3% (95% CI 1.9–2.7) or 0.58 SD (48–0.68) higher, and matrix mineralization density remained 1.23% (1.03–1.43) or 1.28 SD (1.07–1.49) lower (all $p < 0.001$) (Table 2, Fig. 1*A*). There were 0.65 per mm (0.56–0.74) or 1.33 SD (1.15–1.50) fewer trabeculae that were 0.017 mm (0.015–0.020) or 1.54 SD (1.33–1.74) thicker and 0.22 mm (0.19–0.26) or 1.06 SD (0.91–1.22) more separated. Trabecular BV/TV remained 1.07% (0.93–1.21) or 0.70 SD (0.61–0.79) lower (all $p < 0.001$). There was no overall gain in distal tibia total cross-sectional area (–0.005 mm^2 [–2.14, +2.13]).

There was a gain in aBMD of the spine and total hip between baseline and end of follow-up of 0.021 g/cm^2 (95% CI 0.004–0.038) or 0.16 SD (0.07–0.26), $p = 0.016$ and 0.010 g/cm^2

15234681, 2017, 4, Downloaded from https://asbmr.onlinelibrary.wiley.com/doi/10.1002/jbmr.3018 by The University Of Melbourne, Wiley Online Library on [17/06/2023]. See the Terms and Conditions (https://onlinelibrary.wiley.com/terms-and-conditions) on Wiley Online Library for rules of use; OA articles are governed by the applicable Creative Commons License

Table 2. Mean (95% Confidence Intervals [CI]) Changes in Distal Tibial and Distal Radial Microarchitecture Associated With Breastfeeding and in Controls

	Breastfeeding			Controls
	Exclusive 2nd minus first measurement	Intermittent 3rd minus second measurement	Overall 3rd minus first measurement	2nd minus 1st measurement
Distal tibia	Mean (95% CI)	Mean (95% CI)	Mean (95% CI)	Mean (95% CI)
Total cortical porosity (%)	0.6 (0.3, 0.9)[c]	1.8 (1.4, 2.1)[c]	2.3 (1.9, 2.7)[c]	0.8 (0.4, 1.2)[c,f]
Compact cortex porosity (%)	0.3 (0.01, 0.6)[a]	0.8 (0.5, 1.2)[c]	1.2 (0.7, 1.6)[c]	0.3 (–0.1, 0.7)[f]
Outer transitional zone porosity (%)	0.2 (0.004, 0.5)[a]	1.2 (0.9, 1.5)[c]	1.4 (1.1, 1.8)[c]	0.3 (–0.1, 0.7)[f]
Inner transitional zone porosity (%)	0.4 (0.2, 0.5)[c]	0.9 (0.7, 1.1)[c]	1.2 (1.0, 1.5)[c]	0.4 (0.2, 0.6)[c,f]
Matrix mineralization density (%)	–0.26 (–0.41, –0.12)[c]	–0.97 (–1.14, –0.79)[c]	–1.23 (–1.43, –1.03)[c]	–0.29 (–0.51, –0.07)[a,f]
Trabecular number (1/mm)	–0.22 (–0.28, –0.15)[c]	–0.43 (–0.51, –0.36)[c]	–0.65 (–0.74, –0.56)[c]	–0.29 (–0.39, –0.20)[c,f]
Trabecular thickness (mm)	0.004 (0.003, 0.005)[c]	0.014 (0.011, 0.016)[c]	0.017 (0.015, 0.020)[c]	0.008 (0.005,0.010)[c,f]
Trabecular separation (mm)	0.07 (0.05, 0.08)[c]	0.16 (0.13, 0.18)[c]	0.22 (0.19, 0.26)[c]	0.10 (0.07, 0.14)[c,f]
Trabecular bone volume/tissue volume (%)	–0.29 (–0.38, –0.20)[c]	–0.78 (–0.90, –0.66)[c]	–1.07 (–1.21, –0.93)[c]	–0.45 (–0.61, –0.28)[c,f]
Distal radius				
Total cortical porosity (%)	0.6 (0.2, 1.0)[b]	1.6 (1.3, 2.0)[c]	2.2 (1.8, 2.6)[c]	0.8 (0.2, 1.4)[b,f]
Compact cortex porosity (%)	0.3 (–0.1, 0.6)	1.4 (1.1, 1.7)[c]	1.7 (1.3, 2.0)[c]	0.4 (–0.1, 1.0)[f]
Outer transitional zone porosity (%)	0.04 (–0.2, 0.3)	1.2 (0.9, 1.4)[c]	1.2 (0.9, 1.5)[c]	0.3 (–0.2, 0.8)[f]
Inner transitional zone porosity (%)	0.02 (–0.1, 0.1)	0.4 (0.3, 0.6)[c]	0.5 (0.3, 0.6)[c]	0.1 (–0.1, 0.3)[f]
Matrix mineralization density (%)	–0.06 (–0.25, 0.13)	–0.86 (–1.02, –0.69)[c]	–0.92 (–1.13, –0.71)[c]	–0.28 (–0.56, 0.01)[f]
Trabecular number (1/mm)	–0.04 (–0.12, 0.04)	–0.35 (–0.42, –0.27)[c]	–0.39 (–0.46, –0.31)[c]	–0.18 (–0.28, –0.08)[c,e]
Trabecular thickness (mm)	0.002 (–0.0002, 0.004)	0.011 (0.008, 0.013)[c]	0.013 (0.010, 0.015)[c]	0.008 (0.005, 0.011)[c]
Trabecular separation (mm)	0.03 (0.001, 0.05)[a]	0.10 (0.07, 0.13)[c]	0.12 (0.09, 0.15)[c]	0.07 (0.03, 0.10)[c,e]
Trabecular bone volume/tissue volume (%)	–0.08 (–0.14, –0.02)[b]	–0.52 (–0.63, –0.41)[c]	–0.61 (–0.72, –0.49)[c]	–0.22 (–0.33, –0.12)[c,f]

Changes in absolute terms during exclusive and intermittent breastfeeding, overall (exclusive, intermittent, and after cessation of breastfeeding), and in controls.
[a]$p < 0.05$, [b]$p < 0.01$, [c]$p < 0.001$ for within-group changes. [d]$p < 0.05$, [e]$p < 0.01$, [f]$p < 0.001$ comparing overall changes in women who breastfed versus controls.

15234681, 2017, 4, Downloaded from https://asbmr.onlinelibrary.wiley.com/doi/10.1002/jbmr.3018 by The University Of Melbourne, Wiley Online Library on [17/06/2023]. See the Terms and Conditions (https://onlinelibrary.wiley.com/terms-and-conditions) on Wiley Online Library for rules of use; OA articles are governed by the applicable Creative Commons License

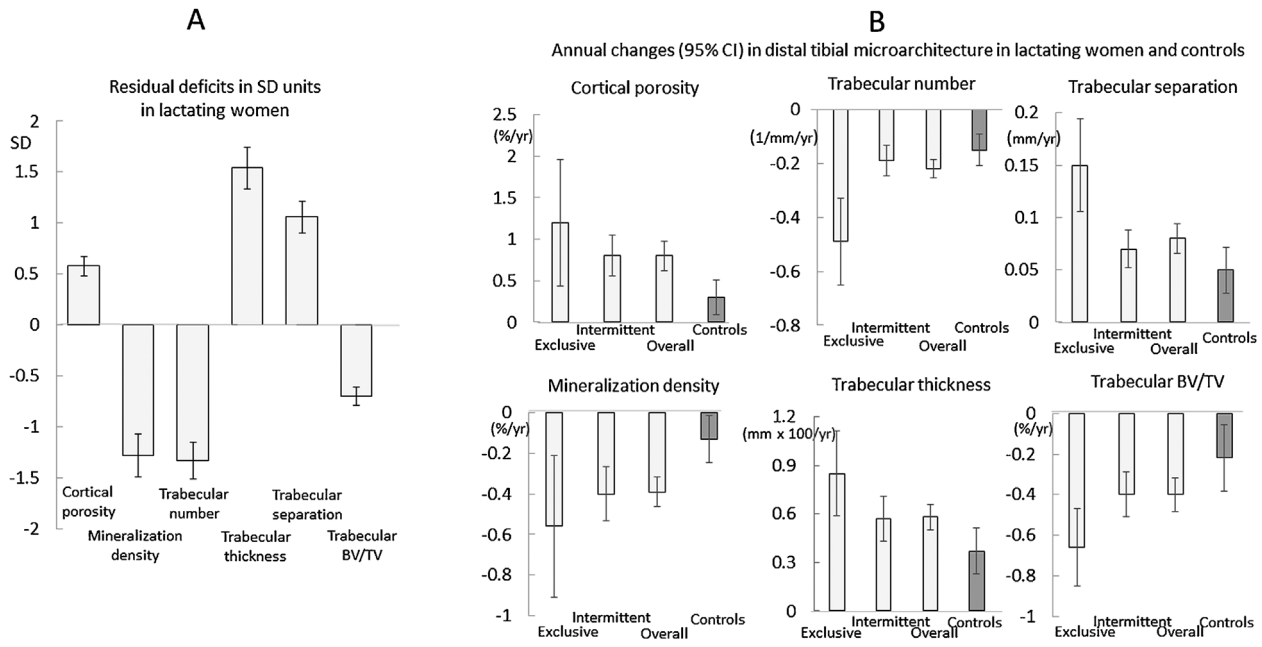

Fig. 1. (*A*) Residual deficits or overall changes (95% confidence intervals) in distal tibia microarchitecture expressed as standard deviation (SD) units relative to beginning breastfeeding for cortical porosity, matrix mineralization density, trabecular number, thickness, separation, and bone volume/tissue volume (BV/TV) (calculated as the difference between first and third measurement, divided by the baseline SD). (*B*) Annualized mean (95% confidence intervals) rate of change in women breastfeeding for distal tibia microarchitecture during exclusive and intermittent breastfeeding and overall (exclusive, intermittent, and after cessation of breastfeeding) and in controls for cortical porosity (%), matrix mineralization density (%), trabecular number (1/mm), thickness (mm × 100), separation (mm), and BV/TV (%) (calculated as the difference between first and second, second and third, and first and third measurement of each trait, divided by its respective follow-up).

(–0.0001, 0.020) or 0.10 SD (0.03–0.18), $p = 0.052$, respectively. The weight loss of 2.2 kg (0.5–4.0) ($p = 0.014$) did not predict the changes in aBMD or microstructure at any site.

All trait changes were greater in women breastfeeding than in controls: Cortical porosity was higher, 2.3% (1.9–2.7) versus 0.8% (0.4–1.2); matrix mineralization density was lower, 1.23% (1.03–1.43) versus 0.29% (0.07–0.51); trabecular number was lower, 0.65 per mm (0.56–0.74) versus 0.29 per mm (0.20–0.39); trabecular thickness was greater, 0.017 mm (0.015–0.020) versus 0.008 mm (0.005–0.010); separation was greater, 0.22 mm (0.19–0.26) versus 0.10 mm (0.07–0.14); and BV/TV was lower, 1.07% (0.93–1.21) versus 0.45% (0.28–0.61) (all $p < 0.001$). Results were similar for distal radius (Tables 1 and 2). Annualized rates of changes in cortical porosity, matrix mineralization density, trabecular number, thickness, separation, and BV/TV were more rapid in breastfeeding women than in controls (all $p < 0.05$, Fig. 1*B*). All these comparisons were adjusted for age, height, weight, and parity.

Discussion

We report that women who breastfed had more rapid deterioration in microstructure than controls. Intracortical remodeling produced porosity and replaced older more completely mineralised bone with younger less completely mineralised bone. Remodeling upon trabecular surfaces removed them producing a reduction in trabecular number and greater separation between them. These morphological effects did not reverse following cessation of lactation and the return of menses. Despite follow-up of a median of 3.6 years post-delivery, residual deficits remained relative to beginning of breastfeeding with higher cortical porosity, fewer trabeculae and lower matrix mineralisation.

Loss of bone mineral and matrix associated with lactation occurs in several ways. First, estrogen deficiency associated with lactation, like menopause, increases the rate of bone remodeling.[23] More remodeling events excavate bone upon the surfaces of intracortical canals, endocortical surface and trabeculae. The rapid increase in cortical porosity and decrease in trabecular BV/TV are the net result of many excavated sites that appear at the same time as refilling occurs in the fewer cavities excavated pre-lactation, before remodeling becomes rapid.[35] The fewer sites excavated pre-lactation do not refill immediately. Refilling is delayed by the reversal phase, and then proceeds slowly, during 3 months, and so occurs during early lactation when rapid remodeling begins.[35] This delay in the initiation and slowness of the refilling phase produces a transient deficit in bone matrix and mineral.[36]

If rapid remodeling was the only abnormality associated with estrogen deficiency, the increase in cortical porosity and decrease in trabecular density produced would be expected to be fully reversed because all the cavities excavated producing the transient deficit in bone matrix and mineral eventually fully reverse with cessation of lactation and restoration of estrogen production.

Estrogen deficiency is also accompanied by the appearance of a remodeling imbalance. Each of the many more remodeling transactions resorb a larger volume of bone and deposit less bone because of the prolongation of the life span

15234681, 2017, 4, Downloaded from https://asbmr.onlinelibrary.wiley.com/doi/10.1002/jbmr.3018 by The University Of Melbourne, Wiley Online Library on [17/06/2023]. See the Terms and Conditions (https://onlinelibrary.wiley.com/terms-and-conditions) on Wiley Online Library for rules of use; OA articles are governed by the applicable Creative Commons License

of osteoclasts and shortening of the life span of osteoblasts respectively.[37] This negative bone 'balance' is small, only about −5%; over 95% of a volume of bone resorbed is replaced by each remodeling transaction. However, this deficit is likely to persist as long as estrogen deficiency is present.

The persisting structural deterioration we report is likely to be due the unbalanced remodeling associated with estrogen deficiency during lactation. This microstructural deterioration is more modest than that found after menopause because lactation is only 6-–9 months in duration. Trabeculae are about 100–200 microns in thickness so that increased resorption depth perforate trabeculae. Perforated trabeculae result in a permanent reduction in trabecular number and connectivity. Complete loss of trabeculae reduces strength more than trabecular thinning.[38] Preferential loss of thinner trabeculae produced an increase in mean thickness of trabeculae; we do not suggest lactation is accompanied by bone formation upon trabeculae making them thicker.

Cortical bone loss occurs more slowly than trabecular bone loss but the slower loss of a larger volume of cortical bone resulted in similar deficits of 0.58 SD higher cortical porosity and 0.70 SD lower trabecular BV/TV. However, intracortical remodeling produces large coalescent pores which may fail to refill after lactation resulting in cortical porosity. Increasing porosity of a compact structure like cortical bone reduces strength more than increasing porosity of an already porous structure like trabecular bone.[32]

The occurrence of cortical porosity is well documented by histomorphometry in lactating beagle dogs but reversibility of porosity in this animal model was not reported.[10] Studies in rodent species variously report reversibility, partial or no reversibility after weaning.[13–18] While trabecular bone is remodeled in rodents, rodents continue to grow throughout life and do not remodel cortical bone, or do so to a limited degree late in life. The synthesis of new trabeculae during continued growth may explain why the loss of trabecular bone is reversible. Rodents are less suitable as a model for examining cortical (Haversian) remodeling and porosity in human subjects.

In addition, the rapid remodeling produces a reduction in matrix mineral content because the smaller volume of newly deposited osteoid replaces mineralised bone matrix. The newly deposited smaller volume of osteoid undergoes rapid primary mineralisation reaching ~80% of its peak mineralisation density within days to weeks but secondary mineralisation, the enlargement of crystals deposited during primary mineralisation takes months if not years to complete so that even after return of menses, a residual deficit in matrix mineralisation density was present.[7,39]

Bone loss also occurs by peri-osteocytic osteolysis - focal osteocytic perilacunar resorption of bone is documented during lactation in rodents.[40] After cessation of lactation, periosteocytic lacunar matrix remineralisation may also occur by rapid primary, but slower secondary mineralisation contributing to the persisting deficits in the mean degree of mineralisation of matrix. This is likely to become fully reversed with time.

The only other study examining bone microarchitecture of the appendicular skeleton during lactation also reported incomplete recovery in bone microarchitecture.[29] However, as 80% of porosity is less than 100 microns in diameter, threshold based segmentation done in that study underestimates cortical porosity because voxels containing pores also contain matrix and are disregarded using that approach. Threshold based segmentation also overestimates trabecular density because intracortical remodeling producing porosity results in cortical fragments which are measured as 'trabecular bone' overestimating recovery of trabecular bone.

Contrary to changes in appendicular microarchitecture,[29] some investigators report either partial or complete reversibility of BMD at the spine or hip after breastfeeding, and some suggest even higher spine BMD after breastfeeding.[7,19–28] The reasons for the reversibility at the central skeleton are not clear.

This study has several limitations. The sample size was modest and follow-up may have been insufficient to detect reversal of structural changes and restoration of matrix mineralisation density produced by high remodeling rate. Measurements were not available prior to pregnancy so that the observations may be confounded by the effects of pregnancy, if any, on bone morphology and the subsequent changes produced at completion of pregnancy. The ideal control, pregnant women who did not breastfeed their offspring, could not be recruited to address this design limitation.

In summary, breastfeeding is associated with deterioration of cortical and trabecular bone microstructure and a reduction in completeness of secondary matrix mineralisation at the appendicular skeleton. The bone loss was irreversible during 2.6 years follow up after the end of lactation, and 3 years after resumption of regular menses. The relevance of the these deficits in terms of compromising bone strength and increasing fracture risk remain to be established. Epidemiological studies report that lactation is neutral or protective against fracture; no long term deleterious effects on fracture risk are reported.[7,41,42] Further studies are needed to establish whether the deterioration in microarchitecture of the appendicular skeleton contributes to fracture risk later in life.

Disclosures

ÅB has received lectures fees from Amgen and Eli Lilly. AG-Z is remunerated by StraxCorp as senior image analyst and is one of the inventors of the StrAx1.0 algorithm. RZ has received grant and/or research support from Amgen, Merck Sharp & Dohme, Servier, Warner-Chilcott, AKP, Genzyme, Sanofi, GSK, and Pfizer. He is a shareholder in StraxCorp, is remunerated by StraxCorp as president of R&D, and is one of the inventors of the StrAx1.0 algorithm. RZ is also a director on the board of StraxCorp. ES has received research support and has lectured at national and international meeting symposia funded by Amgen, Allergan, Asahi, Genzyme, and Merck Sharp & Dohme. He is a director of the board and shareholder in StraxCorp, is remunerated by StraxCorp as chief medical officer, and is one of the inventors of the StrAx1.0 algorithm. All authors state that they have no other conflicts of interest.

Acknowledgments

This study was funded by National Health and Medical Research Council of Australia and by the Research Council of Norway (RCN) Grant (ID 178588/V50).

Authors' roles: Study design and conduct: all authors. Data collection: ÅB, AGZ, and XW. Responsibility for StrAx analysis: RZ. Statistical analyses: ÅB and MB. Drafting manuscript: all authors. Data interpretation and approving final version of manuscript: all authors.

15234681, 2017, 4, Downloaded from https://asbmr.onlinelibrary.wiley.com/doi/10.1002/jbmr.3018 by The University Of Melbourne, Wiley Online Library on [17/06/2023]. See the Terms and Conditions (https://onlinelibrary.wiley.com/terms-and-conditions) on Wiley Online Library for rules of use; OA articles are governed by the applicable Creative Commons License

References

1. Parfitt AM. Skeletal heterogeneity and the purposes of bone remodelling: implications for the understanding of osteoporosis. In: Marcus R, Feldman D, Nelson DA, Rosen CJ, editors. Osteoporosis. San Diego, CA: Academic Press; 2008. p. 71–89.
2. Parfitt AM. Targeted and non-targeted bone remodeling: relationship to basic multicellular unit origination and progression. Bone. 2002;30(1):5–7.
3. Parfitt AM. The physiologic and clinical significance of bone histomorphometric data. In: Recker R, editor. Bone histomorphometry. Techniques and interpretation. Boca Raton, FL: CRC Press; 1983. p. 142–223.
4. Seeman E, Delmas PD. Bone quality—the material and structural basis of bone strength and fragility. N Engl J Med. 2006;354(21):2250–61.
5. Manolagas SC. Choreography from the tomb: an emerging role of dying osteocytes in the purposeful, and perhaps not so purposeful, targeting of bone remodeling. Bonekey. 2006;3:5–14.
6. Eriksen EF, Langdahl B, Vesterby A, Rungby J, Kassem M. Hormone replacement therapy prevents osteoclastic hyperactivity: a histomorphometric study in early postmenopausal women. J Bone Miner Res. 1999;14(7):1217–21.
7. Kovacs CS. Maternal mineral and bone metabolism during pregnancy, lactation, and post-weaning recovery. Physiol Rev. 2016;96(2):449–547.
8. Compston JE. Sex steroids and bone. Physiol Rev. 2001;81(1):419–47.
9. Khosla S, Melton LJ III, Riggs BL. The unitary model for estrogen deficiency and the pathogenesis of osteoporosis: is a revision needed? J Bone Miner Res. 2011;26(3):441–51.
10. Vajda EG, Kneissel M, Muggenburg B, Miller SC. Increased intracortical bone remodeling during lactation in beagle dogs. Biol Reprod. 1999;61(6):1439–44.
11. Vajda EG, Bowman BM, Miller SC. Cancellous and cortical bone mechanical properties and tissue dynamics during pregnancy, lactation, and postlactation in the rat. Biol Reprod. 2001;65(3):689–95.
12. Bowman BM, Siska CC, Miller SC. Greatly increased cancellous bone formation with rapid improvements in bone structure in the rat maternal skeleton after lactation. J Bone Miner Res. 2002;17(11):1954–60.
13. Vanhouten JN, Dann P, Stewart AF, et al. Mammary-specific deletion of parathyroid hormone-related protein preserves bone mass during lactation. J Clin Invest. 2003;112(9):1429–36.
14. Miller SC, Bowman BM. Rapid improvements in cortical bone dynamics and structure after lactation in established breeder rats. Anat Rec A Discov Mol Cell Evol Biol. 2004;276(2):143–9.
15. Miller SC, Anderson BL, Bowman BM. Weaning initiates a rapid and powerful anabolic phase in the rat maternal skeleton. Biol Reprod. 2005;73(1):156–62.
16. Ardeshirpour L, Dann P, Adams DJ, et al. Weaning triggers a decrease in receptor activator of nuclear factor-kappaB ligand expression, widespread osteoclast apoptosis, and rapid recovery of bone mass after lactation in mice. Endocrinology. 2007;148(8):3875–86.
17. Wysolmerski JJ. Conversations between breast and bone: physiological bone loss during lactation as evolutionary template for osteolysis in breast cancer and pathological bone loss after menopause. Bonekey. 2007;4(8):209–25.
18. Liu XS, Ardeshirpour L, Vanhouten JN, Shane E, Wysolmerski JJ. Site-specific changes in bone microarchitecture, mineralization, and stiffness during lactation and after weaning in mice. J Bone Miner Res. 2012;27(4):865–75.
19. Sowers M, Corton G, Shapiro B, et al. Changes in bone density with lactation. JAMA. 1993;269(24):3130–5.
20. Sowers M, Randolph J, Shapiro B, Jannausch M. A prospective study of bone density and pregnancy after an extended period of lactation with bone loss. Obstet Gynecol. 1995;85(2):285–9.
21. Kalkwarf HJ, Specker BL, Bianchi DC, Ranz J, Ho M. The effect of calcium supplementation on bone density during lactation and after weaning. N Engl J Med. 1997;337(8):523–8.
22. Kalkwarf HJ, Specker BL. Bone mineral loss during lactation and recovery after weaning. Obstet Gynecol. 1995;86(1):26–32.
23. Ritchie LD, Fung EB, Halloran BP, et al. A longitudinal study of calcium homeostasis during human pregnancy and lactation and after resumption of menses. Am J Clin Nutr. 1998;67(4):693–701.
24. Laskey MA, Prentice A. Bone mineral changes during and after lactation. Obstet Gynecol. 1999;94(4):608–15.
25. Polatti F, Capuzzo E, Viazzo F, Colleoni R, Klersy C. Bone mineral changes during and after lactation. Obstet Gynecol. 1999;94(1):52–6.
26. More C, Bettembuk P, Bhattoa HP, Balogh A. The effects of pregnancy and lactation on bone mineral density. Osteoporos Int. 2001;12(9):732–7.
27. Pearson D, Kaur M, San P, Lawson N, Baker P, Hosking D. Recovery of pregnancy mediated bone loss during lactation. Bone. 2004;34(3):570–8.
28. Møller UK, Vieth SS, Mosekilde L, Rejnmark L. Changes in bone mineral density and body composition during pregnancy and postpartum. A controlled cohort study. Osteoporos Int. 2012;23(4):1213–23.
29. Brembeck P, Lorentzon M, Ohlsson C, Winkvist A, Augustin H. Changes in cortical volumetric bone mineral density and thickness, and trabecular thickness in lactating women postpartum. J Clin Endocrinol Metab. 2015;100(2):535–43.
30. Bjørnerem Å, Ghasem-Zadeh A, Bui M, et al. Remodeling markers are associated with larger intracortical surface area but smaller trabecular surface area: a twin study. Bone. 2011;49(6):1125–30.
31. Zebaze RM, Ghasem-Zadeh A, Bohte A, et al. Intracortical remodelling and porosity in the distal radius and post-mortem femurs of women: a cross-sectional study. Lancet. 2010;375(9727):1729–36.
32. Schaffler MB, Burr DB. Stiffness of compact bone: effects of porosity and density. J Biomech. 1988;21(1):13–6.
33. Laib A, Hauselmann HJ, Ruegsegger P. In vivo high resolution 3D-QCT of the human forearm. Technol Health Care. 1998;6(5–6):329–37.
34. Zebaze R, Ghasem-Zadeh A, Mbala A, Seeman E. A new method of segmentation of compact-appearing, transitional and trabecular compartments and quantification of cortical porosity from high resolution peripheral quantitative computed tomographic images. Bone. 2013;54(1):8–20.
35. Seeman E, Martin TJ. Co-administration of antiresorptive and anabolic agents: a missed opportunity. J Bone Miner Res. 2015;30(5):753–64.
36. Parfitt AM. Morphologic basis of bone mineral measurements. Transient and steady state effects of treatment in osteoporosis. Miner Electrolyte Metab. 1980;4:273–87.
37. Manolagas SC. Birth and death of bone cells: basic regulatory mechanisms and implications for the pathogenesis and treatment of osteoporosis. Endocr Rev. 2000;21(2):115–37.
38. van der Linden JC, Weinans H. Effects of microarchitecture on bone strength. Curr Osteoporos Rep. 2007;5(2):56–61.
39. Bala Y, Seeman E. Bone's material constituents and their contribution to bone strength in health, disease, and treatment. Calcif Tissue Int. 2015;97(3):308–26.
40. Qing H, Ardeshirpour L, Pajevic PD, et al. Demonstration of osteocytic perilacunar/canalicular remodeling in mice during lactation. J Bone Miner Res. 2012;27(5):1018–29.
41. Yun BH, Chon SJ, Choi YS, Cho S, Lee BS, Seo SK. The effect of prolonged breast-feeding on the development of postmenopausal osteoporosis in population with insufficient calcium intake and vitamin D level. Osteoporosis international: a journal established as result of cooperation between the European Foundation for Osteoporosis and the National Osteoporosis Foundation of the USA. Osteoporos Int. 2016;27(9):2745–53.
42. Bjørnerem Å, Ahmed LA, Jørgensen L, Størmer J, Joakimsen RM. Breastfeeding protects against hip fracture in postmenopausal women: the Tromsø Study. J Bone Miner Res. 2011;26(12):2843–50.

15234681, 2017, 4, Downloaded from https://asbmr.onlinelibrary.wiley.com/doi/10.1002/jbmr.3018 by The University Of Melbourne, Wiley Online Library on [17/06/2023]. See the Terms and Conditions (https://onlinelibrary.wiley.com/terms-and-conditions) on Wiley Online Library for rules of use; OA articles are governed by the applicable Creative Commons License

ORIGINAL ARTICLE

JBMR®

Menopause-Related Appendicular Bone Loss is Mainly Cortical and Results in Increased Cortical Porosity

Åshild Bjørnerem,[1,2] Xiaofang Wang,[3] Minh Bui,[4] Ali Ghasem-Zadeh,[3] John L Hopper,[4] Roger Zebaze,[3] and Ego Seeman[3,5]

[1]Department of Clinical Medicine, UiT The Arctic University of Norway, Tromsø, Norway
[2]Department of Obstetrics and Gynaecology, University Hospital of North Norway, Tromsø, Norway
[3]Endocrine Centre, Austin Health, University of Melbourne, Melbourne, Australia
[4]Centre for Epidemiology and Biostatistics, School of Population and Global Health, University of Melbourne, Melbourne, Australia
[5]Institute for Health and Ageing (IHA), Australian Catholic University, Melbourne, Australia

ABSTRACT

After menopause, remodeling becomes unbalanced and rapid. Each of the many remodeling transactions deposits less bone than it resorbed, producing microstructural deterioration. Trabecular bone is said to be lost more rapidly than cortical bone. However, because 80% of the skeleton is cortical, we hypothesized that most menopause-related bone loss and changes in bone microstructure are cortical, not trabecular in origin, and are the result of intracortical remodeling. Distal tibial and distal radial microstructure were quantified during 3.1 years (range, 1.5 to 4.5 years) of follow-up using high-resolution peripheral quantitative computed tomography and StrAx software in 199 monozygotic and 125 dizygotic twin pairs aged 25 to 75 years in Melbourne, Australia. The annual increases in tibial cortical porosity accelerated, being 0.44%, 0.80%, and 1.40% in women remaining premenopausal, transitioning to perimenopause, and from perimenopausal to postmenopause, respectively. Porosity increased in the compact-appearing, outer, and inner transitional zones of the cortex (all $p < 0.001$). The annual decrease in trabecular bone volume/tissue volume (BV/TV) also accelerated, being 0.17%, 0.26%, and 0.31%, respectively. Little bone loss was observed before menopause. The reduction in BV/TV was due to a decrease in trabecular number ($p < 0.001$). The greatest bone loss, 7.7 mg hydroxyapatite (HA) annually, occurred in women transitioning from perimenopausal to postmenopause and of this, 6.1 mg HA (80%) was cortical. Results were similar for the distal radius. Despite microarchitectural changes, no significant bone loss was observed before menopause. Over 90% of appendicular bone loss occurs during and after menopause, over 80% is cortical, and this may explain why 80% of fractures are appendicular. © 2017 American Society for Bone and Mineral Research.

KEY WORDS: BONE MICROARCHITECTURE; CORTICAL POROSITY; MENOPAUSE; PROSPECTIVE STUDY; TRABECULAR BONE

Introduction

The microstructural design and material composition of bone are maintained by bone remodeling.[1,2] This cell-mediated renewal process is initiated at discrete points upon the surfaces of trabeculae, intracortical canals, and the endocortical surface lining the medullary canal.[3] Trabeculae are thin plate-like structures with a large surface area/matrix volume configuration that is an advantage for damage repair. When remodeling is initiated at points upon this surface, bone matrix is readily accessible to osteoclasts that remove it and osteoblasts that replace it with new bone.[1]

Cortical bone is assembled as a thick compact shell traversed by interconnected canals.[4] These canals are contained within a cortical bone volume that is fourfold larger than trabecular bone volume. Consequently, cortical bone has a lower surface area/matrix volume configuration that is less accessible to cells resorbing and replacing damaged bone. Thus, cortical bone is held to be remodeled more slowly than trabecular bone.[1]

During young adulthood remodeling is balanced; the volume of bone resorbed is replaced by an identical volume of new bone so no net structural deterioration occurs.[1,2] Around the time of menopause or shortly before, remodeling becomes unbalanced and rapid.[5] Now the large trabecular surface area becomes a liability.[6,7] Each of the many more remodeling events deposits less bone than was excavated making plate-like trabeculae more rod-like and producing trabecular perforation and complete loss of trabeculae.[8,9] Unbalanced remodeling upon intracortical canals and upon the endocortical surface lining the medullary canal produces cortical porosity and thinning.[4,6,10]

The rapidity of remodeling of trabecular bone, its reported loss prior menopause, and the appearance of cortical bone loss mainly after menopause, led to the view that the bone fragility predisposing to vertebral and distal radial fractures of postmenopausal osteoporosis is largely due to trabecular

Received in original form September 5, 2017; revised form October 25, 2017; accepted October 31, 2017. Accepted manuscript online November 7, 2017.
Address correspondence to: Ego Seeman, MD, Department of Endocrinology, University of Melbourne, Austin Health, Waterdale Rd, West Heidelberg 3081, Melbourne, Australia. E-mail: egos@unimelb.edu.au
Journal of Bone and Mineral Research, Vol. 33, No. 4, April 2018, pp 598–605
DOI: 10.1002/jbmr.3333
© 2017 American Society for Bone and Mineral Research

bone loss.[11–13] However, not all studies report bone loss before menopause, and some studies suggest bone loss is predominantly cortical in origin.[4,6]

Defining the relative contributions of cortical and trabecular bone to total bone loss is important because over 80% of the skeleton is cortical.[4] Cortical bone is a major determinant of the strength of the appendicular skeleton,[14] the location of over 70% of all fractures in the community.[15] Moreover, making a compact structure such as the cortex porous reduces its strength more greatly that worsening the porosity of an already porous sponge-like structure like trabecular bone.[16]

We therefore hypothesized that (i) little bone loss occurs before menopause because remodeling remains balanced, (ii) most bone loss occurs during and after menopause, (iii) although trabecular bone is believed to be lost more rapidly than cortical bone, most bone loss will be cortical in origin because 80% of the skeleton is cortical.

Subjects and Methods

Subjects

We studied 324 healthy female twin pairs, 199 monozygotic (MZ) pairs, and 125 dizygotic (DZ) pairs, aged 27 to 75 years at baseline in Melbourne, Australia, during 2008–2011.[6,17] The twins were followed-up in 2011–2013. We excluded 39 women treated with hormone replacement therapy. After excluding bone scans with movement artifacts, we had valid measurements of the distal tibia and distal radius at both visits in 388 and 314 women, respectively. Of the 388 women, 180 (46.4%) remained premenopausal (a regular cycle in the last 3 months), 56 (14.4%) premenopausal women became perimenopausal (no cycles for 3 to 12 months), 34 (8.8%) perimenopausal women became postmenopausal (amenorrhea for >1 year), and 118 (30.4%) were postmenopausal at baseline. All women gave written informed consent. The Austin Health Human Research Ethics Committee approved the study.

Bone microstructure

High-resolution three-dimensional (3D) peripheral quantitative computed tomography (HR-pQCT) (XtremeCT; Scanco Medical AG, Brüttisellen, Switzerland; isotropic resolution of 82 μm) was used to obtain images at the nondominant distal tibia and distal radius.[18,19] Images were obtained with the X-ray source potential set to 60 kVp and a current of 900 μA. Scanning (integration) time was 2.8 min.

The cortical and trabecular microstructure derived by image acquisition is based on photon attenuation by mineralized bone. The region of interest consisted of 110 CT slices obtained at 22.5 and 9.5 mm from a reference line at the endplate of the distal tibia and distal radius, respectively. Scanning was done at a fixed distance from the endplate to maintain the same region of interest in this longitudinal study. The 49 most proximal slices were chosen because the relatively thicker cortex allows accurate assessment of porosity.

Table 1. Baseline Microarchitecture of the Distal Tibia and Distal Radius by the Menopausal Stage of the Participants

	Premenopausal remaining premenopausal	Premenopausal to perimenopausal	Perimenopausal to postmenopausal	Postmenopausal
Age (years), mean (range)	40.7 (27–50)	47.5 (40–54)	51.8 (46–55)	60.5 (48–75)
Distal tibia, sample size, *n*	180	56	34	118
Total cortical porosity (%)	57.9 ± 4.57	56.7 ± 4.13	58.4 ± 5.54	64.7 ± 6.47
Compact cortical porosity (%)	39.2 ± 4.55	38.0 ± 4.38	40.7 ± 6.62	48.0 ± 7.47
Outer TZ porosity (%)	40.2 ± 3.39	39.5 ± 2.93	41.7 ± 4.76	48.5 ± 7.16
Inner TZ porosity (%)	84.1 ± 2.88	83.6 ± 2.35	83.9 ± 2.70	86.5 ± 3.18
Cortical BMC (mg HA)	571 ± 74.6	563 ± 69.9	559 ± 73.7	495 ± 82.3
Matrix mineralization density (%)	65.7 ± 1.25	66.4 ± 1.09	65.9 ± 1.29	63.8 ± 1.65
Trabecular number (1/mm)	2.81 ± 0.57	2.94 ± 0.52	2.99 ± 0.57	2.41 ± 0.69
Trabecular thickness (mm)	0.19 ± 0.01	0.19 ± 0.01	0.19 ± 0.01	0.19 ± 0.01
Trabecular separation (mm)	1.30 ± 0.25	1.26 ± 0.22	1.25 ± 0.25	1.47 ± 0.36
Trabecular BMC (mg HA)	228 ± 76.1	219 ± 77.6	230 ± 74.3	207 ± 89.9
Total BMC (mg HA)	799 ± 121	781 ± 110	789 ± 114	702 ± 132
Distal radius, sample size, *n*	157	43	24	90
Total cortical porosity (%)	53.2 ± 5.73	50.8 ± 4.17	51.2 ± 5.52	57.8 ± 7.68
Compact cortical porosity (%)	35.3 ± 4.13	33.5 ± 3.37	34.1 ± 4.30	41.4 ± 7.10
Outer TZ porosity (%)	38.6 ± 3.19	37.1 ± 2.41	37.7 ± 2.92	45.0 ± 6.16
Inner TZ porosity (%)	84.7 ± 3.08	83.8 ± 2.67	84.4 ± 2.60	86.1 ± 3.28
Cortical BMC (mg HA)	267 ± 42.7	271 ± 32.6	278 ± 40.0	238 ± 43.5
Matrix mineralization density (%)	66.4 ± 1.53	67.2 ± 1.13	67.3 ± 1.22	65.0 ± 1.77
Trabecular number (1/mm)	2.30 ± 0.55	2.48 ± 0.39	2.44 ± 0.52	2.07 ± 0.58
Trabecular thickness (mm)	0.19 ± 0.01	0.19 ± 0.01	0.19 ± 0.01	0.20 ± 0.01
Trabecular separation (mm)	1.40 ± 0.34	1.30 ± 0.24	1.35 ± 0.25	1.52 ± 0.40
Trabecular BMC (mg HA)	64.8 ± 26.3	61.4 ± 20.7	62.2 ± 24.9	58.8 ± 28.0
Total BMC (mg HA)	332 ± 55.6	332 ± 42.5	341 ± 47.5	296 ± 56.5

Values are mean ± SD, mean (range), or *n*, as indicated.
TZ = transitional zone; BMC = bone mineral content; HA = hydroxyapatite; SD = standard deviation.

15234681, 2018, 4, Downloaded from https://asbmr.onlinelibrary.wiley.com/doi/10.1002/jbmr.3333 by The University Of Melbourne, Wiley Online Library on [18/06/2023]. See the Terms and Conditions (https://onlinelibrary.wiley.com/terms-and-conditions) on Wiley Online Library for rules of use; OA articles are governed by the applicable Creative Commons License

Porosity within the total cortex and its compartments (compact cortex, outer and inner transitional zones), matrix mineralization density, trabecular number, thickness, separation, and bone volume/tissue volume (BV/TV) were quantified using StrAx, a non–threshold-based method that automatically segments bone from background, and then into its compartments in vivo (Straxcorp, Melbourne, Australia). The in vivo precision was 0.5% to 3.0%.[20] Daily quality control was carried out by scanning a phantom containing rods of hydroxyapatite (HA) (QRM Moehrendorf, Germany).

Porosity is the proportion of voxels within the cortical compartment that contain void. Once deposited, osteoid is mineralized reaching ≥80% of full mineralization (1200 mg HA/cm^3) within days. Matrix mineralization is quantified using StrAx by determining the mean density of voxels with attenuation between 80% and 100% of fully mineralized bone. These voxels are unlikely to contain a pore because a pore results in voxel attenuation <80% of the maximum. So, variation attenuation within 80% to 100% of full mineralization reflects heterogeneity in mineralization. Voxels attenuating photons <80% are used to calculate porosity.

Statistical analysis

Results are presented as means ± standard deviations (SDs) or standard error of the mean (SE). Absolute rates of change were calculated as the difference between the baseline and follow-up divided by years of follow-up. The percentage change was the absolute change divided by the baseline value. We tested whether the trait change differed from zero in women remaining premenopausal or transitioning from premenopausal to perimenopausal, perimenopausal to postmenopause, or moving further into the postmenopausal years. To account for the correlation within pairs we used the generalized estimating equation (GEE) method in regression analysis. All analyses were carried out using STATA software, version 13 (Stata Corporation, Inc., College Station, TX, USA; http://www.stata.com). Values of p were two-sided and significant if <0.05.

Results

Baseline and annual changes during 3.1 years (range, 1.5 to 4.5 years) in microstructure are shown in twins aged 25 to 75 years (Tables 1 and 2; Figs. 1–3). Details below refer to the distal tibia.

Table 2. Annual Absolute Change in Microarchitecture of the Distal Tibia and Distal Radius by the Menopausal Stage of the Participants

	Premenopausal remaining premenopausal	Premenopausal to perimenopausal	Perimenopausal to postmenopausal	Postmenopausal
Distal tibia				
Total cortical porosity (%)	0.44 ± 0.03 (<0.001)	0.80 ± 0.06 (<0.001)[a]	1.40 ± 0.08 (<0.001)[b,c]	0.83 ± 0.06 (<0.001)[d,f]
Compact cortical porosity (%)	0.32 ± 0.03 (<0.001)	0.67 ± 0.07 (<0.001)[a]	1.41 ± 0.12 (<0.001)[b,c]	0.90 ± 0.07 (<0.001)[d,e,f]
Outer TZ porosity (%)	0.33 ± 0.03 (<0.001)	0.61 ± 0.06 (<0.001)[a]	1.33 ± 0.12 (<0.001)[b,c]	0.90 ± 0.07 (<0.001)[d,e,f]
Inner TZ porosity (%)	0.23 ± 0.02 (<0.001)	0.37 ± 0.02 (<0.001)[a]	0.53 ± 0.04 (<0.001)[b,c]	0.31 ± 0.03 (<0.001)[d,f]
Cortical BMC (mg HA)	0.45 ± 0.35 (0.242)	−0.91 ± 0.59 (0.256)	−6.12 ± 0.98 (<0.001)[b,c]	−6.00 ± 0.57 (<0.001)[d,e]
Matrix mineralization density (%)	−0.25 ± 0.02 (<0.001)	−0.41 ± 0.03 (<0.001)[a]	−0.60 ± 0.04 (<0.001)[b,c]	−0.31 ± 0.03 (<0.001)[e,f]
Trabecular number (1/mm)	−0.12 ± 0.01 (<0.001)	−0.15 ± 0.01 (<0.001)[a]	−0.19 ± 0.02 (<0.001)[b]	−0.10 ± 0.01 (<0.001)[e,f]
Trabecular thickness (mm)	0.30 ± 0.02 (<0.001)	0.42 ± 0.03 (<0.001)[a]	0.49 ± 0.03 (<0.001)[b]	0.26 ± 0.03 (<0.001)[e,f]
Trabecular separation (mm)	3.79 ± 0.28 (<0.001)	4.95 ± 0.43 (<0.001)	6.29 ± 0.72 (<0.001)[b]	3.28 ± 0.37 (<0.001)[e,f]
Trabecular BMC (mg HA)	−0.71 ± 0.29 (0.015)	−0.51 ± 0.37 (0.200)	−1.55 ± 0.54 (0.005)	−0.97 ± 0.39 (0.040)
Total BMC (mg HA)	−0.26 ± 0.51 (0.586)	−1.42 ± 0.72 (0.117)	−7.67 ± 1.06 (<0.001)[b,c]	−6.96 ± 0.74 (<0.001)[d,e]
Distal radius				
Total cortical porosity (%)	0.29 ± 0.04 (<0.001)	0.61 ± 0.08 (<0.001)[a]	1.17 ± 0.11 (<0.001)[b,c]	0.85 ± 0.07 (<0.001)[d,e,f]
Compact cortical porosity (%)	0.23 ± 0.04 (<0.001)	0.61 ± 0.09 (<0.001)[a]	1.26 ± 0.14 (<0.001)[b,c]	0.85 ± 0.06 (<0.001)[d,e,f]
Outer TZ porosity (%)	0.19 ± 0.04 (<0.001)	0.54 ± 0.07 (<0.001)[a]	1.19 ± 0.14 (<0.001)[b,c]	0.85 ± 0.07 (<0.001)[d,e,f]
Inner TZ porosity (%)	0.06 ± 0.02 (<0.001)	0.18 ± 0.03 (<0.001)[a]	0.34 ± 0.05 (<0.001)[b,c]	0.22 ± 0.02 (<0.001)[d]
Cortical BMC (mg HA)	0.11 ± 0.23 (0.467)	−0.76 ± 0.37 (0.047)[a]	−3.19 ± 0.70 (<0.001)[b,c]	−3.89 ± 0.35 (<0.001)[d,e]
Matrix mineralization density (%)	−0.18 ± 0.02 (<0.001)	−0.33 ± 0.04 (<0.001)[a]	−0.57 ± 0.05 (<0.001)[b,c]	−0.32 ± 0.03 (<0.001)[d,f]
Trabecular number (1/mm)	−0.08 ± 0.01 (<0.001)	−0.10 ± 0.01 (<0.001)	−0.14 ± 0.01 (<0.001)[b,c]	−0.08 ± 0.01 (<0.001)[f]
Trabecular thickness (mm)	0.31 ± 0.02 (<0.001)	0.44 ± 0.03 (<0.001)[a]	0.45 ± 0.05 (<0.001)[b]	0.27 ± 0.04 (<0.001)[e,f]
Trabecular separation (mm)	2.63 ± 0.28 (<0.001)	3.88 ± 0.35 (<0.001)[a]	4.73 ± 0.50 (<0.001)[b]	3.82 ± 0.55 (<0.001)
Trabecular BMC (mg HA)	0.24 ± 0.11 (0.085)	0.44 ± 0.15 (0.003)	−0.47 ± 0.32 (<0.001)[c]	−0.21 ± 0.18 (0.280)[e]
Total BMC (mg HA)	0.35 ± 0.23 (0.145)	−0.32 ± 0.37 (0.408)	−3.67 ± 0.77 (<0.001)[b,c]	−4.10 ± 0.39 (<0.001)[d,e]

Values are mean ± SE (p value). Values of p represent whether changes differed from 0 within groups.
TZ = transitional zone; BMC = bone mineral content; HA = hydroxyapatite; SE = standard error of the mean; GEE = General Estimating Equation.
[a] $p < 0.05$ for differences in changes between premenopausal to perimenopausal versus premenopausal remaining premenopausal using GEE.
[b] $p < 0.05$ for differences in changes between perimenopausal to postmenopausal versus premenopausal remaining premenopausal using GEE.
[c] $p < 0.05$ for differences in changes between perimenopausal to postmenopausal versus premenopausal to perimenopausal using GEE.
[d] $p < 0.05$ for differences in changes between postmenopausal versus premenopausal remaining premenopausal using GEE.
[e] $p < 0.05$ for differences in changes between postmenopausal versus premenopausal to perimenopausal using GEE.
[f] $p < 0.05$ for differences in changes between postmenopausal versus perimenopausal to postmenopausal using GEE.

15234681, 2018, 4, Downloaded from https://asbmr.onlinelibrary.wiley.com/doi/10.1002/jbmr.3333 by The University Of Melbourne, Wiley Online Library on [18/06/2023]. See the Terms and Conditions (https://onlinelibrary.wiley.com/terms-and-conditions) on Wiley Online Library for rules of use; OA articles are governed by the applicable Creative Commons License

Results for the distal radius were similar and are confined to the tables.

Changes in morphology prior, during, and after menopause

The annual increase in cortical porosity accelerated during menopause, being 0.44% in women remaining premenopausal, doubling to 0.80% in women transitioning from premenopause to perimenopause, and tripling to 1.40% in women transitioning from perimenopause to postmenopause (all $p < 0.001$, Table 2, Fig. 1). In postmenopausal women remaining so, porosity increased by 0.83% annually (all $p < 0.001$). This pattern of increase in porosity was similar in the compact-appearing, outer and inner transitional zones of the cortex (all $p < 0.001$). The increase in porosity was associated with a decrease in matrix mineralization density ($p < 0.001$, Fig. 3).

Trabecular BV/TV decreased in premenopausal women remaining so, in women transitioning from premenopause to perimenopause, perimenopause to postmenopause, and in women remaining postmenopausal (Fig. 2). The reduction in trabecular BV/TV was associated with a decrease in trabecular number, an increase in residual trabecular thickness and separation (all $p < 0.001$, Table 2, Fig. 2).

Absolute amounts of cortical and trabecular bone lost

No significant annual bone loss was observed before menopause (Table 2, Fig. 4). The annual absolute amount of bone lost was 0.3 mg HA in women remaining premenopausal ($p = 0.586$) and 1.4 mg HA in women transitioning from premenopause to perimenopause ($p = 0.117$).

The greatest amount of bone lost annually, 7.7 mg HA, occurred in women transitioning from perimenopause to postmenopause, and of this, 6.1 mg HA (80%) was cortical ($p < 0.001$, Table 2, Fig. 4). Of the 7.0 mg HA lost annually in postmenopausal women remaining so, 6.0 mg HA (86%) was cortical ($p < 0.001$). The annual percentage amount of bone loss and change in bone microstructure are shown in Table 3.

Discussion

We report that cortical and trabecular microarchitecture deteriorate modestly with evidence of trabecular, but no net cortical, bone loss before menopause. Over 90% of bone loss occurs during and after menopause and over 80% of this bone loss is cortical in origin. Cortical bone is lost as a result of unbalanced intracortical remodeling, which increases cortical porosity. Trabecular bone is lost by perforation with complete loss of trabeculae leading to increased trabecular spacing.

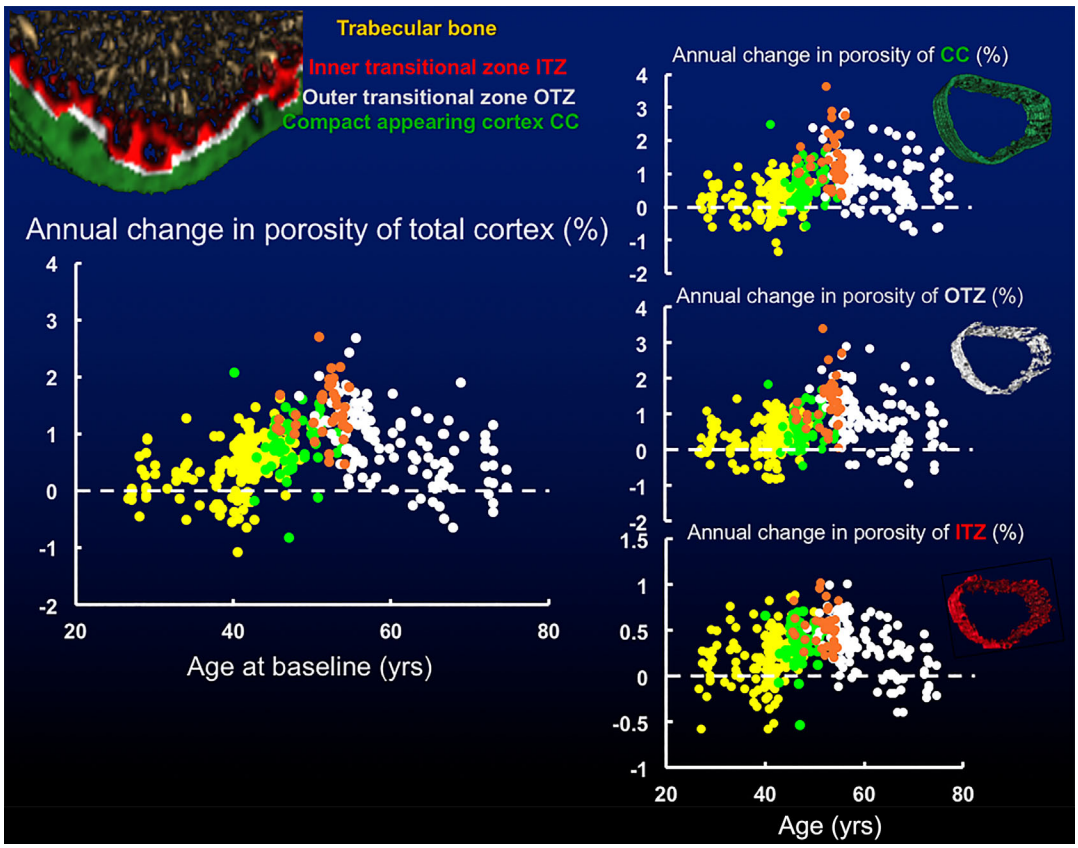

Fig. 1. Annual changes of the distal tibia porosity of the total cortex, CC, OTZ, and ITZ, by baseline age in women remaining premenopausal (yellow dots), becoming perimenopausal (green dots), becoming postmenopausal (orange dots), and remaining postmenopausal (white dots). CC = compact-appearing cortex; OTZ = outer transitional zone; ITZ = inner transitional zone.

15234681, 2018, 4, Downloaded from https://asbmr.onlinelibrary.wiley.com/doi/10.1002/jbmr.3333 by The University Of Melbourne, Wiley Online Library on [18/06/2023]. See the Terms and Conditions (https://onlinelibrary.wiley.com/terms-and-conditions) on Wiley Online Library for rules of use; OA articles are governed by the applicable Creative Commons License

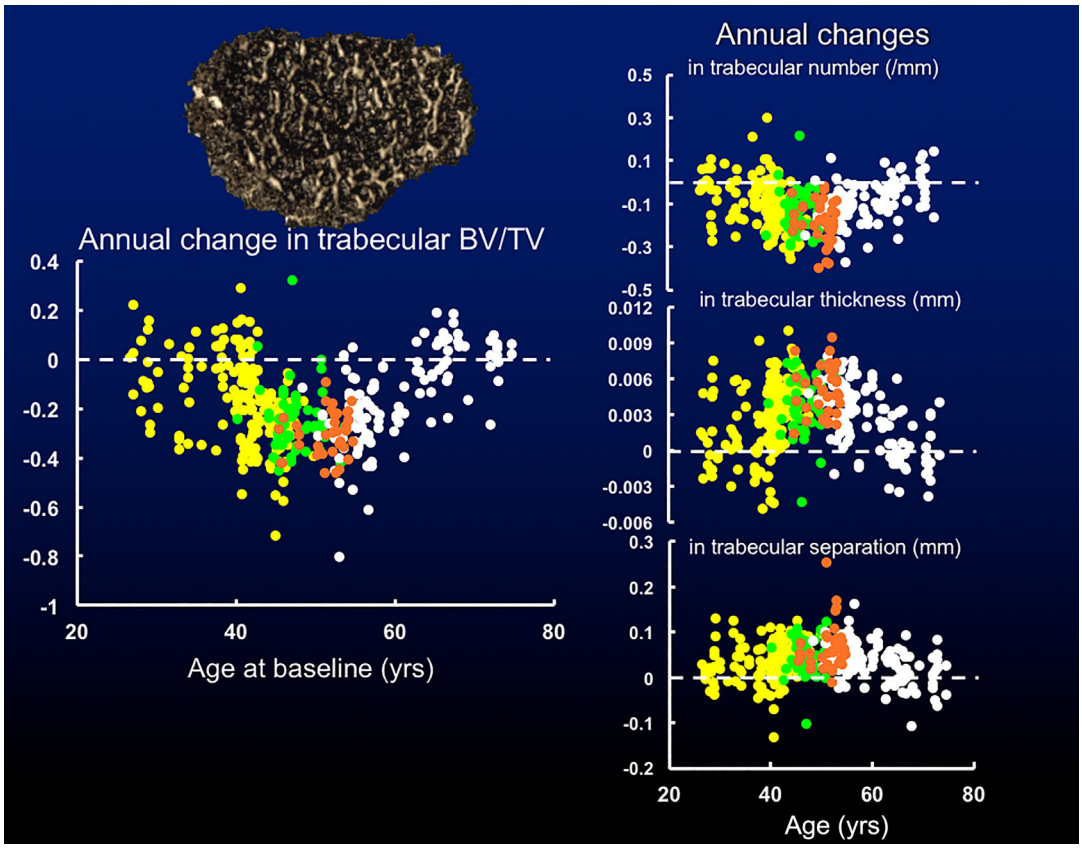

Fig. 2. Annual changes of the distal tibia trabecular BV/TV, trabecular number, trabecular thickness, and trabecular separation by baseline age in women remaining premenopausal (yellow dots), becoming perimenopausal (green dots), becoming postmenopausal (orange dots), and remaining postmenopausal (white dots). BV/TV = bone volume/tissue volume.

The most rapid bone loss occurred in women transitioning from perimenopausal to postmenopause. The inverse association between porosity and matrix mineral density is likely to reflect rapid remodeling, which deteriorates microstructure but also reduces matrix mineral density as younger less mineralized bone replaces older more fully mineralized bone during each remodeling transaction.

Bone loss before menopause is modest

The necessary and sufficient morphological basis of bone loss and microstructural deterioration is remodeling imbalance; the deposition of a smaller volume of bone than was resorbed during a remodeling transaction.[1–3] The appearance of this negative bone balance is reported to occur around 40 to 45 years of age and worsens after menopause.[13] Sex hormone deficiency is accompanied by increases in the lifespan of osteoclasts, which excavate and perforate trabeculae rather than thinning them.[6,8,9] A reduction in the lifespan of osteoblasts also occurs worsening the remodeling imbalance.[7]

We observed both trabecular bone loss with a decrease in trabecular numbers and cortical bone loss with increased cortical porosity before menopause, but the amount of bone lost was modest and much less than observed in women transitioning into the perimenopause and postmenopause.

Bone loss accelerates during menopause and is mainly cortical, not trabecular

Trabecular bone is only 20% of the total bone matrix volume and so accounted for only ~20% of all the bone lost annually during and after menopause. The complete loss of trabeculae resulted in lessening of trabecular bone loss because these structures are completely and irreversibly resorbed leaving disconnected widely spaced trabeculae. Mean trabecular thickness increased because of preferential loss of thinner trabeculae.[6]

Cortical bone constitutes 80% of skeletal mineralized bone volume.[4] This fourfold larger volume is held to be enveloped by *relatively* smaller bone surface area comprising the intracortical surface formed by the canals traversing the cortex and the endocortical surface lining the medullary canal. Consequently, the larger cortical bone volume is believed to be remodeled and lost more slowly than the trabecular bone volume, which is held to have a larger trabecular bone surface area per unit bone volume. We confirm that cortical bone accounted over 80% of all the bone lost during and after menopause but we did not detect more rapid loss of trabecular than cortical bone in this prospective study.[4,6]

Unlike the self-limiting nature of trabecular bone loss, cortical bone loss was self-perpetuating.[6] Intracortical remodeling initiated upon canal surfaces enlarge them focally, they coalesce and so the internal surface area formed by the enlarged canals facilitates more remodeling of an ever-decreasing cortical matrix

15234681, 2018, 4, Downloaded from https://asbmr.onlinelibrary.wiley.com/doi/10.1002/jbmr.3333 by The University Of Melbourne, Wiley Online Library on [18/06/2023]. See the Terms and Conditions (https://onlinelibrary.wiley.com/terms-and-conditions) on Wiley Online Library for rules of use; OA articles are governed by the applicable Creative Commons License

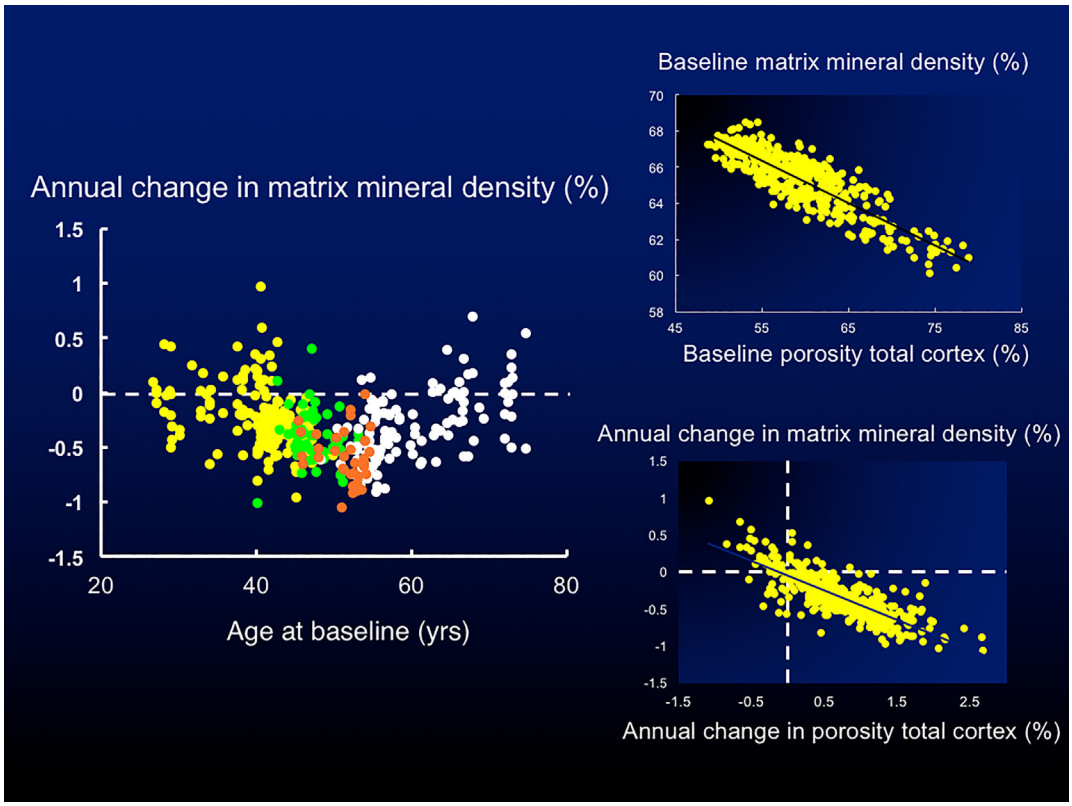

Fig. 3. Annual changes of the distal tibia matrix mineralization density by baseline age in in women remaining premenopausal (yellow dots), becoming perimenopausal (green dots), becoming postmenopausal (orange dots) and remaining postmenopausal (white dots). The inverse association between baseline porosity of the total cortex and matrix mineral density, and the inverse association between annual change in porosity and matrix mineralization density (both $p < 0.001$).

volume. Trabecular surfaces decrease as trabeculae are lost but intra cortical surfaces increase as intracortical porosity increases. The latter provides a greater surface area for remodeling to be initiated upon and so cortical bone loss continues. Indeed, Han and colleagues[21,22] report that remodeling upon intracortical and endocortical envelopes contributes about 50% of the total surface participating in remodeling while the remaining 50% proceeds upon the trabecular envelope. Hence the notion of the greater surface area to bone matrix volume ratio of trabecular than cortical bone may need reassessment.

The inability to detect the rise in cortical porosity before menopause is likely to be the result of errors in image analysis.[20] At a voxel size of 82 μm and spatial resolution of 100 to 120 μm, voxels containing a pore also contain matrix, which excludes that voxel and its porosity from analysis, underestimating the rise in cortical porosity before and during menopause.

The most rapid bone loss occurred in women transitioning from perimenopause to postmenopause. As women become postmenopausal, the number of remodeling sites upon the trabecular, intracortical, and endocortical surfaces increases the surface extent of resorption, which exceeds the surface extent of formation because fewer remodeling sites initiated in early menopause are only now entering their refilling phase.[7] (Refilling is not instantaneous, there is a delay and then refilling occurs over several months, so refilling of cavities dug in early menopause occurs some months later.)

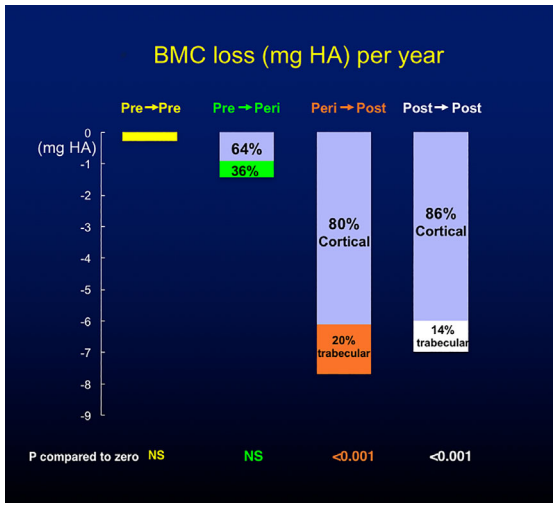

Fig. 4. Amount of tibial cortical and trabecular bone loss as a percentage of annual loss of total (BMC) (mg HA) in women Pre to Pre, Pre to Peri, and Post to Post. Values of *p* within each group tested whether the total annual losses were different from zero. BMC = bone mineral content; HA = hydroxyapatite; Pre to Pre = premenopausal remaining premenopausal; Pre to Peri = premenopausal becoming perimenopausal; Post to Post = postmenopausal remaining postmenopausal.

15234681, 2018, 4, Downloaded from https://asbmr.onlinelibrary.wiley.com/doi/10.1002/jbmr.3333 by The University Of Melbourne, Wiley Online Library on [18/06/2023]. See the Terms and Conditions (https://onlinelibrary.wiley.com/terms-and-conditions) on Wiley Online Library for rules of use; OA articles are governed by the applicable Creative Commons License

Table 3. Annual Percentage Change in Microarchitecture of Distal Tibia and Distal Radius by Menopausal Stage

	Premenopausal remaining premenopausal	Premenopausal to perimenopausal	Perimenopausal to postmenopausal	Postmenopausal
Distal tibia				
Total cortical porosity (%)	0.79 ± 0.06 (<0.001)	1.43 ± 0.11 (<0.001)[a]	2.43 ± 0.15 (<0.001)[b,c]	1.35 ± 0.10 (<0.001)[d,f]
Compact cortical porosity (%)	0.84 ± 0.09 (<0.001)	1.81 ± 0.19 (<0.001)[a]	3.64 ± 0.34 (<0.001)[b,c]	2.00 ± 0.15 (<0.001)[d,f]
Outer TZ porosity (%)	0.86 ± 0.08 (<0.001)	1.56 ± 0.16 (<0.001)[a]	3.19 ± 0.27 (<0.001)[b,c]	1.98 ± 0.15(<0.001)[d,e,f]
Inner TZ porosity (%)	0.27 ± 0.02 (<0.001)	0.44 ± 0.03 (<0.001)[a]	0.63 ± 0.04 (<0.001)[b,c]	0.36 ± 0.03 (<0.001)[d,f]
Cortical BMC (mg HA)	0.09 ± 0.06 (0.184)	−0.14 ± 0.10 (0.305)	−1.08 ± 0.17 (<0.001)[b,c]	−1.23 ± 0.12 (<0.001)[d,e]
Matrix mineralization density (%)	−0.39 ± 0.03 (<0.001)	−0.62 ± 0.04 (<0.001)[a]	−0.91 ± 0.06 (<0.001)[b,c]	−0.48 ± 0.04 (<0.001)[e,f]
Trabecular number (1/mm)	−4.04 ± 0.27 (<0.001)	−5.02 ± 0.36 (<0.001)	−6.41 ± 0.53 (<0.001)[b,c]	−3.86 ± 0.33 (<0.001)[e,f]
Trabecular thickness (mm)	1.60 ± 0.11 (<0.001)	2.26 ± 0.16 (<0.001)[a]	2.66 ± 0.20 (<0.001)[b]	1.38 ± 0.13 (<0.001)[e,f]
Trabecular separation (mm)	3.11 ± 0.22 (<0.001)	3.99 ± 0.34 (<0.001)	4.87 ± 0.48 (<0.001)[b]	2.44 ± 0.26 (<0.001)$_{e,f}$
Trabecular BMC (mg HA)	−0.25 ± 0.14 (0.069)	−0.13 ± 0.18 (0.521)	−0.64 ± 0.20 (0.002)[c]	−0.63 ± 0.23 (0.012)
Total BMC (mg HA)	−0.16 ± 0.17 (0.345)	−0.28 ± 0.22 (0.320)	−1.73 ± 0.26 (<0.001)[b,c]	−1.86 ± 0.28 (<0.001)[d,f]
Distal radius				
Total cortical porosity (%)	0.54 ± 0.09 (<0.001)	1.22 ± 0.16 (<0.001)[a]	2.31 ± 0.22 (<0.001)[b,c]	1.53 ± 0.13 (<0.001)[d,f]
Compact cortical porosity (%)	0.69 ± 0.13 (<0.001)	1.84 ± 0.25 (<0.001)[a]	3.78 ± 0.45 (<0.001)[b,c]	2.18 ± 0.18 (<0.001)[d,f]
Outer TZ porosity (%)	0.53 ± 0.10 (<0.001)	1.45 ± 0.19 (<0.001)[a]	3.23 ± 0.40 (<0.001)[b,c]	1.95 ± 0.16 (<0.001)[d,e,f]
Inner TZ porosity (%)	0.08 ± 0.02 (<0.001)	0.221 ± 0.03 (<0.001)[a]	0.40 ± 0.06 (<0.001)[b,c]	0.26 ± 0.03 (<0.001)[d,f]
Cortical BMC (mg HA)	0.04 ± 0.08 (0.479)	−0.27 ± 0.14 (0.055)[a]	−1.12 ± 0.25 (<0.001)[b,c]	−1.68 ± 0.16 (<0.001)[d,e]
Matrix mineralization density (%)	−0.26 ± 0.04 (<0.001)	−0.49 ± 0.06 (<0.001)[a]	−0.85 ± 0.07 (<0.001)[b,c]	−0.50 ± 0.05 (<0.001)[d,f]
Trabecular number (/mm)	−3.00 ± 0.31 (<0.001)	−4.30 ± 0.41 (<0.001)[a]	−5.87 ± 0.43 (<0.001)[b,c]	−3.69 ± 0.44 (<0.001)[f]
Trabecular thickness (mm)	1.64 ± 0.13 (<0.001)	2.36 ± 0.18 (<0.001)[a]	2.43 ± 0.27 (<0.001)[b]	1.41 ± 0.18 (<0.001)[e,f]
Trabecular separation (mm)	2.00 ± 0.20 (<0.001)	3.02 ± 0.27 (<0.001)[a]	3.61 ± 0.41 (<0.001)[b]	2.66 ± 0.34 (<0.001)[f]
Trabecular BMC (mg HA)	0.44 ± 0.22 (0.079)	0.70 ± 0.24 (0.003)	−0.59 ± 0.49 (0.272)[c]	−0.66 ± 0.35 (0.100)[d,e]
Total BMC (mg HA)	0.48 ± 0.22 (0.048)	0.43 ± 0.25 (0.072)	−1.71 ± 0.53 (0.002)[b,c]	−2.34 ± 0.38 (<0.001)[d,e]

Values are mean ± SE (p value). Values of p represent whether changes differed from 0 within groups.

TZ = transitional zone; BMC = bone mineral content; HA = hydroxyapatite; SE = standard error of the mean.

[a] $p < 0.05$ for differences in changes between premenopausal to perimenopausal versus premenopausal remaining premenopausal using generalized estimating equation (GEE).

[b] $p < 0.05$ for differences in changes between perimenopausal to postmenopausal versus premenopausal remaining premenopausal using GEE.

[c] $p < 0.05$ for differences in changes between perimenopausal to postmenopausal versus premenopausal to perimenopausal using GEE.

[d] $p < 0.05$ for differences in changes between postmenopausal versus premenopausal remaining premenopausal using GEE.

[e] $p < 0.05$ for differences in changes between postmenopausal versus premenopausal to perimenopausal using GEE.

[f] $p < 0.05$ for differences in changes between postmenopausal versus perimenopausal to postmenopausal using GEE.

This perturbation of the surface extent of resorption and formation is responsible for the accelerated net loss of trabeculae and accelerated rise in cortical porosity. Slowing of loss occurs later, not because remodeling slows, but rather because the surface extents of resorption and formation increase, but again resemble each other and proceed as the high rate of remodeling continues in the postmenopause. The many cavities being excavated are now matched by incomplete refilling of the similarly high numbers of resorption sites initiated in perimenopause.[23] Bone loss and structural deterioration continue, but more slowly than during the accelerated phase of bone loss.[24]

Cortical and trabecular bone loss and bone fragility

The notion that rapid trabecular bone loss, vertebral fractures, and forearm fractures are hallmarks of postmenopausal osteoporosis needs reappraisal.[4,25–27] About 80% of all fractures in the community are nonvertebral and occur at locations composed primarily of cortical bone. Cortical bone loss accounts for ~70% of all appendicular bone loss; only ~30% is trabecular.[4] Of the cortical bone lost, most is lost by intracortical remodeling producing intracortical porosity. An increase in porosity in "compact" cortical bone reduces its resistance to bending out of proportion to the amount of bone lost.[16]

This study has several limitations. The sample size and number of twin pairs are modest and follow-up is relatively short. Measurements of microarchitecture are vulnerable to movement artifact, particular at the distal radius. Only microstructure of peripheral sites can be quantified using HR imaging technology, so menopausal changes in microstructure at the spine and proximal femur could not be assessed. Changes at these latter sites during menopause may differ from the observations made at these peripheral sites. We could not determine whether the increase in porosity was due to an increase in the size of existing canal cross-sections, creation of new canals, or both. In the derivation of matrix mineral density, a contribution of pores under 25 μm in diameter cannot be excluded.

In summary, little bone is lost before menopause. Bone loss becomes detectable when remodeling imbalance appears and remodeling rate accelerates at the time of menopause. Trabecular bone loss is self-limiting because perforation removes them. Cortical bone loss is self-perpetuating because

15234681, 2018, 4, Downloaded from https://asbmr.onlinelibrary.wiley.com/doi/10.1002/jbmr.3333 by The University Of Melbourne, Wiley Online Library on [18/06/2023]. See the Terms and Conditions (https://onlinelibrary.wiley.com/terms-and-conditions) on Wiley Online Library for rules of use; OA articles are governed by the applicable Creative Commons License

intracortical remodeling increases the surface available for initiation of remodeling so that more of the larger cortical bone matrix volume is remodeled and lost accounting for most bone loss. Cortical bone loss has a more deleterious effect on cortical strength than does trabecular bone loss on trabecular strength and is likely to contribute to the occurrence of nonvertebral fractures, which constitute 80% of all fractures.

Disclosures

AGZ is remunerated by StraxCorp as senior image analyst. RZ has received grant and/or research support from Amgen, Merck Sharp & Dohme, Servier, Warner-Chilcott, AKP, Genzyme, Sanofi, GSK, and Pfizer; he is a shareholder and a director of the board of StraxCorp. ES has received research support and lecture fees from Amgen, Allergan, Asahi, Genzyme, and Merck Sharp & Dohme; he is a director of the board and shareholder in StraxCorp. The remaining authors state that they have no conflicts of interest.

Acknowledgments

This research was facilitated through access to the Twin Research Australia, a national resource supported by an Enabling Grant (ID 628911) from the National Health & Medical Research Council (NHMRC) of Australia.

Authors' roles: Study design and conduct: ÅB, XW, MB, AGZ, RZ, JLH, and ES. Data collection: ÅB, AGZ, and XW. Responsibility for StrAx analysis: RZ. Statistical analyses: MB. Drafting manuscript: ÅB, XW, MB, AGZ, RZ, JLH, and ES. Data interpretation and approving final version of manuscript: ÅB, XW, MB, AGZ, RZ, JLH, and ES.

References

1. Parfitt AM. Skeletal heterogeneity and the purposes of bone remodelling: implications for the understanding of osteoporosis. In: Marcus R, Feldman D, Nelson DA, Rosen CJ, editors. Osteoporosis. San Diego, CA: Academic Press; 2008. p. 71–89.
2. Parfitt AM. Targeted and non-targeted bone remodeling: relationship to basic multicellular unit origination and progression. Bone. 2002;30(1):5–7.
3. Parfitt AM, Mathews CH, Villanueva AR, Kleerekoper M, Frame B, Rao DS. Relationships between surface, volume, and thickness of iliac trabecular bone in aging and in osteoporosis. Implications for the microanatomic and cellular mechanisms of bone loss. J Clin Invest. 1983;72(4):1396–409.
4. Zebaze RM, Ghasem-Zadeh A, Bohte A, et al. Intracortical remodelling and porosity in the distal radius and post-mortem femurs of women: a cross-sectional study. Lancet. 2010;375(9727):1729–36.
5. Seeman E, Delmas PD. Bone quality—the material and structural basis of bone strength and fragility. N Engl J Med. 2006;354(21):2250–61.
6. Bjørnerem Å, Ghasem-Zadeh A, Bui M, et al. Remodeling markers are associated with larger intracortical surface area but smaller trabecular surface area: a twin study. Bone. 2011;49(6):1125–30.
7. Seeman E. Age- and menopause-related bone loss compromise cortical and trabecular microstructure. J Gerontol A Biol Sci Med Sci. 2013;68(10):1218–25.
8. Eriksen EF, Langdahl B, Vesterby A, Rungby J, Kassem M. Hormone replacement therapy prevents osteoclastic hyperactivity: a histomorphometric study in early postmenopausal women. J Bone Miner Res. 1999;14(7):1217–21.
9. Manolagas SC. Choreography from the tomb: an emerging role of dying osteocytes in the purposeful, and perhaps not so purposeful, targeting of bone remodeling. Bonekey Osteovision. 2006;3:5–14.
10. Shigdel R, Osima M, Ahmed LA, et al. Bone turnover markers are associated with higher cortical porosity, thinner cortices, and larger size of the proximal femur and non-vertebral fractures. Bone. 2015;81:1–6.
11. Riggs BL, Wahner HW, Melton LJ III, Richelson LS, Judd HL, Offord KP. Rates of bone loss in the appendicular and axial skeletons of women. Evidence of substantial vertebral bone loss before menopause. J Clin Invest. 1986;77(5):1487–91.
12. Riggs BL, Melton IL III, Robb RA, et al. Population-based study of age and sex differences in bone volumetric density, size, geometry, and structure at different skeletal sites. J Bone Miner Res. 2004;19(12):1945–54.
13. Riggs BL, Melton LJ, Robb RA, et al. A population-based assessment of rates of bone loss at multiple skeletal sites: evidence for substantial trabecular bone loss in young adult women and men. J Bone Miner Res. 2008;23(2):205–14.
14. Holzer G, von Skrbensky G, Holzer LA, Pichl W. Hip fractures and the contribution of cortical versus trabecular bone to femoral neck strength. J Bone Miner Res. 2009;24(3):468–74.
15. Kanis JA, Oden A, Johnell O, Jonsson B, de Laet C, Dawson A. The burden of osteoporotic fractures: a method for setting intervention thresholds. Osteoporos Int. 2001;12(5):417–27.
16. Schaffler MB, Burr DB. Stiffness of compact bone: effects of porosity and density. J Biomech. 1988;21(1):13–6.
17. Bjørnerem Å, Bui QM, Ghasem-Zadeh A, Hopper JL, Zebaze R, Seeman E. Fracture risk and height: an association partly accounted for by cortical porosity of relatively thinner cortices. J Bone Miner Res. 2013;28(9):2017–26.
18. Laib A, Hauselmann HJ, Ruegsegger P. In vivo high resolution 3D-QCT of the human forearm. Technol Health Care 1998;6(5–6):329–37.
19. Boutroy S, Bouxsein ML, Munoz F, Delmas PD. In vivo assessment of trabecular bone microarchitecture by high-resolution peripheral quantitative computed tomography. J Clin Endocrinol Metab. 2005;90(12):6508–15.
20. Zebaze R, Ghasem-Zadeh A, Mbala A, Seeman E. A new method of segmentation of compact-appearing, transitional and trabecular compartments and quantification of cortical porosity from high resolution peripheral quantitative computed tomographic images. Bone. 2013;54(1):8–20.
21. Han ZH, Palnitkar S, Rao DS, Nelson D, Parfitt AM. Effect of ethnicity and age or menopause on the structure and geometry of iliac bone. J Bone Miner Res. 1996;11(12):1967–75.
22. Han ZH, Palnitkar S, Rao DS, Nelson D, Parfitt AM. Effects of ethnicity and age or menopause on the remodeling and turnover of iliac bone: implications for mechanisms of bone loss. J Bone Miner Res. 1997;12(4):498–508.
23. Seeman E. Pathogenesis of bone fragility in women and men. Lancet. 2002;359(9320):1841–50.
24. Burt LA, Bhatla JL, Hanley DA, Boyd SK. Cortical porosity exhibits accelerated rate of change in peri- compared with post-menopausal women. Osteoporos Int. 2017;28(4):1423–31.
25. Zebaze R, Seeman E. Cortical bone: a challenging geography. J Bone Miner Res. 2015;30(1):24–9.
26. Bala Y, Zebaze R, Ghasem-Zadeh A, et al. Cortical porosity identifies women with osteopenia at increased risk for forearm fractures. J Bone Miner Res. 2014;29(6):1356–62.
27. Ahmed LA, Shigdel R, Joakimsen RM, et al. Measurement of cortical porosity of the proximal femur improves identification of women with nonvertebral fragility fractures. Osteoporos Int. 2015;26(8):2137–46.

15234681, 2018, 4, Downloaded from https://asbmr.onlinelibrary.wiley.com/doi/10.1002/jbmr.3333 by The University Of Melbourne, Wiley Online Library on [18/06/2023]. See the Terms and Conditions (https://onlinelibrary.wiley.com/terms-and-conditions) on Wiley Online Library for rules of use; OA articles are governed by the applicable Creative Commons License

Check for updates

ORIGINAL ARTICLE

JBMR®

Cortical Matrix Mineral Density Measured Noninvasively in Pre- and Postmenopausal Women and a Woman With Vitamin D–Dependent Rickets

Cherie Y Chiang,[1,2] Roger Zebaze,[1,2] Xiao-Fang Wang,[1,2] Ali Ghasem-Zadeh,[1,2] Jeffrey D Zajac,[1,2] and Ego Seeman[1,2,3]

[1]Department of Endocrinology, Austin Health, Heidelberg, Australia
[2]Department of Medicine, University of Melbourne, Parkville, Australia
[3]Institute of Health and Ageing, Australian Catholic University, Melbourne, Australia

ABSTRACT

Reduced bone mineral density (BMD) may be due to reduced mineralized bone matrix volume, incomplete secondary mineralization, or reduced primary mineralization. Because bone biopsy is invasive, we hypothesized that noninvasive image acquisition at high resolution can accurately quantify matrix mineral density (MMD). Quantification of MMD was confined to voxels attenuation photons above 80% of that produced by fully mineralized bone matrix because attenuation at this level is due to variation in mineralization, not porosity. To assess accuracy, 9 cadaveric distal radii were imaged at a voxel size of 82 microns using high-resolution peripheral quantitative computed tomography (HR-pQCT; XtremeCT, Scanco Medical AG, Bruttisellen, Switzerland) and compared with VivaCT 40 (μCT) at 19-micron voxel size. Associations between MMD and porosity were studied in 94 healthy vitamin D–replete premenopausal women, 77 postmenopausal women, and in a 27-year-old woman with vitamin D–dependent rickets (VDDR). Microstructure and MMD were quantified using StrAx (StraxCorp, Melbourne, Australia). MMD measured by HR-pQCT and μCT correlated ($R = 0.87$; $p < 0.0001$). The precision error for MMD was 2.43%. Cortical porosity and MMD were associated with age ($r^2 = 0.5$ and −0.4, respectively) and correlated inversely in pre- and postmenopausal women (both $r^2 = 0.9$, all $p < 0.001$). Porosity was higher, and MMD was lower, in post- than in premenopausal women (porosity 40.3% ± 7.0 versus 34.7% ± 3.5, respectively; MMD 65.4% ± 1.8 versus 66.6% ± 1.4, respectively, both $p < 0.001$). In the woman with VDDR, MMD was 5.6 SD lower and porosity was 5.6 SD higher than the respective trait means in premenopausal women. BMD was reduced (*Z*-scores femoral neck −4.3 SD, lumbar spine −3.8 SD). Low-radiation HR-pQCT may facilitate noninvasive quantification of bone's MMD and microstructure in health, disease, and during treatment. © 2018 American Society for Bone and Mineral Research.

KEY WORDS: BONE QCT/MICRO-CT; MATRIX MINERALIZATION; OSTEOMALACIA AND RICKETS; OSTEOPOROSIS

Introduction

Dual-energy X-ray absorptiometry is a method of radiation transmission that permits quantification of areal bone mineral density (BMD) based on the attenuation of photons by mineralized bone matrix after accounting for the attenuation produced by soft tissue.[1] The attenuation by mineral is determined by the matrix volume and the degree of completeness of primary and secondary mineralization of that matrix.

Thus, a deficit in BMD may be the result of 1) a deficit in the volume of normally mineralized bone matrix as observed in healthy postmenopausal women and in women with osteoporosis relative to premenopausal women; 2) incomplete secondary mineralization produced by rapid remodeling, which replaces older fully mineralized bone with younger incompletely mineralized bone; or 3) failed primary mineralization as occurs in osteomalacia.[2]

These alternatives cannot be distinguished using bone densitometry because it captures the three-dimensional mineralized bone matrix volume as a two-dimensional "areal" projected image. Indeed, failure of primary mineralization in osteomalacia requires demonstration of reduced matrix mineral content with increased surface extent of osteoid, increased osteoid thickness, and mineralization lag time obtained using dynamic histomorphometry.[3,4] However, this approach is not often used because bone biopsy is invasive.[5]

Assessment of bone matrix mineralization using conventional X-ray micro-computed tomography is feasible.[6,7] Burghardt and colleagues reported high correlations between matrix mineral density (MMD) measured using micro-computed tomography (μCT) and synchrotron micro-computed tomography or ash fraction ex vivo ($R^2 = 0.78$ to 0.99).

Quantification of MMD has also been achieved using high-resolution peripheral quantitative computed tomography

Received in original form October 31, 2017; revised form February 5, 2018; accepted February 12, 2018. Accepted manuscript online February 28, 2018.
Address correspondence to: Cherie Chiang, MBBS(Hons), Department of Endocrinology, Austin Health, 145 Studley Road, Heidelberg 3084, Melbourne, Australia. E-mail: Cherie.chiang@mh.org.au
Journal of Bone and Mineral Research, Vol. 33, No. 7, July 2018, pp 1312–1317
DOI: 10.1002/jbmr.3415
© 2018 American Society for Bone and Mineral Research

(HR-pQCT), a noninvasive approach that images bone at low-radiation exposure to quantify matrix mineral density.[8,9] For example, Tsai and colleagues quantified MMD in patients treated with teriparatide, denosumab, or both.[10] Using the same method, Boutroy and colleagues reported a higher MMD in Chinese compared with white American women.[11]

We hypothesized that MMD will decrease after menopause because of increased bone remodeling removing older more mineralized bone and replacing it with younger, less fully mineralized bone, and that because remodeling is unbalanced, cortical porosity will be higher in post- than premenopausal women and that cortical porosity and MMD will correlate inversely. We also hypothesized that a patient with vitamin D–dependent rickets (VDDR) and proven hyperosteoidosis on bone histology will have reduced MMD and increased cortical porosity distinguishing her from age-comparable vitamin D–replete women.

Materials and Methods

Accuracy of measurement of MMD using the StrAx software

Ex vivo experiment

MMD measured using μCT correlates with that quantified using synchrotron μCT or ash fraction.[12] We, therefore, assessed the accuracy of the StrAx measurement of MMD by comparing the result obtained with that using μCT as gold standard ex vivo. Nine radii from the nondominant arm from white female cadavers were imaged using VivaCT 40 μCT (19-μm voxel size, 70 kVp, 114 mA, 381 ms integration time; Scanco Medical, Bruttisellen, Switzerland). Photon attenuation produced by mineralized matrix was converted to hydroxyapatite mgHA/cc concentrations using a linear regression derived by imaging a calibration phantom containing rods of HA-resin mixtures (0, 100, 200, 400, and 800 mg HA/cm^3). The radii were scanned at the same region of interest (ROI) using HR-pQCT (XtremeCT, Scanco Medical AG, 60 kVp, current of 900 μA; stacks of 110 images 9.2 mm were acquired with an isotropic voxel size of 82 μm).

In vivo experiment

For the study of MMD and porosity across age, 296 healthy pre- and postmenopausal women without fragility fractures or exposure to antiresorptive agents were recruited from the Bone Structural Study (see Results). To compare the StrAx method of measuring MMD with that obtained using the Scanco method across the range of MMD values in the community, we studied a separate cohort of 148 healthy ambulant women, mean age 57 years (range 20 to 90 years). The study was approved by Austin Health Ethics Committee (H2006/02704).

Images acquired using HR-pQCT were automatically analyzed using StrAx (StraxCorp, Melbourne, Australia).[8] Bone was segmented from background into its cortical, transitional (cortico-trabecular), and trabecular compartments. Cortical porosity and MMD were quantified and the relative content of mineral in each voxel within the compact-appearing cortex was expressed as a frequency distribution curve.

To quantify porosity, we first identified voxels attenuating photons to the same extent as the attenuation produced by fully mineralized bone (~1200 mg hydroxyapatite) and assigned a value of 100% to these voxels. Voxels with attenuation equal to that produced by background (muscle tissue) were assigned a value of 0%. Between these extremes, voxels in the cortical compartment were classified based on their relative content of mineralized versus nonmineralized tissue into categories: 0%, 1% to 50%, 51% to 70%, 71% to 95%, and 95% or above. The quantification of porosity was restricted to voxels with attenuation value equal to or less than 80% of the attenuation produced in fully mineralized bone matrix because the presence of a pore is unlikely to produce an attenuation above 80% of maximum. Porosity was calculated as the mean level of emptiness in these voxels[13] (Fig. 1).

Quantification of MMD was confined to voxels attenuating photons from 80% to 100% of the attenuation of fully mineralized bone matrix because the likelihood of a pore of 25-micron diameter is less than 5% so that the variation in the attenuation is most likely to be due to variation in matrix mineralization, not porosity. The reason for the choice of threshold of 80% of the maximum for measuring MMD is reported.[9] In brief, heterogeneity in mineralization was assessed in 520 consecutive random points from SEM images of trochanteric cortical bone obtained at post-mortem from 12 white females (mean age 69 years; range 29 to 85 years).[9] The mean MMD was 10% below the maximum with the greatest deviation being within 20% below the maximum. Thus, heterogeneity in MMD produces voxels with attenuation within 80% of that produced by fully mineralized matrix because osteoid undergoes rapid primary mineralization, reaching ~80% of peak matrix mineralization in days to become "bone."[13–15]

Reproducibility of the measurement of MMD using the StrAx software

Fifteen women had three measurements at the distal radius using HR-pQCT. Images were co-registered by an expert (AGZ) and analyzed using StrAx to test the effect of acquisition plus repositioning, co-registration, and processing on segmentation and quantification of porosity.

Statistical analysis

Data were analyzed using SPSS version 24.0 (IBM Corp., Armonk, NY, USA) and expressed in mean and standard deviation. To

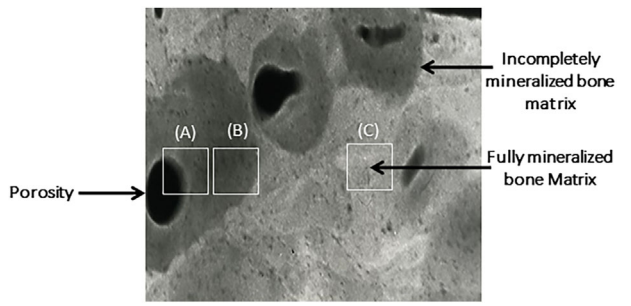

Fig. 1. The attenuation produced by contents of voxel (A) contains both nonmineralized tissue being either a pore containing extracellular fluid or undermineralized bone or both. Voxel (B) contains only undermineralized bone, whereas voxel (C) contains only highly mineralized bone. Because attenuation of photons is produced by mineral, the method cannot distinguish voxels containing osteoid, porosity, or both.

15234681, 2018, 7, Downloaded from https://asbmr.onlinelibrary.wiley.com/doi/10.1002/jbmr.3415 by The University Of Melbourne, Wiley Online Library on [18/06/2023]. See the Terms and Conditions (https://onlinelibrary.wiley.com/terms-and-conditions) on Wiley Online Library for rules of use; OA articles are governed by the applicable Creative Commons License

validate StrAx1.0 segmentation and quantification of porosity, we determined the significance of Pearson's correlation coefficient (r^2) between the gold standard and StrAx1.0 measurements. The precision error was calculated as the coefficients of variation (CV%). Significance levels ($p < 0.05$) were two-tailed.

Results

Accuracy and precision of the matrix mineral density measurement

MMD measured using StrAx1.0 correlated with the gold standard μCT measurements ($R = 0.87$; $p < 0.0001$) (Fig. 2). There was agreement between MMD measured using StrAx1.0 and the manufacturer's measurements ($R = 0.82$; $p < 0.0001$) (Fig. 3). The precision error of StrAx1.0 measurement of MMD expressed as the root mean squared CV was 2.43%.

MMD and bone microstructure in vitamin D–replete pre- and postmenopausal healthy women and in a woman with vitamin D–dependent rickets

For the study of MMD and porosity across age, of the 296 healthy pre- and postmenopausal women without fragility fractures or exposure to antiresorptive agents recruited from the Bone Structural Study, 97 pre- and 28 postmenopausal women were excluded because of low 25-hydroxyvitamin D (25[OH] D) level (<50 nmol/L), leaving 94 premenopausal women (aged 41.8 ± 6.1 years), 77 postmenopausal women (aged 60.7 ± 7.4 years) with serum 25(OH) D ≥50 nmol/L, and a 27-year-old woman with vitamin D–dependent rickets proven by bone biopsy. The pre- and postmenopausal females had, respectively, serum creatinine (66.1 ± 8.5, 67.6 ± 9.3 μmol/L), calcium (2.4 ± 0.1, 2.4 ± 0.1 nmol/L), parathyroid hormone (PTH; 4.2 ± 1.3, 4.7 ± 1.3 pmol/L), 25 hydroxyvitamin D (66.1 ± 11.9, 69.9 ± 15.7 nmol/L), and femoral neck *T*-score (–0.16 ± 0.94, –1.04 ± 0.95).

Cortical porosity and MMD were associated with age ($r^2 = 0.5$ and –0.4, respectively, both $p < 0.001$) (Fig. 4) and was higher in post- than in premenopausal women (40.3% ± 7.0% versus 34.7% ± 3.5%, respectively, $p < 0.001$). MMD was lower in post- than in premenopausal women (65.4% ± 1.8 versus 66.6% ± 1.4, respectively, $p < 0.001$). Cortical porosity and MMD correlated inversely in pre- and in postmenopausal women (both $r^2 = 0.9$, $p < 0.001$) (Fig. 4).

The mineral per voxel frequency distribution curves of the compact cortex varied as a function of age (Fig. 5). In the 30-year-old vitamin D–replete premenopausal woman, the curve was displaced to the right with a greater proportion of voxels containing fully mineralized matrix (red dots), whereas the left tail of the distribution had few voxels containing nonmineralized tissue (either osteoid or porosity). The trabeculae are plentiful and connected (blue). The curves for the 50-, 65-, and 85-year-old postmenopausal women are shifted to the left, reflecting fewer voxels containing fully mineralized bone. Trabeculae are thin and disconnected. In the 85-year-old vitamin D–replete postmenopausal woman, the curve was shifted left with a greater proportion of voxels containing nonmineralized bone (either porosity or osteoid volume), whereas the right tail had few voxels containing fully mineralized bone matrix.

Case report of VDDR subject

This 27-year-old Asian female presented in childhood with hypocalcemia (1.7 mmol/L, reference range 2.1–2.6), elevated alkaline phosphatase (four times the upper limit of normal), secondary hyperparathyroidism (serum parathyroid hormone seven times the upper limit of normal), and an undetectable 1, 25 dihydroxy-vitamin D level. She required regular intravenous calcium during puberty to maintain normocalcemia. In adulthood, she had multiple stress fractures and persistent hypocalcemia despite 2.25 mcg of calcitriol and 3600 mg of elemental calcium daily due to poor compliance. She had bilateral osteotomies to correct bowing deformities. After her HR-pQCT images were taken, she improved her compliance and achieved normocalcemia with the same dose of calcitriol and calcium supplements.

Peripheral leucocyte DNA analysis revealed compound heterozygosity with two mutations in the 1 alpha hydroxylase coding gene (CYP27b1) producing vitamin D–dependent rickets type 1a (VDDR1a, vitamin D 1 alpha-hydroxylase deficiency). Iliac crest bone biopsy showed increased osteoid volume, which comprised 70% of trabecular matrix volume and absence of tetracycline label.

MMD was 5.6 SD lower than the mean in vitamin D–replete premenopausal women. Cortical porosity was 5.6 SD higher than the mean in premenopausal women (Fig. 4). Bone mineral density was reduced (*Z*-scores femoral neck –4.3 SD, lumbar spine –3.8 SD). As can be seen from the mineral per voxel distribution curve in Fig. 5 (hatched red curve), the patient with VDDR has thin cortices with few voxels in the right tail of the

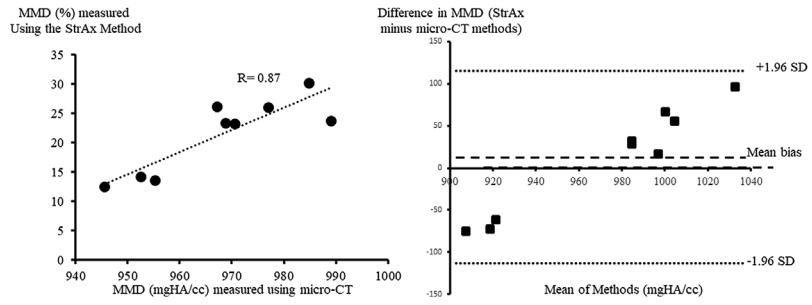

Fig. 2. (Left panel): the correlation between matrix mineral density measured in specimens using StrAx1.0 and Viva40 μCT. (Right panel [Bland and Altman plot]): there was no bias in the matrix mineral density measured using StrAx (after converting the percentage value to mgHA/cc) versus μCT (mean bias ± standard error of the mean) of 9.11 ± 21.4 mg HA/cc (NS).

15234681, 2018, 7, Downloaded from https://asbmr.onlinelibrary.wiley.com/doi/10.1002/jbmr.3415 by The University Of Melbourne, Wiley Online Library on [18/06/2023]. See the Terms and Conditions (https://onlinelibrary.wiley.com/terms-and-conditions) on Wiley Online Library for rules of use; OA articles are governed by the applicable Creative Commons License

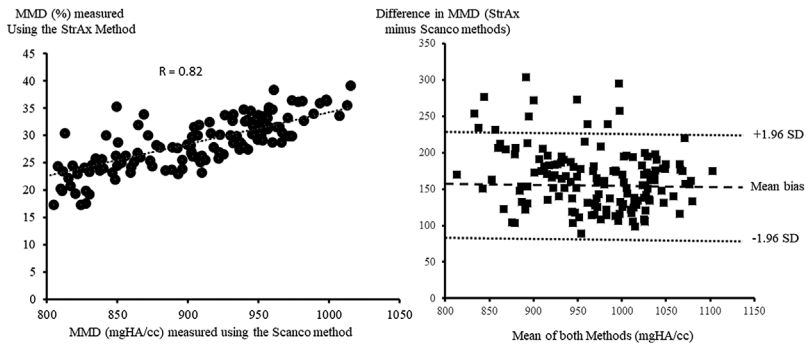

Fig. 3. (Left panel): matrix mineral density measured in vivo using StrAx1.0 versus Scanco HR-pQCT in healthy women. The StrAx and Scanco measurements correlated ($r = 0.82$; $p < 0.001$). (Right panel [Bland and Altman plot]): StrAx MMD measurements (after converting the percentage value to mgHA/cc) were higher than Scanco measurements by 164.2 mgHA/cc $\pm$ 3.45 mgHA/cc; $p < 0.001$).

distribution indicating the cortex contains little fully mineralized bone. Trabeculae are thin and disconnected. There is increased undermineralized bone matrix (blue and green voxels). The curve is shifted left, indicating the cortex is composed of more porosity and unmineralized tissue (osteoid).

Discussion

We present the results of a noninvasive method of measuring MMD in vivo using images acquired by HR-pQCT and analyzed by StrAx in healthy pre- and postmenopausal women and in a patient with biopsy-proven osteomalacia. Quantification of matrix mineral was achieved by examining the attenuation produced by the contents of voxels relative to the attenuation produced by fully mineralized bone and that produced by nonmineralized tissue. The results obtained by this method correlated with results obtained at higher resolution using VivaCT as a gold standard and with MMD measured by Scanco analysis of the same ROI.

Before menopause, remodeling is slow and balanced. Each remodeling event replaces the volume of bone removed with an equal volume of new bone so that there is no net loss of bone, no microstructural deterioration, and no change in mean MMD. After menopause, remodeling becomes unbalanced and rapid. Each remodeling transaction initiated at a point upon an intracortical canal surface removes a volume of bone and replaces it with a smaller volume of bone enlarging the canal focally. The more rapid the remodeling, the greater the numbers of remodeling transactions removing more bone than subsequently deposited, leading to increased cortical porosity.

The rapidity of remodeling also lowers matrix mineralization as older, more mineralized bone is replaced with young, less mineralized bone. The younger bone undergoes rapid primary mineralization, but secondary mineralization, the enlargement of crystals deposited during primary mineralization, takes many months to complete.[13–15] Thus, healthy postmenopausal women had lower MMD and higher cortical porosity than healthy premenopausal women. The correlation between MMD

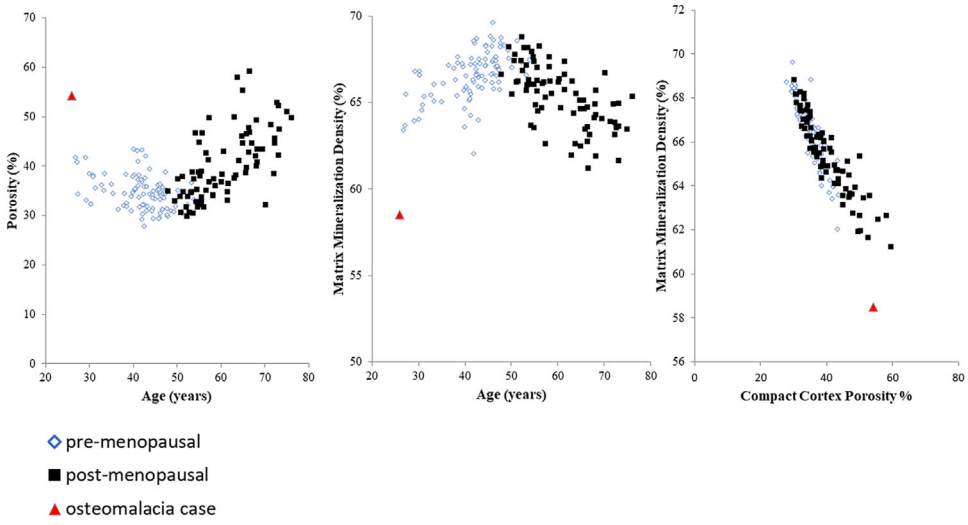

Fig. 4. (Left and middle panels): distal radial cortical porosity and matrix mineral density as a function of age in pre- and postmenopausal women and a woman with VDDR. (Right panel): the correlation between cortical porosity and matrix mineral density in pre- and postmenopausal women and the woman with VDDR.

15234681, 2018, 7, Downloaded from https://asbmr.onlinelibrary.wiley.com/doi/10.1002/jbmr.3415 by The University Of Melbourne, Wiley Online Library on [18/06/2023]. See the Terms and Conditions (https://onlinelibrary.wiley.com/terms-and-conditions) on Wiley Online Library for rules of use; OA articles are governed by the applicable Creative Commons License

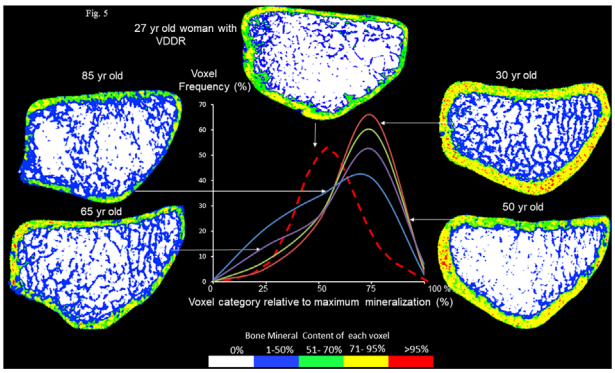

Fig. 5. The *x*-axis is the mineral content of voxel relative to tissue maximum mineralization. The *y*-axis is the frequency of voxels in each category expressed as a percentage. The color code shows the content of mineralized tissue in each voxel in the cross-sectional images of the distal radius: white: 0%, no mineral is present, only porosity or osteoid; blue: 1% to 50% of the maximum mineralization; green: 51% to 70% of the maximum; yellow: 71% to 95% of the maximum mineralization; red: >95% of the maximum mineralization. Red, green, purple, and blue curves show the curves and images in representative vitamin D–replete women aged 30, 50, 65, and 85 years, respectively. Hatched red line shows curve and image in a 27-year-old woman with vitamin D–dependent rickets.

and porosity was likely to be the result of the rapidity of remodeling. The higher the remodeling rate, the higher the prevailing porosity and the lower the MMD.

These changes in bone microstructure and MMD were captured by the left shift in the mineral per voxel frequency distribution curve in the postmenopausal woman compared with the premenopausal woman. In the example of a premenopausal woman, more voxels occupied the right tail of the voxel distribution as more of the cortical bone volume was fully mineralized matrix and fewer voxels contained pores. In the elderly postmenopausal woman, the curve shifted left as there were more voxels containing pores or incompletely secondarily mineralized bone matrix and fewer voxels containing mineralized bone matrix volume.

In osteomalacia, the deficit in mineralization is due to both a reduction in primary mineralization and incomplete secondary mineralization. Early in the pathogenesis of osteomalacia, the reduction in intestinal calcium absorption is compensated for by secondary hyperparathyroidism, which increases the rate of bone remodeling maintaining serum calcium.[15] In the longer term, secondary hyperparathyroidism results in renal phosphate loss, a fall in serum calcium, and the calcium-phosphate product so osteoid no longer undergoes primary mineralization.[16] The subsequent increased rate of remodeling leads to increased cortical porosity as observed in the woman with osteomalacia.

In osteomalacia, distinguishing porosity and unmineralized matrix in the left tail of the curve is not possible, but the paucity of voxels on the right tail of the curve reflects paucity of voxels containing fully mineralized bone matrix or voxels with matrix mineral density at 80% or more of the attenuation produced by fully mineralized bone (1200 mgHA/cc), which is unlikely to contain a pore.[6]

The study has several limitations. Porosity is likely to have been overestimated in the setting of failed primary mineralization because voxels containing void cannot be distinguished from voxels containing osteoid that is devoid of mineral. Nevertheless, the reduction in the frequency of voxels in the right tail of the mineral per voxel distribution curve reflects the deficit of fully mineralized bone matrix that occurs in osteomalacia, not osteoporosis. MMD was studied in the compact cortical bone, not trabecular bone, so that comparison with iliac crest biopsy cannot be made. This method has not yet been used to examine the morphological basis of varying degree of vitamin D deficiency or insufficiency. Whether collinearity contributes to the strong association between porosity and matrix mineral density requires further study.

In summary and conclusion, noninvasive, low-radiation high-resolution peripheral computed tomography allows quantification of bone's MMD and microstructure in health and disease.[17] The deficit in BMD in osteomalacia measured using bone densitometry is likely to be the result of a reduction in bone matrix volume due to bone loss producing high porosity and reduced trabecular density, a reduction in *secondary* mineralization as secondary hyperparathyroidism and rapid remodeling replace more fully mineralized bone with new, less fully mineralized bone, and of course a failure of *primary* mineralization. By contrast, in postmenopausal women and women with osteoporosis, mean MMD is normal or slightly reduced compared with healthy premenopausal controls due to high remodeling, but a substantial proportion of voxels contain fully mineralized matrix. This method is safe and facilitates follow-up of patients to assess treatment efficacy in rickets or other bone diseases accompanied by changes in MMD.

Disclosures

ES has received research support, lectured at national and international meeting symposia funded by Allergan, Amgen, Asahi, Genzyme, Merck Sharp & Dohme. He is a director of the board and shareholder in StraxCorp, is remunerated by StraxCorp as chief medical officer, and is one of the inventors of the StrAx1.0 algorithm. RZ has received grant and/or research support from Amgen, Merck Sharp & Dohme, Servier, Warner-Chilcott, AKP, Genzyme, Sanofi, GSK, and Pfizer. He is a shareholder in StraxCorp, is remunerated by Strax Corp as president of R&D, and is one of the inventors of the StrAx1.0 algorithm. RZ is also a director on the board of StraxCorp. CC has received grant and/or research support from Amgen, Merck Sharp & Dohme, Servier and Sanofi. AG and JZ have nothing to declare.

Acknowledgments

Authors' roles: CC and ES wrote and revised the manuscript, XW performed statistical analysis, RZ and AG performed and analysed the HR-pQCT images, JZ provided clinical information.

References

1. Wahner HW, Dunn WL, Riggs BL. Assessment of bone mineral. Part 1. J Nucl Med. 1984;25(10):1134–41.
2. Farlay D, Panczer G, Rey C, Delmas PD, Boivin G. Mineral maturity and crystallinity index are distinct characteristics of bone mineral. J Bone Miner Metab. 2010;28(4):433–45.
3. Need AG, Horowitz M, Morris HA, Moore R, Nordin C. Seasonal change in osteoid thickness and mineralization lag time in ambulant patients. J Bone Miner Metab. 2007;22(5):757–61.
4. Priemel M, von Domarus C, Klatte TO, et al. Bone mineralization defects and vitamin D deficiency: histomorphometric analysis of iliac

15234681, 2018, 7, Downloaded from https://asbmr.onlinelibrary.wiley.com/doi/10.1002/jbmr.3415 by The University Of Melbourne, Wiley Online Library on [18/06/2023]. See the Terms and Conditions (https://onlinelibrary.wiley.com/terms-and-conditions) on Wiley Online Library for rules of use; OA articles are governed by the applicable Creative Commons License

crest bone biopsies and circulating 25-hydroxyvitamin D in 675 patients. J Bone Miner Metab. 2010;25(2):305–12.

5. Hodgson SF, Johnson KA, Muhs JM, Lufkin EG, McCarthy JT. Outpatient percutaneous biopsy of the iliac crest: methods, morbidity, and patient acceptance. Mayo Clin Proc. 1986;61(1):28–33.
6. Burghardt AJ, Kazakia GJ, Laib A, Majumdar S. Quantitative assessment of bone tissue mineralization with polychromatic micro-computed tomography. Calcif Tissue Int. 2008;83(2):129–38.
7. Kazakia GJ, Hyun B, Burghardt AJ, et al. In vivo determination of bone structure in postmenopausal women: a comparison of HR-pQCT and high-field MR imaging. J Bone Miner Metab. 2008;23(4):463–74.
8. Zebaze R, Ghasem-Zadeh A, Mbala A, Seeman E. A new method of segmentation of compact-appearing, transitional and trabecular compartments and quantification of cortical porosity from high resolution peripheral quantitative computed tomographic images. Bone. 2013;54(1):8–20.
9. Zebaze RM, Jones AC, Pandy MG, Knackstedt MA, Seeman E. Differences in the degree of bone tissue mineralization account for little of the differences in tissue elastic properties. Bone. 2011;48(6):1246–51.
10. Tsai JN, Uihlein AV, Burnett-Bowie SA, et al. Comparative effects of teriparatide, denosumab, and combination therapy on peripheral compartmental bone density, microarchitecture, and estimated strength: the DATA-HRpQCT Study. J Bone Miner Metab. 2015;30(1):39–45.
11. Boutroy S, Walker MD, Liu XS, et al. Lower cortical porosity and higher tissue mineral density in Chinese American versus white women. J Bone Miner Metab. 2014;29(3):551–61.
12. Kazakia GJ, Burghardt AJ, Cheung S, Majumdar S. Assessment of bone tissue mineralization by conventional x-ray microcomputed tomography: comparison with synchrotron radiation microcomputed tomography and ash measurements. Med Phys. 2008;35(7):3170–9.
13. Bala Y, Bui QM, Wang XF, et al. Trabecular and cortical microstructure and fragility of the distal radius in women. J Bone Miner Metab. 2015;30(4):621–9.
14. Akkus O, Polyakova-Akkus A, Adar F, Schaffler MB. Aging of microstructural compartments in human compact bone. J Bone Miner Metab. 2003;18(6):1012–9.
15. Need AG, O'Loughlin PD, Morris HA, Coates PS, Horowitz M, Nordin BE. Vitamin D metabolites and calcium absorption in severe vitamin D deficiency. J Bone Miner Metab. 2008;23(11):1859–63.
16. Sai AJ, Walters RW, Fang X, Gallagher JC. Relationship between vitamin D, parathyroid hormone, and bone health. J Clin Endocrinol Metab. 2011;96(3):E436–46.
17. Seeman E. Bone morphology in response to alendronate as seen by high-resolution computed tomography: through a glass darkly. J Bone Miner Metab. 2010;25(12):2553–7.

15234681, 2018, 7, Downloaded from https://asbmr.onlinelibrary.wiley.com/doi/10.1002/jbmr.3415 by The University Of Melbourne, Wiley Online Library on [18/06/2023]. See the Terms and Conditions (https://onlinelibrary.wiley.com/terms-and-conditions) on Wiley Online Library for rules of use; OA articles are governed by the applicable Creative Commons License

Archives of Osteoporosis (2018) 13: 5
https://doi.org/10.1007/s11657-017-0414-4

ORIGINAL ARTICLE

Upright activity and higher motor function may preserve bone mineral density within 6 months of stroke: a longitudinal study

Karen Borschmann[1,2] · Sandra Iuliano[3,4] · Ali Ghasem-Zadeh[3,4] · Leonid Churilov[2] · Marco Y. C. Pang[5] · Julie Bernhardt[1,2]

Received: 24 May 2017 / Accepted: 18 December 2017 / Published online: 8 January 2018
© The Author(s) 2018. This article is an open access publication

Abstract

Purpose Bone fragility contributes to increased fracture risk, but little is known about the emergence of post-stroke bone loss. We investigated skeletal changes and relationships with physical activity, stroke severity, motor control and lean mass within 6 months of stroke.

Methods This is a prospective observational study. Participants were non-diabetic but unable to walk within 2 weeks of first stroke. Distal tibial volumetric bone mineral density (vBMD, *primary outcome*), bone geometry and microstructure (high-resolution peripheral quantitative computed tomography) were assessed at baseline and 6 months, as were secondary outcomes total body bone mineral content and lean mass (dual energy X-ray absorptiometry), bone metabolism (serum osteocalcin, N-terminal propeptide of type 1 procollagen (P1NP), C-terminal telopeptide of type 1 collagen (CTX)), physical activity (PAL2 accelerometer) and motor control (Chedoke McMaster) which were also measured at 1 and 3 months.

Results Thirty-seven participants (69.7 years (SD 11.6), 37.8% females, NIHSS 12.6 (SD 4.7)) were included. The magnitude of difference in vBMD between paretic and non-paretic legs increased within 6 months, with a greater reduction observed in paretic legs (mean difference = 1.5% (95% CI 0.5, 2.6), $p = 0.007$). At 6 months, better motor control was associated with less bone loss since stroke ($r = 0.46$, $p = 0.02$). A trend towards less bone loss was observed in people who regained independent walking compared to those who did not ($p = 0.053$). Higher baseline daily count of standing up was associated with less change in bone turnover over 6 months: osteocalcin ($r = -0.51$, $p = 0.01$), P1NP ($r = -0.47$, p = 0.01), CTX ($r = -0.53$, p = 0.01).

Conclusion Better motor control and walking recovery were associated with reduced bone loss. Interventions targeting these impairments from early post-stroke are warranted.

Clinical trial registration URL: http://www.anzctr.org.au. Unique identifier: ACTRN12612000123842.

Keywords Stroke · Bone loss · Bone mineral density · Microstructure · HR-pQCT · Physical activity

Electronic supplementary material The online version of this article (https://doi.org/10.1007/s11657-017-0414-4) contains supplementary material, which is available to authorized users.

✉ Karen Borschmann
Karen.borschmann@florey.edu.au

[1] School of Health Science, La Trobe University, Bundoora, Australia

[2] The Florey Institute of Neuroscience and Mental Health, University of Melbourne, Heidelberg, Australia

[3] Department of Medicine, Austin Health, University of Melbourne, Heidelberg, Australia

[4] Department of Endocrinology, Austin Health, University of Melbourne, Heidelberg, Australia

[5] Department of Rehabilitation Sciences, Hong Kong Polytechnic University, Hung Hom, Hong Kong

Introduction

Although age-standardised hip fracture rates vary globally from < 10 to nearly 500/100,000 population [1], increased fracture risk is recognised as a common and serious stroke sequela [2–4]. The likelihood of hip fracture at 12 months post-stroke, particularly in paretic legs, increases two to four times to that of age- and sex-matched controls [2, 5]. Compared to people without stroke, people who fracture after stroke have higher mortality at 1 month (3.3 vs 8.8%, $p = 0.008$) [6] are less likely to regain the ability to walk by hospital discharge (69.2 vs 38.1%, $p < 0.001$) [6] and are more likely to be discharged to residential care (OR 2.69 (95% CI 1.11, 6.54) $p = 0.028$) [3].

Bone mineral density (BMD), a surrogate measure of bone strength, is thought to decline post-stroke due to increased bone resorption and reduced formation, consistent with uncoupling of bone remodelling [7]. While bone loss and increased fracture risk in people with chronic stroke (> 12 months after onset) are well recognised, bone loss likely occurs early after stroke [7]. However, evidence on the timing of post-stroke bone loss, and the contributions of age, gender and stroke impairments, is limited by lack of longitudinal data. Consequently, the magnitude of change that is expected to occur from early after stroke is unknown, and little is known about factors that may influence post-stroke bone loss.

Most studies of post-stroke bone loss have utilised dual energy X-ray absorptiometry (DXA) to estimate areal BMD (g/cm^2) of the paretic side hip. Reduced aBMD has been associated with the length of time people are unable to walk [8], and reductions in muscle strength [9] and mass [10]. However, due to the inherent error in accuracy and reproducibility of DXA imaging, particularly due to difficulty with consistent positioning of people with stroke [9], and the limitations of projecting 3-dimensional structures onto 2-dimensions, areal BMD lacks sensitivity and specificity for fracture prediction [11]. High-resolution peripheral quantitative computed tomography (HR-pQCT, voxel size 82 μm) provides estimation of volumetric BMD (vBMD, $mgHA/cm^3$) and bone microstructure, which are better determinants of bone strength than areal BMD [12], and only scan slices that are common between assessments are included in analyses, which assumes that the bone area is constant over time. Furthermore, trabecular and cortical bone, each of which contributes differently to bone strength, can be quantified separately [11].

To our knowledge, no reports exist of HR-pQCT use to longitudinally evaluate lower limb bone loss from early after stroke. Low-resolution pQCT (voxel size 500 μm) was recently used to examine changes over 12 months in bone structure and density of lower limbs of people who were more than 12 months post-stroke [13]: trabecular bone density at the distal tibia (4% site of bone length) reduced by 1.8% (SD 0.6, $p = 0.006$) in the 20 people who completed the study.

In the present study, we utilised HR-pQCT to determine the magnitude of skeletal changes between 2 weeks and 6 months of first stroke. We hypothesised that total vBMD of the distal tibia would reduce more in paretic compared to non-paretic legs. Moreover, we hypothesised that less vBMD change in paretic legs would be associated with better motor function, and with regaining the ability to walk within 6 months of stroke.

Methods

The full protocol for this prospective observational study has been published [14]; details are provided here in brief. Adults > 40 years admitted to one of two public hospitals in Melbourne (Australia) within 1 week of first stroke, diagnosed with hemispheric stroke, medically stable, unable to walk 10 ft independently and able to follow simple commands were eligible. Exclusion criteria were the following: previous stroke, diabetes, other neurological disease, other condition limiting function (e.g., limb amputation) or use of bone-specific medication (e.g., bisphosphonates). Informed consent was obtained from all participants included in the study.

Outcome measurement

Assessments were undertaken at baseline (within 2 weeks of onset), 1 month post-baseline and 3 and 6 months post-stroke. Demographic and stroke-related data were collected from medical records at baseline. At each assessment, participants reported any falls that they had experienced since the previous assessment. Study-related adverse events were collected, defined as any study-related event that required medical or nursing attention. HR-pQCT scans were undertaken at baseline and 6 months; all other assessments were completed at each time point.

Primary outcome

The primary outcome (change in the magnitude of difference of total vBMD between paretic and non-paretic legs at the distal tibia between baseline and 6 months) was measured at 7% of bone length from the distal end using HR-pQCT (Xtreme CT, Scanco Medical AG, Switzerland. Coefficient of variation (CV, measurement precision) was 1.3% [15]. This is a region that contains both trabecular and cortical bone. Tibial bone strength has been associated with both vertebral fracture (OR 2.92, 95% CI 1.14, 3.03) and non-vertebral fracture (OR = 2.64, 95% CI 1.63, 4.27), and it is therefore considered that properties of the tibia are reasonably representative of other bone sites (Vilayphiou et al. 2010).

Secondary outcomes

Cortical and trabecular vBMD ($mgHA/cm^3$), cortical thickness (mm), cortical and trabecular cross-sectional area (mm^2) and total, cortical and trabecular bone mass (g) at the distal tibiae were also measured. Trabecular bone volume fraction was calculated (bone volume/total volume), and trabecular number (TbN, 1/mm), thickness (TbTh, μm), separation (TbSp, μm) and inhomogeneity of trabecular network (distribution of separation, TbSp SD, μm) were calculated based on the manufacturer's algorithm. CV of density measurements was 0.6–1.4% and structural parameters was 0.9–4.4% [15]. The clinically relevant difference (i.e. least significant change [16]) is calculated $\sqrt{2} \times 1.65 \times CV$; density measures = 1.4–3.3%

and structural measures = 2.1–10.3%. Lean mass and bone mineral content of the total body and legs were determined from total body DXA scans (DPX-L, version 1.3z: Lunar Corp., Madison, USA).

Physical activity was measured using PAL2 accelerometer (Gorman ProMed Pty Ltd., Australia) [17] to register the number of changes in position and the amount of time spent lying, sitting, standing and walking. The device was worn for 1 day from 8AM to 5PM at each time point [18].

Disability was classified using the Modified Rankin Scale [19]. Motor function of the paretic leg was evaluated with Chedoke McMaster Stroke Assessment [20]. Quadriceps muscle strength was assessed seated using hand-held dynamometry (Nicholas Manual Muscle Tester; Lafayette

Table 1 Baseline demographics and stroke characteristics

Characteristic	All recruits	Completed trial			
			Primary outcome analysis		
	n = 37	*n* = 33	Yes *n* = 22	No *n* = 11	*p**
Sex, female	14 (37.8)	13 (39.4)	10 (45.5)	3 (27.3)	0.31
Age, mean (SD)	69.7 (11.6)	69.1 (11.7)	66.0 (12.1)	75.3 (8.3)	0.03
Lived with others prior to stroke	28 (75.7)	25 (75.8)	17 (77.3)	8 (72.7)	0.77
Employed	14 (37.8)	13 (39.4)	10 (45.5)	3 (27.3)	0.32
Primary language not English	7 (18.9)	7 (21.2)	4 (18.2)	3 (27.3)	0.55
Walked prior, no gait aid	32 (86.5)	29 (87.9)	20 (90.9)	9 (81.8)	0.45
BMI, mean (SD)	27.1 (5.4)	27.5 (5.4)	27.3 (5.2)	27.8(6.4)	0.41
Number comorbidities	4.2 (2.9)	4.0 (2.7)	4.2 (3.1)	3.6 (1.9)	0.72
Past medical history					
Previous fracture	12 (32.4)	11 (33.3)	7 (31.8)	4 (36.4)	0.79
Hypertension	18 (48.7)	15 (45.5)	9 (40.9)	6 (54.5)	0.46
High cholesterol	12 (32.4)	10 (30.3)	6 (27.3)	4 (36.4)	0.59
Ischaemic heart disease	7 (18.9)	5 (15.2)	4 (18.2)	1 (9.1)	0.49
Atrial fibrillation	7 (18.9)	6 (18.2)	3 (13.6)	3 (27.3)	0.34
Musculoskeletal	15 (40.5)	14 (42.4)	8 (36.4)	6 (54.5)	0.32
Smoking history					
Current smoker	12 (32.4)	10 (30.3)	6 (27.3)	4 (36.4)	
Never smoked	14 (37.8)	12 (36.4)	9 (40.9)	3 (27.3)	
Previous smoker	11 (29.7)	11 (29.7)	7 (31.8)	4 (36.4)	
Vit D/calcium supplementation	7 (18.9)	7 (21.2)	5 (22.7)	2 (12.9)	0.76
Stroke severity†	12.6 (4.7)	12.9 (4.8)	12.6 (4.8)	13.5 (5.0)	
Group mean (SD)	5 (13.5)	4 (12.1)	4 (18.2)	0	0.30
Mild, *n* (%)	24 (64.9)	21 (63.6)	13 (59.1)	8 (72.7)	
Moderate, *n* (%)	8 (21.6)	8 (24.2)	5 (22.7)	3 (27.3)	
Severe, *n* (%)					
Stroke classification‡					0.67
TACI	18 (48.6)	18 (54.6)	11 (50.0)	7 (63.6)	
PACI	11 (29.7)	10 (30.3)	7 (31.8)	3 (27.3)	
LACI	4 (10.8)	3 (9.1)	3 (13.6)	0	
Haemorrhage	4 (10.8)	2 (6.1)	1 (4.5)	1 (9.1)	

n (%) unless stated otherwise

BMI, body mass index, kg/m^2; *TACI*/*PACI*, total/partial anterior circulation infarct; *LACI*, lacunar circulation infarct; *Vit D*, vitamin D

*Participants who completed the study, comparison of those who did and did not have primary outcome data: Wilcoxon rank-sums or Fisher's Exact Test

†NIHSS (National Institutes of Health Stroke Scale): mild < 8, moderate 8–16, severe > 16

‡Significant difference ($p = 0.02$) between participants who did and did not complete study

Instruments, Lafayette, USA); the average of three test scores were standardised to body mass [21]. Walking ability was classified on Functional Ambulation Classification [22].

Fasting serum markers of bone turnover were assessed (osteocalcin, resorption marker serum C-terminal telopeptide of types 1 collagen (CTX) and formation marker N-terminal propeptide of type 1 procollagen (P1NP)) by electrochemiluminenescence immunoassay (Elecsys 1010 Analytics, Roche Diagnostics, Germany, intra- and inter-assay CV 3–8%) [23].

Sample size calculation

Using the difference between paretic and non-paretic limbs in 6-month change of distal tibia vBMD from pilot data ($n = 10$, mean reduction paretic = − 1.43% (SD 1.92), non-paretic = − 0.45% (SD 1.37)), and assuming one sample, two-tailed test with criterion for significance of $p = 0.05$, 25 participants would provide 80% power to detect a significant effect of this magnitude or larger. Adjusting for an expected mortality of 30% [24], 33 participants were required for the main study.

Statistical analysis

People who did not complete the trial due to death or withdrawal ($n = 4$) were not included in any analyses due to their data being not missing at random [25]. The complete case analysis was conducted on the combined pilot and main study datasets for all outcomes.

The primary outcome (change in the difference in vBMD between paretic and non-paretic legs over 6 months) was compared to zero using a one-sample *t* test. Secondary outcomes: the association between the change in vBMD and paretic leg motor function at 6 months was assessed using Spearman's correlation coefficient, while the relationship between change in vBMD and regaining the ability to walk by 6 months (not able to walk = FAC (Functional Ambulation Classification) 1–4 vs able to walk = FAC 5–6) was investigated using Wilcoxon rank-sum test.

Distributions of secondary outcomes (bone turnover markers, lean mass and bone mineral content) were tested by Shapiro-Wilk test, then log transformed as required. Exploratory analyses of change in secondary outcomes over 6 months were undertaken by generalised estimating equation. Change in secondary HR-pQCT measures was examined as described for the primary outcome. Analyses were performed using STATA v13IC software (StataCorp, College Station, USA). Due to exploratory nature of this research, a significance level of 0.05 was set for all analyses. Separate subgroup analyses (e.g. age, sex, ethnicity) were not undertaken due to small sample.

Results

In total, 2749 patients were screened and 37 provided consent (Table 1). Reasons for exclusion and participant flow through the study are shown in Fig. 1. Participants who completed the study ($n = 33$) had proportionally fewer haemorrhagic strokes compared to those who did not ($n = 4$), ($\chi^2 = 9.4$, $p = 0.02$). No study-related adverse events were reported. Twenty-two people (67%) fell at least once during the course of the study. The median number of falls was 2 (IQR 1, 3), and two people were fractured (1 hip, 1 wrist). Of those who completed the study, 22 (67%) had adequate bone images for primary outcome analysis. Reasons for missing data were the following: movement during scan ($n = 5$), declined or unavailable ($n = 3$), illness ($n = 2$) and scanner not available ($n = 1$). Participants who provided primary outcome data were younger than those who did not (66.0 ± 12.1 years vs 75.3 ± 8.3, $p = 0.03$).

HR-pQCT-derived parameters

At baseline, total vBMD of the paretic leg was 268.4 mgHA/cm^3 (SD 68.4) and non-paretic leg was 272.0 mgHA/cm^3 (SD 67.4) (Table 2). By 6 months, vBMD reduced by 2.4% (SD 2.7, $p = 0.001$) in paretic legs, but did not change in non-paretic legs. The between-limb difference was not significant at either time point. Confirming the primary hypothesis, the

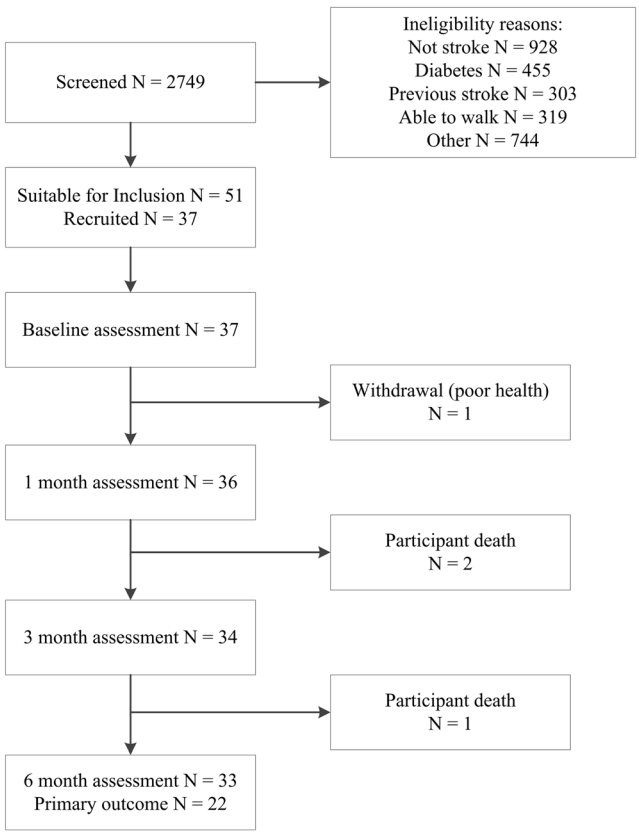

Fig. 1 Participant recruitment and retention

Table 2 HR-pQCT-derived total volumetric bone mineral density, cortical thickness and bone area of distal tibiae within 2 weeks of stroke and 6-month change ($n = 22$)

	Baseline			6-month % change		
	Paretic	Non-par	BW-leg diff %	Paretic	Non-par	BW-leg diff % mean (95% CI)*
Total vBMD, mgHA/cm^3	268.39 (68.41)	272.59 (67.37)	2.15 (5.77)	− 2.4 (2.7)	− 1.0 (2.4)	1.53 (0.46, 2.61) $p = 0.01$
Total bone mass, g	186.2 (52.1)	190.0 (48.7)	3.0 (5.1)	− 2.5 (2.8)	− 1.0 (2.4)	1.56 (0.47, 2.65) $p = 0.01$
Cortical bone mass, g	76.6 (34.7)	75.9 (33.2)	0.2 (12.7)	− 8.5 (10.4)	− 4.2 (7.0) 5.26 (1.91, 8.62) $p = 0.004$	
Trabecular bone mass, g	100.1 (28.8)	104.8 (28.1)	6.2 (9.4)	− 0.4 (1.8)	− 1.2 (2.2)	− 0.84 (− 1.84, 0.17) $p = 0.10$
Cortical area, mm^2	108.28 (42.52)	107.69 (40.74)	0.28 (10.59)	− 7.0 (8.6)	− 3.1 (5.9)	4.42 (1.78, 7.06) $p = 0.002$
Trabecular area, mm^2	691.24 (132.38)	699.51 (136.36)	1.14 (4.39)	0.5 (0.09)	− 0.02 (− 0.79)	− 0.58 (− 0.97, − 0.19) $p = 0.006$

Mean (SD)

Non-par; non-paretic; *vBMD*, volumetric bone mineral density; *BW-leg Diff*. between-leg difference = [(non-paretic–paretic)/paretic] × 100

*One sample *t* test

magnitude of change in the between-limb difference in vBMD increased by 1.53% (95% CI 0.46, 2.61, $p = 0.01$) within 6 months. Similarly, significant changes were observed across 6 months for the between-leg difference in total and cortical bone mass ($p = 0.01$, 0.004, respectively), and cortical and trabecular areas ($p = 0.02$, 0.006, respectively) (Table 2). All HR-pQCT-derived variables are contained in the supplemental table.

DXA derived parameters

At baseline, 21 participants (72.4%) had normal BMD [26], seven (24.1%) were osteopenic (1–2.5 SD below reference range) and one person was osteoporotic (≥ 2.5 SD below reference). Significant changes in bone mineral content were not observed until the 6-month assessment, at which time reductions were observed for total body (2.8%, IQR 0.6, 5.6, $p = 0.001$) and paretic legs (3.4%, IQR 0.5, 6.1, $p < 0.001$), Table 3. Change in lean mass could not be estimated via generalised estimating equation as estimates diverged (correlation > 1); Wilcoxon signed-rank test of baseline and 6-month data showed that lean mass did not change significantly.

Bone turnover markers

Compared to baseline results, P1NP was elevated at every time point, and osteocalcin was elevated by 3 months; both remained elevated at 6 months, Table 3. No significant changes were detected in CTX. By 1 month, P1NP increased by 59.3% (IQR 12.2, 104.5, $p = 0.001$) which is more than its least significant change (19.9%), and at 3 months, osteocalcin was 29.7% (IQR 8.4, 74.4, $p = 0.001$) higher than baseline.

Physical assessments

Independent walking was achieved by 67% of participants ($n = 22$, FAC > 4, Fig. 2), by 54.5 (IQR 27.8, 98.0) days post-stroke. At baseline, participants lay in bed for 57.8% (IQR 40.9, 79.0) of the day, and spent < 2% of time upright, standing (1.4%, IQR 0.3, 5.2) or walking (0.2%, IQR 0.0, 1.6) (Fig. 2). Participants stood up 14 (IQR 6, 28) times in a day. At 6 months, participants sat for 62.5% (IQR 39.9, 82.8) of the day, stood for 12.5% (IQR 2.9, 21.1), walked for 8.7% (IQR 6.1, 15.1) and stood up 53 times (IQR 38, 73), all $p < 0.01$.

Paretic leg motor function was reduced at baseline (2.5, IQR 2, 4) and improved but remained below normal (< 7/7) (5, IQR 3, 6, $p < 0.001$). Quadriceps strength at baseline was 66.0% higher (IQR 11.5, 107.7, $p < 0.001$) in non-paretic legs than paretic legs. Strength increased in both legs during the study; at 6 months, non-paretic legs were 18.9% (IQR 4.3, 44.4, $p < 0.001$) stronger than paretic legs.

Table 3 Bone turnover markers and DXA-derived bone mineral content and lean mass at baseline and 6 months after stroke

	Baseline $N = 30$ BTM/29 DXA	6 months $N = 28$	6-month % change $N = 26$	Significance*
CTX, pg/ml	568.75 (361.2, 735.6)	597.6 (385.55, 847)	4.89 (− 28.01, 45.65)	0.55
P1NP, μg/l	38.45 (26.38, 43.0)	76.17 (51.99, 97.84)	94.42 (64.63, 171.13)	< 0.001
Osteocalcin ng/ml	15.07 (11.18, 20.0)	22.26 (15.61, 29.81)	42.71 (− 0.65, 100.4)	< 0.001
Muscle mass, kg				
Total body	47.00 (40.44, 52.73)	48.20 (40.33, 54.63)	1.2% (− 3.2, 4.2)	0.49
Paretic leg	7.47 (6.58, 8.36)	7.46 (6.69, 8.48)	0.4% (− 3.4, 5.1)	0.82
Non-paretic	7.22 (5.88, 8.45)	7.55 (6.29, 8.66)	1.3% (− 2.8, 6.8)	0.09
BMC, g				
Total body	2919 (2135, 3244)	2705 (2091, 3095)	− 2.8% (− 5.6, − 0.6)	0.039
Paretic leg	533 (439, 603)	512 (423, 585)	− 3.4% (− 6.1, − 0.5)	< 0.001
Non-paretic leg	536 (415, 601)	528 (426, 600)	− 0.3% (− 2.1, 0.3)	0.19

Data presented median (IQR); *BMC*, bone mineral content (grams); *BTM*, bone turnover markers (resorption); *CTX*, carboxyterminal crosslinked telopeptide of type 1 collagen; formation, *P1NP*, N-terminal propeptide of type 1 procollagen

*Generalised estimating equation for all variables except lean mass and non-paretic leg BMC due to estimates diverging (correlation > 1), so assessed by Wilcoxon signed-rank test

As hypothesised, change in vBMD of paretic legs was significantly associated with leg motor function at 6 months ($p = 0.02$), Table 4. The association between change in paretic leg vBMD and regaining the ability to walk independently approached significance ($p = 0.053$): − 1.51% (IQR − 3.67, − 0.09) in those who regained walking compared to − 5.54% (IQR − 6.25, − 3.63) in those who did not. Higher stroke severity, reduced motor function of the paretic leg and lower physical activity at baseline were associated with changes in bone turnover markers but not with change in vBMD.

Discussion

This was the first longitudinal examination of skeletal changes from early post-stroke using HR-pQCT. We observed an increase in the magnitude of difference in total vBMD between paretic and non-paretic legs, with a greater reduction in paretic legs. As expected [27], given the average age of approximately 70 years, the loss was evident predominantly in cortical rather than trabecular bone. Significant changes were observed in both cortical (− 7.0%, SD 8.6) and trabecular bone areas (0.5%, SD 0.09), which is consistent with cortical thinning and the concomitant increase in trabecular area. Bone loss exceeded the machine error margin of 1.4–3.3% and that expected due to ageing alone (0.5–1% in 12 months) [28]. Our observation of 2.4% (SD 2.8) reduction of vBMD in the paretic leg within 6 months is greater than the 1.4% (SD 0.3) reduction previously observed over 12 months in people who were 12–24 months post-stroke [13]. As expected, two thirds of participants fell at least once during the study [29], and two participants (6.1%) fractured within 6 months, in comparison to the annual Australian fracture rate of 0.18% (175/100,000 population) [30]. Combined, these data suggest that bone loss is likely highest within the first 6 months post-stroke, so prevention of bone loss during this rapid phase is critical to prevent fracture risk in this vulnerable patient population.

Our data showed that higher motor control at 6 months after stroke and regaining the ability to walk were associated with less reduction in vBMD of paretic legs. Baseline measures of higher stroke severity, lower paretic leg motor control and lower physical activity were associated with greater changes to bone metabolism markers but not changes in vBMD. The number of times that participants stood up, but not the proportion of time spent on their feet at baseline, was associated with 6-month change in bone resorption (CTX). This likely reflects bone response to discrete loads rather than length of loading, as bone cells desensitise to prolonged loading [36]. Results infer that regular weight bearing within the

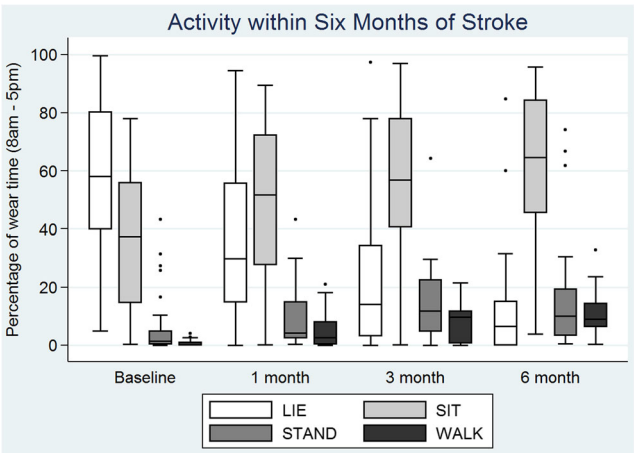

Fig. 2 Physical activity between 2 weeks and 6 months of stroke

Table 4 Associations between 6-month changes in vBMD of paretic leg and bone turnover markers, stroke severity, physical activity and paretic leg motor control

	% change vBMD paretic leg	% change P1NP	% change osteocalcin	% change CTX
Baseline: NIHSS	− 0.04	0.46	0.31	0.52
	0.85	0.01	0.08	0.001
	24	28	28	28
Baseline: daily count of standing up	0.17	− 0.47	− 0.51	− 0.53
	0.44	0.01	0.01	0.01
	23	27	27	27
Baseline: proportion of time sedentary	− 0.08	0.54	0.43	0.28
	0.72	0.003	0.02	0.16
	23	27	27	27
Baseline: paretic-leg motor function†	0.31	− 0.59	− 0.58	− 0.67
	0.16	0.001	0.001	0.0001
	23	28	28	28
6 month: paretic-leg motor function†	0.46	− 0.29	− 0.38	− 0.32
	0.02	0.14	0.047	0.10
	24	28	28	28

Cells contain Spearman's rho, *p*, n.

CTX, C-terminal telopeptide of type 1 collagen; *NIHSS*, National Institute of Health Stroke Scale; *P1NP*, N-terminal propeptide of type 1 procollagen; *vBMD*, volumetric bone mineral density

*Significant at 0.05

†Chedoke McMaster Stroke Assessment

first week of stroke, and targeting leg motor control and reattainment of walking, may protect bone mass after stroke. This needs to be tested.

Similar to a previous longitudinal study of musculoskeletal changes using DXA from early after stroke [31], we did not observe changes in lean mass within 6 months of stroke. Evidence from longer-term longitudinal studies [8, 9] and a systematic review of predominantly cross-sectional chronic stroke data [32] suggest that loss of lean mass may occur after 6 months post-stroke, and the time taken to regain independent walking may mediate changes in both lean mass and BMD in paretic and non-paretic legs.

Previous reports of increased bone resorption in people with chronic stroke [7, 33, 34] are in contrast with our observation that bone resorption marker CTX did not change in the first 6 months of stroke. However, given that bone formation (P1NP) and turnover marker osteocalcin did increase, and studies of young healthy adults show that bone resorption occurs within 2 days of bed rest [35], it is likely that CTX increased early after stroke prior to baseline assessments. Interestingly, our observation of increased bone formation markers at 1 month that remained elevated at 6 months was in contrast with results from Poole (2009) who observed lower histological indices of bone formation in 14 people with moderate physical impairment (71 years (SD 11)) at 10 (SD 2) weeks post-stroke compared to controls.

A study limitation was the proportion of participants not included in the primary outcome (15/37, 41%), and the younger age of those who finished the study, so results may not be generalisable to older stroke survivors. Although movement during scanning is common, the large number of failed scans due to movement artefact may have influenced precision in some parameters [37]; however, clinically and statistically significant differences were observed in results. Due to the expected burden on participants who had high levels of impairment early after stroke, HR-pQCT scans were only assessed at baseline and 6-month follow-up. DXA scans, which only require subjects to lie still, were assessed at all time points. Given that DXA-derived changes in bone mineral content (BMC) were not observed in our participants until 6 months, and that participants could tolerate HR-pQCT testing of lower limbs early after stroke, HR-pQCT assessments within 6 months of stroke are warranted in future studies to examine the rate of change in bone microstructure.

Summary

This was the first longitudinal examination of HR-pQCT-derived vBMD and microarchitecture, bone metabolism, lean mass and physical activity within 6 months of moderately severe stroke. Greatest bone loss was observed in cortical bone of paretic legs, beyond that expected from ageing alone. Recovery of walking and higher motor control were associated with less bone loss; therefore, targeting these impairments from early after stroke is warranted to establish interventions to reduce post-stroke bone loss.

Acknowledgments We thank participants, research nurse Kylie King and staff from the stroke and bone density units. The Florey Institute acknowledges Victorian Government support, particularly the Operational Infrastructure Support Grant.

Sources of funding Australian Research Council (ARCFT09901086), Austin Health Medical Research Fund and La Trobe University Faculty Research Grant. JB was supported by NHMRC Established Researcher Fellowship. KB was supported by La Trobe University Postgraduate Research Scholarship.

Compliance with ethical standards

Conflict of interest None.

Statement of human and animal rights These studies were approved by Austin Health and Northern Health Human Research Ethics Committees and were performed in accordance with the ethical standards as laid down in the 1964 Declaration of Helsinki and its later amendments or comparable ethical standards.

Open Access This article is distributed under the terms of the Creative Commons Attribution 4.0 International License (http://creativecommons.org/licenses/by/4.0/), which permits unrestricted use, distribution, and reproduction in any medium, provided you give appropriate credit to the original author(s) and the source, provide a link to the Creative Commons license, and indicate if changes were made.

References

1. Kanis JA et al (2012) A systematic review of hip fracture incidence and probability of fracture worldwide. Osteoporos Int 23(9):2239–2256. https://doi.org/10.1007/s00198-012-1964-3
2. Kanis J, Oden A, Johnell O (2001) Acute and long-term increase in fracture risk after hospitalization for stroke. Stroke 32(3):702–706. https://doi.org/10.1161/01.STR.32.3.702
3. Fisher A et al (2013) Poststroke hip fracture: prevalence, clinical characteristics, mineral-bone metabolism, outcomes, and gaps in prevention. Stroke Res Treat 2013:641943
4. Dennis M et al (2002) Fractures after stroke: frequency, types, and associations. Stroke 33(3):728–734. https://doi.org/10.1161/hs0302.103621
5. Pouwels S, Lalmohamed A, Leufkens B, de Boer A, Cooper C, van Staa T, de Vries F (2009) Risk of hip/ femur fracture after stroke. A population-based case-control study. Stroke 40(10):3281–3285. https://doi.org/10.1161/STROKEAHA.109.554055
6. Ramnemark A, Nyberg L, Borssén B, Olsson T, Gustafson Y (1998) Fractures after stroke. Osteoporos Int 8(1):92–95. https://doi.org/10.1007/s001980050053
7. Poole K et al (2009) Bone structure and remodelling in stroke patients: early effects of zoledronate. Bone 44(4):629–633. https://doi.org/10.1016/j.bone.2008.11.017
8. Jorgensen L et al (2000) Walking after stroke: does it matter? Changes in bone mineral density within the first 12 months after stroke. A longitudinal study. Osteoporos Int 11(5):381–387. https://doi.org/10.1007/s001980070103
9. Jorgensen L, Jacobsen B (2001) Changes in muscle mass, fat mass, and bone mineral content in the legs after stroke: a 1 year prospective study. Bone 28(6):655–659. https://doi.org/10.1016/S8756-3282(01)00434-3
10. Ashe M et al (2006) Bone geometric response to chronic disuse following stroke: a pQCT study. J Musculoskelet Neuronal Interact 6(3):226–233
11. Vico L, Zouch M, Amirouche A, Frère D, Laroche N, Koller B, Laib A, Thomas T, Alexandre C (2008) High-resolution pQCT analysis at the distal radius and tibia discriminates patients with recent wrist and femoral neck fractures. J Bone Miner Res 23(11):1741–1750. https://doi.org/10.1359/jbmr.080704
12. Geusens P, Chapurlat R, Schett G, Ghasem-Zadeh A, Seeman E, de Jong J, van den Bergh J (2014) High-resolution in vivo imaging of bone and joints: a window to microarchitecture. Nat Rev Rheumatol 10(5):304–313. https://doi.org/10.1038/nrrheum.2014.23
13. Lam FM et al (2016) Chronic effects of stroke on hip bone density and tibial morphology: a longitudinal study. Osteoporos Int 27(2):591–603. https://doi.org/10.1007/s00198-015-3307-7
14. Borschmann K, Pang MYC, Iuliano S, Churilov L, Brodtmann A, Ekinci EI, Bernhardt J (2015) Changes to volumetric bone mineral density and bone strength after stroke: a prospective study. Int J Stroke 10(3):396–399. https://doi.org/10.1111/ijs.12228
15. Boutroy S, Bouxsein ML, Munoz F, Delmas PD (2005) In vivo assessment of trabecular bone microarchitecture by high-resolution peripheral quantitative computed tomography. J Clin Endocrinol Metab 90(12):6508–6515. https://doi.org/10.1210/jc.2005-1258
16. Nelson L, Gulenchyn KY, Atthey M, Webber CE (2010) Is a fixed value for the least significant change appropriate? J Clin Densitom 13(1):18–23. https://doi.org/10.1016/j.jocd.2009.10.001
17. Diggory P, Gorman M, Schwarz J, Helme R (1994) An automatic device to measure time spent upright. Clin Rehabil 8(4):353–357. https://doi.org/10.1177/026921559400800413
18. Bernhardt J, Dewey H, Thrift A, Donnan G (2004) Inactive and alone: physical activity within the first 14 days of acute stroke unit care. Stroke 35(4):1005–1009. https://doi.org/10.1161/01.STR.0000120727.40792.40
19. de Haan R, Limburg M, Bossuyt P, van der Meulen J, Aaronson N (1995) The clinical meaning of Rankin 'handicap' grades after stroke. Stroke 26(11):2027–2030. https://doi.org/10.1161/01.STR.26.11.2027
20. Gowland C, Stratford P, Ward M, Moreland J, Torresin W, van Hullenaar S, Sanford J, Barreca S, Vanspall B, Plews N (1993) Measuring physical impairment and disability with the Chedoke-McMaster Stroke Assessment. Stroke 24(1):58–63. https://doi.org/10.1161/01.STR.24.1.58
21. Hill K, Schwarz J, Flicker L, Carroll S (1999) Falls among healthy, community-dwelling, older women: a prospective study of frequency, circumstances, consequences and prediction accuracy. Aust N Z J Public Health 23(1):41–48. https://doi.org/10.1111/j.1467-842X.1999.tb01203.x
22. Holden M, Gill K, Magliozzi M (1986) Gait assessment for neurologically impaired patients: standards for outcome assessment. Phys Ther 66(10):1530–1539. https://doi.org/10.1093/ptj/66.10.1530
23. Bjornerem A et al (2011) Remodeling markers are associated with larger intracortical surface area but smaller trabecular surface area: a twin study. Bone 49(6):1125–1130. https://doi.org/10.1016/j.bone.2011.08.009
24. Thrift A et al (2000) Stroke incidence on the east coast of Australia: the North East Melbourne Stroke Incidence Study (NEMESIS). Stroke 31(9):2087–2092. https://doi.org/10.1161/01.STR.31.9.2087
25. Twisk J (2003) Applied longitudinal data analysis for epidemiology. A practical guide. Cambridge University Press, Cambridge
26. World Health Organization (2004) WHO Scientific Group on the assessment of osteoporosis at primary health care level
27. Seeman E (2003) The structural and biomechanical basis of the gain and loss of bone strength in women and men. Endocrinol Metab Clin N Am 32(1):25–38. https://doi.org/10.1016/S0889-8529(02)00078-6

28. Henry M et al (2010) Bone mineral density reference ranges for Australian men: geelong osteoporosis study. Osteoporos Int 21(6): 909–917. https://doi.org/10.1007/s00198-009-1042-7
29. Forster A, Young J (1995) Incidence and consequence of falls due to stroke: a systematic inquiry. BMJ 311(6997):83–86. https://doi.org/10.1136/bmj.311.6997.83
30. Australian Institute of Health and Welfare (2011) A snapshot of osteoporosis in Australia 2011. Arthritis series no. 15
31. Carin-Levy G, Greig C, Young A, Lewis S, Hannan J, Mead G (2006) Longitudinal changes in muscle strength and mass after acute stroke. Cerebrovasc Dis 21(3):201–207. https://doi.org/10.1159/000090792
32. English C, Hillier SL (2010) Circuit class therapy for improving mobility after stroke. Cochrane Database Syst Rev 7:CD007513
33. Sato Y, Kuno H, Kaji M, Etoh K, Oizumi K (2000) Influence of immobilization upon calcium metabolism in the week following hemiplegic stroke. J Neurol Sci 175(2):135–139. https://doi.org/10.1016/S0022-510X(00)00298-7
34. Paker N, Bugdayci D, Tekdos D, Dere C, Kaya B (2009) Relationship between bone turnover and bone density at the proximal femur in stroke patients. J Stroke Cerebrovasc Dis 18(2):139–143. https://doi.org/10.1016/j.jstrokecerebrovasdis.2008.09.013
35. Baecker N, Tomic A, Mika C, Gotzmann A, Platen P, Gerzer R, Heer M (2003) Bone resorption is induced on the second day of bed rest: results of a controlled crossover trial. J Appl Physiol 95(3): 977–982. https://doi.org/10.1152/japplphysiol.00264.2003
36. Turner C, Robling A (2003) Designing exercise regimens to increase bone strength. Exerc Sport Sci Rev 31(1):45–50. https://doi.org/10.1097/00003677-200301000-00009
37. Pang M, Ashe M, Eng J (2007) Muscle weakness, spasticity and disuse contribute to demineralization and geometric changes in the radius following chronic stroke. Osteoporos Int 18(9):1243–1252. https://doi.org/10.1007/s00198-007-0372-6

Check for updates

ORIGINAL ARTICLE

JBMR PLUS Open Access ASBMR

Increased Cortical Porosity and Reduced Trabecular Density Are Not Necessarily Synonymous With Bone Loss and Microstructural Deterioration

Roger Zebaze,[1,2] Elizabeth J Atkinson,[3] Yu Peng,[2] Minh Bui,[4] Ali Ghasem-Zadeh,[1] Sundeep Khosla,[3] and Ego Seeman[1,2,5]

[1]Departments of Medicine and Endocrinology, Austin Health, University of Melbourne, Melbourne, Australia
[2]Straxcorp Pty Ltd, Melbourne, Australia
[3]Mayo Clinic, Rochester, MN, USA
[4]Centre for Epidemiology and Biostatistics, School of Population and Global Health, University of Melbourne, Melbourne, Australia
[5]Mary Mackillop Institute for Health Research, Australian Catholic University, Melbourne, Australia

ABSTRACT

Absolute values of cortical porosity and trabecular density are used to estimate fracture risk, but these values are the net result of their growth-related assembly and age-related deterioration. Because bone loss affects both cortical and trabecular bone, we hypothesized that a surrogate measure of bone fragility should capture the age-related deterioration of both traits, and should do so independently of their peak values. Accordingly, we developed a structural fragility score (SFS), which quantifies the increment in distal radial cortical porosity and decrement in trabecular density relative to their premenopausal mean values in 99 postmenopausal women with forearm fractures and 105 controls using HR-pQCT. We expressed the results as odds ratios (ORs; 95% CI). Cortical porosity was associated with fractures in the presence of deteriorated trabecular density (OR 2.30; 95% CI, 1.30 to 4.05; $p = 0.004$), but not if trabecular deterioration was absent (OR 0.96; 95% CI, 0.50 to 1.86; $p = 0.91$). Likewise, trabecular density was associated with fractures in the presence of high cortical porosity (OR 3.35; 95% CI, 1.85 to 6.07; $p < 0.0001$), but not in its absence (OR 1.60; 95% CI, 0.78 to 3.28; $p = 0.20$). The SFS, which captures coexisting cortical and trabecular deterioration, was associated with fractures (OR 4.52; 95% CI, 2.17 to 9.45; $p < 0.0001$). BMD was associated with fracture before accounting for the SFS (OR 5.79; 95% CI, 1.24 to 27.1; $p = 0.026$), not after (OR 4.38; 95% CI, 0.48 to 39.9; $p = 0.19$). The SFS was associated with fracture before (OR 4.67; 95% CI, 2.21 to 9.88) and after (OR 3.94; 95% CI, 1.80 to 8.6) accounting for BMD (both $ps < 0.0001$). The disease of bone fragility is captured by cortical and trabecular deterioration: A measurement of coexisting cortical and trabecular deterioration is likely to identify women at risk for fracture more robustly than absolute values of cortical porosity, trabecular density, or BMD. © 2018 The Authors. *JBMR Plus* Published by Wiley Periodicals, Inc. on behalf of the American Society for Bone and Mineral Research

KEY WORDS: BONE MINERAL DENSITY; CORTICAL POROSITY; MICROSTRUCTURAL DETERIORATION; TRABECULAR DENSITY

Introduction

Fracture risk increases as BMD decreases.[1] However, the diagnostic threshold for osteoporosis, a BMD *T*-score at the femoral neck of −2.5 SDs, is insensitive; it fails to detect most postmenopausal women with fractures because they have osteopenia (*T*-score, −2.5 to −1.0 SD) or so-called normal BMD (> −1.0 SD).[2,3]

A plausible reason for a high fracture risk in postmenopausal women independent of BMD is the presence of microstructural deterioration.[4–6] All women lose bone as their age advances. In women with a high peak BMD, bone loss may only decrease BMD into the low normal or osteopenic range, while bone fragility increases disproportionately to the bone loss producing it and the modest reduction in BMD. The reason for this, as shown in ex vivo studies of bone specimens, is an increase in void volume (porosity) of a compact structure like cortical bone compromises strength as a seventh-power function of porosity, whereas an increase in void volume of an already porous structure like trabecular bone compromises bone strength as a third-power function of trabecular density.[7]

Quantifying microstructure is now feasible,[8] and measurement of cortical porosity and trabecular density does distinguish women with osteopenia with prevalent fractures from women

This is an open access article under the terms of the Creative Commons Attribution License, which permits use, distribution and reproduction in any medium, provided the original work is properly cited.
Received in original form July 17, 2018; revised form August 19, 2018; accepted August 28, 2018. Accepted manuscript online August 31, 2018.
Address correspondence to: Prof E Seeman, Department of Endocrinology, Centaur Building, Repatriation Campus, Austin Health, Waterdale Road, Heidelberg, 3084, VIC, Australia. E-mail: egos@unimelb.edu.au
JBMR® Plus (WOA), Vol. 3, No. 4, Month 2019, e10078.
DOI: 10.1002/jbm4.10078
© 2018 The Authors. *JBMR Plus* Published by Wiley Periodicals, Inc. on behalf of the American Society for Bone and Mineral Research

with osteopenia without fractures.[4–6] However, these findings have not been replicated in all studies,[9–12] perhaps because of unresolved challenges in image acquisition and analyses.

For example, regarding image acquisition, unbalanced remodeling upon intracortical canal surfaces increases cortical porosity. The porosity and the trabecularized fragments of cortex adjacent to the medullary canal are erroneously allocated to the medullary canal void volume by the image segmentation algorithm (rather than being confined to a cortico–trabecular transitional zone). The cortical porosity is measured as part of a seemingly expanded medullary canal, leading to an underestimate of the age-related increase in cortical porosity. The cortical fragments residing within the seemingly expanded medullary canal look like trabeculae, and are measured as part of the trabecular compartment, thus overestimating trabecular density and leaving women at high risk for fracture undetected.[13,14]

The second concern is the use of term "porosity." Porosity is not always synonymous with microstructural deterioration, nor is it always the consequence of bone loss or a cause of bone fragility. Absolute values of cortical porosity are the net result of the growth-related assembly of Haversian canals that are seen as "pores" in cortical cross-sections, and any age-related focal enlargement of the canals produced by unbalanced remodeling.[15,16–19] The canals are part of the osteonal microstructure that confers strength to bone by obstructing microcrack propagation.[20,21] If this "porosity" is erroneously attributed to bone loss and included in the calculation of porosity, women may be misclassified as being at risk for fracture.

The third concern is the need to measure both cortical and trabecular compartments. Finding deficits in both increases the likelihood that the deficits are based on bone loss because bone loss is global: It affects both cortical and trabecular compartments.[13,22] Measuring only one compartment may be misleading because this is likely because of errors in positioning of the region of interest (ROI) as reported elsewhere.[23] In brief, in an individual, a similar volume of mineralized bone matrix assembles adjacent cross-sections along a bone, what differs from cross-section to cross-section is the volume of void (medullary canal and cortical porosity) used to assemble larger and smaller cross-sections.[23,24]

As illustrated in Fig. 1, most of the mineralized bone matrix distally is assembled as trabecular bone; the cortices are thin and porous. Positioning the ROI too far distally results in a trait dissociation with high cortical porosity suggesting bone loss, but high trabecular density suggesting otherwise. Proximally, most of the same amount of mineralized bone matrix is assembled as cortical bone of low porosity, trabeculae are few or absent. Positioning the ROI too far proximally also results in a trait dissociation with low trabecular density suggesting bone loss, but low cortical porosity suggesting otherwise.

These concerns led us to develop a surrogate of bone fragility, a structural fragility score (SFS), a single measurement on a continuous scale that measures the concurrent deterioration in cortical porosity and trabecular density relative to their respective means in premenopausal women. The measurement is relatively free of growth-related determinants of bone strength and errors in positioning of the ROI. We hypothesized that the SFS would identify women with prevalent fractures, would do so with greater sensitivity and specificity than the absolute values of cortical porosity or trabecular density, and would do so independently of BMD; the predictive strength of BMD would be dependent on microstructural deterioration captured by the SFS.

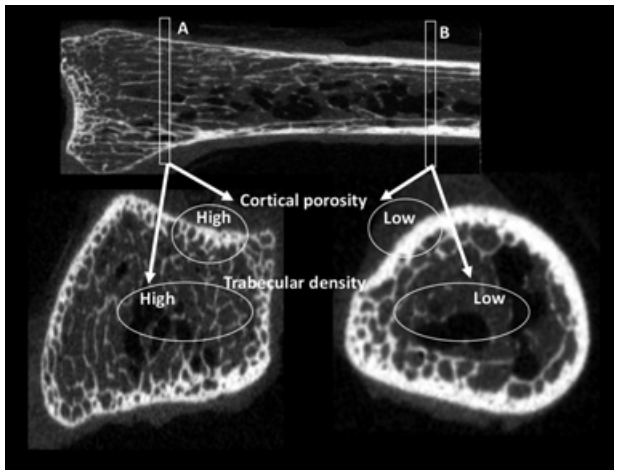

Fig. 1. If the region of interest (ROI) is too distal (position A), cortical porosity will be high, suggesting bone loss, whereas high trabecular density suggests no bone loss. If the ROI is too far proximally along the shaft, the porosity will be low, suggesting no bone loss, but low trabecular density suggests bone loss. Positioning error may produce misleading results (see text).

Subjects and Methods

Participants

As reported, we matched 99 postmenopausal women aged over 50 years with a distal forearm fracture with 105 controls from an age-stratified random sample from Olmsted County, Minnesota, USA.[5] Fracture occurred 7 (3 to 13) months (median interquartile range [IQR]) before measurement of microstructure. Fragility fracture was defined on the basis of moderate trauma from a fall from standing height or less. Controls had no history of a fracture after 35 years of age. The cohort was >96% white. The study was approved by the Mayo Clinic Institutional Review Board (Rochester, MN, USA), and the present analysis was based on deidentified data.

Imaging

Images at the ultradistal radius (on the unfractured side) were obtained using HR-pQCT (XtremeCT; Scanco Medical AG, Brüttisellen, Switzerland) with the X-ray source potential set to 60 kVp and a current of 900 μA. Stacks of 110 images (9.02 mm) were acquired with a voxel size of 82 μm.[8] Quality control was monitored by daily scans of phantoms (hydroxyapatite [HA] rods; QRM, Moehrendorf, Germany). Cortical porosity and trabecular density were measured using StrAx1.0 (StraxCorp, Melbourne, Australia).[13,14] StrAx1.0 is limited to the proximal 49 slices, where cortices at the thickest allow a more robust quantification of porosity. Femoral neck (FN) BMD was measured by DXA (Lunar Prodigy; GE Healthcare, Piscataway, NJ, USA).

Derivation of the SFS

We plotted trabecular density as a function of cortical porosity in 324 healthy ambulant premenopausal women aged 20 to 40 years and 33 postmenopausal women aged 50 to 90 years with fragility fractures in Melbourne, Australia (Fig. 2). Individuals

24734039, 2019, 4, Downloaded from https://asbmr.onlinelibrary.wiley.com/doi/10.1002/jbm4.10078 by National Health And Medical Research Council, Wiley Online Library on [17/06/2023]. See the Terms and Conditions (https://onlinelibrary.wiley.com/terms-and-conditions) on Wiley Online Library for rules of use; OA articles are governed by the applicable Creative Commons License

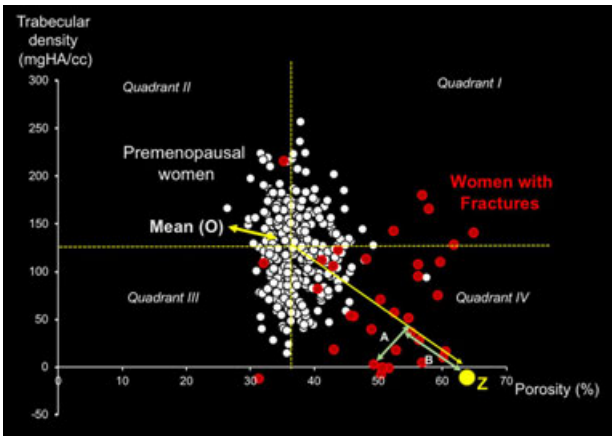

Fig. 2. Trabecular density as a function of cortical porosity in healthy premenopausal women (white dots) and postmenopausal women with fragility fractures (red dots). The mean of each trait in premenopausal women is denoted by "O," the intersection of the horizontal and vertical hatched lines. The line from O to Z is the mean of all the slopes of lines from 0 to each red dot. Quadrants I to IV depict different combinations of high and low trabecular density and cortical porosity (see text).

with cortical porosity and trabecular in quadrant I (high porosity, high trabecular density), quadrant II (low porosity, high trabecular density), or quadrant III (low porosity, low trabecular density) are unlikely to reflect bone loss because bone loss is global and affects both compartments, increasing cortical porosity and decreasing trabecular density. Thus, finding values in quadrant IV (high porosity, low trabecular density) is consistent with bone loss in both compartments, causing bone fragility. Most women with fractures have microstructure in this quadrant.

The SFS is derived by quantifying the coexisting absolute increment in cortical porosity and the absolute decrement trabecular density, relative to their peak values in premenopausal women as a continuous variable. The *x* and *y* coordinates at O are the mean of each trait in premenopausal women. The regression line U from O in the direction of increasing porosity and decreasing trabecular density is the average of all the slopes between point O and all *x* and *y* coordinates, representing absolute values in women with fractures. The length of U captures the absolute deterioration of an individual's cortical and trabecular bone while the slope captures deterioration in porosity relative to deterioration in trabecular density. The point Z along U identifies the maximum deterioration.

For individuals with *x* and *y* coordinates on U, length B measures the deterioration in both traits. The closer an individual's *x* and *y* coordinates are to U (distance A), the more likely there will be coexisting cortical and trabecular bone loss. Values above U reflect greater cortical than trabecular deficits relative to the young normal mean. Values below U reflect the reverse. For these individuals, the perpendicular length A plus length B to Z is a measure of the deterioration of that individual's bone microstructure. The lower (A + B), the closer to Z, the more severe the microstructural deterioration. For ease of comprehension, we express SFS as [100−(A + B)]; so the greater the SFS, the greater the cortical and trabecular deterioration and the higher the fracture risk. The precision of the SFS tests acquisition, repositioning, and coregistration in 15 women having three measurements at the distal radius and was 1.12% expressed as the root mean square of the coefficient of variation.

Statistical analysis

Thresholds used to calculate the odds ratios (ORs) for fracture were 90th centile for cortical porosity, 5th centile for trabecular density, −2.5 SD for BMD, and 70 for the SFS corresponding to the 90th percentile in premenopausal women. ORs were obtained from logistic regression models before and after adjustment for covariates. A $p < 0.05$ (two-tailed) denoted statistical significance.

Results

Among the women with forearm fractures, 10 (10.1%) had osteoporosis, 59 (59.6%) had osteopenia, and 30 (30.3%) had normal BMD. Women with prevalent fractures did not differ in age, but had higher cortical porosity, lower trabecular density, lower BMD, and higher SFS than controls (Table 1). There were significant age-related increments or decrements in cortical porosity, BMD, and the SFS, but not in trabecular density (Fig. 3). The age-related increment in the SFS was greater in women with fractures than in controls ($p = 0.02$).

Associations between microstructure and fractures depend on coexisting deficits in cortical and trabecular bone

Cortical porosity was associated with prevalent fractures before excluding women with deteriorated trabecular density (OR 2.30; 95% CI, 1.30 to 4.05; $p = 0.004$), not after (OR 0.96; 95% CI, 0.50 to 1.86; $p = 0.91$). Trabecular density was associated with prevalent fractures before excluding women with deteriorated cortical porosity (OR 3.35; 95% CI, 1.85 to −6.07; $p < 0.0001$), not after (OR 1.60; 95% CI, 0.78 to 3.28; $p = 0.20$). By contrast, the coexistence of an increment in cortical porosity and a decrement in trabecular density captured by a high SFS women was associated with prevalent fractures (OR 4.52; 95% CI, 2.17 to 9.45; $p < 0.0001$) (Fig. 4).

SFS is associated with fractures independent of BMD and outperforms BMD

As shown in detail in Table 2, BMD had a sensitivity of 10.1% and a specificity of 98.1% giving an OR of 5.79 ($p = 0.026$) before accounting for the contribution of the SFS. However, after accounting for the contribution of the SFS, BMD was no longer associated with fracture, having a sensitivity of 4.04%, a specificity of 99.0%, and an OR of 4.38 ($p = 0.19$). By contrast, the SFS has a sensitivity 35.4%, a specificity of 89.5%, and an OR of 4.67 ($p < 0.0001$) before accounting for the contribution of BMD, and a sensitivity of 29.3%, specificity of 90.5%, and an OR of 3.94% ($p < 0.0001$) after accounting for the contribution of BMD. The results were similar examining women with osteopenia or normal BMD (not shown).

Discussion

All traits, cortical porosity, trabecular density, BMD, and the SFS were associated with prevalent fractures. However, the association between cortical porosity or trabecular density and fracture was contingent upon the copresence of deficits in the other trait as captured by the SFS, which outperformed BMD.

24734039, 2019, 4, Downloaded from https://asbmr.onlinelibrary.wiley.com/doi/10.1002/jbm4.10078 by National Health And Medical Research Council, Wiley Online Library on [17/06/2023]. See the Terms and Conditions (https://onlinelibrary.wiley.com/terms-and-conditions) on Wiley Online Library for rules of use; OA articles are governed by the applicable Creative Commons License

Table 1. Characteristics of All Women With and Without Prevalent Fractures

	Fracture		Nonfracture		
	$N = 99$		$N = 105$		
	Median	IQR	Median	IQR	p value
Age (years)	63.00	14.00	62.00	14.00	0.392
Cortical porosity (%)	42.20	9.20	39.50	7.80	0.003
Trabecular density (mg HA/cc)	55.60	45.50	85.90	46.80	<0.0001
Femoral neck BMD *T*-score	−1.50	1.20	−0.95	1.46	0.0001
SFS (arbitrary unit)	61.60	28.10	51.70	20.40	0.0001

IQR = interquartile range; SFS = structural fragility score.

Early work investigating the microstructural basis of bone fragility focused on trabecular bone because these thin intersecting plates of mineralized bone matrix have a large surface area/matrix volume ratio that facilitates more rapid remodeling and bone loss than cortical bone, which is configured with a smaller surface area/matrix volume and so is remodeled and lost more slowly.[22] Subsequent research focused attention on cortical porosity as a cause of bone fragility because ~80% of the skeleton is cortical and ~80% of all bone loss is cortical. Most of this bone loss is the result of intracortical remodeling, which leaves cortical porosity as a "footprint" of the bone loss.[13]

Measurements of absolute values of cortical porosity and trabecular density do identify women with prevalent or incident fractures,[4–6] but do so inconsistently[9–12] for reasons that may partly relate to challenges in image acquisition and analysis.[13,14] We examined whether a measure of deterioration in both cortical and trabecular bone produces a more sensitive and specific assessment of fracture risk because both cortical and trabecular compartments of bone contribute to bone strength,[7] and unbalanced remodeling, appearing in midlife upon intracortical, endocortical, and trabecular surfaces, causes concurrent cortical and trabecular bone loss, producing microstructural deterioration and fragility of both compartments.[13,22–26]

We developed an algorithm that quantifies coexisting cortical and trabecular deterioration—the deviation from the nadir of cortical porosity and the deviation from the peak trabecular

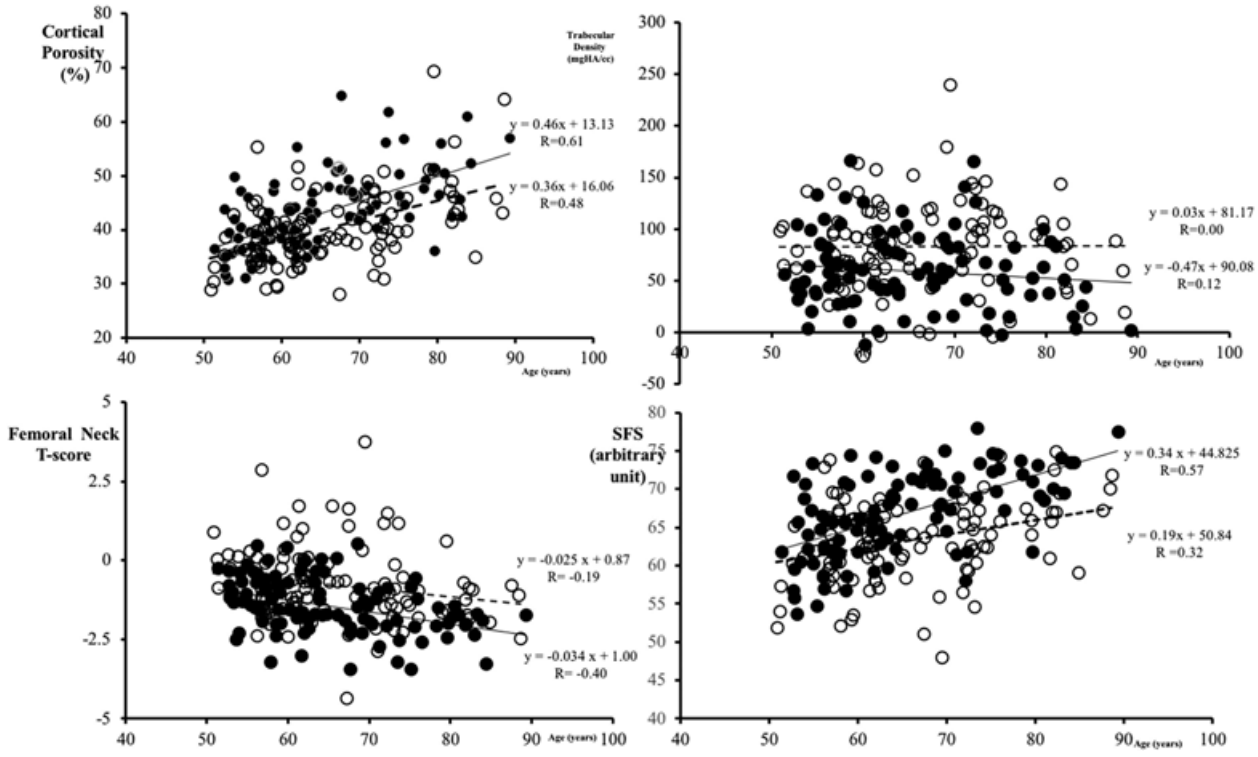

Fig. 3. Advancing age in women with fractures and controls was associated with increments in cortical porosity ($r = 0.61$ and 0.48, respectively; both $ps < 0.0001$), not trabecular density, decrements in BMD ($r = -0.4$, $p < 0.0001$, -0.19, respectively, $p = 0.05$), and increments in structural fragility score (SFS; $r = 0.57$ and 0.32, respectively; both $ps < 0.0001$). The increment in SFS was greater in women with fractures than in controls ($p = 0.02$).

24734039, 2019, 4, Downloaded from https://asbmr.onlinelibrary.wiley.com/doi/10.1002/jbm4.10078 by National Health And Medical Research Council, Wiley Online Library on [17/06/2023]. See the Terms and Conditions (https://onlinelibrary.wiley.com/terms-and-conditions) on Wiley Online Library for rules of use; OA articles are governed by the applicable Creative Commons License

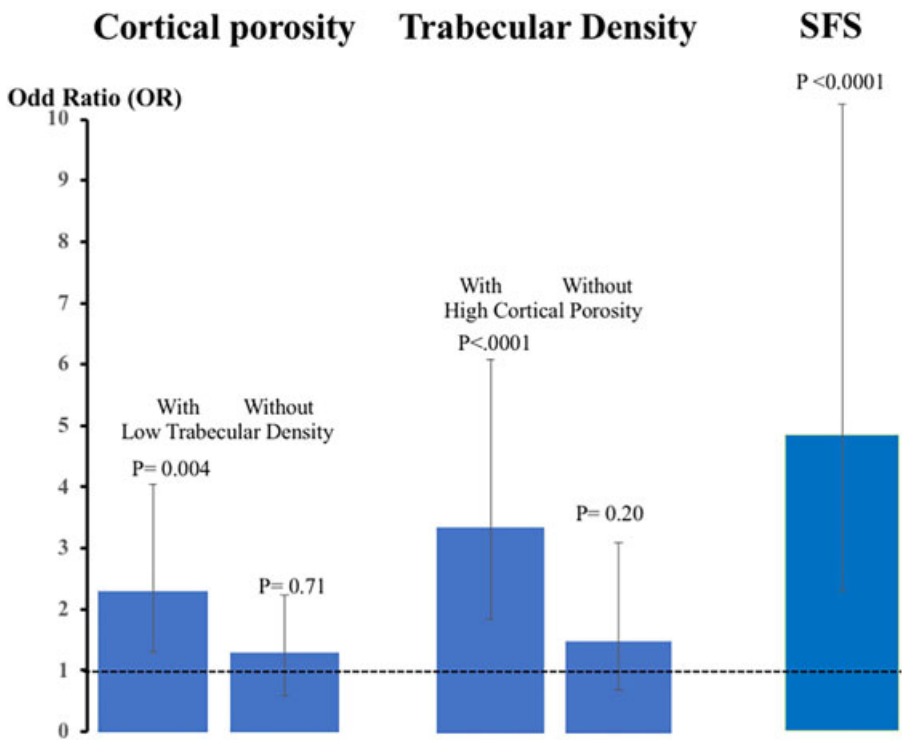

Fig. 4. Cortical porosity was associated with prevalent fractures before, not after, women with deteriorated trabecular density were excluded. Trabecular density was associated with prevalent fractures before, not after, women with deteriorated cortical porosity were excluded. The coexistence of an increment in cortical porosity and a decrement in trabecular density captured by a high structural fragility score was associated with prevalent fractures.

density achieved in young adulthood and subsequently deteriorated by bone loss. We proposed that expressing the deterioration of these traits captures the microstructural basis of bone fragility and minimizes the contribution of peak microstructure.

We also wanted to ensure that the porosity measured was the result of bone loss, not the void volume formed by intracortical canals assembled during growth. Over 80% of the measured porosity is void volume formed by these canals seen as pores in cross-section.[17–19] The porosity of interest is the age-related increment above that achieved during growth. The void formed by canals assembled during growth are a surrogate of bone strength because they are part of the hierarchical structure of the osteon, the bone structural unit. The canal, the surrounding concentric lamellae of mineralized collagen fibers, and the cement line surrounding the osteon and separating it from interosteonal (interstitial) bone form edges or discontinuities, deflecting or obstructing the propagation of microcracks through bone.[20,21]

As another potential source of error, we needed to ensure that there was coexisting cortical and trabecular deterioration because coexisting deficits are more likely to be the result of bone loss than measurement error as discussed in the Introduction and elsewhere.[23] The data confirm that isolated deficits, high porosity with normal/high trabecular density, or low trabecular density with normal/low porosity were not associated with prevalent fractures.

This study has several limitations. Coexisting deficits with an increment in porosity and decrement in trabecular density are likely to be the result of bone loss, but we cannot entirely exclude a contribution of growth, even though we attempted to minimize any contribution of growth to the deficits observed. Cortical porosity and trabecular density were used to quantify

Table 2. Sensitivity, Specificity, and Odds Ratios for the Associations Between BMD, the Structural Fragility Score (SFS), and Fracture Prevalence Before and After Accounting for the Contribution of the Other Predictor

Sensitivity (%) (95% CI)		Specificity (%) (95% CI)		Odd ratios (95% CI; p value)	
Before	After	Before	After	Before	After
BMD before and after accounting for the contribution of the SFS					
10.10 (4.95–17.80)	4.04 (1.11–10.00)	98.10 (93.30–99.80)	99.00 (94.80–100)	5.79 (1.24–27.10; $p = 0.026$)	4.38 (0.48–39.90; $p = 0.19$)
The SFS before and after accounting for the contribution of BMD					
35.40 (26.00–45.60)	29.30 (20.60–39.30)	89.50 (82.00–94.70)	90.50 (83.20–95.30)	4.67 (2.20–9.88; $p < 0.0001$)	3.94 (1.80–8.61; $p = 0.001$)

24734039, 2019, 4, Downloaded from https://asbmr.onlinelibrary.wiley.com/doi/10.1002/jbm4.10078 by National Health And Medical Research Council, Wiley Online Library on [17/06/2023]. See the Terms and Conditions (https://onlinelibrary.wiley.com/terms-and-conditions) on Wiley Online Library for rules of use; OA articles are governed by the applicable Creative Commons License

structural deterioration. However, other traits, such as cortical area, thickness, trabecular number, thickness, and separation, as well as matrix mineral density, may each contribute to bone fragility. Further work is needed to explore the role of other traits singly and in combination. Measurements of the unfractured arm were done at a median of 7 months (IQR 3 to 13) postfracture. Changes in microstructure may have followed rather than preceded a fracture, but are likely to be modest and if found to be higher because of greater post-fracture usage than controls, the observed deficits in cases would be a conservative error.

In summary, unbalanced remodeling at points upon the intracortical surface lining the many Haversian and Volkmann canals produces enlarged, coalesced irregularly shaped cavities, which form stress "concentrators" increasing the focal strain and promoting microcrack propagation.[27] Unbalanced remodeling upon trabecular surfaces perforate and reduce trabecular density.[25–28] The SFS captured deterioration in cortical and trabecular bone and identified women with a prevalent fracture independent of BMD and outperformed current methods such as absolute values of cortical porosity, trabecular density, or BMD alone. The measurement of SFS compliments the measurement of BMD by capturing deterioration in cortical and trabecular microstructure and so identifies women with osteopenia or so-called normal BMD at risk for fracture who would otherwise be regarded as being at low risk based on their BMD alone. Preliminary studies published in abstract form suggest the assessment of microstructure is likely to identify women with osteopenia at risk for fracture.[29] Further studies are needed to demonstrate the SFS serves as a surrogate of bone fragility able to identify women at risk, so that treatment can be targeted to those at imminent risk within 1 to 2 years before the first or a subsequent fracture.

Disclosures

RZ has received grant or research support from Amgen, Asahi, Genzyme; he is a shareholder and a director of the board of Straxcorp. ES has received research support and lecture fees from Amgen, Allergan, Eli Lilly; he is a consultant, director of the board, and shareholder in Straxcorp. YP is an employee of Straxcorp. AG is a shareholder in Straxcorp.

Acknowledgments

Authors' roles: RZ, ES, SK, and EA contributed to the design, analysis, and writing of the manuscript; EA and SK recruited subjects; AG, RZ, and YP provided image analysis; MB did the statistical analysis.

References

1. Kanis JA. Assessment of fracture risk and its application to screening for postmenopausal osteoporosis: synopsis of a WHO report. WHO Study Group. Osteoporos Int. 1994;4(6):368–81.
2. Siris ES, Chen YT, Abbott TA, et al. Bone mineral density thresholds for pharmacological intervention to prevent fractures. Arch Intern Med. 2004;164:1108–12.
3. Pasco JA, Seeman E, Henry MJ, et al. The population burden of fractures originates in women with osteopenia, not osteoporosis. Osteoporos Int. 2006;17:1404–9.
4. Boutroy S, Bouxsein ML, Munoz F, Delmas PD. In vivo assessment of trabecular bone microarchitecture. J Clin Endocrinol Med. 2005;90: 6508–15.
5. Bala Y, Zebaze R, Ghasem-Zadeh A, et al. Cortical porosity identifies women with osteopenia at increased risk for forearm fractures. J Bone Miner Res. 2014;2:1356–66.
6. Åhmed LA, Ghasem-Zadeh A, Bala Y, Zebaze R, Seeman E, Bjørnerem Å. Measurement of cortical porosity of the proximal femur improves identification of women with nonvertebral fragility fractures. Osteop Intern. 2015; 26: 2137–46.
7. Schaffler MB, Burr DB. Stiffness of compact bone: effects of porosity and density. J Biomech. 1988;21:13–6.
8. Laib A, Hauselmann HJ, Ruegsegger P. In vivo high resolution 3D-QCT of the human forearm. Technol Health Care. 1998;6(5–6):329–37.
9. Biver E, Durosier-Izart C, van Rietbergen B, Rizzoli R, Ferrari S. Evaluation of radius microstructure and areal bone mineral density improves fracture prediction in postmenopausal women. J Bone Miner Res. 2018;33(2):328–37.
10. Sornay-Rendu E, Boutroy S, FranScois Duboeuf F, Chapurlat RD. Bone microarchitecture assessed by HR-pQCT as predictor of fracture risk in postmenopausal women: the OFELY Study. J Bone Miner Res. 2017;32(6):1243–51.
11. Ohlsson C, Sundh D, Wallerek A, et al. Cortical bone area predicts incident fractures independently of areal bone mineral density in older men. J Clin Endocrinol Metab. 2017;102(2):516–24.
12. Chevalley T, Bonjour JP, van Rietbergen BV, Ferrari S, Rizzoli R. Fracture history of healthy premenopausal women is associated with a reduction of cortical microstructural components at the distal radius. Bone. 2013;55:377–83.
13. Zebaze RM, Ghasem-Zadeh A, Bohte A, et al. Intracortical remodelling and porosity in the distal radius and post-mortem femurs of women: a cross-sectional study. Lancet. 2010;375:1729–36.
14. Zebaze R, Ghasem-Zadeh A, Mbala A, Seeman E. A new method of segmentation of compact-appearing, transitional and trabecular compartments and quantification of cortical porosity from high resolution peripheral quantitative computed tomographic images. Bone. 2013;54:8–20.
15. Seeman E. Growth in bone mass and size: are racial and gender differences in bone mineral density more apparent than real? J Clin Endocrinol Metab. 1998;83(5):1414–9.
16. Hui SL, Slemebda CW, Johnston CC. Baseline measurement of bone mass predicts fracture in white women. Ann Intern Med. 1989;111:355–61.
17. Techawiboonwong A, Song HK, Leonard MB, Wehrli FW. Cortical bone water: in vivo quantification with ultrashort echo-time MR imaging. Radiology. 2008;248(3):824–33.
18. Smith JW. Observations on the water content of bone. J Bone Joint Surg Br. 1964; 46: 553–62.
19. Cowin SC, Gailani G, Benalla M. Hierarchical poroelasticity: movement of interstitial fluid between porosity levels in bones. Philos Trans A Math Phys Eng Sci. 2009;367:3401–44.
20. Vashishth D, Tanner KE, Bonfeld W. Contribution, development and morphology of microcracking in cortical bone during crack propagation. J Biomech. 2000;33:1169–74.
21. Yeni YN, Brown CU, Wang Z, Norman TL. The influence of bone morphology on fracture toughness of the human femur and tibia. Bone. 1997;21(5):453–9.
22. Bjornerem A, Ghasem-Zadeh A, Minh B, et al. Remodeling markers are associated with larger intracortical surface area but smaller trabecular surface area: a twin study. Bone. 2011;49(6):1125–30.
23. Ghasem-Zadeh A, Burghardt A, Wang XF, et al. Quantifying sex, race, and age specific differences in bone microstructure requires measurement of anatomically equivalent regions. Bone. 2017;101:206–13.
24. Zebaze RM, Jones A, Welsh F, Knackstedt M, Seeman E. Femoral neck shape and the spatial distribution of its mineral mass varies with its size: clinical and biomechanical implications. Bone. 2005;37(2):243–52.
25. Bjornerem A, Wang X, Bui M, et al. Menopause-related appendicular bone loss is mainly cortical and results in increased cortical porosity. J Bone Miner Res. 2018 Apr;33(4):598–605. doi:10.1002/jbmr.3333
26. Khosla S, Riggs BL, Atkinson EJ, et al. Effects of sex and age on bone microstructure at the ultradistal radius: a population-based

24734039, 2019, 4, Downloaded from https://asbmr.onlinelibrary.wiley.com/doi/10.1002/jbm4.10078 by National Health And Medical Research Council, Wiley Online Library on [17/06/2023]. See the Terms and Conditions (https://onlinelibrary.wiley.com/terms-and-conditions) on Wiley Online Library for rules of use; OA articles are governed by the applicable Creative Commons License

noninvasive in vivo assessment. J Bone Miner Res. 2006;21(1): 124–31.

27. Hernandez CJ, Gupta A, Keaveny TM. A biomechanical analysis of the effects of resorption cavities on cancellous bone strength. J Bone Miner Res. 2006;21:1248–55.
28. van der Linden JC, Homminga J, Verhaar JA, et al. Mechanical consequences of bone loss in cancellous bone. J Bone Miner Res. 2001;16(3):457–65.
29. Proriol M, Merle B, Vignoti E, et al. Radius microarchitecture measured by HRpQCT predicts incident fragility fracture in the subset of women with moderately decreased BMD–The QUALYOR Cohort. J Bone Miner Res. 2017;32 Suppl 1. [Poster session presented at: Annual Meeting American Society for Bone and Mineral Research (ASBMR); 2017 Sep 8–11; Denver, CO; Presentation Number: 1084]. Available from: http://www.asbmr.org/meetings/annualmeeting.aspx.

24734039, 2019, 4, Downloaded from https://asbmr.onlinelibrary.wiley.com/doi/10.1002/jbm4.10078 by National Health And Medical Research Council, Wiley Online Library on [17/06/2023]. See the Terms and Conditions (https://onlinelibrary.wiley.com/terms-and-conditions) on Wiley Online Library for rules of use; OA articles are governed by the applicable Creative Commons License

Bone 128 (2019) 115039

Contents lists available at ScienceDirect

Bone

journal homepage: www.elsevier.com/locate/bone

Full Length Article

Dimorphism in axial and appendicular dimensions, cortical and trabecular microstructure and matrix mineral density in Chinese and Caucasian women

Xiao-Fang Wang[a,*], Ali Ghasem-Zadeh[a], Bin Zhou[b], X. Edward Guo[b], Zhendong Zhang[b], Ego Seeman[a,c]

[a] Departments of Medicine and Endocrinology, Austin Health, University of Melbourne, Melbourne, Australia
[b] Bone Bioengineering Laboratory, Department of Biomedical Engineering, Columbia University, New York, NY, USA
[c] Mary MacKillop Institute of Heathly Aging, Australian Catholic University, Melbourne, Australia

ARTICLE INFO

Keywords:
Bone microstructure
Chinese
Caucasians
Females
Racial dimorphism

ABSTRACT

Introduction: Appendicular fractures are less common in Chinese than Caucasian women. Bone mineral density (BMD) is lower, not higher than in Caucasians because Chinese have smaller appendicular dimensions than Caucasians. However, smaller bones may offset the liability to fracture by being assembled with a more robust microstructure. We hypothesized that Chinese assemble an appendicular skeleton with a thicker, less porous and more mineralized cortex that is less deteriorated in advanced age than in Caucasians.

Methods: We compared anthropometry in 477 Chinese and 278 Caucasian women and compared bone microstructure using high-resolution peripheral quantitative computed tomography in another cohort of 186 Chinese and 381 Caucasian women aged 18 to 86 years, all living in Melbourne, Australia. Trabecular plate (p) and rod (r) bone volume/total volume (BV/TV) were quantified using individual trabecula segmentation (ITS). Bone strength was estimated using micro-finite element analysis (μFEA).

Results: Premenopausal Chinese were shorter than Caucasian women, mainly due to shorter leg length. Distal radial total cross sectional area (CSA) was 14.8% smaller ($p < 0.001$). After adjusting for age and total CSA, Chinese had similar cortical and medullary areas but 0.30 SD lower cortical porosity and 0.27 SD higher matrix mineral density (both $p < 0.05$). Trabecular plate-to-rod ratio was 0.55 SD higher due to a 0.41 SD higher pBV/TV and 0.36 SD lower rBV/TV (p ranging 0.001 to 0.023). Chinese also had 0.36 SD greater whole bone stiffness and 0.36 SD greater failure load than Caucasians (both $p < 0.05$). After adjusting for age and total CSA, postmenopausal Chinese had 3.3% smaller cortical area, medullary area was 2.1% larger, cortical porosity was no lower, matrix mineral density and pBV/TV were no higher compared with Caucasians at the distal radius. Whole bone stiffness was 0.39 SD lower and failure load was 0.40 SD lower in Chinese (both $p < 0.05$).

Conclusion: Chinese build a more robust skeleton than Caucasians during growth, an advantage not observed in advanced age due to greater bone loss or race-specific secular trends in bone morphology.

1. Introduction

The incidence of appendicular fractures is lower in Chinese than Caucasians [1–3]. This is not explained by the racial differences in bone mineral density (BMD). Indeed, BMD is lower, not higher than in Caucasians because Chinese have smaller appendicular dimensions than Caucasians [4]. However, resistance to fracturing of a smaller skeleton may be achieved by assembling it more robustly during growth; forming thicker cortices relative to the total cross-sectional area with lower porosity and thicker more connected trabeculae of the metaphyseal region in Chinese [5]. Shorter stature or leg length in Chinese may also be associated with better balance and a lower impact following a fall [6].

Quantification of racial differences in bone microstructure is challenging because meticulous attention is needed in choosing the region of interest (ROI) [7]. In an individual, adjacent cross sections of a long bone are assembled using similar amounts of mineralized bone matrix [7,8]. What differs is how that mineralized matrix is fashioned as cortical and trabecular bone along the length of the bone. Distally the constant amount of material is mainly trabecular with a thin cortical shell whereas proximally in the metaphyseal-diaphyseal region and especially the midshaft more of the constant amount of mineralized

* Corresponding author at: Departments of Medicine and Endocrinology, Austin Health, PO Box 5444, West Heidelberg, 3081, Australia.
E-mail address: wang5@unimelb.edu.au (X.-F. Wang).

https://doi.org/10.1016/j.bone.2019.115039
Received 24 March 2019; Received in revised form 2 August 2019; Accepted 16 August 2019
Available online 19 August 2019
8756-3282/ © 2019 Elsevier Inc. All rights reserved.

matrix is assembled as cortical bone.

For racial comparisons to be valid, the same position of a ROI relative to the length of the bone must be compared. Chinese have a shorter appendicular skeleton than Caucasians. When a ROI of the distal radius or distal tibia is chosen using a fixed distance from the midpoint of the radio-carpal joint space, the ROI is positioned more proximally in Chinese [7]. The more proximal positioning exaggerates the racial difference described above; Chinese will have thicker less porous cortices, the matrix mineral density will be higher and trabecular density will be lower [7]. Several approaches can be taken to correct for this positioning error. The recommended approach is to use a percentage of the radial or tibial bone length (~4–6%). If this is not available, correcting for racial differences in bone length by racial differences in the total bone cross-sectional area (CSA) achieves similar accuracy as using the 4–6% of the bone length [7].

In addition, secular drifts in sitting and standing height are race specific. Height generally increases in more recently born individuals forming the young cohort in a cross sectional sample, but this may differ by race, body segment and sex [9,10]. If the secular increase in height is associated with secular trends towards an earlier puberty then the taller stature, irrespective of race, is likely to be due to greater trunk length (because leg length should be shorter if puberty occurs earlier in life in more recently born women).

We hypothesized that, (i) relative to Caucasians, Chinese are shorter mainly due to their shorter leg length, (ii) more recently born women of each race are taller than earlier born women, (iii) Chinese have an earlier menarche and so will have shorter leg length but comparable trunk length, (iv) across age, the taller stature in younger women is due to trunk length not leg length, irrespective of race, and (v) Chinese have lower cortical porosity, higher matrix mineral density, and higher trabecular plate to rod ratio than Caucasians after adjusted for total bone CSA.

2. Methods

2.1. Subjects

We studied anthropometry on 477 healthy Chinese and 278 Caucasians women and quantified bone microstructure in an additional 186 Chinese and 381 Caucasian women aged 18 to 86 years using high-resolution peripheral quantitative computed tomography (HR-pQCT). All women were ambulatory and recruited from the local community in Melbourne, Australia. They had no illness and received no medication known to affect bone mass or size, and had no history of fractures. About 70% of the Chinese were immigrants who arrived in Australia after aged 18 years with a mean stay of 13.4 years (range 1 month to 41 years) while 7% were born in Australia with parents from China. Approximately 90% were from Southern China and South-east Asia. Recalled age of menarche was recorded on the questionnaire. All participants gave informed consent. The study was approved by the Human Research Ethics Committee of the Austin Health.

2.2. Anthropometry

Standing and sitting heights were measured in the morning using a Holtain stadiometer. Sitting height was measured with the women sitting on a stool with the legs at right angles to the trunk [11]. Leg length was calculated by subtracting sitting from standing height. Arm span was measured by the method of Steele and Mattox [12]. Subjects stood straight with shoulder and heels against the wall. The arms were outstretched horizontally with the palms facing forwards. A calibrated extended ruler was used to measure the two points from the middle finger of the right hand to the middle finger of the left hand along the wall. Measurements were recorded to the nearest 0.1 cm.

Body mass was measured by an electronic scale and was recorded to the nearest 0.1 kg. Femur and tibia lengths were measured by using the ruler function in the total body images from DXA (DPX-L, Lunar Corp., Madison, WI, version 4.6). Femur length was the length of the central long axis of left femur from the junction of the upper rim of the femoral neck and the greater trochanter to the distal end of the intercondylar notch [13]. Tibia length was the distance between the medial condyle and the medial malleolus. The coefficient of variation was 1.5% based on three repeated scans in 10 subjects within three weeks.

2.3. Microstructure

The non-dominant distal radius and distal tibia were scanned using HR-pQCT (Xtreme CT, Scanco Medical AG, Switzerland). The default manufacturer protocol was used and the resolution was 82 μm isotropic voxel size [14]. The 110 slices were obtained at a fixed distance of 9.5 and 22.5 mm from the reference line that was manually placed at the middle point of the endplate of the distal radius and tibia, respectively. Of the 567 subjects had HRpQCT measurements, 8 had motion artefact at the radius and 14 had motion artefact at the tibia and were excluded. There were 559 radius scans and 542 tibia scans included in the analysis. Differing sample size in the radius and tibia was also the result of 11 subjects having only distal radial measurements.

Bone was segmented from background and into its compartments using StrAx1.0, a non-threshold-based segmentation algorithm [15,16]. The method automatically and reproducibly segments bone into the compact-appearing cortex, the outer and inner transitional zones, and trabecular bone. In each cortical compartment, porosity was quantified by estimating the void volume fraction of each voxel. Matrix mineral density is quantified by determining the mean density of voxels with attenuation between 80 and 100% of fully mineralized bone. The precision error was 0.8 to 4.0% [15]. The proximal 49 slices were included in the StrAx1.0 analysis for cortical assessment. Total, cortical and trabecular CSA, and cortical thickness were also quantified.

Individual trabecula segmentation (ITS) methods were applied to quantify trabecular plate and rod microarchitecture from HR-pQCT images of the distal radius and distal tibia. Trabecular elements were classified as a surface or curve that was then classified as a plate or rod [17,18]. Axial bone volume fraction (aBV/TV) along the longitudinal axis, plate and rod bone volume fraction (pBV/TV, rBV/TV), plate-to-rod (P-R) ratio, plate and rod number (pTb.N and rTb.N, 1/mm) and the average thickness of plates and rods (pTb.Th, rTb.Th, mm) were assessed [19,20].

2.4. Bone mechanical properties

Bone stiffness and failure load were estimated using micro-finite element analysis (μFEA) for each image. This was applied to the whole bone to determine axial stiffness. Each voxel was converted to an 8-node elastic brick voxel-based element (82 μm^3). For μFEA, bone tissue was modeled as an isotropic, linear elastic material with a Young's modulus (E_s) of 15 GPa and a Poisson's ratio of 0.3 [21].

2.5. Statistical analysis

Summary statistics were expressed as mean ± standard deviation (SD). Unpaired two-sample *t*-tests were used to determine the significance of trait differences between groups. Differences in standardized terms were calculated by dividing the mean difference between groups by the pooled SD for anthropometry, bone microstructural and mechanical parameters. Analyses were performed initially for each covariate to quantify any association with microstructure. The covariates selected for this study were age, height, body mass, total CSA. Those significant univariate relationships (age, height and total CSA) were then examined in a multivariable analysis. Height was then removed from the model due to its collinearity with total CSA. Analysis of Covariance (ANCOVA) was used to adjust for age and total CSA in cortical and trabecular parameters. T score defined as the number of

Table 1
Age, weight, and anthropometry measurements in pre- (18–45 years) and postmenopausal (55–86 years) Chinese and Caucasian women.

Variables	Premenopausal		Postmenopausal	
	Chinese (n = 146)	Caucasians (n = 153)	Chinese (n = 173)	Caucasians (n = 76)
Age (years)	35.4 ± 8.2	34.5 ± 7.8	64.5 ± 6.3[a]	65.9 ± 7.4[a]
Body mass (kg)	55.7 ± 9.1**	65.5 ± 12.9	56.7 ± 8.2**	68.4 ± 15.1
Height (cm)	158.2 ± 5.6**	164.0 ± 5.8	154.5 ± 5.2**[a]	159.7 ± 5.9[a]
Arm span (cm)	157.3 ± 6.7**	165.3 ± 6.6	154.1 ± 5.8**[a]	162.7 ± 6.3[a]
Arm span — height (cm)	−0.95 ± 3.35**	1.26 ± 3.31	−0.39 ± 3.33**	3.15 ± 3.46[a]
Sitting height (cm)	86.3 ± 3.1*	87.1 ± 2.9	83.6 ± 3.0[a]	84.0 ± 3.8[a]
Leg length (cm)	71.9 ± 3.6**	76.9 ± 3.9	71.0 ± 3.1**[a]	75.8 ± 3.7
Femur length (cm)	37.8 ± 1.9**	40.8 ± 2.2	37.6 ± 1.6**	40.6 ± 2.0
Tibia length (cm)	30.3 ± 1.7**	32.5 ± 2.0	29.6 ± 1.4**[a]	31.9 ± 1.9[a]

Mean ± standard deviation (SD). *$p < 0.05$, **$p < 0.001$ compared with Caucasians.
[a] $p < 0.05$ compared with premenopausal women.

SDs from the mean of premenopausal women of the same race. Associations between cortical porosity and matrix mineral density, trabecular BV/TV was analysed using Pearson's correlation. STATA 14.2 (StataCorp. 2015. Stata Statistical Software. College Station, TX: StataCorp LP.) was used for all statistical analyses and $p < 0.05$ (two tailed) was considered as significant.

3. Results

3.1. Racial dimorphism in premenopausal women

The age of menarche did not differ by race (Chinese 12.8 ± 1.3, Caucasians 13.0 ± 1.5 years). Chinese had 0.27 SD shorter sitting height, 1.31 SD shorter leg length (Table 1, Fig. 1), 14.8% smaller distal radial CSA, 7.9% smaller cortical area and 19.3% smaller medullary area. After adjusting for age and total CSA, Chinese and Caucasians had similar cortical and medullary areas but cortical vBMD was higher in Chinese because they had a 0.30 SD lower total cortical porosity and 0.27 SD higher matrix mineral density (Table 2, Fig. 2). Trabecular BV/TV did not differ by race but in Chinese, pBV/TV was 0.41 SD higher, rBV/TV was 0.36 SD lower producing a favorable P-R ratio ($p = 0.001$) (Fig. 2). Chinese had 0.36 SD greater whole bone stiffness and 0.36 SD greater failure load than Caucasians (both $p < 0.05$).

Findings were similar at the distal tibia (Table 3). Chinese had a 8.9% smaller total CSA, 6.5% smaller cortical area and 10.0% smaller medullary area. After adjusting for age and total CSA, Chinese had a

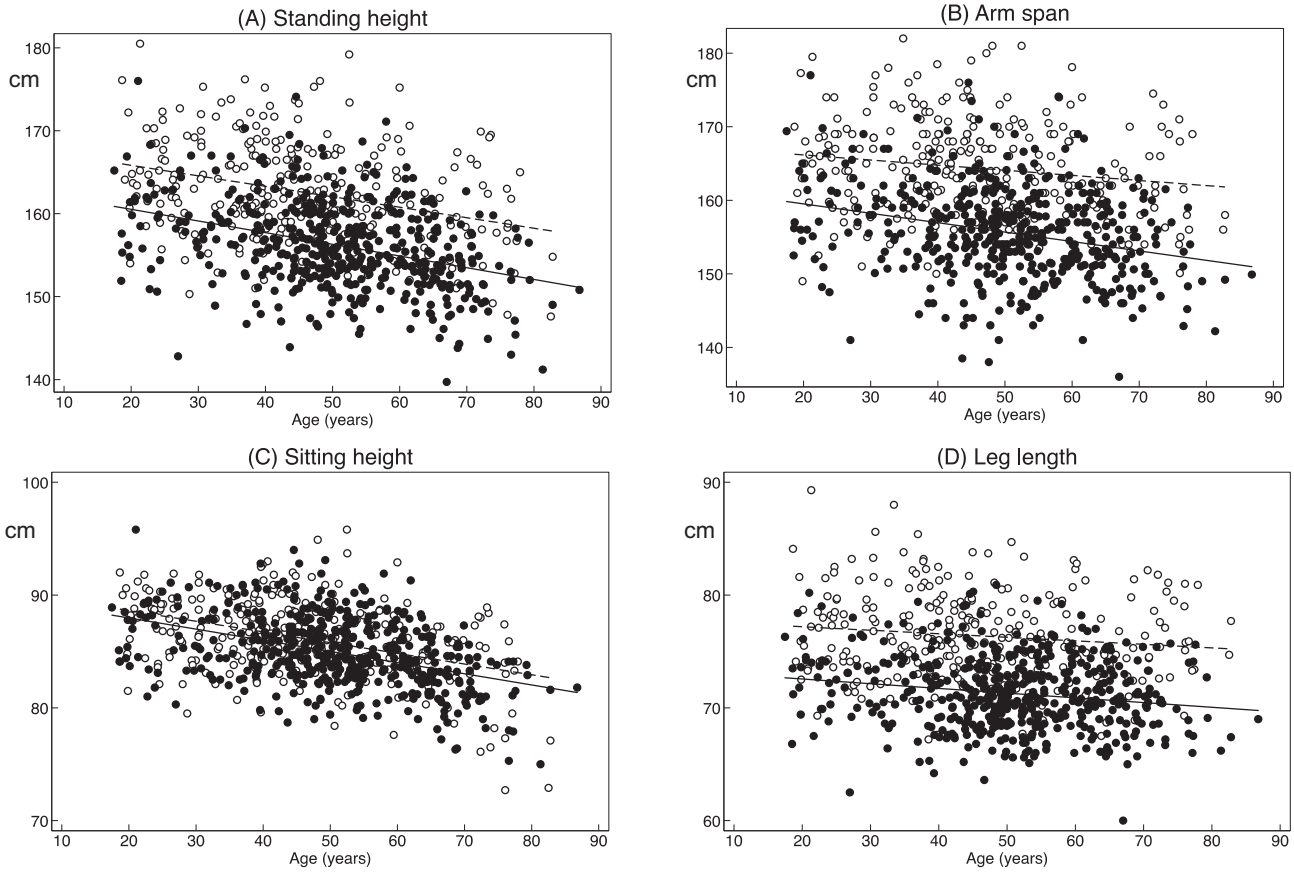

Fig. 1. The age-related differences in (A) standing height, (B) arm span, (C) sitting height and (D) leg length in Chinese (filled circles, solid line) and Caucasian (open circles, dashed line) women.

Table 2
Distal radius microstructure in pre- and postmenopausal Chinese and Caucasian women.

	Premenopausal				Postmenopausal			
	Chinese (n = 67)	Caucasian (n = 155)	*p*	Adj. *p*	Chinese (n = 51)	Caucasian (n = 131)	*p*	Adj. *p*
Age (years)	37.8 ± 8.3	35.6 ± 7.3	0.053		65.0 ± 7.9	64.1 ± 7.2	0.449	
Age at menarche (years)	12.8 ± 1.3	13.0 ± 1.5	0.344		13.7 ± 2.1	13.2 ± 1.3	0.054	
Distal radial CSA								
Total (mm^2)	189.3 ± 32.0	222.1 ± 38.5	< 0.001		198.2 ± 38.2	214.7 ± 37.1	0.009	
Cortical area (mm^2)	80.5 ± 8.7	87.4 ± 9.9	< 0.001	0.325	77.2 ± 8.0	83.2 ± 11.0	< 0.001	0.031
Cortical/total CSA	0.43 ± 0.05	0.40 ± 0.05	< 0.001	0.787	0.40 ± 0.06	0.39 ± 0.05	0.507	0.127
Medullary (mm^2)	108.7 ± 26.8	134.7 ± 32.2	< 0.001	0.325	121.1 ± 33.2	131.5 ± 30.7	0.046	0.031
C.Th (mm)	1.80 ± 0.18	1.81 ± 0.21	0.758	0.129	1.68 ± 0.17	1.76 ± 0.19	0.012	0.003
Cortical porosity (%)								
TC	48.2 ± 4.9	53.0 ± 5.4	< 0.001	0.011	56.5 ± 7.2	56.4 ± 6.2	0.980	0.276
CC	32.4 ± 3.4	35.5 ± 4.0	< 0.001	0.030	40.1 ± 6.1	40.3 ± 6.2	0.789	0.590
Outer TZ	36.8 ± 2.9	39.0 ± 3.2	< 0.001	0.110	45.1 ± 5.6	44.2 ± 5.4	0.292	0.100
Inner TZ	84.4 ± 2.8	85.0 ± 2.8	0.106	0.608	87.6 ± 3.0	86.1 ± 2.9	0.002	< 0.001
MMD (%)	67.3 ± 1.5	66.2 ± 1.5	< 0.001	0.044	65.6 ± 1.8	65.8 ± 1.7	0.348	0.084
Trabecular bone								
BV/TV	0.257 ± 0.046	0.248 ± 0.054	0.195	0.453	0.192 ± 0.058	0.231 ± 0.058	< 0.001	< 0.001
aBV/TV	0.113 ± 0.035	0.096 ± 0.033	0.001	0.009	0.074 ± 0.027	0.085 ± 0.028	0.021	0.012
pBV/TV	0.109 ± 0.045	0.086 ± 0.040	< 0.001	0.008	0.070 ± 0.031	0.077 ± 0.034	0.213	0.098
rBV/TV	0.148 ± 0.029	0.161 ± 0.031	0.004	0.023	0.121 ± 0.038	0.154 ± 0.035	< 0.001	< 0.001
P-R ratio	0.78 ± 0.43	0.55 ± 0.30	< 0.001	0.001	0.60 ± 0.23	0.51 ± 0.22	0.010	0.057
pTb.N (1/mm)	1.42 ± 0.16	1.36 ± 0.18	0.014	0.057	1.24 ± 0.17	1.31 ± 0.18	0.019	0.010
rTb.N (1/mm)	1.77 ± 0.15	1.84 ± 0.15	0.003	0.026	1.65 ± 0.22	1.82 ± 0.17	< 0.001	< 0.001
pTb.Th (mm)	0.214 ± 0.009	0.206 ± 0.008	< 0.001	< 0.001	0.211 ± 0.009	0.208 ± 0.008	0.049	0.176
rTb.Th (mm)	0.215 ± 0.008	0.213 ± 0.006	0.083	0.176	0.209 ± 0.005	0.210 ± 0.006	0.172	0.268
Mechanical properties								
Whole stiffness (N/mm)	86,633 ± 16,011	83,321 ± 18,822	0.210	0.019	60,609 ± 14,947	69,001 ± 17,605	0.003	0.016
Failure load (N)	4115 ± 726	3998 ± 847	0.325	0.020	2880 ± 691	3294 ± 810	0.002	0.011

Mean ± standard deviation (SD). Adj. *p*: adjusted *p* values for racial comparisons were all adjusted for age and total CSA (Premenopausal: at age = 36.3 and total CSA = 212.2; Postmenopausal: at age = 64.3 and total CSA = 210.1). C.Th: cortical thickness; TC: total cortex; CC: compact-appearing cortex; TZ: transitional zone; BV/TV: bone volume/total volume; Tb. Th: trabecular thickness; Tb. N: trabecular number.

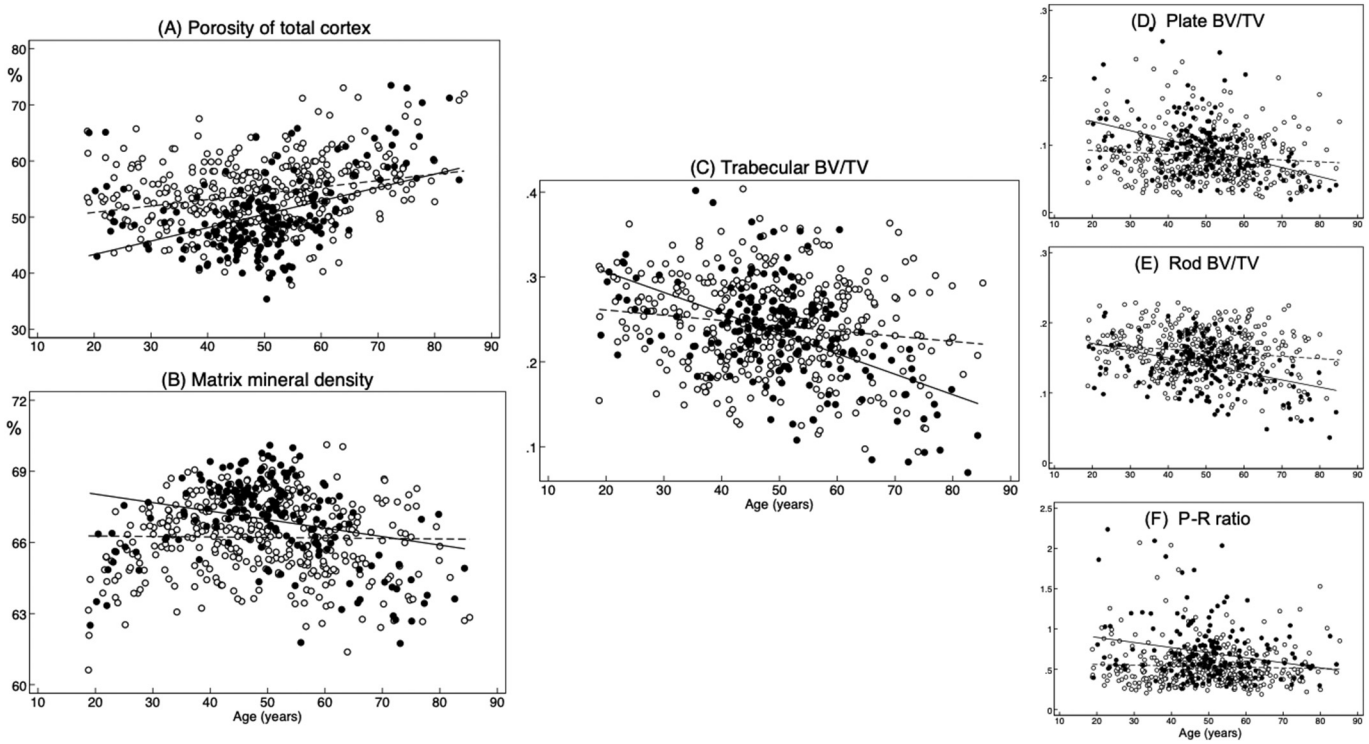

Fig. 2. The age-related differences in (A) porosity of the total cortex and (B) matrix mineral density at the distal radius in Chinese women (filled circles, solid line) and Caucasians (open circles, dashed line). The age-related differences in (C) trabecular BV/TV, (D) plate BV/TV, (E) rod BV/TV and (F) P-R ratio at the distal radius in Chinese women (filled circles, solid line) and Caucasians (open circles, dashed line).

Table 3
Distal tibia microstructure in pre- and postmenopausal Chinese and Caucasian women.

	Premenopausal				Postmenopausal			
	Chinese (n = 65)	Caucasian (n = 151)	*p*	Adj. *p*	Chinese (n = 49)	Caucasian (n = 125)	*p*	Adj. *p*
Age (years)	37.8 ± 8.4	35.8 ± 7.3	0.082		65.2 ± 7.9	64.1 ± 7.3	0.364	
Distal tibial CSA								
Total (mm^2)	568.3 ± 89.4	623.7 ± 118.2	0.001		597.8 ± 110.1	634.5 ± 103.8	0.041	
Cortical area (mm^2)	188.4 ± 20.2	201.6 ± 23.8	< 0.001	0.020	188.8 ± 20.7	194.9 ± 25.0	0.136	0.612
Cortical/total CSA	0.34 ± 0.05	0.33 ± 0.05	0.387	0.015	0.32 ± 0.05	0.31 ± 0.05	0.218	0.824
Medullary (mm^2)	379.8 ± 82.6	422.1 ± 104.7	0.004	0.020	409.0 ± 101.3	439.6 ± 96.7	0.066	0.612
C.Th (mm)	2.27 ± 0.27	2.32 ± 0.26	0.209	0.014	2.22 ± 0.26	2.21 ± 0.30	0.891	0.652
Cortical porosity (%)								
TC	55.1 ± 4.0	58.0 ± 4.6	< 0.001	0.003	65.9 ± 6.1	65.2 ± 6.3	0.533	0.130
CC	35.8 ± 3.4	38.8 ± 4.2	< 0.001	< 0.001	48.6 ± 6.2	49.4 ± 8.2	0.472	0.911
Outer TZ	37.8 ± 2.7	40.3 ± 3.2	< 0.001	< 0.001	50.9 ± 6.3	49.8 ± 7.2	0.345	0.136
Inner TZ	83.7 ± 2.9	84.3 ± 3.1	0.191	0.286	87.7 ± 2.9	86.4 ± 2.8	0.010	0.003
MMD (%)	66.6 ± 1.1	65.7 ± 1.3	< 0.001	0.001	63.7 ± 1.6	64.1 ± 1.6	0.098	0.052
Trabecular bone								
BV/TV	0.267 ± 0.048	0.274 ± 0.054	0.324	0.818	0.220 ± 0.059	0.264 ± 0.049	< 0.001	< 0.001
pBV/TV	0.151 ± 0.048	0.122 ± 0.044	< 0.001	< 0.001	0.118 ± 0.043	0.113 ± 0.038	0.451	0.577
rBV/TV	0.116 ± 0.032	0.152 ± 0.038	< 0.001	< 0.001	0.101 ± 0.032	0.151 ± 0.039	< 0.001	< 0.001
aBV/TV	0.139 ± 0.036	0.116 ± 0.032	< 0.001	< 0.001	0.109 ± 0.035	0.110 ± 0.027	0.899	0.794
P-R ratio	1.44 ± 0.75	0.87 ± 0.49	< 0.001	< 0.001	1.27 ± 0.64	0.82 ± 0.39	< 0.001	< 0.001
pTb.N (1/mm)	1.49 ± 0.12	1.46 ± 0.15	0.204	0.050	1.38 ± 0.17	1.44 ± 0.14	0.013	0.015
rTb.N (1/mm)	1.63 ± 0.18	1.81 ± 0.19	< 0.001	< 0.001	1.54 ± 0.21	1.81 ± 0.20	< 0.001	< 0.001
pTb.Th (mm)	0.229 ± 0.014	0.222 ± 0.012	< 0.001	0.001	0.228 ± 0.011	0.220 ± 0.012	< 0.001	< 0.001
rTb.Th (mm)	0.213 ± 0.007	0.213 ± 0.007	0.950	0.938	0.214 ± 0.007	0.212 ± 0.007	0.198	0.196
Mechanical properties								
Whole stiffness (N/mm)	242,687 ± 46,335	239,671 ± 55,657	0.702	0.030	188,570 ± 57,085	205,462 ± 44,706	0.040	0.156
Failure load (N)	11,258 ± 2129	11,160 ± 2499	0.784	0.033	8770 ± 2575	9626 ± 1999	0.021	0.100

Mean ± standard deviation (SD). Adj. *p*: adjusted p values for racial comparisons were all adjusted for age and total CSA (premenopausal: at age = 36.4 and total CSA = 607.0; postmenopausal: at age = 64.4 and total CSA = 624.2). C.Th: cortocal thickness; TC: total cortex; CC: compact-appearing cortex; TZ: transitional zone; BV/TV: bone volume/total volume; Tb. Th: trabecular thickness; Tb. N: trabecular number.

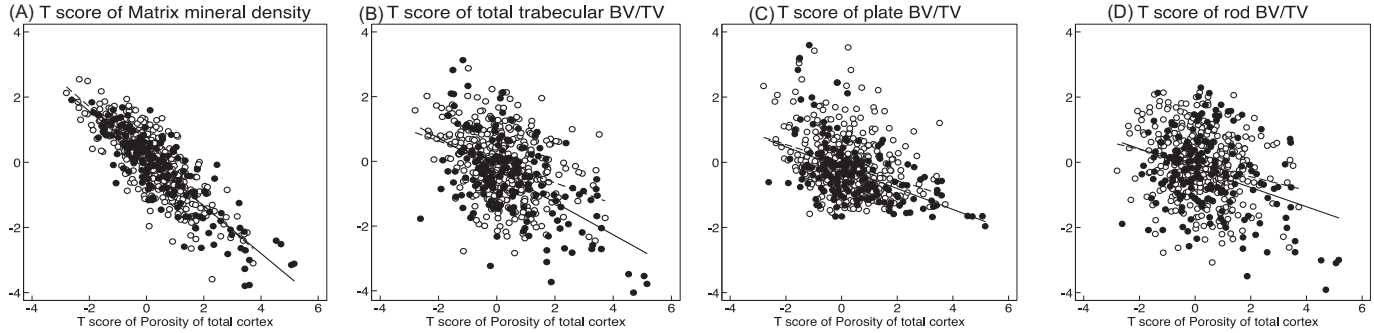

Fig. 3. The scatterplot of T scores of (A) matrix mineral density, (B) total trabecular BV/TV, (C) plate BV/TV, (D) rod BV/TV against T score of porosity of the total cortex in Chinese women (filled circles, solid line) and Caucasians (open circles, dashed line).

3.3% smaller cortical area, a 1.6% larger medullary area, cortical vBMD was higher because porosity was 0.36 SD lower and matrix mineral density was 0.48 SD higher than in Caucasians. Trabecular BV/TV did not differ by race but in Chinese, pBV/TV was 0.64 SD higher, rBV/TV was 0.85 SD lower producing a favorable P-R ratio ($p = 0.001$). Chinese had 0.30 SD greater whole bone stiffness and 0.29 SD greater failure load at the tibia.

3.2. Racial dimorphism in postmenopausal women

Postmenopausal Chinese had later menache than postmenopausal Caucasian women (13.7 ± 2.1 vs 13.2 ± 1.3 years, $p = 0.054$), leg length was 1.46 SD shorter, sitting height was similar, distal radial total CSA was 7.7% smaller, cortical area was 7.2% smaller and medullary area was 6.6% smaller than in Caucasians (Table 1, Fig. 1). After adjusting for age and total CSA, Chinese had a 3.3% smaller cortical area, 2.1% larger medullary area, 5.1% thinner cortices. Total cortical porosity was no longer lower, and matrix mineral density was no longer higher, than in Caucasians (Table 2, Fig. 2). Trabecular BV/TV was lower by 0.69 SD, pBV/TV was similar and rBV/TV was 0.86 SD lower in Chinese so the higher P-R ratio was maintained (after adjustment 0.58 vs. 0.51, $p = 0.057$) (Fig. 2). Chinese had 0.39 SD lower whole bone stiffness and 0.40 SD lower failure load than Caucasians at the distal radius (both $p < 0.05$, Table 2).

Chinese had a 5.8% smaller distal tibial total CSA ($p = 0.041$), 3.1% smaller cortical area ($p = 0.136$) and 7.0% smaller medullary area ($p = 0.066$). After adjusting for age and total CSA, Chinese had similar cortical and medullary areas, similar cortical thickness, total cortical porosity was no lower, and matrix mineral density was no higher than Caucasians (Table 3). Trabecular BV/TV was lower, pBV/TV was similar and rBV/TV was 1.24 SD lower in Chinese so the higher P-R ratio was maintained (after adjustment: 1.24 vs. 0.83, $p < 0.001$). Chinese had similar whole bone stiffness and failure load compared to Caucasians at the distal tibia (Table 3).

In both pre- and post-menopausal Chinese and Caucasian women, there was an inverse correlation between T scores of cortical porosity

and matrix mineral density at both sites (r: −0.71 to −0.87, all $p < 0.001$) (Fig. 3). Inverse correlations were present between T scores of cortical porosity and total trabecular BV/TV, plate and rod BV/TV (r: −0.23 to −0.57, all $p < 0.001$) (Fig. 3).

3.3. Secular trends

Menarche occurred earlier in pre- than post-menopausal Chinese women (12.8 ± 1.3 vs 13.7 ± 2.1 yrs, $p = 0.005$), but did not differ in pre- and post-menopausal Caucasians (Table 2). Premenopausal women were taller than postmenopausal women (Chinese: 0.68 SD; Caucasians: 0.74 SD, NS) due to greater sitting height and leg length in both races. Of the secular difference in height, 74% was truncal and 26% was leg length in both races. Arm span was greater in pre- than post-menopausal women in both races (Chinese: 0.51 SD; Caucasians: 0.40 SD, NS).

4. Discussion

We confirm that growth assembles a smaller but more robust skeleton in Chinese than Caucasians. The shorter stature was mainly due to shorter leg length, an effect that may be partly the result of an earlier menarche. However, we did not detect the earlier age of menarche in Chinese than Caucasians. The shorter appendicular skeleton was associated with smaller total and medullary CSAs. The cortices were less porous with a higher matrix mineral density, trabeculae were more plate- than rod-like and estimated bone strength was higher in premenopausal Chinese than premenopausal Caucasians.

The findings in postmenopausal women were different. Chinese were shorter than Caucasians, but contrary to our hypothesis, the racial dimorphism in bone microstructure was not observed. Distal radial cortices were not relatively thicker, cortical porosity was no lower, matrix mineral density was no higher, and trabecular plate BV/TV was no higher than in postmenopausal Caucasians. However, plate to rod ratio remained higher than postmenopausal Caucasians because postmenopausal Chinese had fewer trabecular rods. Estimated bone strength was lower at the distal radius and no different at the distal tibia compared to postmenopausal Caucasians.

Axial and appendicular dimensions are the result of the differing tempo of growth prior and during puberty [22]. Appendicular growth is more rapid than axial growth before puberty and decelerates at puberty as axial growth accelerates. Consequently, an early puberty produces a longer trunk relative to the legs. Thus, the shorter leg length but similar trunk length in Chinese compared with Caucasians may be partly the result of a shorter period of rapid pre-pubertal linear appendicular growth and an earlier and high peak velocity of truncal growth. Whether shorter leg length is associated with better balance and reduced propensity for falls and less severe falls in Chinese is uncertain [23].

Periosteal apposition ceases around the time of puberty. Closure of the epiphyses results in a smaller total CSA while endocortical apposition thickens the cortex. Trabeculae emerging from the growth plate thicken and coalesce contributing to cortical thickness and a reduction in cortical porosity [24,25]. More plate-like trabecular morphology in premenopausal Chinese women is consistent with the notion that the earlier puberty contributes to trabecular bone formation producing ‘corticalization’ of trabeculae thickening the cortex and forming thicker more highly connected trabeculae. For a fixed bone volume fraction, plate-like trabeculae contribute to mechanical strength [26,27]. Secondary mineralization increases matrix mineral density. Each of these morphological features distinguished appendicular bone in Chinese from Caucasians.

We observed an inverse association with cortical porosity and matrix mineral density in Chinese and Caucasian women. In premenopausal women, remodelling is balanced and slow. Bone multicellular units (BMUs) excavate a transient cavities (porosity) that refill during 3 months with the same volume of bone that is transiently undermineralized until primary and secondary mineralization is complete. Hence, the inverse association between higher porosity and lower matrix mineral density. After menopause, remodelling becomes unbalanced and rapid, now porosity becomes permanent due to less bone being deposited than resorbed. Porosity increases as years since menopause increase and matrix mineral density decreases due to persistent high remodelling replacing more mineralized bone with younger less mineralized bone [28].

After menopause, the racial differences in cortical porosity and matrix mineral density were no longer detected, confirming this observation reported by Boutroy et al. [5]. Whether Chinese lose bone more rapidly after menopause than Caucasians remains uncertain. Some studies support more rapid bone loss in Chinese than Caucasians [29,30], others do not [27]. The lack of consistency may be partly the result of errors introduced by the challenges in the positioning of the ROI. Lower cortical porosity and higher matrix mineral density in Chinese may be partly due to positioning the ROI more proximally, a location of thicker and less porous cortices with higher matrix mineral density [7]. We adjusted for this source of error by correcting for total CSA, an approach shown to largely rectify this potential source of error [7]. We also addressed this by examining a group of Chinese and Caucasian premenopausal women matched by leg length (data not shown) and the racial differences in bone microstructure remained the same. Prospective studies are needed with attention to positioning the ROI within and between individuals to examine this question.

The study has limitations other than the challenges of positioning the ROI. It is cross-sectional. Age of menarche was self-reported so its validity cannot be assured [31]. Chinese living in Australia might have diverse origins and inferences based on the results of this study may not be valid in other cohorts. About 90% of the women were from Southern China and South-east Asian and they arrived in Australia after aged 18 years so the genetic and local environmental factors operative in China may have influenced morphology and remain undefined. FEA models the behaviour of bone under constraints imposed by the model [32]. While the estimated stiffness and peak strength have been tested ex vivo, whether these models describe the mechanical behaviour of the bone in vivo is uncertain. Another limitation is the challenge in segmenting cortical from trabecular bone in advanced age when cortical fragments produced by intracortical remodelling may result in these fragments being ‘seen’ as trabeculae leading to an over estimate of ‘trabecular’ density and an underestimate in cortical porosity (which is ‘seen’ as being part of the medullary canal) [16].

In summary, Chinese assemble a more robust appendicular skeleton with less porous cortices with a higher matrix mineral density and more plate-like than rod-like trabeculae occupying the smaller medullary canal. While this structure may be less accessible to being remodelled, these features were not observed in postmenopausal women; cortices were thinner, porosity and matrix mineral density were no different to Caucasians and trabecular BV/TV was less suggesting the benefits may be lost during advancing age and so may contribute to bone fragility.

Acknowledgements

Authors' roles: XW and ES wrote and revised the manuscript. Data collection: XW and AGZ. Image analysis: AGZ, BZ, ZZ and XEG. Statistical analysis: XW. Data interpretation and approving final version of manuscript: XW, AGZ, BZ, XEG, ZZ and ES. We are grateful the funding support from Australian National Health and Medical Research Council (NHMRC) project grant (ID: 251582).

References

[1] E.M. Lau, J.K. Lee, P. Suriwongpaisal, S.M. Saw, S. Das De, A. Khir, P. Sambrook, The incidence of hip fracture in four Asian countries: the Asian Osteoporosis Study (AOS), Osteoporos. Int. 12 (3) (2001) 239–243.

[2] L. Xu, A. Lu, X. Zhao, X. Chen, S.R. Cummings, Very low rates of hip fracture in

Beijing, People's Republic of China the Beijing Osteoporosis Project, Am. J. Epidemiol. 144 (9) (1996) 901–907.
[3] L. Yan, B. Zhou, A. Prentice, X. Wang, M.H. Golden, Epidemiological study of hip fracture in Shenyang, People's Republic of China, Bone 24 (2) (1999) 151–155.
[4] G.S. Bhudhikanok, M.C. Wang, K. Eckert, C. Matkin, R. Marcus, L.K. Bachrach, Differences in bone mineral in young Asian and Caucasian Americans may reflect differences in bone size, J. Bone Miner. Res. 11 (10) (1996) 1545–1556.
[5] S. Boutroy, M.D. Walker, X.S. Liu, D.J. McMahon, G. Liu, X.E. Guo, J.P. Bilezikian, Lower cortical porosity and higher tissue mineral density in Chinese American versus white women, J. Bone Miner. Res. 29 (3) (2014) 551–561.
[6] J.W. Davis, P.D. Ross, M.C. Nevitt, R.D. Wasnich, Incidence rates of falls among Japanese men and women living in Hawaii, J. Clin. Epidemiol. 50 (5) (1997) 589–594.
[7] A. Ghasem-Zadeh, A. Burghardt, X.F. Wang, S. Iuliano, S. Bonaretti, M. Bui, R. Zebaze, E. Seeman, Quantifying sex, race, and age specific differences in bone microstructure requires measurement of anatomically equivalent regions, Bone 101 (2017) 206–213.
[8] R.M. Zebaze, A. Jones, M. Knackstedt, G. Maalouf, E. Seeman, Construction of the femoral neck during growth determines its strength in old age, J. Bone Miner. Res. 22 (7) (2007) 1055–1061.
[9] J.M. Tanner, T. Hayashi, M.A. Preece, N. Cameron, Increase in length of leg relative to trunk in Japanese children and adults from 1957 to 1977: comparison with British and with Japanese Americans, Ann. Hum. Biol. 9 (5) (1982) 411–423.
[10] S.S. Leung, J.T. Lau, Y.Y. Xu, L.Y. Tse, K.F. Huen, G.W. Wong, W.Y. Law, V.T. Yeung, W.K. Yeung, N.K. Leung, Secular changes in standing height, sitting height and sexual maturation of Chinese—the Hong Kong Growth Study, 1993, Ann. Hum. Biol. 23 (4) (1996) 297–306.
[11] X.F. Wang, Y. Duan, M. Henry, B.T. Kim, E. Seeman, Body segment lengths and arm span in healthy men and women and patients with vertebral fractures, Osteoporos. Int. 15 (1) (2004) 43–48.
[12] M.F. Steele, J.W. Mattox, Correlation of arm-span and height in young women of two races, Ann. Hum. Biol. 14 (5) (1987) 445–447.
[13] X.F. Wang, Y. Duan, T.J. Beck, E. Seeman, Varying contributions of growth and ageing to racial and sex differences in femoral neck structure and strength in old age, Bone 36 (6) (2005) 978–986.
[14] P. Geusens, R. Chapurlat, G. Schett, A. Ghasem-Zadeh, E. Seeman, J. de Jong, J. van den Bergh, High-resolution in vivo imaging of bone and joints: a window to microarchitecture, Nat. Rev. Rheumatol. 10 (5) (2014) 304–313.
[15] R. Zebaze, A. Ghasem-Zadeh, A. Mbala, E. Seeman, A new method of segmentation of compact-appearing, transitional and trabecular compartments and quantification of cortical porosity from high resolution peripheral quantitative computed tomographic images, Bone 54 (1) (2013) 8–20.
[16] R.M. Zebaze, A. Ghasem-Zadeh, A. Bohte, S. Iuliano-Burns, M. Mirams, R.I. Price, E.J. Mackie, E. Seeman, Intracortical remodelling and porosity in the distal radius and post-mortem femurs of women: a cross-sectional study, Lancet 375 (9727) (2010) 1729–1736.
[17] X.S. Liu, A.H. Huang, X.H. Zhang, P. Sajda, B. Ji, X.E. Guo, Dynamic simulation of three dimensional architectural and mechanical alterations in human trabecular bone during menopause, Bone 43 (2) (2008) 292–301.
[18] X.S. Liu, E. Shane, D.J. McMahon, X.E. Guo, Individual trabecula segmentation (ITS)-based morphological analysis of microscale images of human tibial trabecular bone at limited spatial resolution, Journal of Bone and Mineral Research 26 (9) (2011) 2184–2193.
[19] X.S. Liu, P. Sajda, P.K. Saha, F.W. Wehrli, G. Bevill, T.M. Keaveny, X.E. Guo, Complete volumetric decomposition of individual trabecular plates and rods and its morphological correlations with anisotropic elastic moduli in human trabecular bone, J. Bone Miner. Res. 23 (2) (2008) 223–235.
[20] B. Zhou, X.S. Liu, J. Wang, X.L. Lu, A.J. Fields, X.E. Guo, Dependence of mechanical properties of trabecular bone on plate-rod microstructure determined by individual trabecula segmentation (ITS), J. Biomech. 47 (3) (2014) 702–708.
[21] X.S. Liu, X.H. Zhang, K.K. Sekhon, M.F. Adams, D.J. McMahon, J.P. Bilezikian, E. Shane, X.E. Guo, High-resolution peripheral quantitative computed tomography can assess microstructural and mechanical properties of human distal tibial bone, J. Bone Miner. Res. 25 (4) (2010) 746–756.
[22] J. Karlberg, A biologically-oriented mathematical model (ICP) for human growth, Acta Paediatr. Scand. 350 (1989) 70–94.
[23] P.D. Ross, S. Fujiwara, C. Huang, J.W. Davis, R.S. Epstein, R.D. Wasnich, K. Kodama, L.J. Melton 3rd, Vertebral fracture prevalence in women in Hiroshima compared to Caucasians or Japanese in the US, Int. J. Epidemiol. 24 (6) (1995) 1171–1177.
[24] E.R. Cadet, R.I. Gafni, E.F. McCarthy, D.R. McCray, J.D. Bacher, K.M. Barnes, J. Baron, Mechanisms responsible for longitudinal growth of the cortex: coalescence of trabecular bone into cortical bone, J. Bone Joint Surg. Am. 85 (9) (2003) 1739–1748.
[25] Q. Wang, A. Ghasem-Zadeh, X.F. Wang, S. Iuliano-Burns, E. Seeman, Trabecular bone of growth plate origin influences both trabecular and cortical morphology in adulthood, J. Bone Miner. Res. 26 (7) (2011) 1577–1583.
[26] X.S. Liu, A. Cohen, E. Shane, E. Stein, H. Rogers, S.L. Kokolus, P.T. Yin, D.J. McMahon, J.M. Lappe, R.R. Recker, X.E. Guo, Individual trabeculae segmentation (ITS)-based morphological analysis of high-resolution peripheral quantitative computed tomography images detects abnormal trabecular plate and rod microarchitecture in premenopausal women with idiopathic osteoporosis, J. Bone Miner. Res. 25 (7) (2010) 1496–1505.
[27] M.D. Walker, X.S. Liu, B. Zhou, S. Agarwal, G. Liu, D.J. McMahon, J.P. Bilezikian, X.E. Guo, Premenopausal and postmenopausal differences in bone microstructure and mechanical competence in Chinese-American and white women, J. Bone Miner. Res. 28 (6) (2013) 1308–1318.
[28] A. Bjornerem, X. Wang, M. Bui, A. Ghasem-Zadeh, J.L. Hopper, R. Zebaze, E. Seeman, Menopause-related appendicular bone loss is mainly cortical and results in increased cortical porosity, J. Bone Miner. Res. 33 (4) (2018) 598–605.
[29] L. Qin, S.K. Au, P.C. Leung, M.C. Lau, J. Woo, W.Y. Choy, W.Y. Hung, M.A. Dambacher, K.S. Leung, Baseline BMD and bone loss at distal radius measured by peripheral quantitative computed tomography in peri- and postmenopausal Hong Kong Chinese women, Osteoporos. Int. 13 (12) (2002) 962–970.
[30] B.L. Riggs, L.J. Melton, R.A. Robb, J.J. Camp, E.J. Atkinson, L. McDaniel, S. Amin, P.A. Rouleau, S. Khosla, A population-based assessment of rates of bone loss at multiple skeletal sites: evidence for substantial trabecular bone loss in young adult women and men, J. Bone Miner. Res. 23 (2) (2008) 205–214.
[31] R. Cooper, M. Blell, R. Hardy, S. Black, T.M. Pollard, M.E. Wadsworth, M.S. Pearce, D. Kuh, Validity of age at menarche self-reported in adulthood, J. Epidemiol. Community Health 60 (11) (2006) 993–997.
[32] P.K. Zysset, E. Dall'ara, P. Varga, D.H. Pahr, Finite element analysis for prediction of bone strength, Bonekey Rep 2 (2013) 386.

Journal of
Clinical Medicine

MDPI

Article

High Cortico-Trabecular Transitional Zone Porosity and Reduced Trabecular Density in Men and Women with Stress Fractures

Afrodite Zendeli [1,*], Minh Bui [2], Lukas Fischer [3,4], Ali Ghasem-Zadeh [5], Wolfgang Schima [6] and Ego Seeman [5]

1 Medical Department of Internal Medicine, Rheumatology and Endocrinology at Krankenhaus Herz Jesu, 1030 Vienna, Austria
2 Centre for Epidemiology and Biostatistics, Melbourne School of Population and Global Health, University of Melbourne, Melbourne 3000, Australia; mbui@unimelb.edu.au
3 Computational Imaging Research Lab, Department of Biomedical Imaging and Image-Guided Therapy, Medical University of Vienna, 1090 Vienna, Austria; lukas.fischer@scch.at
4 Software Competence Center Hagenberg GmbH (SCCH), 4232 Hagenberg, Austria
5 Departments Medicine and Endocrinology, Austin Health, University of Melbourne, Melbourne 3084, Australia; alig@unimelb.edu.au (A.G.-Z.); egos@unimelb.edu.au (E.S.)
6 Department of Diagnostic and Interventional Radiology–Barmherzige Schwestern Krankenhaus, Goettlicher Heiland Krankenhaus und Sankt Josef Krankenhaus, 1060 Vienna, Austria; wolfgang.schima@khgh.at
* Correspondence: afrodite.zendeli@kh-herzjesu.at; Tel.: +43-664-1245621

Abstract: To determine whether stress fractures are associated with bone microstructural deterioration we quantified distal radial and the unfractured distal tibia using high resolution peripheral quantitative computed tomography in 26 cases with lower limb stress fractures (15 males, 11 females; mean age 37.1 ± 3.1 years) and 62 age-matched healthy controls (24 males, 38 females; mean age 35.0 ± 1.6 years). Relative to controls, in men, at the distal radius, cases had smaller cortical cross sectional area (CSA) ($p = 0.012$), higher porosity of the outer transitional zone (OTZ) ($p = 0.006$), inner transitional zone (ITZ) ($p = 0.043$) and the compact-appearing cortex (CC) ($p = 0.023$) while trabecular vBMD was lower ($p = 0.002$). At the distal tibia, cases also had a smaller cortical CSA ($p = 0.008$). Cortical porosity was not higher, but trabecular vBMD was lower ($p = 0.001$). Relative to controls, in women, cases had higher distal radial porosity of the OTZ ($p = 0.028$), ITZ ($p = 0.030$) not CC ($p = 0.054$). Trabecular vBMD was lower ($p = 0.041$). Distal tibial porosity was higher in the OTZ ($p = 0.035$), ITZ ($p = 0.009$), not CC. Stress fractures are associated with compromised cortical and trabecular microstructure.

Keywords: bone microstructural deterioration; cortical porosity; high resolution peripheral quantitative computed tomography; stress fracture

check for updates

Citation: Zendeli, A.; Bui, M.; Fischer, L.; Ghasem-Zadeh, A.; Schima, W.; Seeman, E. High Cortico-Trabecular Transitional Zone Porosity and Reduced Trabecular Density in Men and Women with Stress Fractures. *J. Clin. Med.* **2021**, *10*, 1123. https://doi.org/10.3390/jcm10051123

Academic Editor: Lorenzo Drago

Received: 9 February 2021
Accepted: 1 March 2021
Published: 8 March 2021

Publisher's Note: MDPI stays neutral with regard to jurisdictional claims in published maps and institutional affiliations.

Copyright: © 2021 by the authors. Licensee MDPI, Basel, Switzerland. This article is an open access article distributed under the terms and conditions of the Creative Commons Attribution (CC BY) license (https://creativecommons.org/licenses/by/4.0/).

1. Introduction

Stress fractures are commonly the result of repetitive loading and are seen in athletes, military recruits and professional dancers, but stress fractures also occur in recreational athletic individuals as vigorous exercise increases the risk for injuries [1–5]. These fractures exist across a spectrum from low-grade stress reactions, bone marrow edema to complete fractures visible radiologically [6–8]. Despite there being little or no deficit in areal bone mineral density (aBMD) reported in most studies, there is evidence suggesting that abnormalities in bone microarchitecture are associated with these fractures and so may contribute to bone fragility [6,9–17].

As stress fractures are commonly reported in young adults abnormalities in bone morphology associated with these fractures are likely to be due, in part, to abnormalities in the growth and development of peak bone macro- and microstructure, not necessarily bone loss. In the diaphysis, a region composed virtually exclusively of cortical bone, growth

in size and mass occurs by periosteal apposition with concurrent endocortical resorptive modeling producing a radial 'modeling drift' so the cortex becomes thinner relative to its increasing total cross-sectional area (CSA) [18,19].

By contrast, the metaphyseal region contains both cortical and trabecular bone. The cortical bone is formed by condensation or 'corticalization' of trabeculae as they arise from the periphery of the growth plate. Adjacent trabeculae coalesce by bone formation upon their surfaces while more centrally placed trabeculae form the metaphyseal trabecular compartment. The cortico-trabecular transitional region so formed between the cortical bone and the more centrally placed trabecular bone is composed of mineralized bone matrix that transitions from the more compact cortical configuration to a more open spongy trabecular configuration with more void volume (porosity) [20].

The purpose of this study was to quantify any association between bone microstructure and the presence of a stress fracture in the lower limb. We hypothesized that young adult individuals sustaining stress fractures have thinner and more porous cortices and reduced trabecular density characterised by reduced numbers and thinner trabeculae.

2. Materials and Methods

This was a cross sectional case control study. Thirty-four patients presenting with acute focal lower limb pain were assessed for possible stress fractures using magnetic resonance imaging (MRI) [21]. Participants were recruited from the osteoporosis outpatients department of the St. Vincent Hospital and the Austrian Military Hospital in Vienna/Austria.

Patients were included if they were above 18 years of age and sustained a recent MRI-diagnosed stress fracture within 14 days prior to inclusion. Patients receiving any medication affecting bone metabolism (parathyroid hormone, intravenous or oral bisphosphonate, strontium ranelate, raloxifene, hormonal replacement therapy or anabolic steroids) were excluded. Other exclusion criteria included the presence of metabolic bone disease, a history of malignancy, hypo- or hyperparathyroidism, pregnancy and lactation.

Of the 34 subjects, 26 were included (11 females, 15 males). The study group included five military recruits, three long distance runners, one sprinter and one professional tennis player, the other 16 patients were recreational sportsmen and women. We compared these results with data obtained from 62 healthy age- and sex matched Caucasian controls (42 Austrian subjects, 20 Australian subjects). The study was approved and supervised by an independent local ethics committee in Vienna/Austria.

2.1. Magnetic Resonance Imaging

Examinations were performed on 1.5 or 3.0 T scanners (Signa HDx, GE Healthcare, USA; Intera, Philips, The Netherlands, Avanto, Siemens, Germany) using a phased-array extremity coil. All MRI examinations included an axial T1-weighted spin-echo (SE) sequence and an axial fat-suppressed T2-weighted turbo spin-echo (TSE) or a short-tau inversion recovery (STIR) sequence. The presence of bone marrow edema and stress fracture was seen as decreased signal intensity on T1 weighted SE images, and markedly increased signal intensity on STIR images or T2 weighted fat-suppressed TSE images [22]. In 16 patients High Resolution Multi-Detector CT (HR-MDCT) scanning was performed with a 128-row MDCT scanner (Somatom AS+, Siemens, Forchheim, Germany). Images were acquired in ultrahigh resolution (UHR) mode covering the area of interest as defined by MRI. Slice thickness was 0.6 mm, field of view of 160–300 mm (x-axis) × 160–300 mm (y-axis), with a matrix of 512 × 512, which equates to a resolution of 0.3–0.6 mm (x-axis) × 0.3–0.6 mm (y-axis) × 0.6 mm slice thickness (z-axis). A linear stress fracture was visible in 16 of 26 cases (61.5%) [23]. In 8 patients the fracture was identified in the metatarsals, in 8 patients in the calcaneus and ankle, in 6 patients in the proximal tibia adjacent to the knee, in 2 patients in the femur condyle, and in 2 patients in the hip (one femoral head and one acetabulum).

2.2. Measurement of Bone Microarchitecture

Scans were obtained from the non-dominant distal radius and unfractured side of the distal tibia using by HR-pQCT scanner (XtremeCT; Scanco Medical AG, Brüttisellen, Switzerland) using the standard in vivo protocol (60 kVp, 900 µA, 100-ms integration time) [24]. StrAx1.0 is a new algorithm that segments bone from background, and then bone into its compact appearing cortex (CC), outer transitional zone (OTZ) and inner transitional zone (ITZ), and trabecular compartments (see Figure 1); and in so doing correctly confines the trabecularized cortex (i.e., cortical fragments) to the transitional zone rather than incorrectly allocating cortical fragments (which look like trabeculae) to the medullary compartment; a segmentation error which overestimates 'trabecular' density [25]. The OTZ is the trabecularized cortex adjacent to the CC whereas the ITZ is the trabecularized cortex adjacent to the medullary cavity. The latter also contains true trabecular bone (of growth plate origin).

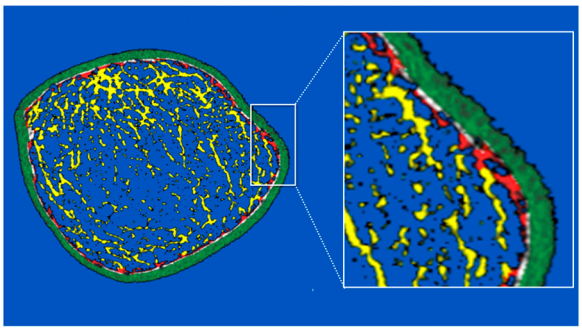

Figure 1. HR-pQCT image of the distal tibia of an 18-year-old male patient with a stress fracture. Compact appearing cortex (green); outer transitional zone (white); inner transitional zone (red); medullary area (yellow).

Of the 110 slices in the region of interest imaged by HR-pQCT the analysis is restricted to the 40 most proximal slices because the 70 distal slices often have very thin cortices, and hence are unsuitable for unambiguous quantification of cortical porosity. Porosity was quantified as previously reported. The coefficient of variation for segmentation and quantification of porosity ranges from 0.54 to 3.98% depending on the compartment [26,27].

2.3. Statistical Analysis

Testing for normality of distribution of a variable was conducted using Shapiro–Wilk test. Two sample *t*-test was used to test the difference in mean between cases and controls if the data was approximate normal, otherwise nonparametric Mann–Whitney test was used to test the difference in the medians. Post hoc power calculations were done. Initially, the statistical test was computed without adjustment for other covariates, and then adjustment for age and height was carried out. Spearman's correlations were used to assess relationships between porosity and medullary CSA/total CSA. Univariate logistic analysis was used to examine the association between porosity of CC, OTZ, ITZ and trabecular volumetric BMD and fracture risk. All variables were standardized to have mean of 0 and SD of 1 and were used to predict the odds ratio (OR). The analyses were performed on data at both tibia and radius site for males and females separately. We used statistical software STATA (StataCorp, 2009), version 11, to conduct all analyses. *p*-values were computed for two-sided tests and values less than 0.05 were considered as significant.

3. Results

Characteristics of the entire study population are described in Table 1.

Table 1. Characteristics of cases and controls.

Males	Cases (15)	Controls (24)	*p*
Age [ys]	29.2 ± 2.6	30.9 ± 1.7	0.450
Weight [kg]	77.5 ± 3.5	84.1 ± 3.1	0.180
Height [m]	1.81 ± 0.02	1.78 ± 0.02	0.140
Females	**Cases (11)**	**Controls (38)**	***p***
Age [ys]	47.8 ± 4.7	40.5 ± 2.3	0.140
Weight [kg]	68.5 ± 5.4	61.8 ± 1.2	0.340
Height [m]	1.67 ± 0.02	1.65 ± 0.01	0.290

Results are shown as mean ± SE (Standard error of mean); *p*-value comparing cases and controls ($p < 0.05$).

3.1. Males

As shown in Figure 1 and Table 2, relative to controls, at the distal radius, cases had smaller cortical CSA ($p = 0.012$) due to a smaller CC CSA ($p = 0.005$) and a smaller OTZ CSA ($p = 0.003$). Cases had higher porosity of the OTZ ($p = 0.006$), ITZ ($p = 0.043$) and CC ($p = 0.023$). Cortical vBMD was lower ($p = 0.002$). Trabecular vBMD was lower ($p = 0.002$). Trabecular thickness was reduced ($p = 0.001$), connectivity was reduced ($p = 0.012$) and separation increased ($p = 0.007$) (Figure 1, Table 2).

Table 2. Comparison of microarchitecture of the distal radius and distal tibia in cases and controls.

	Distal Radius						**Distal Tibia**					
	Males			**Females**			**Males**			**Females**		
	Cases (15)	**Controls (24)**	***p***	**Cases (11)**	**Controls (38)**	***p***	**Cases (15)**	**Controls (24)**	***p***	**Cases (11)**	**Controls (38)**	***p***
TCSA [mm^2]	314 ± 25	287 ± 14	0.418 **	225 ± 8.1	203 ± 5.9	0.878 *	820 ± 54	762 ± 34	0.841 **	625 ± 19	603 ± 16	0.768 *
Medullary CSA [mm^2]	215 ± 24	177 ± 11	0.685 **	149 ± 7.7	126 ± 5.3	0.655 *	629 ± 52	553 ± 32	0.714 **	467 ± 16	437 ± 15	0.941 *
Medullary CSA/TCSA	67.1 ± 1.7	60.9 ± 1.2	0.006 *	66.0 ± 1.7	61.4 ± 1.0	0.161 *	75.8 ± 1.4	71.8 ± 1.1	0.059 *	74.5 ± 0.8	71.9 ± 0.7	0.326 *
Cortical CSA [mm^2]	98.7 ± 2.4	110 ± 4.3	0.012 *	76.0 ± 3.8	76.6 ± 1.5	0.363 *	190.3 ± 6.4	208.7 ± 6.0	0.008 *	159 ± 5.9	166 ± 2.6	0.272 *
CC CSA [mm^2]	62.8 ± 1.8	73.4 ± 3.2	0.005 *	49.6 ± 3.0	49.7 ± 1.2	0.414 **	125 ± 5.9	139 ± 5.3	0.015 *	104 ± 5.2	108 ± 2.2	0.590 *
OTZ CSA [mm^2]	8.12 ± 0.2	9.86 ± 0.5	0.003 *	6.63 ± 0.5	6.47 ± 0.2	0.320 **	17.5 ± 0.9	20.9 ± 1.1	0.012 **	13.8 ± 0.8	14.9 ± 0.4	0.349 *
ITZ CSA [mm^2]	27.8 ± 1.4	26.4 ± 1.4	0.616 *	19.8 ± 0.9	20.4 ± 0.7	0.139 *	48.9 ± 2.9	49.0 ± 1.9	0.512 *	41.4 ± 1.8	43.5 ± 1.5	0.182 *
Cortical CSA/TCSA	32.9 ± 1.7	39.1 ± 1.2	0.006 *	34.0 ± 1.6	38.6 ± 0.9	0.161 *	24.2 ± 1.4	28.2 ± 1.1	0.059 *	25.5 ± 0.8	28.1 ± 0.7	0.326 *
Porosity CC [%]	37.3 ± 2.0	32.2 ± 1.5	0.023 *	33.4 ± 1.8	29.6 ± 0.7	0.054 *	36.4 ± 1.1	33.7 ± 0.9	0.090 *	38.4 ± 2.2	33.8 ± 1.1	0.295 **
Porosity OTZ [%]	55.9 ± 1.2	52.0 ± 0.9	0.006 *	55.2 ± 1.1	52.3 ± 0.4	0.028 **	52.2 ± 0.9	50.4 ± 0.7	0.058 *	54.0 ± 1.0	50.8 ± 0.5	0.035 **
Porosity ITZ [%]	66.0 ± 0.6	64.4 ± 0.6	0.043 *	65.8 ± 0.7	64.3 ± 0.3	0.030 *	61.8 ± 0.7	61.3 ± 0.5	0.245 *	63.5 ± 0.7	61.4 ± 0.3	0.009 *
Total vBMD [mgHA/cm^3]	332 ± 16	412 ± 13	0.001 *	309 ± 21	369 ± 12	0.061	310 ± 15	366 ± 11	0.002 *	266 ± 12	311 ± 8.5	0.104 *
Cortical vBMD [mg HA/cm^3]	657 ± 20	731 ± 16	0.002 *	684 ± 20	721 ± 9.9	0.175 *	674 ± 13	717 ± 11	0.016 *	630 ± 20	684 ± 12	0.106 *
Tr. vBMD [mg HA/cm^3]	168 ± 5.9	205 ± 8.9	0.002 *	113 ± 11	144 ± 5.4	0.041 *	192 ± 9.5	225 ± 8.7	0.001 *	141 ± 8.7	1612 ± 5.4	0.354 *
Tr. thickness [mm]	0.07 ± 0.003	0.10 ± 0.004	0.001 *	0.05 ± 0.006	0.06 ± 0.003	0.056 *	0.08 ± 0.005	0.1 ± 0.004	0.0004 *	0.06 ± 0.004	0.07 ± 0.003	0.332 *
Tr. connectivity density [1/mm^2]	2.89 ± 0.2	3.56 ± 0.2	0.012 *	1.65 ± 0.2	2.16 ± 0.1	0.127 *	3.47 ± 0.2	4.09 ± 0.3	0.006 *	2.27 ± 0.2	2.67 ± 0.1	0.570 *
Tr. separation [mm]	0.89 ± 0.04	0.80 ± 0.03	0.007 *	1.15 ± 0.09	0.96 ± 0.03	0.070 **	0.86 ± 0.04	0.78 ± 0.03	0.007 *	1.06 ± 0.05	1.00 ± 0.03	0.885 *
Tr. number [1/mm^2]	3.16 ± 0.1	3.25 ± 0.1	0.246 *	2.60 ± 0.2	2.87 ± 0.1	0.320 **	3.67 ± 0.1	3.70 ± 0.1	0.166 *	3.21 ± 0.1	3.29 ± 0.08	0.587 *

Results are shown as mean ± SE (standard error of mean); *p*-value comparing healthy controls and fracture patients, adjusted for age and height, using * two-sample *t*-test and ** nonparametric Mann–Whitney test on the residuals of regression of a variable on age and height ($p < 0.05$). TCSA = total cross sectional area, CSA = cross-sectional area; CC = compact-appearing cortex; OTZ = outer transitional zone; ITZ = inner transitional zone; vBMD = volumetric bone mineral density; Tr = trabecular; HA = hydroxyapatite.

At the distal tibia, relative to controls, cases had a smaller cortical CSA ($p = 0.008$) due to smaller CC CSA ($p = 0.015$) and a smaller OTZ CSA ($p = 0.012$). Porosity was not higher at this site. Cortical vBMD was lower ($p = 0.016$). Trabecular vBMD was lower ($p = 0.001$). Trabecular thickness was reduced ($p = 0.0004$), connectivity was reduced ($p = 0.006$) and separation increased ($p = 0.007$) (Table 2).

3.2. Females

The results were similar in females. Relative to controls, at the distal radius, cases had significant higher porosity of the OTZ ($p = 0.028$) and ITZ ($p = 0.030$), but porosity was not significantly higher at CC ($p = 0.054$). Cortical vBMD was not lower, but trabecular vBMD was lower ($p = 0.041$). At the distal tibia, porosity was higher in the OTZ ($p = 0.035$) and ITZ ($p = 0.009$) but not at the CC. Cortical and trabecular vBMD were not lower. No differences in trabecular morphology were detected at either site (Table 2).

In both sexes, at both sites, associations were detected between porosity of CC, OTZ and ITZ and medullary CSA/TCSA ($p < 0.001$, except for the distal radius ITZ in males with $p = 0.004$) (Figure 2). Cortical porosity was associated with an increased odds of stress fracture, with ORs ranging from 1.24 to 3.13 depending on the cortical compartment, though not all sites demonstrated a statistically significant increase in odds. Higher trabecular vBMD was protective, demonstrating a statistically significantly lower odds of fracture at the distal radius in males and females and the distal tibia in males (Figure 3).

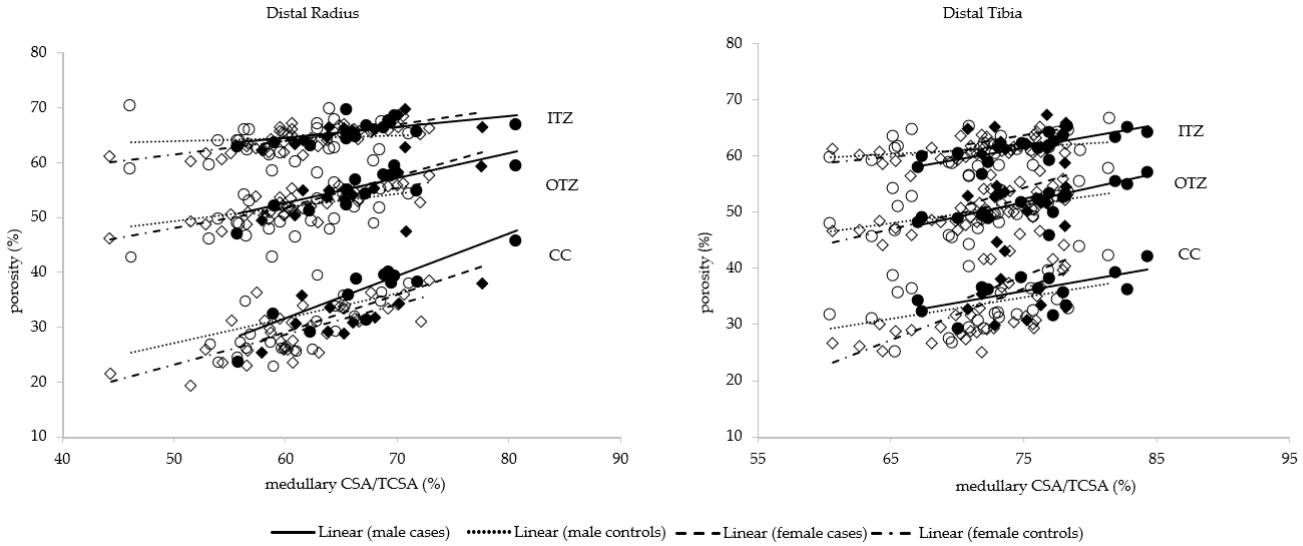

Figure 2. Porosity of the compact appearing cortex (CC), outer and inner transitional zones (OTZ, ITZ) as a function of medullary cross-sectional area (CSA)/total CSA at the distal radius and distal tibia in male cases (filled dots), male controls (open dots), female cases (filled squares) and female controls (open squares). All $p < 0.001$ except for the distal radius ITZ in males ($p = 0.004$).

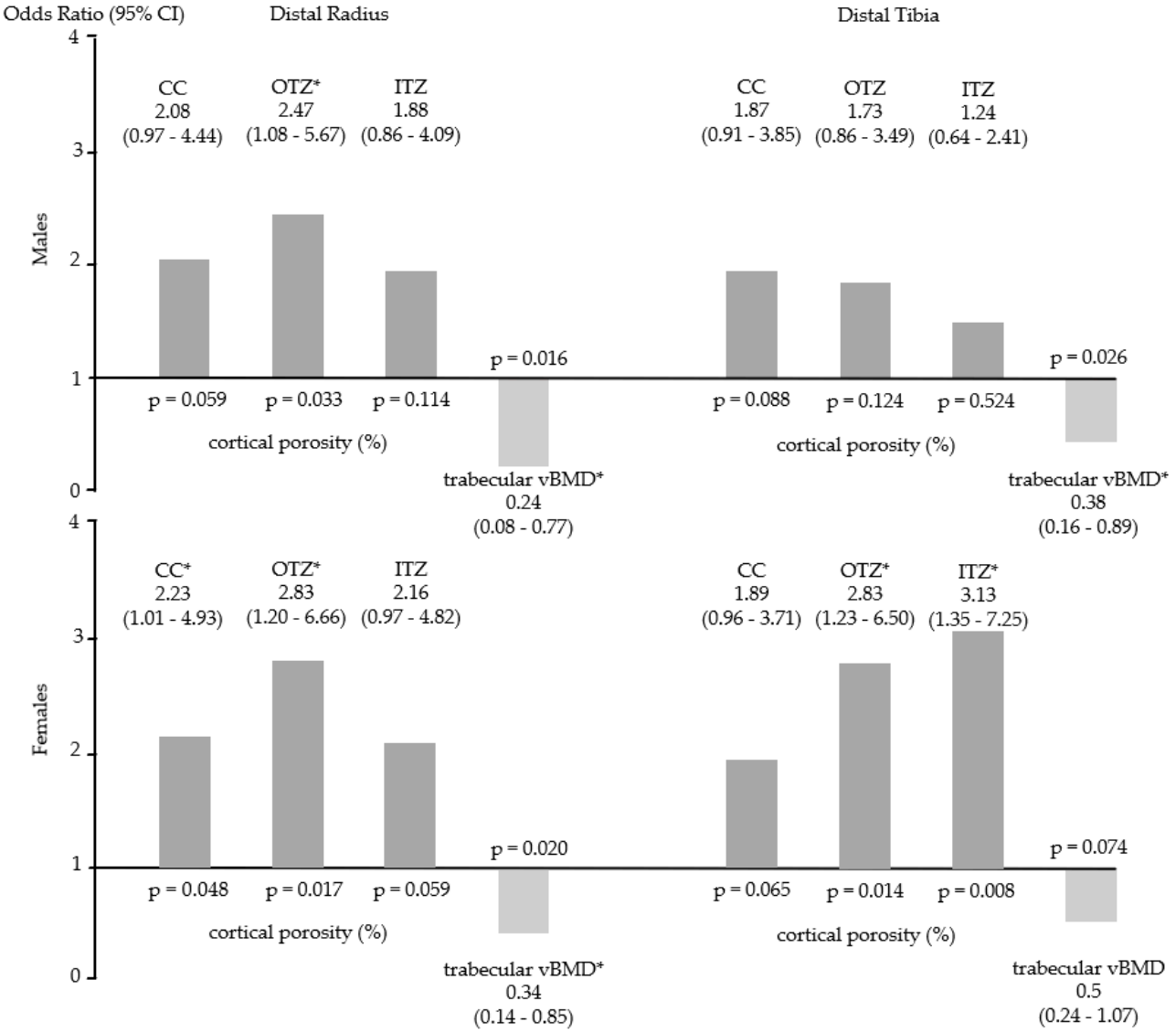

Figure 3. Odds ratio (OR) for fracture (mean and 95% Confidence Intervals, CI) for porosity of the compact appearing cortex (CC), outer and inner transitional zones (OTZ, ITZ) and trabecular volumetric bone mineral density (vBMD) at distal radius and distal tibia in males and females. * = significant *p*-values.

4. Discussion

We report that men and women with stress fractures had increased porosity, observed in the inner and outer cortico-trabecular transitional zones of the distal radius in both sexes and distal tibia in female cases. Porosity of the compact appearing cortex was increased only in males at the distal radius. Odds ratio for a stress fracture was associated with increased porosity of the outer cortico-trabecular transitional zone in three of four locations. Cortical vBMD, which in part, reflects porosity, was also reduced. Furthermore, trabecular vBMD was lower due to reduced trabecular thickness, not numbers. Males with stress fractures had thinner trabeculae with greater separation.

Stress fractures in military cadets and athletes have been subject of most studies using dual x-ray absorptiometry (DXA), x-ray and single photon absorptiometry or nuclear bone scanning [11–14,28]. Fewer studies have used peripheral quantitative computed tomography (pQCT), or HRpQCT to describe bone characteristics in association with stress fractures [10,17,29].

Our findings confirm some, not all previous studies. For example, Beck et al., reported thinner cortices in female cadets and narrower subperiosteal diameters in male cases [12].

Reduced cortical area was also reported by Popp et al., in runners with a stress fracture [30]. While the finding of greater total bone cross sectional was not statistically significant in our study, Weidauer et al., also reported greater periosteal circumference in athletes with a stress fracture [31]. Among military recruits and male runners, Giladi et al., and Popp et al., reported reduced tibial cross sectional area, while HRpQCT-analyses of our cases and work by Schanda et al., reported larger tibial and radial cross sectional area [14,17,29]. These subjects also had reduced cortical vBMD, reduced cortical CSA with increased cortical porosity. In both studies, and work by Schnackenburg et al., trabecular vBMD was found to be reduced [10].

While bone loss cannot be excluded as a cause of these deficits, 20 of the 26 subjects were under 50 years of age. Therefore, higher porosity in the cortico-trabecular junctional zone, with less consistently elevated porosity of the compact cortex, and deficits in trabecular bone may have their origin in the growth-related assembly of bone in some subjects rather than its age-related deterioration [18]. We cannot distinguish these alternatives in a cross sectional study.

We suggest that the thinner and more porous metaphyseal cortex in cases is, in part, the result of a reduction in bone formation upon trabeculae emerging from the periphery of the growth plate. These may fail to coalesce leaving a thinner and more porous cortex (failed corticalization of trabeculae). Reduced bone formation upon trabeculae emerging from the centre of the growth plate may result in the lower metaphyseal trabecular density [32]. This is supported by the presence of a smaller and more porous OTZ suggesting impairment of coalescence as thinner and more separated trabeculae fail to coalesce leaving larger pores adjacent to CC. The more porous cortex will also be thinner due to failure of cortical thickening taking place by adsorption of trabeculae upon the endocortical surface. The thinner cortices are unlikely to be due to reduced periosteal apposition because total CSA was not reduced. Less corticalization of trabeculae may also be partly responsible for the relatively larger medullary canal area as adsorption of trabecular bone upon the endocortical surface is partly responsible for reducing medullary canal area from the 'inside'.

The relatively larger medullary canal area, thinner cortices and higher porosity in the cases may also be due to greater growth-related endocortical resorptive modeling excavating a larger medullary canal during growth and concurrent intracortical resorptive remodeling forming osteons, each with their central Haversian canal. The cases were slightly taller and had wider bones. Taller persons assemble their wider bones by excavation of a disproportionately larger medullary canal such that the wider bone has a thinner cortex relative to its total CSA [19]. Wider bones are assembled with less material relative to their size because resistance to bending is a fourth power function of their radius–less material is needed to achieve a given bending strength than is needed in a narrower bone [33,34].

Wider bones may also be more porous. The greater amount of modeling required to assemble a larger total and medullary CSA is accompanied by more intracortical remodeling forming secondary cortical osteons, each with their Haversian canal (which forms most 'porosity' as seen in cross section) [35]. This is suggested by the positive correlation between medullary canal area and porosity reported here, and elsewhere [19]. This correlation is consistent with the notion of coordinated assembly of the external size, shape and internal architecture of bone by periosteal, intracortical, endocortical surface dependent modeling and remodeling [36].

The increased risk for fracture reported in taller persons is inconsistent with greater resistance to bending observed in wider bones [19]. However, the greater porosity and relatively thinner cortices of wider bones may offset the advantage of greater width. Resistance to bending is a 4th power function of the distance a unit volume of bone is placed from the neutral axis of a long bone [33]. However, resistance to bending is a 7th power function of cortical porosity and a 3rd power function of trabecular density, so the deleterious effect of microstructural abnormalities may offset any benefit achieved by greater bone width [37]. The ability of bone to deform without cracking decreases

as porosity increases [37,38]. The porosity may form stress concentrators predisposing a higher risk to fracture following repetitive loading [39]. Additionally, porosity may reduce compressive strength as the cross-sectional area of the cortex is less mineralized bone matrix and more void area [38].

Both deterioration in cortical and trabecular bone may result from impaired growth, particularly because cortical bone at metaphysis is partly formed by condensation of trabeculae in the periphery of the growth plate to form the cortex while trabeculae emerging from the center of the growth plate form metaphyseal trabecular bone.

Bone loss contributing to the deficits cannot be excluded but appears to be less likely given the age of the cases. Remodeling initiated upon Haversian canal surfaces excavate resorptive cavities enlarging the canal focally producing higher intracortical porosity and stress concentrators predisposing to micro cracks in cortical bone [39]. Even though remodeling may be still balanced in young adults, the refilling phase takes about 3 months, so resorption cavities upon trabeculae surfaces form stress concentrators which may predispose to microdamage in the face of repetitive strain [40]. The repetitive strains lead to accumulation of unrepaired microdamage ultimately producing a stress fracture [41–43].

This study has several limitations. First, it was a cross-sectional case control study. We cannot distinguish whether the porosity contributed to the stress fracture or whether the sequence of events was the reverse. However, measurements were performed within 14 days after injury on the contralateral side, which makes the latter less likely. Most of the cases were recreational sportsmen and women as were controls. We have no data concerning daily physical activity of the controls. Second, most of the male controls were from Australia. However, results were similar in females. Female cases and controls were Austrian. Third, the small number of cases, particularly in females, may have limited the power to achieve statistical significance of differences between cases and controls. Further investigation with a prospective study design and larger sample size are needed. The stress fractures in the cases were diagnosed in their lower limbs whereas differences in bone microstructure were measured at the distal tibia and the distal radius [26,44–46]. Despite this limitation Mikolajewicz et al., and others have reported fracture prediction using HRpQCT. [24,47,48]. Finally, the contribution of pore size and pore number to the reduction in total porosity was not evaluated.

5. Conclusions

In summary, stress fractures are common among young adults and are likely to be partly the result of deficits in cortical and trabecular bone microstructure. Whether these deficits have their origin established during growth, during advancing age or both requires further study.

Author Contributions: Study design: A.Z. Study conduct: A.Z. and E.S. Data collection: A.Z., L.F., A.G.-Z. and W.S. Data analysis and statistical calculations: A.Z., M.B. and E.S. Data interpretation: all authors; Drafting manuscript: A.Z. and E.S. All authors contributed to the development and critical revision of the manuscript and approved the final version for submission. A.Z. takes responsibility for integrity of the data analysis. All authors have read and agreed to the published version of the manuscript.

Funding: This study was not sponsored by any pharmaceutical company. Vinforce receives academic funding grants.

Institutional Review Board Statement: The study was approved by the local ethical committee (VINFORCE-013AZ) and conducted in accordance with the Declaration of Helsinki.

Informed Consent Statement: All patients agreed to participate to the study and signed an informed consent form.

Data Availability Statement: The data presented in this study are available on request from the corresponding author.

Acknowledgments: The authors thank Colonel Christian Rizzi (Van Swieten Kaserne-Austrian Military Hospital Vienna/Austria) for the help in recruitment of several cases with stress fracture. We further thank Christina Marterer and Rahbarnia Arastoo for HR-pQCT scanning of the participants.

Conflicts of Interest: A.G.-Z. is one of the inventors of the StrAx1.0 algorithm. E.S. is an inventor of the StrAx1.0 algorithm and Directors of Straxcorp. All other authors state that they have no conflicts of interest.

References

1. Saunier, J.; Chapurlat, R. Stress fracture in athletes. *Jt. Bone Spine* **2018**, *85*, 307–310. [CrossRef]
2. Waterman, B.R.; Gun, B.; Bader, J.O.; Orr, J.D.; Belmont, P.J.J. Epidemiology of Lower Extremity Stress Fractures in the United States Military. *Mil Med.* **2016**, *181*, 1308–1313. [CrossRef]
3. McInnis, K.C.; Ramey, L.N. High-Risk Stress Fractures: Diagnosis and Management. *PM&R* **2016**, *8*, S113–S124. [CrossRef]
4. Bennell, K.L.; Malcolm, S.A.; Thomas, S.A.; Reid, S.J.; Brukner, P.D.; Ebeling, P.R.; Wark, J.D. Risk Factors for Stress Fractures in Track and Field Athletes: A Twelve-Month Prospective Study. *Am. J. Sports Med.* **1996**, *24*, 810–818. [CrossRef] [PubMed]
5. Tschopp, M.; Brunner, F. Diseases and overuse injuries of the lower extremities in long distance runners. *Z. Rheumatol.* **2017**, *76*, 443–450. [CrossRef]
6. Burr, D.B.; Martin, R.B.; Schaffler, M.B.; Radin, E.L. Bone remodeling in response to in vivo fatigue microdamage. *J. Biomech.* **1985**, *18*, 189–200. [CrossRef]
7. Schaffler, M.B.; Jepsen, K.J. Fatigue and repair in bone. *Int. J. Fatigue* **2000**, *22*, 839–846. [CrossRef]
8. Rosenberg, Z.; Zanetti, M. Imaging of the Foot and Ankle. In *Musculoskeletal Diseases*; Springer: Berlin/Heidelberg, Germany, 2005; pp. 39–47.
9. Turner, C.H.; Burr, D.B. Basic biomechanical measurements of bone: A tutorial. *Bone* **1993**, *14*, 595–608. [CrossRef]
10. Schnackenburg, K.E.; Macdonald, H.M.; Ferber, R.; Wiley, J.P.; Boyd, S.K. Bone Quality and Muscle Strength in Female Athletes with Lower Limb Stress Fractures. *Med. Sci. Sports Exerc.* **2011**, *43*, 2110–2119. [CrossRef]
11. Beck, T.J.; Ruff, C.B.; Mourtada, F.A.; Shaffer, R.A.; Maxwell-Williams, K.; Kao, G.L.; Sartoris, D.J.; Brodine, S. Dual-energy X-ray absorptiometry derived structural geometry for stress fracture prediction in male U.S. marine corps recruits. *J. Bone Miner. Res.* **1996**, *11*, 645–653. [CrossRef] [PubMed]
12. Beck, T.J.; Ruff, C.B.; Shaffer, R.A.; Betsinger, K.; Trone, D.W.; Brodine, S.K. Stress fracture in military recruits: Gender differences in muscle and bone susceptibility factors. *Bone* **2000**, *27*, 437–444. [CrossRef]
13. Armstrong, D.W.; Rue, J.-P.H.; Wilckens, J.H.; Frassica, F.J. Stress fracture injury in young military men and women. *Bone* **2004**, *35*, 806–816. [CrossRef]
14. Giladi, M.; Milgrom, C.; Simkin, A.; Stein, M.; Kashtan, H.; Margulies, J.; Rand, N.; Chisin, R.; Steinberg, R.; Aharonson, Z. Stress fractures and tibial bone width. A risk factor. *J. Bone Jt. Surg. Ser. B* **1987**, *69*, 326–329. [CrossRef] [PubMed]
15. Jepsen, K.J.; Evans, R.; Negus, C.H.; Gagnier, J.J.; Centi, A.; Erlich, T.; Hadid, A.; Yanovich, R.; Moran, D.S. Variation in tibial functionality and fracture susceptibility among healthy, young adults arises from the acquisition of biologically distinct sets of traits. *J. Bone Miner. Res.* **2013**, *28*, 1290–1300. [CrossRef]
16. Cosman, F.; Ruffing, J.; Zion, M.; Uhorchak, J.; Ralston, S.; Tendy, S.; McGuigan, F.E.; Lindsay, R.; Nieves, J. Determinants of stress fracture risk in United States Military Academy cadets. *Bone* **2013**, *55*, 359–366. [CrossRef] [PubMed]
17. Schanda, J.E.; Kocijan, R.; Resch, H.; Baierl, A.; Feichtinger, X.; Mittermayr, R.; Plachel, F.; Wakolbinger, R.; Wolff, K.; Fialka, C.; et al. Bone Stress Injuries Are Associated with Differences in Bone Microarchitecture in Male Professional Soldiers. *J. Orthop. Res.* **2019**, *37*, 2516–2523. [CrossRef]
18. Seeman, E. From Density to Structure: Growing Up and Growing Old on the Surfaces of Bone. *J. Bone Miner. Res.* **1997**, *12*, 509–521. [CrossRef]
19. Bjørnerem, Å.; Bui, Q.M.; Ghasem-Zadeh, A.; Hopper, J.L.; Zebaze, R.; Seeman, E. Fracture risk and height: An association partly accounted for by cortical porosity of relatively thinner cortices. *J. Bone Miner. Res.* **2013**, *28*, 2017–2026. [CrossRef]
20. Cadet, E.R.; Gafni, R.I.; McCarthy, E.F.; McCray, D.R.; Bacher, J.D.; Barnes, K.M.; Baron, J. Mechanisms responsible for longitudinal growth of the cortex: Coalescence of trabecular bone into cortical bone. *J. Bone Jt. Surg. Am.* **2003**, *85*, 1739–1748. [CrossRef]
21. Matcuk, G.R.J.; Mahanty, S.R.; Skalski, M.R.; Patel, D.B.; White, E.A.; Gottsegen, C.J. Stress fractures: Pathophysiology, clinical presentation, imaging features, and treatment options. *Emerg. Radiol.* **2016**, *23*, 365–375. [CrossRef]
22. Boks, S.S.; Vroegindeweij, D.; Koes, B.W.; Bernsen, R.M.D.; Hunink, M.G.M.; Bierma-Zeinstra, S.M.A. MRI Follow-Up of Posttraumatic Bone Bruises of the Knee in General Practice. *Am. J. Roentgenol.* **2007**, *189*, 556–562. [CrossRef] [PubMed]
23. Kaeding, C.C.; Miller, T. The Comprehensive Description of Stress Fractures: A New Classification System. *J. Bone Jt. Surg.* **2013**, *95*, 1214–1220. [CrossRef] [PubMed]
24. Boutroy, S.; Bouxsein, M.L.; Munoz, F.; Delmas, P.D. In VivoAssessment of Trabecular Bone Microarchitecture by High-Resolution Peripheral Quantitative Computed Tomography. *J. Clin. Endocrinol. Metab.* **2005**, *90*, 6508–6515. [CrossRef] [PubMed]
25. Zebaze, R.; Ghasem-Zadeh, A.; Mbala, A.; Seeman, E. A new method of segmentation of compact-appearing, transitional and trabecular compartments and quantification of cortical porosity from high resolution peripheral quantitative computed tomographic images. *Bone* **2013**, *54*, 8–20. [CrossRef] [PubMed]

26. Bala, Y.; Zebaze, R.; Ghasem-Zadeh, A.; Atkinson, E.J.; Iuliano, S.; Peterson, J.M.; Amin, S.; Bjørnerem, Å.; Melton, L.J.; Johansson, H.; et al. Cortical Porosity Identifies Women with Osteopenia at Increased Risk for Forearm Fractures. *J. Bone Miner. Res.* **2014**, *29*, 1356–1362. [CrossRef]
27. Zebaze, R.M.; Libanati, C.; Austin, M.; Ghasem-Zadeh, A.; Hanley, D.A.; Zanchetta, J.R.; Thomas, T.; Boutroy, S.; Bogado, C.E.; Bilezikian, J.P.; et al. Differing effects of denosumab and alendronate on cortical and trabecular bone. *Bone* **2014**, *59*, 173–179. [CrossRef]
28. Giladi, M.; Milgrom, C.; Simkin, A.; Danon, Y. Stress fractures. Identifiable risk factors. *Am. J. Sports Med.* **1991**, *19*, 647–652. [CrossRef] [PubMed]
29. Popp, K.L.; Frye, A.C.; Stovitz, S.D.; Hughes, J.M. Bone geometry and lower extremity bone stress injuries in male runners. *J. Sci. Med. Sport* **2020**, *23*, 145–150. [CrossRef]
30. Popp, K.L.; Hughes, J.M.; Smock, A.J.; Novotny, S.A.; Stovitz, S.D.; Koehler, S.M.; Petit, M.A. Bone Geometry, Strength, and Muscle Size in Runners with a History of Stress Fracture. *Med. Sci. Sports Exerc.* **2009**, *41*, 2145–2150. [CrossRef] [PubMed]
31. Weidauer, L.A.; Binkley, T.; Vukovich, M.; Specker, B. Greater Polar Moment of Inertia at the Tibia in Athletes Who Develop Stress Fractures. *Orthop. J. Sports Med.* **2014**, *2*. [CrossRef]
32. Wang, Q.; Wang, X.-F.; Iuliano-Burns, S.; Ghasem-Zadeh, A.; Zebaze, R.; Seeman, E. Rapid growth produces transient cortical weakness: A risk factor for metaphyseal fractures during puberty. *J. Bone Miner. Res.* **2010**, *25*, 1521–1526. [CrossRef] [PubMed]
33. Ruff, C.B.; Hayes, W.C. Subperiosteal expansion and cortical remodeling of the human femur and tibia with aging. *Science* **1982**, *217*, 945–948. [CrossRef] [PubMed]
34. Zebaze, R.M.D.; Jones, A.; Welsh, F.; Knackstedt, M.; Seeman, E. Femoral neck shape and the spatial distribution of its mineral mass varies with its size: Clinical and biomechanical implications. *Bone* **2005**, *37*, 243–252. [CrossRef]
35. Thomas, C.D.L.; Feik, S.A.; Clement, J.G. Increase in pore area, and not pore density, is the main determinant in the development of porosity in human cortical bone. *J. Anat.* **2006**, *209*, 219–230. [CrossRef] [PubMed]
36. Seeman, E. Age- and Menopause-Related Bone Loss Compromise Cortical and Trabecular Microstructure. *J. Gerontol. Ser. A Boil. Sci. Med Sci.* **2013**, *68*, 1218–1225. [CrossRef] [PubMed]
37. Schaffler, M.B.; Burr, D.B. Stiffness of compact bone: Effects of porosity and density. *J. Biomech.* **1988**, *21*, 13–16. [CrossRef]
38. Yeni, Y.N.; Brown, C.U.; Wang, Z.; Norman, T.L. The influence of bone morphology on fracture toughness of the human femur and tibia. *Bone* **1997**, *21*, 453–459. [CrossRef]
39. Currey, J.D. The many adaptations of bone. *J. Biomech.* **2003**, *36*, 1487–1495. [CrossRef]
40. Parfitt, A.M. Targeted and nontargeted bone remodeling: Relationship to basic multicellular unit origination and progression. *Bone* **2002**, *30*, 5–7. [CrossRef]
41. Schaffler, M.B.; Radin, E.L.; Burr, D.B. Mechanical and morphological effects of strain rate on fatigue of compact bone. *Bone* **1989**, *10*, 207–214. [CrossRef]
42. Pattin, C.A.; Caler, W.E.; Carter, D.R. Cyclic mechanical property degradation during fatigue loading of cortical bone. *J. Biomech.* **1996**, *29*, 69–79. [CrossRef]
43. Hughes, J.M.; Popp, K.L.; Yanovich, R.; Bouxsein, M.L.; Matheny, J.R.W. The role of adaptive bone formation in the etiology of stress fracture. *Exp. Biol. Med.* **2017**, *242*, 897–906. [CrossRef]
44. Patsch, J.M.; Burghardt, A.J.; Kazakia, G.; Majumdar, S. Noninvasive imaging of bone microarchitecture. *Ann. N. Y. Acad. Sci.* **2011**, *1240*, 77–87. [CrossRef]
45. Szulc, P.; Boutroy, S.; Chapurlat, R. Prediction of Fractures in Men Using Bone Microarchitectural Parameters Assessed by High-Resolution Peripheral Quantitative Computed Tomography-The Prospective STRAMBO Study. *J. Bone Miner. Res.* **2018**, *33*, 1470–1479. [CrossRef]
46. Vilayphiou, N.; Boutroy, S.; Szulc, P.; Van Rietbergen, B.; Munoz, F.; Delmas, P.D.; Chapurlat, R. Finite element analysis performed on radius and tibia HR-pQCT images and fragility fractures at all sites in men. *J. Bone Miner. Res.* **2011**, *26*, 965–973. [CrossRef] [PubMed]
47. Mikolajewicz, N.; Bishop, N.; Burghardt, A.J.; Folkestad, L.; Hall, A.; Kozloff, K.M.; Lukey, P.T.; Molloy-Bland, M.; Morin, S.N.; Offiah, A.C.; et al. HR-pQCT Measures of Bone Microarchitecture Predict Fracture: Systematic Review and Meta-Analysis. *J. Bone Miner. Res.* **2020**, *35*, 446–459. [CrossRef]
48. Sornay-Rendu, E.; Boutroy, S.; Duboeuf, F.; Chapurlat, R.D. Bone Microarchitecture Assessed by HR-pQCT as Predictor of Fracture Risk in Postmenopausal Women: The OFELY Study. *J. Bone Miner. Res.* **2017**, *32*, 1243–1251. [CrossRef] [PubMed]

OPEN ACCESS

Check for updates

Effect of dietary sources of calcium and protein on hip fractures and falls in older adults in residential care: cluster randomised controlled trial

S Iuliano,[1] S Poon,[1] J Robbins,[1] M Bui,[2] X Wang,[1] L De Groot,[3] M Van Loan,[4] A Ghasem Zadeh,[1] T Nguyen,[5,6] E Seeman[1]

[1]Departments of Medicine and Endocrinology, Austin Health, University of Melbourne, Melbourne, Australia
[2]School of Population and Global Health, University of Melbourne, Melbourne, Australia
[3]Division of Human Nutrition, Wageningen University, Wageningen, Netherlands
[4]US Department of Agriculture-ARS, University of California, Davis, CA, USA
[5]Garvan Institute of Medical Research, Sydney, Australia
[6]University of Technology Sydney, Sydney, Australia

Correspondence to: S Iuliano
sandraib@unimelb.edu.au
(ORCID 0000-0003-3900-2030)

Additional material is published online only. To view please visit the journal online.

Cite this as: *BMJ* 2021;375:n2364
http://dx.doi.org/10.1136/bmj.n2364

Accepted: 23 September 2021

ABSTRACT

OBJECTIVE

To assess the antifracture efficacy and safety of a nutritional intervention in institutionalised older adults replete in vitamin D but with mean intakes of 600 mg/day calcium and <1 g/kg body weight protein/day.

DESIGN

Two year cluster randomised controlled trial.

SETTING

60 accredited residential aged care facilities in Australia housing predominantly ambulant residents.

PARTICIPANTS

7195 permanent residents (4920 (68%) female; mean age 86.0 (SD 8.2) years).

INTERVENTION

Facilities were stratified by location and organisation, with 30 facilities randomised to provide residents with additional milk, yoghurt, and cheese that contained 562 (166) mg/day calcium and 12 (6) g/day protein achieving a total intake of 1142 (353) mg calcium/day and 69 (15) g/day protein (1.1 g/kg body weight). The 30 control facilities maintained their usual menus, with residents consuming 700 (247) mg/day calcium and 58 (14) g/day protein (0.9 g/kg body weight).

MAIN OUTCOME MEASURES

Group differences in incidence of fractures, falls, and all cause mortality.

RESULTS

Data from 27 intervention facilities and 29 control facilities were analysed. A total of 324 fractures (135 hip fractures), 4302 falls, and 1974 deaths were observed. The intervention was associated with risk reductions of 33% for all fractures (121 *v* 203; hazard ratio 0.67, 95% confidence interval 0.48 to 0.93; P=0.02), 46% for hip fractures (42 *v* 93; 0.54, 0.35 to 0.83; P=0.005), and 11% for falls (1879 *v* 2423; 0.89, 0.78 to 0.98; P=0.04). The risk reduction for hip fractures and falls achieved significance at five months (P=0.02) and three months (P=0.004), respectively. Mortality was unchanged (900 *v* 1074; hazard ratio 1.01, 0.43 to 3.08).

CONCLUSIONS

Improving calcium and protein intakes by using dairy foods is a readily accessible intervention that reduces the risk of falls and fractures commonly occurring in aged care residents.

TRIAL REGISTRATION

Australian New Zealand Clinical Trials Registry ACTRN12613000228785.

WHAT IS ALREADY KNOWN ON THIS TOPIC

Few studies have investigated the efficacy and safety of a nutritional approach to reduction of fracture risk in institutionalised older adults

One study using pharmacological doses of calcium and vitamin D reduced hip fractures in female nursing home residents with low calcium intakes and vitamin D deficiency

WHAT THIS STUDY ADDS

Supplementation using high calcium, high protein dairy foods reduced falls and fractures in vitamin D replete older adults in aged care

Introduction

Longevity increases the proportion of older adults in the population. The accompanying increased prevalences of chronic illnesses, loss of musculoskeletal mass, frailty, and bone fragility increase the risk of falls and fractures.[1] Loss of independence increases the number of people needing full time institutionalised care, the source of around 30% of all hip fractures in the community.[2] Thus, targeting an intervention to all aged care residents is a rational approach to reducing the fracture burden in the whole community.

The widespread use of antiresorptive therapy is unlikely to reduce this fracture burden because of a paucity of evidence of antifracture efficacy in people over 80 years of age, the common occurrence of adverse events, and high cost given the large numbers of people that must be treated.[3] However, these people often have calcium intakes below 700 mg daily, an amount unlikely to offset obligatory loss of calcium.[4] They also often have protein intakes below 1 g/kg body weight/day, predisposing to loss of lean muscle mass.[5] Thus, an alternative approach is to target all institutionalised older adults with a non-pharmaceutical nutritional intervention.

Few studies have investigated the efficacy and safety of a nutritional approach to reduction of fracture risk in aged care residents. Chapuy and colleagues showed antifracture efficacy with pharmacological doses of calcium and vitamin D in female nursing home residents with low calcium intakes and vitamin D deficiency.[6] No studies have examined the effects of protein supplementation on reduction of fracture risk, despite evidence of improved muscle function and reduced falls.[7]

Consumption of milk, yoghurt, and cheese, foods rich in calcium and protein, slows bone loss and improves insulin-like growth factor 1.[8 9] These foods are widely available, palatable, and low cost and so are likely to be adhered to. Accordingly, we conducted a prospective,

BMJ: first published as 10.1136/bmj.n2364 on 20 October 2021. Downloaded from http://www.bmj.com/ on 18 June 2023 by guest. Protected by copyright.

two year, cluster randomised controlled trial to test the hypothesis that achieving recommended intakes of 1300 mg/day calcium and 1 g protein/kg body weight will reduce the risk of fragility fractures and falls when targeted to institutionalised older adults replete in vitamin D but with intakes below these levels.

Methods

Study design

This two year, cluster randomised controlled trial involved recruitment of 60 residential aged care facilities housing 7195 older adults in metropolitan Melbourne and regional Victoria, Australia, between December 2013 and August 2016. To ensure similar standards of care, we recruited only facilities accredited with the Australian Aged-Care Accreditation Agency that housed predominantly ambulant residents. These facilities are similar to residential care in the UK and assisted care facilities in the US. Facilities recruited were representative of charitable, private, and religious organisations, with an even distribution of small (≤50 beds), medium (51-100 beds), and large (>100 beds) facilities (supplementary figure C). The ratio of women to men and the age of residents were representative of the national average.[10]

Inclusion criteria

Randomisation was by facility, not by individuals. For inclusion, facilities were required to provide no more than two servings of dairy foods daily, which was assessed from menu audits, as this level of provision is associated with dietary intakes of <1 g/kg body weight and 600 mg calcium daily.[11] Vitamin D adequacy is maintained in residents through routine supplementation as foods are not fortified with vitamin D. We included only permanent residents in data analyses—that is, we excluded data from respite residents.

Randomisation procedure

The unit of randomisation was facility, as the intervention was delivered to all residents by the food service at each facility. Eligible facilities were randomly assigned in a 1:1 ratio to either intervention (n=30) or control (n=30), with the control facilities maintaining their existing menus. The randomisation was done with the use of a computer, with block sizes being varied according to organisation (to ensure similar procedures and policies), and was stratified by geographical location (to ensure similar socioeconomic status). A statistician independent of the study did the randomisation and provided the concealed group allocation to the principal investigator (SI) who, in turn, conveyed this allocation to the facility. SI was not involved in any data collection. An organisation may have between two and 10 facilities, and randomisation was done within an organisation.

Consent

Facility managers consented to provide de-identified details of age and sex of residents, as well as access to all incident reports including those for falls and fractures. Reporting of all incidents of any nature is a mandatory requirement of all accredited aged care providers. The accreditation agency regularly audits incident reports. Facilities are sanctioned if breaches are observed, with potential for accreditation to be revoked and government funding terminated. Falls (time, location, circumstances, and outcome/injury), fractures, and other adverse events were verified from these incident reports. These reports were maintained at all facilities. An independent medically trained person blinded to study allocation verified fractures by using hospital radiographs and radiographic reports. Residents and families were informed of the study during regular meetings. A subset of 371 residents from all facilities voluntarily consented to have dietary intake recorded, medical records reviewed, blood sampling, and measurement of body composition, bone mineral density, and bone microarchitecture performed. A next of kin consented for an additional 345 residents to allow dietary intake to be recorded and medical records reviewed.

Intervention

We classified dairy foods by using the Australian Dietary Guidelines, with a "serving" defined as 250 mL of milk, 200 g of yoghurt, and 40 g of cheese.[12] Lactose-free options were provided to accommodate the few participants (<0.001%) with reported lactose intolerance. Butter, cream, and ice cream were not provided, as they contain little calcium or protein. All facilities prepared and cooked foods on site. We assigned intervention facilities a food service dietician to assist food service staff to increase the provision of dairy foods at all meals and snacks. Methods used to increase dairy foods included use of milk powder to fortify milk used in recipes and beverages. Dairy based desserts and snacks were offered in place of less nutritious foods such as cakes and biscuits. Foods provided were based on the preferences expressed by the residents at intervention sites.

Dairy foods were provided in-kind by Fonterra International (New Zealand) and distributed by a commercial food distribution company not associated with the project (Bidfoods, Australia). Use of a single distributor ensured accurate recording of costs for all dairy foods provided, with invoices used to verify compliance data. During dietary assessments, foods and beverages were weighed on a food scale (±1 g) (Sohnele Page Profi, Germany) at all facilities. During two days every three months, dieticians assessed compliance by using the validated visual estimation of plate waste, with data collected from 55 000 foods and beverages during the study.[13] We used nutritional analysis software (FoodWorks, Australia) or the Australian food composition database NUTTAB 2010 to calculate nutrient intakes.

Data monitoring

Data safety monitoring was carried out by the Study Trial Review Board, which was provided with quarterly reports.

BMJ: first published as 10.1136/bmj.n2364 on 20 October 2021. Downloaded from http://www.bmj.com/ on 18 June 2023 by guest. Protected by copyright.

Outcomes

As per the approved study protocol, all pre-specified primary and secondary outcomes have been reported. The primary outcome was time to fragility fracture. Secondary outcomes were time to fall and changes in bone morphology and biochemistry. The tertiary outcomes of all cause mortality and changes in body composition are also reported. Exploratory outcomes including quality of life and muscle function were not examined (see original and final study protocols). Fasting morning serum samples were obtained from 189 residents at baseline and 12 months for measurement of 25-hydroxy-vitamin D (baseline only), C terminal telopeptide of type 1 collagen (a measure of bone resorption), procollagen type 1 N propeptide (a measure of bone formation), parathyroid hormone (Roche Cobas E170), and insulin-like growth factor 1 (LIASON) (supplementary figure A).

Body composition and bone morphology were assessed at baseline and 12 months in 72 residents (supplementary figure B). Total and appendicular (arms and legs) lean mass and fat mass were determined from total body scans, and bone mineral density was measured at the lumbar spine and femoral neck using dual x-ray absorptiometry (Prodigy, GE Lunar, Madison, WI, CV=1%). Volumetric bone mineral density (the amount of bone contained within the external volume of bone, in g/cm^3) was measured at the distal tibia and distal radius by using high resolution peripheral quantitative computed tomography (Scanco Medical AG, Switzerland, CV 0.5–4.0%).[14] Cortical porosity was determined using automated image processing (StrAx1.0, Straxcorp, Melbourne, Australia).

Blinding and sample size

Once a facility was randomised, only the principal investigator, food service research dieticians, facility managers, and food service staff were aware of the allocation. Data acquisition and analyses were carried out by staff blinded to group allocation (SP, XW, MB, AGZ, and TN). Residents were blinded to the study; permission to conduct the study was obtained from the aged-care provider and facility managers. Some of the intervention strategies were not visible—for example, fortification of milk with milk powder or modification of recipes. Some residents may have been aware of some changes, such as provision of cheese and biscuits for snacks, but not the reason for the changes.

The sample size was determined on the basis of a hypothesised effect size and intra-cluster correlation coefficient (r). Under the hypothesis that the intervention reduces the risk of fracture by 30%, based on previous antifracture calcium/vitamin D intervention in this setting, and that r ranges from 0.10 to 0.50, the sample size needed was 25 to 50 residents per facility and 25 facilities per arm to achieve the power of 80%.[6] From falls data, we used an r of 0.20 to calculate the sample size.[15] To account for approximately 20% annual attrition, we recruited 60 facilities with a minimum of 50 residents per facility.

At the start of the study, 3980 permanent residents were living in the participating facilities. We refer to these residents as the inception cohort. Recruitment continued throughout the 24 months to ensure that the required sample size was maintained, so we included data from residents admitted to facilities that replaced initial residents lost to follow-up due to death or discharge in analyses. We refer to these residents as the replacement cohort. In total, an additional 3215 residents were admitted to facilities after the study had started. We obtained details of new residents and those lost to follow-up from admission and discharge records from each facility.

Analyses

We expressed baseline data as mean and standard deviation, with the unit of analysis being clusters. We expressed fracture incidence, falls, and deaths per 100 person years of follow-up. We used the product limit (Kaplan-Meier) method to determine the cumulative risk of an event. No data were missing for these primary and secondary outcomes. The duration of follow-up was based on date of study entry to date of an event. When no event occurred, duration of follow-up was date of study entry to date of study termination.

As individuals were "nested" within clusters (facilities), the primary analysis was based on the mixed effects Cox's proportional hazards model; effects of intervention, age, and sex were fixed effects, and the facility was considered the random effect (see supplementary methods for additional statistical analysis). We expressed the results as a hazard ratio with 95% confidence limits. We used the "coxme" package to estimate model parameters. We also used the Fine-Gray sub-distribution method with the "cmprsk" package to do mortality competing risk analysis.

We tested between group differences in serum biomarkers and measurements of body composition and bone morphology at baseline with the weighted t test, with cluster being the unit of analysis. Biomarkers were log transformed if they were not normally distributed. We analysed effects of the intervention by using the mixed effects model in which the within person change in outcome was modelled as a function of treatment or control group, time of follow-up, age, weight, and sex. All analyses used the R Statistical Environment.

Amendments to protocol and statistical analysis plan

Initially, facilities were matched only by location to account for socioeconomic status. We also accounted for organisations, as they contributed varying numbers of facilities and had different policies and procedures. We included facilities providing less than two servings of dairy food daily, as dietary assessments for all residents was not feasible. We quantified two day instead of three day diets, as this was adequate to capture regular intakes.[11] We did not assess osteocalcin, as sufficient information is obtained from C terminal telopeptide of

BMJ: first published as 10.1136/bmj.n2364 on 20 October 2021. Downloaded from http://www.bmj.com/ on 18 June 2023 by guest. Protected by copyright.

type 1 collagen and procollagen type 1 N propeptide. We used only all cause mortality as a tertiary outcome, as cardiovascular events were not obtainable and causes of death were poorly documented. We did not examine exploratory outcomes related to quality of life and muscle function, as unanticipated attrition reduced the sample size resulting in insufficient power to detect an effect of treatment. We did not include bayesian analyses and imputations, as no values were missing for falls and fracture outcomes (original and final study protocols).

Patient and public involvement

We consulted aged care residents, providers, and food service staff after the initial feasibility study that guided the design of this intervention.[16] The manuscript was read by non-academics.

Results

Of the 60 facilities, 54 completed the 24 month intervention (fig 1). One control facility and three intervention facilities withdrew after randomisation. Two intervention facilities closed at months 15 and 20, but we included the data up to the date of closure. At baseline, the two groups had comparable demographics and were vitamin D replete. Daily baseline calcium and protein intakes were 689 (SD 266) mg and 57 (16) g respectively (table 1; supplementary figure D).

Nutritional changes

Dairy food intake increased from 2.0 to 3.5 servings daily in the intervention facilities (fig 2). The additional dairy foods, equivalent to 250 mL of milk plus 20 g cheese or 100 g yoghurt, provided 562 (166) mg calcium, achieving 1142 (353) mg calcium daily, and 12 (6) g protein, achieving an intake of 69 (15) g (1.1 g/kg body weight) daily. In control facilities, residents' dairy intakes remained at less than two servings daily providing 700 (247) mg calcium and 58 (14) g protein (0.9 g/kg body weight) daily. No adverse gastrointestinal events related to the intervention were reported. No detectable within or between group differences in energy intake were observed during follow-up (fig 2). However, we observed group differences for the change in body weight (table 2). In absolute terms, no weight change occurred in the intervention group (0.3 (95% confidence interval −0.8 to 1.4) kg; P=0.56). In controls, a weight loss of 1.4 (0.6 to 2.1) kg, (P<0.001) was due to a 0.3 (−0.6 to 0.0) kg decline in appendicular lean mass (P=0.03) and 0.8 kg (−1.6 to −0.2) decline in total body fat mass (P=0.02).

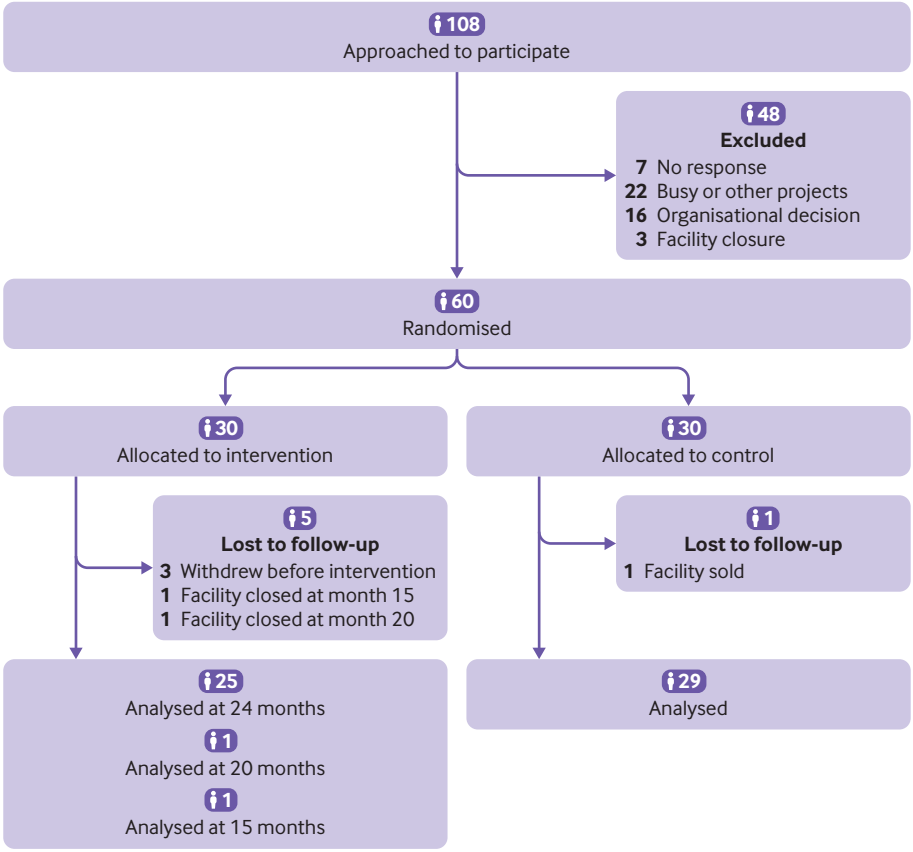

Fig 1 | Flowchart for participating aged care facilities. Of 108 eligible facilities, 48 were excluded, leaving 60 randomised to intervention or control. Three intervention facilities and one control facility did not start study, leaving 27 intervention and 29 control facilities participating, of which two intervention facilities closed during study period. Median number of residents in intervention and control groups were 111 (interquartile range 75-147) and 125 (88-163), respectively; P=0.42 by Wilcoxon's rank test

BMJ: first published as 10.1136/bmj.n2364 on 20 October 2021. Downloaded from http://www.bmj.com/ on 18 June 2023 by guest. Protected by copyright.

Table 1 | Baseline characteristics of residents in clusters assigned to two years of dairy supplementation (intervention) or maintenance of existing menu (controls). Values are mean (standard deviation) unless stated otherwise

Characteristics	Intervention (n=3301)	Controls (n=3894)
No of clusters (facilities)	27	29
Median No of residents per cluster	111	125
No (%) female	2311 (70)	2609 (67)
Age, years	86 (2.3)	86 (2.2)
Height (m)	1.60 (0.02)	1.61 (0.03)
Weight (kg)	66 (6.3)	68 (8.4)
Median (IQR) medications*	11 (8-14)	12 (9-16)
Median (IQR) medical conditions*	9 (7-12)	10 (7-14)
No (%) with previous fracture*	184 (41)	183 (37)
No (%) with cognitive impairment*	189 (52)	237 (53)
No (%) with cardiovascular disease*	301 (66)	309 (63)
No (%) malnourished, at risk, normal†	70 (17), 272 (66), 70 (17)	25 (11), 158 (66), 55 (23)
Biochemistry	**(n=170)**	**(n=135)**
25-hydroxy-vitamin D, nmol/L	72 (15)	72 (21)
C terminal telopeptide of type 1 collagen, ng/mL	0.41 (0.14)	0.39 (0.11)
Procollagen type 1 N propeptide, µg/L	52.9 (19.1)	48.5 (9.7)
Parathyroid hormone, pg/mL	6.85 (2.04)	7.27 (1.74)
Insulin-like growth factor 1, nmol/L	15.4 (2.8)	15.1 (3.1)
Body composition	**(n=77)**	**(n=79)**
Total lean mass, kg	39.7 (8.6)	39.8 (8.1)
Appendicular lean mass, kg	16.3 (1.2)	16.4 (3.7)
Fat mass, kg	22.5 (9.5)	27.2 (11.0)
Bone morphology	**(n=77)**	**(n=79)**
Femoral neck BMD, g/cm^2	0.76 (0.08)	0.74 (0.12)
Lumbar spine BMD, g/cm^2	1.08 (0.22)	1.13 (0.23)
Distal tibia:		
Total volumetric BMD, mgHA/cm^3	215 (44)	228 (63)
Cortical porosity, %	75 (5.6)	75 (6.6)
Trabecular volumetric BMD, mgHA/cm^3	155 (35)	167 (47)
Distal radius:		
Total volumetric BMD, mgHA/cm^3	257 (41)	247 (68)
Cortical porosity, %	68 (3.8)	69 (7.5)
Trabecular volumetric BMD, mgHA/cm^3	155 (34)	148 (47)

BMD=bone mineral density; IQR=interquartile range.
*n=457 intervention; n=494 controls.
†Mini Nutrition Assessment Score: 24-30=normal nutritional status; 17- 23.5=at risk of malnutrition; <17=malnourished (n=412 intervention; n=238 controls).

Fractures, falls, and mortality

During 90 557 person months of follow-up (mean 12.6 (8.9) months), 324 fractures occurred: 121 (3.7%) in the intervention group and 203 (5.2%) in controls—a 33% risk reduction (hazard ratio 0.67, 95% confidence interval 0.48 to 0.93; P=0.02). Post hoc analysis indicated that the incidence of hip fracture was 1.3% (n=42) in the intervention group and 2.4% (n=93) in controls—a 46% risk reduction (hazard ratio 0.54, 0.35 to 0.83; P=0.005). The separation in cumulative incidence of fractures between the groups achieved significance at five months for all fractures (P=0.02) and hip fractures (P=0.02) (fig 3). Competing risk analysis adjusted for mortality showed that the intervention was associated with average reductions in fracture risk of 27% (hazard ratio 0.73, 0.58 to 0.92) for all fractures and 44% (0.56, 0.39 to 0.82) for hip fractures.

The cumulative incidence of falls was 57% (n=1879) in the intervention group and 62% (n=2423) in controls—an 11% relative risk reduction (hazard ratio 0.89, 0.78 to 0.98; P=0.04). The separation in the incidence of falls between groups achieved significance at three months (P=0.04) (fig 3). All but one fracture was the result of a fall. Mortality did not differ between the intervention and control groups (27% (n=900) *v* 28% (n=1074), respectively; hazard ratio 1.01, 0.43 to 3.08; P=0.91) (fig 3). The numbers needing treatment to prevent any fracture, hip fracture, or a fall were 52, 82, and 17, respectively.

To explore the veracity of the observations made in the entire cohort (n=7195), we examined the effects of the intervention on fracture risk and falls relative to controls in a post hoc analyses of residents present at the start of the study (n=3980, the inception cohort) and residents added after its start (n=3215, the replacement cohort), separately. The inception cohort was older than the replacement cohort (mean 86.5 (8.1) *v* 85.2 (8.4) years; P<0.001). However, age did not differ between the intervention and control groups in either the inception cohort (mean 86.7 (8.2) *v* 86.4 (8.0) years, respectively; P=0.25) or the replacement cohort (85.1 (8.5) *v* 85.3 (8.2) years, respectively; P=0.601). We observed significant reductions in all fractures, hip fractures, and falls in the intervention group relative to the controls in both the inception and replacement cohorts (see supplementary figure E).

Biochemistry and bone morphology

The subgroup providing data for biochemistry, body composition, and bone morphology did not differ from

BMJ: first published as 10.1136/bmj.n2364 on 20 October 2021. Downloaded from http://www.bmj.com/ on 18 June 2023 by guest. Protected by copyright.

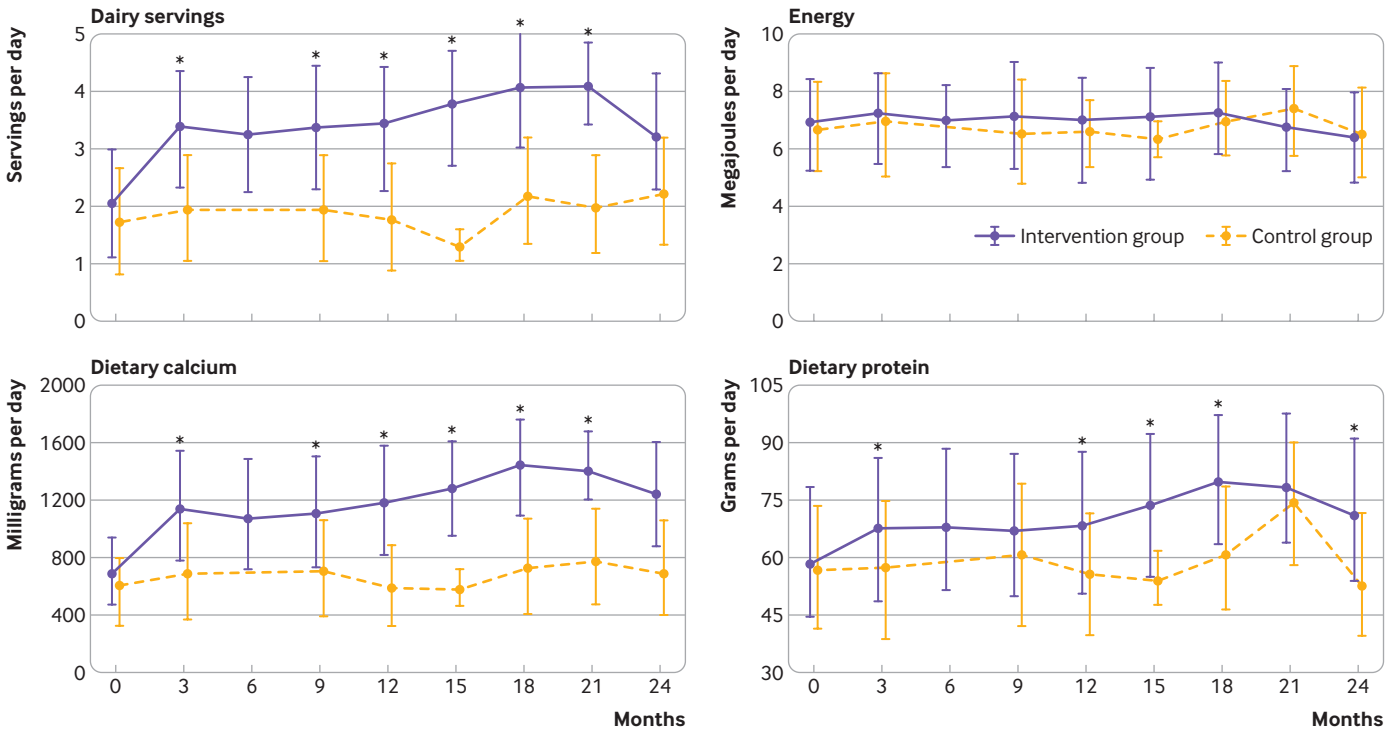

Fig 2 | Mean (SD) daily dietary intake of dairy servings, energy, calcium, and protein at baseline (regular menu) and during two year study period in intervention group compared with controls. *P<0.05 denotes significant difference between groups at corresponding time point

the entire cohort in age (mean 85.9 (8.2) *v* 85.6 (8.2) years), proportion of women to men (70% (n=74) *v* 69% (n=57)), and proportion with previous fractures (38% (n=40) *v* 39 (n=32)). As shown in table 2, at 12 months, we observed a 20.4% between group difference in serum C terminal telopeptide of type 1 collagen (P=0.002), the result of no change in the intervention group and a 13.1% increase in controls (P<0.05). We observed no between group difference in procollagen type 1 N propeptide or parathyroid hormone, but we observed a 7.9% between group difference in serum insulin-like growth factor 1 (P=0.04), the result of a 5.9% increase in the intervention group (P<0.05) and no change in controls.

We observed a 1.8% between group difference in spine bone mineral density (P=0.04), the result of a

Table 2 | Mean (standard deviation) percentage change from baseline at month 12 in biochemistry and bone morphology in each group and between group mean percentage difference with 95% confidence interval.

	Intervention	Control	Mean between group difference (95% CI)	P value
Biochemistry	(n=106)	(n=83)		
Bone resorption marker (CTX)	−7.3 (40.7)	13.1 (45.5)*	−20.4 (−33.2 to −7.6)	0.002
Bone formation marker (P1NP)	−4.7 (35.4)	−3.9 (55.1)	−0.8 (−14.6 to 12.9)	0.90
Parathyroid hormone	1.1 (20.7)	−0.16 (32.0)	1.3 (−6.7 to 9.2)	0.76
Insulin-like growth factor-1	5.9 (27.0)*	−2.0 (22.4)	7.9 (15.7 to 0.2)	0.04
Bone morphology	(n=33)	(n=39)		
Lumbar spine BMD	2.1 (2.7)**	0.3 (2.4)	1.8 (0.1 to 3.5)	0.04
Femoral neck BMD	0.7 (3.0)	−1.0 (4.4)	1.7 (−0.3 to 3.7)	0.09
Distal radius:				
Total volumetric BMD	0.7 (2.7)	−2.6 (5.6)*	3.3 (0.6 to 6.0)	0.02
Trabecular volumetric BMD	0.9 (2.3)	−3.5 (8.7)	4.6 (0.4 to 8.2)	0.03
Cortical porosity	0.0 (1.7)	0.7 (3.3)	−0.6 (−2.3 to 1.0)	0.43
Distal tibia:				
Total volumetric BMD	−0.1 (2.5)	−2.1 (4.4)*	2.0 (−0.1 to 4.2)	0.07
Trabecular volumetric BMD	0.2 (2.3)	−2.2 (8.5)	2.4 (−1.4 to 6.2)	0.21
Cortical porosity	0.4 (1.3)	0.7 (1.2)*	−0.3 (−1.1 to 0.4)	0.39
Body composition	(n=33)	(n=39)		
Body weight	0.6 (8.3)	−1.9 (5.2)**	2.5 (0.6 to 4.1)	0.009
Lean mass	−0.2 (2.7)	−0.4 (2.8)	0.3 (−0.9 to 1.6)	0.60
Appendicular lean mass	0.3 (4.5)	−1.7 (5.0)*	2.0 (0.02 to 4.1)	0.05
Fat mass	3.8 (20.6)	−3.3 (8.1)*	7.3 (0.1 to 14.5)	0.05

BMD=bone mineral density; CTX=C terminal telopeptide of type 1 collagen; P1NP=procollagen type 1 N propeptide.
*P<0.05 for difference from baseline within group.
**P<0.001 for difference from baseline within group.

BMJ: first published as 10.1136/bmj.n2364 on 20 October 2021. Downloaded from http://www.bmj.com/ on 18 June 2023 by guest. Protected by copyright.

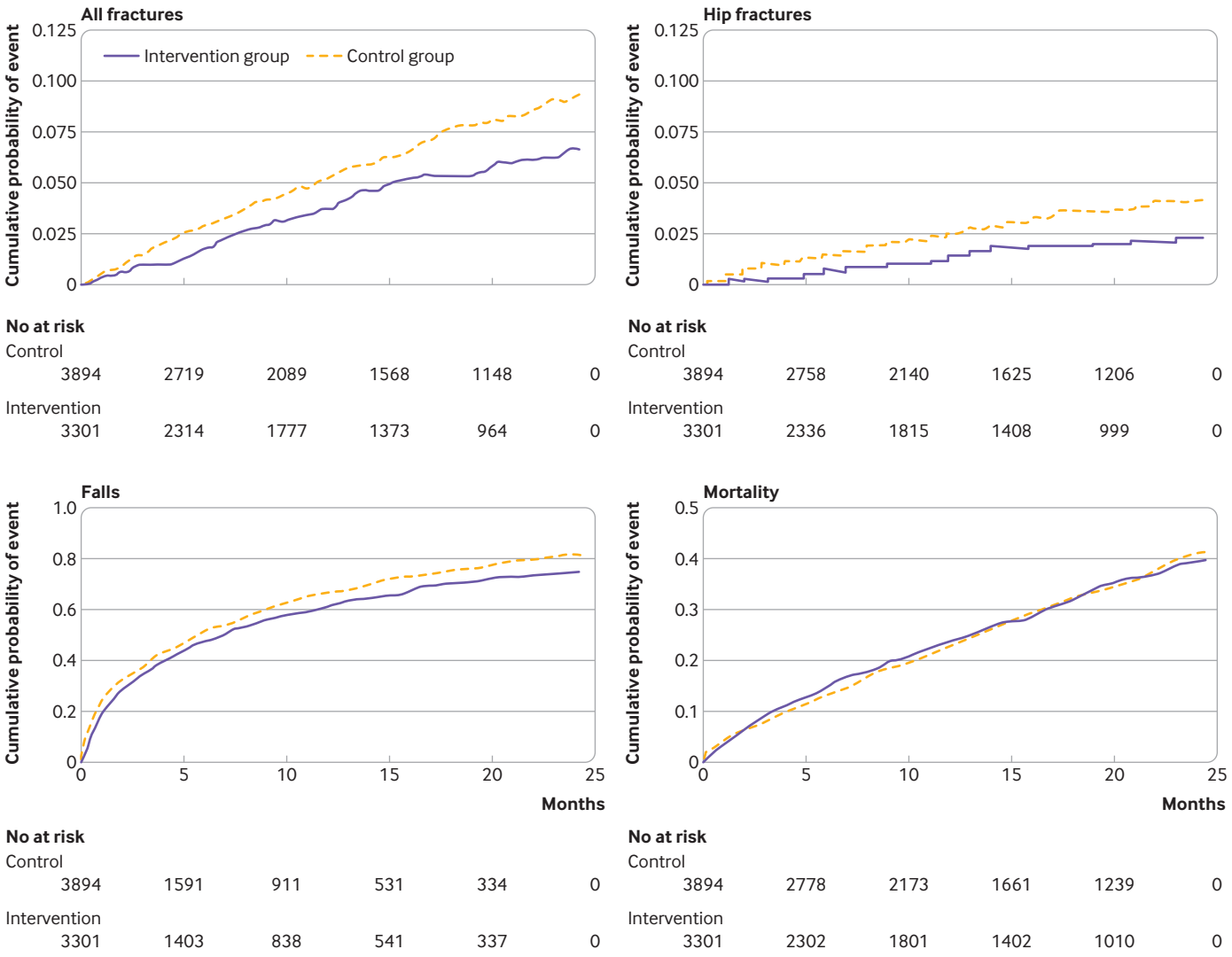

Fig 3 | Cumulative probability of event over 24 months for all fractures, hip fractures, falls, and mortality in intervention group and controls. Numbers of participants in two groups at risk for each event are shown below panels

2.1% increase in the intervention group (P<0.001) and no change in controls. The 1.7% between group difference in femoral neck bone mineral density was not significant (P=0.09). The 3.3% between group difference in distal radius total volumetric bone mineral density (P=0.02) and 2.0% between group difference in distal tibial total volumetric bone mineral density (P=0.07) were the result of decreases at each site in controls (both P<0.05). We observed a 4.6% between group difference in distal radial trabecular volumetric bone mineral density (P=0.03) due to a non-significant decrease in controls and a 0.7% increase in distal tibia cortical porosity in controls (P<0.05).

Discussion

This nutritional approach using high calcium and high protein dairy foods to increase calcium and protein intakes in institutionalised older adults replete in vitamin D was associated with a 33% reduction in risk of fractures of any type, a 46% reduction in risk of hip fractures, and an 11% reduction in risk of falls relative to controls. We found no group difference in all cause mortality.

Most interventions aimed at reducing fracture risk target a drug therapy to people with osteoporosis because they are at high risk of fracture. This approach confers a large benefit to the individual and does so cost effectively, because few people need to be treated to avert one event. However, averting fractures in small numbers of people at high risk does not reduce the burden of fractures in the community.

The population burden of fractures—the number of events, morbidity, mortality, and cost to the community—arises from the vast numbers of people with risk factors that confer a modest attributable risk to the individual.[17] For example, most fragility fractures in the community arise among women with osteopenia (bone mineral density T score −2.5 to −1 SD) because they form the largest segment of the community.[18] Likewise, most fractures attributable to nutritional inadequacy arise among the great many people with intakes of calcium and protein that are below recommended levels.[19] This nutritional inadequacy confers a small attributable risk to the individual but accounts for a large attributable fraction

BMJ: first published as 10.1136/bmj.n2364 on 20 October 2021. Downloaded from http://www.bmj.com/ on 18 June 2023 by guest. Protected by copyright.

of the fracture burden in the community as a whole. This is the Geoffrey Rose prevention paradox—a community based approach producing a small benefit to an individual may still confer a large benefit to the community.[17] Safety is essential because most individuals treated may derive little or no benefit from the intervention. For example, the Dietary Approach to Stop Hypertension study reduced blood pressure by replacing a "western" diet with a diet rich in fruit, vegetables, and low fat dairy foods—an approach associated with fewer cardiovascular events.[20]

Comparison with other studies

Most nutrition based studies assessing antifracture efficacy in aged care residents and people in the community used pharmacological doses of calcium with or without vitamin D.[21] In a meta-analysis of 17 of these studies, only two studies reported a reduction in fracture risk—a study of nursing home residents with calcium intakes <600 mg/day and vitamin D concentrations <50 nmol/L and a community based study in women and men ≥65 years of age with mean calcium intakes of 700 mg/day.[21] In the remaining 15 studies, poor compliance, large numbers of dropouts, and a low prevalence of the risk factor may have contributed to the null findings.[22 23] Benefits are unlikely if the prevalence of a risk factor (such as inadequate calcium and protein intakes) is low.[24] For example, in the meta-analysis, reduction in fracture risk reported with treatment was confined to the 7272 individuals with calcium intakes <700 mg/day (risk ratio 0.80, 95% confidence interval 0.71 to 0.89), not the 45 241 individuals with calcium intakes above 700 mg daily.[21] The reduction in fracture risk observed with calcium and protein rich foods in this study may have been the result of attention to several of the above factors. Compliance was optimised by supervised provision and consumption of the foods. Participants lost to follow-up were replaced by newly admitted residents. We intentionally targeted a cohort at high risk for fracture in whom low calcium and protein intakes were common and so were likely to partly contribute to the already high fracture burden in this community.

Mechanisms of fracture risk reduction

This nutritional intervention produced two unanticipated novel observations. The risk reduction for falls and fractures was detected by three and five months, respectively, and the relative risk reduction for fractures was similar to that found in trials using potent antiresorptive therapy to treat people at high risk due to osteoporosis. The two most likely explanations for each of these observations is a risk reduction for falls and slowing progression of bone fragility. Insulin-like growth factor 1 increased in the intervention group only, whereas the decrease in appendicular lean mass was confined to controls, consistent with the notion that protein intakes of 1-1.5 g/kg/day is needed to prevent protein catabolism and preserve or increase muscle mass in older adults, particularly those at risk of malnutrition or frailty.[25] The increase in serum C terminal telopeptide of type 1 collagen and deterioration in tibial and radial total volumetric bone mineral density in controls was not seen in the intervention group, consistent with slowing of bone loss and slowing of microstructural deterioration.[26] These changes were modest, but slowing microstructural deterioration disproportionately reduces progression of bone fragility because fragility increases as a power function to the bone loss producing it.[27]

Mortality did not differ between the groups. Some, but not all, studies suggest that milk consumption is associated with increased mortality but consumption of yoghurt and cheese (fermented foods) with reduced mortality and favourable blood lipid profiles.[28-30] Fermented and non-fermented dairy foods were used during the intervention. Milk consumption did not differ between the intervention and control groups (data not shown).

Limitations of study

The study has several limitations. Less than half of the participants had follow-up longer than 15 months. However, the reduction in risk of fractures and falls was detected within six months. Measures of dietary intakes and causes of secondary osteoporosis were obtained from the subgroup of 716 consented participants, not all 7195 residents, so compliance was monitored in about 10% of residents. However, recorded intakes of 55 000 foods and beverages are likely to be representative of all residents as most, if not all, food is provided by facilities. Assessment of body composition, bone morphology, and biochemistry was confined to a subgroup of residents. Attrition of these participants limited the power to examine differences in body composition, bone morphology, and biochemistry between the groups. Therefore, our ability to make inferences concerning the role of this intervention in slowing microstructural deterioration and loss of muscle mass is limited. Serum parathyroid hormone remained unchanged, perhaps owing to administration of around 1100 mg of calcium throughout the day as food, not as a single supplement of elemental calcium.[31] Moreover, this intervention used whole dairy foods, so any potential benefit of other components of the dairy matrix cannot be determined.

Summary and conclusions

In summary, ageing of the population is associated with a greater number of older adults needing full time institutionalised care. These individuals are often malnourished.[5] Although the risk of fracture attributable to undernutrition may be small in an individual, the large number of older adults in aged care confers a large fracture burden in the community; institutionalised people are the source of about 30% of all hip fractures.[2 17] A high calcium and high protein nutritional intervention reduced the risk of falls and fractures. This intervention was tailored to the preferences of the residents and was successfully

BMJ: first published as 10.1136/bmj.n2364 on 20 October 2021. Downloaded from http://www.bmj.com/ on 18 June 2023 by guest. Protected by copyright.

delivered through the food service using regular retail milk, yoghurt, and cheese incorporated into existing menus. In conclusion, this nutritional intervention has widespread implications as a public health measure for fracture prevention in the aged care setting and potentially in the wider community.

We thank dieticians Anishya Gangadharan, Annemarie Murrell, Caryn Batchelor, Deanna Lavanty, Ella Smits, Lexie Griffin, Stephanie Renehan, Samantha Chiodo, Sally Collins, Simone Karafilis, Simone Mastronado, and Kako Choi for assisting in data collection; food service specialists Brenda Cook, Denise Burbidge, and Megan Dodds for their work with food service staff; and research nurses Angela Sones and Kylie King. We dedicate this manuscript to the late Gonca Pasin of the California Dairy Research Foundation, whose drive, enthusiasm, and vision were instrumental in the initiation of this project.

Contributors: SI was involved in the conception, design, planning, and management of the study, data acquisition, interpretation of results, drafting the manuscript, and critically reviewing or revising the manuscript for important intellectual content. SP and JR were involved in data acquisition and management and critically reviewing or revising the manuscript. MB and XW were involved in data analysis, interpretation of results, and critically reviewing or revising the manuscript for important intellectual content. LDG was involved in the design of the study and critically reviewing or revising the manuscript. MVL was involved in the design of the study, data acquisition, and critically reviewing or revising the manuscript. AGZ was involved in data acquisition and interpretation of results. TN was involved in the design of the study, data analysis, interpretation of results, and critically reviewing or revising the manuscript. ES was involved in the conception and design of the study, interpretation of results, drafting the manuscript, and critically reviewing or revising the manuscript for important intellectual content. SI and ES are the guarantors. The corresponding author attests that all listed authors meet authorship criteria and that no others meeting the criteria have been omitted.

Funding: This study was support by grants from Dairy Australia (grant number TP 701722), California Dairy Research Foundation, National Dairy Council, Aarhus University Hospital and Danish Dairy Research Foundation, Fonterra Co-operative Group Ltd, Dutch Dairy Association, Dairy Council of California, Dairy Farmers of Canada, the Centre national interprofessionnel de l'economie laitiere, University of Melbourne, Austin Hospital Medical Research Foundation, and Sir Edward Dunlop Medical Research Foundation. The funding groups played no role in the design, execution, analyses, interpretation of the data, writing of the manuscript, preparation of slides or presentation at congresses, or any other aspect of the study.

Competing interests: All authors have completed the ICMJE uniform disclosure form at www.icmje.org/disclosure-of-interest/ and declare: funding support from the organisations listed above; SI has received lecture fees from Abbott; TVN has received research support and lecture fees from Amgen, MSD, and Novartis; ES has received research support from Amgen and MSD and lecture fees from Amgen, Eli Lilly, and Allergan; ES is a scientific consultant for StraxCorp and shareholder; no other relationships or activities that could appear to have influenced the submitted work.

Ethical approval: The study was approved by the Austin Hospital Human Research Ethics committee (project number 04958).

Data sharing: The dataset is available from the corresponding author.

The lead and senior authors affirm that the manuscript is an honest, accurate, and transparent account of the study being reported; that no important aspects of the study have been omitted; and that any discrepancies from the study as planned and registered have been explained.

Dissemination to participants and related patient and public communities: Once published, a national (and international) promotional strategy will be implemented using mainstream and social media. Training for food service staff to implement the methods used in the trial is planned. Outcomes from the trial will be used to improve policy and good clinical practice. Participants and participating facilities will be provided with plain language statements and copies of the publication.

Provenance and peer review: Not commissioned; externally peer reviewed.

This is an Open Access article distributed in accordance with the Creative Commons Attribution Non Commercial (CC BY-NC 4.0) license, which permits others to distribute, remix, adapt, build upon this work non-commercially, and license their derivative works on different terms, provided the original work is properly cited and the use is non-commercial. See: http://creativecommons.org/licenses/by-nc/4.0/.

1 Prince MJ, Wu F, Guo Y, et al. The burden of disease in older people and implications for health policy and practice. *Lancet* 2015;385:549-62. doi:10.1016/S0140-6736(14)61347-7
2 Australian Institute of Health and Welfare. *Hip fracture incidence and hospitalisations in Australia 2015-16*. AIHW, 2018.
3 Greenspan SL, Perera S, Ferchak MA, Nace DA, Resnick NM. Efficacy and safety of single-dose zoledronic acid for osteoporosis in frail elderly women: a randomized clinical trial. *JAMA Intern Med* 2015;175:913-21. doi:10.1001/jamainternmed.2015.0747
4 Nordin BE. Calcium and osteoporosis. *Nutrition* 1997;13:664-86. doi:10.1016/S0899-9007(97)83011-0
5 Iuliano S, Poon S, Wang X, Bui M, Seeman E. Dairy food supplementation may reduce malnutrition risk in institutionalised elderly. *Br J Nutr* 2017;117:142-7. doi:10.1017/S000711451600461X
6 Chapuy MC, Arlot ME, Duboeuf F, et al. Vitamin D3 and calcium to prevent hip fractures in elderly women. *N Engl J Med* 1992;327:1637-42. doi:10.1056/NEJM199212033272305
7 Neelemaat F, Lips P, Bosmans JE, Thijs A, Seidell JC, van Bokhorst-de van der Schueren MA. Short-term oral nutritional intervention with protein and vitamin D decreases falls in malnourished older adults. *J Am Geriatr Soc* 2012;60:691-9. doi:10.1111/j.1532-5415.2011.03888.x
8 Moschonis G, Katsaroli I, Lyritis GP, Manios Y. The effects of a 30-month dietary intervention on bone mineral density: the Postmenopausal Health Study. *Br J Nutr* 2010;104:100-7. doi:10.1017/S000711451000019X
9 Heaney RP, McCarron DA, Dawson-Hughes B, et al. Dietary changes favorably affect bone remodeling in older adults. *J Am Diet Assoc* 1999;99:1228-33. doi:10.1016/S0002-8223(99)00302-8
10 Australian Government and Australian Institute of Health and Welfare. People using aged care. 2021. https://www.gen-agedcaredata.gov.au/Topics/People-using-aged-care.
11 Iuliano S, Olden A, Woods J. Meeting the nutritional needs of elderly residents in aged-care: are we doing enough?*J Nutr Health Aging* 2013;17:503-8. doi:10.1007/s12603-013-0042-7
12 Australian Government, Department of Health and Ageing. Australian Guide to Healthy Eating. 2017. https://www.eatforhealth.gov.au/guidelines/australian-guide-healthy-eating.
13 Sherwin A, Nowson CA, McPhee J, et al. Nutrient intake as meals in residential care facilities at the aged: validated visual estimation of plate waste. *Australian Journal of Nutrition and Dietetics* 1988;55:188-93.
14 Chapurlat R, Bui M, Sornay-Rendu E, et al. Deterioration of Cortical and Trabecular Microstructure Identifies Women With Osteopenia or Normal Bone Mineral Density at Imminent and Long-Term Risk for Fragility Fracture: A Prospective Study. *J Bone Miner Res* 2020;35:833-44. doi:10.1002/jbmr.3924
15 Iuliano-Burns S, Woods J, King K, et al. A dairy-based protein, calcium and vitamin D supplement reduces falls and femoral neck bone loss in aged care residents: a cluster randomised trial. *J Aging Res Clin Pract* 2012;2:141-6.
16 Iuliano S, Woods J, Robbins J. Consuming two additional serves of dairy food a day significantly improves energy and nutrient intakes in ambulatory aged care residents: a feasibility study. *J Nutr Health Aging* 2013;17:509-13. doi:10.1007/s12603-013-0025-8
17 Rose G. Sick individuals and sick populations. 1985. *Bull World Health Organ* 2001;79:990-6.
18 Siris ES, Chen YT, Abbott TA, et al. Bone mineral density thresholds for pharmacological intervention to prevent fractures. *Arch Intern Med* 2004;164:1108-12. doi:10.1001/archinte.164.10.1108
19 Australian National Health and Medical Research Council, Australian Government Department of Health and Ageing, New Zealand Ministry of Health. Nutrient Reference Values for Australia and New Zealand. 2006. www.nrv.gov.au.
20 Jones NRV, Forouhi NG, Khaw KT, Wareham NJ, Monsivais P. Accordance to the Dietary Approaches to Stop Hypertension diet pattern and cardiovascular disease in a British, population-based cohort. *Eur J Epidemiol* 2018;33:235-44. doi:10.1007/s10654-017-0354-8
21 Tang BM, Eslick GD, Nowson C, Smith C, Bensoussan A. Use of calcium or calcium in combination with vitamin D supplementation to prevent fractures and bone loss in people aged 50 years and older: a meta-analysis. *Lancet* 2007;370:657-66. doi:10.1016/S0140-6736(07)61342-7
22 Reid IR, Mason B, Horne A, et al. Randomized controlled trial of calcium in healthy older women. *Am J Med* 2006;119:777-85. doi:10.1016/j.amjmed.2006.02.038

BMJ: first published as 10.1136/bmj.n2364 on 20 October 2021. Downloaded from http://www.bmj.com/ on 18 June 2023 by guest. Protected by copyright.

23 Grant AM, Avenell A, Campbell MK, et al, RECORD Trial Group. Oral vitamin D3 and calcium for secondary prevention of low-trauma fractures in elderly people (Randomised Evaluation of Calcium Or vitamin D, RECORD): a randomised placebo-controlled trial. *Lancet* 2005;365:1621-8. doi:10.1016/S0140-6736(05)63013-9
24 Heaney RP. Vitamin D--baseline status and effective dose. *N Engl J Med* 2012;367:77-8. doi:10.1056/NEJMe1206858
25 Bauer J, Biolo G, Cederholm T, et al. Evidence-based recommendations for optimal dietary protein intake in older people: a position paper from the PROT-AGE Study Group. *J Am Med Dir Assoc* 2013;14:542-59. doi:10.1016/j.jamda.2013.05.021
26 Johansson H, Odén A, Kanis JA, et al, IFCC-IOF Joint Working Group on Standardisation of Biochemical Markers of Bone Turnover. A meta-analysis of reference markers of bone turnover for prediction of fracture. *Calcif Tissue Int* 2014;94:560-7. doi:10.1007/s00223-014-9842-y
27 Schaffler MB, Burr DB. Stiffness of compact bone: effects of porosity and density. *J Biomech* 1988;21:13-6. doi:10.1016/0021-9290(88)90186-8
28 Michaëlsson K, Wolk A, Langenskiöld S, et al. Milk intake and risk of mortality and fractures in women and men: cohort studies. *BMJ* 2014;349:g6015. doi:10.1136/bmj.g6015
29 Dehghan M, Mente A, Rangarajan S, et al, Prospective Urban Rural Epidemiology (PURE) study investigators. Association of dairy intake with cardiovascular disease and mortality in 21 countries from five continents (PURE): a prospective cohort study. *Lancet* 2018;392:2288-97. doi:10.1016/S0140-6736(18)31812-9
30 Kiessling G, Schneider J, Jahreis G. Long-term consumption of fermented dairy products over 6 months increases HDL cholesterol. *Eur J Clin Nutr* 2002;56:843-9. doi:10.1038/sj.ejcn.1601399
31 Bristow SM, Gamble GD, Stewart A, Kalluru R, Horne AM, Reid IR. Acute effects of calcium citrate with or without a meal, calcium-fortified juice and a dairy product meal on serum calcium and phosphate: a randomised cross-over trial. *Br J Nutr* 2015;113:1585-94. doi:10.1017/S000711451500080X

Web appendix: Supplementary materials
Web appendix: Original and final protocols

BMJ: first published as 10.1136/bmj.n2364 on 20 October 2021. Downloaded from http://www.bmj.com/ on 18 June 2023 by guest. Protected by copyright.

No commercial reuse: See rights and reprints http://www.bmj.com/permissions Subscribe: http://www.bmj.com/subscribe